MARTIN MARIETTA ENERGY SYSTEMS LIBRARIES

3 4456 0298911 2

ORNL/TM-11116

ornl

OAK RIDGE NATIONAL LABORATORY

MARTIN MARIETTA

Ceramic Technology for Advanced Heat Engines Project Semiannual Progress Report for April Through September 1988

Prepared for
U.S. Department of Energy
Assistant Secretary for
Conservation and Renewable Energy
Office of Transportation Systems
Advanced Materials Development Program

OAK RIDGE NATIONAL LABORATORY
CENTRAL RESEARCH LIBRARY
CIRCULATION SECTION
4500N ROOM 175
LIBRARY LOAN COPY
DO NOT TRANSFER TO ANOTHER PERSON
If you wish someone else to see this report, send in name with report and the library will arrange a loan.

CERAMIC TECHNOLOGY FOR ADVANCED HEAT ENGINES

CERAMIC TECHNOLOGY PROJECT
DOE/ORNL

OPERATED BY
MARTIN MARIETTA ENERGY SYSTEMS, INC.
FOR THE UNITED STATES
DEPARTMENT OF ENERGY

Printed in the United States of America. Available from
National Technical Information Service
U.S. Department of Commerce
5285 Port Royal Road, Springfield, Virginia 22161
NTIS price codes—Printed Copy: A22 Microfiche A01

This report was prepared as an account of work sponsored by an agency of the United States Government. Neither the United States Government nor any agency thereof, nor any of their employees, makes any warranty, express or implied, or assumes any legal liability or responsibility for the accuracy, completeness, or usefulness of any information, apparatus, product, or process disclosed, or represents that its use would not infringe privately owned rights. Reference herein to any specific commercial product, process, or service by trade name, trademark, manufacturer, or otherwise, does not necessarily constitute or imply its endorsement, recommendation, or favoring by the United States Government or any agency thereof. The views and opinions of authors expressed herein do not necessarily state or reflect those of the United States Government or any agency thereof.

ORNL/TM-11116

Metals and Ceramics Division

CERAMIC TECHNOLOGY FOR ADVANCED HEAT ENGINES PROJECT SEMIANNUAL PROGRESS REPORT FOR APRIL THROUGH SEPTEMBER 1988

D. R. Johnson
Project Manager

Date Published: March 1989

NOTICE: This document contains information of a preliminary nature. It is subject to revision or correction and therefore does not represent a final report.

Prepared for
U.S. Department of Energy
Assistant Secretary for Conservation and Renewable Energy
Office of Transportation Systems
Advanced Materials Development Program
EE 04 00 00 0

Prepared by the
OAK RIDGE NATIONAL LABORATORY
Oak Ridge, Tennessee 37831-6285
operated by
MARTIN MARIETTA ENERGY SYSTEMS, INC.
for the
U.S. DEPARTMENT OF ENERGY
under Contract DE-AC05-84OR21400

MARTIN MARIETTA ENERGY SYSTEMS LIBRARIES

3 4456 0298911 2

REPORTS PREVIOUSLY ISSUED

ORNL/TM-9325	Period March 1983–September 1983
ORNL/TM-9466	Period October 1983–March 1984
ORNL/TM-9497	Period April 1984–September 1984
ORNL/TM-9673	Period October 1984–March 1985
ORNL/TM-9947	Period April 1985–September 1985
ORNL/TM-10079	Period October 1985–March 1986
ORNL/TM-10308	Period April 1986–September 1986
ORNL/TM-10469	Period October 1986–March 1987
ORNL/TM-10705	Period April 1987–September 1987
ORNL/TM-10838	Period October 1987–March 1988

CONTENTS

SUMMARY 1

0.0 PROJECT MANAGEMENT AND COORDINATION 3

1.0 MATERIALS AND PROCESSING 5

INTRODUCTION 5

1.1 MONOLITHICS 7

1.1.1 Silicon Carbide 7

Turbo-Milling of SiC Whiskers (Southern Illinois University) 7

1.1.2 Silicon Nitride 16

Sintering of Silicon Nitride (AMTL) 16

Synthesis of High Purity Sinterable Si_3N_4 Powders (Ford) 20

Microwave Processing of Silicon Nitride (ORNL) . . . 28

1.1.4 Processing of Monolithics 31

Improved Processing (ORNL) 31

1.2 CERAMIC COMPOSITES 35

1.2.2 Silicon Nitride Matrix 35

SiC-Whisker-Toughened Silicon Nitride (Garrett) . . 35

Silicon Nitride-Metal Carbide Composites (GTE) . . . 48

Development of Toughened Si_3N_4 Composites by Glass Encapsulated Hot Isostatic Pressure (Norton) 64

Fabrication of Si_3N_4 SiC Composites by Transient Liquid Phase Sintering (University of Michigan) . . 83

1.2.3 Oxide Matrix 92

Dispersion-Toughened Oxide Composites (ORNL) 92

Processing of Improved Transformation-Toughened Ceramics (Norton) 98

Processing and Characterization of Transformation-Toughened Ceramics with Strength Retention to Elevated Temperatures (Ceramatec) 118

1.2.4 Silicate Matrix 125

Low Expansion Ceramics for Diesel Engine Applications (VPI) 125

1.3 THERMAL AND WEAR COATINGS 153

1.3.1 ZrO_2 Base Coatings 153

Advanced Coating Technology (ORNL) 153

Development of Adherent Ceramic Coatings to Reduce Contact Stress Damage of Ceramics (GTE) . . . 154

Wear-Resistant Coatings (Caterpillar) 160

Development of Wear Resistant Ceramic Coatings for Diesel Engine Components (Cummins) 166

1.4 JOINING 177

1.4.1 Ceramic-Metal Joints 177

Joining Ceramics for Heat Engine Applications (ORNL) 177

Analytical and Experimental Evaluation of Joining Silicon Nitride to Metal and Silicon Carbide to Metal for Advanced Heat Engine Applications (GTE) 184

Analytical and Experimental Evaluation of Joining Ceramic Oxides to Ceramic Oxides and Ceramic Oxides to Metal for Advanced Heat Engine Applications (BCL) 206

Analytical and Experimental Evaluation of Joining Silicon Carbide to Silicon Carbide and Silicon Nitride to Silicon Nitride for Advanced Heat Engine Applications (Norton) 224

2.0 MATERIALS DESIGN METHODOLOGY 235

INTRODUCTION 235

2.1 MODELING 237

2.1.1 Modeling 237

Microstructural Modeling of Cracks (UT) 237

2.2 CONTACT INTERFACES 241

2.2.2 Dynamic Interfaces 241

Studies of Dynamic Contact of Ceramics and Alloys for Advanced Heat Engines (Battelle) 241

2.3 NEW CONCEPTS 253

Advanced Statistical Concepts of Fracture on Brittle Materials (GE) 253

3.0 DATA BASE AND LIFE PREDICTION 257

INTRODUCTION 257

3.1 STRUCTURAL QUALIFICATION 259

Microstructural Analysis of Structural Ceramics (NIST) 259

Physical Properties of Structural Ceramics (ORNL) 274

Effect of Translucence of Engineering Ceramics on Heat Transfer in Diesel Engines (ITI) 284

Project Data Base (ORNL) 287

3.2 TIME-DEPENDENT BEHAVIOR 291

Characterization of Advanced Transformation Toughened Zirconias (AMTL) 291

Fracture Behavior of Toughened Ceramics (ORNL) . . . 301

Cyclic Fatigue of Toughened Ceramics (ORNL) 305

Rotor Data Base Generation (ORNL) 318

Toughened Ceramics Life Prediction (NASA-Lewis Research Center) 322

3.3 ENVIRONMENTAL EFFECTS 331

Environmental Effects in Toughened Ceramics (University of Dayton) 331

Low Heat Rejection Diesel Coupon Tests (ORNL) . . . 399

3.4 FRACTURE MECHANICS 409

Testing and Evaluation of Advanced Ceramics at High Temperature in Uniaxial Tension (North Carolina A&T University) 409

Standard Tensile Test Development (NIST) 416

Fracture Toughness of Thin Coatings (Vanderbilt) . . 436

3.5 NONDESTRUCTIVE EVALUATION DEVELOPMENT 447

Nondestructive Characterization (ORNL) 447

Nuclear Magnetic Resonance Imaging (ANL) 453

Powder Characterization (ORNL) 462

4.0 TECHNOLOGY TRANSFER 467

Technology Transfer (ORNL) 467

IEA Annex II Management (ORNL) 468

Standard Reference Materials (NIST) 472

Ceramic Characterization (NIST) 478

CERAMIC TECHNOLOGY FOR ADVANCED HEAT ENGINES PROJECT SEMIANNUAL PROGRESS REPORT FOR APRIL THROUGH SEPTEMBER 1988

SUMMARY

The Ceramic Technology For Advanced Heat Engines Project was developed by the Department of Energy's Office of Transportation Systems (OTS) in Conservation and Renewable Energy. This project, part of the OTS's Advanced Materials Development Program, was developed to meet the ceramic technology requirements of the OTS's automotive technology programs.

Significant accomplishments in fabricating ceramic components for the Department of Energy (DOE), National Aeronautics and Space Administration (NASA), and Department of Defense (DoD) advanced heat engine programs have provided evidence that the operation of ceramic parts in high-temperature engine environments is feasible. However, these programs have also demonstrated that additional research is needed in materials and processing development, design methodology, and data base and life prediction before industry will have a sufficient technology base from which to produce reliable cost-effective ceramic engine components commercially.

An assessment of needs was completed, and a five-year project plan was developed with extensive input from private industry. The objective of the project is to develop the industrial technology base required for reliable ceramics for application in advanced automotive heat engines. The project approach includes determining the mechanisms controlling reliability, improving processes for fabricating existing ceramics, developing new materials with increased reliability, and testing these materials in simulated engine environments to confirm reliability. Although this is a generic materials project, the focus is on the structural ceramics for advanced gas turbine and diesel engines, ceramic bearings and attachments, and ceramic coatings for thermal barrier and wear applications in these engines. This advanced materials technology is being developed in parallel and close coordination with the ongoing DOE and industry proof-of-concept engine development programs. To facilitate the rapid transfer of this technology to U.S. industry, the major portion of the work is being done in the ceramic industry, with technological support from government laboratories, other industrial laboratories, and universities.

This project is managed by ORNL for the Office of Transportation Systems, Heat Engine Propulsion Division, and is closely coordinated with complementary ceramics tasks funded by other DOE offices, NASA, DoD, and industry. A joint DOE and NASA technical plan has been established, with DOE focus on automotive applications and NASA focus on aerospace applications. A common work breakdown structure (WBS) was developed to facilitate coordination. The work described in this report is organized according to the following WBS project elements:

0.0 Management and Coordination

1.0 Materials and Processing

- 1.1 Monolithics
- 1.2 Ceramic Composites
- 1.3 Thermal and Wear Coatings
- 1.4 Joining

2.0 Materials Design Methodology

- 2.1 Modeling
- 2.2 Contact Interfaces
- 2.3 New Concepts

3.0 Data Base and Life Prediction

- 3.1 Structural Qualification
- 3.2 Time-Dependent Behavior
- 3.3 Environmental Effects
- 3.4 Fracture Mechanics
- 3.5 NDE Development

4.0 Technology Transfer

This report includes contributions from all currently active project participants. The contributions are arranged according to the work breakdown structure outline.

0.0 PROJECT MANAGEMENT AND COORDINATION

D. R. Johnson
Oak Ridge National Laboratory

Objective/scope

This task includes the technical management of the project in accordance with the project plans and management plan approved by the Department of Energy (DOE) Oak Ridge Operations Office (ORO) and the Office of Transportation Systems. This task includes preparation of annual field task proposals, initiation and management of subcontracts and interagency agreements, and management of ORNL technical tasks. Monthly management reports and bimonthly reports are provided to DOE; highlights and semiannual technical reports are provided to DOE and program participants. In addition, the program is coordinated with interfacing programs sponsored by other DOE offices and federal agencies, including the National Aeronautics and Space Administration (NASA) and the Department of Defense (DoD). This coordination is accomplished by participation in bimonthly DOE and NASA joint management meetings, annual interagency heat engine ceramics coordination meetings, DOE contractor coordination meetings, and DOE Energy Materials Coordinating Committee (EMaCC) meetings, as well as special coordination meetings.

1.0 MATERIALS AND PROCESSING

INTRODUCTION

This portion of the project is identified as project element 1.0 within the work breakdown structure (WBS). It contains four subelements: (1) Monolithics, (2) Ceramic Composites, (3) Thermal and Wear Coatings, and (4) Joining. Ceramic research conducted within the Monolithics subelement currently includes work activities on green state ceramic fabrication, characterization, and densification and on structural, mechanical, and physical properties of these ceramics. Research conducted within the Ceramic Composites subelement currently includes silicon carbide and oxide-based composites, which, in addition to the work activities cited for Monolithics, include fiber synthesis and characterization. Research conducted in the Thermal and Wear Coatings subelement is currently limited to oxide-base coatings and involves coating synthesis, characterization, and determination of the mechanical and physical properties of the coatings. Research conducted in the Joining subelement currently includes studies of processes to produce strong stable joints between zirconia ceramics and iron-base alloys.

A major objective of the research in the Materials and Processing project element is to systematically advance the understanding of the relationships between ceramic raw materials such as powders and reactant gases, the processing variables involved in producing the ceramic materials, and the resultant microstructures and physical and mechanical properties of the ceramic materials. Success in meeting this objective will provide U.S. companies with new or improved ways for producing economical highly reliable ceramic components for advanced heat engines.

1.1 MONOLITHICS

1.1.1 Silicon Carbide

Turbo-Milling of SiC Whiskers

D. E. Wittmer (Associate Professor, SIU-C, Carbondale, IL)

Objective/scope

The purpose of this work is to investigate the turbomilling process as a means of improved processing for SiC whisker-ceramic matrix composites, and to design and fabricate prototype turbomilling units.

Technical progress

The potential feasibility of using turbomilling as a process to improve deagglomeration of whiskers and subsequent enhanced dispersion and homogenization was demonstrated in FY87. Based on these results the current sub-contract was awarded. This subcontract contains the following three tasks:

Task 1. Design, fabrication and testing of prototype turbomills.
Task 2. Dispersion and homogenization of SiC whisker/alumina matrix composites.
Task 3. Dispersion and homogenization of SiC whisker/silicon nitride matrix composites.

Task 1. Prototype Turbomills

In Task 1 developmental turbomills were redesigned to allow the use of various sized rotor, shaft and body assemblies which shall make it possible to make smaller batches and determine the effects of upscaling on the processing parameters. Additional design considerations allow for real-time data acquisition of the turbomill operating parameters.

During this reporting period, delays in construction of the protypye turbomills were encountered due to unexpected delivery problems and machine shop scheduling. Presently the first prototype mill with about a 0.75 liter volume is nearing completion, and the major components for the additional turbomills are being fabricated. A new completion date for this task was given as November 1, 1988.

Task 2 and 3. Dispersion and Homogenization of SiCw Ceramic Matrix Composites

Due to anticipated delays in the construction and development of the prototype turbomills, turbomilling equipment at the U.S. Bureau of Mines Tuscaloosa Research Center was utilized to process several batches of SiCw/alumina matrix and SiCw/silicon nitride matrix mixtures. The whisker content for two whisker sources (Tateho, Grade SC-1 and American Matrix, Inc.,Grade 1) was varied between 20 to 45 vol./o for the SiCw/alumina matrix and 15 to 35 vol./o for the

SiCw/silicon nitide matrix composites. The turbomilling parameters were the same as utilized in the prior feasibility study. Following turbomilling, green preforms for hot-pressing were prepared by pressure casting 6.5 cm diameter discs approximately 3 cm in thickness from the flocculated suspensions. After drying, the discs were hot-pressed at ORNL and then sent to an outside vendor (Bomas Machine Specialties) for machining into 3 X 4 X 25 mm test bars (MIL Spec. 1942). MOR (4-pt), Vicker's microhardness, indentation fracture toughness, and controlled flaw fracture toughness were determined on the hot-pressed bars according to standard techniques. Optical and scanning electron microscopy techniques were used to examine the machined and polished surfaces of the microhardness specimens for dispersion and homogenization of the composites and the fractured surfaces of the MOR bars for indentification of the fracture origins.

The data resulting from these trials are given in Figures 1 through 6. As observed from these results, strength and fracture toughness values for both SiC whisker reinforced alumina and silicon nitride matrix composites were found to be improved by the turbomilling and pressure filtration process used in this study. For both matrix materials, American Matrix SiC whiskers resulted in higher strength and toughness values, compared to the same whisker loading for Tateho SiC whiskers. A strength of 593 MPa and fracture toughness of 7.3 MPa-$m^{1/2}$ was measured for a 40 vol.% American Matrix SiC whisker/RCHP-DBM alumina, and a strength of 865 MPa and a fracture toughness of 8.8 MPa-$m^{1/2}$ was determined for a 35 vol.% American Matrix SiC/UBE silicon nitride with the addition of 2 wt.% alumina and 6 wt.% yttria.

The detailed results and discussion for these studies will be given in the final report and will also appear in the Proceedings of the Third Annual Symposium on Ceramic Materials and Components for Heat Engines, Las Vegas, NV November 28-30, 1988.

Status of milestones

Design, fabrication and testing of prototype turbomills.	November 1988
Dispersion and homogenization of SiC whisker/ alumina matrix composites. Completed ahead of schedule.	November 1988
Dispersion and homogenization of SiC whisker/ silicon nitride matrix composites. Completed ahead of schedule.	November 1988

Presentations

D.E. Wittmer, "Improved Processing of Ceramic Composites", 90th Annual American Ceramic Society Meeting, Cincinnati, OH May 1-5, 1988.

Publications

D. E. Wittmer, "Alternative Processing Through Turbomilling", The American Ceramic Society Bulletin, Vol. 67, No. 10, Oct. 1988, pp. 1670-72.

D. E. Wittmer and W. Trimble, "Ceramic Composites Processed by Turbomilling", Proceedings of the Third International Symposium on Ceramic Materials and Components for Heat Engines, Las Vegas, NV November 28-30, 1988 (Manuscript completed)

Figure 1. Vickers Microhardness Results for SiC Whisker/RCHP Alumina Composites

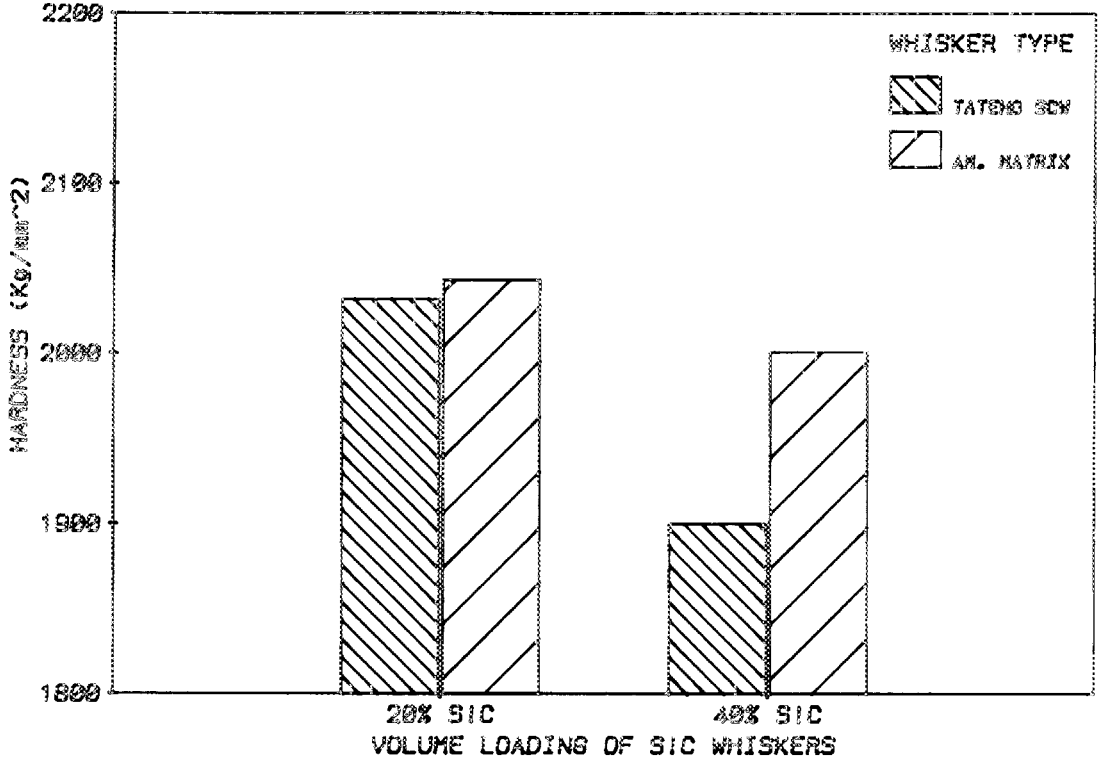

Figure 2. 4-Pt MOR Results for SiC Whisker/RCHP Alumina Composites

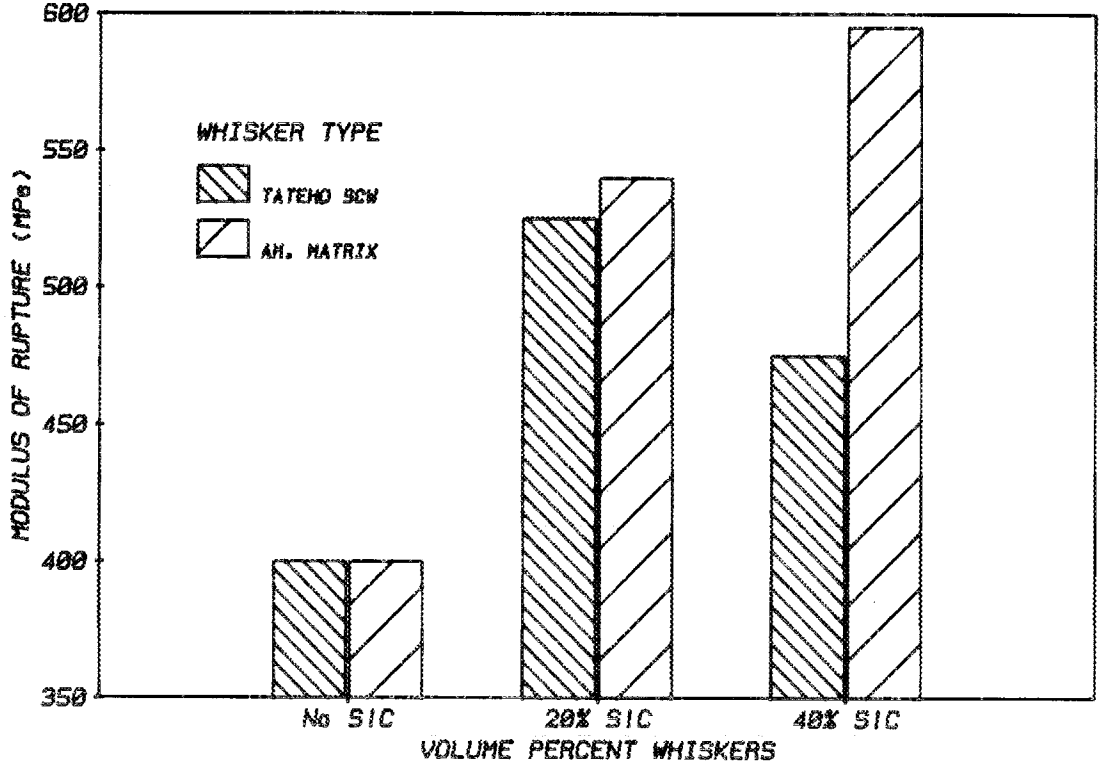

Figure 3. Fracture Toughness Results for SiC Whisker/RCHP Alumina Composites

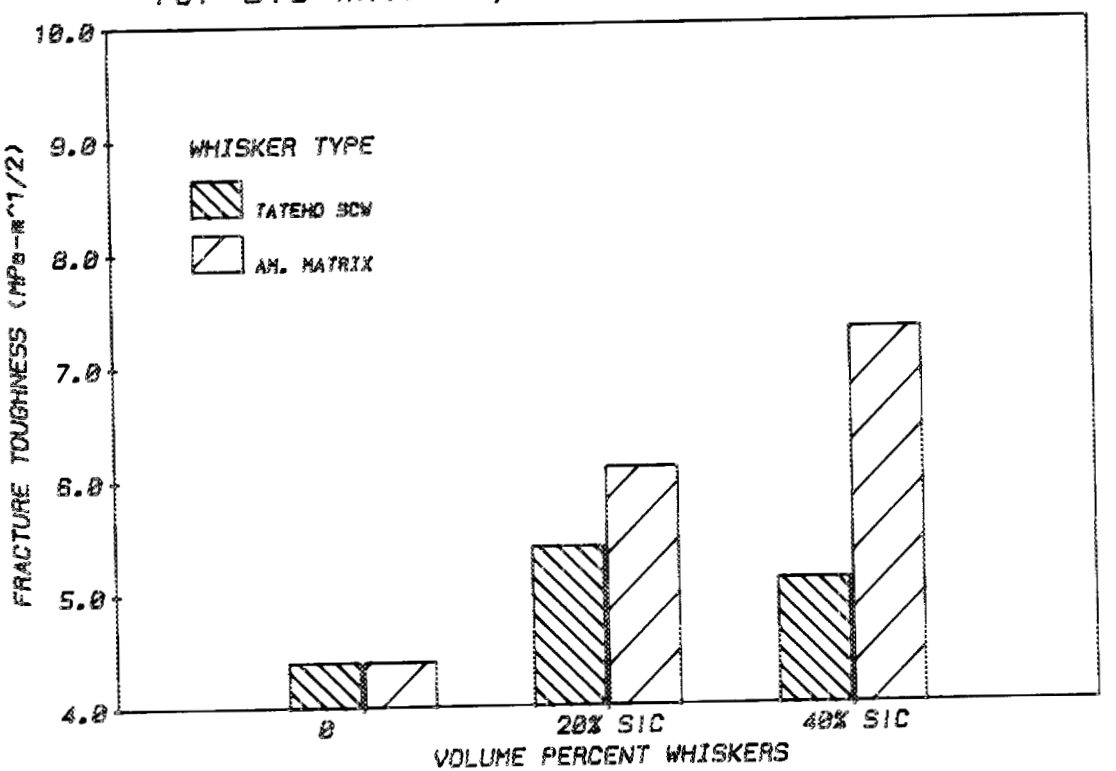

Figure 4. Microhardness Results for SiC Whisker/Silicon Nitride Composites

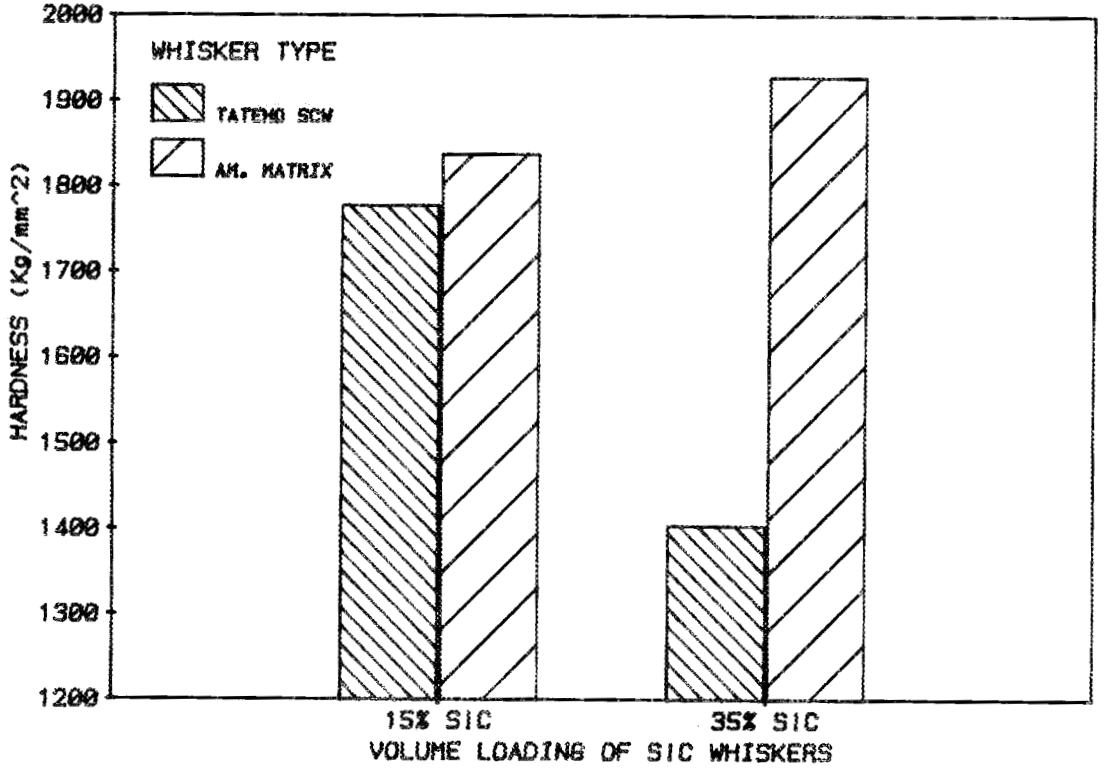

Figure 5. 4-Pt MOR Results for SiC Whisker/Silicon Nitride Composites

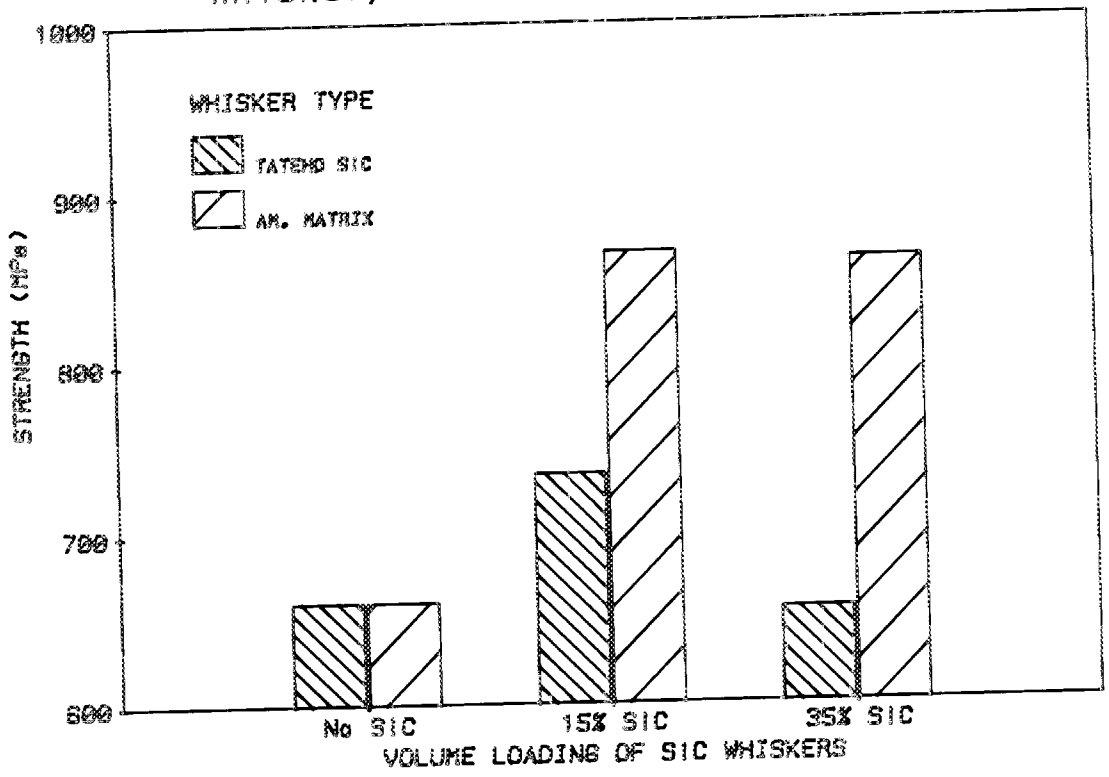

Figure 6. Fracture Toughness Results for SiC Whisker/Silicon Nitride Composites

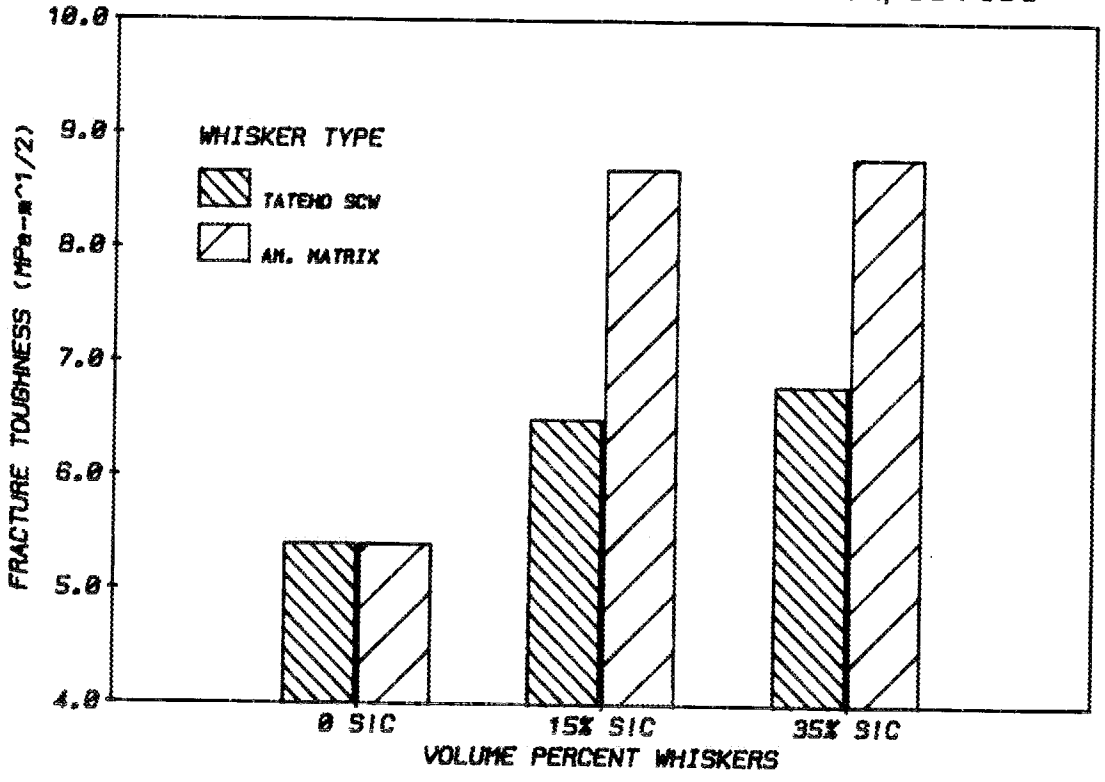

1.1.2 Silicon Nitride

Sintering of Silicon Nitride
G. E. Gazza (Army Materials Technology Laboratory)

Objective/scope

This program is concentrating on sintering compositions in the Si_3N_4-Y_2O_3-SiO_2 system using a two-step sintering method where the nitrogen gas pressure is raised to 7-8 MPa during the second step of the process. During the sintering, dissociation reactions are suppressed by the use of high nitrogen pressure and cover powder of suitable composition over the specimen. Variables in the program include the sintering process parameters, source of starting powders, milling media and time, and specimen composition. Resultant properties determined are room temperature modulus of rupture, high temperature stress-rupture, oxidation resistance, and fracture toughness. Successful densification of selected compositions with suitable properties will lead to densification of injected molded or slip cast components for engine testing.

Technical progress

The composition selected for further scale-up and property evaluation is designated as nos.39 which is 85.8m/o silicon nitride - 4.73m/o yttria - 9.47m/o silica. The addition of approximately 1.0m/o of Mo_2C to the base composition promotes sintering of these compositions. Starting silicon nitride powders being investigated have been restricted Toyo-Soda's TS-7 and TS-10 grades. The TS-10 grade is reportedly a higher alpha phase powder than TS-7 with a finer particle size distribution. A sedigraph analysis of both powders indicated that the shape of the particle size distribution curves are similar but the TS-10 powder curve is displaced to lower particle size sizes. The 50% cumulative mass percent value for the TS-7 powder is 0.9um while the TS-10 powder value is 0.6um. High density specimens have been obtained with both powders after high gas pressure sintering.

Fractographic examination of specimens which have failed at lower than average MOR values have shown that various defects associated with either powder processing, machining, or impurities in the starting materials can result in low strength. Flaws produced from powder processing are pores or metallic inclusions. An EDX analysis of the inclusion shows Fe-Ni-Co present. Another flaw type present at the fracture origin was found to contain K and Cl by EDXA. This is believed to be a residual impurity in the starting powder from the powder synthesis method. Other fracture origins were found to be machining flaws or large grains.

Further sintering runs were made with composition designated as #39 (containing 4.73m/o Y_2O_3 and 9.45/o SiO_2) with additions of either Mo_2C (1.5%) or $MoSi_2$ (1.5%). The sintering experiments were used to determine differences in sintering behavior between the different compositions. In particular, whether sintering is affected by Mo_2C added and reacting with Si_3N_4 to form Mo_5Si_3-$MoSi_2$ as opposed to $MoSi_2$ added directly. Sintering runs were conducted under 1.5 MPa nitrogen gas pressure and stopped at temperatures of 1650C, 1800C and 1900C after holding for 60 minutes at temperature. The results are shown in as follows:

TABLE 1

Sintering of standard compositions (#39), with additions of 1.5% Mo_2C, or additions of $MoSi_2$.

Composition	T (C)	D (gr.) g/cc	D (sint.) g/cc	%wt.loss
Std.#39	1650	1.58	2.39	1.01
	1800	1.58	2.80	1.74
	1900	1.56	3.23	2.12
Std.+$MoSi_2$	1650	1.59	2.42	0.74
	1800	1.59	2.79	1.51
	1900	1.58	3.19	2.31
Std.+Mo_2C	1650	1.62	2.67	1.67
	1800	1.61	3.09	2.40
	1900	1.61	3.31	3.67

Although further sintering runs will be conducted to confirm results, the sintering behavior of the standard composition and that containing $MoSi_2$ appear similar. The more reactive Mo_2C addition appears to promote densification of the compacts at lower sintering temperatures as well. Specimens are being prepared for phase and microstructural analysis.

Similar sintering runs were conducted using pure Si_3N_4 compacts and compacts containing only 1.5% and 3.0% Mo_2C. The addition of only Mo_2C is not an effective densification aid. It does, however, appear to promote the formation of beta phase by reacting with the Si_3N_4.

Microscopy

Sintered specimens were microstructurally examined by SEM to determine grain size, morphology and distribution of minor phases. Grains were typically elongated with diameters of approximately 1-2um. Finer microstructures formed as the sintering temperature was reduced. Aspect ratios were difficult to determine but usually fall between 6:1 and 10:1 for sintered Si_3N_4. Phase determinations found the Si_3N_4 to be essentially all beta-phase. A secondary phase dispersed throughout the microstructure was determined to be Y_2Si2O7. This appeared to be present in gamma or beta polymorophic form. The presence of fine, equiaxed particles containing Mo and Si by EDXA was also dispersed in the microstructure. These particles were approximately 1-2um maximum diameter and found to be approximately 70w/o Mo and 30w/o Si. This represents a composition between Mo_5Si_3 and $MoSi_2$. It has been reported (1) that $MoSi_2$ is dimorphic and undergoes a eutectoidal transformation upon cooling below 1850C to yield the low temperature form, alpha $MoSi_2$, plus Mo_5Si_3. Such compositions might also be formed by the reaction of Mo_2C with SiO and/or Si_3N_4 where the Mo_5Si_3 particle may form a $MoSi_2$ shell by further reaction with Si, SiO_2 or SiO.

Discussion of results

The addition of Mo_2C to Si_3N_4 compositions containing Y203 and SiO_2 was found to promote densification of the specimens at temperatures of 1850-1960C. The Mo_2C particle additions were kept fine (1-2um diameter) to avoid/minimize strength degradation as reported (2-3) for Fe-based inclusions. The result molybdenum silicide particles were not observed to be associated with fracture origins in MOR specimens. Best sintering temperatures appear to be in the range of 1925-1960C. Although most specimens survived the established stress-rupture conditions, examination by TEM is necessary to determine whether cavitation occurred near molybdenum silicide particle sites. For long term applications, operating temperatures of 1200-1250C appear maximum for these materials if a small amount of creep, as indicated by the permanent strain values, is tolerable. Post heat treatments to crystallize grain boundary phases was not extensively explored but may improve creep resistance.

The mechanism involved in promoting densification, however, is not yet clear. Suspected formation of a lower viscosity liquid phase by molybdenum carbide reaction with the yttrium silicate phase does not appear likely. EDX analysis of areas of yttrium silicate phase near molybdenum silicide particles did not indicate the presence of Mo. The absence of such a reaction may be consistent with Lange's observation (4) that the presence of tungsten silicide (from WC) in hot pressed compositions prepared in the Si_3N_4-Y_2O_3-$Y_2Si_2O_7$ triangle did not produce surface pitting during oxidation. In MgO doped Si_3N_4, pitting is produced by enhanced oxygen diffusion through a low viscosity glassy phase formed by the reaction of magnesium silicate with WC impurity. Another mechanism being investigated involves the decomposition of Si_3N_4 by reaction of Mo_2C particles with Si_3N_4, SiO_2, and/or SiO. As indicated by Negita (5), the decomposition of Si_3N_4 by MoO_2 is favored by comparing standard free energies of reactions between Si_3N_4 and various metal oxides. In this study, it was observed that Mo_2C accelerates the formation of beta phase in TS-7 powder compacts (without Y_2O_3 additions) at sintering temperatures above 1700C. After 60 minutes at 1935C, TS-7 powder without Mo_2C retains 25% alpha phase while powder containing 1m/o Mo_2C becomes essentially 100% beta phase. The acceleration of the alpha to beta transformation by Mo_2C with increasing temperature may produce a higher beta phase nucleation density and restrict coarsening of the structure before sufficient solution-reprecipitation of beta phase can occur via the yttrium silicate grain boundary liquid phase.

References

1. Brewer, L. and Lamoreaux, R.H., II "Phase Diagrams", Atomic Energy Rev. Spec. Issue No. 7 (Molybdenum: Physico-Chemical Properties of It Compounds and Alloys), p.320, L. Brewer, Editor, International Atomic Energy Agency, Vienna, 1980.

2. Pasto, A.E., "Cause and Effects of Fe-Bearing Inclusions in Sintered Si_3N_4", Communications of the American Ceramic Society, Sept. 1984, C-178-180.

3. Neil, J.T., Pasto, A.E.,, and Bowen, L.J., "Improving the Reliability of Silicon Nitride: A Case Study", Advanced Ceramics Materials, 3, [3], 225-30, 1988.

4. Lange, F.F., "Reaction of Iron With Si_3N_4 Materials to Produce Surface Pitting", Jour. American Ceramic Society, 61, [5-6], 270-71,1978.

5. Negita, K., "Effective Sintering Aids for Ceramics", Jour. of Material Science Letters, 4, (1985), 755-758.

Synthesis of High Purity Sinterable Si_3N_4 Powders -- G. M. Crosbie, J. M. Nicholson, R. L. Predmesky, and E. D. Stiles (Research Staff, Ford Motor Company, Dearborn, Michigan)

Objective/scope

The goal of this task is to achieve major improvements in the quantitative understanding of how to produce sinterable Si_3N_4 powders having highly controlled particle size, shape, surface area, impurity content and phase content. Through the availability of improved powders, new ceramic materials are expected to be developed to provide reliable and cost-effective structural ceramics for application in advanced heat engines.

Of interest to the present powder needs is a silicon nitride powder of high cation and anion purity without carbon residue.

The process study is directed towards a modification of the low temperature reaction of $SiCl_4$ with liquid NH_3 which is characterized 1) by absence of organics (a source of carbon contamination), 2) by pressurization (for improved by-product extraction efficiency), and 3) by use of a non-reactive gas diluent for $SiCl_4$ (for reaction exotherm control).

In the "further development" phase begun October 1987, our goal is to test for unique properties of the ceramics sintered from the low carbon powders, before committing to a pilot plant of the 110 L scale designed. In view of powder quantities needed to allow tests of the ceramics, the major task is to design and implement a scaled-up version of the silicon nitride synthesis processing equipment to produce greater amounts of powders with high cation and anion purity and low carbon residue.

Technical progress

Introduction

Silicon nitride based ceramics are often considered to represent the toughest of the high-temperature (above 1000°C) monolithic ceramics intended for advanced heat engine use. Also, due to a desirable combination of lower temperature properties (wear resistance, low density, high hardness, and toughness), the nitride ceramics are already finding commercial applications in certain passenger vehicles.

Ceramic reliability and cost depend on powder qualities and subsequent processing. Because powders can limit the capability to achieve unique sintered properties and to fabricate complex shapes, the availability of appropriate powders is critical to advanced ceramics research. In the case of silicon nitride ceramics, the powder purity is especially important, since a low solubility in silicon nitride for many impurities leads to high concentrations of those impurities in grain boundary phases. Also, carbon residues (which are found in some otherwise high purity powders) are considered to be detrimental to second phase oxynitride development, thermal stability, and mechanical properties.

Previous work

The primary points of reference for the previous process work are the 1986 and 1987 Automotive Technology Development Contractors' Coordination Meeting proceedings papers[1,2] and the previous semiannual report.[3]

In the previous lab demonstration work, we prepared a novel process flowsheet for preparation of Si_3N_4 with a block flow diagram and a mathematical model of mass and heat balances for the "vapor chloride--liquid ammonia" process. We observed that the cooling from latent heat of vaporization of NH_3 more than offsets the heat of reaction at 0°C and 75 psig.

Powder characteristics met or were approaching target values. Key results were achieved in the areas of phase and microstructure, and carbon purity. Si_3N_4 powder was produced with phase content, particle size and shape which are close to those characteristics considered desirable for pressureless sinterability.

Specifically, the powder derived by thermal decomposition of an intermediate imide product (from reaction of $SiCl_4$ with liquid NH_3 at 0°C and 75 psig) was principally alpha silicon nitride (as determined by x-ray diffraction, which has little sensitivity to amorphous phases) with crystallite size of 0.2 to 0.3 micron and primarily equi-axed particle shape.

The process was identified to have features which are important for scale-up. Key features of near-neutral heat balance and liquid-like materials handling were demonstrated.

Also, improvements were achieved in yield, laboratory production rate, cation purity, and alpha/beta ratios.

In the extension period work, we prepared a pilot plant design for the "vapor-chloride - liquid ammonia" process, carried out additional process development including the "liquid chloride - liquid ammonia" direct reaction, campaigned runs to test process stability, carried out sintering tests, and reported on a new analytical method for discriminating amorphous and crystalline phases in silicon nitride powders.

Summary of current period work

We found evidence for rapid rinsing out of the chloride by-product with the use of agitation. We installed additional subsystems to the pre-pilot plant, found high oxygen contents in initial nitride powders produced, and extended transient flow modeling of the saturator.

Pre-pilot plant work

In the "further development" phase begun in this period, we increased reactor volume, took steps to improve quality of sealing of vessels and piping, and incorporated direct mechanical agitation while under pressure. By this means, we have equipment to produce 100 g lots of powder (by liquid-liquid and vapor-liquid routes) for sintering tests and characterization of the sintered materials.

Through joint work with an engineering firm, the 4 L scale skid-mounted imide reactor system was installed in a dynamometer test cell and pressure tested to 225 psig (1.65 MPa absolute) with nitrogen in March 1988.

In the design of this system, the reactor working volume is increased to one gallon (4 L) and a pressure-sealed mechanical agitator is provided. The piping system is of welded construction with flanged fittings that are mostly of a type to allow simplified helium leak testing. All vessels are jacketed and pressure-rated to 300 psig (2.2 MPa absolute) to permit tests with ammonia remaining liquid to room temperature (to demonstrate reduced

refrigeration requirement). The equipment was received with certification plates and corresponding rupture disks for these pressure ratings.

The pre-pilot plant is located in larger quarters in a nearby building at the Research and Engineering Center in Dearborn. The new location is a dynamometer test cell which provides suitable facilities for the pre-pilot scale plant. These facilities include: 1) a high volumetric air flow rate (with up to three air changes per minute), 2) a high ceiling to accommodate the condenser (4 meter height) and other desired lay-out features, 3) adequate floor space to allow access to all sides of the equipment, and 4) an adjacent control room with a large window for monitoring.

In an initial run leading to nitride powder, 40 shots of liquid $SiCl_4$ were put into the reactor. The 40 shots at 9.9 cm^3 each, if full, would correspond to 162 g of Si_3N_4 potential. (Subsequent inspection revealed that the entry system had remained clear by use of the purge flow.) Agitation was used during the injection, but turned off during rinsing/settling for 10 minutes before decantation. A total of three rinses were made with agitation during the refillings. In opening the reactor bottom valve, an outward leak of ammonia into the N_2 pneumatic valve actuation circuit occurred as product was moved to the jacketed product vessel.

A transfer vessel was used to collect the powder and bleed off NH_3, because the <u>in situ</u> decomposition furnace electrical connection was not completed. In lieu of a continuous piping connection to the decomposition furnace, transfer of the intermediate reaction product was made to an air-locked pressure vessel. After bleeding off NH_3 gas, an glove bag was used to shield ambient during transfer of powder intermediate to a silicon nitride sagger. The imide was loaded as a 0.25 inch layer in a 6 inch sagger vessel with Si_3N_4 coverplate. The sagger was transferred (with limited air exposure) to a sintering furnace (vacuum for initial heat-up, then backfilled with N_2) and thermally decomposed at 1410°C. (A day was required to pump down vacuum before heating.)

In the course of the transfers, 52.4 grams of intermediate was found left in the reactor, none in the jacketed product vessel, and 10.0 g residue in the temporary transfer vessel. A sample of the transfer vessel intermediate was retained for Cl analysis. Only 4.5 g of product was obtained from this run.

Characterizations of the product were made by x-ray diffraction and Leco methods. X-ray analysis of the powder showed a Si_3N_4 phase ratio of 95% alpha/(alpha+beta) and also showed presence of Si_2N_2O. Leco analyses showed 26.7 wt.% nitrogen and 17.4% oxygen. Leco total carbon was 0.031%. The low yield was attributed to Cl residual in the intermediate.

Subsequently, we made consecutive pre-pilot plant runs with removal of at least 90% of the theoretical removal of by-product chloride with a rinse-and-settle-and-decant time of 45 min for each subbatch (40 g Si_3N_4 equivalent).

Three runs made with $SiCl_4$ introduced in amounts equivalent to 120, 120, and 40 g Si_3N_4 equivalent. Due to high ambient temperatures, reactor temperatures were 10-15°C (not 0-2°C) in two of the runs.

We used the mechanical agitation during rinsing and changed the theoretical rinsing ratio for each rinse: To lower the theoretical residue per rinse, we increased the volume of liquid ammonia rinse and also increased the proportion of liquid decanted from that used in initial runs (reported in the April-May 1988 period). The principal design change

was a lengthening of a syphon tube to reduce the volume left (of solids-containing slurry) after decantation. Ammonia refill volumes were then increased beyond that due to the lengthened tube to provide additional leverage for each of the rinse stages. The theoretical rinsing per rinse stage was thereby changed from 0.84 (for the first run of the present period) to 0.315 (for the last). These per-stage rinse values are raised to the third power to estimate theoretical rinsing ratios.

To compare to theoretical rinsing, samples of the imide intermediate from each run were analyzed for silicon and chlorine content. With no chloride rinsing out, the atom ratio of Cl/Si would be 4 and the weight ratio of Cl/Si would be 5.05.

In Figure 1, the Cl/Si weight ratio is plotted versus the theoretical value. The lowest value corresponds to removal of 95.6% of the chlorine. The intermediate value corresponds to removal of most of the chlorine in two of three subbatches combined with one subbatch with no rinsing at all. The high value corresponds to a case with a shorter syphon tube and a smaller NH_3 rinse volume.

These values can be compared with values from last year's upgraded lab apparatus (500 mL scale, no mechanical agitation, three rinse stages, each rinse-settle period about 10 minutes). In those tests, a bimodal distribution was obtained for rinse-out values, with 4% and 38% as modes. Previously reported characterization of the imide intermediate product pointed to little, if any, Si-Cl bonding, which, in turn, suggested that agitation in the 4 L build would be effective in removing NH_4Cl.

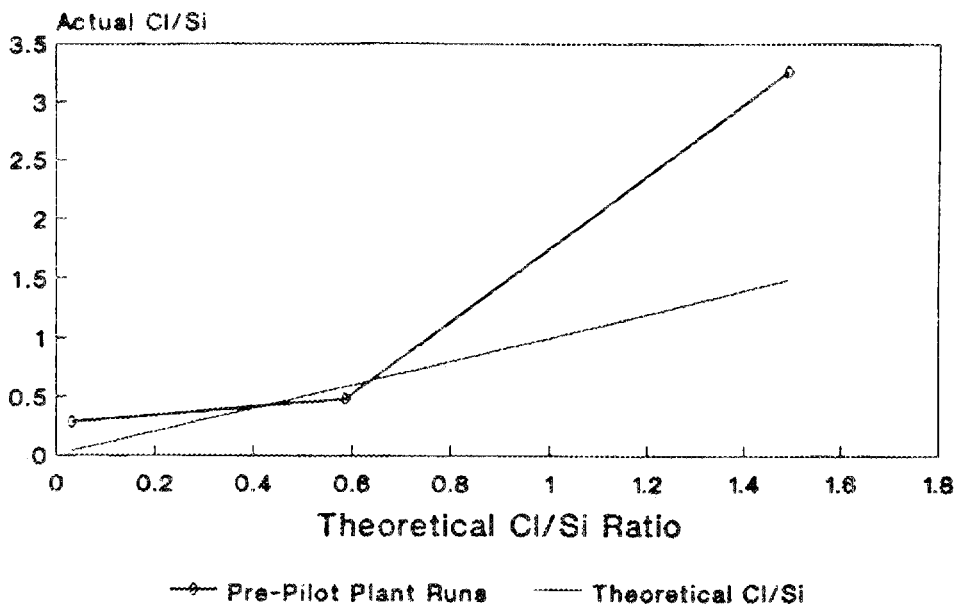

Figure 1. Comparison of actual chlorine-to-silicon ratios with theoretical Cl/Si ratios based on rinsing and decant volumes (assuming ideal dilution).

Now, with the agitated pre-pilot plant we have greater than 90% removal for the last two runs. Although the pre-pilot runs were at a higher temperature than last year's 500 mL scale tests (10-15°C versus 0°C), the differences in rinsing effectiveness are believed to be primarily attributable to the mechanical agitation in the pre-pilot plant.

The values can be compared with values from glass vacuum line experiments reported by others. Working at approximately -60°C and ambient pressure, Morgan[1] was able to remove most of the chlorine from the liquid-liquid reaction product by Soxhlet extraction with recycling (rinsing) once per hour for a week. We have now shown we can remove more than 90% of the chlorine from a liquid-liquid reaction product in less than 1 hour. The difference in removal time is attributable to the present use of a higher temperature (10-15°C, not -60°C) while keeping the ammonia liquefied by a nitrogen-ammonia gas pressure of about 110 psig. This advantage was anticipated by Morgan and is now demonstrated in 40 to 120 g Si_3N_4 equivalent lot sizes.

We did not succeed in decomposing the intermediate products to powders with oxygen contents as low as those of the 500 mL scale tests. For example, in the last run of the previous reporting period, valve stem leakages occurred in depressurizing and transferring the intermediate slurry to the decomposition furnace. In the early part of the current period, the transfer valve leakages recurred and decant/wastage line leakages arose. We stepped back to analyze the problem.

The valve vendor's analysis confirmed that the materials of valve construction were according to specification (and were materials which had been used previously with a measure of success). However, an unspecified adhesive used to join the teflon to the 316 stainless steel was attacked by the liquid ammonia. Also, the vendor expressed concern about the capacity of the valve to tolerate rapid temperature changes as boiling ammonia passed over it. With the vendor's cooperation, a new valve type was specified without the adhesive interlayer and with a tolerance to a wider range of temperature.

Our analysis of the system pointed to valve failures where intermediate product solids had passed. The intermediate has Si-N bonds present and could be expected to be abrasive. In one case of failure, optical microscope examination revealed corrosion of the 316 alloy, verified independently by x-ray fluorescence. Because the stainless quality of the alloy is based on forming a Cr_2O_3 coating in oxidizing environment, fresh metal surfaces may not be self-protected when exposed by abrasion by imide in an anhydrous ammonia slurry. Alloys other than stainless may provide better resistance and lower cost in a future pilot plant.

Decomposition furnace

Due to the large driving force for reaction of water with ammonia and for reactions of oxygen and water with the intermediate imide to form silica, the strategy we have followed (in the 500 mL scale apparatus) is

---

[1] P. E. D. Morgan, "Research on Densification, Character and Properties of Dense Silicon Nitride," Annual Report, March 1972 - March 1973, NTIS AD-757-748, (Contract No. N00014-72-C-0262, Office of Naval Research).

to do all processing in a pipe. A dedicated furnace was purchased for the pre-pilot plant, to follow the same strategy. However, the furnace installation is delayed.

The furnace is the one subsystem which was still not available at the end of September 1988. (Electrical supply installation to the apparatus was completed in mid-October and the vendor is being contacted for commissioning.) In lieu of its operation, we continue to an alternate decomposition route with a slightly pressurized transfer vessel for transport and glove-box and glove-bag handling for decomposition in a N_2 furnace in the lab building.

Process monitoring

We are also learning to use the instrumental readings to judge what is happening unseen in the pressure vessels. There are no surprises here, but one can "see" consistent patterns and use the computational base to display the critical control information to the operator.

For example, for a particular system backpressure drop, the onset of boiling is noted by a drop in reactor thermocouple well temperature and a rise in the condenser wall temperature. Avoidance of such boiling is especially critical during the settling period before decantation (or filtration). A near-real time display of the margin of safety (above the vapor pressure of ammonia) is now available, based on reactor well temperature and system pressure to show the present margin of pressure before boiling. Temperature and pressure sensors were recalibrated to increase the precision of the calculation.

Transient flow modeling

Through discussions continued with L.-F. Chen of the Control Systems Department (Ford Research), flow transients were modeled for the saturator that was built for use with the pre-pilot plant. In previous laboratory demonstration tests of the "vapor $SiCl_4$ -- liquid NH_3" process, flow transients have caused clogging when the vapor repeatedly supersaturates at the reactor entry during operation. It had been suggested that a computer simulation could aid in designing a system to minimize the supersaturation transients.

Mr. Chen proposed the use of a state function approach to model the gas flows in the reactor system for the vapor-liquid process. We provided him with various system size parameters and steady-state mass balance calculations for use as input to the digital simulation.

Initial modeling results showed that supersaturations can readily occur with less than 2 psig step changes in system pressure. This model was used to examine means to identify critical values of system parameters (such as flow resistance and vessel volumes) to avoid the transient supersaturations.

A more complex transient flow model was generated with an additional balanced volume to provide symmetrical flows during pressure transients. In this case, no sharp flow restrictions were necessary. With the added volume, the response to a pressure drop was a simple relaxation, shown in Fig. 3, rather than the overshoot of Fig. 2. This more complex version was used to show that supersaturations could be avoided without sharp flow constrictions as long as appropriate volume parameters were chosen.

The changes suggested in the report are being incorporated in the current saturator build and an experimental verification of the transient model is being attempted. The flowmeters and other hardware for the

balanced flow design were installed and electrically connected to the data acquisition system. Following discussions, pressure sensors and flow constrictions were located at critical points upstream and downstream of the mixing point. The pressure sensor signals were calibrated with the data acquisition system.

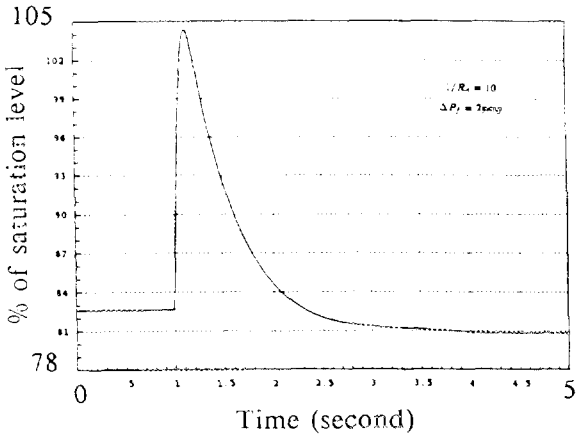

Fig. 2. Initial design with a sharp flow restriction added before the mixing point.

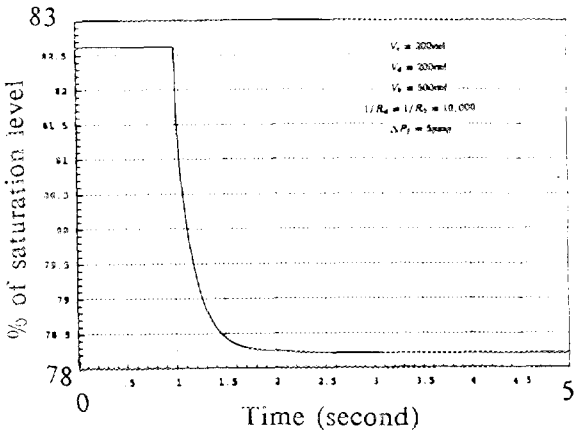

Fig. 3. Balanced flow design with added volume, but no sharp flow restrictions.

(Percent of saturation is plotted as a function of time after a drop in system backpressure for the "vapor $SiCl_4$ -- liquid NH_3" process. Courtesy L.-F. Chen)

Economic analysis

As part of the preparation for licensing discussions, we are adapting and refining previous cost estimates into formats of likely interest to particular companies. Where possible, we are formulating quantitative models for capital and utility costs. We plan, then, to tie these models with process options in the range that is testable for process feasibility with the pre-pilot plant. For example, operation under higher pressure allows less refrigeration but requires thicker pressure vessel walls.

The rinsing effectiveness demonstration in a pre-pilot scale lot size (100 g) is important support for assumptions made for processing costs which must be added on to the relatively low cost silicon tetrachloride precursor for both the liquid-liquid and vapor-liquid processes.

Status of milestones

This two-year follow-on contract was initiated October 1, 1987 for the "Further Development of Synthesis of High-Purity Sinterable Silicon Nitride (Si_3N_4) Powders for Application in Ceramic Technology for Advanced Heat Engines Project." Key milestones are the commissioning of scale-up equipment and the modeling of saturator transient performance.

The milestones are on schedule.

Publications

G. M. Crosbie, J. M. Nicholson, R. L. Predmesky, E. D. Stiles, "Pre-Pilot Scale Synthesis of Low-Carbon Si_3N_4," presented at the 90th Annual Meeting of the American Ceramic Society, May 1-5, 1987, at Cincinnati, Ohio.

G. M. Crosbie, J. M. Nicholson, R. L. Predmesky, and E. D. Stiles, "Silicon Nitride Powder Synthesis Program," pp. 127-135 in: Proc. of the 25th Automotive Technology Development Contractors' Coordination Meeting, Soc. of Automotive Engineers, Warrendale, Pa., 1988. (P-209)
ISBN 0-89883-469-4

G. M. Crosbie, J. M. Nicholson, R. L. Predmesky, E. D. Stiles, "Pre-Pilot Synthesis of Low-Carbon Si_3N_4," abstract accepted for presentation at the Second International Conference on Ceramic Powder Processing Science, October 12-14, 1988, at Berchtesgaden (Bavaria), Fed. Rep. of Germany.

"About the Project: Ford Motor Company," Ceramic Technology Newsletter, No. 20, p. 1-2, July-September, 1988. Published by Oak Ridge National Laboratory, Oak Ridge, Tenn.

"Silicon Nitride Powder for Advanced Engine Components," Research Staff Highlights, Ford Motor Company, July, 1988. (Ford Motor Company distribution only)

K. R. Carduner, R. O. Carter III, G. M. Crosbie, and E. D. Stiles, "Silicon-29 Magic Angle Spinning Nuclear Magnetic Resonance of Sintered Silicon Nitride Ceramics," submitted for publication.

References

1. G. M. Crosbie, "Silicon Nitride Powder Synthesis," pp.255-265 in: Proc. of the 24th Automotive Technology Development Contractors' Coordination Meeting, Soc. of Automotive Engineers, Warrendale, Pa., 1987. (P-197).

2. G. M. Crosbie, J. M. Nicholson, R. L. Predmesky, and E. D. Stiles, "Silicon Nitride Powder Synthesis Program," pp. 127-135 in: Proc. of the 25th Automotive Technology Development Contractors' Coordination Meeting, Soc. of Automotive Engineers, Warrendale, Pa., 1988. (P-209)

3. G. M. Crosbie, "Synthesis of High Purity Sinterable Si_3N_4 Powders," pp. 17-23 in Ceramic Technology for Advanced Heat Engines Project Semiannual Report for October 1986 Through March 1987, ORNL/TM-10469, Oak Ridge National Laboratory, Oak Ridge, Tenn., August 1987.

Microwave Processing of Silicon Nitride

H. D. Kimrey, M. A. Janney, and M. K. Ferber (Oak Ridge National Laboratory)

Objective/scope

The objective of this research element is to identify those aspects of microwave processing of silicon nitride that might (1) accelerate densification, (2) permit sintering to high density with much lower levels of sintering aids, (3) lower the sintering temperature, or (4) produce unique microstructures.

Technical progress

This research element is examining the sintering and heat treatment of silicon nitride in the Oak Ridge National Laboratory (ORNL) 2.45-GHz and 28-GHz microwave furnaces. The types of experiments that are to be performed include the following:

1. annealing of dense silicon nitride parts to examine the effects of microwave heating on grain growth and grain boundary recrystallization,

2. development of a microwave furnace dilatometer to provide the capability to monitor the densification of silicon nitride at all stages in the sintering process,

3. sintering of conventional silicon nitride compositions (e.g., 6 Y_2O_3 and 2 Al_2O_3) to establish a baseline of densification rates and microstructural states for microwave-sintered materials, and

4. sintering of silicon nitride with reduced levels of sintering aids (e.g., <2% Y_2O_3) to produce a dense sintered body possessing superior mechanical properties at elevated temperatures.

Our efforts during the past six months have focused on two areas: (1) design and construction of a microwave-compatible dilatometer for sintering studies in the 28-GHz microwave furnace, and (2) annealing of dense Si_3N_4-6 wt % Y_2O_3 in the 2.45-GHz microwave furnace.

Dilatometer design and construction

The microwave-compatible dilatometer design, construction, and test has been completed. Milestone 1.1.2.4.01 was successfully met on time in September 1988.

The dilatometer posed several design problems that were unique to a microwave furnace. First, the materials of construction had to be compatible with the microwave field. We chose BN as the most likely candidate that would satisfy the needs of high-temperature stability as well as low microwave absorption. Second, no leakage of microwaves could be allowed along the feedthroughs for the dilatometer. Several designs for blocking the transmission of microwaves were considered. Third, the components of

the dilatometer needed to be compatible with high vacuum as well as furnace atmosphere operation.

The microwave-compatible dilatometer will greatly enhance our capabilities with respect to the gathering of sintering data in the microwave furnace. With the present instrument, we will be able to follow the entire course of densification from initial thermal expansion of the green part to the final densification and thermal contraction of the dense sintered body. The dilatometer has the following specifications with respect to its performance:

1. It is compatible with the 28-GHz microwave field by virtue of its materials of construction and special microwave chokes that prevent leakage of the microwaves into the linear variable differential transformer (LVDT) chamber, which is below the microwave furnace chamber. Potential leakage is monitored using a microwave-sensitive diode.
2. The range and sensitivity of the instrument are ±1 cm (0.5 in.) and 2 μm (0.0001 in.), respectively. For a standard sintering sample 2.5 cm (1 in.) long, this provides a range of linear shrinkage >50% and a sensitivity of 0.01 lin %.
3. Temperature is measured using a Type C thermocouple that is a part of the central pushrod; hence, temperature is measured at approximately the midpoint of the sample.

Figure 1 shows a typical test and checkout run that was made with the dilatometer. We are able to measure and record the temperature, the displacement of the LVDT, the relative electric field strength, and the rate of temperature change [dT/dt (not shown, for clarity)]. The test part was alumina (Reynolds RC152DBM) with a particle size of about 1.5 μm. It was a cylindrical specimen, approximately 3 cm (1.2 in.) tall × 2.5 cm (1.0 in.) diam. The LVDT trace in Fig. 1 shows the thermal expansion of the sample up to a temperature of about 1400°C, followed by rapid sintering at the soak temperature of 1550°C. An additional enhancement that remains to be added is interfacing the system to a microcomputer for data reduction and analysis.

Annealing studies

Annealing studies have been initiated in the 2.45-GHz microwave furnace using dense PY6 from GTE Labs. (PY6 is Si_3N_4 with 6 wt % Y_2O_3 as the sintering aid.) A matrix of time-temperature conditions has been established; temperature was varied from 1600°C (1-10 h annealing time) to 1850°C (1-2 h).

Initial results at 1800 and 1850°C indicated that there was excessive migration of silicon and yttrium from the sample into the pure silicon nitride insulation/packing powder. To alleviate the problem, a packing powder consisting of Si_3N_4-6 wt % Y_2O_3 was used. Under the same annealing conditions, the yttria-containing insulation/packing powder greatly reduced the amount of silicon and yttrium migration to the surface of the samples.

A reaction zone that extends into the center of the sample has been observed in all of the samples that have been annealed. The extent of the

ORNL-DWG 89-2129

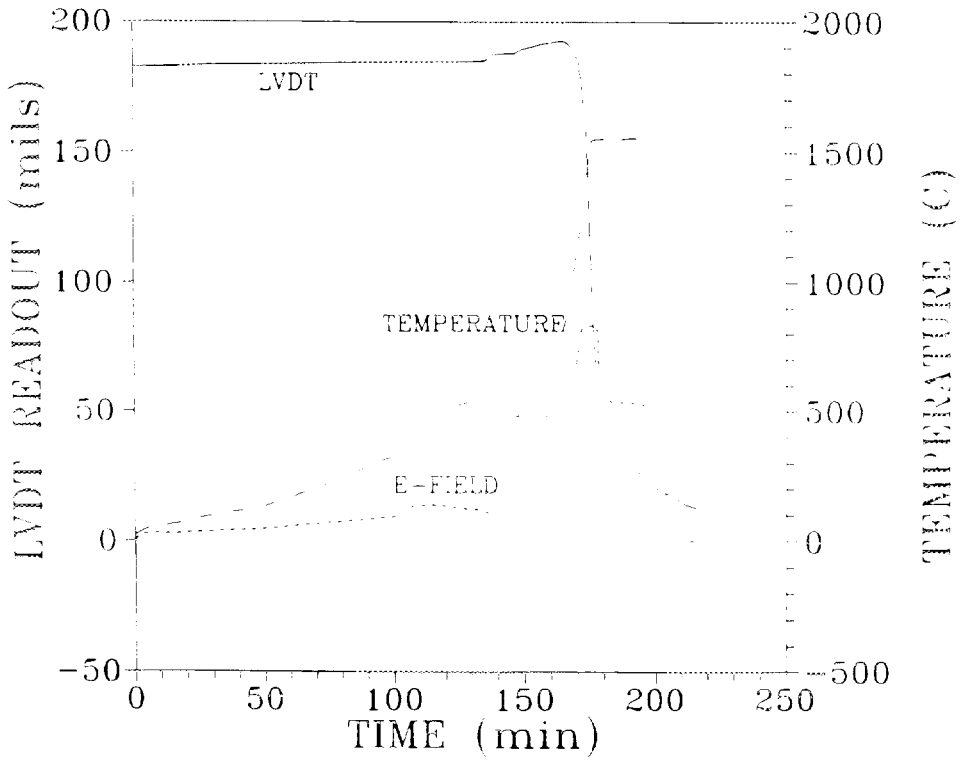

Fig. 1. Typical strip chart traces for displacement (LVDT), temperature, and relative electric-field strength (E-field) for the 28-GHz microwave-compatible dilatometer.

reaction layer increases with time and temperature. The cause of this layer is not known at this time. A complete microstructural and mechanical properties characterization of these samples is in progress and will be reported in the next semiannual report.

Status of milestones

Milestone 1.1.2.4.01 was completed on time in September 1988.

1.1.4 Processing of Monolithics

Improved Processing

R. L. Beatty and R. A. Strehlow (Oak Ridge National Laboratory)

Objective/scope

The objective of this project is to determine and develop the reliability of selected advanced ceramic processing methods. This project is to be conducted on a scale that will permit the potential for manufacturing use of candidate processes to be evaluated.

Technical progress

Introduction

The experimental plan for these studies is to make tensile specimens in sufficient number to permit the uniaxial tensile strength to be used as a principal independent variable in analyzing process reliability.

The gel-casting process has been chosen for study. This project has as its objective the application of this process to the casting of a silicon-nitride composition. However, initial tests have been conducted with a fine-grained alumina. This material is intended to serve as a surrogate for the silicon nitride, especially with reference to the centrally important drying step of the process. It is recognized that several of the steps of the process for alumina will need to be altered for the silicon nitride studies.

Tensile specimen design

The tensile specimen design for this experimental program was completed. This design uses a straight machined ceramic bar with machined metal end pieces that are fastened to the ceramic with a commercially available premixed epoxy formulation (chosen in order to minimize the sample-to-sample variation). The design requires simpler ceramic machining than do specimen designs that change the ceramic cross section for direct gripping.

Three reference sample tensile specimens from a commercially available dense alumina (AD-94) were machined to the dimensions 6.00 × 6.00 × 94 mm and were broken using recently developed specimen grips. Insignificant bending moment was observed in these tests. The tensile data for the two specimens that broke due to material failure were within the scatter band for the tensile strength of the material. Improvements and refinements of design are expected to come with further development work.

A plate mold large enough to produce 12 tensile specimens is now being used for development of the gel-casting process. The anodized aluminum mold is used to form a gel-cast plate, 22.9 × 8.9 × 1.0 cm (9 × 3.5 × 0.375 in.). This mold design was found to simplify several steps of the process, including casting, drying, and debindering. The resulting ceramic slab formed from each preparative run is machined into tensile specimens.

Processing studies

The gel-casting process involves several steps that are continuing subjects for testing in this project. Each is associated with several variables. The basic steps of the process are:

1. powder preparation (as-received or wet-milled and dried),
2. mixing of the powder with an aqueous solution of polymerizable components (loading level and concentration of organic compounds including dispersant),
3. addition of polymerization initiator,
4. casting,
5. thermal treatment to form a polymer gel,
6. unmolding,
7. drying in a controlled humidity environment,
8. debindering (removal of residual organic compounds), and
9. sintering.

The process tests conducted included casting at different solids loading, several different drying schedules, and the inclusion of a polymerization catalyst. Successful casting of a relatively coarse alumina produced two sintered plates, one cast at 55 vol % solids loading and one at 60 vol %. Tests with the more difficult fine-particle alumina, RC-HP-DBM, as received, were cast successfully at the 52 vol % solids level, and four plates were made. All specimens had sintered densities of at least 95.5% of the theoretical density.

Studies of drying schedules were conducted. Successful plates utilized a 48-h gel drying schedule beginning at 20°C and 100% relative humidity (RH) and ending with a 16-h soak at 100°C and approximately 0% RH. Drying cycles ending at lower temperatures have led to a successful product only after a 48-h soak at 55°C. Shorter soak periods led to subsequent part cracking that occurs during debindering. More cracking progressively occurs as the 55°C soak time decreases. Additional drying studies will be part of the subsequent studies.

The polymer removal schedule was designed conservatively as based on the results of thermogravimetric studies and has been satisfactory. This schedule will be one of the processing variables in later studies.

Experimental work was concluded on an initial test composition for gel-casting the fine-particle alumina powder. In the continuing development work, however, both alumina and silicon nitride of similar particle size distributions will be studied. The work will concentrate on the formation of slab specimens for the tensile testing project, although casting of selected large form pieces will also be developed. Tests to choose the significant variables and define their levels for systematic study are in progress.

Milling media preparation

In a related study, a milled powder mixture was prepared for the experimental forming of silicon nitride milling media for use in this project. Approximately 20 kg of UBE-SN-E10 silicon nitride powder premix containing 5% alumina and 7% yttria as sintering aids and approximately

5% PEG-8000 as a water-soluble binder was milled, dried, and screened. The mixture was milled with alumina media in an isopropanol-water mixture. The forming of the media was done with a Vector/Freund CF Granulator. The forming produced a somewhat wider size distribution of spheroidal and elongated particles than expected from previous experience, but should produce suitable media.

Status of milestones

Decision on mold preparation procedures for tensile specimens will be made and a test composition will be chosen.	June 30, 1988 Complete
Status report written on test composition results and estimates of process reliability.	Sept. 30, 1988 Complete
Production of numbers of cast specimens using the initial casting system.	Jan. 31, 1989 On schedule

Publications

None.

1.2 CERAMIC COMPOSITES

1.2.2 Silicon Nitride Matrix

SiC-Whisker-Toughened Silicon Nitride

H. Yeh, E. Solidum (Garrett Ceramic Component Div.), K. Karasek, S. Bradley (Engineered Materials Research Center) and J. Schienle (Garrett Auxiliary Power Div.)

Objective/scope

The objective of this program (Phase II) is to maximize the toughness in a high strength, high temperature SiC whisker/Si_3N_4 matrix material system that can be formed to shape by slip casting and densified by a method amenable to complex shape mass production. The ASEA glass encapsulation hot isostatic pressing (HIP) technique shall be used for densification throughout the program.

The program is divided into five technical tasks with multiple iterations of process development and evaluation. Parametric studies shall be conducted to optimize processing steps developed in the Phase I effort(Ref. 1), guided by established analytical and NDE techniques. The five technical tasks are: Task I - Selection of SiC whiskers; Task II - Baseline Casting Process; Task III - Parametric Densification Study; Task IV - Effect of Specimen Size and Shape; and Task V - Alternate Whiskers.

The technical effort was initiated in May 1988. During this reporting period, only Task I efforts were conducted.

Technical progress

Task I - Selection of Whisker

The purpose of this Task is to select a SiC whisker (SiC_w) to be used as the reinforcement in GN-10 Si_3N_4 matrix, prior to the start of the process optimization and property evaluation studies, conducted under Tasks II through IV.

Advanced Composite Material Corporation, (ACMC, formerly ARCO), SC-9 SiC_w was found to be the best among those available for evaluation during the course of Phase I (Ref.1). At the start of Phase II, two whiskers, Tateho 1S-105 SiC_w and American

Matrix (AM) SiC_w appeared to be very promising and were available in commercial production quantities. Thus, these two whiskers were selected for evaluation.

A) Processing

The most direct method to evaluate the effectiveness of a reinforcing whisker is to measure the mechanical properties of a composite containing the whiskers. Composite billets (approximately 2 1/2" Dia. x 3" Ht.) of each of the two whiskers at 20 wt. %, were formed by a baseline slip casting process and densified to full density using the ASEA glass encapsulated HIP technique. Table 1 lists the green processing data and the final billet densities. Two composite billets containing each whisker were densified. The two billets containing AM whiskers cracked into two or three large pieces during/after densification, while the two containing Tateho whiskers did not. The cracking behavior of the AM composite was believed to be due to the high silica surface layer on the whiskers as suggested by the evidence presented below. The densified composite billets were subsequently machined into test bars and other samples for characterization.

B) Characterization

o <u>Whisker Surface Chemistry</u>

X-ray photoelectron spectroscopy (XPS) was used to analyze the surface chemistry. The Tateho SCW#1-S-105 SiC whiskers was received in several large bags, all designated as Lot 297. To check the uniformity of the material, samples from different locations from two bags were analyzed. The American Matrix, Inc. (AM) SiC whiskers were received (March 1988) in a single bag and only one sample taken from the middle of the bag was analyzed. The results are summarized in Table 2. As seen in Table 2, there is little variation among the four Tateho samples; however, there is a significant difference between Tateho and AM whiskers, in particular, the high level of SiO_2 on AM whiskers, as reflected by the higher oxygen content. The high surface SiO_2 content could be the cause of the cracking problem observed in the American Matrix composite, because SiO_2 has a tendency to react at high temperature with SiC, forming SiO and CO gases. It is anticipated that removal of the SiO_2 surface layer would eliminate the cracking problem.

o <u>Whisker Morphology</u>

STEM was used to examine the whiskers. The Tateho SiC whiskers used in this Task were similar to the lot examined

under Phase I (Ref. 1). Whisker diameters ranged from 0.1μm to 1μm. lengths of some whiskers were over 100 μm. Many whiskers were bent or consisted of irregularly shaped segments. Some debris was present as well. About 10% of the whiskers appeared to hollow. Occasionally 20 nm particles of Fe with trace Ca were found on the whisker surfaces. Both type-a Iwanga and stacking fault type-b defects (Ref. 1) were noted.

The AM whiskers were also similar to the lot that was examined under Phase I effort. Diameters ranged from 0.2μm to 5μm with the average being a little less than 1μm. Whisker lengths varied from 5μm to 50μm. As with the earlier versions the rough irregular surface morphology tended to be dominant. There did, however, appear to be an increased fraction of smooth whiskers. Whiskers were straight. Some debris was present; the amount appeared to be similar to that found in the earlier version. Fe-Ni-Ca particles were seen on whisker surfaces.

o <u>X-ray Diffraction of Composites</u>

Conventional X-ray diffraction analysis was performed on the samples cut from the composite billets. The results showed that the Tateho composite contains a substantial amount of α - Si_3N_4 in addition to β - Si_3N_4 and SiC, while the AM composite only contains
β - Si_3N_4 and SiC. The presence of α - Si_3N_4 in the Tateho composite indicates that not all of the starting powder reacted with the sintering aids. The minor phases present in the grain boundaries will be presented under STEM analysis section.

o <u>Microscopy of Composites</u>

a) Optical Metallography

Polished cross-section of American Matrix and Tateho SiC whisker reinforced composites were prepared to evaluate whisker distribution and orientation. The American matrix composite (Figures 1 and 2) exhibited good whisker dispersion. However, the whiskers exhibit some degree of preferred orientation along the test bar length. The Tateho whiskers appear agglomerated (Figures 3 and 4) and do not exhibit any evidence of preferred orientation. In addition, the whisker morphology observed in the Tateho composite is less distinct than for the American Matrix composite, suggesting that the Tateho whiskers may have reacted during processing.

b) <u>STEM Analysis</u>

The scanning transmission electron microscopy (STEM)

results showed a small amount of void content in the Tateho composite but much higher in American Matrix composite (Fig. 5), consistent with the cracking behavior discussed earlier. The grain boundary pockets in both composites contained two crystalline phases, H-phase and J-phase, plus a non-crystalline phase. The amount of H-phase in both composites is higher than that of the J-phase. The Tateho composite contained more non-crystalline phase than American Matrix composite.

As noted in Phase I effort (Ref. 1), a significant fraction of the Tateho SiC whiskers used in this task were also hollow. Grain boundary material flowed into these holes (Figure 6); however, only the J-phase and the non-crystalline phase were present.

The SiC whisker to Si_3N_4 grain and Si_3N_4 grain boundaries were both non-crystalline.

A comparison of the morphologies between the two composites indicates the presence of finer grains in the Tateho composite. The Tateho composite also had a lower volume fraction of whiskers in the area examined by STEM; this is consistent with the optical metallography observation of whisker agglomeration. The observation that the hollow Tateho whiskers soaked up a certain amount of grain boundary material may be one of the reasons for the presence of the unreacted starting α-Si_3N_4 in the Tateho composite observed by x-ray diffraction.

o Mechanical Property Testing and Fractography

Ten MOR bars of each composite were tested in four-point bending at room temperature. The test parameters and results are shown in Table 3. The American Matrix whisker reinforced composites exhibited higher flexural strength (94.9 ksi) than the Tateho composites (78.2 ksi). The fracture surfaces were examined at 40X using a binocular microscope. The American Matrix composite exhibited both surface and internal fracture origins. The Tateho composite fractures primarily originated from the surface, but a few internal failures were noted.

SEM analysis was performed on selected specimens to better document the failure origins and look for evidence of whisker toughening. Typical failure origins of the American matrix whisker composite are shown in Figure 7. The failure origins of the American Matrix whisker composite appear to be agglomerate defects. Typical failure origins of the Tateho whisker composite are shown in Figure 8. The failure origins are similar in appearance to the remainder of the fracture surface. Consequently, the nature of the flaws was not evident.

In the American Matrix composite, SiC whiskers normal to the plane of fracture were observed for which the whisker fracture surface was below the matrix fracture surface (Figure 9). This observation suggests crack bridging toughening may have occurred. For the Tateho composite, no distinct evidence of SiC whiskers was observed. The whisker impressions on the fracture surface were believed to be pulled-out Si_3N_4 grains rather than SiC whiskers since the impressions better match the Si_3N_4 grain morphology (Figure 10).

The five K_{IC} bars of each composite were notched (Chevron) at the mid-span and subsequently tested at room temperature in three-point bending. The test parameters and toughness results are shown in Table 4. The American Matrix whisker composites exhibited an average K_{IC} of 6.02 ksi*in$^{1/2}$, which is equivalent in toughness to monolithic GN-10 Si_3N_4, 5.98 ksi*in$^{1/2}$ (average of 16 data points). The Tateho whisker composite exhibited lower toughness, 5.34 ksi*in$^{1/2}$.

Reference

1. H. Yeh, J. Schienle, K. Karasek, and S. Bradley, *Development of Ceramic Matrix Composites for Application in the Ceramic Technology for Advanced Heat Engines, Final Report*, ORNL/Sub/85-22008/1.

Status of milestones

As a result of recent information on whisker availability and the results of the existing Task 1 effort, the milestones and the Statement of Work of this program are under revision.

Publications

A paper entitled "SiC Whisker Stability During Processing of Si_3N_4 Matrix Composites" by S.A. Bradley, K.R. Karasek, M.R. Martin, H.C. Yeh, and J.L. Schienle was accepted for publication by the J. American Ceramic Society.

A paper entitled "Composition and Microstructure of Silicon Carbide Whiskers," by K.R. Karasek, S.A. Bradley, J.T. Donner, M.R. Martin, K.L. Haynes, and H.C. Yeh was accepted for publication by the J. Materials Science.

A talk entitled "Process Parameters Affecting Slip Cast SiC Whisker Reinforced Si_3N_4 Composites" by K.R. Karasek, S.A. Bradley, H.C. Yeh, and J.L. Schienle was presented at the World Materials Congress in Chicago on September 29, 1988.

A paper entitled "Characterization of Silicon Carbide Whiskers" by K.R. Karasek, S.A. Bradley, J.T. Donner, H.C. Yeh, J.L. Schienle, and H.T. Fang was submitted to the American Ceramic Society for publication.

TABLE 1 COMPOSITE PROCESSING DATA

SiC_w Loading wt %	COMPOSITE SLIP			Green Density (g/cc)	Final Density (g/cc)
	% Solids	Viscosity (cp)	pH		
20% American Matrix *	62.1	23	9.35	1.83	3.28
20% Tateho 15-105	55.6	670	9.25	1.43	3.27

* Uncleaned, batch received at GCCD on May 1988

Table 2

XPS Data
Atomic Percent (Binding Energy in eV)

Sample No.	5562-101-1	5562-101-4	5562-59-3	5562-59-4	American Matrix
	Tateho SCW#1-S-105				
Location	Bag 1 Bottom	Bag 2 Middle	Bag 1 Top	Bag 2 Top	
Si 2p	35.6(100.5)	37.6(100.6)	37.4(100.6)	35.8(100.5)	15.9(100.5)
Si 2p	5.2(101.9)	4.9(102.0)	5.3(101.9)	6.7(101.7)	17.3(103.2)
C 1s	36.2(282.4)	36.7(282.4)	31.9(282.4)	35.2(282.4)	13.6(282.4)
C 1s	9.3(283.8)	9.3(283.8)	13.2(283.4)	9.9(283.6)	2.8(283.9)
C 1s	2.1(285.4)				1.9(285.3)
O 1s	1.9(529.6)	2.7(529.8)	3.4(530.1)	3.0(530.0)	8.1(531.3)
O 1s	9.2(531.4)	8.0(531.4)	7.4(531.5)	8.3(531.5)	37.5(532.4)
O 1s			1.1(533.1)		
Fe 2p	0.6(711.3)	0.7(711.0)	*0.5(710.7)	*1.0(711.5)	
Ca 2p3		0.2(346.6)			1.7(347.9)

* The Fe 2p value was taken from the broad energy survey scan instead of a high resolution scan. Therefore, the accuracy will not be as high as for other values shown.

TABLE 3 ROOM TEMPERATURE MOR OF COMPOSITES

SiC Whisker	MOR* ksi (MPa)
20% American Matrix	94.9 8.1 (654 56)
20% Tateho	78.2 6.3 (539 43)

* Average of ten test bars

Test Bar Dimensions (nominal)
Width: 0.250 inch (6.35 mm)
Thickness: 0.125 inch (3.175 mm)
Length: 2.0 inch (50.8 mm)

Test Parameters (four point bending)
Outer Span: 1.50 inch (38.1 mm)
Inner Span: 0.75 inch (19.05 mm)
Crosshead Speed: 0.02 inch/minute (0.51 mm/minute)

TABLE 4 ROOM TEMPERATURE CHEVRON NOTCH TOUGHNESS OF COMPOSITES

SiC Whisker	Fracture Toughness* $ksi*in^{1/2}$ ($MPa*m^{1/2}$)
20% American Matrix	5.02 0.17 (6.62 0.19)
20% Tateho	5.34 0.26 (5.87 0.29)

* Average of five test bars

Test Bar Dimensions (nominal)

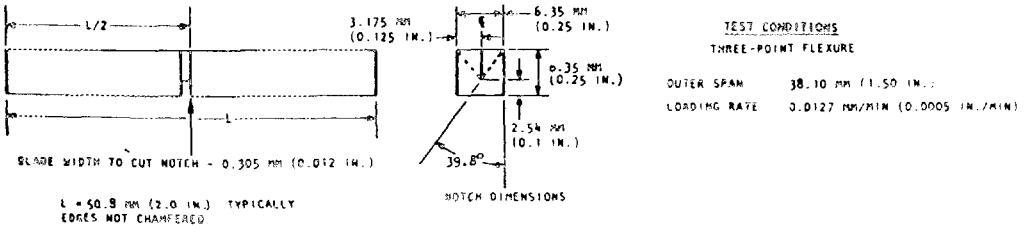

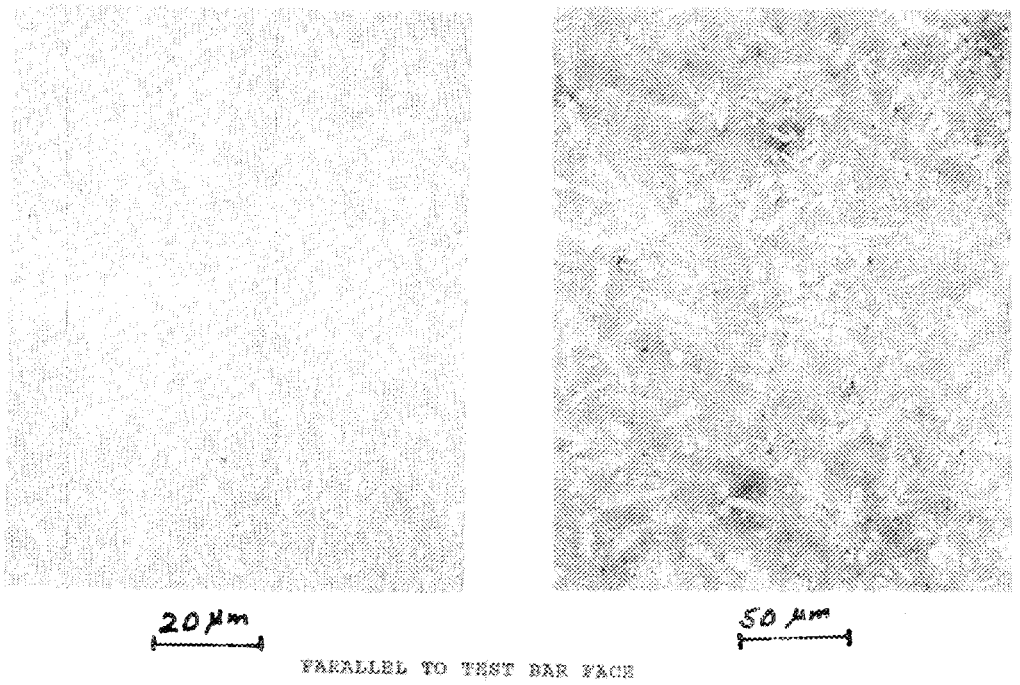

FIGURE 1 - AMERICAN MATRIX WHISKERS ARE WELL DISPERSED

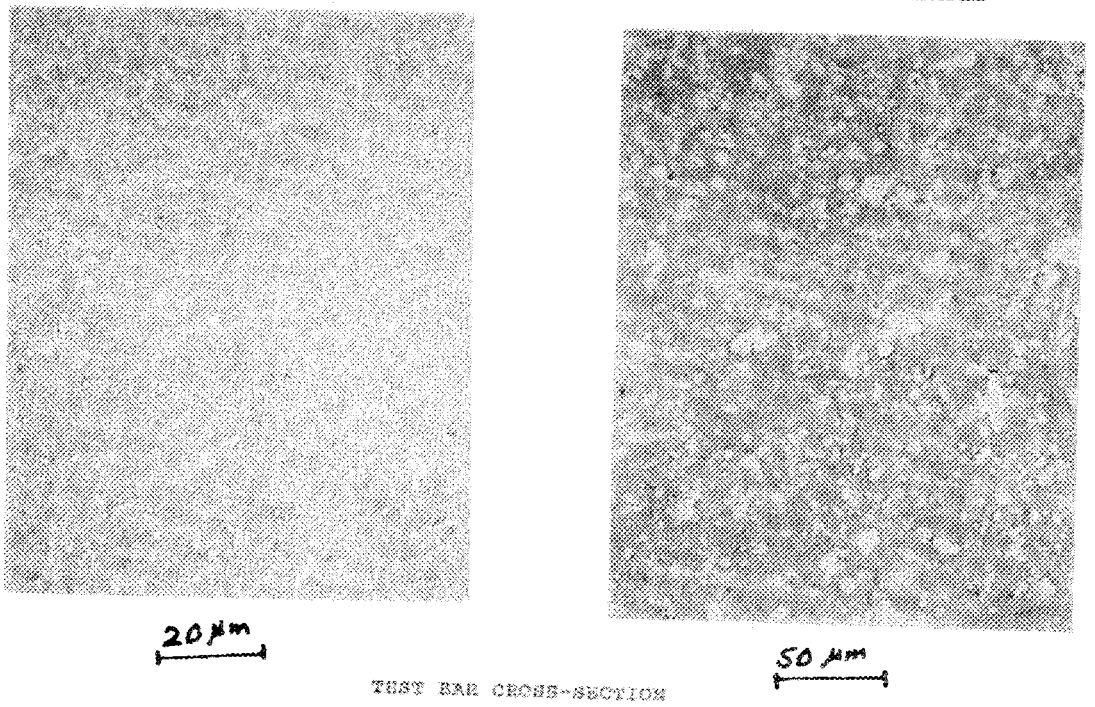

FIGURE 2 - FEW AMERICAN MATRIX WHISKERS LIE IN THE PLANE OF THE BAR CROSS-SECTION SUGGESTING PREFERRED ORIENTATION

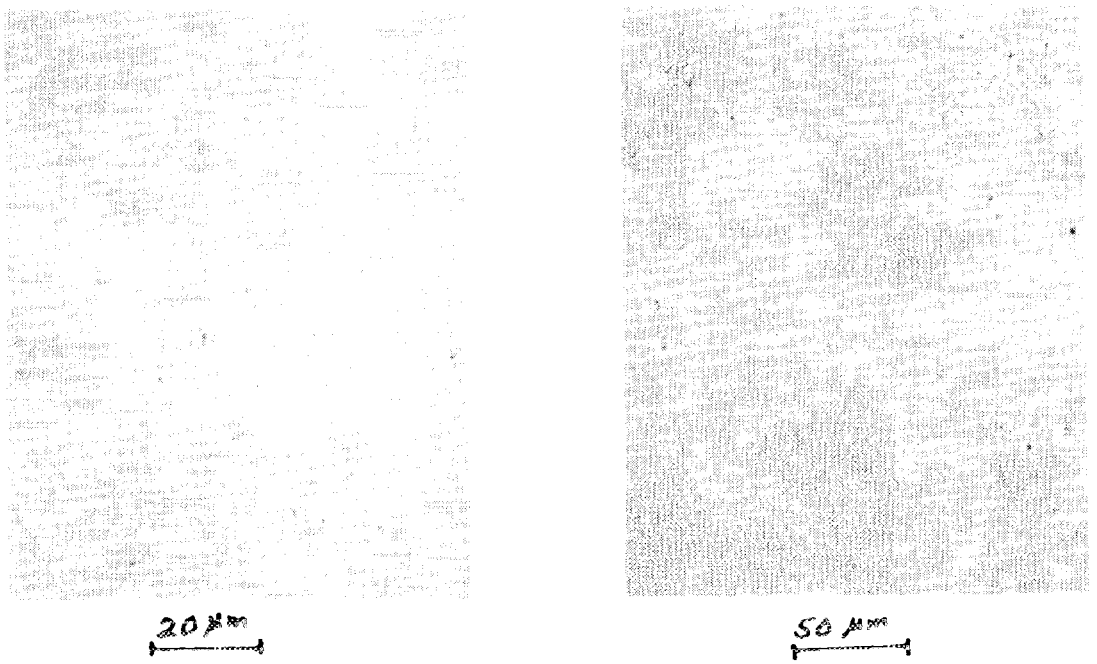

PARALLEL TO TEST BAR FACE

FIGURE 3 - AGGLOMERATED WHISKERS IN TATEHO COMPOSITE

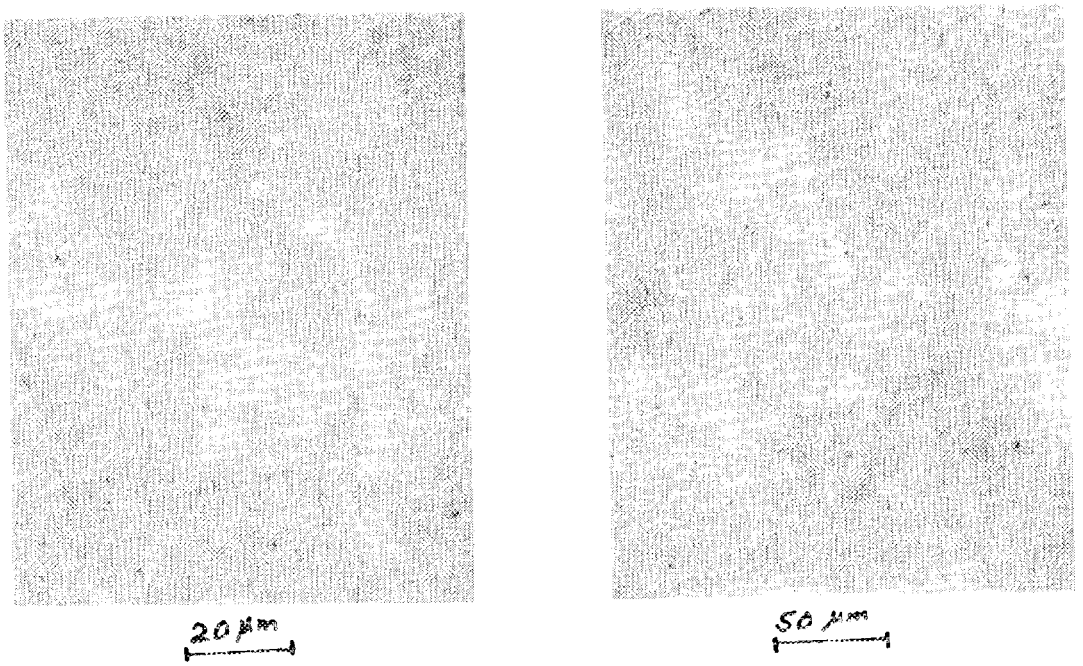

TEST BAR CROSS-SECTION

FIGURE 4 - AGGLOMERATED WHISKERS IN TATEHO COMPOSITE

FIGURE 5 - STEM MICROGRAPH SHOWING THE PRESENCE OF THE VOIDS IN THE AMERICAN MATRIX COMPOSITE SAMPLE

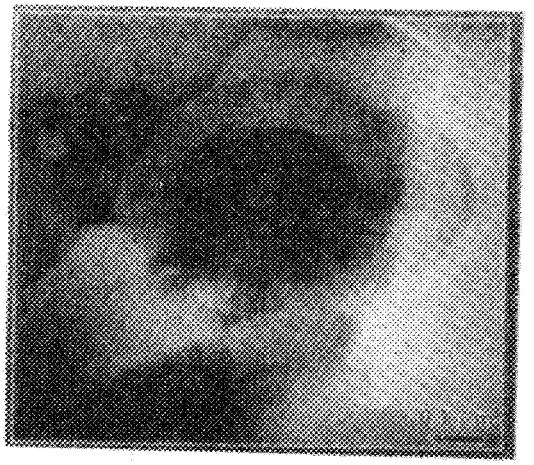

FIGURE 6 - STEM MICROGRAPH SHOWING THE LOSS OF SINTERING AIDS INTO THE AXIAL HOLE OF THE WHISKER IN THE TATEHO COMPOSITE

FIGURE 7 - SEM MICROGRAPHS SHOWING EXAMPLES OF AMERICAN MATRIX WHISKER REINFORCED COMPOSITE FAILED FROM AGGLOMERATE TYPE DEFECT

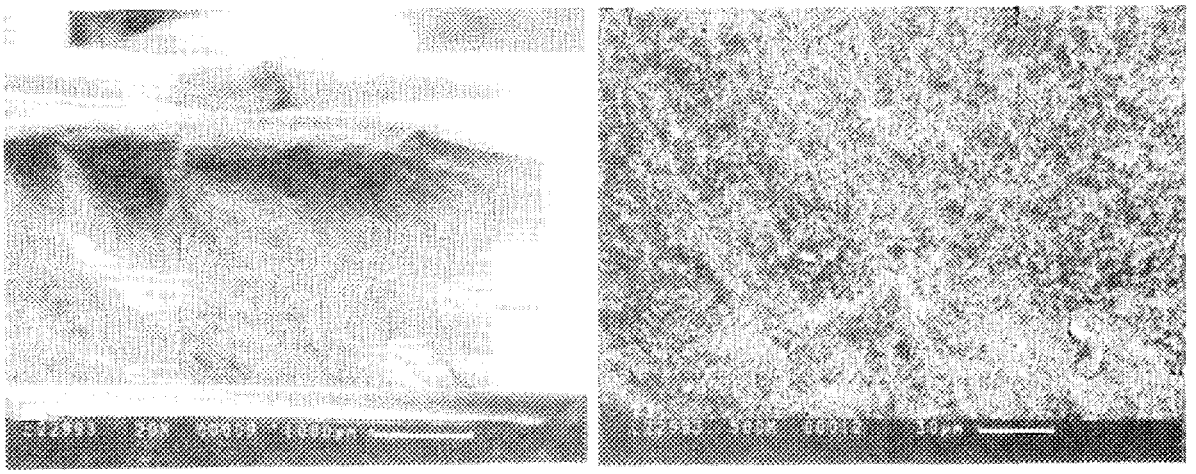

FIGURE 8 - SEM MICROGRAPH SHOWING TATEHO WHISKER REINFORCED COMPOSITE FRACTURE ORIGIN SIMILAR TO REMAINDER OF FRACTURE SURFACE

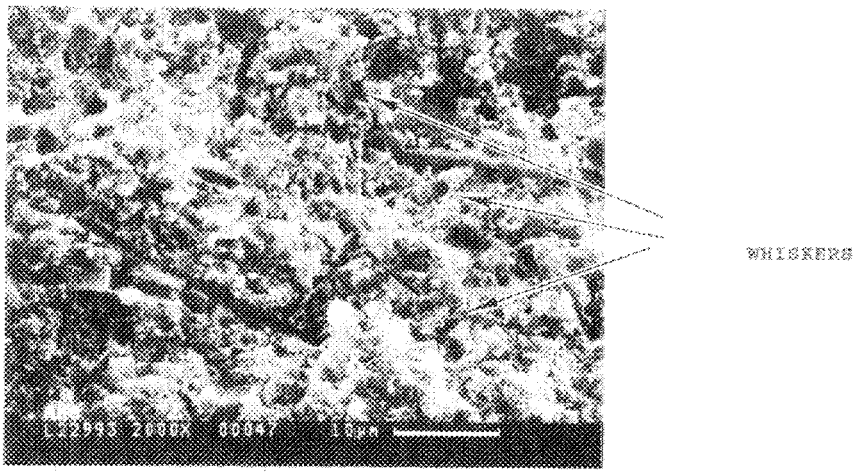

FIGURE 9 - SEM MICROGRAPH SHOWING WHISKERS OBSERVED ON FRACTURE SURFACE OF AMERICAN MATRIX COMPOSITE SUGGESTS CRACK BRIDGING TOUGHENING

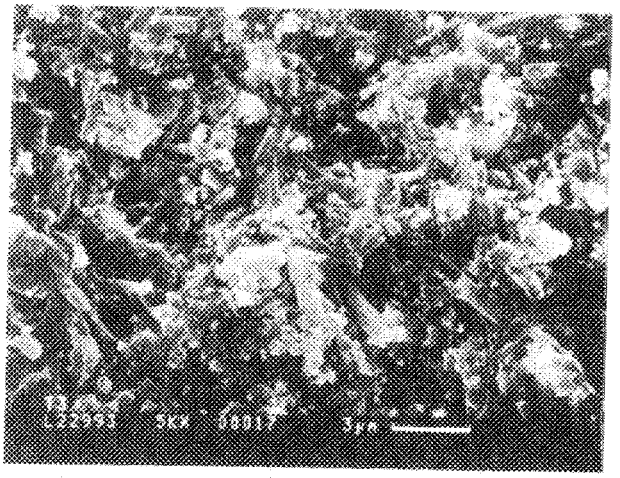

FIGURE 10 - SEM MICROGRAPH SHOWING NO EVIDENCE OF WHISKER TOUGHENING FOR TATEHO COMPOSITE

Silicon Nitride-Metal Carbide Composites

S. T. Buljan (GTE Laboratories, Inc.)

Objective/Scope

The objective of the proposed effort is to study the effect of sintering aids on microstructure and properties of Si_3N_4-SiC(w) composites and utilize the results obtained to design and synthesize an advanced composite of improved properties. It is also an objective of this effort to refine forming and consolidation processes and develop technology for prototype part fabrication.

Technical Progress

In the course of the preceding period, research has addressed three general areas.

I. Precursor Materials: The objective of this task was to characterize Si_3N_4 and SiC whiskers from several different manufacturers and evaluate their potential to replace GTE SN502 silicon nitride and Arco SC9 SiC whiskers in composites. This task was completed. Ube Si_3N_4 and Tokai SiC whiskers were identified to be acceptable alternate materials.

II. Microstructural Design: These studies are focused on bonding glass phase modifications through sintering aid additions and processing and evaluation of effects of microstructure on fracture toughness of silicon nitride monoliths and composites.

III. Process for Near Net Part Fabrication: Work has concentrated on improvement of injection molding mix preparation, forming, and HIP densification techniques. This effort has resulted in development of a process which yields parts of high strength (1150 MPa) and fracture toughness (6.9 $GPa \cdot m^{1/2}$).

A part of the effort was also devoted to studies of creep behavior of Si_3N_4-SiC whisker composites. The results of these studies are discussed in detail in the following sections.

I. Precursor Materials

Based on the results of screening studies, Ube Si_3N_4 was identified to be, at this point in time, the best alternative to GTE SN502 and was selected as a source material for further studies. Hot pressing studies have examined the behavior of powders of different particle size (E03, E10) and shown that (Table 1) Ube Si_3N_4 exhibits somewhat lower rate of $\alpha \rightarrow \beta$-Si_3N_4 transformation and requires an increase in sintering temperature to obtain complete conversion to β form, which can be attributed to the difference in SiO_2 content. Increased densification temperature results in improved fracture toughness. Ube Si_3N_4 yields an AY6 "monolithic" body of higher average strength than SN502 (Table 1). Minor variations in strength are thought to be associated with processing related flaws. A blend (80/20) of E03 and E10 powders is a preferred choice for injection molding.

Table 1: Properties of Hot-Pressed Si_3N_4-AY6

Ube Grade	HP Parameters T(°C)	t(min)	Mechanical Properties K_{IC}(CSF) ($Mpa \cdot m^{1/2}$)	MOR (MPa)	Phase Characterization % α-Si_3N_4	% β-Si_3N_4
	1725	100	4.7±0.3	845±51	9.1	90.9
E-10	1800	100	4.4±0.3	876±84	-	100
	1800	400	5.1±0.3	916±29	-	100
	1725	100	4.7±0.2	932±92	48.7	51.3
80/20	1800	100	5.2±0.1	823±88	-	100
E03/E10	1800	400	5.2±0.2	841±13	-	100
	1725	100	4.1±0.3	995±30	65.8	34.2
E03	1800	100	5.0±0.2	871±69	4.8	95.2
	1800	400	4.8±0.2	821±90	-	100
SN502	1725	100	4.6±0.2	773±69	-	100

Further studies were focused on composites containing AY6 (Si_3N_4 + 6 w/o Y_2O_3 + 1.5 w/o Al_2O_3) with 30 v/o Silar SC-9 SiC whiskers. SiC whiskers were not beneficiated. AY6 powders containing SN502 Ube E-10 and 80/20 E-O3, E-10 were prepared at GTE Labs and shipped to Advanced Composites Materials Corp., Greer, SC, where the powders were blended with SiC whiskers using ACMC's proprietary processing. The blended powders were hot pressed at 1725°C and 1800°C under 25.1 MPa maximum pressure for 400 minutes. Typical densification curves for the hot-pressing runs are shown in Figure 1. At the same hot-pressing temperature, the Ube E-10 densifies at a faster rate. The faster rate may be due to easier rearrange-

ment during the initial stages of densification for the more equiaxed E-10 grains. All hot-pressed densities were greater than 99.5 of the calculated theoretical density. X-ray analysis showed the presence of only β-Si_3N_4 and SiC in the hot-pressed materials.

The mechanical properties for the hot-pressed composites are compared in Tabled 2. For the materials with as-received whiskers hot pressed at 1725°C, the values for fracture toughness and MOR are the same. Raising the hot-pressing temperature to 1800°C clearly increases the fracture toughness and strength for the composite made with Ube Si_3N_4, while the composites made with SN502 do not show the same increases. Composites prepared with E-03//E-10 blend and densified at 1800°C show superior fracture toughness and strength.

Table 2: Properties of Si_3N_4-Based Composites Containing 30 v/o ACMC SiC Whiskers (Hot Pressed at 25.1 MPa and 100 Minutes)

Matrix	Hot Press Temperature (°C)	Mechanical Properties K_{IC} (CSF) ($MPa \cdot m^{1/2}$)	(MOR) (MPa)	Comments
	1725	6.4±0.4	975±39	Beneficiated
SN502	1725	6.1±0.6	796±40	As-received
	1800	6.0±0.6	880±101	"
Ube E-10	1725	5.8±0.4	823±13	"
	1800	6.9±0.3	913±47	"
Ube Mix 80/20 E-03/E-10	1800	7.3±0.6	1043±50	"

Evaluation of alternate SiC whiskers has considered several sources (Tateho, Tokai, Am. Matrix). The results of whisker characterization were reported earlier. At present, the one deemed the most suitable alternative of ACMC SC-9 are whiskers produced by Tokai. Composites with Tokai SiC whiskers prepared using processing conditions developed for SC-9 SiC exhibit fracture toughness equivalent to that of composites with ACMC SC-9 (Table 3). These composites possess somewhat lower strength, which may be in part due to the difference in morphology and composition of the Tokai whisker.

Table 3: Properties for Hot-Pressed Composites Containing 30 v/o Additions of Different SiC Whiskers (1725°C, 25.1 MPa, 400 min)

Matrix	Whisker	K_{IC} ($MPa \cdot m^{1/2}$)	MOR (MPa)
Si_3N_4*-AY6	ACMC	6.4 (±0.4)	975 (±39)
(SN502)	Tokai	6.3 (±0.2)	871 (±42)

II. Microstructural Design

The observations on monolith and composite silicon nitride have provided an excellent illustration of the need to consider grain size and shape of the matrix as well as dispersoid in composite design. It is also clear that grain boundary strength deserves equal consideration. Strong bonding across the grain boundaries reduces the amount of intergranular fracture and restricts crack deflection toughening. Weak bonding reduces the energy to propagate the cracks and may result in a net decrease in fracture toughness despite an increase in intergranular fracture.

It was observed that silicon nitride bodies prepared with 8.8 v/o of different sintering aids and essentially the same average grain size, aspect ratio, and elastic modulus exhibit considerably different fracture toughness (Table 4).

Table 4: Properties of Si_3N_4 Prepared with Equivalent Volumes of Different Sintering Aids

	Relative IFT	Young's Modulus E (GPa)	Grain Size Equiv. Dia. D (μm)	Avg. Aspect Ratio A
$Si_3N_4 + (Y_2O_3)$	1.00	301	0.22	3.0
$Si_3N_4 + (MgO)$	0.70	306	0.29	3.4
$Si_3N_4 + CeO_2$	0.91	308	0.27	3.3

In the absence of intergranular fracture, the fracture toughness of these composites could be expected to be quite similar. It follows then that for improved fracture toughness the strength of the grain boundary needs to be carefully tailored to optimize the trade-off between the amount of intergranular fracture and the energy used to fracture a grain boundary in the matrix and along the dispersoid.

Additional data for this study related to sintering aid species is given in Table 5 and again indicate that increases in fracture toughness can be effected by ex-

tended time at densification temperature most likely as a result of grain growth. Equivalent gains in IFT can be realized by pressure-assisted sintering at higher temperature for shorter time as is observed at lower temperature for extended time. The AM4 composition, containing the volume equivalent of MgO substituted for Y_2O_3 consistently yields a monolithic body with inferior mechanical properties compared to AY6 densified under identical conditions. The ceria-containing monolith shows comparable room temperature mechanical properties to the AY6 composition at the densification conditions employed to date.

The above observations support the premise that grain size/shape and the strength of intergranular bond dictate the crack path and control the fracture toughness of polycrystalline ceramic bodies.

Table 5: Room Temperature Mechanical Properties of Si_3N_4 (Ube E-10 Si_3N_4 Powder) Based Ceramics*

Material[x]	HP Temp/Time (°C/min)	Relative MOR	Relative IFT[xx]
AY6	1725/90	1.00	1.00
	1725/120	0.95	1.00
	1725/240	0.98	1.14
	1775/90	0.93	1.07
	1775/120	0.99	1.20
AM4	1725/90	0.61	0.70
	1725/120	0.58	1.02
	1725/240	0.69	1.09
	1775/90	0.52	1.00
	1775/120	0.64	1.11
AC8	1725/90	0.96	0.91
	1775/120	0.96	1.16

*All values normalized to standard AY6 hot pressed 1725°C/90 min.

[x]AY6 - 6.0 w/o Y_2O_3 + 1.5 w/o Al_2O_3 + Bal Si_3N_4 (Ube E-10)

AM4 - 4.4 w/o MgO + 1.5 w/o Al_2O_3 + Bal Si_3N_4 (Ube E-10)

AC8 - 6.3 w/o CeO_2 + 1.5 w/o Al_2O_3 + Bal Si_3N_4 (Ube-10)

[xx]Measured in a cross section parallel to HPD

III. Process for Complex Part Fabrication

Previous studies of injection-molded parts prepared from composite material containing SiC whiskers indicated nonsymmetrical whisker orientation resulting from the flow pattern of the whisker into the die to be a major source of warpage produced by nonuniform shrinkage. In an effort to obtain improved dimensional control, two areas were addressed. The first was reduction in shrinkage by increasing the solids loading of the injection molding mix. The second area was control of the whisker orientation during injection molding by alteration of the gate configuration.

Figure 2 shows representative HIPed bars produced from the mix with higher solids loading and formed in a mold of earlier design (1987). The reduced distortion of the bottom bar can be attributed to a higher solids loading content, leading to an apparent reduction in shrinkage. Single axial CATE turbine blades from the current higher solids-loaded material also exhibit somewhat reduced distortion.

To study the effect of whisker orientation, a number of test bars were also prepared with Ube Si_3N_4 and Advanced Composites Materials Corporation SiC whiskers and molded using four different gate configurations.

Selected cross sections of bars for each gate configuration have been mounted after binder removal and epoxy impregnation, and examined. SEM micrographs of the burned-out bars have been digitized and used to determine the whisker orientation differences related to gate configuration.

Samples fabricated by employing each configuration were densified using a revised ASEA HIP cycle. Shrinkage values were based on dimensional measurements before and after HIPing (Table 6).

Table 6: Summary of Results for HIPed Composites

Gate Configuration	Normalized Shrinkage*			Density (%TD)
	ΔLength	ΔWidth	ΔThick.	
1	0.34	1.34	1.34	98.2-98.5
2	0.38	1.26	1.19	98.4-98.6
3	0.57	1.04	1.05	98.1-98.5
4	0.62	1.21	1.17	98.4-98.6

*Normalized shrinkage values less than 1 indicate lower shrinkage than design value.

The gate 1 and 2 designs exhibit little shrinkage in length during densification, and whisker orientation measurements showing alignment primarily along the bar

length. However, gate 3 produced more warpage than gate 1. The type 4 design showed substantial bending during densification (see Figure 3), which was again in agreement with the orientation measurements. The gate type 3 bars were generally straight but showed numerous surface ripples which appear to be relics of the differential shrinkage of the thin stream which had folded many times during the mold filling. The gate type 1 bars appear most suitable for mechanical property testing based on the whisker orientation uniformity and the lack of bending during densification. Bars of this design processed through HIPing were ground into test samples for mechanical property characterization.

Results of mechanical testing of the bars fabricated from the Type 1 gate configuration are given in Table 7. The results are compared to the same material hot pressed at 1800°C, 25.1 MPa and 400 minutes. From these results, it appears that the room temperature properties are essentially equivalent. In summary, higher solids loading and modified gate configurations have produced a relatively distortion-free bar of Si_3N_4-SiC whisker composite material with good fracture toughness and high strength.

Table 7: Comparison of Mechanical Property Data for AY6 + 30 v/o SiC Whisker Composites

Process	K_{IC} ($MPa \cdot m^{1/2}$)	MOR (MPa)
Hot Pressed	7.3 ± 0.6	1043 ± 50
Injection-Molded and HIPed	6.9 ± 0.4	1143 ± 48

IV. Creep Studies

Testing to compare the creep behavior (four-point flexure) of monolithic AY6 to AY6-SiC composites were continued. Data generated in this study indicated a constant creep rate after approximately 0.05% strain (Figure 4). Linear regression analysis of the creep strain-time data after 40 h of testing yielded straight lines with correlation coefficients of greater than 0.95. Therefore, the slopes of these lines were assumed to be steady state creep rates. Additionally, multiple tests conducted with a single material under identical conditions (Figure 5) showed a variation in the steady state creep rate of ±12%, indicating very good data reproducibility.

Figure 6a compares typical strain-time data at 1200°C and imposed stresses of 206.7 MPa (30 ksi) and 137.8 MPa (20 ksi) for the AY6 monolith and the AY6 + 30 v/o SiC whisker composite. The primary creep portions of the data were very similar. Once steady state creep was attained, the strain of the whisker-containing composite was lower. At 1200°C, the steady state creep rate of the whisker-containing composite was lower than its monolithic counterpart over the entire stress range investi-

gated (Figure 6b). The stress exponent from the relationship $\dot{\epsilon} \propto \sigma^n$ of both materials had a value of approximately two over the range of conditions investigated. The value of the stress exponent is consistent with those obtained in other investigations of the creep behavior of Si_3N_4-based materials with different sintering aids using flexure, tension, or compression loading. The mechanism which has been ascribed to the creep of Si_3N_4 bodies containing an intergranular glass phase is grain boundary sliding controlled by the viscous flow of the glass phase. Due to geometric restraints, the motion of the intergranular phase is restricted by the Si_3N_4 grains and a stress exponent greater than one is observed. Since the reduced creep rate of the Si_3N_4-SiC whisker composite did not result in a change in stress exponent, it appears that the same mechanism may control the creep resistance of both materials. The whisker additions apparently retard grain boundary sliding and cavitation.

Data generated in the testing of a material containing 30 v/o SiC particles support this hypothesis (Figure 7). At 1200°C, the strain-time data of the particulate composite (Figure 7a) showed a higher strain at a given time compared to monolithic AY6. Over the range of stress examined, the strain rate was consistently higher than that of the monolith (Figure 7b), with a stress exponent of approximately two. The two SiC-containing composites contained the same reduced amount of $Al_2O_3 + Y_2O_3$, compared to monolithic AY6, although somewhat different total sintering aid contents (Table 8), due to the different amounts of SiO_2 present in the SiC raw materials. It appears that replacing a substantial portion (30%) of acicular β-Si_3N_4 grains with large equiaxed particles (8 μm SiC) detrimentally affects the material's resistance to time-dependent deformation at elevated temperature.

Other studies[1,2] of AY6 and AY6 + SiC whisker composites reported that, at 1200°C in the stress range 50 to 350 MPa, the creep rate in compression of a composite containing 20 v/o SiC whisker was slightly higher than the monolith. The compression samples were annealed in N_2 at the temperature of creep prior to the application of load and subsequently tested in nitrogen. Extensive devitrification of the intergranular glass phase of the monolithic material occurred during annealing, while significantly less devitrification was observed in the composite. After the creep tests, the degree of crystallinity of the intergranular phase of the composite was reported to have increased. If grain boundary sliding controlled by the intergranular phase is assumed to be the operative mechanism of creep, these results, i.e., higher creep resistance of the monolith compared to the composites, follow since the more extensively devitrified glass phase of the monolith would be more resistant to deformation. The higher $SiO_2/Y_2O_3 + Al_2O_3$ ratio of the whisker-containing composite (Table 8), resulting in a more stable glass phase, accounts for this behavior. In the present study, x-ray diffraction of Si_3N_4-based samples crept for as long as 500 hr showed no indication of glass devitrification. It may be speculated that the intergranular glass phases of these materials are less prone to devitrification in an air environment than in nitrogen. Flexure testing in air at 1200°C, where

glass devitrification is assumed to be minimal, clearly shows that the addition of 30 v/o SiC whiskers to AY6 increases resistance to creep.

Table 8: Creep Rates in Four-Point Bending and Sintering Aid Contents of the Si_3N_4-Based Ceramics Shown in Figure 1

Material	Normalized Steady State Strain Rate (1200°C/206.7 MPa)	Sintering Aid Content (Wt % of Composition) Al_2O_3	Y_2O_3	SiO_2*	$SiO_2/Al_2O_3+Y_2O_3$
AY6	1.0	1.50	6.00	2.60	0.35
AY6 + 30 v/o SiCp (8 μm)	2.0	1.05	4.23	2.0	0.38
AY6 + 30 v/o SiCw	0.1	1.05	4.25	2.82	0.53
AY6 + 30 v/o Si_3N_4	0.4	1.05	4.25	2.66	0.50

*Based on O_2 analysis of Si_3N_4 and SiC raw materials

In order to further evaluate the silicon nitride phase, a monolithic material with reduced amounts of sintering aids was prepared as an analog to the composite matrix. In this instance, α-Si_3N_4 powder was milled with the prepared AY6 composition in a manner identical to the one used with the SiC particulate composite. This material required 110 min to densify. The density was 99% of theoretical with K_{IC} = 3.9 ± 0.1 MPa•m$^{1/2}$ and MOR = 684 ± 25 MPa at room temperature. Limited testing at 1200°C showed that reducing the amount of sintering aids did significantly improve the resistance to creep at 206.7 MPa (30 ksi) (Figure 8 and Table 8). The steady state strain rate of the AY6 + 30 v/o Si_3N_4 monolith was 605 less than that of the baseline AY6 material. These data also serve to more dramatically illustrate the effect of dispersoid shape on the creep rate of Si_3N_4-based composites. Although the resistance to creep of the matrix phase of the composites increased when the amount of sintering aids was reduced, this was detrimentally offset by replacing 30 v/o of the small acicular Si_3N_4 grains with equiaxed large (8 μm) SiC particles. Substituting larger (≈ 2 μm equivalent diameter) acicular SiC whiskers for 30 v/o of the smaller (0.3 μm equivalent diameter) acicular β-Si_3N_4 grains further increases the material's resistance to creep at 1200°C.

These data show that the addition of SiC whiskers to a (Si_3N_4 + 6 w/o Y_2O_3 + 1.5 w/o Al_2O_3) composition results in a composite ceramic body with substantially increased resistance to creep at 1200°C in air in the stress range 68.9 to 275.6 MPa.

The reduced content of sintering aid in the composites and the addition of acicular SiC dispersoids to the microstructure both contribute to the observed behavior. The whiskers appear to improve creep resistance by retarding grain boundary sliding. The substitution of equiaxed dispersoids for acicular matrix grains in silicon nitride ceramics containing intergranular glass phases can detrimentally affect time-dependent properties at elevated temperature.

References

1. R.D. Nixon, et al., "Deformation Behavior of SiC Whisker-Reinforced Si_3N_4," *Mat. Res. Soc. Symp. Proc. 78*, 78, 295-302 (1987).

2. D.A. Koester, et al., "High Temperature Creep of SiC Whisker-Reinforced Ceramics," *Proc. Int. Conf. on Whisker and Fiber-Toughened Ceramics, ASM* (in print).

Status of Milestones

Program execution is on schedule.

Communications/Visits/Travel

6/6-9/88 - S.T.Buljan attended a meeting on Whiskers and Fiber-Toughened Ceramics at Oak Ridge National Laboratories, Oak Ridge, TN and presented a paper entitled "Microstructure and Fracture Toughness of Si_3N_4 Composites."

9/6-8/88 - J.G. Baldoni visited S. Wiederhorn (National Bureau of Standards) and R.F. Davis North Carolina State University) regarding testing of composites.

10/18/88 - T.A. Nolan and K.L. More (Oak Ridge National Laboratories) visited GTEL to discuss TEM evaluation of Si_3N_4-based composites.

Problems Encountered

None.

Publications

S.T. Buljan, J.G. Baldoni, M.L. Huckabee and G. Zilberstein, "Microstructure and Fracture Toughness of Si_3N_4 Composites," *Proc. Intl. Conf. on Whisker and Fiber-Toughened Ceramics*, ASM, 1988 (in print).

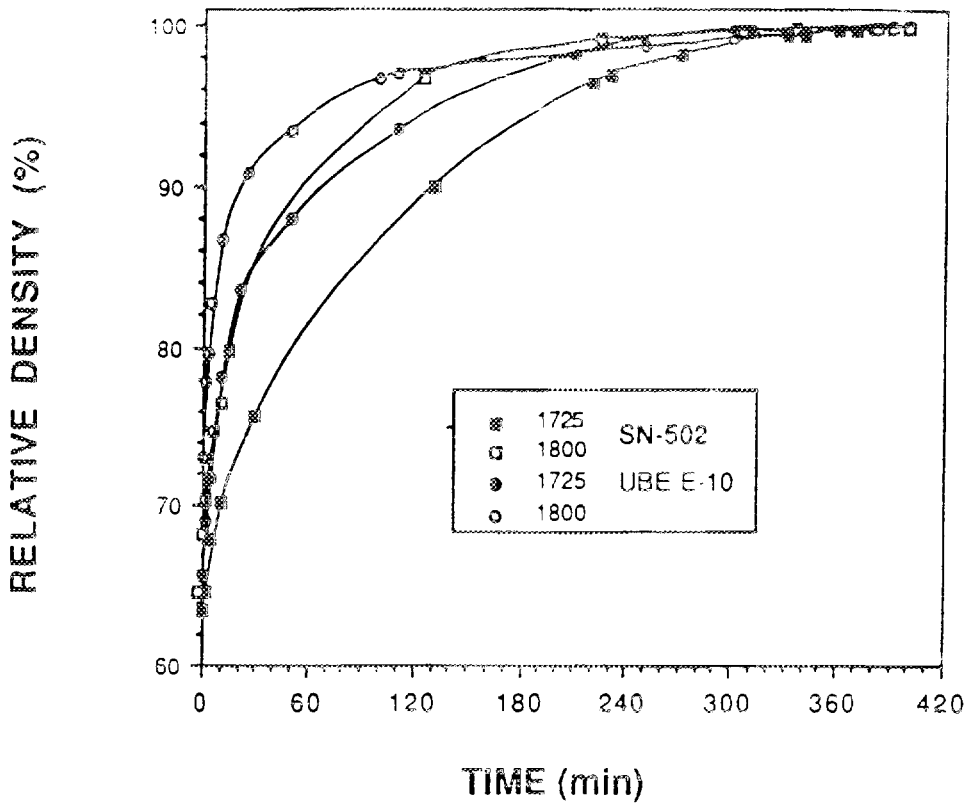

Figure 1: Relative Density vs Time for Hot-Pressed AY6 + 30 v/o SiC Whiskers at 1725°C and 1800°C Containing SN502 and Ube E-10 Si_3N_4

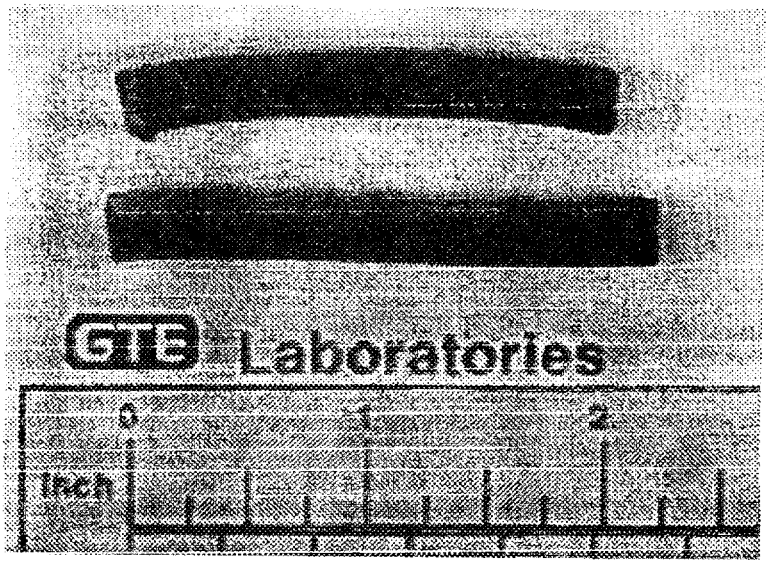

Figure 2: Injection-Molded and HIPed Test Bars Made Using (1987) Mold Containing Two Levels of Solids Loading. Bottom Bar Shows 1988 Material with Higher Solids Loading.

Figure 3: As-HIPed Composite Test Bars Produced by Different Gate Configurationss Shown from Top to Bottom: (2), (1), (3), and (4). Numbers Refer to Table 6.

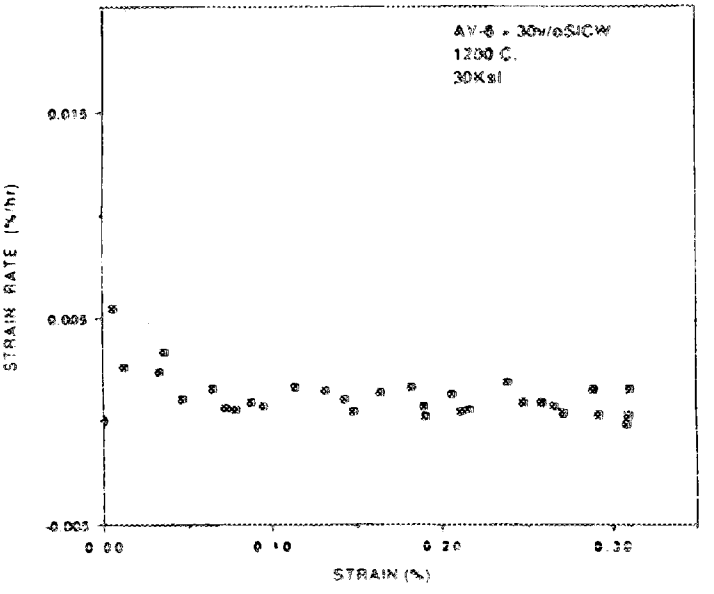

Figure 4: Effect of Increasing Strain on the Strain Rate of Silicon Nitride Ceramics

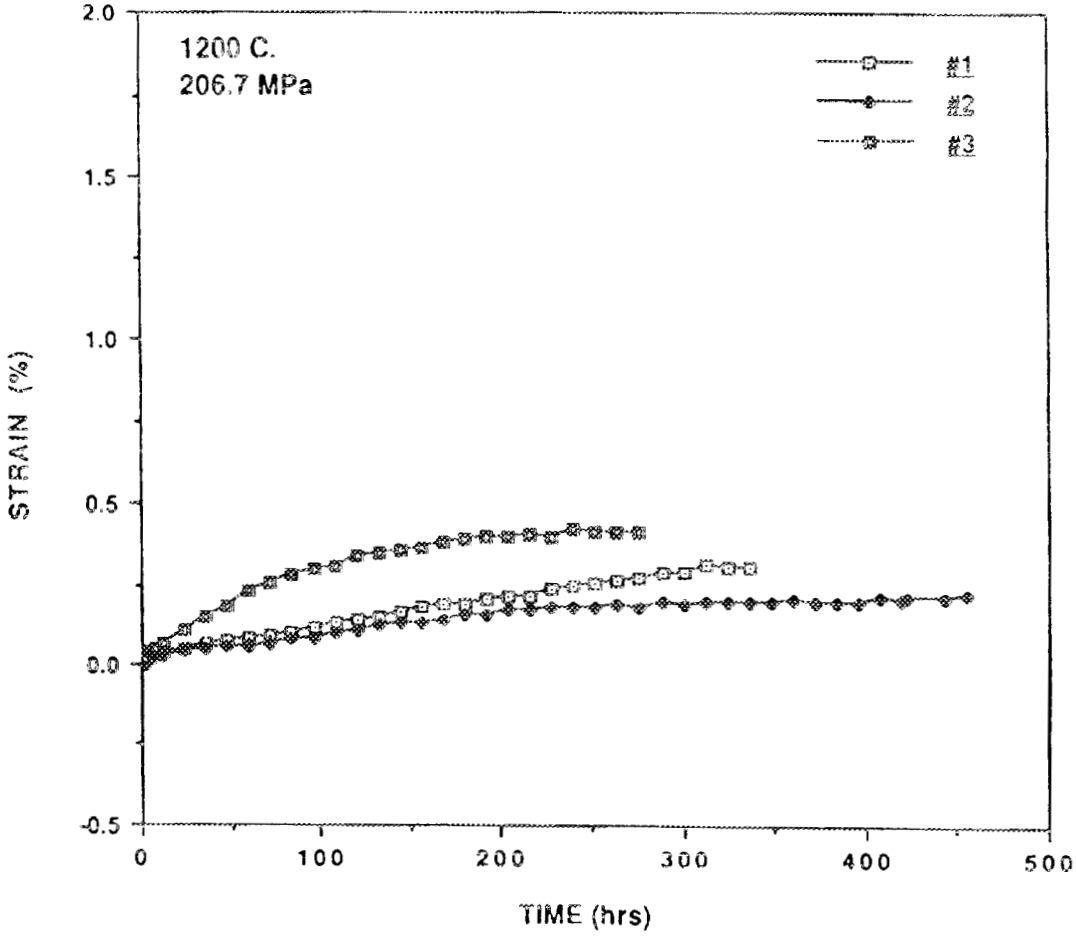

Figure 5: Reproducibility of Creep Data

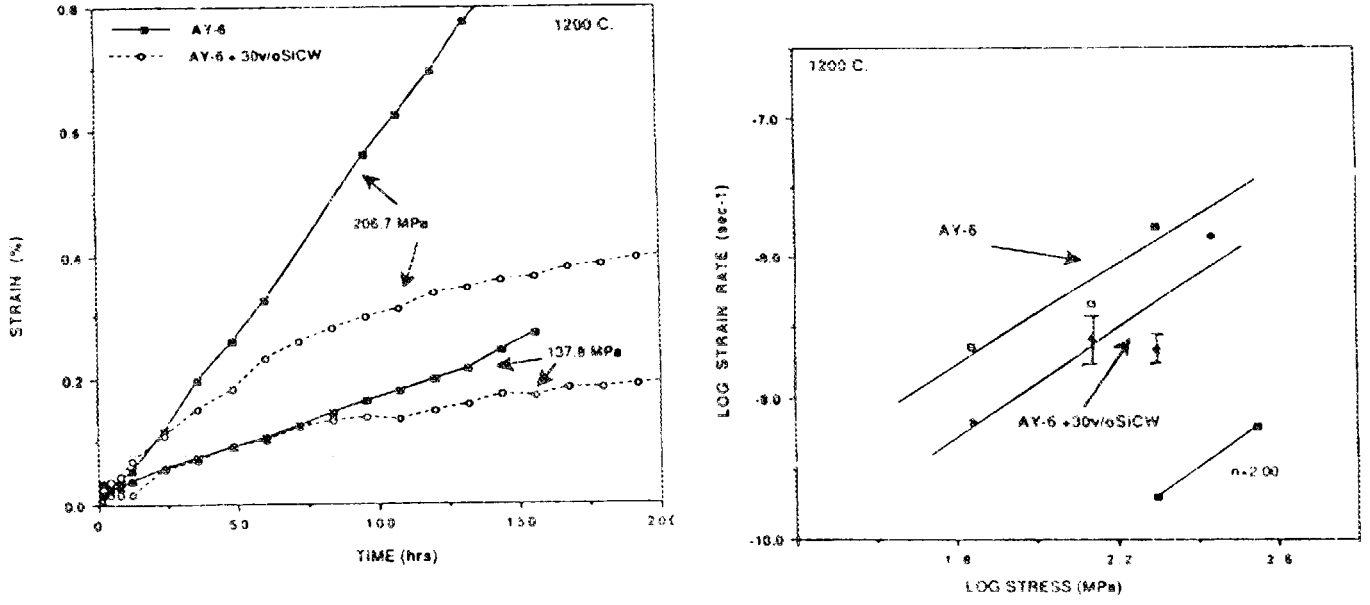

(a) (b)

Figure 6: (a) Strain-Time Data and (b) Strain Rate Data as a Function of Stress of Monolithic AY6 and an AY6-30 v/o SiC Whisker Composite at 1200°C

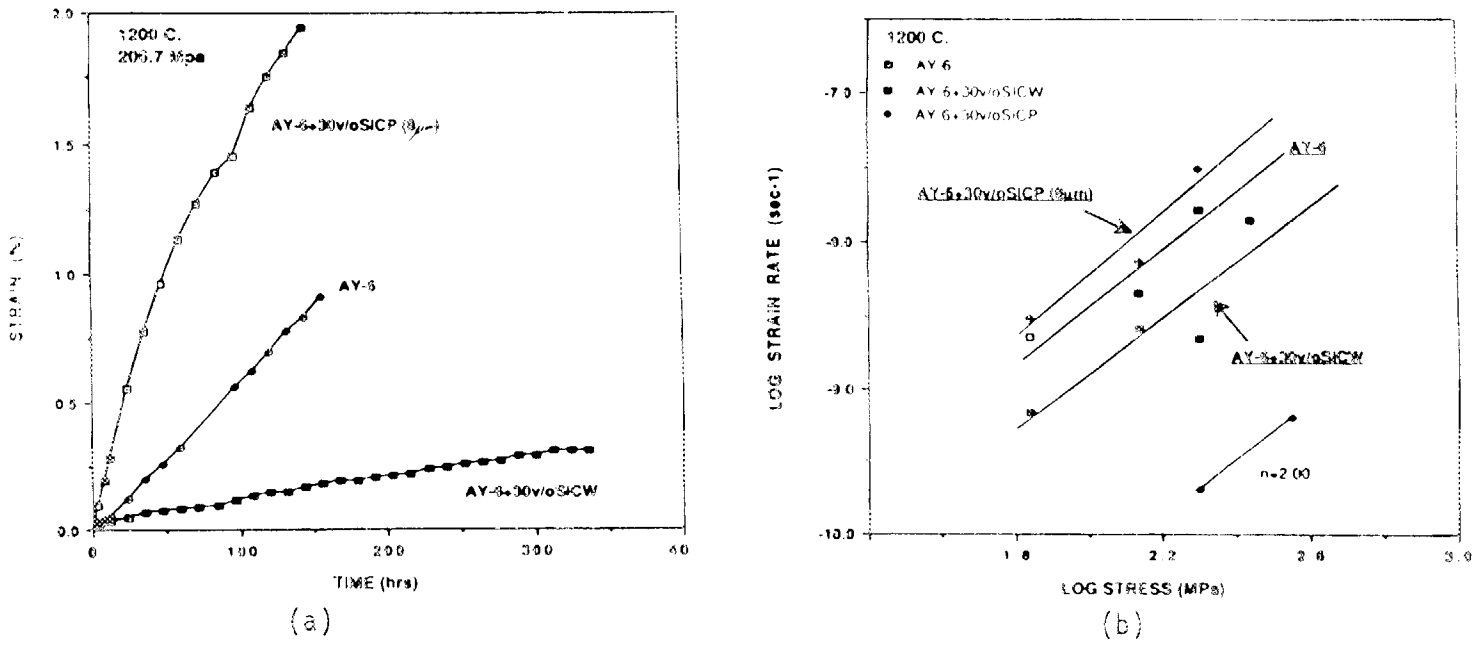

Figure 7: Effect of SiC Dispersoid Morphology on (a) Strain and (b) Strain Rate

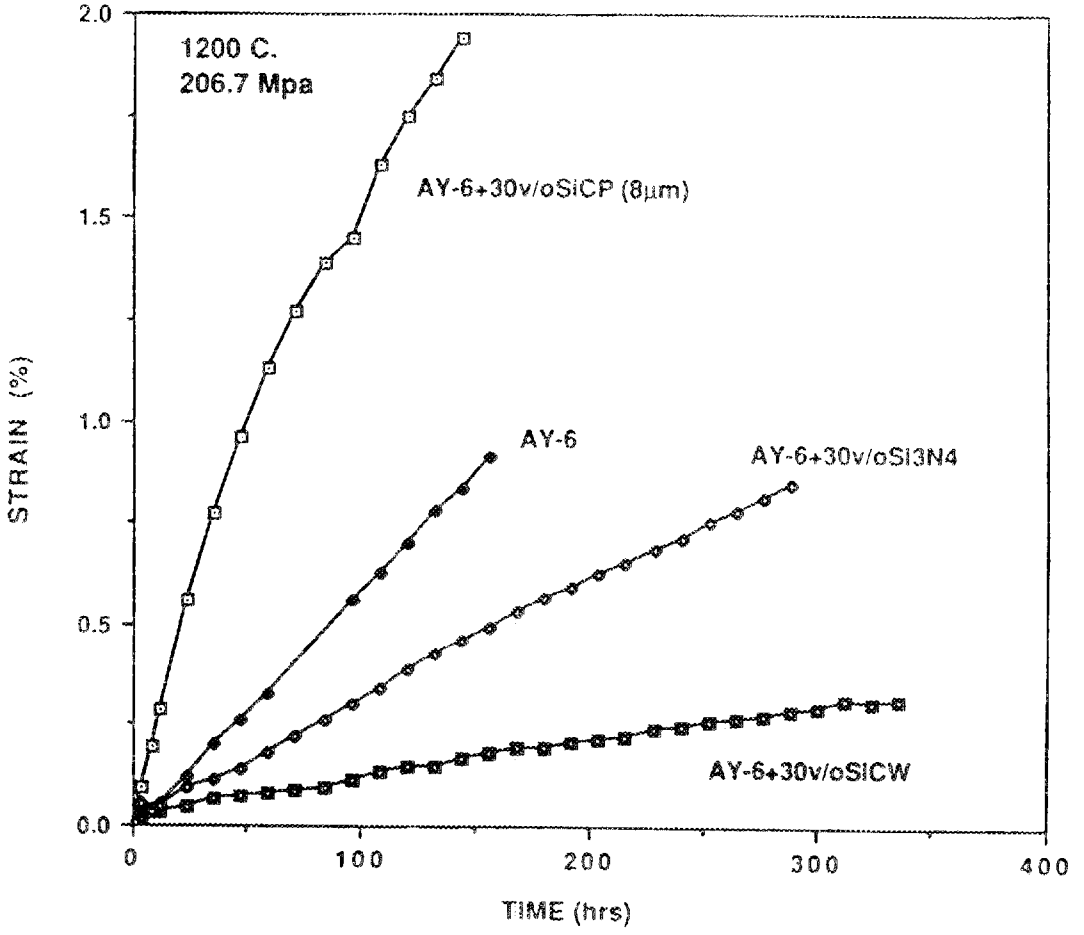

Figure 8: Strain-Time Data of Silicon Nitride Ceramics

Development of Toughened Si_3N_4 Composites by Glass Encapsulated Hot Isostatic Pressure

Norman D. Corbin, Craig A. Willkens, Vimal K. Pujari, Guilio A. Rossi, Jeffrey S. Hansen, Kerry N. Siebein, and Chow Ling Chang (Norton Company)

Objective/scope

This two year program is to develop fully dense Si_3N_4 matrix SiC whisker composites which show enhanced properties over monolithic Si_3N_4 materials. Materials will be processed using an RBSN approach followed by high pressure glass encapsulation HIPing. The primary goal is to develop a composite with a fracture toughness >10 MPa(m)$^{.5}$ and capable of operating up to 1400°C.

Studies will be conducted to tailor the whisker/matrix interface and determine the optimum whisker morphology for fracture toughness improvements. The effect of forming on whisker orientation, fracture toughness, and shape distortion will also be addressed.

1.0 EVALUATION PROCEDURES

Procedures for analytical evaluations and mechanical property determinations have previously been described in detail[1]. Flexural strength is determined using the U.S. Army recommended procedures for a cross-section of 3x4mm[2]. Fracture toughness is determined by either an indentation method[3] or a controlled flaw method[4] depending on material availability.

As previously detailed[5] a technique was developed for determining the surface composition of individual SiC whiskers by Scanning Auger Microanalysis (SAM). This method was used to evaluate additional whisker materials.

A Chevron notch four point bend specimen will be used for determining the high temperature plane strain fracture toughness of the composite materials. This specimen type was chosen because no precracking is required, the test load passes through a maximum at a constant material independent crack length/width ratio for a specific geometry and no post test crack measurement is required. [6] The four point bend specimen was chosen

because specimen alignment is not critical since a constant moment is applied between the upper load points. Fracture toughness for the four point chevron notch specimen is calculated by:

$$K_{IC} = P_{max} \ (Y^* \ / \ B \ W^{.5})$$

where P_{max} is the maximum test load, B is the specimen width, W is the specimen thickness and Y* is dependent on the specimen geometry and the manner of specimen loading. The value of Y* is calculated using the strength through crack assumption (STCA) [7]:

$$Y^* = (2.92+4.52a_o+10.14a_o^2)*((S_1-S_2/W)((a_1-a_o)/(1-a_o))^6$$

where the variables are presented in Fig. 1.

Initial data was collected on NC-132 to qualify the test procedure for using bars with 3mm x 4mm cross-sections. Tests were performed at room temperature on an Instron 4206 unit with a cross head speed of 0.13 mm/min. The test fixture was SiC with a 5mm top span and 4 mm lower span. Using specimens with a 40.9° notch resulted in load deflection curves exhibiting non-linear behavior and noncatastrophic failure. The resulting fracture toughness was 4.74 ± .06 MPa $(m)^{.5}$ which is the same (4.8 MPa $(m)^{.5}$) as that reported in the literature by a double torsion technique.[8] High temperature evaluation with this geometry are planned. Room temperature toughness evaluation of composites will be initiated using the described procedure.

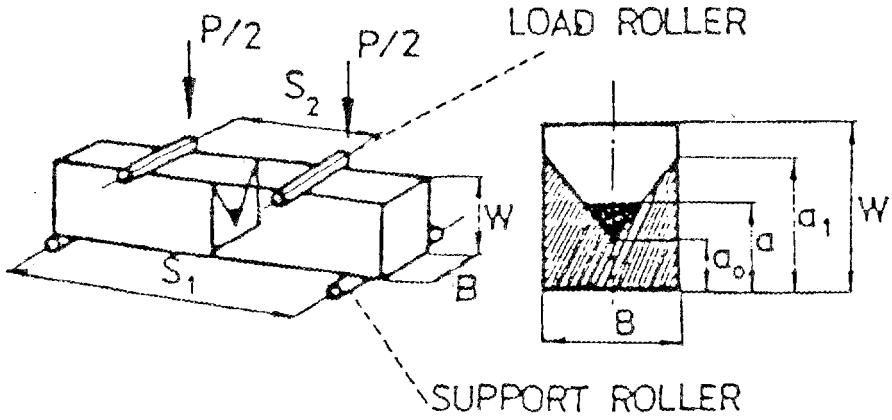

Fig. 1. Geometry, fixings, and loadings of a chevron-notch four-point-bend specimen: $\alpha = a/W$; $\alpha_0 = a_0/W$; $\alpha_1 = a_1/W$. (Ref #22)

2.0 REINFORCEMENTS

Whisker Sources - New whiskers received and under evaluation this period were a Tateho[9] 0.8 um diameter experimental grade (see Aspect Ratio), C-Axis, Inc.[10], Tokai carbon-coated, and Tokai[11] 1.0 um. Advanced Composite Materials (ACMC)[12] and C-coated American Matrix, Inc.[13] whiskers were reevaluated in a Si_3N_4 powder matrix to preserve the C-rich surface (see Section 4.0). Reportedly, next year Tateho will not make their Japanese produced whiskers available in the United States.

Aspect Ratio - Tateho SiC whiskers with different diameters have been evaluated under similar processing conditions (isotropic, unmodified interface). The results, shown in Table 1, indicate very little influence of this whisker diameter range (0.4-0.8 micron) on toughness for the matrix system studied.

Table 1: Whisker diameter effect on composite fracture toughness.

v/o Tateho Reinforcement	Average Diameter(2)	Toughness(3) MPa $\sqrt{m}$	Sample Code
0%		4.6 ± .2	2139-38
20%	0.4 um	5.1 ± .1	2138-38
30%	0.4 um	5.2 ± .1	2122-32
20%	0.6 um	5.4 ± .3	2073-22
30%	0.8 um	4.9 ± .1	2176-44

1) HIP RBSN (4% Y_2O_3) as matrix
2) Per product data sheet from Tateho
3) Control flaw by Chantikul method

3.0 FORMING

Injection Molding/Extrusion - Injection molding and extrusion processes have been developed for coated and uncoated whiskers in either silicon nitride powder or silicon powder.

For the extrusion process, barrel temperature was found to exert considerable influence upon extrusion quality. Barrel and die temperature requirements for extrusion are approximately 15°C lower than that of injection molding. Based upon this information void free rods have been extruded. High extrusion temperature caused considerable bubble formation. Attempts are also underway to extrude rods with rectangular (3mm x 4mm final dimensions) cross-section. These rods will be tested as-HIPed for fracture toughness determination. If successful, this approach will eliminate the need for machining the round bars into rectangular test specimens.

Microstructures of an extruded composite made with American Matrix SiC whiskers are shown in Fig. 2 and 3. The whisker distribution is very uniform and there is a significant degree of whisker orientation. This type of microstructure results in improved sensitivity for studying interface/coating effects on toughness.

A direct comparison was made of microstructures produced by injection molding rectangular test bars and extruding 8mm diameter rods, using 30% ACMC SiC-w/ Si_3N_4 composites. Both produce highly oriented microstructures. The alignment of whiskers in the injection molded bars (Fig. 4) were more uniform through the cross-section as compared to the extruded rods. Extruded bars showed islands of swirled regions in the cross-section. This is explained by the higher back-pressure and stepped changes in cross-section (velocity) that occur for injection molding, which tend to force a more uniform whisker alignment.

Orientation vs Toughness - Injection molded and extruded composites were used to study the effect of whisker orientation on fracture toughness. For the 30% ACMC/ Si_3N_4 material, indentation toughness values (Table 2) were measured parallel (3.5 $MPa(m)^{.5}$) and perpendicular (6.0 $MPa(m)^{.5}$) to the whisker axis (flow direction) . The indent value of 6.0 is the highest obtained in this study. Fig. 5 shows the effect of orientation on toughness as measured using the controlled flaw technique. The

Figure 2: Extruded 20 v/o American Matrix SiC-w/Si3N4, parallel to rod length (flow direction).

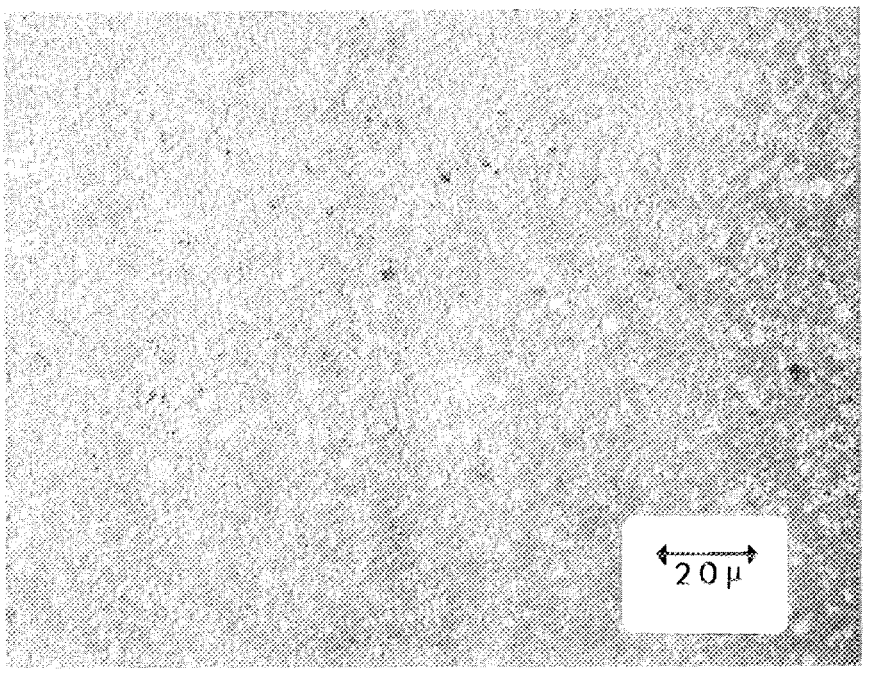

Figure 3: Extruded 20 v/o American Matrix SiC-w/Si3N4, cross-section of rod.

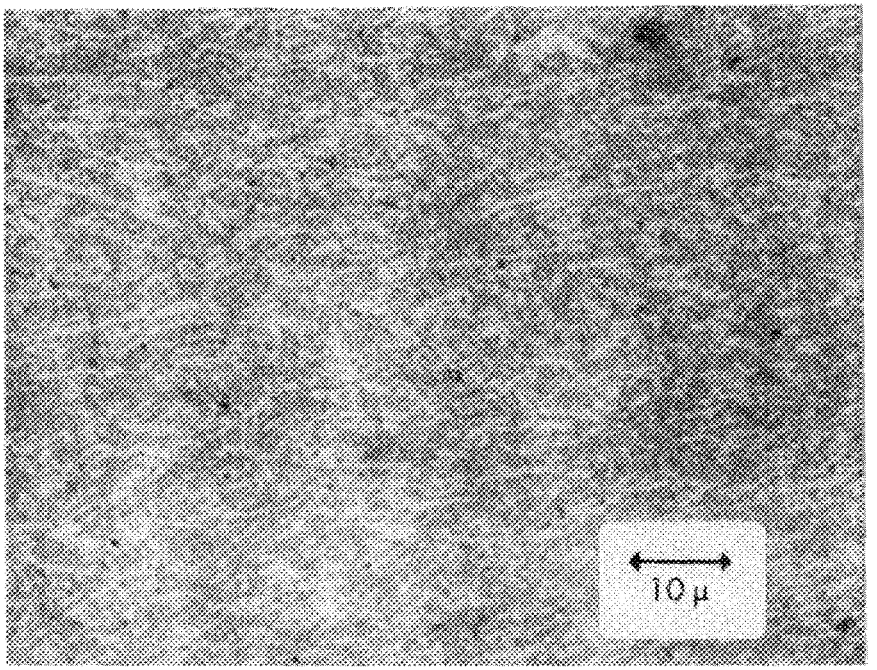

Figure 4: Injection molded 30 v/o ACMC SiC-w/Si3N4, parallel to bar length (flow direction).

injection molded bars had a value of 6.9 MPa(m)$^{.5}$, again the highest value obtained using the controlled flaw technique.

A Si_3N_4 composite reinforced with carbon coated American Matrix whiskers has also been used to study the effect of whisker orientation. The CIPed material has a controlled flaw toughness of 6.4 MPa (m)$^{.5}$, the highest toughness obtained on composites with randomly oriented whiskers to date. Indent toughness values (Table 2) were measured in three directions for an extruded rod.

Table 2: Effect of whisker orientation on fracture toughness.

Sample	Toughness $MPa\sqrt{m}$ (1)		
Angle between crack plane and whisker axis	0^0	0^0	90^0
Surface polish (see below)	A	B	B
30% ACMC SiC-w/ Si_3N_4 (IM)2	-	3.5	6.0
30% ACMC SiC-w/ Si3N4 (EX)	-	3.7	5.6
20% SiC coated American Matrix SiC-w/Si_3N_4 (EX)	4.6	4.3	4.9
20% Uncoated Tateho T44 SiC-w/Si_3N_4 (EX)	3.8	3.6	4.4

(1) Indentation by Anstis method
(IM) Injection molded bar
(EX) Extruded Rod

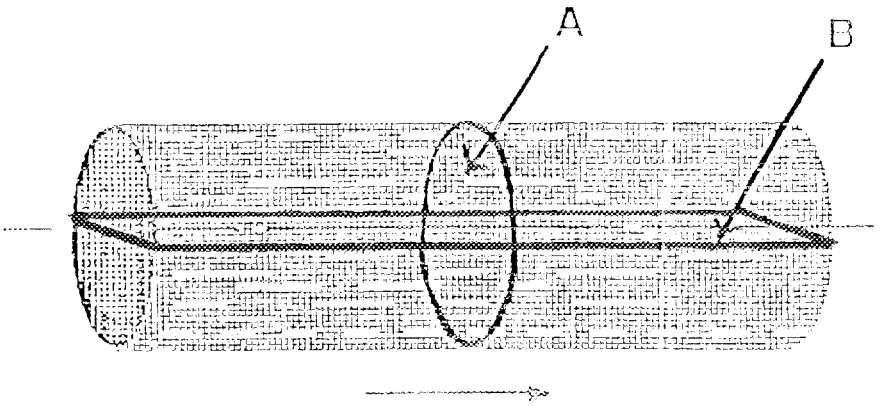

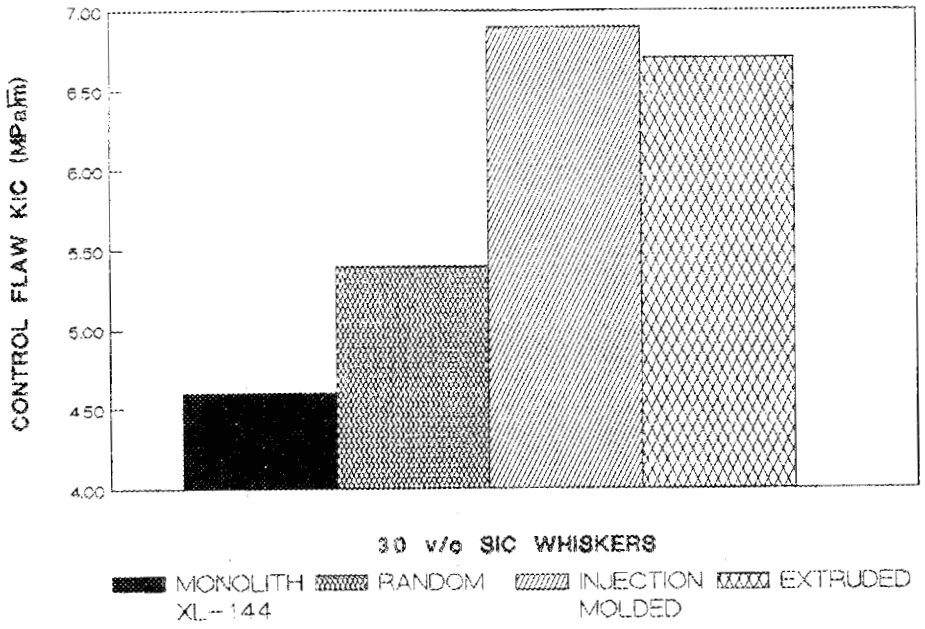

Figure 5: Effect of whisker orientation on fracture toughness. 30% ACMC SiC-w/Si3N4.

Packing/Distortion Issues - Initial efforts to minimize distortion during densification are concentrated on differential shrinkage by maximizing packing density. Mixtures made with chemically derived silicon nitride powder[14] showed the highest packing density (58%) and in turn required minimum binder to achieve a moldable mix. This packing density was significantly higher than that achieved previously (51-55%) using a nitrided silicon nitride powder[15]. Higher packing density is felt to be the result of a greater whisker/powder size ratio due to the fine, narrow size distribution of the chemically derived powder. Larger diameter whiskers also contributed to a higher packing density.

These powder/whisker packing results are being factored into our effort on using an SRBSN route, which is expected to further increase pre-HIP density and minimize distortion. Silicon powder was milled and then classified to produce a fine, (D50=0.4um) narrow size distribution. Combined with 20 v/o American Matrix whiskers, this blend has produced our highest CIP'd (random orientation) packing density (57%). After nitriding, the density would increase to 68% of theoretical, with a linear shrinkage on HIPing of 12% compared to 18% prior to this work. The forming process used also has a significant effect. Slip casting and injection molding provide approximately 5% higher packing density than CIPing due to whisker orientation, improved dispersion and/or high shear rearrangement.

4.0 INTERFACE STUDIES

We have an effort to increase the fracture toughness of whisker reinforced materials by modifying the matrix/whisker interface. Currently three interface compositions are under evaluation: yttria-silica, carbon, and boron nitride. The results will be discussed separately.

Yttria-Silica - Materials under development in this program use Y_2O_3 and SiO_2 as sintering aids. During densification the sintering aids react and segregate to grain boundaries, the matrix/SiC interface and triple points. Upon cooling they tend to crystallize in the triple points and remain amorphous at the grain boundaries. In Fig. 6 an amorphous interface ~2 nm thick can be observed between a SiC whisker and a Si_3N_4 grain. Fracture toughness of composite materials with this characteristic tends to be ~5.0 MPa(m)$^{.5}$. TEM evaluations on these materials have shown that debonding and crack bridging can occur (Fig. 7) even with the thin interface present.[16] The microstructure just described are typical for a composite with 4 w/o Y_2O_3 in the matrix and the SiO_2 content dependent on the oxygen content of the Si_3N_4 powders and/or SiC whiskers.

Previous results had shown that fracture toughness is effected by the bulk oxygen content of composites [5]. To further address these results, a study was conducted to determine the effect of sintering aid composition (Y_2O_3:SiO_2) and quantity (Y_2O_3+SiO_2) on composite fracture toughness. Table 3 lists the compositions evaluated and the resulting fracture toughness values. An improvement of 15% was obtained over standard materials by modifying the matrix composition.

To increase the SiO_2 content at the interface silica was applied to the surface of whiskers by two different approaches. A solution coating method was developed to precipitate fine SiO_2 onto the whisker surfaces.[5] The other method involves partial oxidation to form a SiO_2 surface on the whiskers. Using TGA data an oxidation treatment was selected to result in an ~.05um thick oxide coating. Composites prepared with the oxidized whiskers were evaluated for fracture toughness. Results show its toughness to be 10% higher than when whiskers are used in the as-received condition.

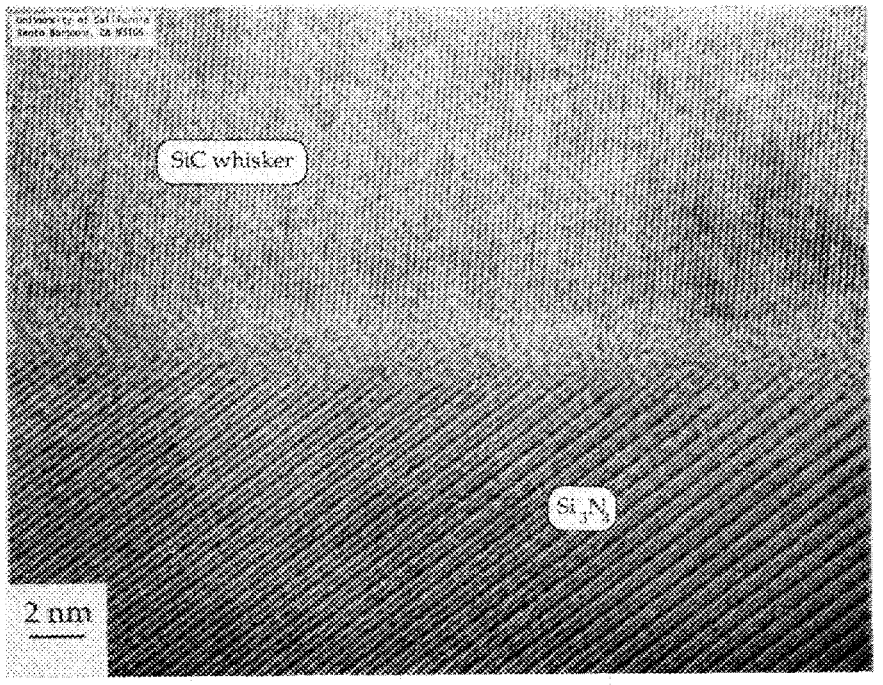

Figure 6: TEM lattice image of interface in a SiC-w/Si3N4 composite. Courtesy of M.Ruhle and J.Campbell. (16)

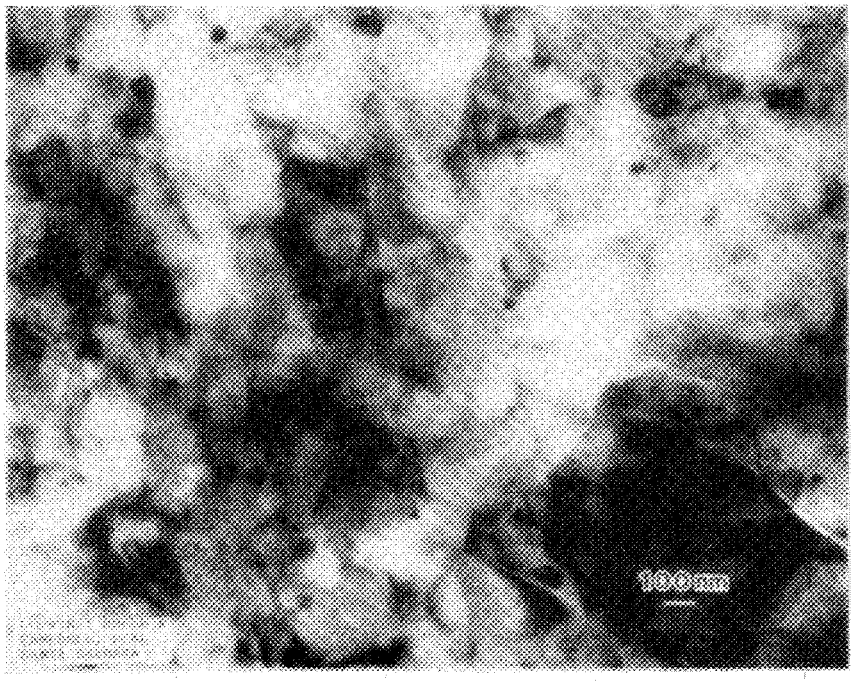

Figure 7: TEM of crack path in a SiC-w/Si3N4 composite showing debonding and bridging. Courtesy of M.Ruhle and J.Campbell.(16)

Table 3: Influence of sintering aid content and composition on toughness.

v/o SiC(1)	Matrix Composition (2) Molar % $Y_2O_3 + SiO_2$	Molar Ratio SiO_2/Y_2O_3	K_{IC}(3)	% Δ (4)	SAMPLE CODE
30	50	9:1	4.4 ± .5	-15.4	2166 #40
30	55	2.7:1	4.1	-21.2	2170 #40
30	55	1.2:1	5.4 ± .3	+3.8	2168 #40
20	37	17.5:1	5.6 ± .1	+7.8	2097 #27
20	27	12.5:1	6.0 ± .1	+15.4	2096 #27
20	36	2.6:1	5.8 ± .5	+11.5	2126 #32
30	8.9	2.6:1	5.2 ± .1	-	7x014(5)

1) Tateho T44 whisker
2) Si_3N_4 powder used
3) Control flaw by Chanikul method
4) % change in toughness from standard 4 w/o Y_2O_3 material
5) SRBSN matrix

Carbon - It has been demonstrated that SiC whiskers with carbon rich surfaces improve the fracture toughness of alumina[17] and spinel[18] matrix composites. Whiskers with thin (50-100 Å) carbon surfaces are currently available from several manufacturers. Results utilizing these materials to reinforce Si_3N_4 are summarized below.

Whiskers manufactured by Advanced Composite Materials Corporation (ACMC,[12]) were evaluated for surface composition by Auger. As shown in Fig. 8 this material has a pure carbon surface approximately 1600 Å thick. Composites were prepared with a loading of 30 v/o SiC and Si_3N_4 powders. Fracture toughness results for materials with randomly oriented whisker are given in Table 4.

Carbon coated whiskers are also available from American Matrix Inc. (AMI[13]). Analysis of the as-received materials for surface composition are underway. Composites were prepared by blending with Si_3N_4 and the sintering aids for a whisker loading of 20 v/o. Its fracture toughness of 6.5 ± .2 MPa(m)$^{.5}$ (Table 4) is the highest value obtained in our work to date for composites with randomly oriented whiskers. Transmission electron

microscopy was conducted in a similarly prepared composite to determine if the carbon coating remained on the whiskers during processing of the composite. In the composite most of the whiskers had a discontinuous, crystalline coating on their surface. The coating morphology was thin and layered, thickness ranged from approximately 10 nm to 30 nm. The composition and crystal structure of the coating could not be determine due to its thinness, it is assumed to be carbon. The whisker matrix interface is presented in Fig. 9 illustrating the morphology of the crystalline film on the whiskers. This coating is similar to the graphitized film observed by M. Yamamoto et al[18] in a spinel matrix composite reinforced with an initially amorphous carbon coated silicon carbide whisker.

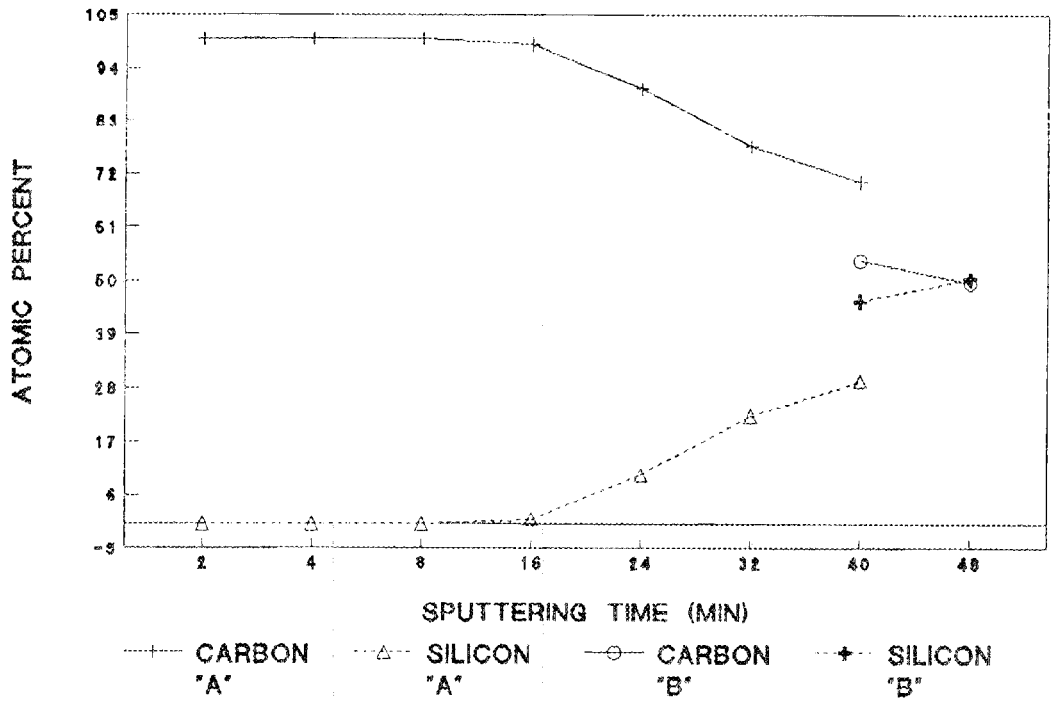

Figure 8: Auger analysis of ACMC SiC whisker.

Table 4: Fracture toughness results on composites with modified interfaces.

Reinforcement	K_{IC} Control Flaw	Specimen Code
30 v/o ACMC as-rec.	5.4 ± .1 (R)	3054 #50
20 v/o AMI, C-coated	6.5 ± .2 (R)	2148 #39
20 v/o AMI, oxidized	5.9 ± .7 (H)	2194IM #52
30 v/o ACMC as-rec.	6.9 ± .2 (H)	3054IM #18
20 v/o AMI as-rec.	5.3 ± .3 (H)	2146IM #48
30 v/o Tateho, BN coated	4.3 ± .2 (H)	2175IM #48
20 v/o AMI, SiO_2 by Solution	TBD	2195IM #53
30 v/o AMI, BN coated	TBD	2188IM #53

H = High toughness direction, injection molded bar
R = Randomly oriented whiskers
TBD = To be determined

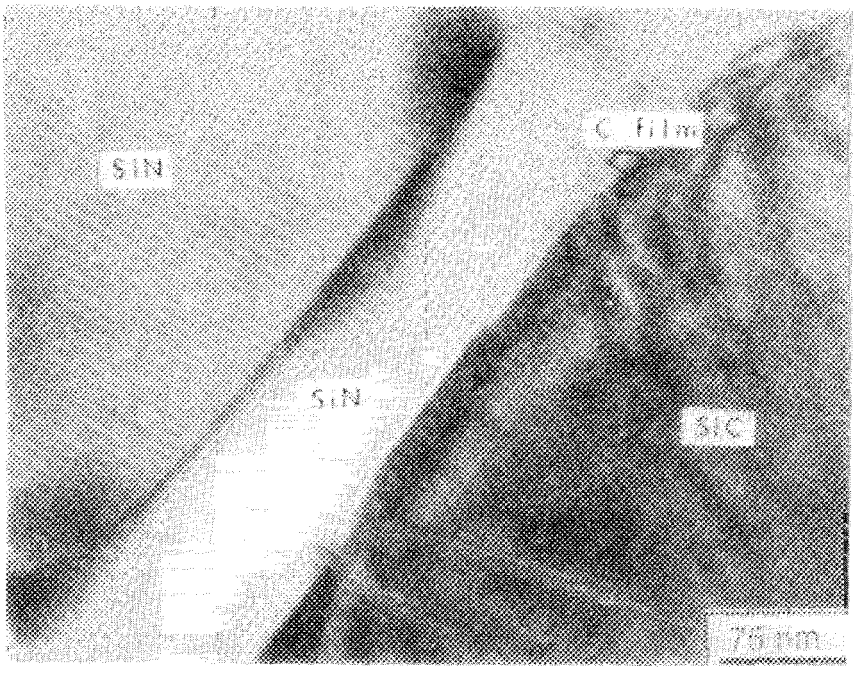

Figure 9: TEM of carbon coated American Matrix SiC-w/Si3N4 composite showing intact carbon coating after HIP.

Boron Nitride - Boron nitride has been shown to act as a debonding layer in fiber reinforced composites[19]. Considering this, we are evaluating it as a debonding layer in our material. This effort includes developing methods to apply a thin layer of stoichiometric BN to SiC whisker surfaces. Coating work is being conducted by a vendor[20] and within Norton Company.

The analytical results on the whiskers coated by the vendor were previously described[5]. Fracture toughness results on composites reinforced with these coated whiskers are listed in Table 4. The fracture toughness, 4.3 $MPa(m)^{.5}$, is equivalent to monolith material. It is expected that reaction of the BN layer has resulted in its elimination. Earlier results[1] had shown this to occur in similar materials.

Norton Company's CVD effort consisted of modifying their current fluidized bed reactor for the deposition of BN. Initial work used 100um SiC grit. Table 5 lists Auger analysis of the coating. The stoichiometry is ~1:1 with some carbon and oxygen also detected. X-ray diffraction shows the coating to be microcrystalline and matches well with the hexagonal BN structure (PDF#34-421). The coating was also examined using TEM. The specimen was prepared by immersing a carbon coated copper grid in the powder. Using this technique only the smaller silicon carbide particles, typically less than 1 micron stuck to the grid. Analysis showed the particles are coated with a layered film. The thickness of the coating varied from area to area on a particle, typical coating thickness ranged from 20 nm to 140 nm. A typical BN coated silicon carbide particle is presented in Fig. 10. The crystallinity of the film was not determined because the coating was very thin and the particles very thick.

With the successful deposition of BN, the CVD coating apparatus was redesigned for coating whiskers using a stationary bed method. Whiskers from initial coating runs were evaluated for coating composition by Auger. The results revealed that a significant quantity of carbon contamination had occurred and only a small proportion of the whiskers were coated. As a result, additional processing and equipment modifications were made to increase the quantity of the whiskers coated and coating thickness. As shown in Fig. 11, whiskers coated by this modified process have a thick coating (est. >0.5 um). Hexagonal BN was clearly evidenced by X-ray diffraction. Plans are to evaluate this material by Auger and incorporate into Si_3N_4 for determining the effect of the coating on composite fracture toughness.

Table 5: Auger analysis of CVD boron nitride coated SiC grit prepared at Norton Company.

		Grit "B"	Grit "C"	Grit "D"
Atomic percent	Boron	42.4 } 1.0	42.2 } 1.2	45.0 } 1.1
	Nitrogen	43.0 }	36.0 }	41.3 }
	Carbon	10.7	13.0	6.9
	Oxygen	3.9	8.9	6.9

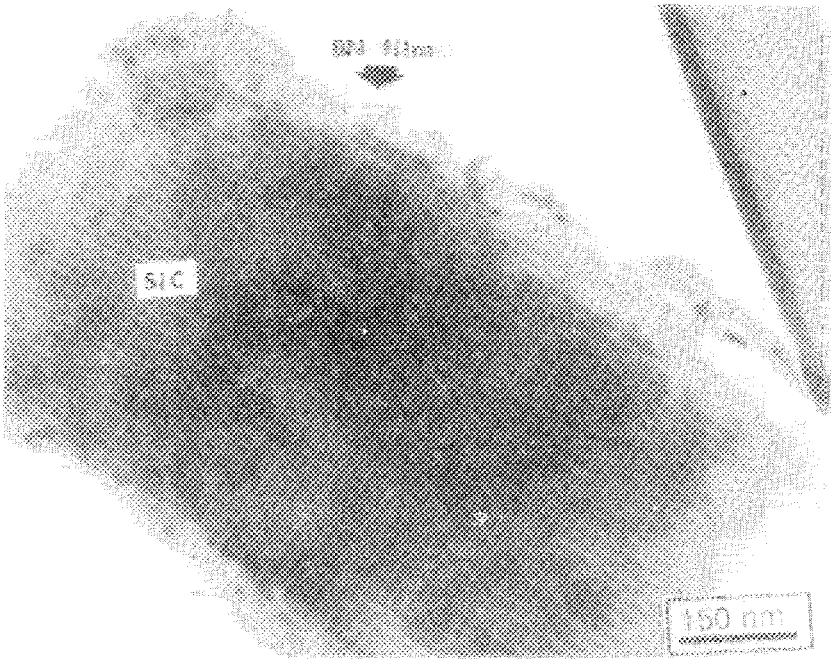

Figure 10: TEM of fluidized bed CVD boron nitride coated SiC grit prepared at Norton Company.

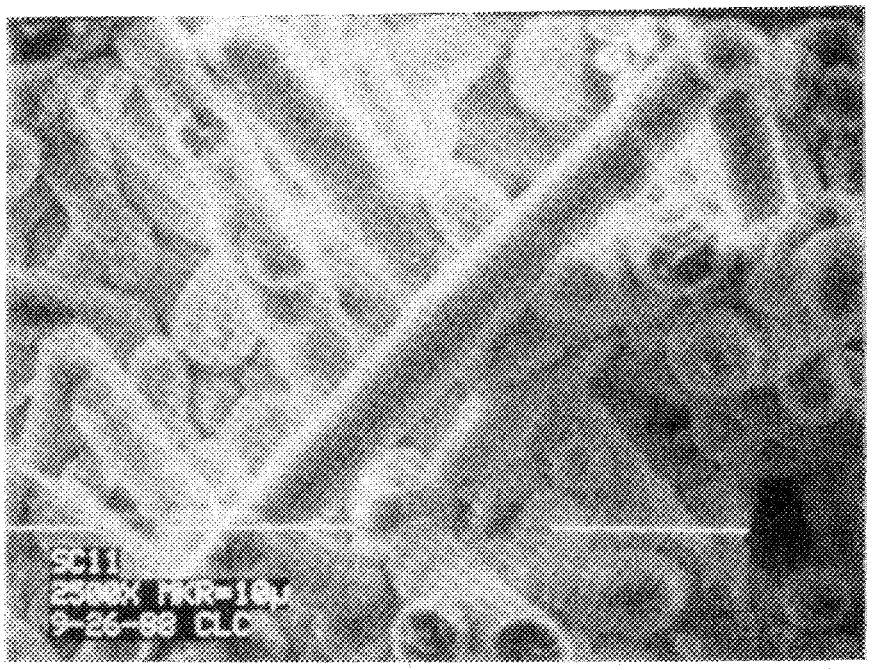

Figure 11: SEM of CVD boron nitride coated AMI SiC whiskers prepared at Norton Company

5.0 PROPERTY PROGRESS

Composites which show promise from the screening studies will be prepared into large batches to allow for extensive property evaluations. Of particular emphasis are Weibull modulus, fracture toughness to 1400°C, oxidation resistance, and stress rupture behavior at 1400°C. Four materials were previously prepared; the data is reported elsewhere.[1,5]

During the past six months several materials which showed promising results during small batch screening were prepared into large batches. At this time property determinations are just initiating. One of these materials was processed to improve room temperature strength. All

processing steps were scrutinized to ensure that flaw sizes and impurities were kept to a minimum. Table 6 shows the results as compared to previous materials. The strength of the monolith was significantly improved (143 ksi). Composite strength was slightly improved (123 ksi) but was lower than the monolith for the first time. Although the composite materials have different whisker loading, earlier work had reported no difference in strength or toughness with whisker loadings of 20 or 30 v/o%.(1) Failure origin analysis is ongoing, but it is believed that SiC particulates in the whiskers are still limiting composite strength. Another material previously discussed[5] was supplied to NASA for further testing. Their high temperature fracture toughness data showed the monolith and composite increases to ~7.0 MPa(m)$^{.5}$ at 1000°C.

Table 6: Material property progress - RT strength.

	RT Strength (Ksi)	% Improvement	Sample Code
Current Monolith	143 ± 3	49.0%	2154M-43
Past Monolith	96 ± 2	-	3X015
Current Composite 20% Tateho T44	123 ± 14	9.8%	2154C-43
Past Composite 30% Tateho T44	112 ± 8	-	7X014

(1) CIP/HIP RBSN (4% Y_2O_3)

6.0 SUMMARY

Program emphasis is now on interface modification to improve fracture toughness by debonding, bridging and pullout. The in-house CVD coatings of BN are promising in terms of thickness and stoichiometry. Carbon coatings continue to give high toughness values as compared to similar uncoated reinforcements (6.5 vs. 5.3 MPa (m)$^{.5}$, isotropic). The carbon coating can be retained through the HIPing step. Pullout is still limited indicating further room for toughness improvements. Chevron notch testing is being incorporated for high temperature toughness measurements.

Injection molding parameters have been established to achieve controlled orientation of the whiskers. Combined with C-coated whiskers, composites with aligned whiskers give toughness values of 6.9 $MPa(m)^{.5}$ by controlled flaw and 6.0 $MPa(m)^{.5}$ by indentation. Distortion is initially being addressed by incorporating features that will maximize packing density and minimize shrinkage.

References

1) N.D. Corbin and C.A. Willkens "Development of Toughened Si_3N_4 Composites by Glass Encapsulated Hot Isostatic Pressure Final Report", ORNL/SUB/86-95906/1.

2) MIL-STD-1942 (MR), Flexural Strengths of High Performance Ceramics at Ambient Temperature, November 21, (1983).

3) Antis, G., et al, Journal of the American Ceramic Society, Vol. 64, #9, p.533-538, Sept. 1981.

4) Chantikul, et al, Journal of the American Ceramic Society, Vol. 64, #9, p.539-543, Sept. 1981.

5) N.D. Corbin et al, "Material Development in the Si_3N_4/SiC-w System using Glass Encapsulated HIP'ing - Phase II" Semi-annual report to ORNL, March 1988.

6) D. Munz, J.L. Shannon, R.T. Bubsey, Int J Fract, 16, (1980) PA RR137-RR142.

7) J.E. Srawley, B. Gross, Cracks and Fracture, STP 601, ASTM, Philadelphia (1976) PA 559-579.

8) A.G. Evans, S.M. Wiederhorn, J Mat Sci, 9 (1974) PA 270-278.

9) Tateho Chemical Industries, Hyogo-Ken JAPAN.

10) C-Axis Technology, Jonquiere, Quebec, CANADA.

11) Tokai Carbon Co. Ltd, JAPAN.

12) Advanced Composites Materials Corp., Greer, SC.

13) American Matrix Inc., Knoxville, TN

14) Ube Industries, Ltd., Tokyo, JAPAN.

15) KemaNord Industrikemi AB, Ljungaverk, Sweden.

16) Private Communication; Prof. M. Ruhle and G. Campbell, University of California - Santa Barbara.

17) T.N. Tiegs, et al, ORNL Report #CONF-860714-3.

18) Yamamoto et all., to be published in the Proceedings of the "ASM Conf. on Composites," Oak Ridge, TN, June 1988.

19) R.W. Rice, U.S. Patent #4,642,271.

20) Synterials, Herndon, VA.

21) Courtesy of N. Shaw, NASA Lewis Res Center, Cleveland, OH.

22) J. Joch et al, J. Am. Ceramic Society, 71[3] C154-C155 (1988).

Status of milestones

- All on schedule.

Publications

- None.

Fabrication of Si_3N_4 SiC Composites by Transient Liquid Phase Sintering

S. D. Nunn and T. Y. Tien (The University of Michigan)

Objective/scope

The goal of this project is to obtain dense silicon nitride composites containing silicon carbide whiskers by transient liquid phase sintering. The systems SiAlON, SiAlON-Garnet ($Y_3Al_5O_{12}$), and SiAlON-Cordierite ($Mg_2Al_4Si_5O_{18}$) were selected for this study. Mixtures of the starting materials form a sufficient amount of liquid to aid densification at the sintering temperatures. After sintering, the liquid can be crystallized by heat treatment.

Technical progress

Having demonstrated that liquid phase sintering techniques could be used to obtain high density Si_3N_4/SiC whisker composites containing 20 vol % whiskers,[1] efforts during this reporting period were concentrated on evaluating some of the properties of the sintered composites, comparing the effects of the different sintering aids, and preparing compositions with increased whisker loading and reduced sintering additives.

The effects of liquid phase sintering aid composition and heat treatment on the fracture toughness of Si_3N_4/SiC whisker composites was evaluated. Additionally, the effect of sinterability of varying the composite compositions was investigated. Finally, planar orientation of the SiC whiskers due to the processing method used to form the ceramic green body is reported.

Fracture toughness

The fracture toughness of composites consisting of a Beta-20 SiAlON matrix containing 20 vol.% SiC whiskers and 10 vol.% of either yttrium aluminum garnet ($Y_3Al_5O_{12}$, YAG) or cordierite ($Mg_2Al_4Si_5O_{18}$) was measured. The samples were sintered at 1850 C for one

hour, and half of the samples received an additional crystallization anneal at 1400 C for 20 hours.

The measurements were made using the indentation method at loads of 3, 4, and 5 kilograms. Five indentations were made at each load setting. The data were reduced using a computer program originally developed for analyzing the fracture toughness of high density silicon carbide.[2]

Compositional variations

To determine the effect of increased whisker loading on the sinterability of Si_3N_4/SiC composites, compositions with a Beta-20 SiAlON matrix containing 10 vol.% YAG and either 30 or 40 vol.% SiC whiskers were formulated. The samples were prepared by attrition milling the matrix and liquid-forming starting powders. The whiskers were then added and the slurry was pressure slip cast to form the green ceramics. After drying, the samples were compacted in a cold isostatic press and then placed in graphite crucibles for firing in a graphite resistance furnace. The samples were sintered at 1850-1950 C in a nitrogen atmosphere. A more detailed description of the processing procedure is given in the previous report.[1]

A new series of compositions was made to evaluate the effects of reducing the amount of sintering aid compared to previous compositions. Samples having a matrix consisting of Si_3N_4 plus 5 eq.% Al and 3 eq.% of either Y or Mg, and containing 0 to 30 wt.% SiC whiskers were prepared by the method described above. The samples were sintered at 1550 to 1950 C.

The raw material additions used to make the compositions which were compared are shown in Table 1. The bulk density and porosity for all of the compositions evaluated were determined using the Archimedes method.

SiC whisker orientation

To reveal SiC whisker orientation in the pressure slip cast (PSC) green bodies, x-ray diffraction patterns were obtained from two perpendicular surfaces of the specimens. The green ceramics formed by PSC are disk-shaped, with the thickness dimension of the disk being parallel to the PSC direction. The flat disk surface and a surface exposed by cutting through the thickness of the disk were used for x-ray analysis. Sintered ceramics were also evaluated.

Results and discussion

Fracture toughness

The measured values of fracture toughness for the sintered composites are shown in Table 2. These values compare quite favorably with those for hot pressed samples containing 20 vol.% SiC whiskers reported by Shalek et al.[3] using chevron notch bend test specimens (6.8 to 10 $MPa \cdot m^{1/2}$) and by Tiegs and Geer[4] using bend test specimens with indentation precracks on the tensile surface (4.8 to 9.1 $MPa \cdot m^{1/2}$).

The difference seen in the as-fired toughness values may be due to the slightly better sinterability of the YAG-containing samples compared to the cordierite samples. As shown in Table 3, the Y70/10/20 composition sintered at 1850 C has a lower detectable porosity level than the C70/10/20 composition.

The lower fracture toughness for the cordierite sample after annealing is probably due to an increase in the interfacial bond strength between the matrix and the whiskers. The YAG composition, however, showed an increase in fracture toughness after annealing. Yttrium aluminum garnet has a relatively high thermal expansion coefficient compared to silicon nitride and silicon carbide. If the liquid YAG phase coats the boundaries between the Si_3N_4 grains and the SiC whiskers, this thermal expansion mismatch may cause tensile stresses to develop at the interfaces upon cooling from high temperature. Such tensile stresses would result in weakened bonding between the whiskers and the matrix and allow increased energy absorbing interactions with an advancing crack tip.

Compositional variations

Some properties of the sintered composites which are related to the sinterability of the various compositions are listed in Table 3. For the Beta-20 SiAlON plus 10 vol.% YAG composites (Yxx/xx/xx in the table), increasing the whisker content from 20 to 30 vol.% required sintering at a higher temperature, but otherwise did not reduce sinterability. Compositions containing 40 vol.% whiskers, however, could not be densified.

Properties for the compositions consisting of Si_3N_4 plus 5 eq.% Al and 3 eq.% of either Y or Mg, and containing 0 to 30 wt.% (approx. equal to vol.%) SiC whiskers are also listed in Table 3. The amount of total oxide additions, as shown in Table 4, is considerably reduced compared to previously studied compositions. Correspondingly, the sinterability was reduced for comparable whisker loadings as can be seen in Table 3. Samples with 0

and 10 wt.% whiskers showed excellent sinterability, while the composites containing 20 wt.% whiskers showed moderate porosity. However, both the 10 and 20 wt.% whisker samples appear to have higher densities than those reported by Tiegs and Geer[5] for pressureless sintering with comparable whisker and sintering aid additions. The 30 wt.% whisker compositions sintered poorly and contained excessive porosity.

SiC whisker orientation

It has been observed that the SiC whiskers in the samples prepared in this study have a strong crystallographic orientation. The green ceramic bodies are formed by pressure slip casting (PSC) a slurry which contains the starting raw materials. This processing step was described in the previous report.[1] During PSC, the solids in the slurry are deposited on a filter to form a thin disk. The SiC whiskers tend to be oriented with the long axis nearly parallel to the plane of the disk. This 2-dimensional, planar orientation is revealed by x-ray diffraction analysis.

When compared to a random powder pattern, the x-ray diffraction peak intensities will be enhanced for crystallographic planes which lie perpendicular to the x-ray beam and suppressed for planes which lie parallel to the beam. The SiC whiskers (Tateho) are primarily cubic Beta-phase. The growth direction (length) of the whiskers is <111>. This means that the {111} planes are perpendicular to the length direction, while the {220} planes are parallel to the length.

For the face of the PSC disk, as seen in Fig. 1a), the {111} peak intensity is suppressed and the {220} peak intensity is enhanced relative to the pattern for the disk edge shown in Fig. 1b). This indicates that the {111} planes are nearly perpendicular to the face (parallel to the beam) and that the {220} planes are parallel to the face. The pattern for the edge shows nearly normal peak intensities as would be expected for a random planar orientation.

The {111} and {220} peak intensities for the face, edge, and a standard powder pattern are listed in Table 5 along with the {111}/{220} peak intensity ratio which gives an indication of the degree of orientation. The same whisker orientation has been observed in sintered composite samples.

Summary

1). Fracture toughness was measured for composites containing either YAG or cordierite as the liquid phase sintering aid, both in the as-fired and annealed conditions. The

cordierite composition showed a higher as-fired fracture toughness (7.83 vs. 5.34 $MPa \cdot m^{1/2}$), but the toughness was reduced by annealing (6.52 $MPa \cdot m^{1/2}$). The YAG composition, however, showed an increase in toughness after annealing (6.32 $MPa \cdot m^{1/2}$).

2). For composites with a matrix consisting of Beta-20 SiAlON with 10 vol.% YAG, good sinterability was obtained for samples with up to 30 vol.% SiC whisker loading. However, samples containing 40 vol.% whiskers did not densify.

3). For composites with a matrix consisting of Si_3N_4 plus 5 eq.% Al and 3 eq.% of either Y or Mg, good sinterability was obtained for samples with 0 and 10 wt.% SiC whisker additions. With 20 wt.% whiskers, the samples showed moderate porosity. And with 30 wt.% whiskers, the samples did not densify.

4.) Composites which are prepared by pressure slip casting (PSC) of a slurry to form the green body show orientation of the SiC whiskers. The length direction of the whiskers lies in the plane of the PSC disk.

References

[1] S. D. Nunn and T. Y. Tien, Semi-annual report submitted to ORNL under Contract No. SC-19X-SA125C, April, 1988.

[2] Prof. E. E. Hucke, The University of Michigan.

[3] P. D. Shakek, et al., Am. Ceram. Soc. Bull. 65 [2] 351-56 (1986).

[4] T. N. Tiegs and J. W. Geer, CTAHE Bi-monthly report to DOE, August, 1988.

[5] T. N. Tiegs and J. W. Geer, CTAHE Bi-monthly report to DOE, April, 1988.

Table 1. Composite sample compositions.

	Weight Percent					
	Si3N4	SiO2	AlN	Al2O3	MgO/Y2O3	SiC
Y87.5/12.5/0*	62.24		8.11	19.85	9.79	
Y70/10/20	50.15		6.53	15.99	7.89	19.44
Y60/10/30	42.91		5.59	14.53	7.87	29.10
Y50/10/40	35.69		4.65	13.07	7.86	38.73
Y75/5/20	54.91		7.15	14.05	4.04	19.86
5Al/3Y/0**	84.46			6.67	8.87	
5Al/3Y/10	76.02			6.00	7.98	10.00
5Al/3Y/20	67.56			5.34	7.10	20.00
5Al/3Y/30	59.12			4.66	6.20	30.00
C87.5/12.5/0*	67.38	5.30	8.78	17.11	1.42	
C70/10/20	53.42	4.21	6.96	13.57	1.13	20.71
C75/5/20	56.68	2.09	7.39	12.79	0.56	20.50
5Al/3Mg/0**	88.09			6.96	4.95	
5Al/3Mg/10	79.28			6.26	4.46	10.00
5Al/3Mg/20	70.48			5.56	3.96	20.00
5Al/3Mg/30	61.66			4.88	3.46	30.00

* Letter indicates liquid phase composition: Y = YAG; C = Cordierite
First number is vol.% Beta-20 SiAlON; second number is vol.% liquid phase; third number is vol.% SiC whiskers.

** 5 eq.% Al; 3 eq.% Y or Mg; last number is wt.% SiC whiskers.

Table 2. Composite sample fracture toughness comparison.

Sample	Heat Treatment	Fracture Toughness
C70/10/20	As-fired	7.83
C70/10/20	Annealed	6.52
Y70/10/20	As-fired	5.34
Y70/10/20	Annealed	6.32

Table 3. Properties of sintered composite samples.

	Temperature (C)	Time (min)	Bulk Density (gm/cc)	Porosity (vol.%)	Wt. Loss (%)
Y87.5/12.5/0	1550	60	3.141	0.19	0.29
	1650	60	3.219	0.08	2.27
Y70/10/20	1650	60	2.859	12.99	3.55
	1750	60	3.015	1.31	4.51
	1850	60	3.185	0.21	6.47
Y60/10/30*	1950	5	3.078	0.06	1.14
Y50/10/40*	1950	5	2.770	16.36	1.83
Y75/5/20	1850	60	3.066	0.08	5.12
	1900	20	3.063	0.12	4.27
	1950	5	3.002	0.12	3.46
5Al/3Y/0	1550	420	3.242	0.16	1.20
	1650	60	3.178	0.31	0.97
	1750	60	3.112	0.15	0.90
5Al/3Y/10	1750	60	3.189	0.26	1.08
	1850	20	3.205	0.12	0.75
	1950	10	3.201	0.09	3.22
5Al/3Y/20	1750	60	2.855	10.71	1.03
	1850	20	2.908	5.84	0.81
	1950	10	2.897	7.10	3.21
5Al/3Y/30	1750	60	2.342	34.92	1.27
	1850	20	2.370	35.07	1.41
	1950	10	2.390	33.38	2.48
C87.5/12.5/0	1550	60	2.781	13.90	2.35
	1650	60	3.071	0.14	3.89
C70/10/20	1650	60	2.747	11.72	6.88
	1750	60	2.942	3.84	7.71
	1850	60	3.033	0.86	8.03
C75/5/20	1850	60	2.563	16.66	3.81
	1900	20	2.614	12.86	3.67
	1950	5	2.672	12.97	3.02
5Al/3Mg/0	1550	420	3.112	0.11	3.30
	1650	60	3.089	0.21	2.14
	1750	60	3.063	0.11	2.50
5Al/3Mg/10	1750	60	3.054	0.29	2.34
	1850	20	3.001	0.15	1.87
	1950	10	2.956	0.00	2.12
5Al/3Mg/20	1750	60	2.798	8.41	5.20
	1850	20	2.846	4.64	5.20
	1950	10	2.791	4.23	6.68
5Al/3Mg/30	1750	60	2.379	23.93	5.83
	1850	20	2.507	12.38	5.26
	1950	10	2.255	39.82	7.73

* Firing schedule was: 5 min. at 1950 C, followed by 15 min. at 1900 C, and 45 min. at 1850 C.

Table 4. Comparison of oxide additions to the composite samples.

	MgO/Y2O3 (Wt. %)	Total Oxides (Wt. %)	Best Density (gm/cc)	Temperature (C)
Y87.5/12.5/0	9.79	29.64	3.219	1650
Y70/10/20	7.89	23.88	3.185	1850
Y60/10/30	7.87	22.40	3.078	1950
Y50/10/40	7.86	20.93	2.770	1950
Y75/5/20	4.04	18.09	3.066	1850
5Al/3Y/0	8.87	15.54	3.242	1550
5Al/3Y/10	7.98	13.98	3.205	1850
5Al/3Y/20	7.10	12.44	2.908	1850
5Al/3Y/30	6.20	10.82	2.390	1950
C87.5/12.5/0	1.42	23.83	3.071	1650
C70/10/20	1.13	18.91	3.033	1850
C75/5/20	0.56	15.44	2.672	1950
5Al/3Mg/0	4.95	11.91	3.112	1550
5Al/3Mg/10	4.46	10.72	3.054	1750
5Al/3Mg/20	3.96	9.52	2.846	1850
5Al/3Mg/30	3.46	8.34	2.507	1850

Table 5. Beta SiC x-ray diffraction peak intensities.

Surface Analyzed	Peak Intensity {111}	{220}	Peak Ratio {111}/{220}
Face	38	100	0.38
Edge	100	30	3.33
Powder	100	35	2.86

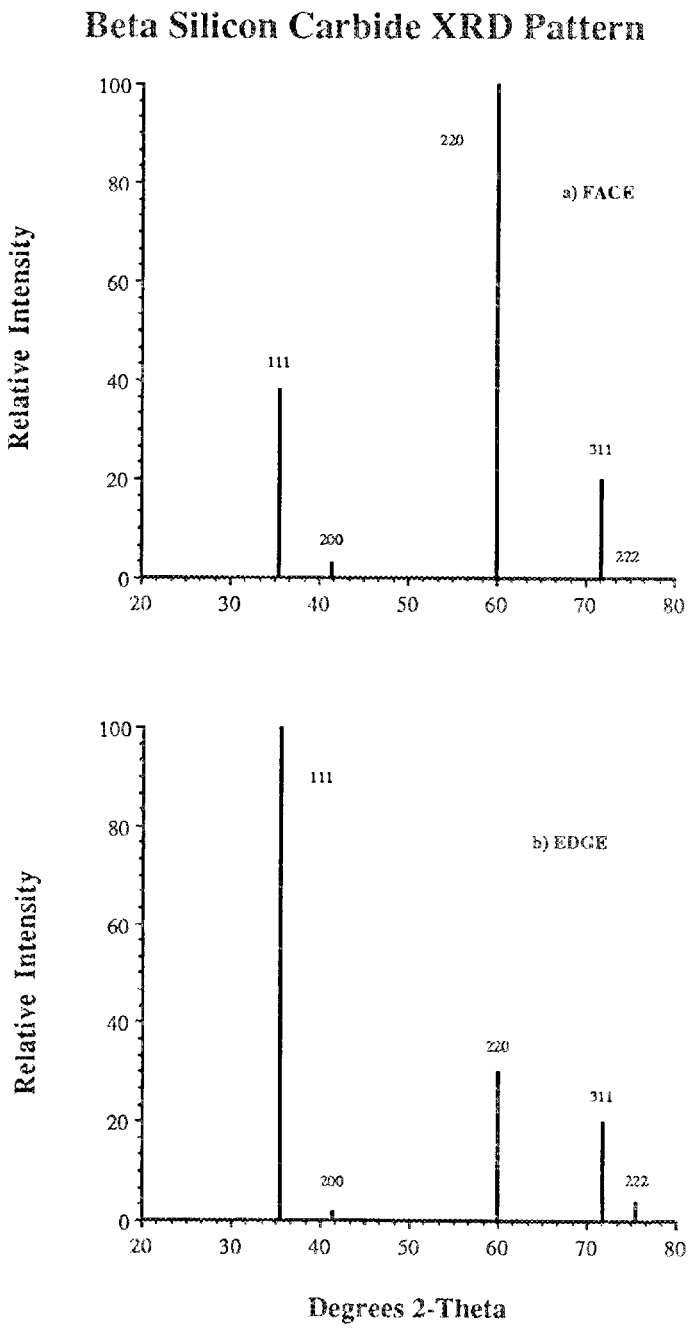

Figure 1. Comparison of the Beta-silicon carbide x-ray diffraction peak intensities for a green ceramic body containing 40 vol.% SiC whiskers. a) Flat surface of pressure slip cast disk. b) Edge of the disk exposed by cutting through the thickness.

1.2.3 Oxide Matrix

Dispersion-Toughened Oxide Composites

T. N. Tiegs, J. W. Geer, P. D. Tennis, and S. M. Leahy (Oak Ridge National Laboratory)

Objective/scope

This work involves development and characterization of SiC whisker-reinforced oxide composites for improved mechanical performance. To date, most of the work has dealt with alumina as the matrix because it was deemed a promising material for initial study. However, a new effort in SiC whisker-reinforced sialon is being initiated. Emphasis in the new system will be on pressureless sintering and control of the whisker-matrix interface properties.

Technical progress

Interface characterization of sialon-SiC whisker composites

Initial results indicated that, in the silicon nitride-SiC whisker composites where considerable amounts of liquid phases are present during densification, the bonding at the whisker-matrix interface is controlled by that liquid phase. The surface chemistry of the whisker is secondary, which is in contrast to the alumina-SiC whisker system. To further examine this effect, a series of composites with various whiskers, whisker surface chemistry, and matrix compositions were hot-pressed. Results on the mechanical property testing are summarized in Tables 1 and 2.

As shown, the fracture toughness was measured by two different methods,[1,2] and each gave a different value. An assessment of the two methods is being made to determine which is more applicable. In any case, the addition of the SiC whiskers into the silicon nitride matrix using the Ube E10 powder improved both the flexural strength and the fracture toughness over the monolithic material. No improvement was observed in the materials using the Ube E2 Si_3N_4 powder.

Of particular importance is the affect of whisker surface chemistry on the fracture toughness. The whisker treatments used were intended to lower the surface oxide and increase the surface carbon contents. These methods were successful in the alumina matrix system at increasing debonding at the whisker-matrix interface and increasing the composite fracture toughness. However, in the silicon nitride system there appears to be no affect of the whisker surface chemistry. This is further evidence that the liquid phases present are much more effective at controlling the whisker-matrix bonding than the initial whisker surface chemistry. This is exemplified in the sialon-matrix composites, which have high levels of transient liquid phases. In those cases, the fracture toughness values were extremely low.

Ceramographic polished sections of the silicon nitride and sialon composites showed the SiC whiskers to be clearly visible. However, only the silicon nitride composites showed any significant crack-whisker interaction on fracture surfaces examined with the scanning electron microscope, as shown in Fig. 1.

Table 1. Summary of results on silicon nitride matrix-SiC whisker composites

Si_3N_4 matrix type[a]	Whisker type	Whisker content (vol %)	Flexural strength (MPa)	Fracture toughness, (K_{IC} (MPa$\sqrt{m}$)		Flaw size (μm)		Elastic modulus (GPa)
				CSF[1]	MIF[2]	CSF	MIF	
E2	--	--	694 ± 56	5.3 ± 0.1	6.5 ± 0.5	37	57	313
E2	American Matrix[b,c]	10	657 ± 36	4.7 ± 0.4	6.0 ± 0.8	33	53	--
E2	American Matrix[b,c]	20	699 ± 29	5.3 ± 0.2	6.6 ± 0.6	37	57	--
E2	Tateho[d]	20	638 ± 77	4.8 ± 0.1	6.2 ± 0.5	38	63	--
E10	--	--	660 ± 58	5.5 ± 0.2	6.4 ± 0.6	46	61	314
E10	American Matrix[b]	20	771 ± 39	6.9 ± 0.2	8.8 ± 0.5	52	84	325
E10	American Matrix[b,c]	20	757 ± 17	6.7 ± 0.1	8.5 ± 0.6	37	81	329
E10	American Matrix[b,e]	10	721 ± 44	6.1 ± 0.1	7.9 ± 0.6	46	78	328
E10	American Matrix[b,e]	20	793 ± 34	6.7 ± 0.3	9.0 ± 1.1	46	83	332
E10	American Matrix[b,e]	30	726 ± 58	6.8 ± 0.2	9.1 ± 0.5	57	102	312
E10	American Matrix[b,f]	20	787 ± 35	7.0 ± 0.1	8.7 ± 0.4	51	78	322
E10	American Matrix[b,e,f]	20	802 ± 38	6.8 ± 0.2	8.9 ± 0.7	47	80	319
E10	Tokai Carbon[g]	20	648 ± 38	6.8 ± 0.1	8.8 ± 0.6	72	120	317
E10	Tokai Carbon[g,h]	20	573 ± 38	6.5 ± 0.2	8.2 ± 0.4	83	132	--
E10	Tokai Carbon[g,i]	20	608 ± 20	6.6 ± 0.3	8.7 ± 1.0	85	131	--
E10	Tateho[d]	20	591 ± 35	6.3 ± 0.1	7.8 ± 0.5	74	111	--
E10	Ube[j]	20	473 ± 23	6.7 ± 0.4	9.1 ± 0.8	129	240	--

[a]Matrices contained 6 wt % Y_2O_3 and 2 wt % Al_2O_3; Si_3N_4 was either E2 or E10, both manufactured by Ube Industries, Japan.

[b]American Matrix, Inc., grade 1, received 9/87.

[c]Heat-treated, vacuum, 1450°C.

[d]Tateho Corp., grade SCW-1S, received 1/86.

[e]Heat-treated, Ar-4% H_2, 1450°C.

[f]Acid-leached in HCl followed by HF.

[g]Tokai Carbon Co., Tokai whisker, received 3/86.

[h]Coated with ~25 Å carbon.

[i]Coated with ~50 Å carbon.

[j]Ube Industries, ß-Si_3N_4 whisker, grade SN-B.

Pressureless sintering of sialon-SiC whisker composites

Pressureless sintering of sialon-SiC whisker composites was examined as an alternative densification method to hot-pressing or encapsulated HIPing. Previous results[3,4] on sintering of Al_2O_3-SiC_w and Si_3N_4-SiC_w composites showed that the densification is highly dependent on the amount of liquid phase sintering aid present, the whisker volume content, and the whisker aspect ratio. The effects of whisker volume content and aspect

Table 2. Summary of results on sialon matrix-20 vol % SiC whisker composites

Sialon matrix composition[a]	Elastic modulus (GPa)	Flexural strength (MPa)	Fracture toughness, K_{Ic} (MPa$\sqrt{m}$)		Flaw size (μm)	
			CSF[1]	MIF[2]	CSF	MIF
$Si_4Al_2O_2N_6$	269	189 ± 8	2.3 ± 0.1	2.2 ± 0.1	88	96
$Si_3Al_3O_3N_5$	223	163 ± 13	2.1 ± 0.1	1.9 ± 0.2	108	88
$Si_2Al_4O_4N_4$	263	281 ± 7	3.6 ± 0.1	4.5 ± 0.1	105	165

[a]All compositions contain 8 wt % Y_2O_3 and the whiskers were treated in Ar-4% H_2 at 1450°C.

ratio have been fairly well defined in the alumina system and were held as constants in the current work. Parameters that were examined were the amount of liquid phase sintering aid and the sialon composition.

The results on the pressureless sintering of sialon-20 vol % SiC_w composites with various amounts of sintering aid are summarized in Table 3. As shown, with low sintering aid contents (≤0.5 wt %) very little densification occurs. The sialon matrix compositions made with the mixture of starting powders showed better densification than the fully reacted starting powder. This is probably due to the presence of transient liquid phases that form as the powders react with one another. As the sintering aid content is increased to 8 wt %, particle-whisker rearrangement is promoted and high densities are easily obtained.

The effect of sialon matrix composition is given in Table 4. As the Al:Si ratio is increased, densification is increased, which is again probably a result of higher amounts of liquid phase content during sintering.

The flexural strength and fracture toughness of the sialon-20 vol % SiC_w composites with densities >95% T.D. were determined. The results on the flexural strength are given in Table 5. The measured fracture toughnesses were in the 4-5 MPa$\sqrt{m}$ range for all compositions. As shown in Table 5, the overall strengths were low; however, a comparison with hot-pressed materials showed actually better strengths for the sintered compositions. In all cases, the poor strength is attributable to a degradation of the whiskers at the matrix-whisker interface. This is also reflected in the fact that the strengths generally decreased at the higher sintering temperatures. Thus, it appears that if sialons are to be used with SiC whisker reinforcement, coatings or some other means will be necessary to minimize reactions at the matrix-whisker interface.

Status of milestones

Milestone 123106, "Complete Characterization Study of Whisker-Sialon Interfaces," was completed in June 1988.

Milestone 123107, "Complete Fabrication Study of Whisker-Sialon Composites by Pressureless Sintering," was completed in September 1988.

M27679

(a)

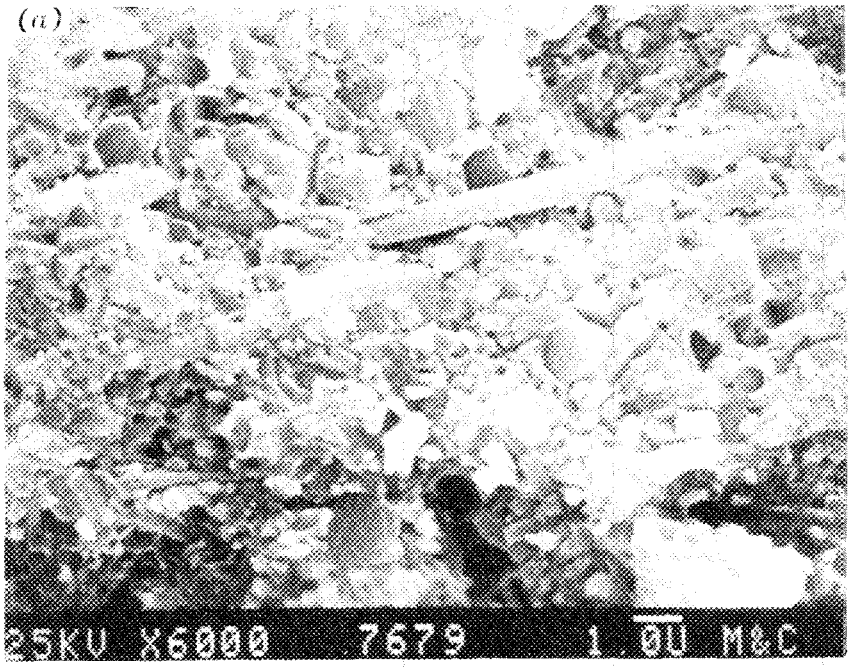

M28150

(b)

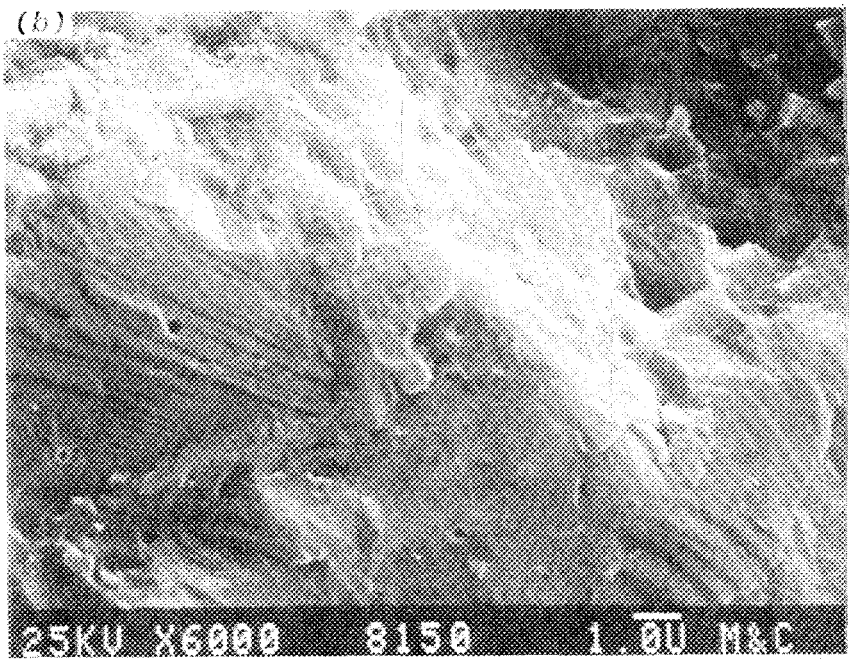

Fig. 1. Fracture surfaces of (*a*) Si_3N_4-6 wt % Y_2O_3-2 wt % Al_2O_3/20 vol % SiC_w composite showing extensive crack-whisker interaction and (*b*) $Si_2Al_4O_4N_4$-8 wt % Y_2O_3/20 vol % SiC_w composite showing no crack-whisker interaction.

Table 3. Summary of results on pressureless sintering of sialon-20 vol % SiC whisker composites with various liquid phase sintering aid contents

Sialon composition	Nominal sintering aid content (wt %)[a]	Density at various sintering temperatures (% T.D.)		
		1700	1750	1800
$Si_3Al_3O_3N_5$[b]	0	57.6	57.2	53.3
$Si_3Al_3O_3N_5$[b]	0.5	N.D.	83.1	83.4
$Si_3Al_3O_3N_5$[b]	2	N.D.	78.9	90.5
$Si_3Al_3O_3N_5$[b]	8	97.0	98.0	97.1
$Si_{4.5}Al_{1.5}O_{1.5}N_{6.5}$[c]	0.5	N.D.	58.1	60.0
$Si_{4.5}Al_{1.5}O_{1.5}N_{6.5}$[c]	2	N.D.	75.6	94.0

[a] $3Y_2O_3 \cdot 5Al_2O_3$.

[b] Mixture of Si_3N_4 (Ube E10), Al_2O_3 (Reynolds RCHP-DBM) and AlN (ART AlNel-100).

[c] Vesuvius Crucible Co., Sialon grade AA.

Table 4. Summary of results on pressureless sintering of sialon-20 vol % SiC whisker composites with various sialon matrix compositions

Matrix composition[a]	Density at various sintering temperatures (% T.D.)			
	1700	1750	1800	1850
Si_3N_4[b]	71.7	70.6	69.5	71.7
$Si_4Al_2O_2N_6$[c]	95.0	96.4	96.2	--
$Si_3Al_3O_3N_5$[c]	97.0	98.0	97.1	--
$Si_2Al_4O_4N_4$[c]	99.3	99.7	99.8	--

[a] All compositions contained American Matrix SiC whiskers.

[b] Si_3N_4 (Ube E10), 12 wt % Y_2O_3 (Molycorp), 4 wt % Al_2O_3 (Reynolds RCHP-DBM).

[c] Mixture of appropriate amounts of Si_3N_4 (Ube E10), Al_2O_3 (Reynolds RCHP-DBM), AlN (ART AlNel-100) and 8 wt % Y_2O_3 (Molycorp).

Table 5. Summary of results on flexural strength of pressureless sintered sialon-20 vol % SiC whisker composites

Matrix composition[a]	Flexural strength of composites pressureless-sintered at various temperatures (MPa)			Flexural strength of hot-pressed[b] composites (MPa)
	1700	1750	1800	
$Si_4Al_2O_2N_6$	298	277	218	281
$Si_3Al_2O_2N_5$	291	254	251	163
$Si_2Al_4O_4N_4$	252	300	197	189

[a]8 wt % Y_2O_3 contained in all compositions.

[b]Hot-pressed at 1650°C.

References

1. P. Chantikul et al., "A Critical Evaluation of Indentation Techniques for Measuring Fracture Toughness: II, Strength Method," *J. Am. Ceram. Soc.* **64**(9), 539-43 (1981).

2. R. F. Cook and B. R. Lawn, "A Modified Indentation Toughness Technique," *Comm. Am. Ceram. Soc.* **11**, C-200-1 (1983).

3. T. N. Tiegs and P. F. Becher, "Sintered Al_2O_3-SiC Whisker Composites," *Am. Ceram. Soc. Bull.* **66**(2), 339-42 (1987).

4. T. N. Tiegs, L. A. Harris, and J. W. Geer, "Dispersion Toughened Oxide Composites," pp. 60-66 in *Ceramic Technology for Advanced Heat Engines Project Semiannual Progress Report for October 1987 through March 1988*, ORNL/TM-10838 (December 1988).

Processing of Improved Transformation-Toughened Ceramics

E. Lilley and G. A. Rossi (Norton Company)

Objective/scope

The objective of Phase IIA is to optimize the properties of two classes of transformation toughened ceramics, which were already studied in Phase I of this contract. These ceramics are Y-TZP (Y_2O_3 stabilized Tetragonal Zirconia Polycrystals) and Ce-ZTA (CeO_2-ZrO_2 toughened Al_2O_3).

For the Y-TZP materials, one of the main efforts will be to study the low temperature degradation and understand how it is affected by microstructure and composition. In the case of the Ce-ZTA ceramics, the main goal is to optimize the high temperature mechanical properties by minimizing the flaw size and controlling the microstructures.

Technical progress

1. Y-TZP Ceramics

Materials

Yttria doped zirconia crude has been prepared by arc melting and rapid solidification for compositions of 4.5 and 5.3 wt.% Y_2O_3. This crude was Sweco milled to produce powder with an average diameter of 0.7 microns, measured by a Sedigraph. The resulting powders were dry pressed and CIPed at 30 ksi and fired at 1500°C. Gas pressure sintering is also being employed.

Some powders are being prepared with different particle sizes using different milling times in order to obtain different grain sizes in fully dense bodies. These materials are intended for study: (a) to optimize the microstructures and mechanical properties between RT and 700°C; and (b) to investigate the resistance to low temperature degradation.

Results

Four point strength study MOR measurements have been performed on both Mil Spec and Norton size bars (1.375 x 1.25 x 1.28 inches with a fixture 0.5 and 1.0 inch spans). Two batches of each composition were tested with Norton size bars with strengths as follows:

Code	Yttria Wt.%	MOR MPa	Std.Dev. %	# of Bars
MG-008	4.66	1164	19	18
MG-032/34	4.7	1137	18	10
MG-024	5.27	1220	15	14
MG-026	5.52	909	20	16

It interesting to see that the higher yttria composition in the case of MG-024 has not led to a significant decrease in strength when compared to the two lower yttria concentrations. MG-026 presumably has larger processing defects giving a lower strength. This result is important because the higher yttria concentrations are expected to exhibit greater resistance to low temperature degradation.

Low Temperature Degradation

Three kinds of tests are being used for the study of low temperature degradation. These will be discussed.

The first test is done at 250°C in moist nitrogen. The samples are held in an oven at atmospheric pressure through which slightly moist nitrogen is passed having been bubbled through water at RT (P_{H_2O} = 0.0023 MPa). This is equivalent to air on a humid day. The mechanical degradation which is associated with the transformation of tetragonal to monoclinic structure has been tracked in two ways; first, with XRD monoclinic % measurements and secondly, with MOR measurements. Typically, about 10 MOR bars are required for each data point to give a reasonable average value. Once serious degradation occurs, the scatter in the results become significantly reduced and the number of bars may be reduced to 5 or even 3 in some cases.

Fig. 1 shows the change in strength for both HIPed and sintered bars with exposure times up to 1000 hrs. for the HIPed and to 4000 hrs. for the sintered material. The

HIPed material shows a more dramatic decrease in strength than the sintered material. This is because the micro-cracks which form during the transformation have a size greater than that of the preexisting defects in the HIPed materials, whereas this is not the case for the sintered Y-TZP.

XRD has been used to follow the initial temperature degradation reaction at 250°C. This method only examines <10 micron surface depth due to absorption of the X-rays. The % monoclinic formed for two different materials is shown in Fig. 2 as a function of exposure time. MG008 has 4.7 w% Y_2O_3 and MG024 has 5.3 w% Y_2O_3 and a finer grain size. The latter material is more resistant to degradation, as expected.

The second test was to hold samples at 200°C and 200 psi in water vapor for 50 hours. This is a test that has been used by Swab at the Army Materials Technology Lab to evaluate a number of Japanese Y-TZP ceramics. This is a much more severe test than the last one described. The bars, after autoclaving, were tested for MOR and the results are given in Fig. 3. The change in strength is comparable to that found by Swab.

The third test involved immersing bars in water at 120°C in a pressure cooker for different times. The results are shown in Fig. 4 for exposure times 0, 200 and 400 hours. Again, the HIPed bars show a more precipitous decline but the resultant strengths are ~800 MPa with Norton size bars. Mil Spec bars would have a strength ~10% lower than this.

In future studies, we plan to measure the depth of the monoclinic zone by Raman microprobe measurements.

2. Ce-ZTA CERAMICS

During this contract period, the main accomplishments were the preparation and characterization of the CeO_2-ZrO_2 powders made from the rapidly solidified (R/S) crude, the fabrication of sintered/HIPed billets of Ce-ZTA ceramics of three compositions and their characterization (mechanical properties, fractography, microstructures, phase content by XRD). The powders used to make the billets were prepared by mixing R/S CeO_2-ZrO_2 and Sumitomo AKP-30 Al_2O_3 powders. The best composition was identified on the basis of the mechanical properties measured. This composition is made up of 40 w/o (16 w/o CeO_2-ZrO_2) and 60 w/o Al_2O_3 and is abbreviated as Z16CE60A. Finally, a crude of this composition was prepared at NORTON Plasma Materials in Manchester, NH, by rapid solidification of a melt of three three oxides.

This crude is now being milled to a submicron powder which will be used to make billets for mechanical property characterization.

2.1 Preparation and characterization of the R/S CeO_2-ZrO_2 powders

Two CeO_2-ZrO_2 crudes (about 50 lbs. each) of compositions 16 w/o CeO_2-ZrO_2 (12 m/o CeO_2) and 24 w/o CeO_2-ZrO_2 (18 m/o CeO_2) were prepared in our facility in Chippawa, Ontario, by co-fusion and rapid solidification. The two crudes are abbreviated as Z16CE and Z24CE. The dark and shiny R/S bubbles were characterized by XRD and TGA analysis. The two XRD patterns were virtually identical and showed only the presence of t-ZrO_2 (possibly t'-ZrO_2 formed from the c-ZrO_2 phase upon quenching). Fig. 5 shows the XRD pattern for the Z16CE crude. The TGA curves for the two materials appear also very similar. Fig. 6 shows that of the Z16CE crude. It can be noticed that a weight gain occurs upon heating up to about 700°C after which the weight remains constant and then slightly drops at higher temperatures. The percent weight gain was found to be slightly higher for crude Z24CE, i.e. 0.6% vs. 0.5%. The samples after the TGA runs appeared yellow-orange. These results indicate that the as-received crudes are oxygen deficient and that they are reoxidized in air. The fact that neither curve shows weight loss at intermediate temperatures seems to indicate that no free carbon was incorporated in the bubbles. The slight weight loss beyond 1000°C could be due to the thermal reduction of CeO_2 to Ce_2O_3.

The chemical analysis of the two crudes have shown 15.92 and 24.46 w/o CeO_2, compared to the nominal 16 and 24 w/o.

Powders were obtained from the two crudes by milling with water in a vibratory mill (Sweco). It was found that the Z24CE bubbles were harder to mill than the Z16CE ones. The former material had to be milled for 144 hrs. and classified by sedimentation, in order to get a particle size distribution curve similar to that of crude Z16CE milled for 96 hrs. and not classified. The particle size distributions of the two powders used to prepare the Ce-ZTA billets are shown in Fig. 7.

The two powders were also characterized for BET area and phase content by XRD. The BET areas (single point) were 7.0 m^2/g and 5.3 m^2/g, in agreement with the particle size distribution curves.

The XRD patterns (short scan in the 25-35 2 theta range) of the two powders are shown in Fig. 8. About 25% m-ZrO_2 is present in the Z16CE powder, whereas no m-ZrO_2 appears in the Z24CE powder. This result is consistent with the expectation, since a lower amount of stabilizer makes the t-ZrO_2 easier to transform to m-ZrO_2.

Powder Z16CE was analyzed for impurities by spectrographic analysis. The result, shown below, has shown that virtually no contamination has occurred during milling.

	Si	Fe	Ti	Al	Ca	Mg	Na
Z16CE crude	.04	.05	.05	.11	.05	.005	.01
Z16CE powder	.08	.1	.03	.15	.05	.01	--

The crude of composition Z16CE60A, made at Plasma Materials, was vibratory milled with water in order to get a submicron powder. The particle size distribution vs. milling time is given in Fig. 9 for three milling times. The powder milled for 109 hrs. has been used to make billets, which have shown virtually theoretical density after firing at 1600°C/1 hr. The billets were submitted for machining into MOR bars and K_{IC} (double torsion) samples.

2.2 Processing/shape forming

The R/S Z16CE and Z24CE powders were mixed with Sumitomo AKP-30 powder in water in a planetary mill for 2 hrs. The aqueous slurry was poured into liquid N_2 and the frozen mass was freeze-dried. This was done in order to prevent phase segregation and to produce a powder with soft agglomerates.

The powders of the three compositions, prepared as described above, were die pressed at 69 MPa and cold isostatically pressed at 207 MPa into billets.

In parallel with dry powder pressing, the Moffatt technique of coacervation (1) was investigated. This technique consists in preparing an aqueous solution of two powders of different density, electrostatically stabilized, containing polyvinyl alcohol (PVA). The addition of acetone, a non-solvent for PVA, causes the precipitation (coacervation) of the two powders in the form of a "cheese curd", which is collected on a sieve and colloid pressed, to squeeze the liquid out through a porous stainless steel disc. Problems

were encountered at first, mainly due to the loss of powder with the liquid during colloid pressing. A trip was made to MIT to discuss this problem. Recently, we have found the solution, by vacuum filtering the cheese curd on a filter paper before colloid pressing, in order to consolidate the flocs by draining out the excess liquid.

Recently a 3" diameter disc, about 1/4" thick, was successfully made, dried and fired at 1500°C. The green density after drying was 55% of TD, 58% after cold isostatic pressing at 207 MPa and 98.5% of TD after firing. No cracking was observed. The disc will be HIPed and then characterized for microstructure and mechanical properties.

2.3 Densification

The billets of the three compositions were first fired in air at 1500°C/3 hrs. and then HIPed in Ar at 1550°C for 45 minutes to eliminate the residual porosity.

Table 1 shows green, sintered and HIPed densities in Mg/m^3.

Table 1

Composition	Green	Sintered	HIPed	Theor.
Z16CE80A	2.47	4.36	4.37	4.30
Z24CE80A	2.46	4.34	4.37	4.30
Z16CE60A	2.63	4.67	4.65	4.67

2.4 Characterization of the Ce-ZTA ceramics

MOR bars (3x3x30 mm) were machined from the billets and tested in 4 PT bending with spans of 12.3 and 25.4 mm, with a cross-head speed of 0.5 mm/min. The MOR bars were broken at 25°C and 1000°C.

Samples of 50x25x1 mm were also machined for the toughness measurement at 25°C and 1000°C with the double torsion method.

Table 2 shows the results for strength and K_{IC} at 25°C and 1000°C.

Table 2

Strength and Toughness of Ce-ZTA Ceramics at 25°C and 1000°C

Comp.	MOR (25°C)	MOR (1000°C)	K_{IC}(25°C)	K_{IC}(1000°C)
Z16CE80A	889 (10)	544 (10)	6.1 (5)	3.0 (5)
Z24CE80A	840 (10)	461 (10)	5.2 (5)	2.5 (5)
Z16CE60A	1020 (10)	537 (10)	7.5 (2)	N/A

Note: Strength values are in MPa; Toughness values are in $MPa.m^{\frac{1}{2}}$; numbers in parenthesis are samples tested.

Z16CE80A = 20 w/o (16 w/o CeO_2-ZrO_2)-80 w/o Al_2O_3
Z24CE80A = 20 w/o (24 w/o CeO_2-ZrO_2)-80 w/o Al_2O_3
Z16CE60A = 40 w/o (16 w/o CeO_2-ZrO_2)-60 w/o Al_2O_3

In the case of the Z16CE60A composition, three of the five K_{IC} samples to be tested at 25°C broke while being notched with the diamond blade. The five samples to be tested at 1000°C broke in an anomalous way, most likely because they had been, by mistake, machined transversely, and the K_{IC} values could not be calculated. (The crack did not follow the notch line, but deviated sharply to the right or to the left).

The data of Table 2 shows that the Z16CE60A composition gives the highest strength and toughness, although the 1000°C K_{IC} values is missing. We feel that it is safe to assume that the high temperature toughness for this composition is not lower than the values shown by the other compositions.

The microstructures (SEM) of the sintered/HIPed billets of the three compositions are shown in Figs. 10, 11 and 12 below. It appears that the distribution of the CeO_2-ZrO_2 dispersed phase in the Al_2O_3 matrix is fairly homogenous. As described in the previous report, the powders used to make the billets were prepared by mixing CeO_2-ZrO_2 and Al_2O_3 powders in a planetary mill with water (pH = 6.5), after which the slurry was frozen in liquid N_2 and freeze-dried.

Fractographic analysis was performed on the broken MOR test bars to identify the fracture origins. Figs. 13, 14, and 15 show typical examples of strength reducing defects. In general, the bars with highest strengths showed regions rich in either ZrO_2 or Al_2O_3, as fracture

origins, whereas the weakest bars failed due to machining damage along the chamfers and/or porous regions close to the tensile surface.

Status of milestones

All milestones are on schedule. The list of milestones for Phase IIA of the contract is shown below.

List of milestones

Y-TZP (YZ-110) Study

1. Complete preliminary evaluation of low temperature degradation (LTD). Obtain rapidly solidified (R/S) crude from Chippawa of different Y_2O_3 compositions for microstructural studies ....June '88

2. Choose best YZ-110 composition and forming method based on previous measurements of LTD and mechanical properties to be used in optimizational studies in the remaining period. At Penn State prepare and carry out initial mechanical testing of TiO_2/ZrO_2 ceramic bodies made from R/S Chippawa crude .....Oct. '88

3. Complete (i) processing/microstructural studies for optimization of mechanical properties; (ii) measurements of MOR, K_{IC} between RT and 700°C; (iii) low temperature degradation testing.....Feb. '89

4. Finish all documentation and supply test bars to ORNL.....May '89

Ceria-Zirconia Toughened Alumina Ceramics

1. Choose best composition on the basis of mechanical properties obtained at room temperature and at high temperature. Use HIPing to quickly evaluate compositions. Demonstrate and perfect Moffatt's technique.....June'88

2. Evaluate rapidly solidified powders made in Chippawa and PMI and choose between chemically derived and rapidly solidified powders, based on mechanical properties obtained at RT and high temperature .....Oct. '88

3. Complete study on processing/microstructure/property organization.....Feb. '89

4. Finish all documentation and supply test bars to ORNL .....May '89

Publications

G. A. Rossi and P. J. Pelletier have submitted a manuscript which, if accepted, will be published in the Proceedings of the 3rd International Symposium on Materials and Ceramics for Engines, to be held in Las Vegas, NV, in November, 1988. The paper contains the results of the study on the Ce-ZTA ceramics performed during Phase I of this contract.

References

1. W. C. Moffatt and H. K. Bowen, "Composite Ceramic Production by Precipitation of Polymer Solutions Containing Ceramic Powder", J. Matls. Sci. Letters, Vol 6, pp. 383-385, April, 1987.

FLEXURAL STRENGTH WITH EXPOSURE TO HUMID NITROGEN @ 250 C, MG008

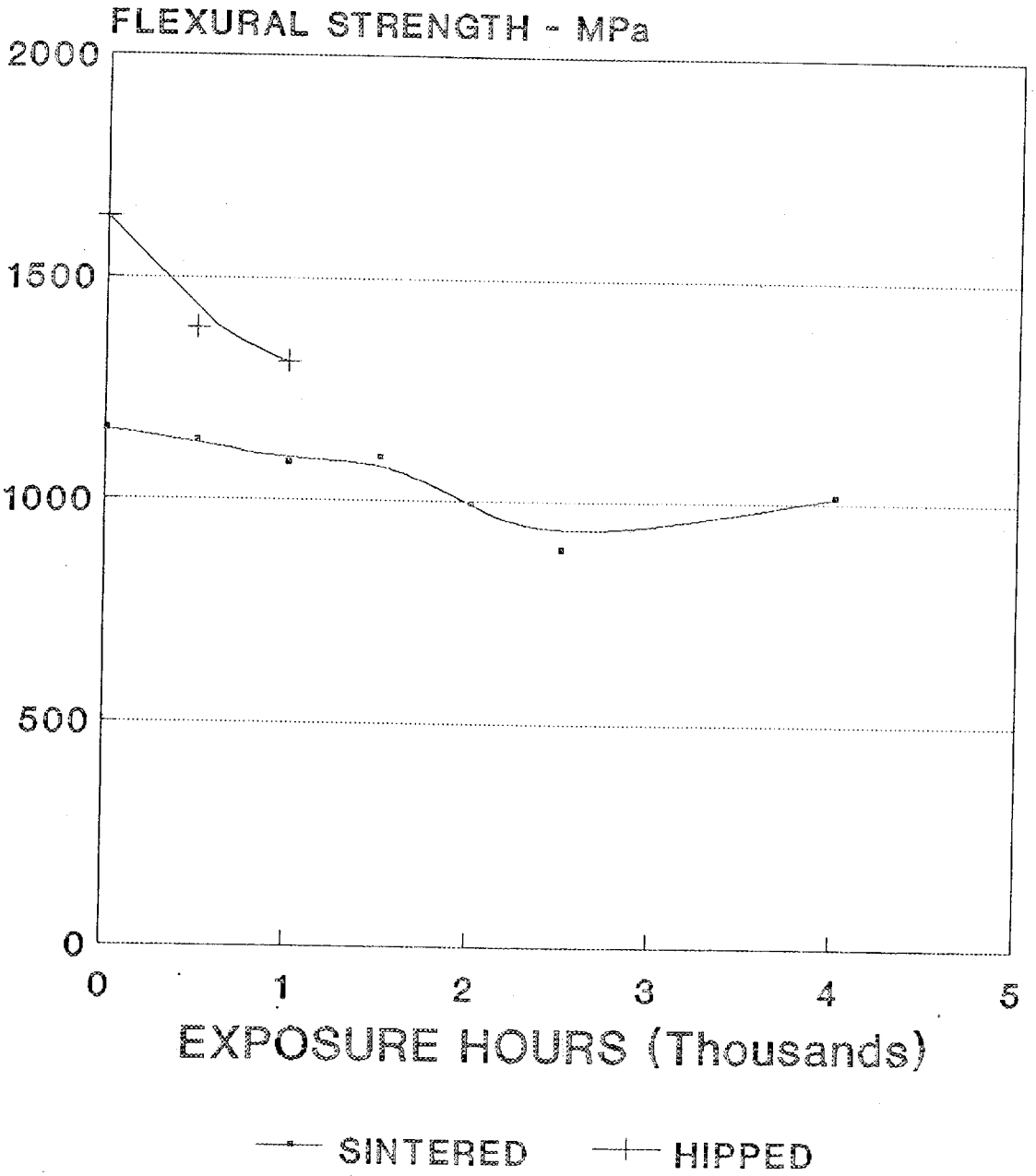

FIGURE 1

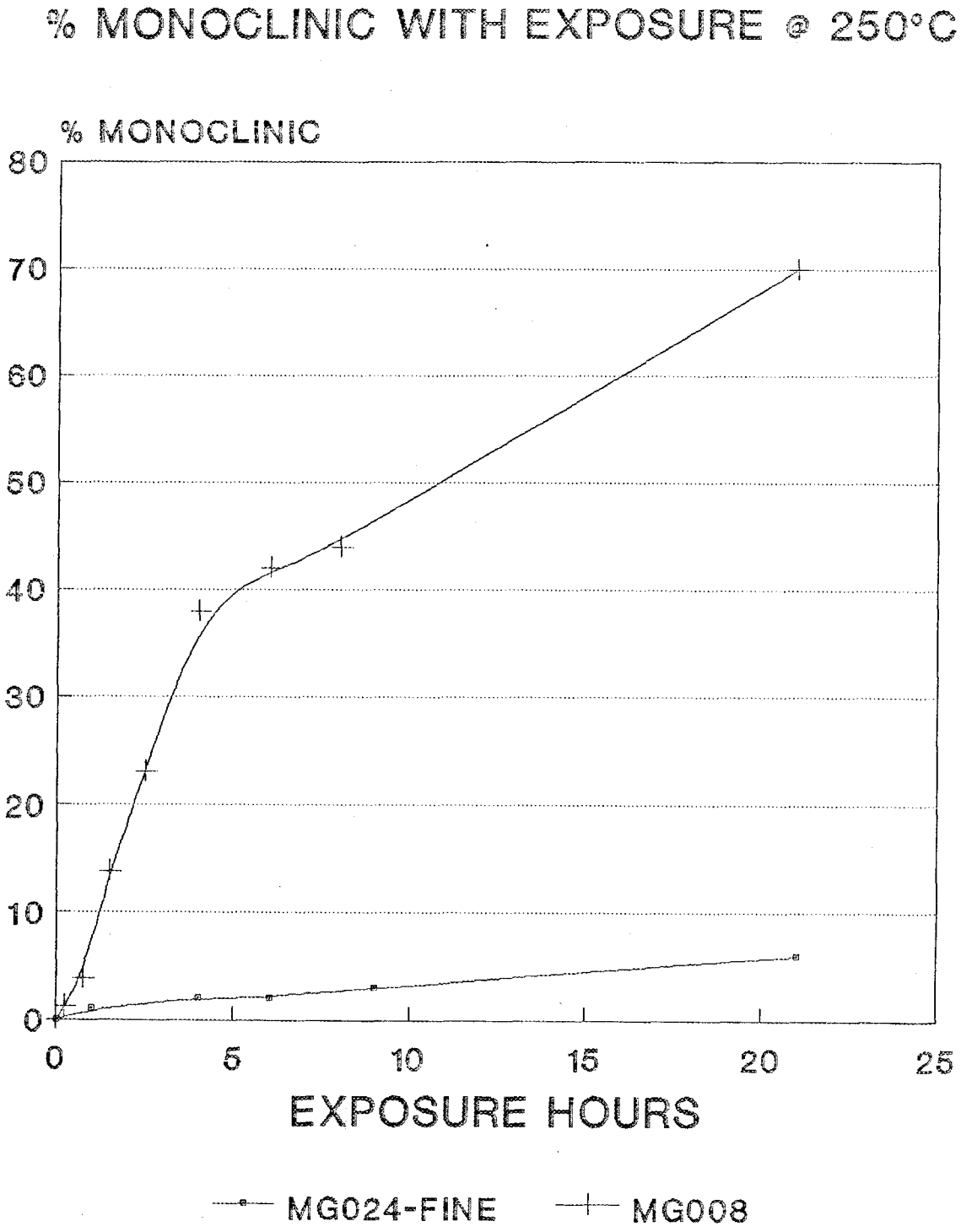
% MONOCLINIC WITH EXPOSURE @ 250°C
% MONOCLINIC
80
70
60
50
40
30
20
10
0
0
5
10
15
20
25
EXPOSURE HOURS
MG024-FINE
MG008

FIGURE 2

LOW TEMPERATURE DEGRADATION

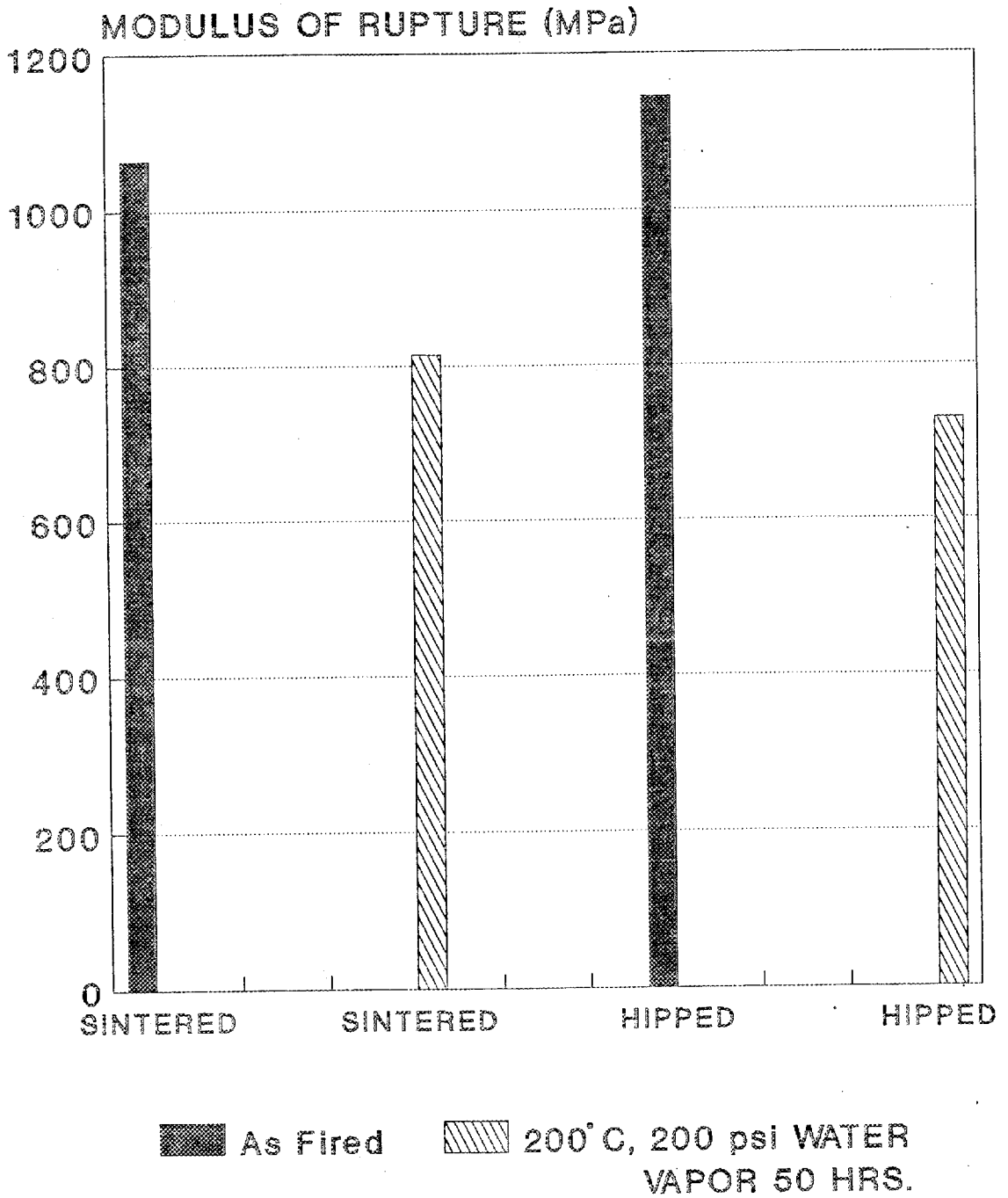

FIGURE 3

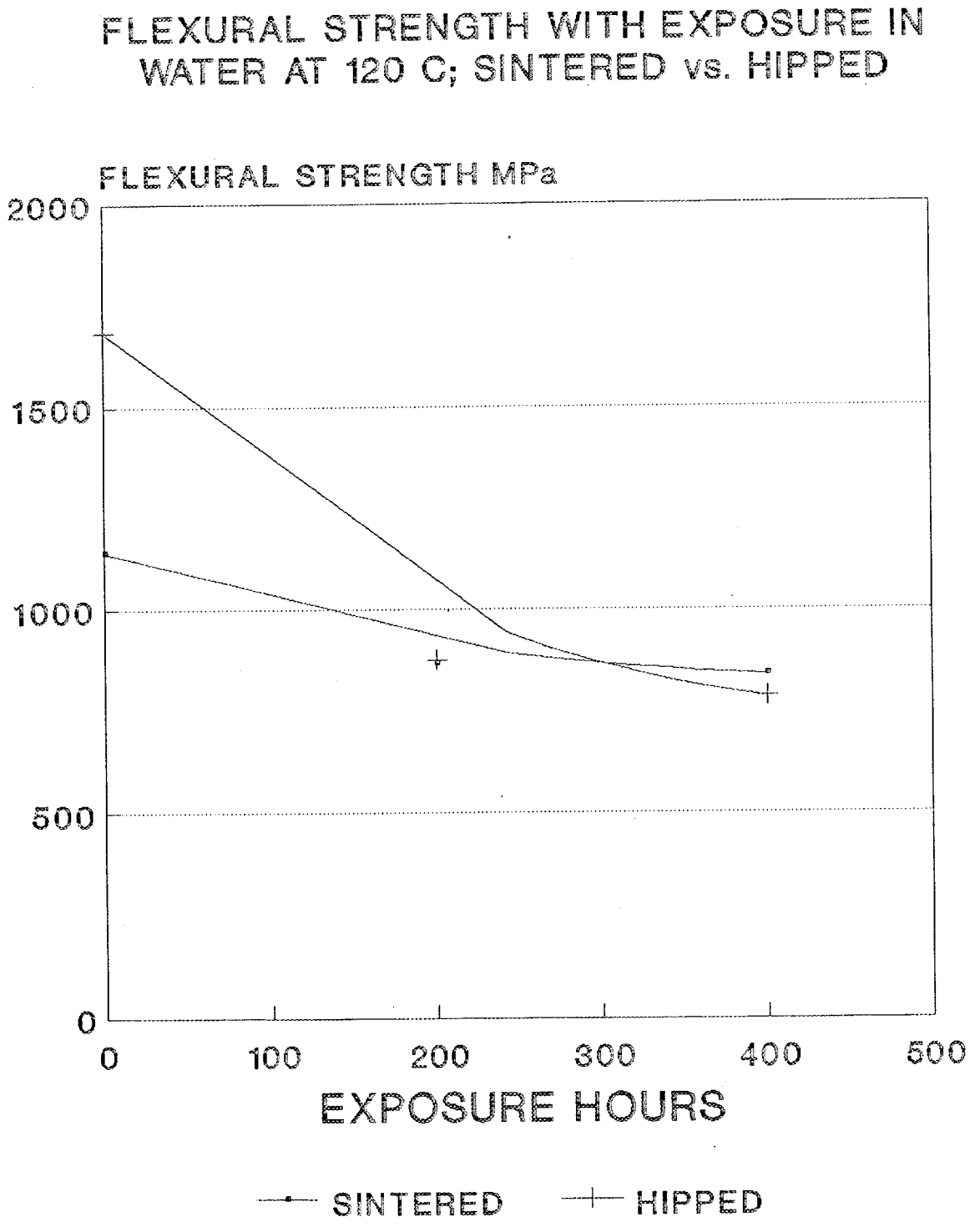
FLEXURAL STRENGTH WITH EXPOSURE IN WATER AT 120 C; SINTERED vs. HIPPED
FLEXURAL STRENGTH MPa
2000
1500
1000
500
0
0
100
200
300
400
500
EXPOSURE HOURS
SINTERED
HIPPED

FIGURE 4

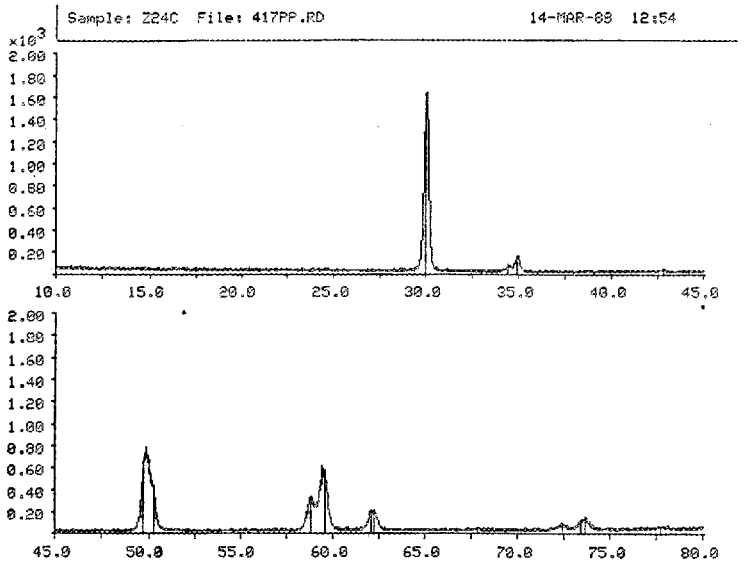

Fig. 5: XRD pattern of the Z16CE R/S crude

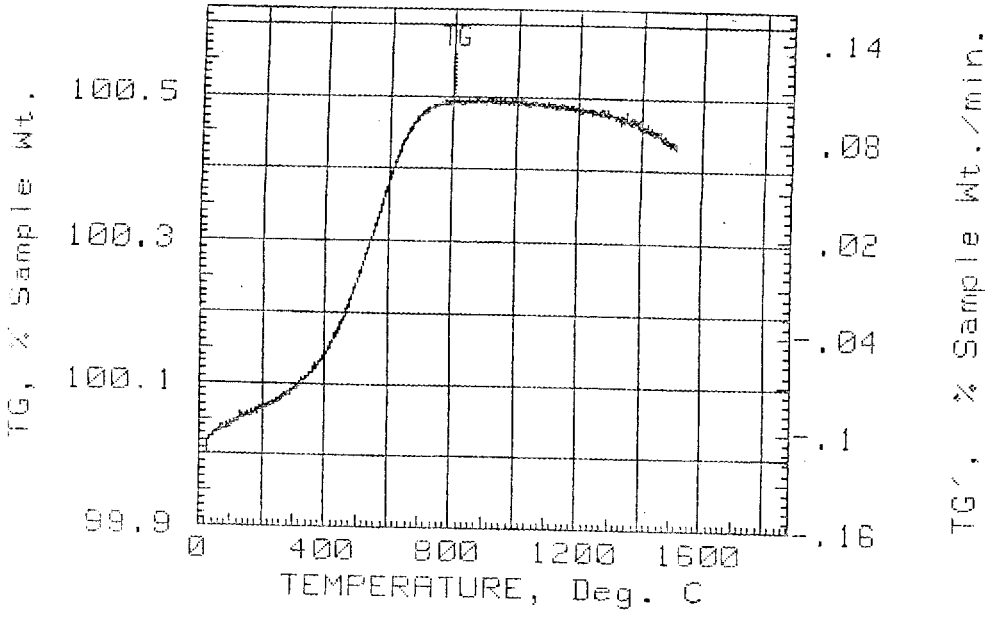

Fig. 6: TGA curve of the Z16CE R/S crude

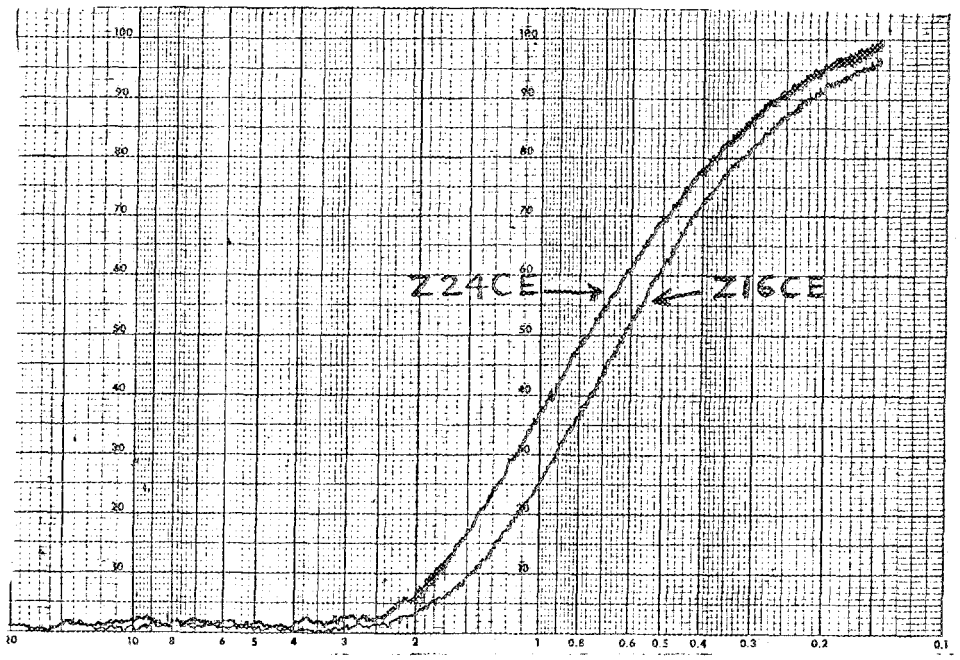

Fig. 7: Particle size distribution curves for powders Z16CE and Z24CE used to prepare the Ce-ZTA billets.

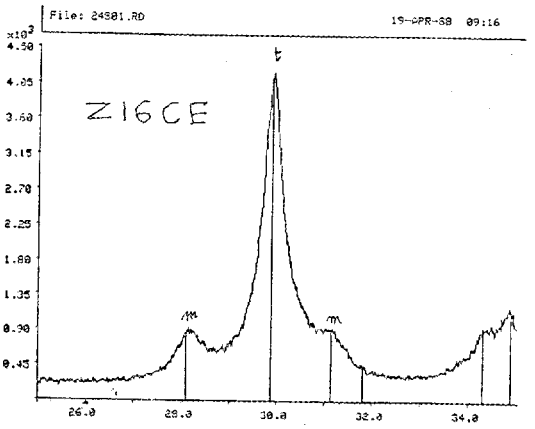

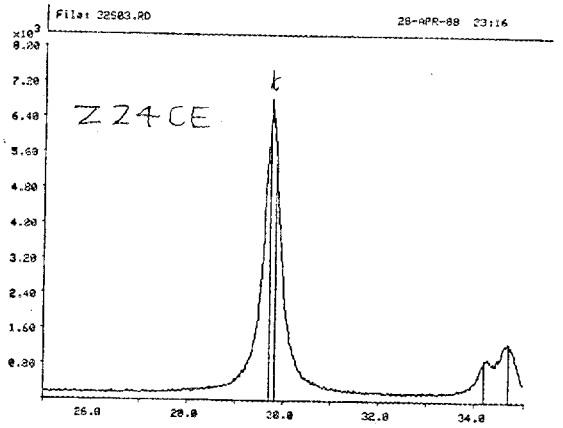

Fig. 8: XRD patterns of the powders obtained from the Z16CE and Z24CE crudes by vibratory milling.

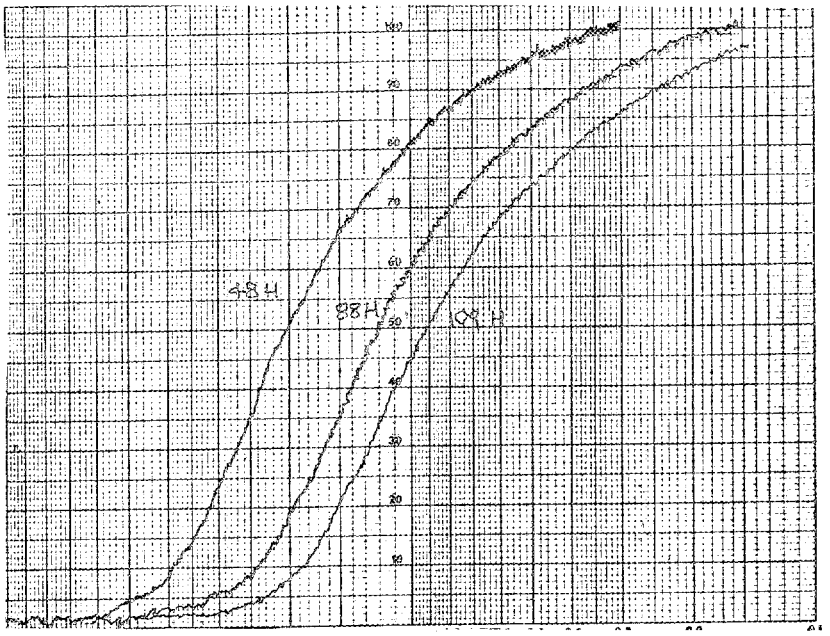

Fig. 9: Particle size distribution curves of powders obtained by Sweco milling the CeO_2-ZrO_2-Zl_2O_3 crude for three different times.

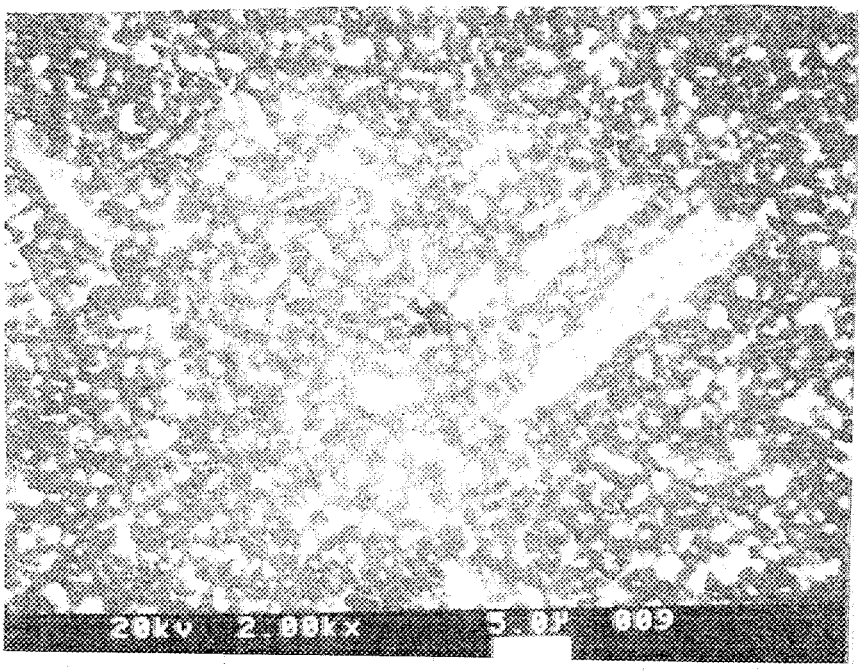

Fig. 10: Microstructure (SEM) of sintered/HIPed Ce-ZTA ceramic with composition Z16CE80A.

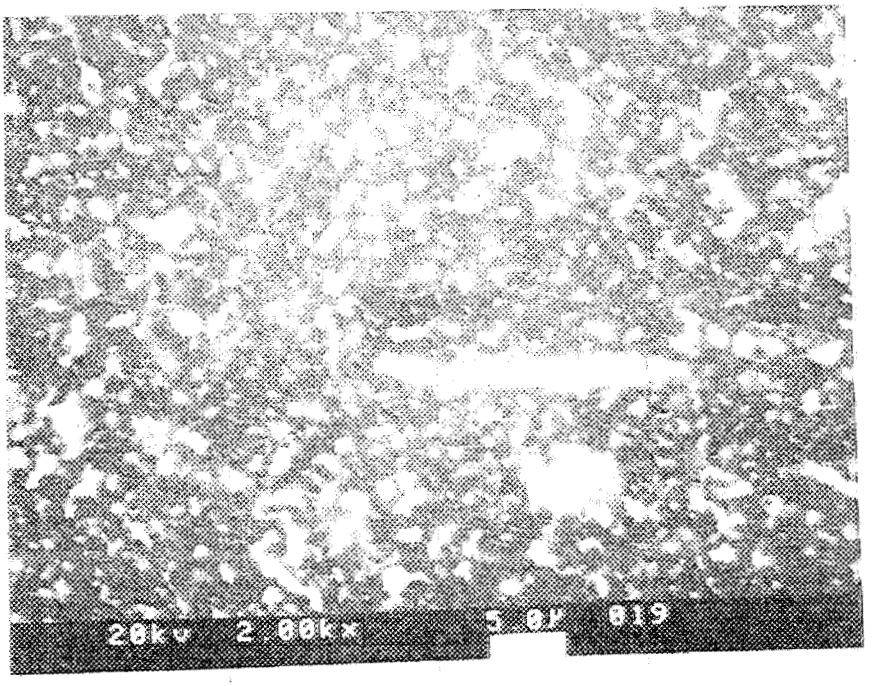

Fig. 11: Microstructure (SEM) of sintered/HIPed Ce-ZTA ceramic with composition Z24CE80A.

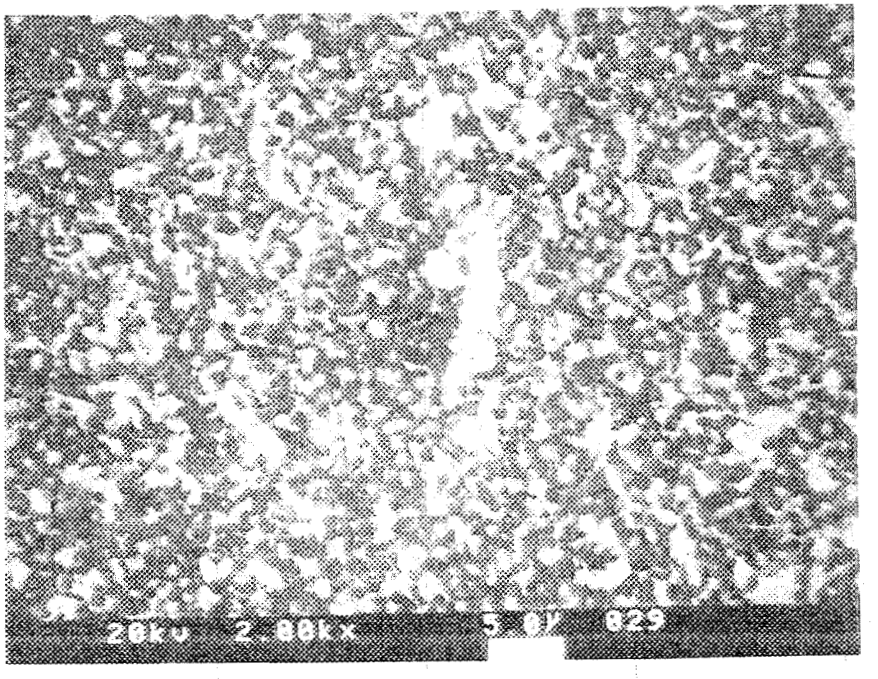

Fig. 12: Microstructure (SEM) of sintered/HIPed Ce-ZTA ceramic of composition Z16CE60A.

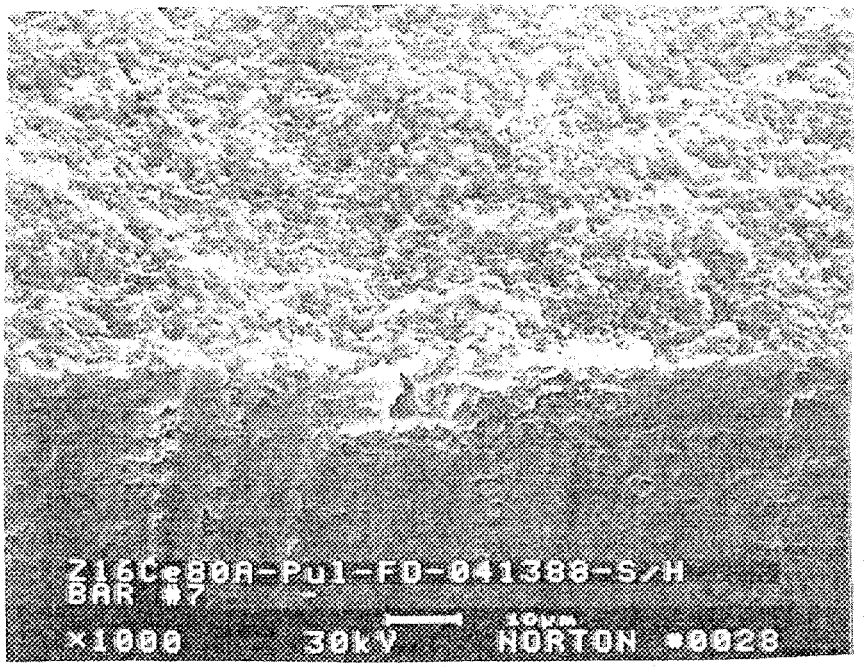

Fig. 13: Fractography of an MOR bar of material Z16CE80A, showing surface defect.

Fig. 14: Fractography of an MOR bar of material Z24CE80A, showing a large Al_2O_3-rich grain near the surface.

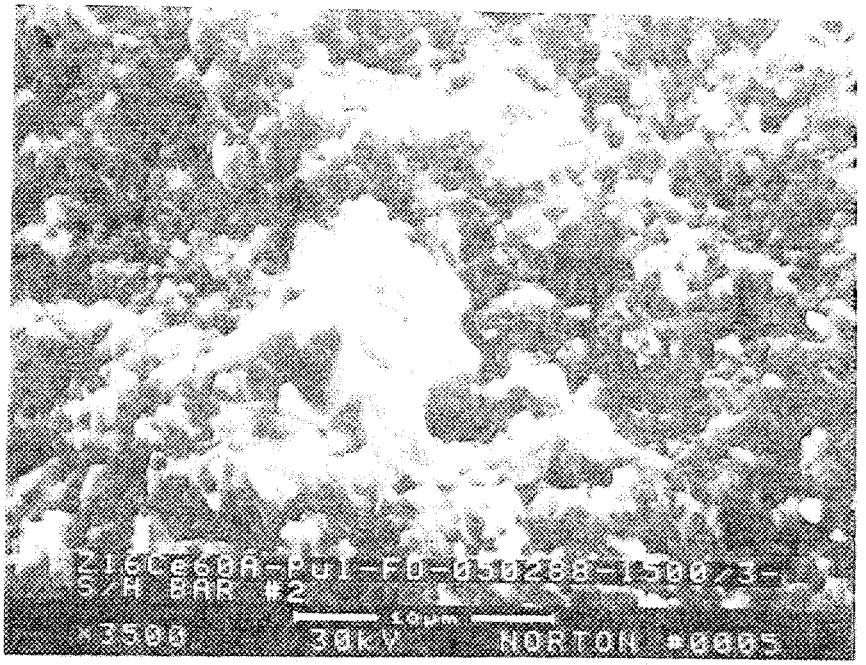

Fig. 15: Fractography of an MOR bar of material Z16CE60A, showing dense, Al_2O_3-rich agglomerate in the interior.

Processing and Characterization of Transformation-Toughened Ceramics with Strength Retention to Elevated Temperatures

R. A. Cutler, S. L. Bruner, and D. W. Prouse (Ceramatec, Inc.)
A. V. Virkar and D. K. Shetty (University of Utah)

Objective/Scope

Previous work[1] has shown that it is possible to increase the strength of Al_2O_3-ZrO_2 ceramics by incorporating transformation-induced residual stresses in sintered specimens consisting of three layers. The outer layers contained Al_2O_3 and unstabilized ZrO_2, while the central layer contained Al_2O_3 and partially stabilized ZrO_2. When cooled from the sintering temperature, some of the zirconia in the outer layers transformed to the monoclinic form while zirconia in the central layer was retained in the tetragonal polymorph. The transformation of zirconia in the outer layers led to the establishment of surface compressive stresses and balancing tensile stresses in the bulk. In theory, the residual stress will not decrease with temperature until the monoclinic to tetragonal transformation temperature is reached since monoclinic and tetragonal ZrO_2 polymorphs have nearly the same coefficients of thermal expansion.

During the first two years of ORNL funding it was demonstrated that 1) three layer composites could be made with retention of compressive surface stresses to temperatures of 750°C[2,3]; 2) residual stresses could be detected by strength testing[2,3], strain gauge measurements[4], characterization of monoclinic content by x-ray diffraction[2], or indentation/strength measurements[5]; 3) the three layer composites have excellent damage resistance[5]; and 4) significant (300-400 MPa) residual compressive stress which is not transformation-induced can be introduced by grinding monolithic Al_2O_3-15 vol. % ZrO_2(3.0 mol. % Y_2O_3).

The objectives of the present two year subcontract are 1) to increase the use temperature of three-layer composites by substituting HfO_2 for ZrO_2, 2) develop aqueous and nonaqueous slip casting techniques for three layer composites in order to obtain better layer uniformity and to maximize residual compressive stress by optimizing the outer layer thickness, 3) superimpose temperature stresses on transformation-induced stresses in three layer composites, and 4) demonstrate improved thermal shock resistance and damage resistance in optimized composites.

Technical Highlights

Residual Stresses Introduced During Grinding

Previous testing of both monolithic and three layer compositions was performed in the as-sintered condition to avoid transformation of the outer layer upon grinding[2,3]. Strength data recently reported (see Table 1) for the monolithic inner layer material (Al_2O_3-15 vol. % ZrO_2(3 mol. % Y_2O_3)) show nearly a doubling of strength upon grinding[6].

Table 1
Strengthening of Al_2O_3-15 vol. % ZrO_2(3 mol. % Y_2O_3)
Due to Grinding

Specimen Preparation	Test Temp. (°C)	No. Spec. Tested	Strength (MPa)
Unground	25	6	452±11
Ground (220 Grit)	25	6	835±85
Ground, 1200°C Anneal	25	5	731±168
Ground, 1600°C Anneal	25	6	666±68
Ground, 1200°C Anneal	750	3	621±47
Ground, 1200°C Anneal	850	3	606±5
Ground, 1200°C Anneal	950	3	528±21
Ground, 1200°C Anneal	1200->750	3	627±95

The strength degraded slightly with temperature (see Table 1) but testing at 750°C (after cooling from 1200°C) showed that transformation-induced stresses are not the primary strengthening mechanism since strength was identical to that measured upon heating to 750°C. This is consistent with x-ray diffraction data which showed no transformation to monoclinic zirconia upon grinding (see Table 2). Specimens polished to a 1 μm finish without grinding showed only a moderate strength improvement (strength of 551±49 MPa) despite a significant improvement in surface finish, demonstrating that grinding does more than improve surface finish. In order to see if it is possible that grinding introduces compressive stresses due to plastic deformation, Al_2O_3, ZrO_2, monolithic outer layer material (Al_2O_3-15 vol. % ZrO_2) and three-layer composites were all tested (see Table 2) in the unground (edges chamfered before HIPing) and ground state (220 grit wheel at down feed of 2.5 microns/pass before sparking out). The strength increased (by 30-67%) for all specimens, although the magnitude of the strength increase was greatest for ZrO_2 and the monolithic inner layer specimen. Fractography showed alumina, zirconia, and monolithic outer layer bars all failed from the tensile surface, whereas monolithic inner layer and three-layer bars showed a large percentage of bars failing from near the chamfers.

A number of factors affect the strength increase including improved surface finish and transformation-induced stresses for the ZrO_2, monolithic outer, and three-layer specimens. The inner layer monolithic ZrO_2 is unique in that no measurable monoclinic ZrO_2 was observed on the ground or fracture surface (see Table 2). While others[7-10] have seen a strengthening via grinding for transformation toughened ceramics, it has always been accompanied by an increase in monoclinic content. It is for this reason that the stresses introduced during grinding are not dependent on the m-->t transformation temperature[6] and ground monolithic inner

Table 2
Strength Comparison of Ground and Unground Bars

Material	Density (g/cc)	Strength (MPa) Unground[b] # [d]	x [e]	s [f]	Ground[c] #	x	s	m-ZrO_2 Content[a] (%) U[b]	G[c]	F.S.[d]
Al_2O_3[g]	3.98	8	308	30	8	434	64	---	---	---
ZrO_2[h]	6.04	8	677	63	5	998	73	<1	1.9	24.8
Outer[i]	4.29	8	389	23	5	650	59	83.1	85.6	88.5
Inner[j]	4.32	8	485	34	8	806	52	<1	<1	<1
Three-layer[k]	4.32	7	679	56	4	879	51	---[l]	---[l]	---[l]

a. Monoclinic content of ZrO_2 in specimen[11].
b. Chamfered before HIPing with no other grinding.
c. Ground with a 220 grit wheel at a down feed of 2.5 μm/pass before spark out.
d. Number of specimens tested in four point bending.
e. Mean value.
f. Standard deviation.
g. Reynold's ERC-DBM alumina.
h. Daiichi's HSY-3.0 zirconia.
i. Outer layer composition.
j. Inner layer composition.
k. Three-layer composition[2,3] with outer layers 1/12 total thickness.
l. Not measured but has substantial monoclinic ZrO_2[2,3].

layer specimens have higher strength than three-layer composites at temperatures in excess of 950°C. The lack of monoclinic zirconia on ground and fracture surfaces and prior work showing that the effect is not solely due to improved surface finish, suggests that plastic deformation during grinding may account for part of the improved strength of the inner layer composition.

In order to optimize the stresses introduced into the monolithic inner material during grinding, the rate of down feed was varied. Table 3 shows that strengths over 900 MPa were observed when the down feed was increased to 10.2 microns/pass. Furthermore, grinding on the sides of the bar decreased the tendency for the bars to fail from chamfers and increased the strength.

Monolithic Al_2O_3, ZrO_2(3 mol. % Y_2O_3), Al_2O_3-15 vol. % ZrO_2 and three layer Al_2O_3-15 vol. % ZrO_2 (with and without post HIP grinding) specimens were sent to Rockwell International for determination of residual stresses by x-ray diffraction. In an effort to determine the depth of compressive stresses introduced by grinding (believed to be due to plastic deformation) Al_2O_3-15 vol. % ZrO_2, specimens

Table 3
Effect of Grinding Parameters on the Room Temperature Strength of Al_2O_3-15 vol. % $ZrO_2(Y_2O_3)$ Composites

Sides Ground[a]	Down feed[b] (μm/pass)	Strength (MPa) #[c]	x[d]	s[e]
0	2.5	8	485	34
2	2.5	8	806	52
4	2.5	6	876	100
2	5.1	6	749	105
4	5.1	6	862	119
1	7.6	8	806	52
4	10.2	6	926	78
4	15.2	6	849	102

a. Sides of samples ground with a 220 grit diamond wheel. Tensile surface was ground for all samples except for unground bars.
b. Down feed of 220 grit wheel prior to spark out.
c. Number of bars tested.
e. Mean strength.
f. Standard deviation.

were prepared for strength/indentation measurements as before[5]. The strength at indentation loads of 37, 64, 125, and 296 N agreed with previous data for unground monolithic inner layer specimens[5], indicating that residual stresses introduced by grinding are very shallow, as expected. The fact that the stresses are shallow, as compared to stresses in three layer specimens, further supports the need for a protective compressive stress layer of at least 100 μm[1].

Slip Casting

Aqueous slip casting was used to make monolithic and three layer Al_2O_3-15 vol. % ZrO_2 plates (approximately 70 mm x 70 mm x 6 mm). The slip cast plates were sectioned into bars using a diamond wire saw. The sintered bars had densities greater than 99% of theoretical. Strengths of slip cast monolithic and three layer Al_2O_3-15 vol. % ZrO_2 bars made by aqueous slip casting[6] ranged between 800 and 930 MPa, which was no improvement over previous slip cast composites (The strength of monolithic inner bars cut from a similar plate and diamond ground was 922 MPa (std. dev. of 49 MPa). This strength is comparable to that of ground dry pressed inner layer bars). It is believed that the main limitation in achieving higher strengths is associated with eliminating surface cracks created during drying. Experiments using microwave drying in a controlled humidity environment are in progress. Several other approaches are being pursued including nonaqueous slip casting. The uniformity in outer

layer thickness is excellent for three layer plates and two layer crucibles (and cylinders) made via aqueous slip casting.

Partially stabilized and unstabilized hafnia powders are expected from Teledyne Wah Chang Albany during the next month. These hafnia powders will be used to make Al_2O_3-15 vol. % HfO_2 compositions for three layer composites.

Temperature Stresses

The feasibility of using temperature stresses to improve the room temperature strength of three layer composites was investigated by making a ZrO_2(3 mol. % Y_2O_3)-30 vol. % Al_2O_3 composition (thermal expansion expected to be $9.4 \times 10^{-6}/^{o}C$) as the inner layer composition and using Al_2O_3-15 vol. % ZrO_2(3 mol. % Y_2O_3) ($\alpha = 8.3 \times 10^{-6}/^{o}C$) as the outer layer composition. Assuming a square wave stress distribution, a temperature differential of $1000^{o}C$ over which stresses are present, inner layer thickness/total thickness of 0.833 (i.e., outer layers 1/12 the total thickness of the part), and identical Poisson's ratio (0.25) and Young's modulus (300 GPa) for inner and outer materials, the predicted compressive residual stress in the outer layers is 367 MPa.

The strength of the three layer 1/12-5/6-1/12 composite was increased by 210 MPa over the strength of the monolithic outer layer specimens. The strength of the unground three layer bars was 787 MPa. Assuming that a residual stress of 400 MPa can be superimposed by grinding the outer layers before testing, the strength of the ground three layer composite is expected to be approximately 1.2 GPa. The strength of ground specimens will be investigated as well as efforts to maximize the magnitude of the compressive residual stress. Further work on temperature stresses and the superposition of stresses is in progress.

Status of Milestones

On schedule.

Publication

A paper entitled "Indentation Fracture Response and Damage Resistance of Al_2O_3-ZrO_2 Composites Strengthened by Transformation-Induced Residual Stresses" by J. J. Hansen, R. A. Cutler, D. K. Shetty and A. V. Virkar was accepted by the Am. Ceram. Soc. for publication.

References

1. A. V. Virkar, J. L. Huang, and R. A. Cutler, "Strengthening of Oxide Ceramics by Transformation Induced Stresses," J. Am. Ceram. Soc., 70 [3] 164-170 (1987).

2. R. A. Cutler, J. J. Hansen, A. V. Virkar, D. K. Shetty, and R. C. Winterton, "Strength Improvement in Transformation Toughened Ceramics using Compressive Residual Surface Stresses," Advanced Structural Ceramics Vol. 78, ed. by P.F. Becher, M. V. Swain, and S. Somiya (Materials Research Society, Pittsburgh, PA, 155-163, 1987).

3. R. A. Cutler, J. D. Bright, A. V. Virkar, and D. K. Shetty, "Strength Improvement in Transformation-Toughened Alumina by Selective Phase Transformation," J. Am. Ceram. Soc., 70 [10] 714-18 (1987).

4. A. V. Virkar, J. F. Jue, J. J. Hansen and R. A. Cutler, "Measurement of Residual Stresses in Oxide-ZrO_2 Three-Layer Composites," J. Am. Ceram. Soc., 71[3] C-148-C-151 (1988).

5. J. J. Hansen, R. A. Cutler, D. K. Shetty and A. V. Virkar, "Indentation Fracture Response and Damage Resistance of Al_2O_3-ZrO_2 Composites Strengthened by Transformation-Induced Residual Stresses" to appear in J. Am. Ceram. Soc.

6. R. A. Cutler, J. J. Hansen, D. W. Prouse, A. V. Virkar, and D. K. Shetty, "Processing and Characterization of Transformation Toughened Ceramics with Strength Retention to Elevated Temperatures," in Ceramic Technology for Advanced Heat Engines Project Bimonthly Technical Progress Report ORNL/CF-87/380 (Feb.-Mar. 1988), Oak Ridge National Laboratory, Oak Ridge, Tenn. pp. 129-134 (1988).

7. T. K. Gupta, "Strengthening by Surface Damage in Metastable Tetragonal Zirconia," J. Am. Ceram. Soc., 63 [1-2] 117 (1980).

8. N. Claussen and M. Rühle, "Design of Transformation-Toughened Ceramics," Advances in Ceramics Vol. 3, ed. by A. H. Heuer and L. W. Hobbs, The Am. Ceram. Soc., Columbus, Ohio, pp 137-163 (1981).

9. D. J. Green, F. F. Lange, and M. R. James, "Residual Surface Stresses in Al_2O_3-ZrO_2 Composites," Advances in Ceramics Vol. 12, ed. by N. Claussen, M. Ruhle, and A. H. Heuer, The Am. Ceram. Soc., Columbus, Ohio, pp. 240-250 (1983).

10. D. J. Green, F. F. Lange, and M. R. James, "Factors Influencing Residual Surface Stresses due to a Stress-Induced Phase Transformation," J. Am. Ceram. Soc., 66 [9] 625-629 (1983).

11. H. Toraya, M. Yoshimura, and S. Somiya, "Calibration Curve for Quantitative Analysis of the Monoclinic-Tetragonal ZrO_2 System by X-Ray Diffraction," J. Am. Ceram. Soc., 68[6] C-119-C-121 (1984).

1.2.4 Silicate Matrix

Low Expansion Ceramics for Diesel Engine Applications

J. J. Brown, R. E. Swanson (Virginia Polytechnic Institute and State University), and F. A. Hummel (Consultant)

Objective/scope

The major objective of this research is to investigate selected oxide systems for the development of a low expansion, high thermal shock resistant ceramic. Specifically, it is the goal of this study to develop an isotropic, ultra-low expansion ceramic which can be used above 1200°C and which is relatively inexpensive.

Technical progress

This research program includes the synthesis, property characterization, and fabrication of candidate low thermal expansion ceramics from four systems based upon aluminum phosphate, silica, mullite, and zircon. In the first two systems, the goal is to stabilize low thermal expansion, high temperature, high crystal symmetry phases via solid solution formation. In mullite, deviation from stoichiometry and solid solution formation are utilized to reduce the thermal expansion. In zircon, the crystal anisotropy and thermal expansion are reduced via solid solution formation. Based upon earlier data of the investigators, compositional ranges are evaluated by fabricating experimental specimens and determining phase content plus microstructure, thermal expansion, solidus temperature, and density. Those compositions which exhibit acceptable sintering, phase composition, and expansion characteristics are studied in more detail, including flexure strength, creep, thermal conductivity, and crystal structure. Finally, those ceramic compositions exhibiting the best combination of properties are evaluated as to their fabrication behavior in the form of specimens having masses up to about 0.5 kg.

β-Eucryptite-$AlPO_4$ System

$AlPO_4$ is a well-known high-melting compound with crystal structures and polymorphism similar to that of SiO_2. Solid solutions of β-eucryptite ($Li_2 \cdot Al_2O_3 \cdot 2SiO_2$) with $AlPO_4$ are being studied in an effort to stabilize the high temperature polymorphs such as β-cristobalite. Current work has focused on high $AlPO_4$ content solid solution formation between $AlPO_4$ and β-$LiAlSiO_4$, and elemental substitution in some of the solid solutions.

Experimental

Samples were prepared by either the solid state reaction method or sol-gel technique. Raw materials included silicic acid, $Al(OH)_3 \cdot nH_2O$, $(NH_4)_2HPO_4$ or $NH_4H_2PO_4$, Li_2CO_3, $MgCO_3$, TiO_2, GeO_2, $Si(OC_2H_5)_4$, $(CH_3O)_3P(O)$, $[(CH_3)_2CHO]_3Al$, and $Ti[OCH(CH_3)_2]_4$. X-ray diffraction (XRD) and petrographic phase identifications were made on the resulting sample powders. Samples showing single phase compositions were pressed into bars and sintered at the desired temperature for subsequent thermal expansion measurements. Linear thermal expansion was measured from room temperature to 1000°C with an automatic dual push rod dilatometer (Netzsch 402 ED). Axial thermal expansion to 1100°C was was measured by high temperature XRD at the High Temperature Materials Lab at Oak Ridge National Lab. The high temperature XRD was performed using a Scintag θ-θ goniometer equipped with a Buehler high temperature attachment. Platinum powder was used as an internal standard. Scanning rate was 2°2θ/min in a 2θ range of 19° to 50°. Three major reflections, (100), (102), and (114), were used.

Phase stability of specimens was studied by differential thermal analysis (DTA) with a Perkin-Elmer thermal analysis system 7/4(20°C/min heating rate to 1300, 1400, or 1500°C). Thermal shock tests for compositions having low thermal expansion were conducted by quenching bars from progressivley higher temperatures into water of room temperature until cracking was observed. For retained flexural strength, or modulus of rupture (MOR) measurements, more than 20 rectangular specimens were pressed and sintered from the sample powders

for each of the compositions exhibiting low thermal expansion. The 4-point bend method was used for these measurements. For each composition, 10 specimens were tested as originally formed; others were tested after undergoing different thermal shock cycles. At least 3 specimens were tested for each condition.

Results and Discussion

<u>β-$LiAlSiO_4$-$AlPO_4$ system and elemental substitution</u>. The possibility of forming solid solution between β-$LiAlSiO_4$ and $AlPO_4$ within the $AlPO_4$ content range of 56-90 mol% was studied. Sample composition, processing, phase analysis, and thermal expansion details are summarized in Table 1. Samples 1-5 were prepared by the solid-state reaction method and fired at 1200°C or higher for more than 100 hours to achieve equilibrium. XRD phase identification revealed the presence of more than one phase in all samples after the heat treatments. It is likely that a single phase solid solution cannot form within this $AlPO_4$ range.

The effects of SiO_2 content in β-$LiAlSiO_4$-$AlPO_4$ solid solution on thermal expansion behavior of compositions were further studied. With an increased SiO_2 content in the compositions $Li_{0.5}AlP_{0.5}Si_{0.5}O_4$, $Li_{0.5}AlP_{0.5}Si_{0.6}O_{4.2}$, and $Li_{0.5}AlP_{0.5}Si_{0.7}O_{4.4}$ (samples 6-8 in Table 1), the average coefficient of thermal expansion (CTE) (30-100°C) decreased from $-10.3 \times 10^{-7}/°C$ to $-11.9 \times 10^{-7}/°C$ to $-15.6 \times 10^{-7}°C$, respectively. The results were similar in the case of compositions $Li_{0.48}AlP_{0.52}Si_{0.48}O_4$, $Li_{0.48}AlP_{0.52}Si_{0.576}O_{4.19}$, and $Li_{0.48}AlP_{0.52}Si_{0.672}O_{4.384}$ (samples 9-11 in Table 1), where the CTE decreased from $-7.6 \times 10^{-7}/°C$ to $-10.5 \times 10^{-7}/°C$ to $-12.9 \times 10^{-7}/°C$, respectively. It appears that an increase in SiO_2 content increases the negative thermal expansion of β-$LiAlSiO_4$-$AlPO_4$ solid solution.

Work has continued on the effect of the substitution of Mg^{++} ions for Li^+ ions in β-$LiAlSiO_4$-$AlPO_4$ solid solutions. As shown in Table 1, compositions $Mg_{0.01}Li_{0.46}AlP_{0.52}Si_{0.48}O_4$ (sample 12), $Mg_{0.02}Li_{0.44}AlP_{0.52}Si_{0.48}O_4$ (sample 13), $Mg_{0.03}Li_{0.42}AlP_{0.52}Si_{0.48}O_4$ (sample 14), $Mg_{0.035}Li_{0.41}AlP_{0.52}$ (sample 16), and

Table 1. Sample processing and thermal expansion results for the $AlPO_4$-β-$LiAlSiO_4$ system.

Sample No.	Initial Composition	Sample and Bar Processing Temp/Time(°C/h)	Phase Composition	Linear Thermal Expansion $\alpha(x10^{-7}/^{o}C)$
1	$Li_{0.44}AlP_{0.56}Si_{0.44}O_4$	1210/48,1200/63, 1200/36	M.P.	N.A.
2	$Li_{0.25}AlP_{0.75}Si_{0.25}O_4$	1200/58,1250/35, 1300/24	M.P.	N.A.
3	$Li_{0.2}AlP_{0.8}Si_{0.2}O_4$	1200/58,1250/35, 1300/24	M.P.	N.A.
4	$Li_{0.15}AlP_{0.8}Si_{0.2}O_4$	1200/58,1250/35 1300/24	M.P.	N.A.
5	$Li_{0.1}AlP_{0.9}Si_{0.2}O_4$	1200/58,1250/35, 1300/24	M.P.	N.A.
6	$Li_{0.5}AlP_{0.5}Si_{0.5}O_4$	1200/72 Bar: 1200/10	S.S.	-10.3
7	$Li_{0.5}AlP_{0.5}Si_{0.6}O_{4.2}$	1200/53,1200/36 Bar: 1200/10	S.S.	-11.9
8	$Li_{0.5}AlP_{0.5}Si_{0.7}O_{4.4}$	1200/53,1200/36 Bar: 1200/10	S.S.	-15.6
9	$Li_{0.48}AlP_{0.52}Si_{0.48}O_{0.4}$	1200/72 Bar: 1200/10	S.S.	-7.6
10	$Li_{0.48}AlP_{0.52}Si_{0.576}O_{4.192}$	1200/53,1200/36 Bar: 1200/10	S.S.	-10.5
11	$Li_{0.48}AlP_{0.52}Si_{0.672}O_{4.384}$	1200/53,1200/36 Bar: 1200/10	S.S.	-12.9
12	$Mg_{0.01}Li_{0.46}AlP_{0.52}Si_{0.48}O_4$	1200/72,1200/44 Bar: 1200/10	S.S.	-3.8

Table 1 (cont'd)

13	$Mg_{0.02}Li_{0.44}AlP_{0.52}Si_{0.48}O_4$	1200/72,1200/44 Bar: 1200/10	S.S.	-3.1
14	$Mg_{0.03}Li_{0.42}AlP_{0.52}Si_{0.48}O_4$	1200/72,1200/44 Bar:1200/10	S.S.	-2.6
15	$Mg_{0.04}Li_{0.4}AlP_{0.52}Si_{0.48}O_4$	1200/72,1200/44 Bar: 1200/10	S.S.	-2.0
16	$Mg_{0.035}Li_{0.41}AlP_{0.52}Si_{0.48}O_4$	1200/84,1200/36	S.S.	-2.3
17	$Mg_{0.05}Li_{0.38}AlP_{0.52}Si_{0.48}O_4$	1200/54,1200/60 1200/74	M.P.	N.A.
18	$Li_{0.45}Al_{0.95}Ti_{0.05}P_{0.5}Si_{0.5}O_4$	1200/84,1200/48 1200/40	S.S. with Rutile	N.A.
19	$Li_{0.45}Al_{0.95}Ti_{0.05}P_{0.5}Si_{0.5}O_4$	Sol-gel;1200/36	S.S. with Rutile	N.A.
20	$Li_{0.4}Al_{0.9}Ti_{0.1}P_{0.5}Si_{0.5}O_4$	1200/84,1200/60 1200/36	S.S. with Rutile	N.A.
21	$Li_{0.4}AlP_{0.5}Si_{0.45}Ti_{0.05}O_4$	1200/48 (melted) 1180/48	Multiphase	N.A.
22	$Li_{0.42}Al_{0.95}Ge_{0.05}P_{0.52}Si_{0.48}O_4$	1180/48,1190/36 1205/25	S.S. with small amount of $AlPO_4$	-10.4
23	$Li_{0.48}AlP_{0.52}Si_{0.24}Ge_{0.24}O_4$	1180/48 1190/36(melted) 1170/30	Multiphase	N.A.
24	$Li_{0.48}AlP_{0.52}Si_{0.32}Ge_{0.16}O_4$	1180/48,1170/30 1180/30	S.S. with small amount of $AlPO_4$	N.A.
25	$Li_{0.48}AlP_{0.52}Si_{0.40}Ge_{0.08}O_4$	1180/48,1170/28	S.S.	-2.5

M.P. = More than one phase.
S.S. = β-$LiAlSiO_4$ Solid solution.
N.A. = Not available.

$Mg_{0.04}Li_{0.4}AlP_{0.52}Si_{0.48}O_4$ (sample 15), prepared by solid state reactions, exhibited single phases and decreasing negative expansion (30-1000°C) with increasing Mg^{++} content. Composition $Mg_{0.05}Li_{0.38}AlP_{0.52}Si_{0.48}O_4$ (sample 17, 20 mol% of Li^+ replaced by Mg^{++}), however, was multiphase after the heat treatment, indicating that although the substitution of Mg^{++} for Li^+ may lower the negative expansion of the material, the maximum replaceable amount of Li^+ by Mg^{++} in this system appears to be about 20 mol%.

The possibilities of ion substitution of $Ti^{4+} \rightleftharpoons Al^{3+} + Li^+$ or $Ti^{4+} \rightleftharpoons Si^{4+}$ and $Ge^{4+} \rightleftharpoons Al^{3+} + Li^+$ or $Ge^{4+} \rightleftharpoons Al^{3+} + Li^+$ were studied. In an attempt to introduce the ion exchange $Ti^{4+} \rightleftharpoons Al^{3+} + Li^+$, two samples having the composition of $Li_{0.45}Al_{0.95}Ti_{0.05}P_{0.5}Si_{0.5}O_4$ (samples 18-19) were prepared by the solid state reaction method and sol-gel techniques. Sample 18, processed via solid state reaction, was fired at 1200°C 3 times (for 84, 48, and 40 hours) with powder grinding and mixing between each firing. Sample 19, processed using the sol-gel technique, was fired at 1200°C for 36 hours. Both final samples had a phase composition of β-$LiAlSiO_4$ solid solution with a small amount of rutile. In the cases of composition $(Li_{0.4}Al_{0.9}Ti_{0.1})P_{0.5}Si_{0.5}O_4$ (sample 20) and composition $Li_{0.5}AlP_{0.5}(Si_{0.45}Ti_{0.05})O_4$ (sample 21), second phases were present after the heat treatment. It is likely that, due to its larger size, Ti^{4+} cannot easily enter the 4-coordinated position to replace either the Al^{3+} or Si^{4+} in the solid solution.

In the composition $(Li_{0.42}Al_{0.95}Ge_{0.05})P_{0.52}Si_{0.48}O_4$ (sample 22), Ge^{4+} was initially introduced to replace Al^{3+} and Li^+ ($Ge^{4+} \rightleftharpoons Al^{3+} + Li^+$). In the composition $Li_{0.48}AlP_{0.52}(Si_{0.32}Ge_{0.16})O_4$ (sample 24) and $Li_{0.48}AlP_{0.52}(Si_{0.24}Ge_{0.24})O_4$ (sample 23), Ge^{4+} was initially introduced to replace Si^{4+} ($Ge^{4+} \rightleftharpoons Si^{4+}$). All three compositions showed second phases after heat treatment. However, with a decreased Ge^{4+} substitution for Si^{4+} in the composition $Li_{0.48}AlP_{0.52}(Si_{0.4}Ge_{0.08})O_4$ (about 16.7 mol% Si^{4+} was substituted by Ge^{4+}, sample 25), single phase β-$LiAlSiO_4$ solid solution was formed. This composition exhibited an average CTE value of $-2.5 \times 10^{-7}/°C$ (30-1000°C), a substantial

reduction in negative thermal expansion when compared to composition $Li_{0.48}AlP_{0.52}Si_{0.48}O_4$ ($-6.6 \times 10^{-7}/^{o}C$).

(DTA) results. Compositions showing a single phase by XRD analysis were analyzed by DTA to evaluate the thermal stability and the effects of composition change on melting behavior. Peaks corresponding to phase transformation were not observed for any of the samples analyzed.

The DTA results shown in Table 2 indicate that the melting point of the β-$LiAlSiO_4$-$AlPO_4$ solid solution increased with $AlPO_4$ content. This is illustrated by compositions No. 2, No. 4, and No. 5 where the $AlPO_4$ content increases from 50 to 54 mol percent. The melting point of the solid solution appears to increase with increased SiO_2 content, as illustrated by the first three compositions in Table 2. Partial substitution of Mg^{++} for Li^{+} (No. 7) and Ge^{4+} for Si^{4+} (No. 9) appeared to lower the melting temperature when compared to composition No. 4 (without substitutions).

Axial thermal expansion. The axial thermal expansion behavior of specimens having compositions $Li_{0.5}AlP_{0.5}Si_{0.465}O_{3.93}$ and $Li_{0.41}Mg_{0.035}AlP_{0.52}Si_{0.48}O_4$ are shown in Figures 1 and 2. The former had an average CTE value of $-0.56 \times 10^{-7}/^{o}C$ (30-1000°C) and was described in our previous semiannual progress report;[1] the latter had an average CTE value of $-2.3 \times 10^{-7}/^{o}C$ (30-1000°C). The expansions are anisotropic, but compared with pure α-$LiAlSiO_4$, appear to be much lower.

The average bulk CTE value, calculated on the basis of the axial thermal expansion results, for composition $Li_{0.5}AlP_{0.52}Si_{0.465}O_{3.93}$ is $-17.7 \times 10^{-7}/^{o}C$, for composition $Li_{0.41}Mg_{0.035}AlP_{0.52}Si_{0.48}O_4$ is $-16 \times 10^{-7}/^{o}C$, both between 18 to 1100°C. These CTE values are more negative than those measured by the dilatometer.

Thermal shock experiments. Thermal shock resistance and relative retained strength (normalized) were determined for the compositions of $Li_{0.46}AlP_{0.54}Si_{0.46}O_4$, $Li_{0.5}AlP_{0.5}Si_{0.465}O_{3.93}$, and $Li_{0.41}Mg_{0.035}AlP_{0.52}Si_{0.48}O_4$. Results of these tests are summarized in

Table 2. DTA results of single phase compositions.

Composition	Maximum temperature reached (°C)[a]	Results
1. $Li_{0.5}AlP_{0.5}Si_{0.465}O_{0.393}$	1300	O.T.P.[b] ~ 1205°C
2. $Li_{0.5}AlP_{0.5}Si_{0.5}O_4$	1300	O.T.P. ~ 1213°C
3. $Li_{0.5}AlP_{0.5}Si_{0.6}O_{4.2}$	1400	O.T.P. ~ 1241°C
4. $Li_{0.48}AlP_{0.52}Si_{0.48}O_4$	1500	O.T.P. ~ 1222°C
5. $Li_{0.46}AlP_{0.54}Si_{0.46}O_4$	1400	O.T.P. ~ 1246°C
6. $(Li_{0.46}Mg_{0.01})AlP_{0.52}Si_{0.48}O_4$	1300	O.T.P. ~ 1218°C
7. $(Li_{0.41}Mg_{0.035})AlP_{0.52}Si_{0.48}O_4$	1300	O.T.P. ~ 1210°C
8. $(Li_{0.4}Mg_{0.04})AlP_{0.52}Si_{0.48}O_4$	1300	O.T.P. ~ 1208°C
9. $Li_{0.48}AlP_{0.52}(Si_{0.4}Ge_{0.08})O_4$	1300	O.T.P. ~ 1175°C

[a]Heating rate = 20°C/min.
[b]O.T.P. = Onset temperature point on melting peak of DTA curve.

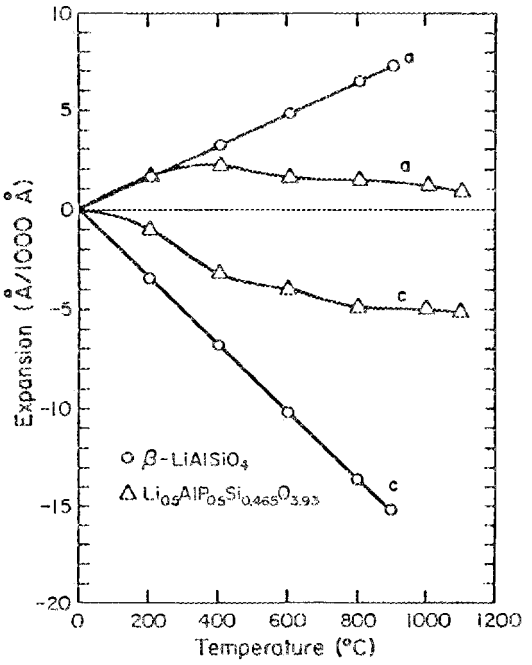

Figure 1. Axial expansion of $Li_{0.5}AlP_{0.5}Si_{0.465}O_{3.93}$.

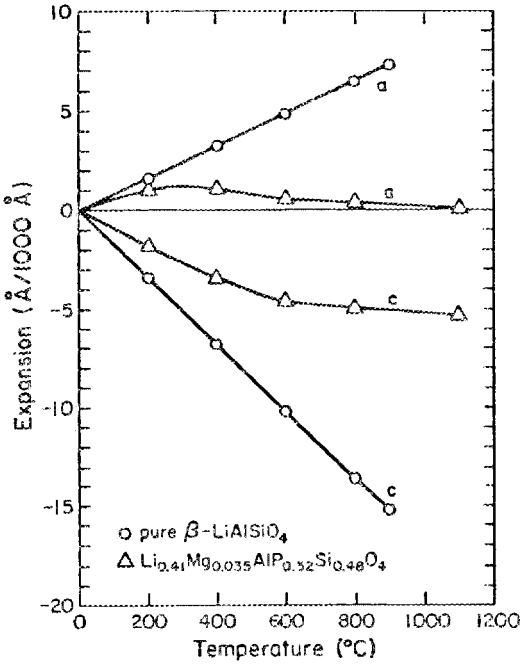

Figure 2. Axial expansion of $Li_{0.41}Mg_{0.035}AlP_{0.52}Si_{0.48}O_4$.

Table 3. The relative retained MOR values are shown in Figure 3, plotted as a function of the number of thermal shock cycles.

Table 3. Results of thermal shock experiments.

Composition	Thermal expansion (30-1000°C) $\alpha(\times 10^{-7}/^{\circ}C)$	ΔT_{max} (°C)	Relative retained strength* (%)
$Li_{0.46}AlP_{0.54}Si_{0.46}O_4$	-5.8	1150	39.3
$Li_{0.41}Mg_{0.035}AlP_{0.52}Si_{0.48}O_4$	-2.3	1175	46
$Li_{0.5}AlP_{0.5}Si_{0.465}O_{3.93}$	-0.96	1175	63.4

*MOR of specimen after 10 thermal shock cycle/MOR of specimen as originally formed without any thermal shock cycle) x 100%.

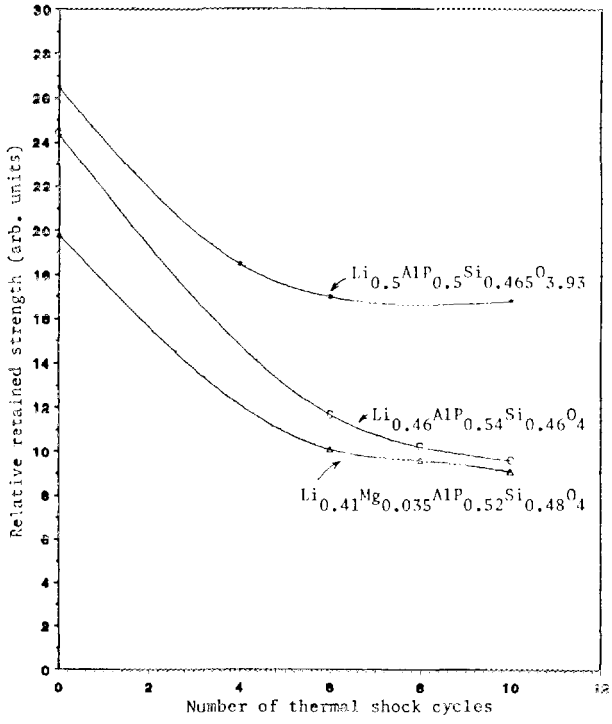

Figure 3. Relative retained strength of thermally shocked specimens.

For the composition $Li_{0.46}AlP_{0.54}Si_{0.46}O_4$, the maximum temperature difference at which cracking was observed (ΔT_{max}) was 1150°C (quenched from 1175°C into water at 25°C). In the case of the other two compositions quenched from 1200°C into water at 25°C, no cracking was observed. Because 1200°C was approaching the melting points of the compositions (see Table 2), higher temperature quenching was not performed.

As shown in Table 3, with the negative thermal expansion decreasing from $-5.8 \times 10^{-7}/°C$ for composition $Li_{0.46}AlP_{0.54}Si_{0.46}O_4$, to $-2.3 \times 10^{-7}/°C$ for composition $Li_{0.41}Mg_{0.035}AlP_{0.52}Si_{0.48}O_4$, to $-0.76 \times 10^{-7} \times 10^{-7}/°C$ for composition $Li_{0.5}AlP_{0.5}Si_{0.465}O_{3.93}$, the relative retained strength (MOR of specimens following 10 thermal shock cycles/MOR of specimens as-formed) x 100% increased from 39.3% to 46% to 63.4%, respectively.

The results indicate that the MOR values of composition $Li_{0.41}Mg_{0.035}AlP_{0.52}Si_{0.48}O_4$ were obviously lower than that of the other two compositions (see Figure 3). More work should be done to investigate the effect of $Mg^{++} \rightleftharpoons Li^{+}$ ion exchange on the strength of the material.

Summary

Attempts to form a single phase solid solution between β-$LiAlSiO_4$ and $AlPO_4$ within the $AlPO_4$ content range of 55-90 mol% were unsuccessful. The limit of solid solubility was found to be 54 mol%.

SiO_2 content can change within a small range in the solid solutions without the structural changes. A decrease in SiO_2 content will reduce the negative thermal expansion and, on the other hand, decrease the melting temperature of the solid solutions.

About 20 mol% of Li^{+} can be substituted by Mg^{++} in the solid solutions. This substitution can further decrease the negative thermal expansion and expansion anisotropy of the solid solutions. On the other hand, this substitution decreases the melting temperature and may lower the strength of the solid solutions.

Due to its large size, Ti^{4+} could not be introduced into

4-coordinated positions to replace Al^{3+} or Si^{4+} in the solid solutions.

Si^{4+} was substituted (up to about 16.7 mol%) by Ge^{4+}, leading to a decrease in the negative thermal expansion of the solid solution. Al^{3+} could not be substituted by Ge^{4+} in the solid solution.

Silica System

The effect of the presence of foreign species on the high-low inversion behavior of cristobalite has been studied in detail in the present work. It was found that solid state reactions from starting oxides would not stabilize β-cristobalite due to a limited solid solution range in the cristobalite end; however, in some cases the inversion temperature of the cristobalite solid solution was shifted to a significantly lower value. Therefore, the sol-gel decomposition technique has been employed in preparing stabilized β-cristobalite. The goal is to achieve the fine-scale homogeneous mixing offered by sol-gel preparations and the preformed network structure in the gel. The fine particle size may also have some kinetic effects on the phase transformation. Two basic systems, $CaO-Al_2O_3-SiO_2$ and $MgO-Al_2O_3-SiO_2$, were selected for the present studies. Phase formation and the thermal expansion behavior of the stabilized silica phases were characterized.

Experimental

The starting material used for sol-gel preparation of the compositions shown in Table 4 included tetraethyl orthosilicate $[Si(OC_2H_5)_4]$, aluminum tri-sec butoxide $[Al(OC_4H_9)_3]$, calcium propionate $[Ca(O_2C_3H_5)_2]$, calcium nitrate $[Ca(NO_3)_2 \cdot 4H_2O]$, magnesium ethoxide $[Mg(OC_2H_5)_2]$, and magnesium nitrate $[Mg(NO_3)_2 \cdot 6H_2O]$. Both $Ca(NO_3)_2 \cdot 4H_2O$ and $Ca(O_2C_3H_5)_2$ were used as sources of calcium, and $Mg(NO_3)_2 \cdot 6H_2O$ and $Mg(OC_2H_5)_2$ were used as sources of magnesium, the difference being that nitrates are more soluble in alcohol. Sample compositions were prepared by mixing the starting materials in ethyl alcohol until the calcium or magnesium species dissolved. The solution was then hydrolyzed by adding distilled water. The molar ratio of water to the framework cations (Al + Si) was kept at 2:1 and the pH

Table 4. Phase analyses of compositions on the $CaO \cdot Al_2O_3 \cdot 2SiO_2$–$SiO_2$ join.

Sample No.	Composition	Phase Present
TS-125	$CaO \cdot Al_2O_3 \cdot 2SiO_2$	anorthite, β-crist. amorphous
TS-126	$CaO \cdot Al_2O_3 \cdot 5SiO_2$	anorthite, β-crist. amorphous
TS-127	$CaO \cdot Al_2O_3 \cdot 10SiO_2$	β-crist., anorthite
TS-128	$CaO \cdot Al_2O_3 \cdot 15SiO_2$	β-crist., anorthite
TS-129	$CaO \cdot Al_2O_3 \cdot 20SiO_2$	β-crist., anorthite (tr)
TS-130	$CaO \cdot Al_2O_3 \cdot 25SiO_2$	β-crist., anorthite (tr)
TS-131	$CaO \cdot Al_2O_3 \cdot 30SiO_2$	β-crist., anorthite (tr)
TS-132	$CaO \cdot Al_2O_3 \cdot 35SiO_2$	β-crist., anorthite (tr)
TS-133	$CaO \cdot Al_2O_3 \cdot 40SiO_2$	β-crist., anorthite (tr)
TS-134	$CaO \cdot Al_2O_3 \cdot 50SiO_2$	β-crist.
TS-135	$CaO \cdot Al_2O_3 \cdot 60SiO_2$	β-crist., amorphous
TS-136	$CaO \cdot Al_2O_3 \cdot 70SiO_2$	β-crist., amorphous, α-quartz

value was adjusted to 8 with ammonium hydroxide solution. A transparent gel resulted after the solution was allowed to stand at ambient temperature for 24 hours. The gel was dried at 60~70°C and then gradually heated to 1000°C for 48 hours. Phase identification was carried out by XRD and petrographic microscopy. Differential scanning calorimetry (DSC) and DTA were used to study the phase transformation of the silica phase. The powder samples without phase transformation and showing single phase composition were pressed into bars and sintered at 1000°C for 24 hours. These bars were used for thermal expansion measurements, using a dual push rod dilatometer. Axial thermal expansion of the composition $CaO \cdot Al_2O_3 \cdot 40SiO_2$ was measured by high temperature XRD using Pt as the internal standard.

Results and Discussion

<u>$CaO-Al_2O_3-SiO_2$ System.</u> The compositions studied were prepared using, as a basis, the chemical formula $CaAl_2Si_xO_{2(2+x)}$, $x \geq 2$, to form a three dimensional framework structure linked by the Al and Si tetrahedra. All the oxygen atoms are bridging oxygen and the calcium ions fit into the intersticies to balance the charge. The compositions selected also lie on the $CaO \cdot Al_2O_3 \cdot 2SiO_2-SiO_2$ binary join of the $CaO-Al_2O_3-SiO_2$ ternary system as shown in Figure 4.[2]

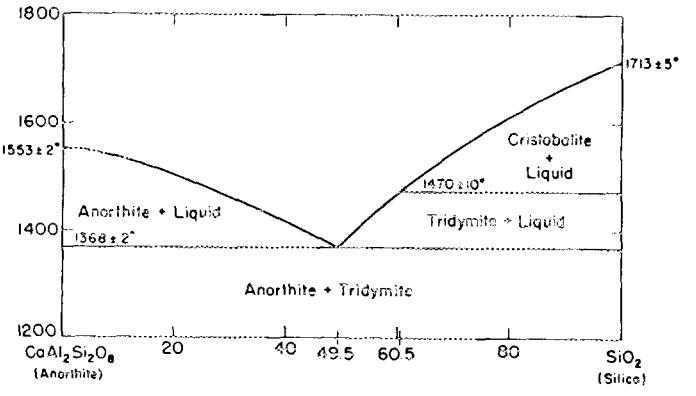

Figure 4. The $CaAl_2Si_2O_8-SiO_2$ binary join.[2]

Results from both XRD and DSC measurements showed that β-cristobalite was chemically stabilized in all the compositions prepared. Repeated scanning in the cristobalite inversion range revealed no phase transformation, and that the observed cristobalite phase is indeed high cristobalite. The concentration of about 5% ($CaO + Al_2O_3$), as in the composition $CaO \cdot Al_2O_3 \cdot 5OSiO2$, appears to be critical. Above this concentration, anorthite is always present; and below this concentration, either α-quartz or amorphous phase coexists with β-cristobalite (Table 4).

The axial thermal expansion of the gel-derived β-cristobalite is shown in Figure 5. The aggregate thermal expansion curves for most of the compositions follow the trend shown in Figure 5; however, these data are not reported because of the presence of multiple phases. The observed non-linear behavior indicates that the structure still shows a significant flexibility at low temperatures. It is the flexibility of the bond angle that results in the high expansion in the initial stage. This appears to be in contrast to the anticipated result for β-cristobalite, since the characteristic expansion curve of cristobalite usually shows a linear region after the inversion with a linear CTE value in the vicinity of $30 \times 10^{-7}/^{o}C$ for β-cristobalite. The speculation is that the bond angle stretching is typical for framework silicates, including silica. During the stretching, phase transformation may or may not occur depending on whether a new symmetry is generated, while dimensional changes always result. By the same token, a framework silicate will normally exhibit high expansion unless its thermal expansion is highly anisotropic.

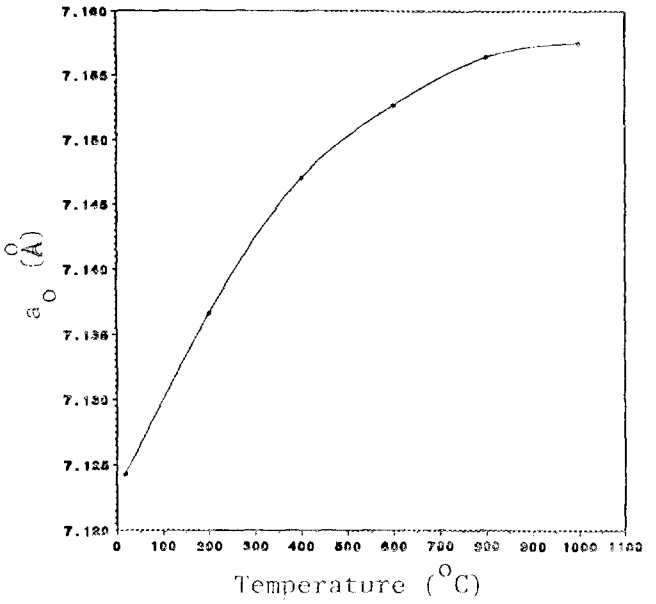

Figure 5. Axial expansion of β-cristobalite.

MgO-Al_2O_3-SiO_2 System. The compositions prepared are based on the chemical formula $MgAl_2Si_xO_{2(2+x)}$, x>2, as listed in Table 5. Figure 6 shows the $2MgO \cdot 2Al_2O_3 \cdot 5SiO_2$-$SiO_2$ join in the MgO-Al_2O_3-SiO_2 phase diagram[2] from which the compositions were selected. Unlike the $CaO \cdot Al_2O_3 \cdot 2SiO_2$-$SiO_2$ join, the $2MgO \cdot 2Al_2O_3 \cdot 5SiO_2$-$SiO_2$ join is not a true binary join.

Phase analyses and thermal expansion measurements are also presented in Table 5. The results are surprisingly different from the CaO-Al_2O_3-SiO_2 system since β-quartz was stabilized instead and repeated DTA scanning detected no phase transformation in the α⟷quartz range. The presence of amorphous phase is probably related to incomplete condensation reactions during gel formation. Another interesting result is that cordierite was not observed in any of the compositions, including the specimen with a stoichiometric cordierite composition (TS-137). In this case, the phase present was β-quartz and spinel. The solubility of (MgO + Al_2O_3) in β-quartz appears to be much higher than that of (CaO + Al_2O_3) in β-cristobalite. The thermal expansion appears to depend on the concentration of (MgO + Al_2O_3). As

Table 5. Phase analyses and CTE of compositions lying on the $2MgO \cdot 2Al_2O_3 \cdot 5SiO_2$-$SiO_2$ join.

Sample No.	Composition	Phase Present	Thermal expansion 30-1000°C $\alpha(10^{-7}/^{o}C$
TS-137	$2MgO \cdot 2Al_2O_3 \cdot 5SiO_2$	β-quartz, spinel	N.A.
TS-138	$MgO \cdot Al_2O_3 \cdot 10SiO_2$	β-quartz	41
TS-139	$MgO \cdot Al_2O_3 \cdot 15SiO_2$	β-quartz, amorphous(tr)	43
TS-140	$MgO \cdot Al_2O_3 \cdot 20SiO_2$	β-quartz, amorphous	N.A.
TS-141	$MgO \cdot Al_2O_3 \cdot 25SiO_2$	β-quartz, amorphous	N.A.
TS-142	$MgO \cdot Al_2O_3 \cdot 30SiO_2$	β-quartz	31
TS-143	$MgO \cdot Al_2O_3 \cdot 40SiO_2$	β-quartz	46
TS-144	$MgO \cdot Al_2O_3 \cdot 50SiO_2$	β-quartz, amorphous	N.A.
TS-145	$MgO \cdot Al_2O_3 \cdot 60SiO_2$	β-quartz	102

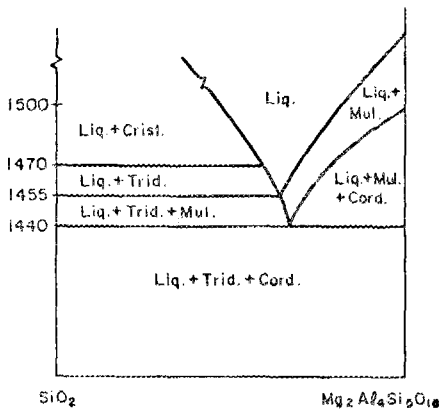

Figure 6. The SiO_2-Mg_2Al_4-Si_5O_{18} join.

shown in Figure 7, the expansion of β-quartz becomes increasingly non-linear as the concentration of (MgO + Al_2O_3) decreases. The decrease in (MgO + Al_2O_3) concentration may result in a more flexible (relaxed) structure and, therefore, a higher expansion. On the other hand, when sufficiently high in concentration, the presence of (MgO + Al_2O_3) may play an important role in hindering the bond angle stretching.

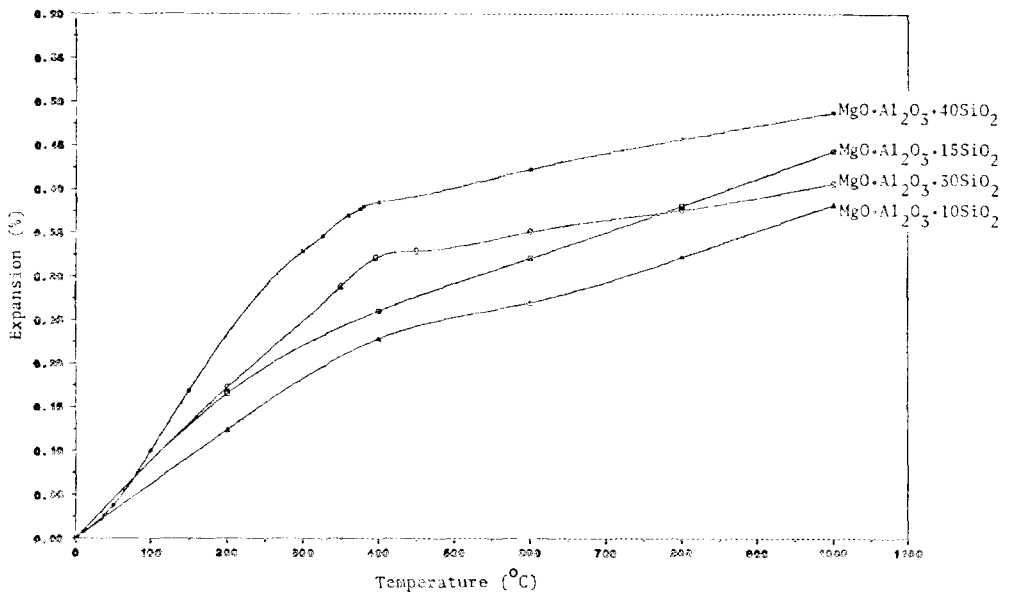

Figure 7. Thermal expansion of β-quartz structure.

The phases obtained in the above two systems after firing at 1000°C are compared to their corresponding phase diagrams. According to the phase diagrams, the formation temperature of β-cristobalite should be above 1360°C (Figure 4), and the temperature to form β-quartz may be well below 1000°C (Figure 6). Except for anorthite, none of the observed phases agrees with the predicted results. Furthermore, to test the sol-gel results, some of the compositions were separately prepared using oxides and carbonates as starting materials and following the same heat treatment. Neither β-cristobalite nor β-quartz was observed. To explain this discrepancy, the concept of topotaxy may be applied, that is, the product phase of a solid state reaction

usually bears a close resemblance in structure to the parent phase.[3] In studying the possible crystal model for the ordered region of amorphous silica, both high cristobalite and high quartz structures have been proposed from different experimental data.[4-6] After complete hydrolyses and condensation, the structure of the gel can be approached by that of a silica glass. Therefore, it is thought that the silica phase which crystallized from the gel depends on the crystal model of the gel; the gel structure may then depend on the chemistry of the solution or the coordination polyhedra of the interstitial cations. This hypothesis requires future Raman and infrared spectrum studies. The kinetic aspect explaining how the gel-derived high silica structure remained untransformed is presently unclear.

Summary

Experimental results show that both β-cristobalite and β-quartz can be chemically stabilized using sol-gel techniques. β-cristobalite can be stabilized by the $CaO-Al_2O_3-SiO_2$ system with a 1:1 ratio of $CaO:Al_2O_3$, and β-quartz is stabilized by substituting Mg for Ca. Both high structure phases may occur as a result of topotactic reactions, and the gel structure determines which phase is favored. The thermal expansion of both structures proceeds via bond angle stretching, and is is independent of the presence of phase transformation.

Mullite

Thermal expansion investigations are continuing in the mullite crystal structure. Recently, two procedures for producing pure mullite have been optimized using sol-gel synthesis. Crystallization conditions, such as time and temperature, vary by controlling the reaction time allowed for partial hydrolysis of the tetraethyl-orthosilicate (TEOS) prior to the addition of aluminum trisisopropoxide.

For the first process, partial hydrolysis (5 min) of the TEOS results in the formation of pure mullite at approximately 1000°C. The minimum time for crystallization is still under investigation.

Preliminary results indicate the crystallization time is on the order of a few hours. For the second process, if partial hydrolysis of the TEOS is allowed to take place for twenty minutes, crystallization takes place at 1400°C in about 24 hours. Both mullites are formed from the crystallization of an amorphous oxide (stoichiometric mullite composition) which itself was formed by calcining the $Al_6Si_2(OH)_{13}$ gel at 650°C for one hour.

The above two processes, along with the standard solid state mullite formation from simple oxides at 1550°C, will be used in an attempt to introduce oxygen vacancies into the mullite lattice. Each of the above processes will be carried out under an oxygen deficient atmosphere formed by using a CO_2-CO mixture. The oxygen partial pressure will then be systematically varied along with the time and temperature of sample exposure. The resulting material will be tested for a possible increase in oxygen vacancies. The effect of the vacancies on the thermal expansion properties will then be evaluated.

Zircon-Based System

We have previously reported on the synthesis of several modified $NaZr_2(PO_4)_3$-type (NZP) structures (i.e. $RbZr_2(PO_4)_3$, $CsZr_2(PO_4)_3$, solid solution of (Rb-Cs) zirconium phosphate, and $Ca_{0.5}Mg_{0.5}Zr_4(PO_4)_6$) which exhibit very low thermal expansion behavior.[1] From among these compounds, $Rb_{0.5}Cs_{0.5}Zr_2(PO_4)_3$ with a CTE value $-0.3 \times 10^{-7}/°C$, and $Ca_{0.5}Mg_{0.5}Zr_4(PO_4)_6$ with a CTE value of $-5 \times 10^{-7}/°C$, were selected for more detailed examination. This study included characterization of the compositions in terms expansion anisotropy, thermal shock resistance, and phase stability.

Experimental

Bar specimens pressed and fired at 1300°C for 8 h were used in the characterization studies. (No attempt was made to optimize the heat treatment schedule.) Lattice parameter measurements were conducted at the Oak Ridge National Laboratory to determine axial thermal expansion. High temperature XRD was performed up to 1400°C at 200°C intervals using a scintag $\theta - \theta$ goniometer equipped with a Buehler high temperature

attachment. The diffraction patterns were obtained in a 2θ range of 18° to 42° with a scanning rate of 2°2θ/min. The six major peaks selected to calculate the lattice parameters included (110), (113), (024), (116), (214) and (300).

The critical maximum temperature water quench test and repeated water quench tests[7] were conducted to characterize thermal shock resistance. DTA was used to determine phase stability up to 1500°C, using a heating rate of 20°C/min. Long-term stability was evaluated by exposure at 1400°C for 96 h, followed by cooling to room temperature and XRD analysis.

Results and Discussion

Axial thermal expansion values for compounds $Ca_{0.5}Mg_{0.5}Zr_4(PO_4)_6$ and $Rb_{0.5}Cs_{0.5}Zr_2(PO_4)_3$ are tabulated in Table 6 and shown in Figures 8 and 9. $Rb_{0.5}Cs_{0.5}Zr_2(PO_4)_3$ showed axial expansion of $-11 \times 10^{-7}/^{\circ}C$ for the a-axis and $21 \times 10^{-7}/^{\circ}C$ for the c-axis. These two axial CTE values provided a calculated average linear CTE value of $-0.3 \times 10^{-7}/^{\circ}C$ [based on $\alpha_L = [(2\alpha_a + \alpha_c)/3]$, which correlates well with the measured linear aggregate CTE value ($-0.3 \times 10^{-7}/^{\circ}C$).

Table 6. Axial expansion results.

Composition	Axial CTE values ($\times 10^{-7}/^{\circ}C$)						
	25-600°C		600-1400°C		Calculated α_L		Measured α_L
	a-axis	c-axis	a-axis	c-axis	25-600°C	600-1400°C	
$Ca_{0.5}Mg_{0.5}Zr_4(PO_4)_6$	-39	66	-14	47	-4	6	-5
$Rb_{0.5}Cs_{0.5}Zr_2(PO_4)_3$	-11	21	-11	21	-0.3	-0.3	-0.3

$Ca_{0.5}Mg_{0.5}Zr_4(PO_4)_6$ exhibited a discontinuity in expansion behavior at about 600°C, where the CTE changed from $-39 \times 10^{-7}/^{\circ}C$ to $-14 \times 10^{-7}/^{\circ}C$ for the a-axis and from $66 \times 10^{-7}/^{\circ}C$ to $47 \times 10^{-7}/^{\circ}C$ for the c-axis. Linear aggregate expansion values of $-4 \times 10^{-7}/^{\circ}C$ and $6 \times 10^{-7}/^{\circ}C$ for the range of 25 to 600°C and 600°C to 1400°C, respectively, were calculated from the axial CTE values. These values

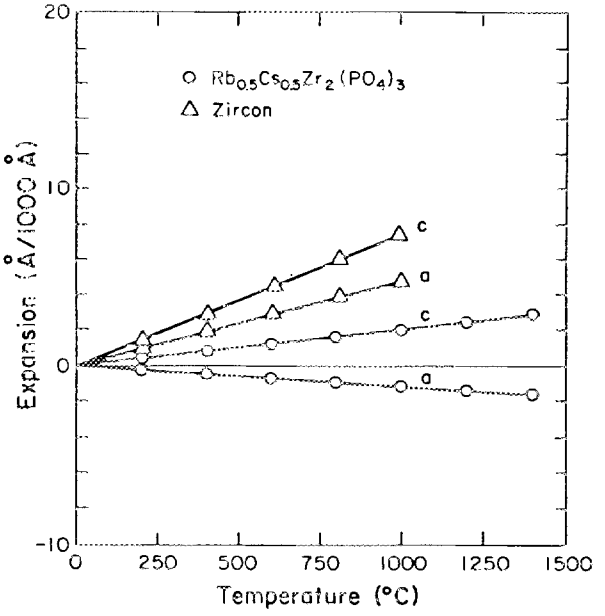

Figure 8. Axial expansion of $Rb_{0.5}Cs_{0.5}Zr_2(PO_4)_3$.

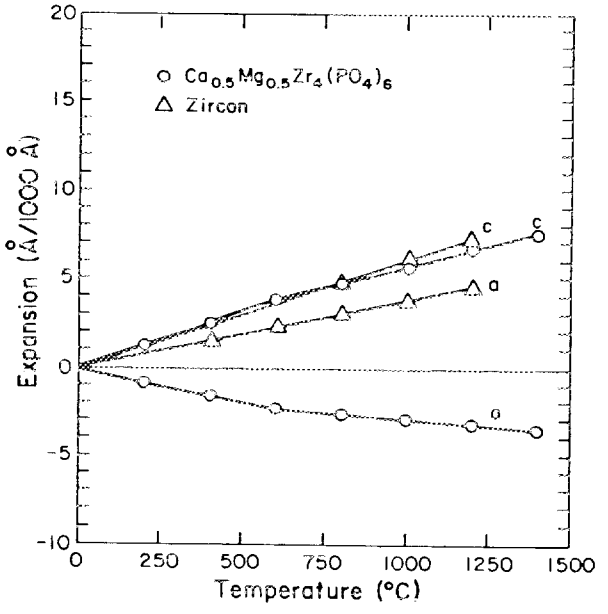

Figure 9. Axial expansion of $Ca_{0.5}Mg_{0.5}Zr_4(PO_4)_3$.

were calculated from the axial CTE values. These values agree with the measured linear CTE values which changed from negative to positive, around 700°C, as previously reported.[1]

Thermal shock resistance was characterized by the water quench method to determine the maximum quench temperature difference (ΔT_{max}) and the number of repeated quench cycles needed to form cracks. Results are summarized in Table 7. One sample of each composition was quenched into ice water from successively higher temperatures until surface cracks were detected by visual observation. For the compound $Ca_{0.5}Mg_{0.5}Zr_4(PO_4)_6$, ΔT_{max} = 1475°C. The compound $Rb_{0.5}Cs_{0.5}Zr_2(PO_4)_3$ resisted fracture up to 1625°C.

Table 7. Characterization of thermal shock resistance for $Ca_{0.5}Mg_{0.5}Zr_4(PO_4)_6$ and $Rb_{0.5}Cs_{0.5}Zr_2(PO_4)_3$.

Compound	ΔT_{max} (°C)	Allowable Repeated Quench with ΔT = 1200°C
$Ca_{0.5}Mg_{0.5}Zr_4(PO_4)_6$	1475	5 times
$Rb_{0.5}Cs_{0.5}Zr_2(PO_4)_3$	>1625[a]	>20 times[b]

[a]No cracking was observed up to the maximum value of 1625°C used in the current experiments.
[b]No cracking was observed after 20 quench cycles.

Repeated water quenching from 1225°C to R.T. was done for both compounds. Specimens were held at 1225°C for 30 minutes and then quenched into ice water. $Ca_{0.5}Mg_{0.5}Zr_4(PO_4)_6$ was cracked after 6 quench cycles. No cracks were observed in $Rb_{0.5}Cs_{0.5}Zr_2(PO_4)_3$ after 20 quench cycles.

DTA revealed no transformation or reaction to 1500°C for either composition. In long-term stability studies, no changes were detected in $Ca_{0.5}Mg_{0.5}Zr_4(PO_4)_6$ after holding at 1400°C for 96h; however, XRD phase identification results indicated the presence of ZrO_2, Rb_2O, and Cs_2O in compound $Rb_{0.5}Cs_{0.5}Zr_2(PO_4)_3$ following thermal exposure. This instability is likely due to the decomposition of P_2O_5.

At this time, it is apparent that $Ca_{0.5}Mg_{0.5}Zr_4(PO_4)_6$ shows much

promise as a thermal shock resistant ceramic composition which is chemically stable to temperatures well above 1200°C. It should be noted, however, that no optimization studies have been conducted. Efforts to optimize strength and porosity are presently underway.

References

1. J. J. Brown, Jr., R. E. Swanson, and F. A. Hummel, "Low Expansion Ceramics for Diesel Engine Applications," *Semi-Annual Progress Report for the Period October 1, 1987 - March 31, 1988*, VPI & SU, Dept. Materials Engineering, April 10, 1988.

2. E. M. Levin, C. R. Robbins, and H. F. McMurdie, "Phase Diagram for Ceramist," *The American Ceramic Society*, Columbus, Ohio (1964).

3. J. R. Gunter and H-R Oswald, "Attempt to a Systematic Classification of Topotactic Reactions," *Bull. Inst. Chem. Res.*, Kyoto Univ., 53 [2] 249-55 (1975).

4. E. Gorlich, K. Blaszczak, and G. Sieminska, "Infra-red Studies of Vitreous Silica at Elevated Temperature," *J. Mat. Sci.*, 9, 1926-32 (1974).

5. J. B. Bates, "Raman Spectra of α and β Cristobalite," *J. Chem. Phys.*, 57 [9], 4042-47 (1972).

6. A. H. Narten, "Diffraction Pattern and Structure of Noncrystalline BeF_2 and SiO_2 at 25°C," *J. Chem. Phys.*, 56 [5], 1905-9 (1972).

7. D. Lewis, III, "Thermal Shock and Thermal Shock Fatigue Testing of Ceramics with the Water Quench Test," *Fracture Mechanics of Ceramics*, Vol. 6 edited by R. C. Bradt, A. G. Evans, D. P. H. Hasselman and F. F. Lange, Plenum Press, New York, 1983.

Status of Milestones

Status of milestones is presented in Table 8 and Figure 10. In support of this program, a Perkin Elmer Series 7 Thermal Analysis System was purchased using $52,000 from the State Equipment Fund. This system includes DSC and DTA capabilities.

Publications

None this period.

Table 8. Key to major milestones

VPI 1.1	Process selection for phosphate- and silicate-based systems (Oct. 31, 1986)
VPI 1.2	Process selection for mullite- and zircon-based systems (Oct. 31, 1986)
VPI 2.1	Complete literature review (Oct. 31, 1986)
VPI 3.1	Complete upgrade of characterization facility (Dec. 31, 1986)
VPI 3.2	Complete upgrade of specimen fabrication, processing facilities (June 30, 1987)
VPI 4.1	Complete initial screening of phosphate-based systems (Dec. 31, 1987)
VPI 4.2	Complete initial screening of silicate-based systems (Dec. 31, 1987)
VPI 4.3	Complete initial screening of zircon-based systems (Dec. 31, 1987)
VPI 4.4	Complete initial screening of mullite-based systems (Dec. 31, 1987)
VPI 5.1	Complete second-stage property and characterization evaluation of phosphate-based systems (Sept. 30, 1988)
VPI 5.2	Complete second-stage property and characterization evaluation of silicate-based systems (Oct. 31, 1988)
VPI 5.3	Complete second-stage property and characterization evaluation of mullite-based systems (Nov. 30, 1988)
VPI 5.4	Complete second-stage property and characterization evaluation of zircon-based systems (Dec. 31, 1988)
VPI 6.0	Complete scale-up specimen fabrication of most promising low-expansion ceramics (Feb. 28, 1989)

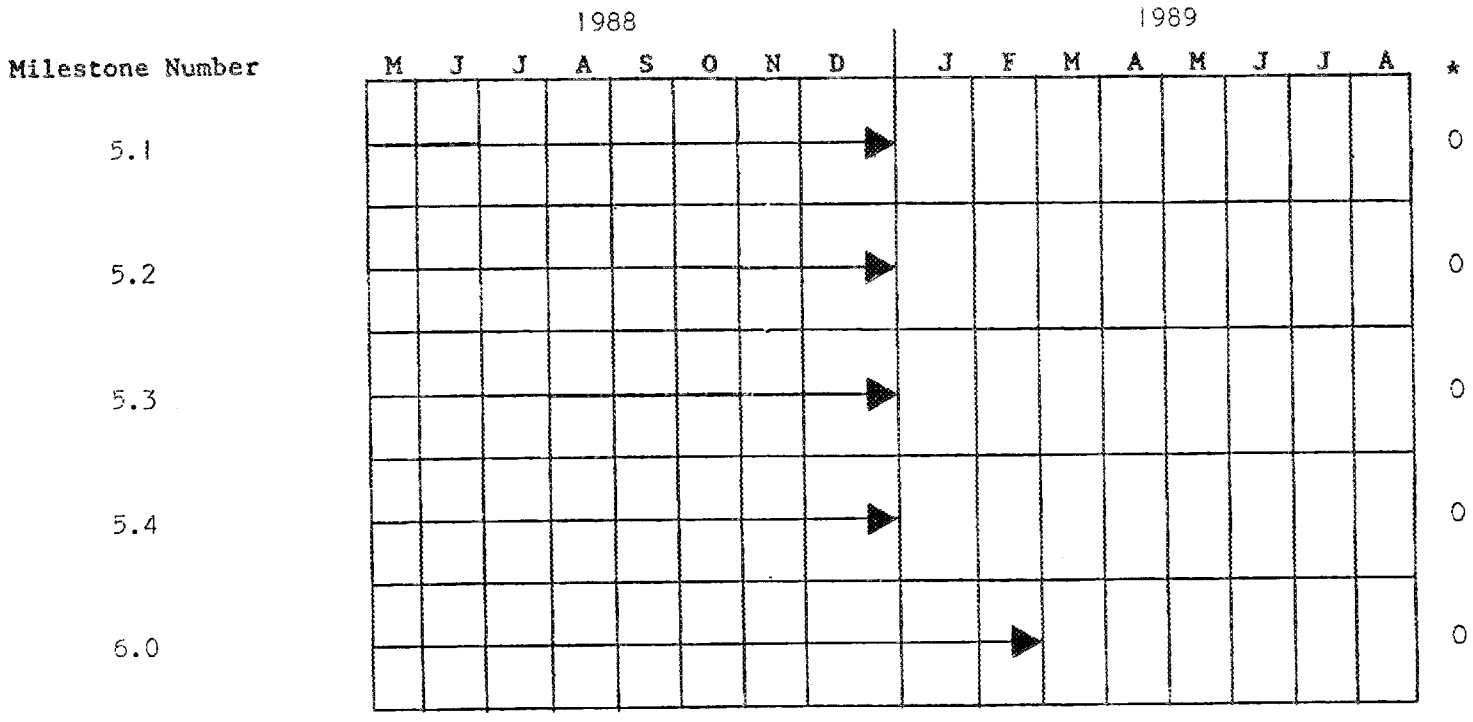

*On, Ahead of, or Behind Schedule.

Figure 10. Milestone status.

1.3 THERMAL AND WEAR COATINGS

1.3.1 ZrO_2 Base Coatings

Advanced Coating Technology
D. P. Stinton and D. W. Dellinger (Oak Ridge National Laboratory)

Objective/scope

Contact stress damage at ceramic-ceramic interfaces in gas turbine engines has been identified as a major source of ceramic component failure in experimental engine tests. Therefore, the objective of this program is to reduce or eliminate the contact stress damage at these interfaces. Contact stresses will be reduced by chemically vapor depositing a coating that consists of Al_2O_3 and a solid lubricant to minimize the coefficient of sliding friction. This work supports a larger contract with GTE where chemically vapor deposited zirconia-toughened alumina coatings are being developed to reduce contact stress damage to silicon carbide and silicon nitride components. After satisfactory Al_2O_3-lubricant coatings have been produced at ORNL, tribological testing will identify the optimum composition and concentration of lubricant to minimize the coefficient of friction.

Technical progress

Equipment modifications made this period significantly improved the quality of the Al_2O_3 coatings being deposited. Homogeneous nucleation of Al_2O_3 in the gas phase was reduced by replacing all metallic components within the coating system with fused silica components. By utilizing fused silica, chlorides of iron, nickel, and chromium that are thought to aggravate the homogeneous nucleation problem were avoided. Changes to the chlorination and piping design also increased the efficiency of the $AlCl_3$ generator. A set of coatings was produced this period using varying amounts of $AlCl_3$, CO_2, and H_2. High oxygen supersaturations were used to enhance the formation of very fine-grained deposites. The best coatings with the least gas phase nucleation were deposited at low H_2:CO_2 ratios.

Recent research at NASA-Lewis Research Center has shown that silicon carbide and silicon nitride are quite susceptible to corrosion, particularly from sodium. Other research has indicated that the inclusion of a lubricant phase such as MoO, CoO, or MoS_2 could aggravate the corrosion problem. Since little progress has been made toward identifying a solid lubricant to codeposit with alpha alumina, this program will be redirected to develop a coating for corrosion protection of silicon carbide and silicon nitride. The coating system to be described in detail next period will include a layer of the refractory compound $Na_2O.11Al_2O_3$, referred to as beta-alumina. Therefore, the effort expended to date in development of alumina coating capability can be utilized in the redirected program.

Status of milestones

The milestone due September 30, 1988, "Identify promising Al_2O_3-lubricant systems for optimization," was delayed because of the difficulty depositing high quality coatings.

Development of Adherent Ceramic Coatings to Reduce Contact Stress Damage of Ceramics

V. K. Sarin (GTE Laboratories)

Objective/Scope

The objective of this program is to develop oxidation-resistant, high-toughness, adherent coatings for silicon-based ceramic substrates, namely, reaction-bonded Si_3N_4, sintered SiC, and HIPed Si_3N_4 for use in an advanced gas turbine engine. The program will utilize a singular coating technique, chemical vapor deposition (CVD), to develop appropriate coating configurations to accommodate as many of the mechanical, thermal and chemical requirements demanded of the application as possible.

Technical Highlights

Protective Layer Coating Process Development

Task 1.3, Protective Layer Deposition Studies, was completed. A CVD process for growing the $Al_2O_3 + ZrO_2$ composite layer was developed. Dense, adherent coatings were grown on the $AlN/Al_xO_yN_z$ intermediate layer on all three substrates over a range of pressures and temperatures. These ranges, 50 - 100 torr and 950°C - 1050°C, were also used for the intermediate layer deposition. Although composite layers of 2-3 µm thickness can be reproducibly grown, precise control of the composition has not yet been addressed due to lack of manpower for characterization of the layer. To address this concern, arrangements were made with Case Western Reserve University and the University of California at Santa Barbara to perform electron microscopy work. Samples were sent to each for analysis. No results have been received yet.

Statement of Work

The Statement of Work for Phase I of the contract was modified and approved by ORNL. The following changes were implemented:

1. Thermal shock, oxidation, and contact stress testing will be done at 1200°C in addition to 1000°C and 1375°C.

2. Contact stress tests will be performed by Garrett in conjunction with GTEL. These tests will use specially designed MOR bars and pins, both of which must be fabricated and coated.

3. The number of samples tested at each temperature will be reduced to accommodate the addition of 1200°C to the test matrices and extensive oxidation and thermal shock studies.

The milestones for the remainder of Phase I of the contract were modified accordingly. Arrangements were also made with Garrett to perform the contact stress tests.

Substrate Characterization

Since 1200°C was added to the test matrices under the new Work Statement, mechanical property characterization of uncoated substrates had to be done at this temperature. Table 1 shows MOR values measured at 1200°C. Previously reported MOR measurements at room temperature, 1000°C, and 1375°C are also included for comparison.

Table I: Room Temperature and High Temperature Strength of Substrate Materials As Determined by a Four-Point Bend Test. Dimensions of Test Bars: 2" x 1/4" x 1/8".

Substrate	MOR (MPa)			
	room temp.[1]	1000°C[2]	1200°C[2]	1375°C[2]
RBSN	272.7±36.8	271.8±12.9	232.5±40.4	254.2±15.7
SSC	401.2±55.2	352.1±20.4	398.2±67.6	415.6±68.4
HSN	821.5±117.1	608.4±21.9	411.0±37.4	120.7±7.7

[1]Reported MOR values are average of 20 measurements.
[2]Reported MOR values are average of 5 measurements.

Long-term Oxidation.

1000°C

The long-term oxidation studies at 1000°C of the coated and uncoated substrates have been completed out to 550 hours. The HSN and SSC samples, coated and uncoated, showed no significant weight gains, but the uncoated RBSN did. The results for RBSN are shown in Figure 1, where $(\Delta W/m^2)^2$ is plotted as a function of time in hours. Weight changes observed for the uncoated RBSN follow a parabolic growth law. If weight gain is assumed to be directly proportional to SiO_2 formation, the uncoated RBSN gained 10.6 mg/cm², which translates into a 45-μm thick layer of SiO_2. However, cross-sectional studies so far have not revealed such a region near the surface. The coated RBSN samples also showed significant weight gain (relative to HSN and SSC) after 250 hours, but no additional gains out to 550 hours. Significant quantities of Fe were often detected in the EDS spectrum and in most instances the surfaces of the coated RBSN samples were discolored with a reddish-brown deposit. Some cracking and/or spalling was observed in specific samples in all three substrates around 500 hours; however, typically the coating configuration looked reasonably good. In the case of RBSN, this coating configuration definitely offers oxidation protection at 1000°C.

1200°C

The oxidation studies at 1200°C have also been completed out to 500 hours. The coated HSN and SSC samples gained approximately .70 mg/cm^2 after 25 hours and are unchanged thereafter out to 500 hours. The uncoated HSN and SSC gained no weight. These results are shown in Figure 2. The coatings on HSN showed some cracking and spalling after 25 hours, which became more extensive after 50 hours. Blistering was also observed after 250 hours. For RBSN, cracking of the coating was observed in the 50-100 hour range. For SSC, more cracking of the coating was observed after 50 hours, leading to extensive cracking and some blister formation after 250 hours.

The uncoated RBSN gained an average of 3.6 mg/cm^2, which is approximately 1/3 of the weight gained after the same time period at 1000°C. For the coatings on RBSN, there is a small amount of cracking and some blister formation after 50 hours. Spalling and blistering were detected after 250 hours. The coated RBSN samples heated for 25 and 50 hours, respectively, are being examined in cross section by SEM-EDS to determine the extent of chemical and diffusional effects.

1375°C

Oxidation experiments at 1375°C produced severe changes in the coating on all three substrates. Additionally, samples with only the composite coating and only the AlN coating were also investigated. In all cases there was cracking and sometimes blistering of the coating configuration. After 25 hours the coating on HSN showed extensive blistering and spalling and a transformation into a glassy type structure that was rich in Si and Al, as determined by EDS. Additionally, in one case, the coating spalled off the HSN and was found by x-ray diffraction to be α-Al_2O_3 with a large fraction of a mullite phase. The coated RBSN substrate also showed extensive spalling and some blistering, but to a lesser degree than the HSN and did not show the same glass formation. It also showed a Si-rich surface. The coated SSC substrates were heated for an additional 50 and 100 hours at 1375°C. There was a small additional increase in weight after 50 hours with somewhat greater frequency of surface deformation accompanied by some cracking. After 100 hours there was extensive cracking and blistering.

By way of comparison, studies were also conducted using CVD α-Si_3N_4 as the substrate with the full coating configuration and with only the AlN intermediate layer. This material does not contain the glass phase present in the HSN and the SSN samples. Although a small amount of cracking of the coating was observed for the full coating configuration, none was detected for the AlN coating alone. Furthermore, no spalling or blistering was detected after heating for 2 hours at 1375°C.

Studies were also conducted on coated substrates that had been heated in an N_2 atmosphere (30 psi) for 2 hours at 1375° prior to heating in air. The heating in N_2 produced no apparent change in the appearance of the surface; however, after the oxidation step the results were similar to those obtained earlier: severe blistering and spalling for the coating on the HSN substrate, blistering and spalling for the RBSN substrate, and a small amount of surface deformation for the SSC substrate.

Thermal Shock.

Arrangements were made with A. G. Associates in Sunnyvale, CA to perform the thermal shock tests using a modified thermal anneal apparatus. Pieces of MOR bars (2/3" x 1/4" x 1/8") were coated with the full coating configuration and the samples needed for testing were sent (6 coated and 3 uncoated of each substrate). Prior to conducting the tests, the equipment had to be calibrated for the test temperatures (1000°C, 1200°C, and 1375°C). For this purpose, 6 additional samples were sent. These samples were specially prepared by drilling 0.040" diameter holes into them for thermocouple wells. In attempts to calibrate the equipment for 1375°C, it was determined that the apparatus could not be used at this temperature, so 1375°C was dropped from the test matrix.

The tests were carried out in flowing argon at 1000°C and 1200°C. The samples were placed on a SiC-coated susceptor within the anneal chamber and heated by ramping to the maximum temperature in 30 seconds, starting at 150°C. There was a 10-second hold at the maximum temperature, and the samples were cooled for 300 seconds prior to the next cycle. The cycle was repeated 50 times. All samples were returned to GTE Laboratories where they were examined by SEM for cracking and spalling. No deleterious effects to the coating or the substrate as a result of the thermal shock were observed.

Status of Milestones

The third and fourth milestones, due in June and August 1988, were completed on time. The fifth milestone due in September, 1988 is delayed due to insufficient time for coating the MOR bars.

Communications/Visits/Travel

On 4/20-21/88, V.K. Sarin and J.T. Smith traveled to Oak Ridge National Laboratory to present the status of the project and to discuss modification of the Statement of Work.

On 5/11-13/88, V.K. Sarin traveled to Garrett Turbine Engine Company to discuss contact stress testing of MOR bars.

On 7/12/88, V.K. Sarin traveled to A.G. Associates, Sunnyvale, CA to make arrangements for them to perform the thermal shock tests.

On 7/13/88, V.K. Sarin visited Prof. M. Ruhle at the University of California Santa Barbara to discuss electron microscopy of the interfaces and the composite layer.

Problems Encountered

Due to equipment limitations, the required number of samples for testing could not be coated in time to meet the fifth milestone. Delays in getting pins made for contact stress testing also occurred and will result in failure to complete the sixth milestone on schedule.

Publications

None.

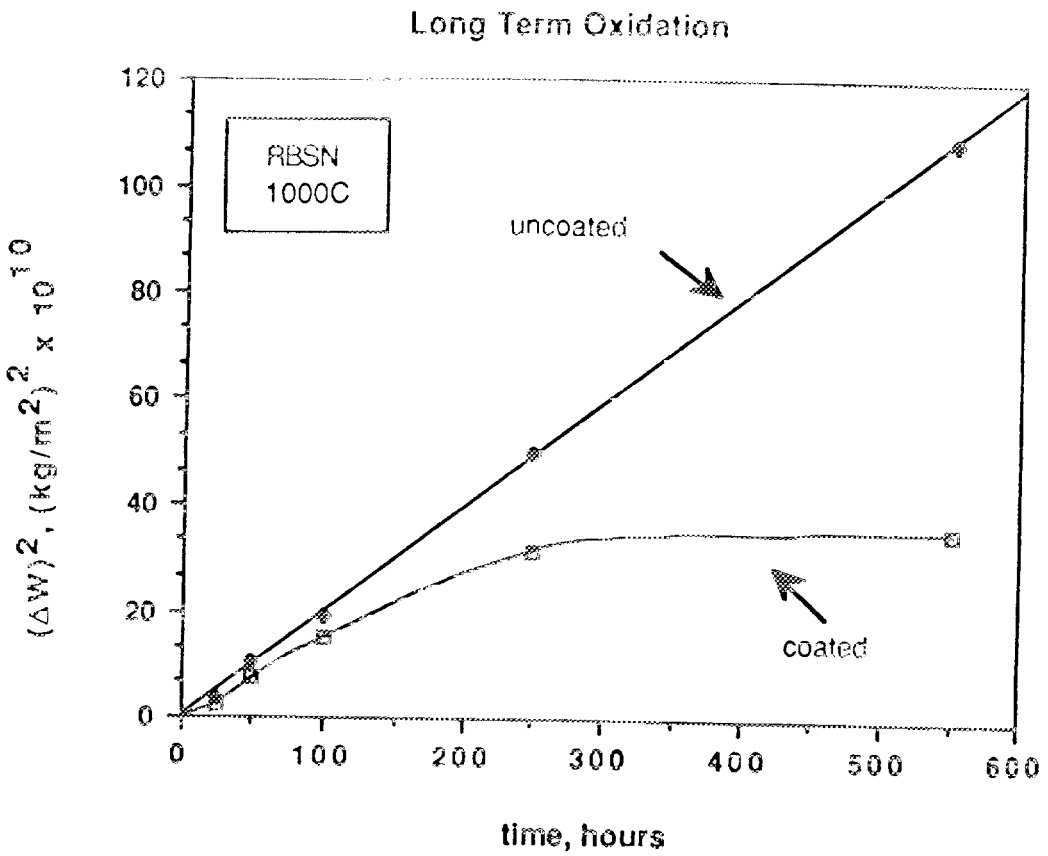

Figure 1: Change in (Sample Weight/Unit Area) as a Function of Time of Coated and Uncoated RBSN during Oxidation in Static Air at 1000°C

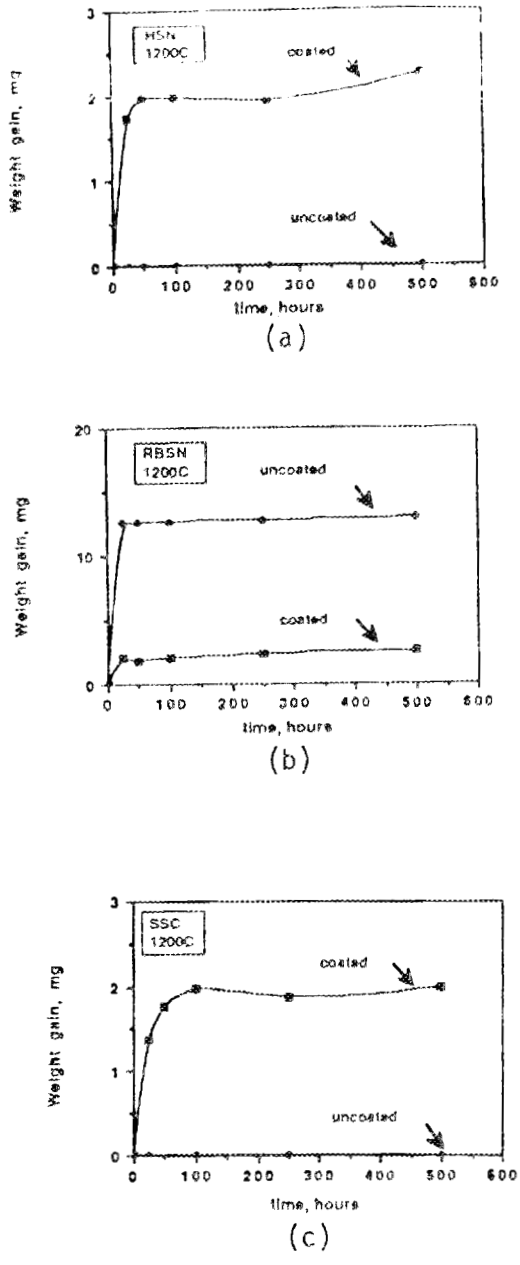

Figure 2: Weight Gain of Coated and Uncoated Substrates during Oxidation in Static Air at 1200°C up to 500 Hours for a) HSN, b) RBSN, and c) SSC

Wear-Resistant Coatings
C. D. Weiss (Caterpillar, Inc.)

Objective/Scope

The goal of this technical program is to develop wear-resistant coatings for piston ring and cylinder liner components for low heat-loss diesel engines.

Wear resistant coatings will be applied to metallic substrates utilizing plasma spraying, vapor deposition (CVD-PVD) and enameling coating processes. First the adherence of each coating for each coating process to the metallic substrates will be optimized. Methods which can be utilized for improving the adherence of these coatings include development of unique substrate preparation methods before application of the coating, grading coating compositions to match thermal expansion, compositional changes, laser or electron beam fusing and/or optimizing coating thickness. Once the adherence of each coating system is optimized, each coating will be screened for wear and friction at 350°C under lubricated conditions. Coatings which show promise after this initial screening will be further optimized by adjustments to chemistry and hard particle content to meet the wear and friction requirements. Then the optimized coating systems will be fully characterized for oxidation resistance, adherence, uniformity, thermal shock resistance, wear and friction.

Selection of the most promising coatings and coating processes will be made after completion of the characterization task. Criteria for selection will include not only performance (i.e. wear, adhesion, friction coefficient, thermal shock resistance and thermal stability) but manufacturability/cost factors, as well. Utilizing both criteria a coating system having acceptable cost/benefit relationships will be selected.

Technical Progress

Plasma Spraying

The thermal expansion coefficients for the following plasma sprayed coatings were determined: Metco 750 (CaF_2), Metco 70C (Cr_3C_2), Metco 63NS (Mo), Metco 350 (Mo-Fe-C), Metco 136CP (Cr_2O_3), Metco 66F-NS (High Co, Mo, Cr), Hohman PS212, Metco 461 (bond coat), Amdry 961 (bond coat), Metco 143 (ZrO_2-TiO_2-Y_2O_3), Metco 19E (Ni, Cr) and Zircoa ZrO_2. All the thermal expansion specimens were obtained by spraying the various coatings on a salt coated rod and then removing the coating from the rod. Thus, the thermal expansion coefficients were determined on cylinders of each plasma sprayed coating.

The thermal expansion data included in Table I illustrates that the following plasma spray coatings can be applied to either the gray cast iron or H-13 tool steel substrates without creating a significant mismatch in thermal expansion.

Metco 19E (Ni, Cr Powder)
Metco 66F-NS (High Co, Mo, Cr powder)
Hohman PS212
Eetco 750F (high Mo, Ni, Cr powder)
Metco 350A (high carbon iron, Mo powder)

Plasma coatings such as Metco 143, Zircoa and Metco 70C have significantly lower coefficients of thermal expansion than the H-13 or gray iron substrates. These coatings will have to be graded with the Metco 461 (bond coat) in order to match the thermal expansion of the substrate and the coating.

The effect of grading plasma spray coatings on thermal expansion coefficient was determined by Caterpillar in contract DEN3-332 of the DOE/NASA Heavy Duty Transport Technology program. In contract DEN3-332 it was learned that when blending plasma sprayed coatings, if the as sprayed microstructure of the coating is uniform, the thermal expansion coefficient of the blended coating will follow the rule of mixtures. That is, a 50/50, by volume, blend will have a thermal expansion coefficient midway between that of each individual plasma sprayed coatings.

Table II illustrates the effect of grading or blending both the Metco 143 and Zircoa coatings with a Metco 461 bond coat. By utilizing the following grading schedule the difference in thermal expansion between the substrate and coating can be significantly reduced:

100% Metco 461
75% Metao 461/25% Top Coat (either Metco 143 or Zircoa)
50% Metco 461/50% Top Coat
25% Metco 461/75% Top Coat
100% Top Coat

CVD/PVD Coating

H-13 tool steel specimens were chemical vapor deposited (CVD) with Cr_3C_2 and a layered TiC/TiN coatings at Sylvestor and Co., Cleveland, Ohio. H-13 tool steel specimens were also physical vapor deposited (PVD) with a TiN coating at Caterpillar. Finally, 17-4 PH stainless-steel specimens were mid-temperature CVD coated with Ti(C,N).

The mid-temperature CVD Ti(C,N) coating on 17-4 stainless-steel was included as part of this program because it offers two advantages over the higher temperature CVD processes. First, the processing temperature of the mid-temperature CVD process is 200-250°C lower than a normal CVD process. This lower processing temperature will cause less distortion of the 17-4 PH stainless steel rings during coating. Second, while the maximum thickness of a Cr_3C_2 and TiC/TiN CVD coating is limited to six and 12 microns respectively, the mid-temperature Ti(C,N) coating can be applied to thicknesses up to 20 microns. To achieve the program goals of 10,000 hours operation, CVD coatings with thickness greater than six or 12 microns might be required, even with very low friction coefficients and wear ratios.

The PVD, CVD and mid-temperature CVD coated H-13 or 17-4 PH adherence specimens all had an excellent physical appearance. In addition, no flaking and/or spalling was observed. An optical microscopy examination of these specimens illustrated that all the coatings were uniformly applied and that no chemical reactions occurred during the coating operation which would adversely affect the adherence, chemical stability of the coating or the mechanical properties of the H-13 or 17-4 PH substrates. Using the cross-sectioned optical photomicrographs the thicknesses of each coating was determined to be:

High Temperature CVD - Cr_3C_2 - 5 microns
High Temperature CVD-TiC/TiN - 8 microns
Mid-Temperature CVD-Ti(C,N) - 14 micron
PVD TiN - 2-3 microns

The CVD and PVD coatings conformed to the surface of the metal substrate to which they were applied. As a result, these specimens had a 5 to 10 micron surface finish after coating. One significant advantage for the CVD/PVD coatings is they will not require costly machining after coating to obtain the desired surface finish.

A Revetest was utilized to measure the adherence of the CVD and PVD coatings. However, the Revetest gave inconclusive adherence results because the data obtained was very scattered. For this reason, a modified tensile pull test is being designed for adherence testing of these specimens.

Enamel Coating

Two methods of loading an A.I. Andrew's cobalt enamel base were evaluated. One method consisted of plasma spraying the hard particles on top of the enamel after the enamel coating was applied to and fired on the metallic substrate. The second method evaluated consisted of sprinkling the hard particles on top of the molten enamel when the enamel was fired onto the metallic substrate.

Zirconia (ZrO_2), chrome oxide (Cr_2O_3), and chrome carbide (Cr_3C_2) were successfully plasma sprayed on top of an A.I. Andrews' cobalt based enamel. Silicon carbide (SiC) and silicon nitride (Si_3N), when sprinkled on the molten enamel, produced very porous hard particle coatings which were not bonded very well to the enamel. After evaluating the initial specimens produced by this sprinkling method, it was decided to drop this approach and concentrate on the plasma spray technique.

Cast iron Falex specimens containing plasma sprayed ZrO_2, Cr_2O_3 or Cr_3C_2 on top of an A.I. Andrews' cobalt enamel were screened for wear and friction, lubricated at 350°C, using a ZrO_2 pin. Preliminary wear data indicated that the friction coefficient for these material pairs were:

A. ZrO_2 pin - plasma sprayed ZrO_2 over enamel - 0.25
B. ZrO_2 pin - plasma sprayed Cr_2O_3 over enamel - 0.09
C. ZrO_2 pin - plasma sprayed Cr_3C_2 over enamel - 0.04

The plasma sprayed ZrO_2 over enamel specimen failed after less than 30 minutes of wear testing. Examination of this specimen after testing indicated that the failure occurred because the enamel disbonded from the metal substrate during the test causing large portions of the coating to spall. Both the plasma sprayed Cr_3C_2 over enamel and plasma sprayed Cr_2O_3 over enamel coatings did not spall during the initial wear testing. The plasma sprayed Cr_2O_3 over enamel coating did, however, wear the ZrO_2 pin significantly during the test. Both the plasma sprayed Cr_3C_2 over enamel coating and ZrO_2 pin exhibited very little wear after 120 minutes of testing lubricated at 350°C.

Another method of improving the wear and friction properties of an enamel is to incorporate the hard particles within the enamel. An enamel composition was developed which would bond to SAE 1018 mild steel utilizing a firing schedule which would not adversely affect the mechanical properties of the mild steel. However, when this enamel composition was loaded with 50 volume percent of 1-5 micron Cr_2O_3 particles an adherence problem developed.

A metallographic investigation illustrated that the reason for the poor adherence was the lack of a chemical reaction between the enamel and the oxides which develop on the mild steel during the firing of the enamel. This problem was overcome by reducing the alkali content of the enamel composition while substantially increasing the boric acid content.

Four (4) enamel compositions containing 0, 50, 60 and 70 volume percent 1-5 micron Cr_2O_3 particles were applied to mild steel Falex and adherence specimens. The adherence of all the enamel compositions was excellent. The physical properties of the Cr_2O_3 loaded enamel coatings were as follows:

Coating	Percent Cr_2O_3 Weight/Volume	Density (gr/cc)	Thermal Exp. (cm/cm/°C)	Hardness (15-y)
Base Coat	0/0	2.42	$7.9X10^{-6}$	95.5
C-1B	50/31.7	3.30	$7.7X10^{-6}$	95.3
C-1D	60/41.0	3.57	$7.7X10^{-6}$	94.7
C-1E	70/51.9	3.87	$7.5X10^{-6}$	89.7

The enamels containing 50 and 70 volume percent 1-5 micron Cr_2O_3 particles could not be evaluated for wear and friction because the enamel coating spalled within the first five (5) minutes of testing. Examination of the specimens after testing illustrated the coatings spalled because at these Cr_2O_3 volume loads there was not enough enamel between the individual Cr_2O_3 particles to hold them in place. As a result, the particles could be easily removed from the enamel by the ZrO_2 pin.

Material Substrates	Thermal Expansion Coefficient ($x10^{-6}$ °C) 200°C	400°C
H-13 Tool Steel(1)	11.5	12.2
Gray Cast Iron(2)	12.3	14.4
Plasma Spray Coatings		
Metco 461 (Bond Coat)	12.33	13.70
Andry 961 (Bond Coat)	12.58	13.79
Metco 143	7.57	8.46
Metco 19E	10.7	11.79
Metco 66F-NS	9.9	11.38
Hohman PS212	9.76	11.37
Zircoa	7.95	8.09
Metco 70C	8.35	9.48
Metco 750F	10.62	11.30
Metco 63NS	4.27	4.75
Metco 350A	8.85	11.09

Table I - Thermal Expansion Coefficients

Plasma Spray Coating	Thermal Expansion Coefficient - 400°C 10^{-6}°C
Gray Cast Iron	14.4
Metco 461 Bond Coat	13.70
Metco 143	8.46
75% Metco 143/25% Metco 461	9.77
50% Metco 143/50% Metco 461	11.08
25% Metco 143/75% Metco 461	12.39
Zircoa	8.09
75% Zircoa/25% Metco 461	9.50
50% Zircoa/50% Metco 461	10.9
25% Zircoa/75% Metco 461	11.0

(All percentages are volume percent)

Table II - Effect of Grading Plasma Spray Coatings

Status of Milestones

MS1 Manufacture 400 adherence test specimens - complete
MS2 Manufacture friction and wear test specimens - complete
MS3 Identify a minimum of 12 adherent coating systems - complete

Publications

Weiss, C.D., "Wear-Resistant Ceramic Coatings for Diesel Engine Components," Proceedings of the 1987 Coatings for Advanced Heat Engines Workshop, 1987.

References

Book

1. Metals Handbook,9th Edition
2. Iron Casting Handbook Iron Casting Society, 1981

Development of Wear Resistant Ceramic Coatings for Diesel Engine Components

M.G.S. Naylor
Cummins Engine Company, Inc.

Objective/Scope

The objective of this program is to develop advanced wear resistant coatings for in-cylinder components for future, low heat rejection diesel engines. Coatings and substrates (for piston rings and cylinder liners) are to be developed to meet the following requirements.

: Low wear (as measured in laboratory rig tests at ambient temperature and 350°C). Wear coefficients in the range $5x10^{-12}$ to $5x10^{-11}$ $mm^3/mm/N$ are targeted (at 350°C).

: Low friction coefficients when tested under boundary lubricated conditions (target 0.1) and unlubricated conditions (target 0.2) at ambient temperature and 350°C.

: Good thermal shock resistance.

: High adherence and compatibility with the substrate materials up to 650°C.

: High uniformity and reproducibility.

Technical Progress

Wear Testing

Wear testing and microstructural characterization of chromium oxide wear coatings is in progress. Tests were performed with a commercial Air Plasma Spray (APS) chromium oxide 'piston ring' coating sliding against slurry-sprayed silica-chromia-alumina (SCA) and grey cast iron 'cylinder liners'. The test conditions and results are summarized in table 1.

Results Using Fresh Lubricant

Wear data is plotted in figure 1, together with best-fit curves for the conventional electroplated chromium-grey cast iron (baseline) tribological system. The lubricant was a mineral oil based CE/SF 15W40 oil.

The APS chromium oxide/SCA wear couple was found to reduce total wear (ring + liner) by approximately a factor of three compared to the baseline. This wear improvement was caused by a significant reduction in the wear of the liner sample. On the other hand the ring sample had a higher wear rate than for the conventional system. Much lower ring wear rates were obtained when testing APS chromium oxide against grey cast iron, but at the expense of significantly higher liner wear (figure 1).

Table 1. Cameron Plint wear test data. Load = 225 N, stroke = 5mm, frequency = 20 Hz, duration = 360 min (lubricated), 60 min (unlubricated). Lubricant supply rate = 10.7 cm³/hour.

Ring Material	Liner Material	Lubricant	Temperature (C)	Ring Wear Coeff $mm^3/mm/N$	Liner Wear Coeff $mm^3/mm/N$	Friction Coeff
APS Cr_2O_3	SCA	None	436	2.60×10^{-9}	7.53×10^{-10}	>0.75
APS Cr_2O_3	SCA	CE/SF 15W40 Mineral Oil: Fresh	275	2.35×10^{-10}	6.30×10^{-11}	0.108
APS Cr_2O_3	SCA	CE/SF 15W40 Mineral Oil: Fresh	344	7.70×10^{-11}	6.42×10^{-11}	0.109
APS Cr_2O_3	SCA	CE/SF 15W40 Mineral Oil: Fresh	353	4.49×10^{-11}	1.71×10^{-10}	0.110
APS Cr_2O_3	SCA	CE/SF 15W40 Mineral Oil: Engine-Tested	259	1.03×10^{-10}	1.23×10^{-10}	0.223
APS Cr_2O_3	Grey Cast Iron	CE/SF 15W40 Mineral Oil: Fresh	262	4.59×10^{-12}	7.94×10^{-10}	0.196

In this study, the wear rate of the SCA coating was found to be approximately the same as for the APS chromium oxide. In previous tests using self-mated APS chromium oxide (from another supplier), much lower wear rates were obtained than in the present work (figure 2). The differences are attributed to microstructural effects (discussed below).

Results Using Engine-Tested Oil

Significant differences between metallic and ceramic tribological systems have been observed when testing with a degraded lubricant obtained from an engine test (figure 3). For the Cr/grey iron system, ring and liner wear rates were accelerated by up to an order of magnitude compared with the tests run using fresh lubricant. The APS chromium oxide/SCA wear couple, by comparison, showed no increase in wear rate, which suggests that ceramic wear coatings may be much more tolerant of degraded oil conditions than conventional materials.

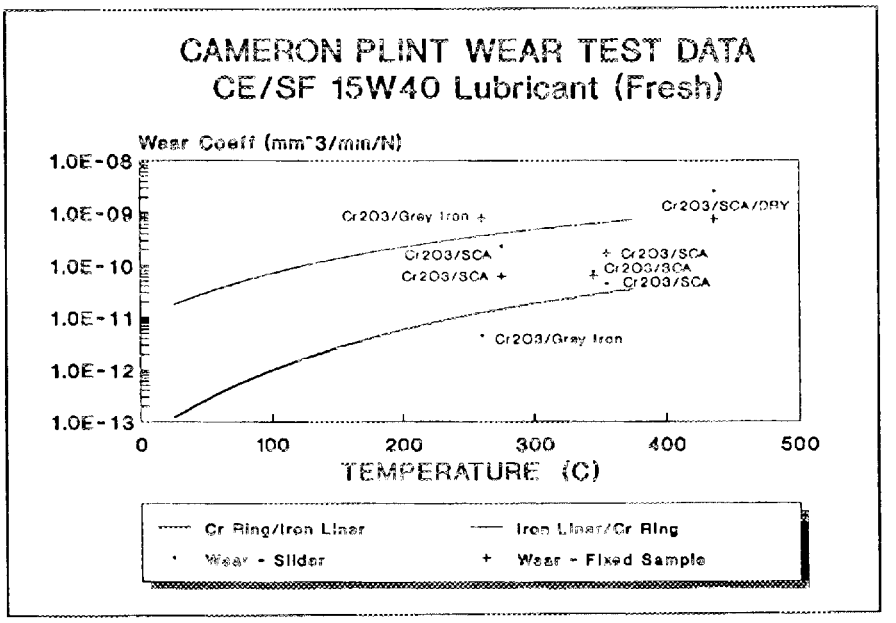

Figure 1 *Wear coefficients for APS chromium oxide sliding against SCA and grey cast iron in fresh oil. Lower curve shows variation of wear coefficient with temperature for Cr plated ring sliding against grey iron liner (best-fit). Upper curve = best-fit for iron liner sliding against Cr ring.*

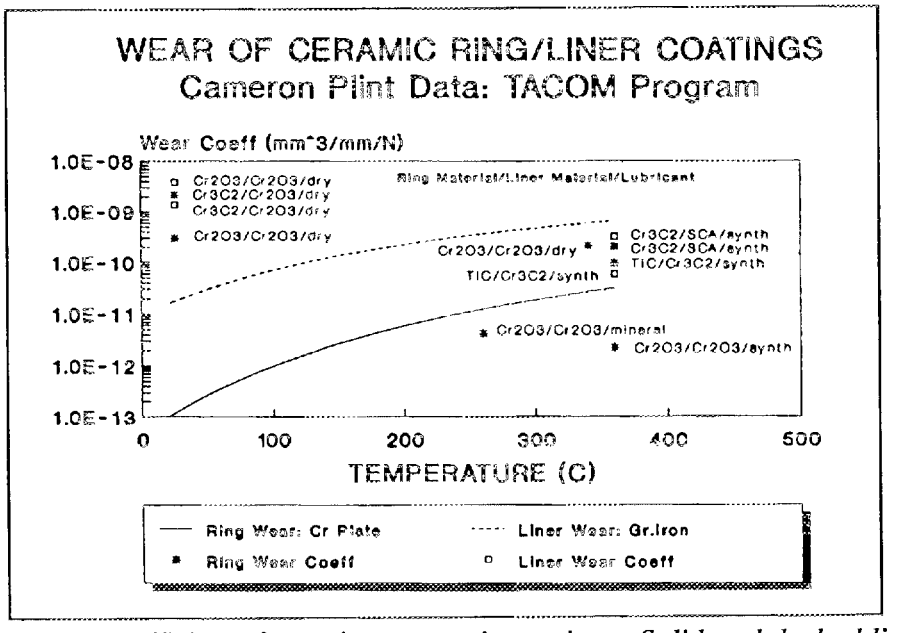

Figure 2 *Wear coefficients for various ceramic coatings. Solid and dashed lines show best-fit for baseline system. 'Mineral' = CE/SF 15W40 mineral oil, 'Synth' = polyol ester based lubricant. Cr2O3 = APS chromium oxide, Cr3C2 = APS chromium carbide-Ni-Cr, TiC = APS titanium carbide with CaF_2-Ni-Cr-Fe. SCA = SiO_2-Al_2O_3-Cr_2O_3 dipped coating.*

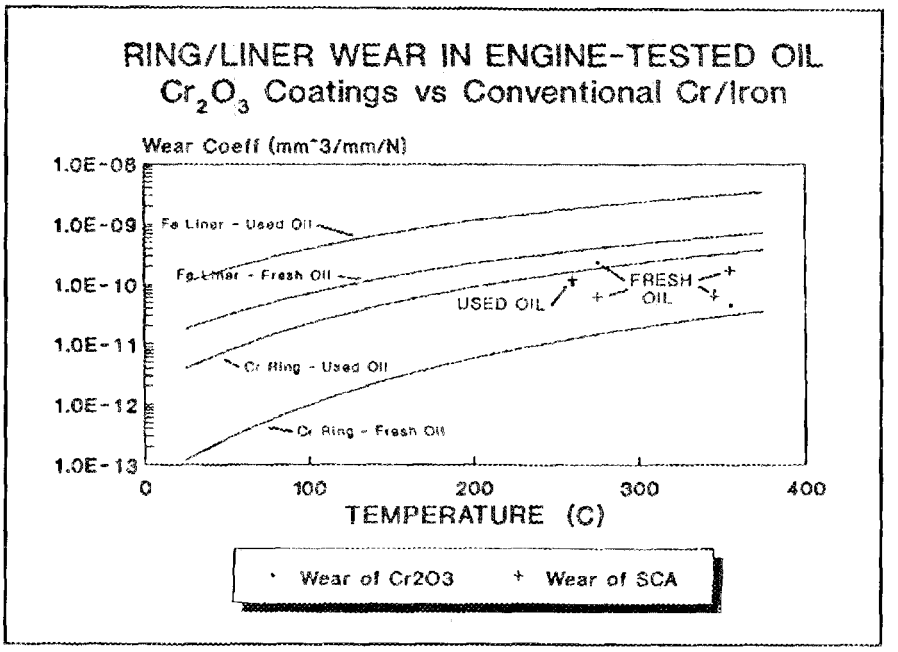

Figure 3 *Wear coefficients of conventional materials and chromium oxide coatings in fresh and engine-tested lubricants. Solid lines show variation of wear with temperature for conventional Cr plated rings vs grey iron liners (best-fit). Lubricant = CE/SF 15W40 mineral oil.*

The degradation of lubricant wear performance for metallic materials is not fully understood. Contributing factors may include:

: build-up of products derived from fuel combustion (e.g. soot, sulphuric acid)

: depletion of anti-wear additive by oxidation or other processes

: build-up of corrosive oxidation products of the lubricant

: build-up of dirt/wear debris (below minimum size removed by filtration)

Figure 4 shows the difference in friction coefficient between fresh and engine-tested lubricants for APS chromium oxide sliding against SCA. The used oil generally showed higher friction and less variation with time than the fresh oil. At one point, the fresh oil showed a transition in friction coefficient from 0.1 to 0.15 followed by the reverse transition after approximately 50 minutes. This may be evidence of formation of metastable surface films during the test.

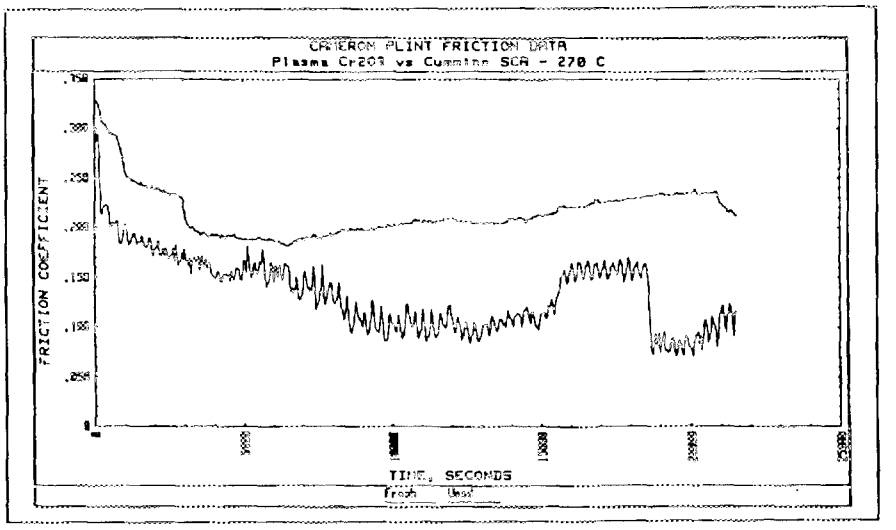

Figure 4 Friction coefficient versus test time for APS chromium oxide sliding against SCA with fresh and engine-tested lubricants. Test temperature = 270°C.

Microstructural Characterization of Coatings

The microstructures of APS chromium oxides A and B are compared in figures 5 - 8. Material B (higher wear) contains higher porosity, more microcracking and a greater proportion of unmelted material (clusters of fine particles) than material A. The chemical composition of the two coatings is similar, comprising a few percent TiO_2 and SiO_2 in addition to Cr_2O_3 (figures 7 and 8). Variations in composition through the microstructure are visible as changes in grey scales in the backscattered electron SEM images (figures 5 and 6).

The microstructure of the slurry-sprayed silica-chromia-alumina (SCA) coating is shown in figure 9. The coating was produced by 12 densification cycles (impregnation with chromic acid followed by heating) with no surface finishing operations. The coating was fully dense, comprising a mixture of SiO_2 and Al_2O_3 particles (from the original sprayed slurry) with Cr_2O_3 formed in the densification cycles. The grain size is approximately 5 microns, much less than the coating thickness (20 microns). A thin layer of pure Cr_2O_3 has formed on the surface, and in places extends into the bulk of the coating, to fill cracks in the original slurry coating. The composition of the coating was determined by EDS analysis to be 55% Cr_2O_3 - 41%SiO_2 - 4% Al_2O_3 by weight.

X-ray diffraction was performed to compare the phase content of the present coating with a sample obtained from Kaman Sciences Inc (Boulder, Colorado) (1986 vintage). The current material was found to contain more Cr_2O_3 and less Al_2O_3 than the Kaman coating (figure 10).

Microhardness values for the APS chromium oxide (A and B) and SCA coatings were similar: approximately 1000 $kgfmm^{-2}$ (Knoop) (table 2).

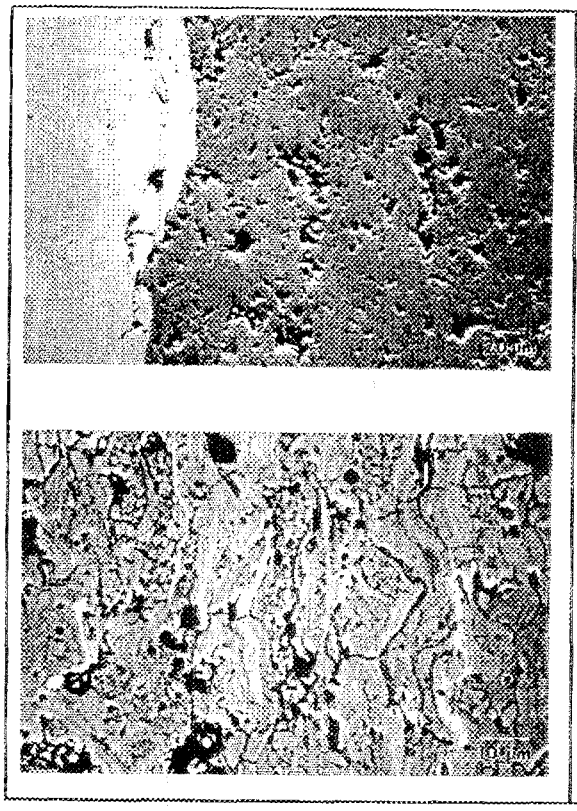

Figure 5 *SEM micrographs of APS chromium oxide coating used in the present study (coating B).*

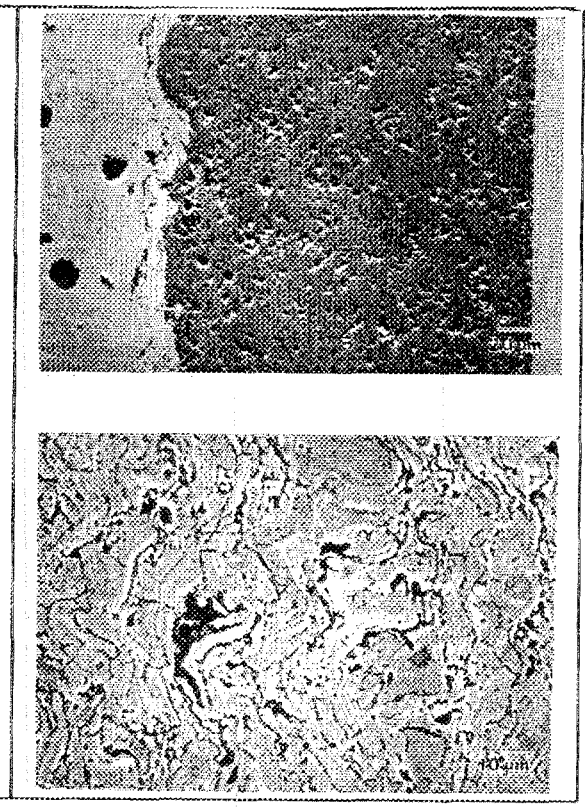

Figure 6 *SEM micrographs of APS chromium oxide coating used in previous study (coating A).*

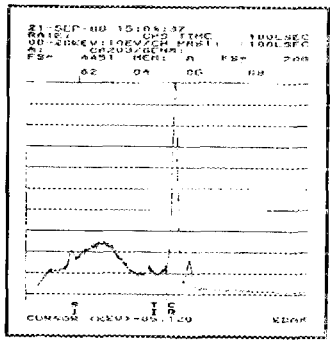

Figure 7 *EDS spectrum from coating B, showing the presence of Ti and Si (TiO_2 and SiO_2) in addition to Cr (Cr_2O_3).*

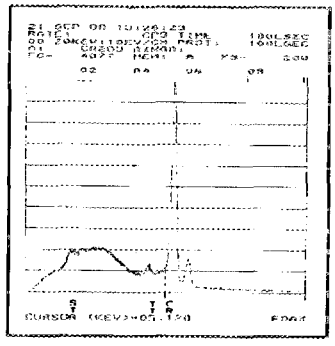

Figure 8 *EDS spectrum from coating A, showing similar composition to coating B.*

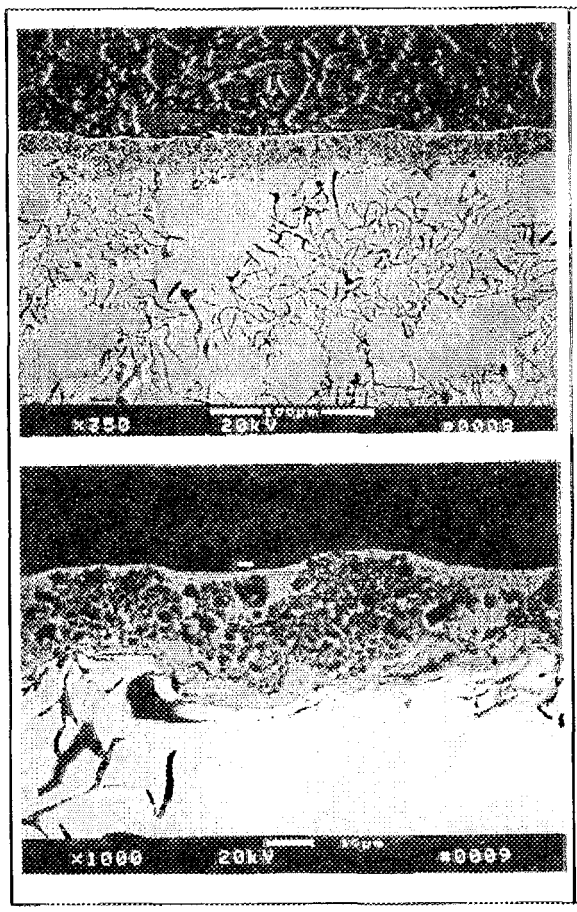

Figure 9 *SEM micrographs of silica-chromia-alumina slurry sprayed coating (12 densification cycles). Note light-imaging surface layer (pure Cr_2O_3).*

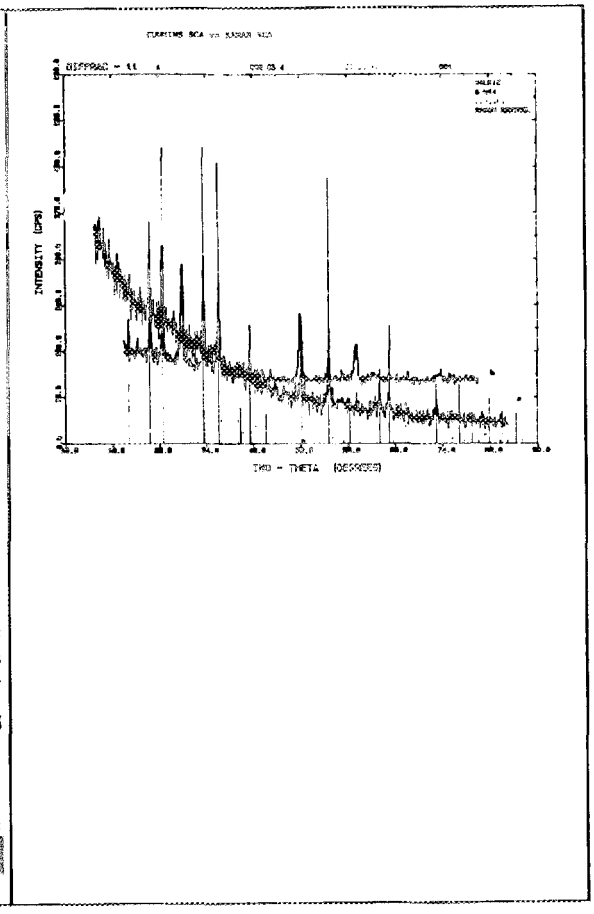

Figure 10 *X-ray diffraction spectra from two SCA samples: (a) current material (b) sample obtained from Kaman Sciences (1986 vintage).*

Table 2 Microhardness of Cr_2O_3 Coatings

Coating	Knoop Hardness $kgfmm^{-2}$	Standard Error
Plasma Sprayed Cr_2O_3 (A)	1051	66
Plasma Sprayed Cr_2O_3 (B)	1013	35
SCA (12 densifications)	961	39

Analysis of Worn Surfaces

Worn surfaces were examined in the scanning electron microscope (SEM) in order to establish correlations between microstructure and wear behaviour. Lubricated tests with the APS chromium oxide (B) against SCA produced a relief polish in which the coating microstructure was clearly visible (figure 11). Shallow pits in the surface suggest that spalling at 'splat' interfaces may be an important wear mechanism for this material. Debonding of small particles from regions containing high levels of unmelted powder may also contribute to the wear process.

The SCA counterface (figure 12) showed two distinct microstructures: in some regions, the surface Cr_2O_3 skin (figure 9) was still intact (light-imaging areas), while in other regions, the underlying SiO_2-Cr_2O_3-Al_2O_3 microstructure was visible (mottled dark areas). For these tests, the SCA coating was tested in the as-coated condition, with no surface finishing. The worn-through areas may thus correspond to high spots on the original surface.

Worn SCA surfaces from lubricated and unlubricated tests are compared in figures 13 and 14. For this material, there was very little difference in wear morphology between the two cases (although wear rates were much lower when lubricated - figure 1). In both cases, the worn surface was highly polished, especially in the SiO_2-Cr_2O_3-Al_2O_3 regions.

Figures 15 and 16 show the wear morphologies of the two forms of APS chromium oxide (A and B) when tested at high temperature without lubrication. Coating B (higher wear) showed extensive spalling and small fragmented debris particles adhering to the surface. The size of the spalled regions was clearly greater than in the lubricated tests (compare figures 11 and 15). Coating A also showed inter-splat fracture/spallation but, in this case, the wear surface between the spalls was highly polished, with no evidence of wear grooves (figure 16). Evidently, the splat adherence was much greater in coating A than in B, which may be related to the microstructural differences discussed above. It is speculated that in coating B, the spray powder particles were not heated in the plasma for a sufficient amount of time to produce complete melting.

Status of Milestones

Task 1	Experimental Plan and Coating Deposition
Task 2	Characterization
Task 3	Selection of Coating
Task 4	Fabricate Components
Task 5	Reporting
Task 6	Quality Assurance

Tasks 1 (18 months) and 2 (16 months) are in progress and on schedule.

Publications

None

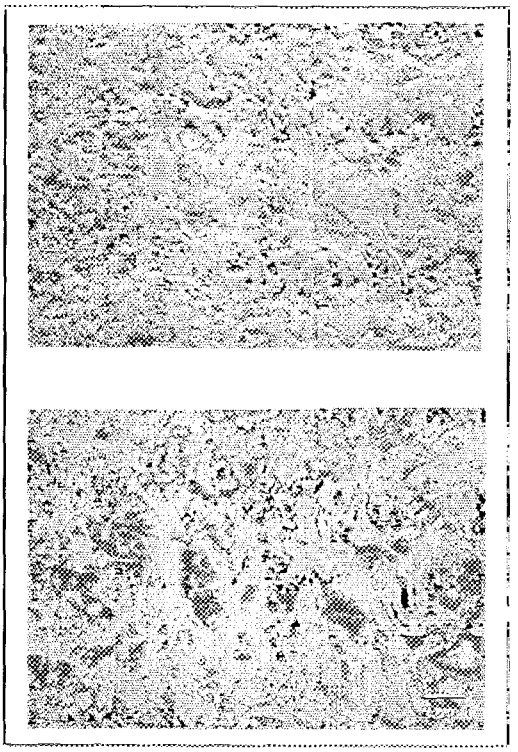

Figure 11 *Wear Surface: APS Cr_2O_3 (B)*
Counterface: SCA (12 dens)
Lubricant: CE/SF 15W40
Cameron Plint, 353°C, 225 N,
20 Hz, 5 mm stroke, 6 hrs.

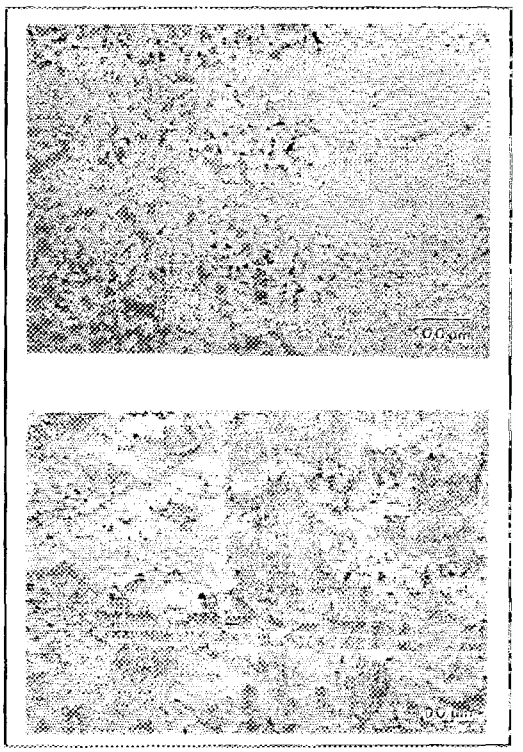

Figure 12 *Wear Surface: SCA (12 dens)*
Counterface: APS Cr_2O_3 (B)
Lubricant: CE/SF 15W40
Cameron Plint, 353°C, 225 N,
20 Hz, 5 mm stroke, 6 hrs.

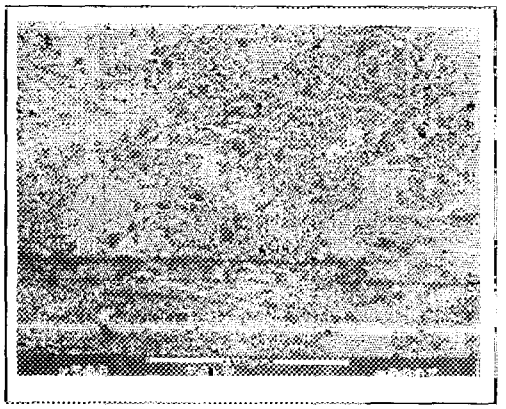

Figure 13 *Wear Surface: SCA (12 dens)*
Counterface: APS Cr_2O_3 (B)
Lubricant: CE/SF 15W40
mineral-based
Cameron Plint, 353°C, 225 N,
20 Hz, 5 mm stroke, 6 hrs.

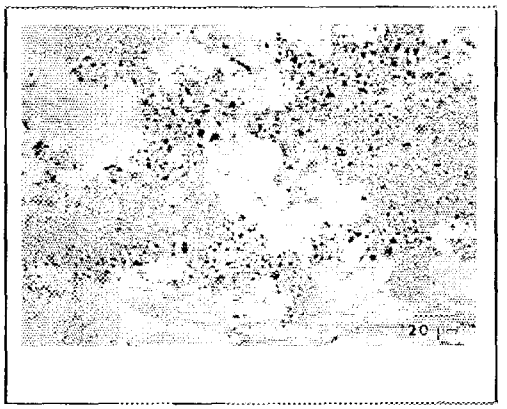

Figure 14 *Wear Surface: SCA (12 dens)*
Counterface: APS Cr_2O_3 (B)
Lubricant: none
Cameron Plint, 436°C, 225 N,
20 Hz, 5 mm stroke, 1 hr.

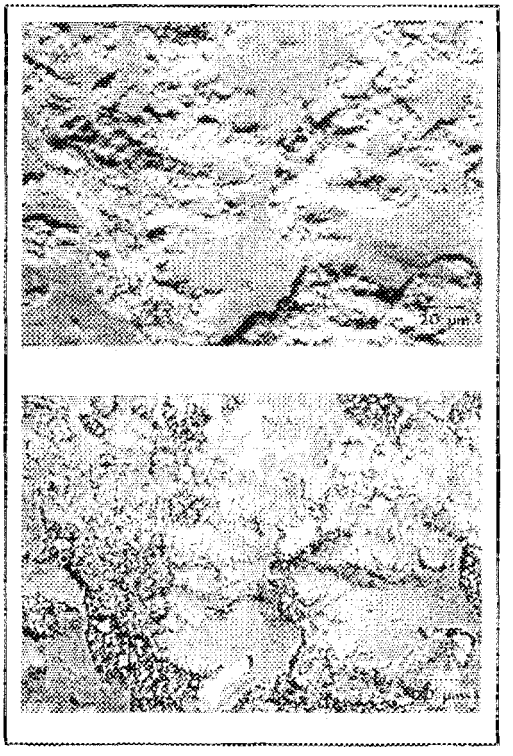

Figure 15 *Wear Surface: APS Cr_2O_3 (B)*
Counterface: SCA (12 dens)
Lubricant: none
Cameron Plint, 436°C, 225 N,
20 Hz, 5 mm stroke, 1 hr.

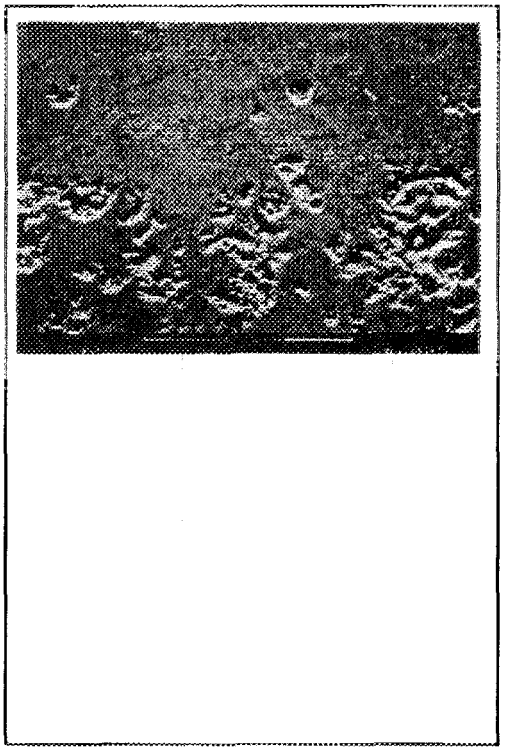

Figure 16 *Wear Surface: APS Cr_2O_3 (A)*
Counterface: APS Cr_2O_3 (A)
Lubricant: none
Cameron Plint, 343°C, 250 N,
10 Hz, 5 mm stroke, 1 hr.

References

1. M.G.S. Naylor, "Development of Advanced Diesel Wear Coatings", in *Proc. 1987 Coatings for Advanced Heat Engines Workshop*, July 27-30, 1987, Castine, Maine, U.S. Department of Energy, Office of Transportation Systems.

1.4 JOINING

1.4.1 Ceramic-Metal Joints

Joining Ceramics for Heat Engine Applications
M. L. Santella (Oak Ridge National Laboratory)

Objective/scope

The objective of this task is to develop strong reliable joints containing ceramic components for applications in advanced heat engines. Currently, this work is focused on the joining of partially stabilized zirconia to nodular cast iron by brazing. Joints of this arrangement will be required for attaching monolithic pieces of partially stabilized zirconia to cast iron piston caps in order for the ceramic to provide the insulation necessary for use in low-heat-rejection diesel engines. A novel method for brazing zirconia to cast iron has already been established. The emphasis of this activity during FY 1988 was on investigating: (1) the effects of testing temperature and zirconia surface finish on the flexure strength of zirconia-to-zirconia, and zirconia-to-cast iron joints, (2) correlating zirconia braze joint microstructures with strength data to identify any factors that may limit joint strength, (3) flexure testing of silicon nitride braze joints, and (4) developing a method of calibrating the indentation fracture technique to determine the accuracy of residual stress measurements in ceramic-to-metal joints.

Technical progress

Areas in which there was significant technical activity are outlined in the following sections.

Brazing of zirconia

A series of 3.5 × 4.5 × 50 mm ZrO_2-ZrO_2 and ZrO_2-cast iron braze joint flexure test specimens was prepared for eventual exposure in the combustion chamber of a small laboratory diesel engine. The TS grade of Nilcra zirconia was used for these joints. Sixteen ZrO_2-ZrO_2 and 13 ZrO_2-cast iron joint specimens were tested at room temperature by four-point bending to establish a reference point, and these data are shown plotted in Fig. 1. The highest strengths recorded were 328 MPa for ZrO_2-ZrO_2 and 311 MPa for ZrO_2-cast iron. The average strengths and scatter for both types of joints were also similar, indicating that the effects of residual stress in the ZrO_2-cast iron joints were perhaps overshadowed by other factors. A complete analysis of these specimens will be performed when the diesel-engine-exposed specimens are available.

A set of ZrO_2-ZrO_2 (MS grade) joint coupons were made using Incusil-15 ABA active brazing alloy (Ag-24Cu-14In-1.25Ti). Twenty-four 3.5 × 4.5 × 50 mm flexure bars were made from these coupons and tested at room temperature by four-point bending. These data are shown in Fig. 2 along with the data for the TS grade ZrO_2-ZrO_2 joints shown in Fig. 1 and data for monolithic MS-ZrO_2. The average strength of the Incusil joints was 334 ± 106 MPa, and the Weibull modulus was 2.46. The highest strength

ORNL-DWG 88-10270

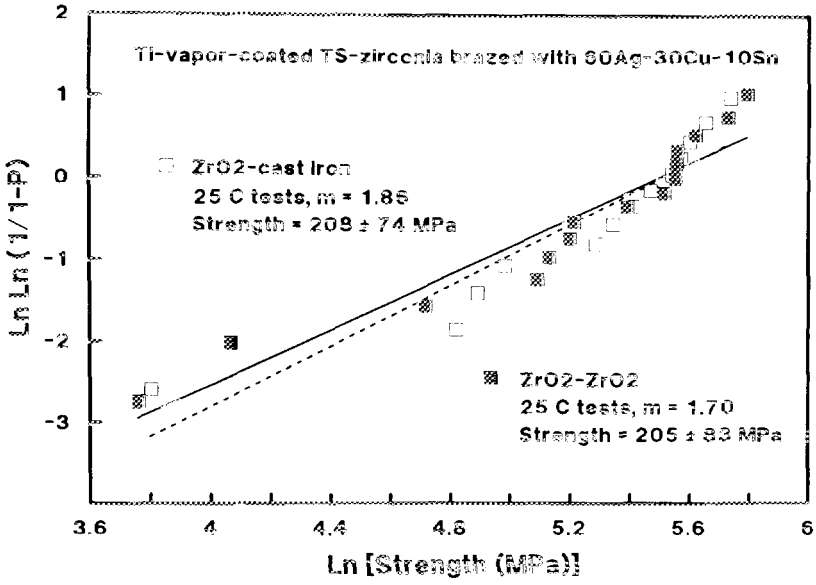

Fig. 1. Weibull plot of joint strength data for TS-grade ZrO_2-ZrO_2 and ZrO_2-cast iron joints tested at room temperature.

ORNL-DWG 88-10269

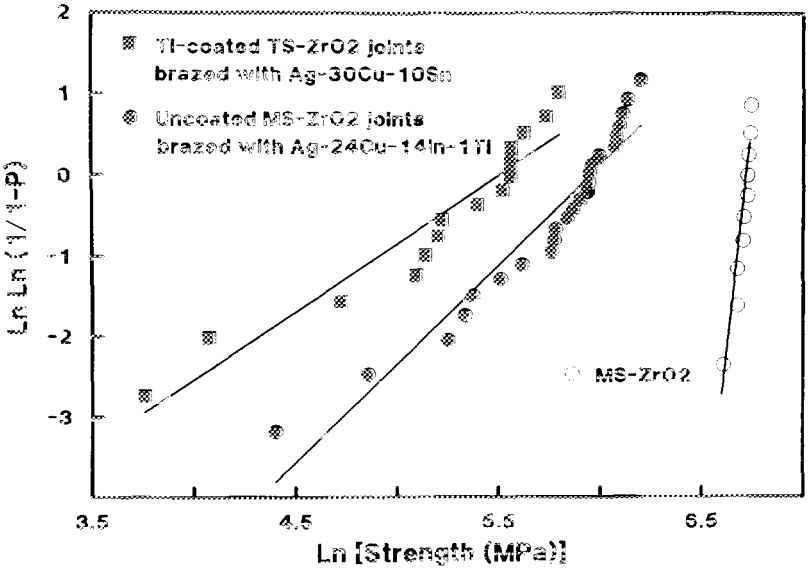

Fig. 2. Weibull plot of strength data for TS-grade titanium-vapor-coated ZrO_2-ZrO_2 braze joints, MS-grade ZrO_2-ZrO_2 active filler metal joints, and monolithic ZrO_2 tested at room temperature.

value recorded was 493 MPa. The fractured specimens were examined in some detail and the fracture initiation site was typically in the zirconia within about 10 μm of the brazed surface. The region near the brazed interface on the tensile surface of a broken flexure bar is shown in Fig. 3. This fracture behavior indicates that bonding to the zirconia is relatively good. This region of the zirconia, however, is typically darkened by reaction with the brazing materials (either titanium-vapor coating or titanium in the braze filler metal), suggesting that chemical reactions between the zirconia and the brazing materials may be degrading the strength of the zirconia near the brazed surface. Another possible explanation is that residual stresses produced by thermal expansion mismatch between the filler metal and the zirconia are reducing the load-carrying capacity of the zirconia near the brazed surface. No unusual microstructural features or compositional variations were identified.

Residual stress measurement

The possibility of using an indentation technique for estimating residual stress levels in ceramic-to-metal joints is still being explored. The technique is based on a comparison of the crack patterns resulting from indentations made under identical conditions on unstressed and

ORNL-PHOTO 02239-88

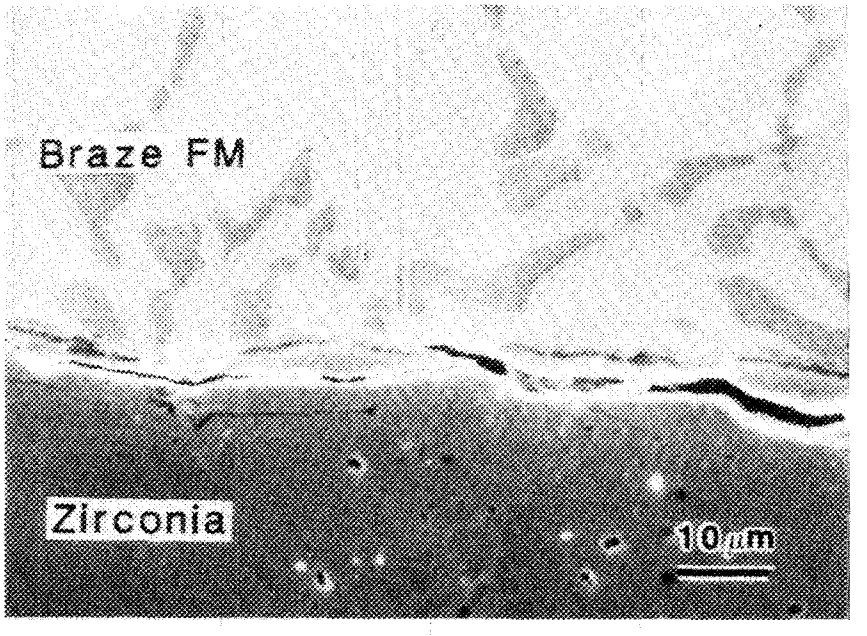

Fig. 3. Scanning electron micrograph of tensile surface of a broken ZrO_2-ZrO_2 active filler metal braze joint flexure test bar in vicinity of brazed zirconia surface.

stressed surfaces of the same material. Residual stresses in the stressed specimen can then be estimated using the expression:

$$\sigma_r = [K_c/(\Gamma \cdot c_r)^{1/2}][(c_0/c_r)^{3/2} - 1] \ , \qquad (1)$$

where K_c is the fracture toughness, Γ is a geometrical constant, and c_0 and c_r are the crack lengths in unstressed and stressed material, respectively. The fracture toughness K_c and hardness H can be determined from indentation also:

$$K_c = \Phi(E/H)^{1/2}(P/c_0{}^{3/2}) \ ,$$

$$H = P/\alpha a^2 \ ,$$

where E is Young's modulus, Φ is a material independent constant, P is indentation load, α is a geometrical constant with a value of 2 for a Vickers indenter, and a is the half-diagonal of a hardness indent.

The ceramic we have been using in this work is Kyocera SN-220 silicon nitride. It was decided to generate the hardness and fracture toughness values required by the residual stress expression as a means of checking the calibration of our equipment and because only manufacturers' material property data are available for the Si_3N_4. For the estimates of H and K_c, 20 indentations were made on an annealed Si_3N_4 specimen at indentation loads of 0.2, 0.5, 2, 5, and 10 kg. The results for the hardness determination are given in Table 1. Hardness should not vary with load, and the calibration of our equipment is currently being checked. According to the manufacturer, the hardness of SN-220 is 14.7 GPa.

Table 1. Hardness of Si_3N_4

Indentation load (kg)	Hardness (GPa)
0.2	3.6 ± 0.3
0.5	7.1 ± 0.6
2.0	8.3 ± 0.5
5.0	11.5 ± 0
10.0	12.8 ± 0

The general behavior of the expression for σ_r given above was also investigated, and the results are shown in Fig. 1 where calculated residual stress is plotted against the ratio c_0:c_r. The fracture toughness value used for the calculation was 7 MPa-m$^{1/2}$, and the crack length in the stressed state was allowed to increase as a fraction of c_0 starting at a value of $c_r = c_0$ which implies a tensile residual stress. The c_0 values were experimentally determined although, because of the calibration problem in our indenter, the loads indicated in Fig. 4 are not accurate. The data show, however, that the sensitivity of the indentation technique

ORNL-DWG 89-2130

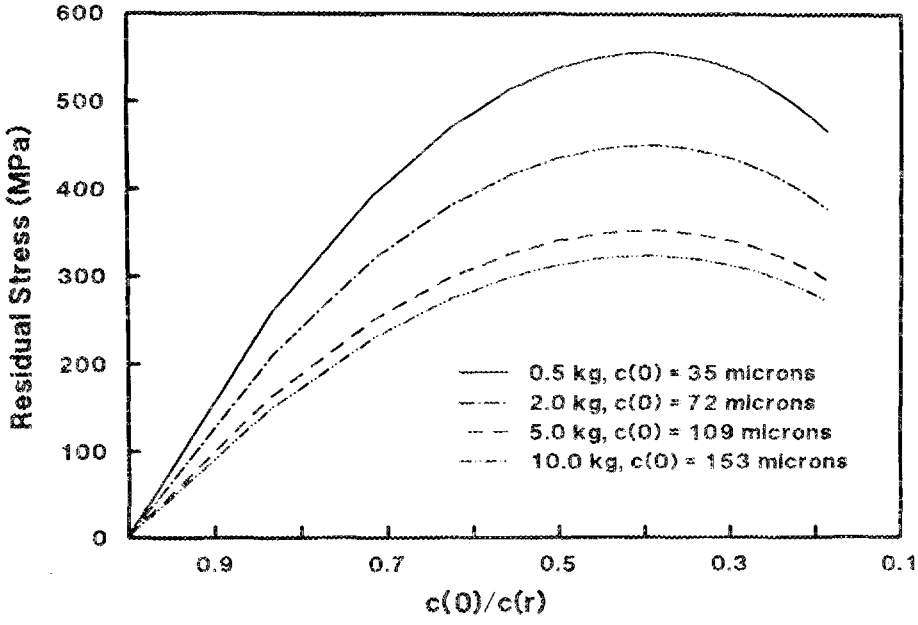

Fig. 4. Calculated residual stress shown as a function of indentation load.

decreases considerably at high indenter loads. At an indenter load of approximately 10 kg the maximum residual stress value that can be determined using Eq. (1) is about 300 MPa, while at an indenter load of about 0.5 kg residual stresses as high as the the fracture strength of the Si_3N_4 (reportedly 500–600 MPa) can be measured.

Brazing of silicon nitride

The titanium-vapor-coated Si_3N_4 was brazed to itself with two commercial brazing filler metals: BAg-8a with a composition in wt % of 71.7Ag-28Cu-0.3Li, and BVAu-7 Gr 1 with a composition in wt % of 50Au-25Ni-25-Pd. The BAg-8a and BVAu-7 Gr 1 alloys were in the form of thin foil, 50 and 25 μm thick, respectively. The Si_3N_4 surfaces used for brazing were vapor coated with a 1.0-μm-thick layer of titanium by melting a titanium source with an electron beam in a vacuum chamber. All brazing was done under a vacuum pressure of about 130 μPa. The brazing temperatures used were: (1) BAg-8a, 790°C; and (2) BVAu-7 Gr 1, 1130°C. The holding time at each brazing temperature was 5 to 10 min. The assemblies made for flexure testing were held on edge in a graphite fixture with the brazed interface in the horizontal plane. No load was applied to any of the assemblies during brazing. Braze joint assemblies were surface ground on both faces, polished to a 1-μm finish on one face, and cut into flexure test bars with dimensions of 28 × 2.5 × 2 mm having a brazed joint in the

center of each bar. Testing was done by four-point bending at a loading rate of 22.7 kg/s. The test bars broken at 400°C were equilibrated at the test temperature for 30 min prior to fracture.

The Weibull strength distribution of the Si_3N_4-Si_3N_4 joints brazed with the Au-Ni-Pd (BVAu-7 Gr 1) alloy and tested at room temperature is shown in Fig. 5. Twelve of these specimens were tested and their average strength was 264 ± 102 MPa with a Weibull modulus of 2.4. The highest strength value recorded was 474 MPa.

Specimens of the Si_3N_4-Si_3N_4 joints brazed with the Ag-Cu (BAg-8a) alloy were tested at room temperature and 400°C, and these data are shown in Fig. 6. At room temperature the average joint strength was 326 ± 38 MPa with a Weibull modulus of 7.7 and a maximum strength value of 406 MPa. The average strength of the joint specimens tested at 400°C was 280 ± 37 MPa with a Weibull modulus of 6.4. The highest joint strength measured at this temperature was 334 MPa.

Metallographic examination was performed on specimens from each testing condition and indicated that fracture paths traveled almost exclusively through the Si_3N_4 rather than through the filler metal or along one of the titanium-vapor-coating interfaces. In most specimens the fracture path was within about 50 μm of the interface between the titanium vapor coating and the Si_3N_4, although the fracture origin and path in several of the higher strength bars was 1 to 2 mm from the brazed surface. The examination of the broken flexure test bars confirmed that adhesion of the

ORNL-DWG 88-10274

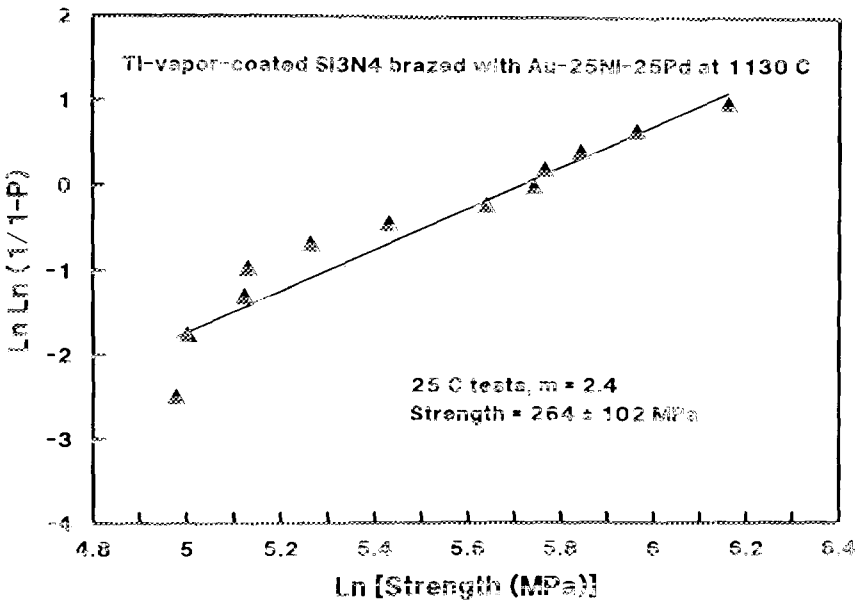

Fig. 5. Weibull plot for flexure strength specimens of Si_3N_4-Si_3N_4 joints made with Au-Ni-Pd braze filler metal at 1130°C.

ORNL-DWG 88-10273

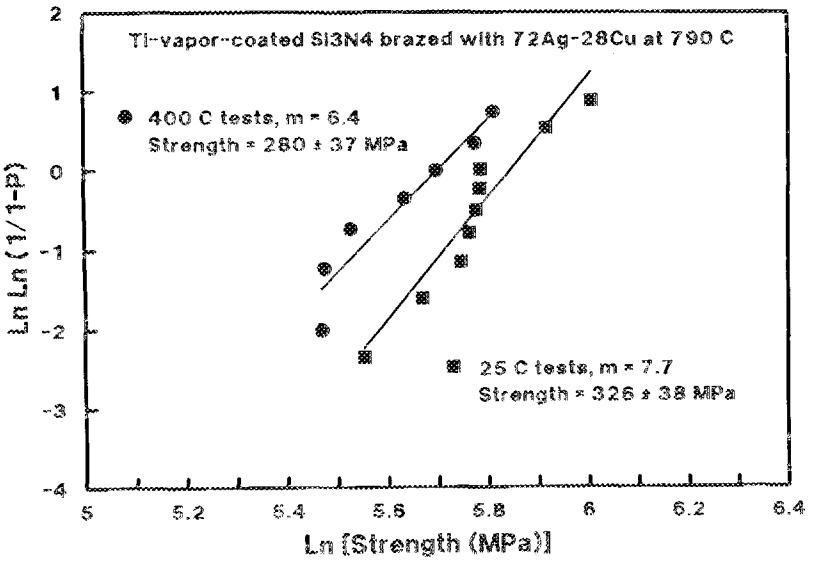

Fig. 6. Weibull plot for flexure strength specimens of Si_3N_4-Si_3N_4 joints made with Ag-Cu braze filler metal at 790°C.

titanium vapor coating to the Si_3N_4 surfaces after brazing was high, and suggested that joint strength was not limited by adhesion of the coating to the ceramic. The coupons used for producing the flexure bars were ground to their final dimensions before brazing, and no attempt was made to remove surface damage that may have resulted from machining. Surface cracks were never observed on metallographically prepared joint specimens, or on specimens examined in the scanning electron microscope, but an exhaustive search for the presence of surface defects was not done. The proximity of the fractures to the interfaces between the Si_3N_4 and the titanium coating suggests near-surface microcracking in the Si_3N_4 controlled joint strength. Analysis of these test data is continuing.

Status of milestones

On schedule.

Publications

M. L. Santella, "Brazing of Titanium-Vapor-Coated Silicon Nitride," *Advanced Ceramic Materials* 3(5), 457–62 (1988).

Unpublished work

"Strength and Microstructure of Brazed Partially-Stabilized Zirconia," by M. L. Santella, J. J. Pak, and R. J. Fruehan, presented at the ASM World Materials Congress, Chicago, Sept. 27–29, 1988.

Analytical and Experimental Evaluation of Joining Silicon Nitride to Metal and Silicon Carbide to Metal for Advanced Heat Engine Applications

E. M. Dunn (GTE Laboratories Incorporated)

Objective/Scope

The goal of this work is to demonstrate analytical tools for use in designing ceramic-to-metal joints including the strain response of joints as a function of the mechanical and physical properties of the ceramic and metal, the materials used in producing the joint, the geometry of the joint, externally imposed stresses both of a mechanical and thermal nature, temperature, and the effects of joints exposed for long times at high temperature in an oxidizing (heat engine) atmosphere. The maximum temperature of interest for application of silicon carbide to metal and silicon nitride to metal containing joints is 950°C. The initial joint fabrication work shall include "experimental" joints whose interfacial area is not less than two square centimeters. The work shall also include demonstration of the potential for scale-up of the joint size to interfacial areas of commercial significance, applicability of the analytical joint modeling tools and the ability to use these tools to design and predict the mechanical and thermal stability of the larger joints. These joints, referred to as "scale-up" joints, shall have an interfacial area of at least twenty square centimeters.

Technical Highlights

Finite element analysis of a variety of braze joint configurations was undertaken. The superiority of a tapered metal sleeve around a ceramic cylinder, compared with a butt joint, was demonstrated.

Braze alloy development work has resulted in acceptable brazes for the 650°C application using an Au-Pd-Ni-Ti alloy. The 950° Application is being evaluated with the Au-Pd-Ti system.

Materials systems development focused on selection and thickness optimization of interlayers for SiC and Si_3N_4 brazing to Incoloy 909. Satisfactory results were obtained for SiC with a .040" interlayer of either Cu or Mo. In Si_3N_4 brazing, a test grid was conducted to examine the relative effectiveness of two different categories of interlayers, low yield stress materials such as copper and low expansion coefficient alloys such as molybdenum. The joint material system with a copper interlayer showed a significant improvement in joint strength compared with samples having Mo interlayer.

Silicon nitride brazing studies with Mo interlayers have shown that a wide range of temperature and time results in acceptable brazes. In coating studies on MOR bars of AY6 and PY6, the latter was shown to be less strongly affected by coatings than alumina-containing silicon nitride.

Design/Criteria/Stress Analysis

An examination of the mechanics of various joint geometries was undertaken in order to minimize the residual tensile thermal stresses in the ceramic shaft after brazing. The basic geometry of the joint is given in Figure 1. The ceramic shaft is 14 mm diameter and the metal shaft is a solid or hollow section as described later. The braze has a thickness of 0.05 mm and an area of 154 mm^2. The length of each component is taken to the 30 mm so that end effects are eliminated. The joining is done by heating the components to the melting point of the braze, applying the braze and allowing the components to cool down to the room temperature (20°C).

Two sets of materials (set A and B) are considered, and the ceramic is assumed to be linearly elastic. Material A included Inconel 718 as the structural alloy; material B used Incoloy 909. Material A included a braze with 4 times the yield stress of material B.

Geometries considered in this study are shown in Figure 2. Because of symmetry, only a half section is considered in the analysis. The dimensions of the metal shaft and the braze were chosen so that

1. Braze area is constant at 154 mm^2 (this is strictly not correct in the parabolic cases).

2. Limit torque of the metal shaft is not less than that which can be carried by the braze.

The flat joint (Figure 2a) has a circular braze area of 154 mm^2 and a thickness of 0.05 mm. Figure 2b shows the parabolic joint. Here the braze has a parabolic shape with a downward or an upward dip. The parabolic cross section of the braze is given by

$$y = h\left(\frac{x}{b}\right)^2, \; b = 7mm$$

where h is the dip at the outer surface. The vertical distance between the lower and upper surfaces of the braze is kept constant at 0.05 mm. The conical joint and the hollow metal shaft with an inner radius a and outer radius b= 7 mm. Since the braze area is constant at πb^2, the parameters shown in Figure 2c are related by

$$a^2 = b^2(1 - \sin\alpha)$$

and

$$h = (b - a)\cot\alpha$$

If τ_o^M and τ_o^B are the yield stresses in shear for the metal and the braze, respectively, the fully plastic torque (neglecting residual stresses) are given by:

$$T_o^M = \frac{2\pi}{3}(b^3 - a^3)\tau_o^M$$

for the metal, and

$$T_o^B = \frac{2\pi}{3\sin\alpha}(b^3 - a^3)\tau_o^B$$

for the braze.

Hence

$$\frac{T_o^M}{T_o^B} = \left(\frac{\tau_o^M}{\tau_o^B}\right)\sin\alpha \geq 1$$

This gives limiting values for α and $\frac{a}{b}$ for each material, as follows. For material A,

$$\sin\alpha \geq \frac{\tau_o^B}{\tau_o^M} = \frac{271}{1033} = 0.26$$

i.e.

$$\alpha \geq 15.2^\circ \text{ and } \frac{a}{b} \leq 0.86$$

For material B,

$$\alpha \geq 3.8^\circ \text{ and } \frac{a}{b} \leq 0.97$$

Two values for $\frac{a}{b}$ ratio were considered in the present study.

1. $\frac{a}{b} = 0.8$ *giving* a = 5.6 mm, b = 7.0 mm
   $\alpha = 21^\circ$ and h = 3.63 mm

2. $\frac{a}{b} = 0.5$ *giving* a = 3.5 mm, b = 7.0 mm
   $\alpha = 49^\circ$ and h = 3.09 mm

In the case of the cylindrical joint (Figure 2d), the metal shaft of outer radius b and inner radius 7.05 mm, fits outside the ceramic shaft. In order to have constant braze area, the length of the joint (h) must be half the radius of the inner shaft, i.e.,

h = 3.5 mm.

Two details were considered for the lower edge of the metal shaft.

1. A square edge as shown in Figure 2d(i)
2. A bevel edge as shown in Figure 2d(ii).

This study was carried out using the facility available at the University of Illinois Department of Mechanical and Industrial Engineering. It consists of the following:

1. HP 9000 mini-computer operating under unix system
2. ABAQUS - general purpose finite element package - version 4.5

Numerical analysis was done using 8 node, parabolic-isoparametric axi-symmetric finite elements with reduce integration. The normal element CAx8R was used for the ceramic, and the hybrid element CAx8RH was used for the metal and the braze.

Since the aim of this study is to compare stress in the ceramic with different joint geometries and select the one which gives lower stress levels, the finite element modeling has to be done carefully so that the differences in stresses among different models are due to their geometry differences and not due to modeling differences. This means that the finite element modeling errors should be approximately the same for different models. The error estimation of finite element models is not an easy task and hence the approach taken was to use similar element sizes and distributions at critical locations for all models. It is hoped that this will give rise to similar errors for different models, so that their stresses obtained from the analysis could be compared directly. Output from ABAQUS runs consistent of element stress and strains at integration points (4 pt. element) and the displacements at the nodes. Nodal stress can also be obtained, but they are not as accurate as those at element integration points. Hence comparisons were mainly done using element stress.

Since the primary concern is about tensile stress in the ceramic, results presented in this report are for the critical tensile regions in the ceramic. This region was found to be near the outer surface of the joint where the braze is in contact with the ceramic and the metal.

In the previous reporting period, it was shown that ceramic near surface stress was unfavorable in the butt joint compared with the cylindrical joints, particularly the tapered or beveled joint. In this reporting period, similar analysis was performed using different brazing materials systems. Specifically, Incoloy 909 was replaced with Inconel 718 and the braze yield strength was increased by a factor of 4. These changes had the effect of increasing near surface stresses by a factor of about 3. However, the relative ranking of the different joint configurations remained unchanged.

Figure 3 shows the results of FEM applied to three different joint configurations and the von Mises equivalent stress. Of particular interest is the stress level in the ceramic. Beveling the metal end was shown to reduce ceramic stress near the thin end. Similar stress reductions were obtained by placing a groove near the ceramic rod end. Plots of this type demonstrate the capability of the model to evaluate the effectiveness of candidate joint designs.

Brazing Alloy Development

An alloy of Au-Pd-Ni-Ti was developed that meets the application criteria. The ductile alloy wets both silicon nitride and molybdenum at 1100°C under 10^{-5} torr vacuum. A high-temperature braze between silicon nitride to silicon nitride was made at 1450°C using an alloy of Au-Pd-Ti. To meet the mechanical property at 650°C, a solidus temperature of about 1050°C was targeted. The developed alloy with a solidus of 1078°C should meet the creep resistance at 650°C application temperature.

Table 1

Alloy No.	Composition Weight Percent				Liq.°C/Sol.°C	Knoop Hardness
53-0	92 Au	5Pd	2Ni	1.0 Ti	1114/1084	117
53-21	91.75Au	5Pd	2Ni	1.25Ti	1113/1078	138
53-15	91.50Au	5Pd	2Ni	1.50Ti	1133/1078	170
53-22	91.25Au	5Pd	2Ni	1.75Ti	1124/1078	190
53-16	91.0 Au	5Pd	2Ni	2.00Ti	1119/1082	209

The alloy with 1.5% Ti and above is too hard and will not allow the brazing alloy layer to plastically flow during post-braze cooling cycle (see Table 2).

Table 2

Alloy No.	Composition Weight Percent			Liq.°C/Sol.°C
53-07	94Au	5PD	1Ti	1178/1116
53-10	93Au	5Pd	2Ti	1150/1117
53-17	94Au	5Pd	1Zr	1181/1125
53-18	93Au	5Pd	2Zr	1168/1116

The recommended brazing practice of brazing silicon nitride to molybdenum using alloy composition 53-21 is to use 4 mil thickness foil and braze at about

1110°C ± 10°C (part temperature) for 2 - 4 minutes under 10^{-5} torr vacuum. Excess temperature and time will alter the brazing alloy composition, making the alloy less ductile.

The braze joint to survive the 950°C temperature for extended time in oxidizing air atmosphere required that the alloy be based on precious metal. The braze temperature or the solidus temperature of the brazing alloy should be about 1450°C. For purposes of this study, silicon nitride-silicon nitride joints were made:

Alloy No.	Composition Weight Percent		
53-6	39.2Au	60Pd	0.8Ti
53-9	48.5Au	50Pd	1.5Ti

No DTA was made on the above two alloys. Brazes were carried out at 1400°C, 1450°C, and 1500°C.

An alloy for joining silicon nitride to molybdenum was developed with a composition of 91.75% Au, 5% Pd, 2% Ni, 1.25% Ti. Substitution of Ti with Zr resulted in a degraded alloy system. An alloy of 39.2% Au, 60% Pd, 0.8% Ti was developed to join silicon nitride to silicon nitride at 1450°C under vacuum.

Silicon Carbide Metal Joint Development

Coating

In order to develop a candidate list of possible coatings for SiC brazing, it was first necessary to address the mechanism of adhesion between the braze and the ceramic. This effort utilized the approach demonstrated earlier for silicon nitride. The possible chemical reactions were examined from a thermodynamic standpoint using the JANAF Thermochemical Data. Reactions of the type listed below were considered.

$SiC + Hf \rightarrow Si + HfC$ ΔG_f° at 1500K = Unavailable

$SiC + Ta \rightarrow Si + TaC$ ΔG_f° at 1500K = -33.561 Kcal/mol

$SiC + Ti \rightarrow Si + TiC$ ΔG_f° at 1500K = -40.185 kcal/mol

$SiC + Zr \rightarrow Si + ZrC$ ΔG_f° at 1500K = -43.453 kcal/mol

ΔG_f° for SiC at 1500K = -17.943 $K_{cal/mol}$

Based on these thermodynamic data, TaC, TiC, and ZrC have lower free energy of formation than SiC and are strongly favored. Hf was included in the test grid based on previous experience with silicon nitride. Thermodynamic data for reactions of Hf with SiC were not available.

In order to evaluate the effect of ceramic coatings on the mechanical strength of the ceramic, a series of coated SiC MOR bars were prepared in a manner similar to the earlier study on silicon nitride. The samples were polished to a 3-micron finish. Groups of fifteen samples were coated with 3 microns of either Hf, Ta, Ti, Zr, or were uncoated. They were then subjected to a thermal cycle which is prototypical of Nioro brazing, 980°C for ten minutes. During MOR testing, the coated side was placed in tension so that the mechanical ramifications of any interfacial reactions would be seen. The results of these procedures are shown in the now familiar format in Figure 4. The uncoated specimens serve as a set of baseline values. Ta coating was seen to result in a small but noticeable improvement in MOR. Ti and Zr each had small negative effects on mechanical behavior. Hf had an extremely damaging impact on the mechanical performance of the SiC samples.

Based on consideration of ceramic-coating interactions and its effect on mechanical properties, Ta was judged to be the preferred coating material with Ti and Zr as second and third choices, respectively. Hf was considered to be unacceptable.

The mechanism by which the coatings interact with the ceramics and alter properties is still the subject of some speculation. Of particular interest is the apparent improvement offered by Ta coating. Attempts to more clearly define the nature of coating-ceramic interactions will be addressed at later stages of the program.

Interlayers

Materials system development for silicon carbide brazing continued during this reporting period. A series of coupon samples were brazed using the coupon-type samples developed for silicon nitride. Such samples offer the capability of being tested in the available shear test fixture for convenient characterization of properties.

Figure 5 shows a schematic illustrating the configurations of the specimens used for the study. Type I specimens consisted of a small coupon of SiC coated with either Hf, Ta, Ti, or Zr. Coating thicknesses were 3 μm with the exception of Ta, which was only deposited to .4 μm. The large coupon was Incoloy 909, which is the structural alloy selected for 650°C service. Type II specimens were geometrically the same as Type I with molybdenum used in place of Incoloy 909. Such samples would be exposed to smaller differential strains than Type I because of the relatively good expansion match between Mo and SiC. They would not, however, demonstrate the effectiveness of Mo in shielding the ceramic from the thermal

shrinkage associated with Incoloy 909. For that purpose, Type III specimens were used. Previous experience with such interlayer specimens has shown large unbonded areas associated with warping of the layers. To avoid this problem, a two-step brazing practice was used. During the first step, Nioroni was selected to braze the Cu or Mo interlayer to Incoloy 909. This braze consists of 73.8 wt. % Au and 26.2 wt. % Ni. Its liquidus and solidus are 1010°C and 980°C, respectively. After this first step, the sample surface was repolished and was then brazed to SiC with Nioro. The 950°C liquidus of this alloy made it possible to perform the second braze without remelting the first. A fourth group of specimens were coated with SiC brazed to coated SiC.

The results of this series of tests (Table 811-I) provide a considerable amount of information concerning the quantitative effect of differential contraction on residual stress, SiC cracking, and interlayer effectiveness and shear properties. The Type I samples all failed on cooling to room temperature. They were unable to withstand the relatively large differential contraction between Incoloy 909 and SiC. The lower expansion of Mo made it possible for the Type II samples to be shear tested with reasonable results. The Type III samples also survived cooling to room temperature when the interlayer was .040″ thick using either Cu or Mo. Their lower level properties is a measure of the extent to which the interlayers protected the SiC from the Incoloy 909. Samples using thin, .010″ Cu or Mo were unable to survive the cooling cycle. The results of these tests are shown in Table 3.

Table 811-I: Shear Test Results

	Materials System	No. of Samples	Mean Shear Test (ksi)
I.	Incoloy 909-Nioro-Hf Coating-SiC	1	0
	Incoloy 909-Nioro-Ta Coating-SiC	1	0
	Incoloy 909-Nioro-Ti Coating-SiC	1	0
	Incoloy 909-Nioro-Zr Coating-SiC	1	0
II.	Mo-Nioro-Hf Coating-SiC	4	1.6
	Mo-Nioro-Ta Coating-SiC	4	2.4
	Mo-Nioro-Ti Coating-SiC	3	2.9
	Mo-Nioro-Zr Coating-SiC	3	3.5
III.	Incoloy 909-Nioroni-.010 in. Cu-Nioro-Ta Coating-SiC	2	0
	Incoloy 909-Nioroni-.040 in. Cu-Nioro-Ta Coating-SiC	2	.7
	Incoloy 909-Nioroni-.040 in. Cu-Nioro-Zr Coating-SiC	1	2.6
	Incoloy 909-Nioroni-.010 in. Mo-Nioro-Ta Coating SiC	2	0
	Incoloy 909-Nioroni-.040 in. Mo-Nioro-Ta Coating SiC	1	.29
IV.	SiC-Hf Coating-Nioro-Hf Coating-SiC	2	13.9

All of the failed samples had a common macrostructural feature: they all failed entirely in the ceramic. This is significant in terms of interpretation of results, since it makes it possible to rule out the effect of unbonded areas. All coatings were equally effective in one sense because no joints delaminated at the ceramic-braze interface. It is possible, however, that coating-ceramic interactions weakened the ceramic promoting failure at a low value of shear. Referring to the Type II samples for which the best statistics are available, it is seen that the lowest failure strength was obtained with the Hf-coated specimens. This coating was shown to cause the most ceramic degradation in the coated MOR test previously reported.

The work on SiC joining with the fourth group of samples included two pairs of SiC-to-SiC joints. Each piece of SiC was coated with 3 μm of Hf, brazed with Nioro, and sheared. The mean shear stress of these samples was 13.9 ksi. This was significantly higher than was obtained with SiC-Metal joints in the variety of configurations discussed above. The low values reported for metal-SiC joints raised the concern that perhaps chemical degradation, rather than residual stress from differential expansion was responsible. The coating used for the SiC-to-SiC joints, Hf, had re-

sulted in the largest reduction in properties in the coated MOR tests. The fact that even the most chemical damaging coating yielded high shear strength values in the absence of differential expansion demonstrated that chemical attack was not responsible for the low strength of SiC-metal pairs. Future work on Incoloy 909-Mo-SiC joints will utilize thicker layers of Mo to address the residual stress problem and its effect on joint strength.

A number of conclusions can be drawn from this study.

1. An interlayer of either a soft, compliant material such as Cu, or a low coefficient of expansion material, such as Mo, must be used to braze SiC to Incoloy 909.

2. Interlayer thicknesses of .010″ were ineffective.

3. Interlayer thicknesses of .040″ showed a measurable ability to partially offset the effect of Incoloy 909 contraction.

4. All observed failures were in the ceramic, indicating that unbonded areas did not play a role. Ceramic coatings appear to affect the ceramic strength in brazed coupons.

5. Residual stress, not chemical degradation, is the principal factor affecting strength level in brazed pairs.

Further data will be needed to determine the optimal interlayer thickness and to quantify the relative effectiveness of different types of interlayers. Finite element calculations to be provided by the University of Illinois will be used to direct the effort.

Silicon Nitride-Metal Joint Development

Interlayers

According to the analytical expression for joint failure, low thermal expansion and low yield strength properties are needed in interlayer materials to prevent cracking. Unfortunately, in real materials it is not possible to have both of these properties simultaneously. In this report, two different interlayer materials, i.e., Mo and Cu, have been used (1) to determine the effectiveness of these materials as an interlayer, and (2) to find the optimum thickness of each interlayer material for practical use. Mo was selected for its low thermal expansion coefficient, high stiffness, and yield strength, while Cu was chosen for low yield strength and stiffness.

Specimen geometry is similar to that shown in Figure 5-iii, with SNW1000 in place of SiC. Interlayer materials were brazed in the step formed in the Incoloy 909 coupon using Nioro braze. Subsequently, Zr-coated SNW1000 was brazed onto the top of the interlayer material with Nioro at 980°C for 10 min. in vacuum. Shear tests were performed with the Instron 1320 at 4,000 lbs of full scale load in compression mode.

Table 4 shows the results of testing. A dramatic difference in bond strength was found between two interlayer materials, even though these materials were processed with the same brazing conditions. In particular, the joint strength values obtained from the Mo interlayer system were very low compared with those from the Cu interlayer system. Also, the values did not reach those reported previously for the Mo interlayer system (June bimonthly). It was found that the Mo layer suffered inconsistent, improper bonding with ceramic, resulting in 40 - 90% unbonded area. The Cu interlayer system provided excellent bonding performance (> 95% of bonding area) with high shear strength for failure. Samples with a 0.020″-thick Cu interlayer showed the highest shear value (23.1 ksi). It is difficult to say that this is due solely to thickness effect.

Fractography revealed that the system with the Cu interlayer fractured predominantly at the interface between braze and ceramic. For the system with Mo, fracture occurred in the ceramic material. Overall results showed that the system with the copper interlayer (low strength and high thermal expansion coefficient materials) was effective in the reduction of residual stress generated by the thermal expansion mismatch. Shear strength of the ceramic-ceramic joint was in the range of 40 - 45 ksi, which represented the case of no thermal mismatch.

Debonding of the braze joint between the Mo interlayer and SNW1000 could be explained as follows. At the brazing temperature, diffusion of the interlayer materials to liquid Nioro will be assisted by thermal convection with a diffusivity in the vicinity of 10^{-4} cm^2/sec. As the local concentration of Mo in the vicinity of the interface (between the Mo interlayer and liquid Nioro) increases, the liquid braze will be undercooled due to the increase in the solidus temperature. Therefore, the brazing process would be sensitive to brazing temperature and holding time. It is expected that higher temperature with long holding time will induce extensive alloying with Mo, enhancing diffusion solidification. In contrast, binary phase diagrams show that the Cu interlayer has a relatively small effect on the solidus temperature of the braze alloy, even after being alloyed. This makes the brazing process more controllable, minimizing the effect of diffusion solidification. However, it cannot be ruled out at this point that alloying with Mo or Cu may exert significant effect on the wetting behavior of the braze.

Table 4: Results of Shear Test with Mo and Cu Interlayers

Thickness (in.) of Interlayer Material	Shear Strength (ksi) Molybdenum (Avg.)	Copper (Avg.)
0.010	3.1 2.2 (4.4) 7.8	9.8 11.2 (10.5) 10.5
0.020	3.2 7.3 (5.3) 5.4	26.9 Not fractured 23.2 (23.1) 19.3
Brazing Condition	980°C for 10 min in vac	980°C for 10 min in vac
Bonding	All samples have poor bonding between Mo & SNW (40-90% unbonded area)	Excellent bonding for samples (≈100%) the interface between braze and SNW1000

A series of tests were performed to determine whether molybdenum diffusion into the liquid braze, with the resultant effect on liquidus temperature, would limit the acceptable window of processing variables. Figure 6 is the microprobe result showing the extent of molybdenum diffusion in the (Zr-coated) SNW1000-Nioro-molybdenum-Incoloy 909 system. Significant diffusion of molybdenum is noted in the braze layer after 980°C for 10 min. Based on this observation, two extreme processing conditions were selected: 1) brazing at 960°C for 3 min. and 2) brazing at 1100°C for 30 min. in order to determine the effect of the diffusion on bonding performance.

From optical microscopy, it was noted that fast diffusion of molybdenum is evident in both cases. Brazing at 960°C for 3 min. resulted in a braze layer of 40 - 45 µm in thickness which has moderate alloying with molybdenum (20 µm thick). Brazing at 1100°C for 30 min. extended the molybdenum diffusion further and caused severe alloying with braze alloy (30 µm in thickness). From these micrographs, it was noted that the diffusion and the reaction between braze alloy and molybdenum (even at 960°C for 3 min.) in the presence of liquid phase are extensive in both cases. However, acceptable brazes were obtained over the wide range of processing variables. A faceted phase was shown in the braze layer after brazing at 1100°c

for 30 min., which is probably due to the interaction between Zr and a Mo-Nioro phase.

Table 5 shows the results of shear strength testing. As shown in this table, there is no noticeable difference in strength among three different processing conditions. Also, excellent bonding was obtained in all three cases. It was concluded from this investigation that brazing conditions such as temperature and holding time have little effect on bonding performance.

Table 5: The Effect of Processing Parameters on Bond Strength

Sample #	Brazing Conditions	Shear Strength (ksi)	Avg. (ksi)	Bonding Result
1	960°C for 3 min.	5.4	12.1	Excellent
2	960°C for 3 min.	21.5	12.1	Excellent
3	960°C for 3 min.	9.4	12.1	Excellent
4	960°C for 3 min.	11.9	12.1	Excellent
1	1100°C for 30 min.	18.9	12.0	Excellent
2	1100°C for 30 min.	5.7	12.0	Excellent
3	1100°C for 30 min.	12.7	12.0	Excellent
4	1100°C for 30 min.	10.8	12.0	Excellent
1	980°C for 10 min.	11.3	11.5	Excellent
2	980°C for 10 min.	18.9	11.5	Excellent
3	980°C for 10 min.	4.2	11.5	Excellent

Coatings

MOR tests were done to evaluate the effect of coatings on the mechanical properties of AY6 and PY6 as part of materials system development. Samples were made out of 3 and 5 different blanks of PY6 and AY6, respectively, to avoid misinterpretation of data. Those bars were coated with various materials in vacuum and were exposed to 980°C for 7 min.

Figure 7 shows the Weibull plots of AY6 material. As with the results reported for SNW1000, Ti coating caused a dramatic reduction in MOR. The influence of Zr- or Hf-coating on the MOR strength was minimal. Ta coating decreased the MOR strength by 20 - 30 ksi. On the other hand, the impact of Ti coating on the MOR strength of PY6 is almost insignificant as illustrated in Figure 8.

These results indicate that the primary cause of Ti coating damage is attributed to Ti interaction with Al_2O_3 in the ceramic materials. SNW1000 and AY6 were strongly affected by Ti coating, with each containing 2 wt. % Al_2O_3 (Table 6). This is

also supported by the same experiments with SNT which also showed reasonably small decrease in strength by Ti coating. SNT has about 1.2 wt. % of Al_2O_3 along with 39 wt. % TiC, which can minimize the impact on strength from Ti coating. Further study is underway to identify the mechanism for the ceramic weakening due to coating materials.

Table 6: Ceramic Compositions (w/o) and Ti Coating Effects on MOR

	Y_2O_3	Al_2O_3	TiC	Balance	Avg. MOR Strength (ksi) Coated	Uncoated
SNW1000	13	2	-	Si_3N_4	60	80
AY6	6	2	-	"	100	200
PY6	6	-	-	"	100	110
SNT	3.6	1.2	40	"	65	75

Status of Milestones

The milestone Analytical Strength Prediction, scheduled for 8/1/88, was completed 3/1/88, and the milestone Brazing Alloy Development, scheduled for 8/1/88, was rescheduled for 11/1/88.

Communications/Visits/Travel

Frequent discussions were held by phone with Professor K-S. Kim of the University of Illinois and Howard Mizuhara of GTE Wesgo. On 5/13/88, Professor Kim visited GTE Labs to discuss mechanics modeling.

6/16-17/88 - H. Mizuhara (GTE Wesgo) visited the Labs to discuss alloy development and program status.

6/24/88 and 7/25/88 - E. Dunn and S. Kang met with Professor K-S. Kim of the University of Illinois to discuss mechanics modeling and milestone status.

Problems Encountered

None.

Publications

None.

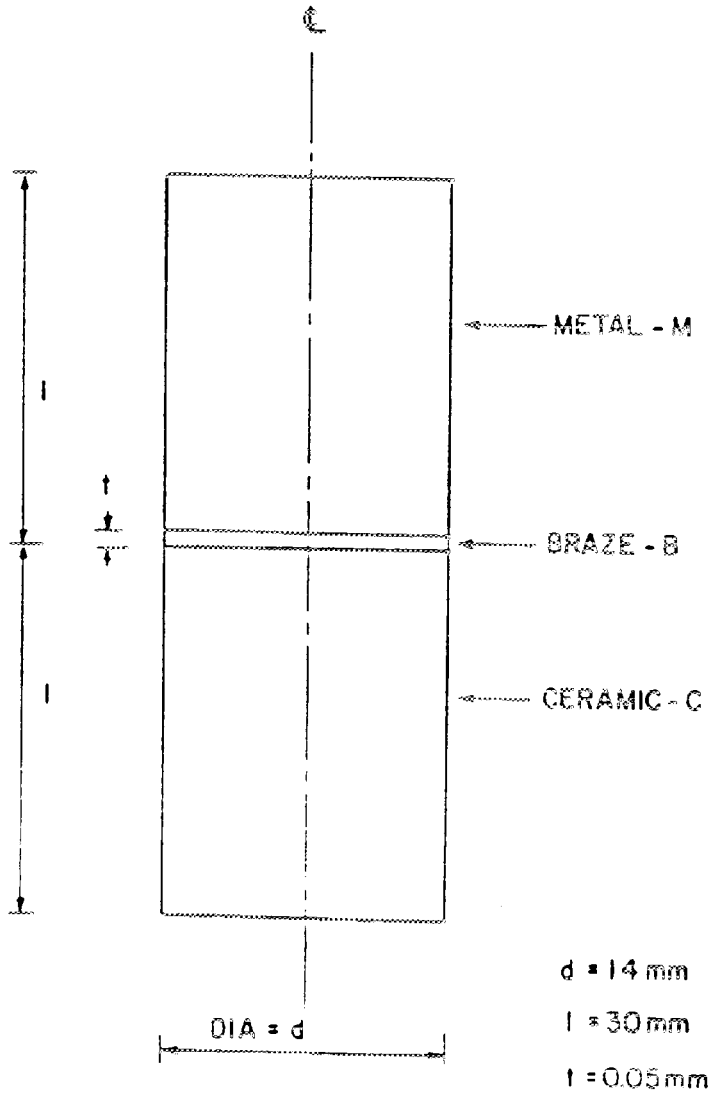

Figure 1: Basic geometry of Ceramic-to-Metal braze joint

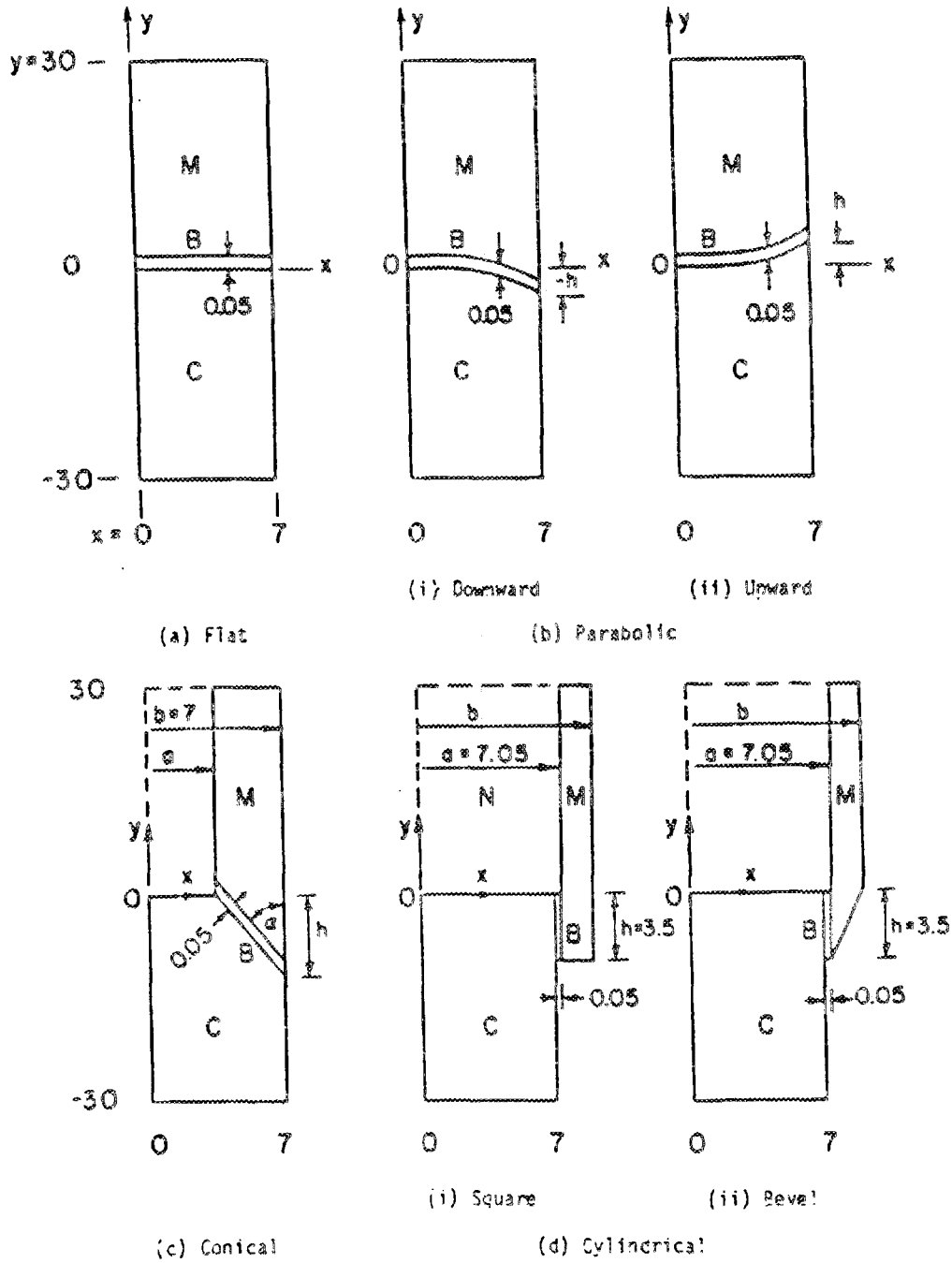

Figure 2: Types of geometry for different configurations with same brazing area; all dimension in mm.
Note: Torque(load) capacity of socket joint is 1.5 times that of butt joint for same area of brazing.

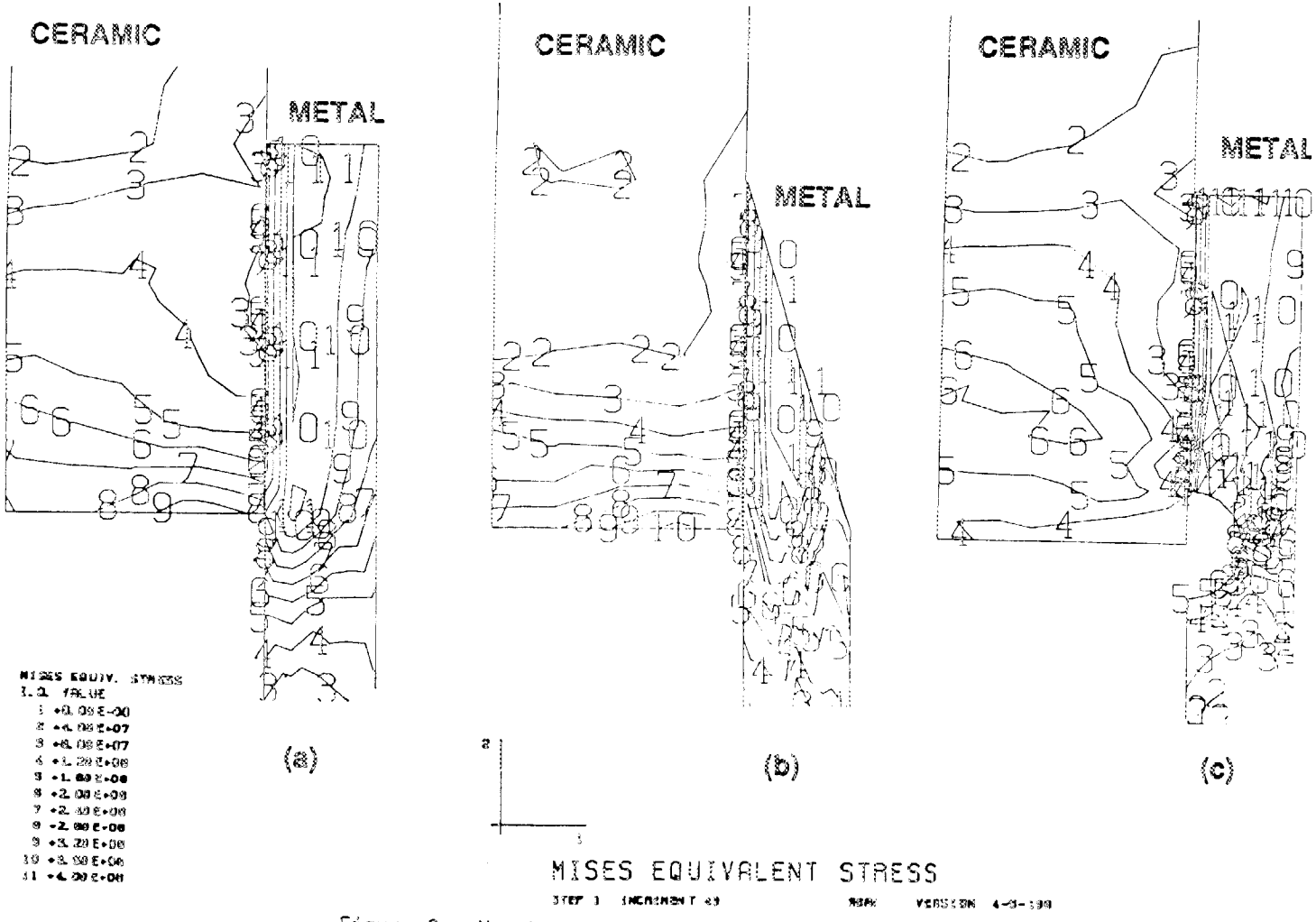

Figure 3: Von Mises Equivalent Stress for Three Joint Designs

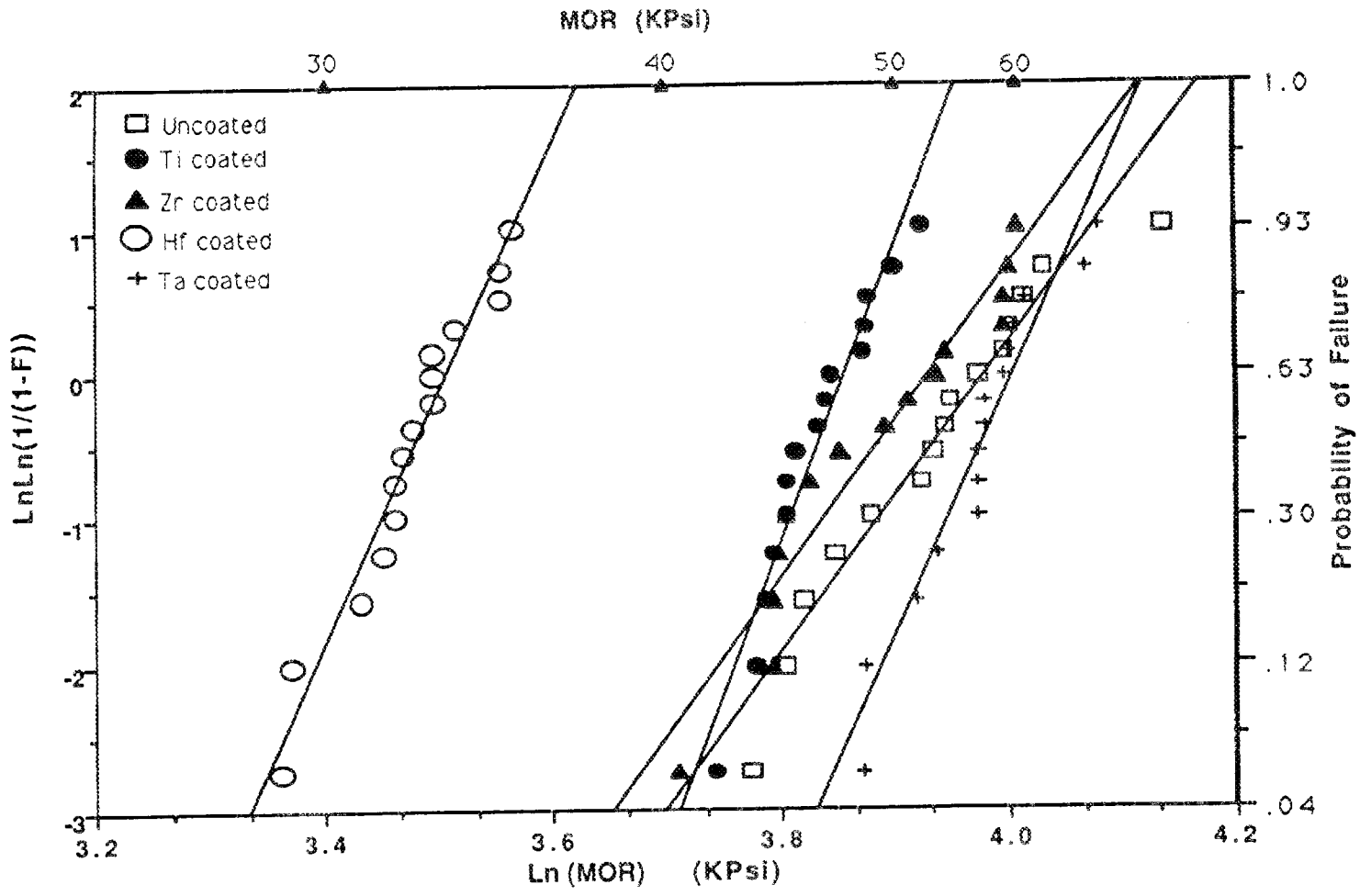

Figure 4. Weibull Plot of Hexaloy SiC MOR Bars at Room Temperature

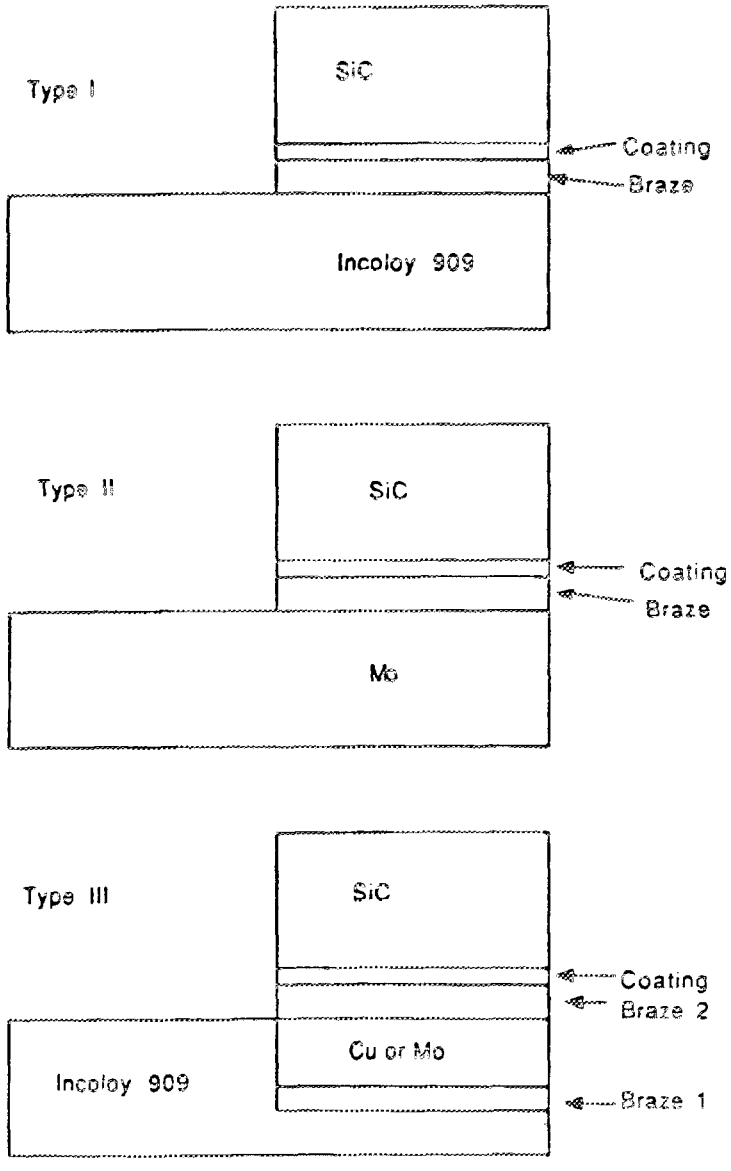

Figure 5: Schematic Illustrating Shear Test Specimens

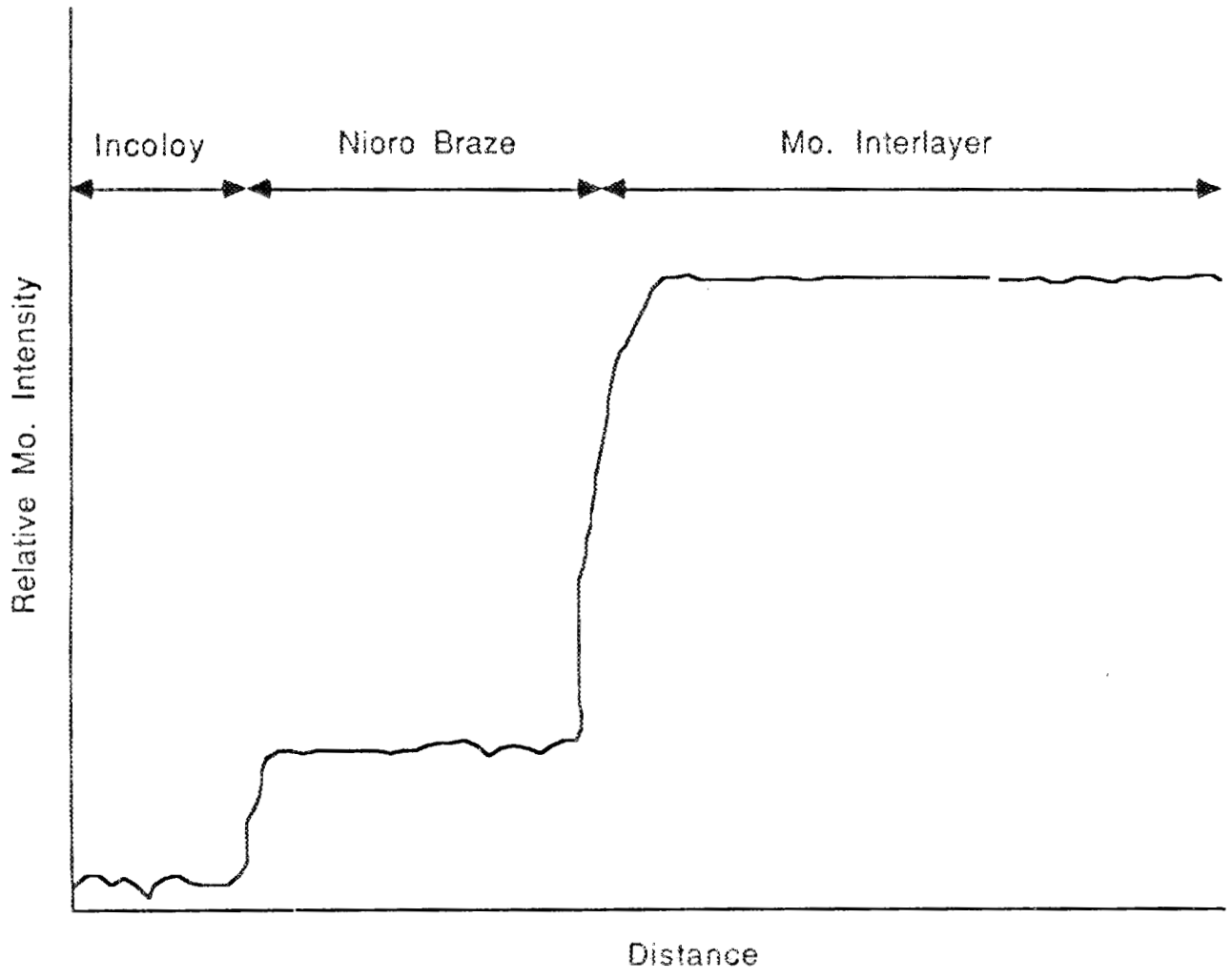

Figure 6 : Microprobe result on Mo diffusion in SNW1000-Nioro-Mo interlayer-Nioro-Incoloy 909 system

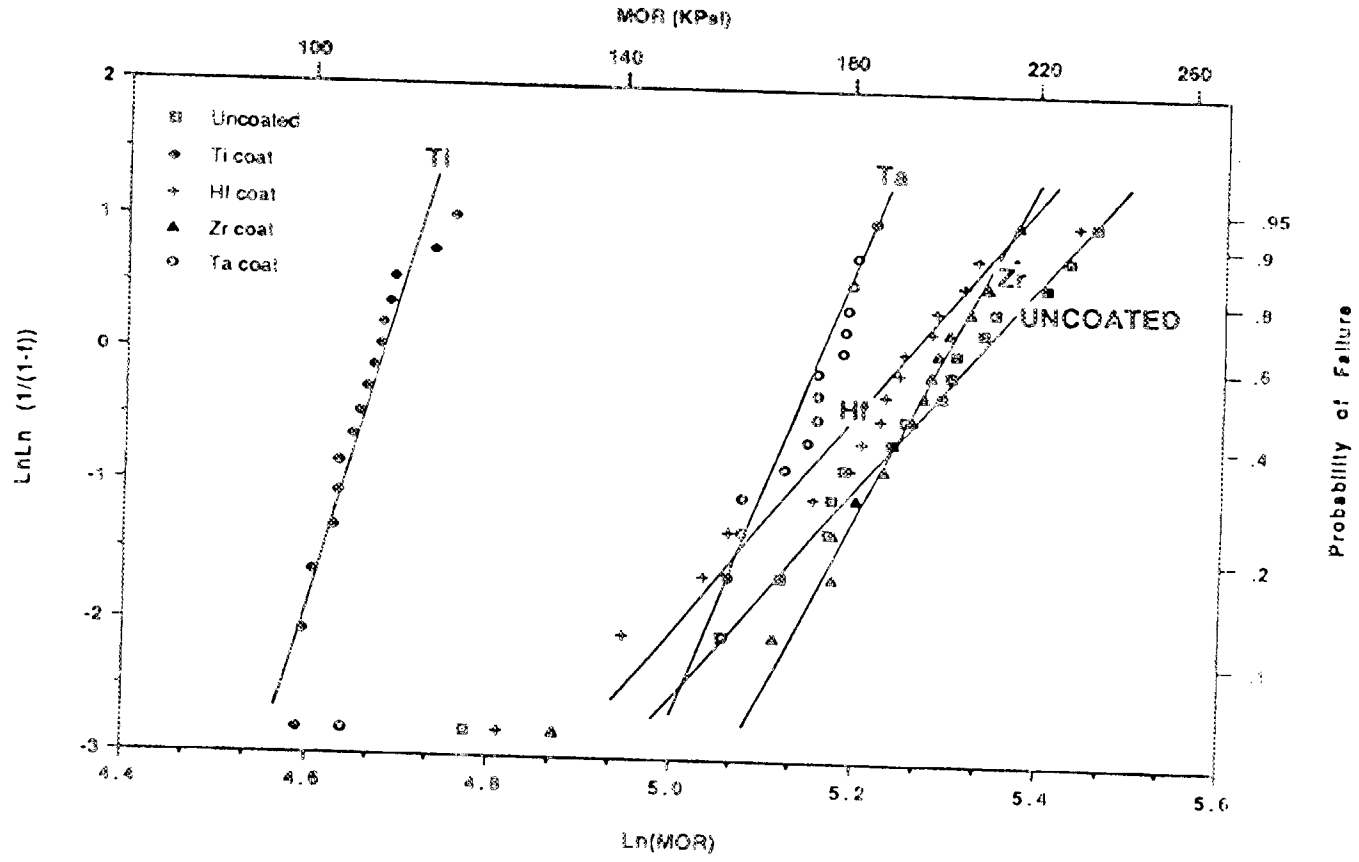

Figure 7: Weibull plot of AY6 silicon nitride MOR bars with various coatings at room temperature (after heat treatment at 980°C for 10 minutes)

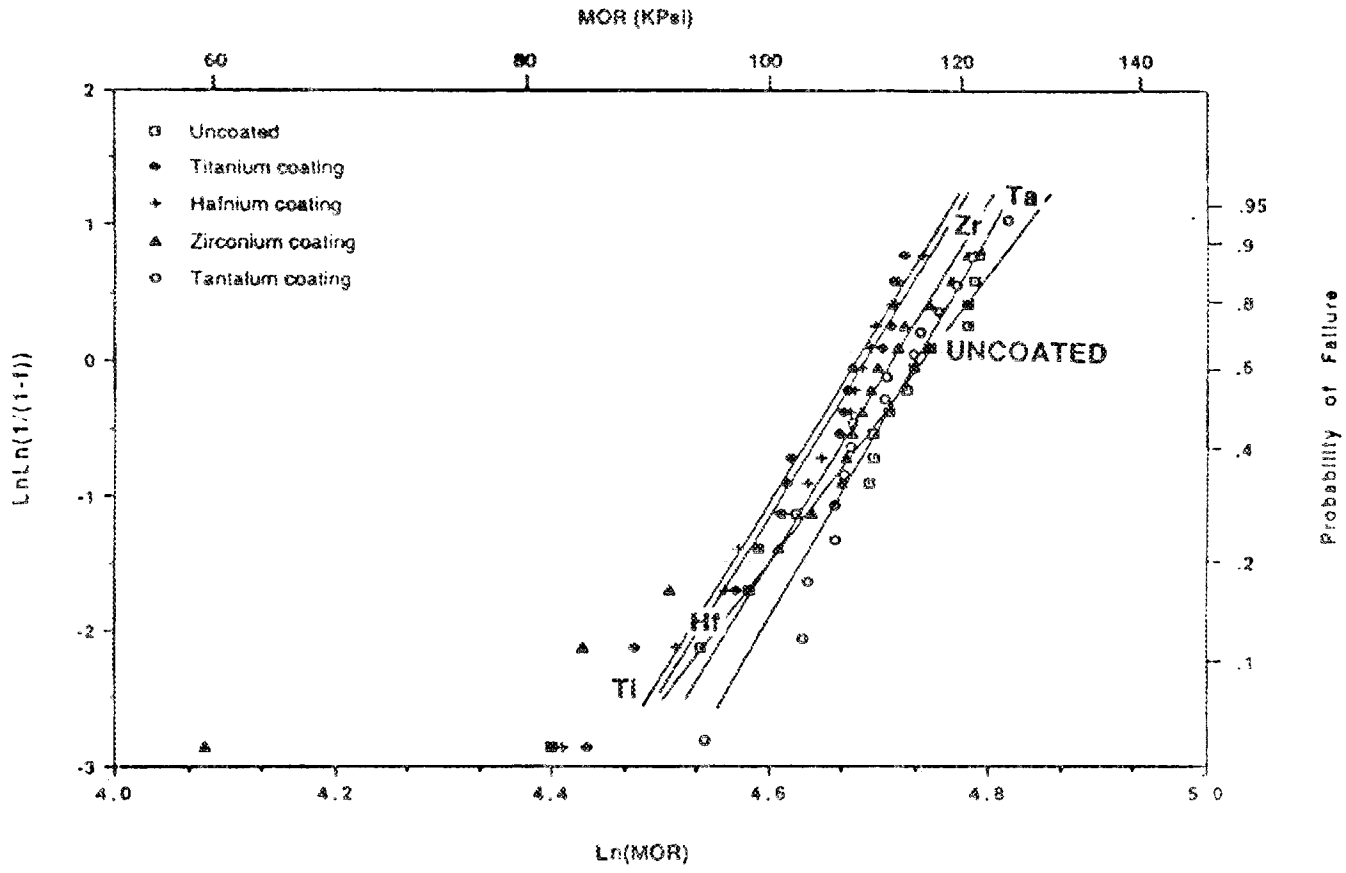

Figure 8 : Weibull plot of PY6 silicon nitride MOR bars with various coatings at room temperature (after heat treatment at 980°C for 10 minutes)

Analytical and Experimental Evaluation of Joining Ceramic Oxides to Ceramic Oxides and Ceramic Oxides to Metal for Advanced Heat Engine Applications

A. T. Hopper, J. Ahmad, and A. Rosenfield
(Battelle Columbus Division)

Objective/Scope

The objective of this project is the development of procedures necessary for design of reliable, high strength ceramic oxide-to-ceramic oxide and ceramic oxide-to-metal joints. The research program consists of analytical and experimental tasks.

The goal of the analytical work is a predictive model that can be used in engineering design of ceramic joints. This work consists of several subtasks involving residual stress modeling, deterministic stress and fracture mechanics modeling, engineering design modeling, probablistic modeling, and model validation. Inputs to these models come from the experimental efforts.

The experimental work involves the fabrication and testing of small scale and scaled up joints to determine the mechanical behavior of these ceramic joints. Experiments will be performed to determine elastic constants and stress-strain curves as a function of temperature, tensile strength, shear strength, Mode I and Mode II fracture toughness, creep deformation, time dependent strength, and strength degradation from hot oxidizing gases and from thermo-mechanical cycles.

Technical Progress

1.0 Analytical Efforts

In the present reporting period, analytical effort was focused on estimating potential residual stress influence on joint performance. Specifically, a zirconia/nodular cast iron disk (see Figure 1) was subjected to finite element analyses. The disk diameter in this analysis was 31.75 mm.

Residual stresses in the disk are induced because the joining of the ceramic and metal halves is done at an elevated temperature followed by cooling to room temperature. The mismatch in the thermomechanical properties of the two halves induces residual stresses.

In the analysis, the following material properties were used:

Young's Modulus: 138 GPa (Zirconia), 168 GPa (cast iron)
Poisson's Ratio: 0.26 (Zirconia), 0.31 (cast iron)
Coefficient of Thermal Expansion: 10.8×10^{-6}/C (Zirconia), 13.7×10^{-6} (cast iron)

Since the analysis was linear, the computed strains and stresses scale linearly with temperature. The results in Figures 2 through 5 correspond to a joining temperature of 1000 C. Figure 2 shows the high localized stress (S_{xx}) across the bond line, close to the edge of the disk. The local nature of this high stress component can be seen in Figure 3 in which S_{xx} is plotted along the bond line.

Toward the center of the disk, where the crack will be located in the experiments, both S_{xx} and the shear stress (S_{xy}) components are relatively small. This can be seen from Figures 3 and 4. The normal stress component S_{yy} (see Figure 5) is large in the center but this is expected to have only a small effect on the behavior of the crack.

Overall, the analyses suggest that residual stresses may not be important in analyzing the disk specimen experiments. However, the high S_{xx} close to the free edge will need to be addressed in developing a predictive model for joint integrity.

Work was also started on developing the capability to calculate energy release rates and stress intensity factors for the zirconia-cast iron compression disk specimens. Since these solutions would depend on the elastic properties of the constituent materials, the computational work must await completion of the planned material characterization tests.

Recent discussions with Professor C. F. Shih of Brown University have lead to the conclusion that, at least initially, the joint failure-prediction model can be formulated in terms of the path independent integral J. Under linear elastic conditions, J is equivalent to the energy release rate G for the interface crack problems of interest.

Recent work indicates that under nonlinear crack tip conditions, J may provide an approximate description of the local stress-strain field. Based on this information, the joint failure prediction model is envisioned to be similar to the failure assessment diagram (FAD).

2.0 Experimental Efforts

The objective of this task is to design, fabricate, and test small-area ceramic oxide-to-ceramic oxide and ceramic oxide-to-metal joints. Statistically significant numbers of experimental-sized joints in which the interfacial area is a minimum of two-square centimeters are first being fabricated and both physical and mechanical properties needed for model inputs evaluated. This task will result in validated joining procedures and, in combination with analytical efforts, validated analysis procedures.

2.1 Oxide/Oxide Joints

Small (0.56-inch diameter) Mg-PSZ billets have been joined by air-ambient hot-pressing with a $CaO-Ti_2-SiO_2$ interlayer powder, using a modified creep-testing apparatus. The joining method and the microprobe characterization results have been described in a paper submitted to Materials Letters. Figure 6 shows a bond produced using CTS. Further results are described below.

2.1.1 Joining. The joining technique under investigation for Mg-PSZ ceramics involves both hot-pressing and a ceramic interlayer that is molten at the hot-pressing temperature. One limitation of the use of high temperature hot-pressing for joining MG-PSZ ceramics is that the Mg-PSZ ceramics will be seriously degraded if the temperature cycle is not carefully designed. Mg-PSZ ceramics typically require a post-sintering annealing heat treatment at temperatures in the range of 1400 to 1450 C. In a production process, it may be appropriate to combine the annealing and joining steps. Consequently, the hot-pressing temperature for joining Mg-PSZ ceramics should be in the annealing range. For this reason, a hot-pressing temperature of 1420 C was selected. Appropriate interlayer materials include ceramic compositions or eutectics with melting temperatures below the joining temperature.

The $CaO-TiO_2-SiO_2$ (CTS) system is appealing because it has several eutectic compositions with melting temperatures below 1400 C (and would thus be molten at the joining temperature). The initial small-scale joining experiment with 0.56-inch diameter MG-PSZ billets and a CTS interlayer gave promising results. In this experiment, the modified creep-testing unit limited the joining pressure to 650 psi; the resulting interlayer was thin (10 microns), and extremely uniform over the entire joint area. Significant diffusion of the interlayer constituents into the Mg-PSZ base material was observed. The air-ambient hot-press was subsequently employed to join large (2-inch diameter) Mg-PSZ billets with the CTS interlayer, and a pressure of 2000 psi was applied at the hot-pressing temperature of 1420 C. However, the quality of the CTS joints was poor because of thermal expansion mismatch between the CTS interlayer (α = 3 ppm/C) and the Mg-PSZ base material (α = 10 ppm/C). Optical microscopy of polished cross-sections indicated the presence of numerous cracks propagating

through the interlayer; these cracks were likely caused by the thermal expansion mismatch. The thermal expansion of the CTS interlayer was increased by the addition of 30 wt% ZrO_2, and the joint quality improved (i.e., the density of interlayer cracks was reduced).

2.1.2. Evaluation. To evaluate the joint strength, bend bars were machined from a 2-inch diameter by 1.5-inch long cylinder of CTS-bonded zirconia. The bars were of nominal dimensions 0.1"x0.2"x2.5", and were tested in 4-point bending using a bend fixture with inner and outer spans of 0.75-inch and 1.25-inch respectively. The following are the test results.

TABLE 1. Bend Strength of Zirconia-Zirconia Joint

Specimen No.	Fracture Load lbf	Bend Strength ksi	MPa
ZZB-3	30.5	11.9	81.9
ZZB-4	23.6	9.3	63.7
ZZB-5	26.5	10.4	71.5
ZZB-6	29.4	11.5	79.5

Specimen numbers ZZB-3 and ZZB-4 were machined from one part of the cylinder, and specimens numbers ZZB-5 and ZZB-6 were machined from a different part of the block. Thus, the strengths appear to be fairly reproducible. A piece of the joined block was polished and observed under an optical microscope. It was confirmed that the low strength (80 MPa vs the 300 MPa target) was associated with a number of voids and crack-like defects along the bond line. Figure 7 shows a fracture surface, indicating primary failure within the interlayer.

More recent experiments have indicated that interlayers of the $CaO-Al2O_3-SiO_2$ (CAS) system may be more appropriate for joining Mg-PSZ ceramics. There are also several low-temperature eutectics in the CAS system; two of these eutectic compositions have high thermal expansion (α = 8-9 ppm/C), closely matching that of Mg-PSZ. These two CAS compositions have been prepared and two joining experiments have been performed using them. No strength data are available yet, but from optical microscopy, the CAS joints appear to be much improved over earlier CTS joints. No interlayer cracks were observed, and there was excellent continuity between the Mg-PSZ and the CAS interlayer.

2.2 OXIDE/METAL JOINTS

2.2.1. Procedure

Joining of zirconia to cast iron was done by the "active substrate process" which was invented by Hammond, David, and Woodhouse[2]. The process involves coating the zirconia surface with titanium to enable it to be brazed with a non-reactive filler metal as well as plating the cast iron surface with copper to prevent carbon from the graphite nodules from dissolving in the filler metal.

Three grades of zirconia were included in the program:

yttria stabilized PSZ (Toya Soda)
Nilsen grade MS (supplied by ORNL)
Magnesia stabilized PSZ (Corning)

The nodular cast iron used for bonding was either a high pearlite (60%) grade or a graphite grade supplied to Battelle by Sandia. The bronze was Ag-30Cu-10Sn (Lucas-Milhaupt No. 604). Both surfaces to be bonded were ground to a surface finish of 0.3μm in order to insure intimate physical contact.

Because of the high affinity of oxygen for titanium, the zirconia must be coated in a high vacuum (at least 3×10^{-2} torr.). Two procedures were examined:

a. NASA-Lewis Lab

Plasma ion etching was for 1 min. followed by coating using an RF source for 15 min. at 5×10^{-7} torr. Thickness = 0.9 micron (Y_2O_3-ZrO_2) and 1.4 micron (MgO-ZrO_2)

b. ORNL Ion Beam Vapor Coating

Thickness not measured.

Eleven bonding runs were carried out. Most unsuccessful joints were obtained mainly due to the oxidation of the Ti film on PSZ. However, it was later found that another cause of failure was due to poor Cu electroplating. The adhesion of a Cu layer on NCI was poor and carbon was easily diffused out through the Cu layer providing a non-wetting condition. So electroplating was replaced by vacuum evaporation and an excellent coating was obtained. Evaporation was carried out using a Kinney vacuum evaporator with 99.9% Cu beads at a pressure of 10^{-4} torr. for 4 minutes. The resulting thickness was 20 μm.

Use of several furnaces was also investigated. Successful bonding was achieved using a graphite-resistance furnace with the material to be bonded inserted in a graphite hot-pressing fixture. The pressure was $4\text{-}5 \times 10^{-5}$ torr. and the temperature cycle was 750 C for 10 minutes.

2.2.2. Evaluation of Ti Vapor Coated Joint

This joint involved Nilsen zirconia bonded to the graphitic iron. Two specimens, one as-brazed the other brazed and as-fractured were metallographically examined. Optical metallographic examination of the as-fractured specimen did not reveal titanium on the ceramic or copper on the cast iron. The braze alloy was bonded to the cast iron and contained some porosity. There was a dark band, parallel to the interface which extended from the joint interface into the ceramic. This dark band probably is partially reduced (oxygen depleted) zirconia.

The as-brazed specimen examined by optical metallography also was fractured, probably by stress imposed during the mounting operation. A dark band also was observed in the ceramic near the joint interface. Along the cast iron/braze alloy interface, there was some dark grey constituent intermittently scattered along the joint length. There also were regions along the joint length at the ceramic/braze interface that contained a thin layer of light grey material, possibly titanium or Ti_xO_y. The fracture appeared to have propagated primarily through the ceramic and this phase, although there were occasional small amounts of braze alloy bonded to the ceramic. This phase will be identified further by EDS analysis using the scanning electron microscope (SEM).

2.2.3. Evaluation of Ti-sputter Coated Joint

Bend bars with the same nominal dimension as the zirconia-zirconia specimens were machined from the joined block. These were then tested in 4-point bending. The bend strengths were calculated from the fracture loads using standard bend formulas for monolithic materials.

The fracture toughness of the joints were also evaluated using chevron-notched bend bars of nominal dimension 0.2-inch wide by 0.25-inch deep. The tip of the chevron notch was at a distance of approximately 0.042 inch from the tensile face of the bend bar, giving an initial a/W (a is the crack length and W is the beam depth) of approximately 0.17. The chevron notch extended all the way to the compression face of the bend bar. The notch was approximately 15 mils thick, and was located approximately in the middle of the interlayer. The notched bend specimens were also tested in 4-point bending.

In calculating the fracture toughness from the fracture load, the formula proposed by Munz et al[3] was used. This formula is derived for a monolithic material, and it assumes that crack growth occurs at a constant value of stress intensity factor. Analytical work is being undertaken to determine what corrections are necessary for our composite specimen. With regard to the second point, the assumption of a constant stress intensity factor leads to the result that for a given crack geometry the maximum load and instability occurs at a specific value of crack length. For our specimen geometry, the instability should occur at an a/W of approximately 0.35. On the other hand, the test record as well as the fracture surface markings indicated that the

crack was propagating intermittently, and that final fracture could have occurred at an a/W as high as 0.71. The load versus displacement plot indicated a number of pop-ins. It appears that the joint has an R-curve behavior, however, further experiments and observations are necessary to substantiate this initial finding.

The following table summarizes the results of the mechanical tests on the zirconia-cast iron specimens:

TABLE 2. Bend Strength and Fracture Toughness of Zirconia-Cast Iron Joint

Specimen No.	Maximum Load lbf	Bend Strength ksi	Bend Strength MPa	Fracture Toughness MPa√m
		Strength Data		
MCB-1	34	12.9	88.9	-
MCB-2	31	11.8	81.4	-
MCB-3	31	11.7	80.9	-
		Toughness Data		
MCF-1	41.2	-	-	3.75
MCF-2	53.2	-	-	5.03

While the scatter in the data for strengths is low, there is large separation in the two fracture toughness values. The fracture surfaces indicate that final fracture could have occurred at a/W of 0.71 and 0.63 for specimen numbers MCF-1 and MCF-2 respectively. If these final crack lengths are taken into account, the toughness values for the two specimens would be 6.88 MPa√m respectively. Further observations are necessary to validate these initial estimates.

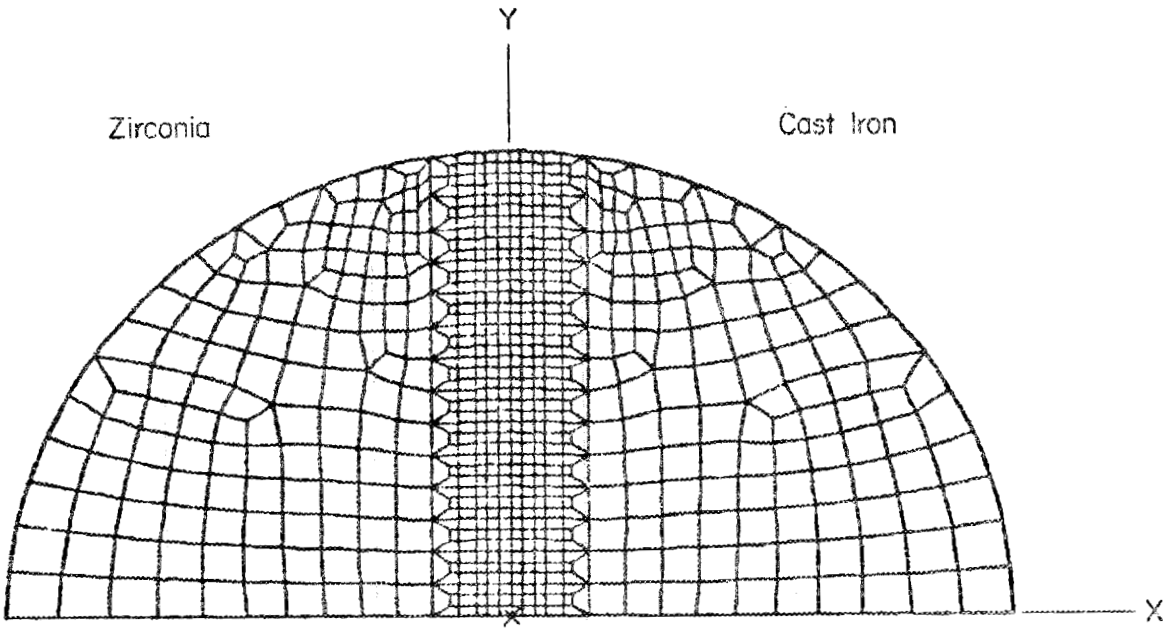

FIGURE 1. Finite element mesh of the bimaterial disk specimen without a crack.

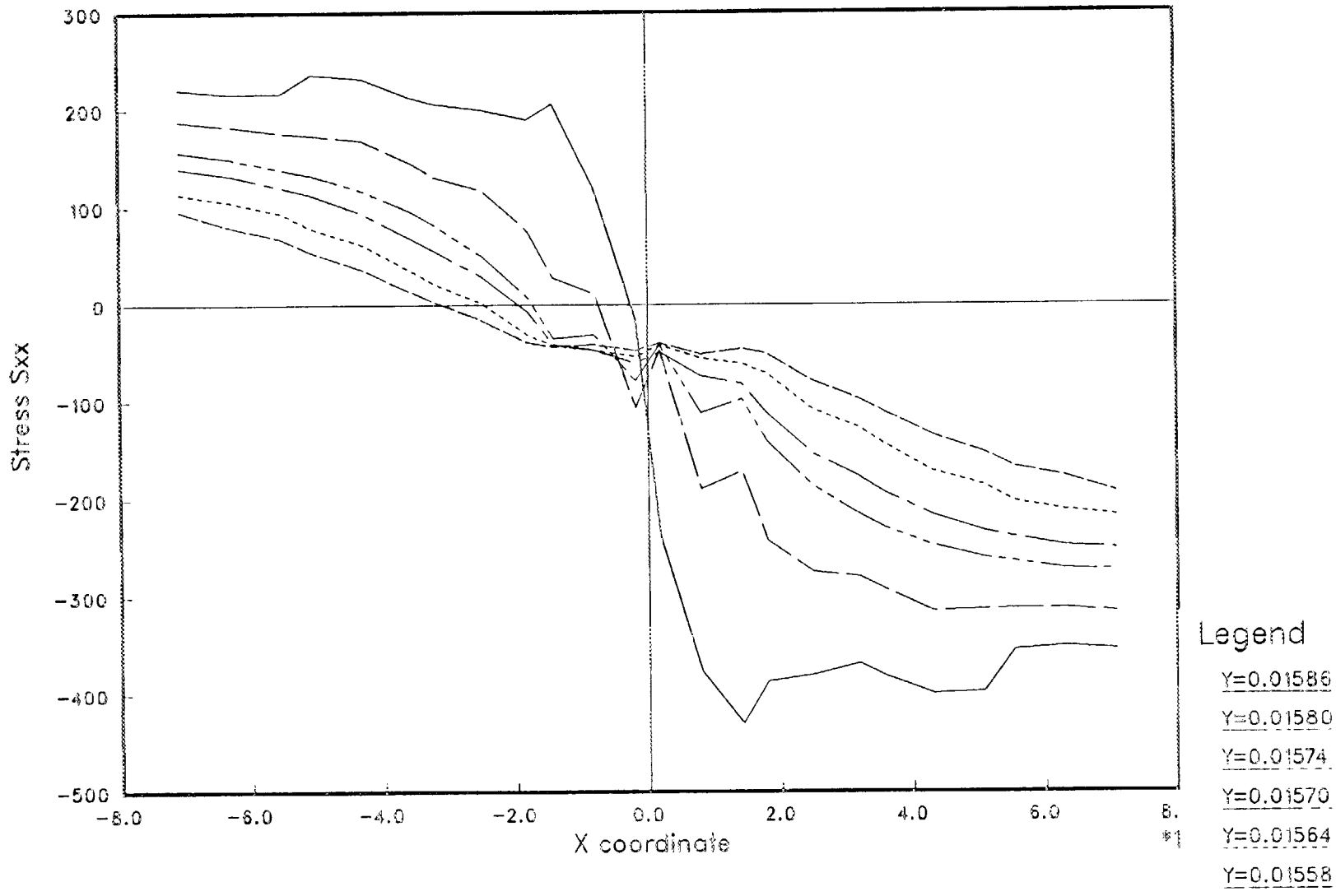

FIGURE 2. The s_{xx} stress distribution across the bond line, close to the free edge.

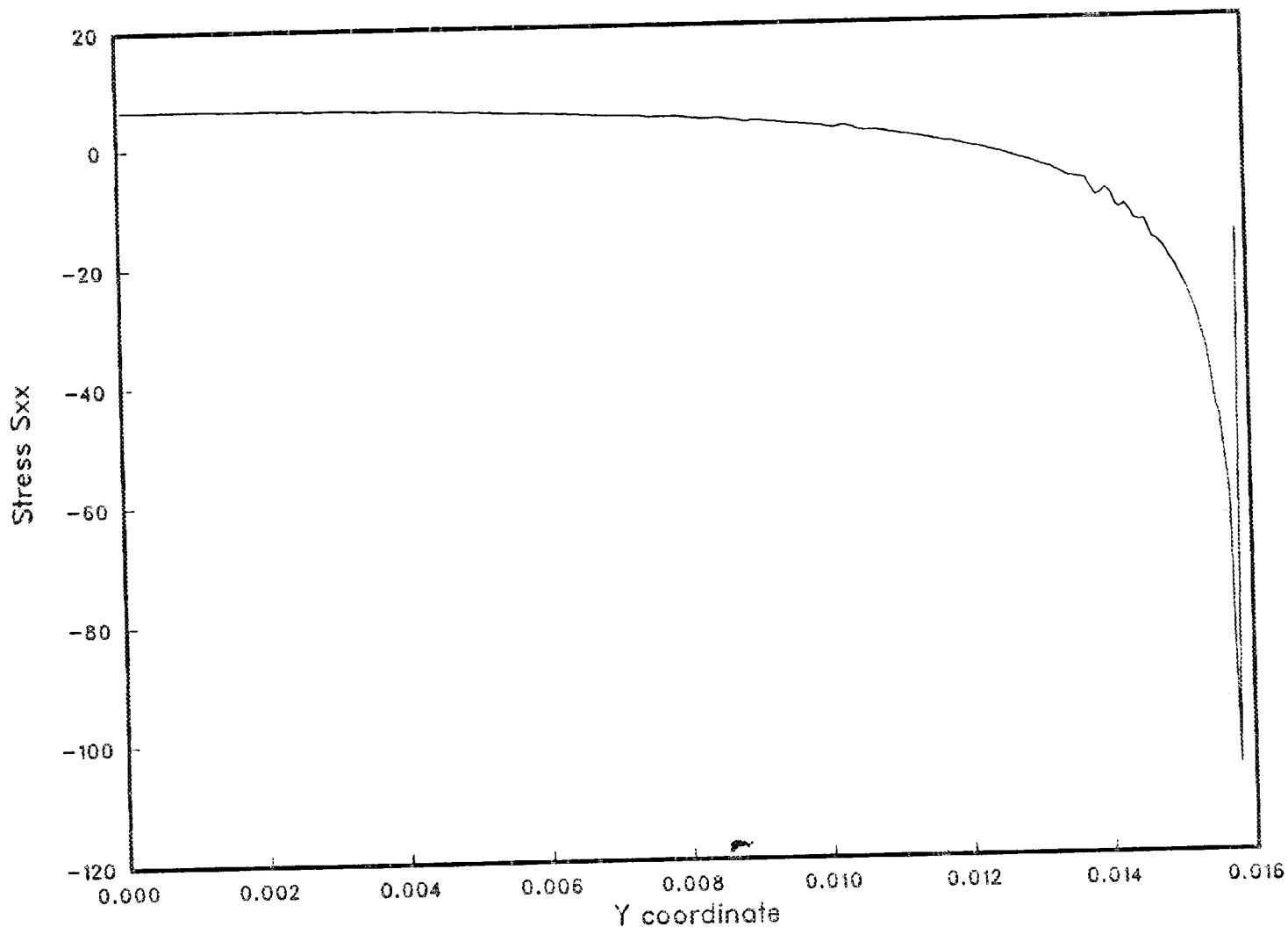

FIGURE 3a. The s_{xx} stress distribution along the bond line in ceramic.

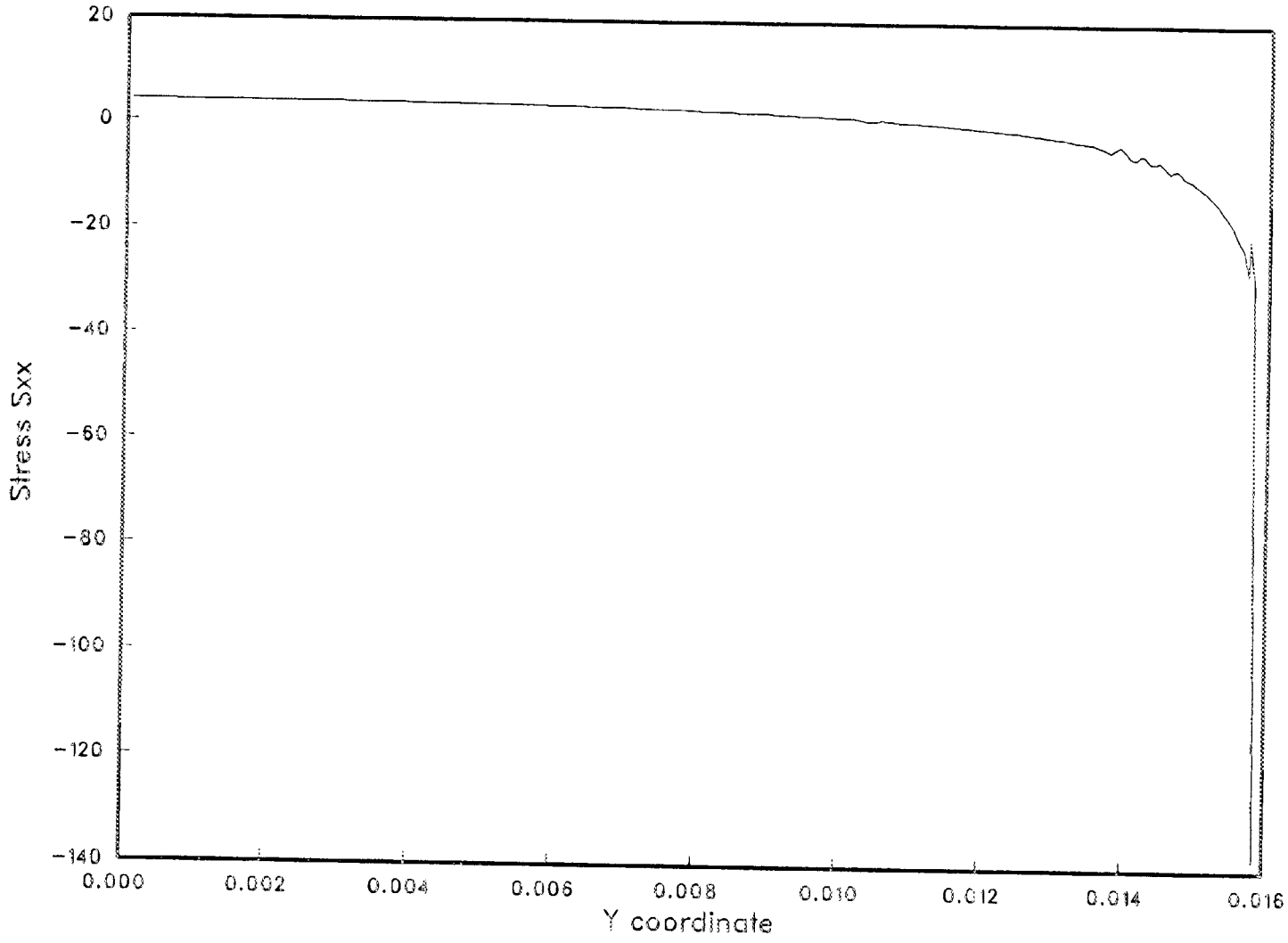

FIGURE 3b. The s_{xx} stress distribution along the bond line in cast iron.

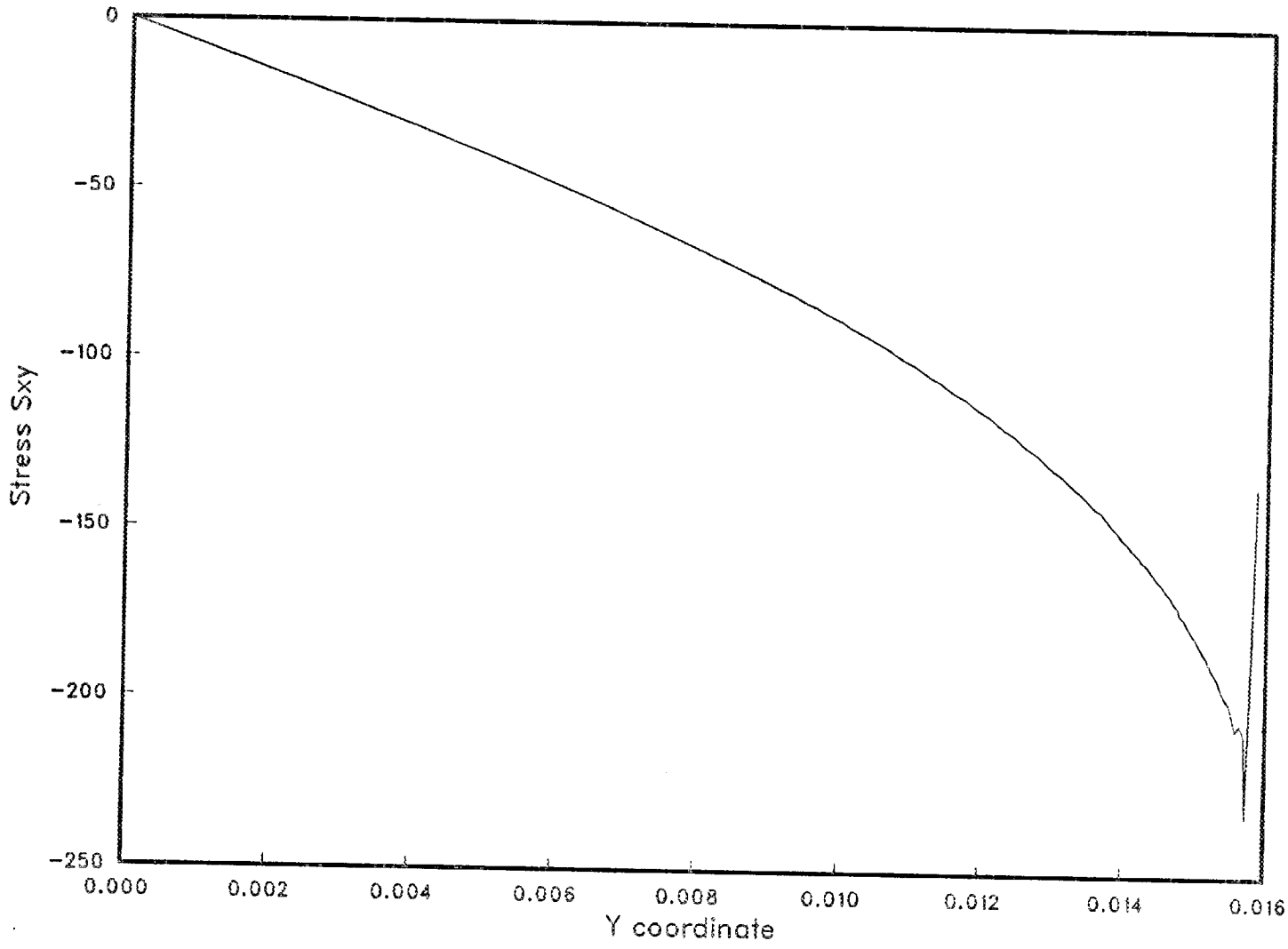

FIGURE 4a. The shear stress distribution along the bond line in ceramic.

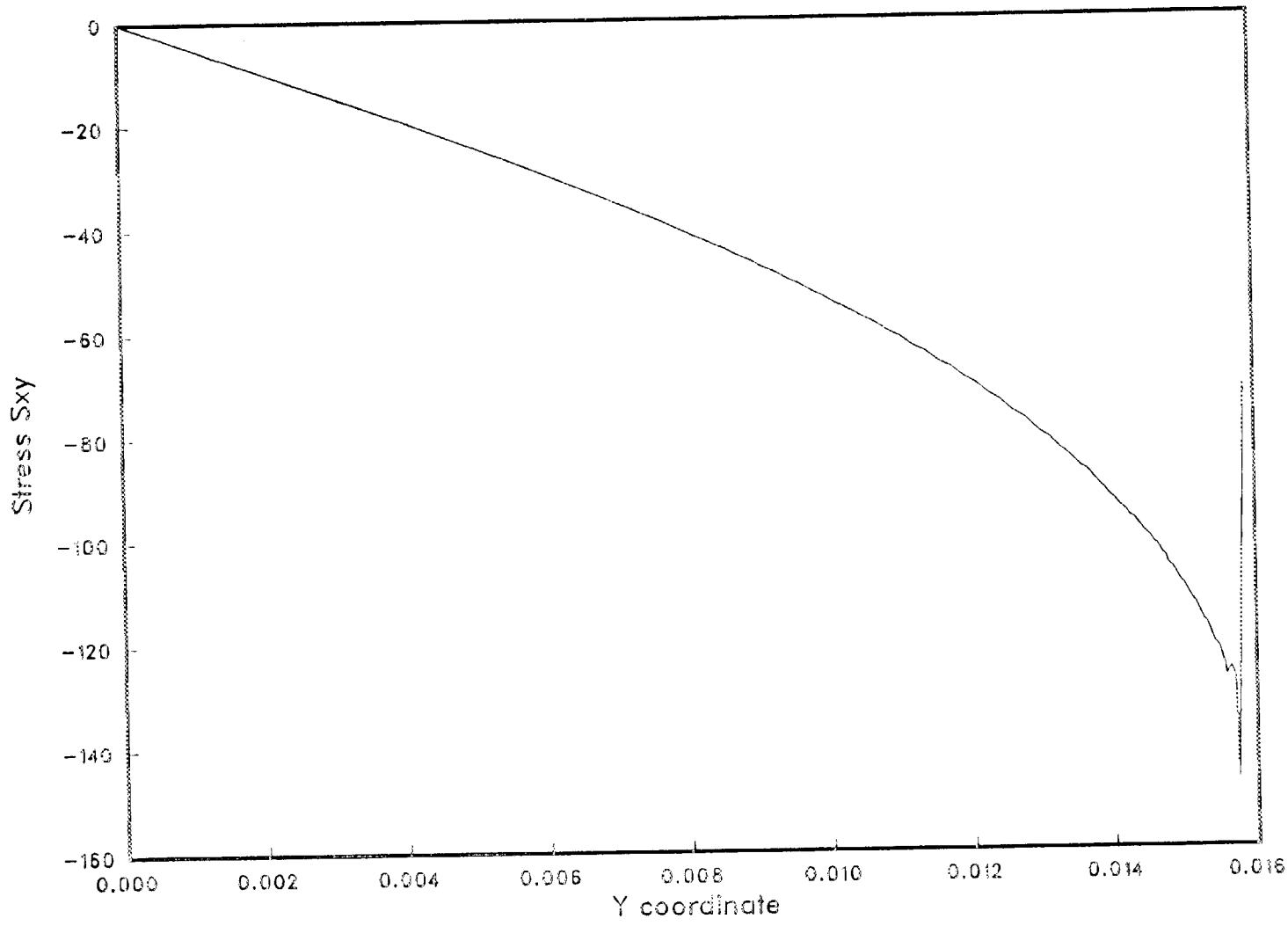

FIGURE 4b. Shear stress distribution along the bond line in cast iron.

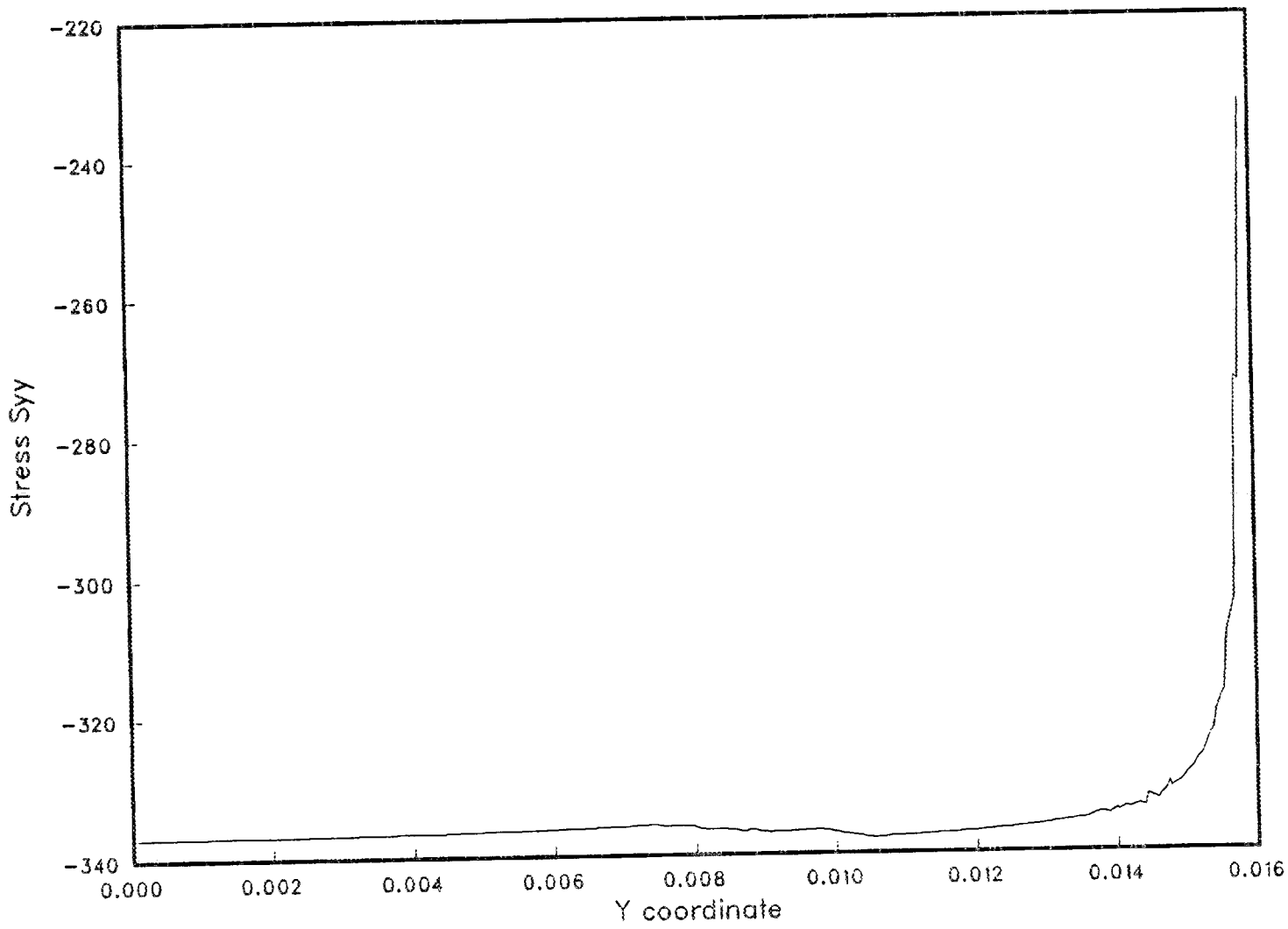

FIGURE 5a. The s_{yy} stress distribution along the bond line in ceramic.

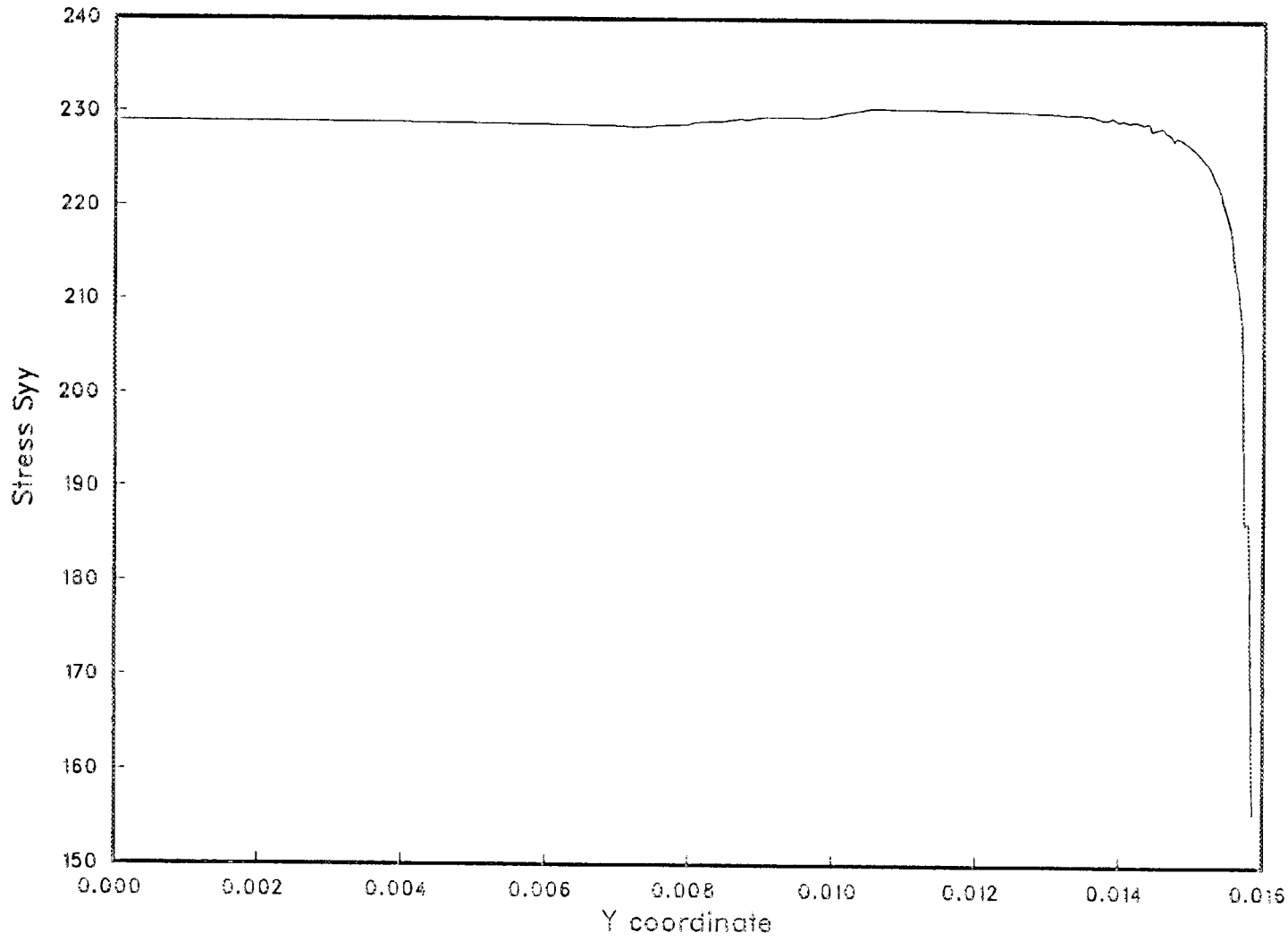

FIGURE 5b. The s_{yy} stress distribution along the bond line in cast iron.

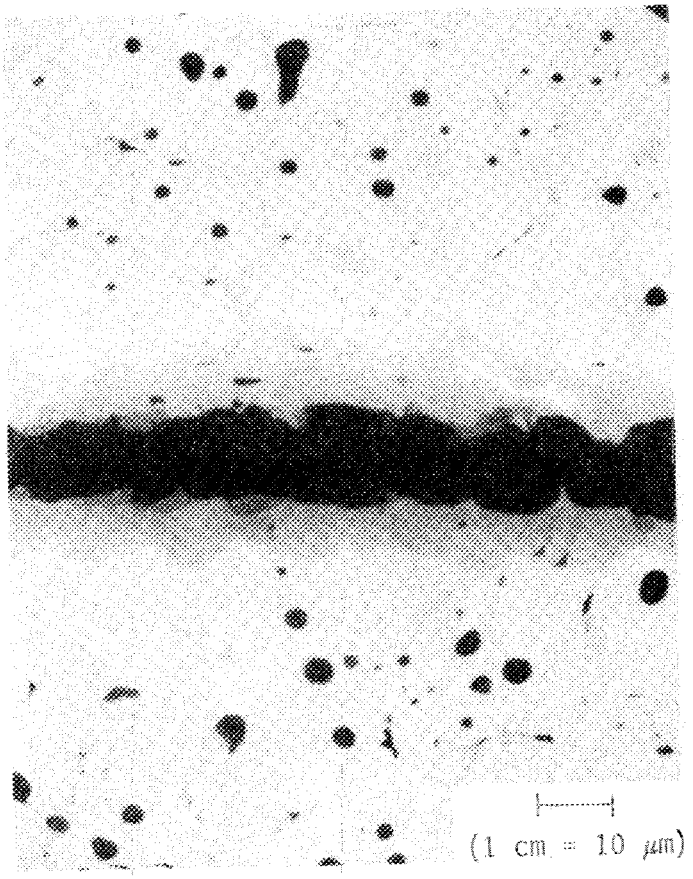

FIGURE 6. Back-scattered electron micrograph of a zirconia-zirconia joint obtained by using a $CaO-TiO_2-SiO_2$ interlayer.

Note: the dark band is the interlayer material, while the darkish bands on either side indicate the diffusion of interlayer material into the substrate.

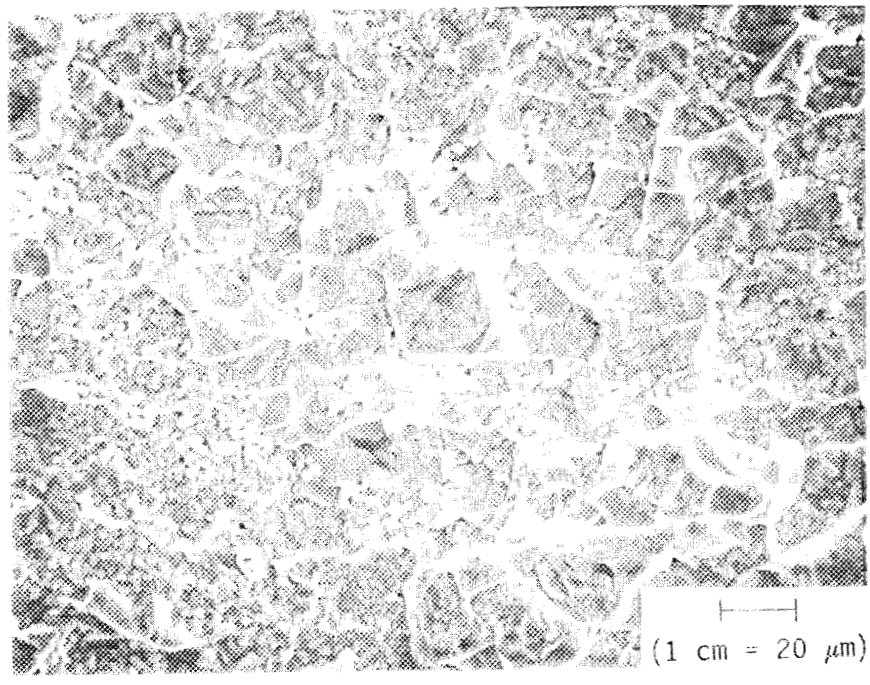

FIGURE 7. Fracture surface of a zirconia-zirconia joint, obtained by using a $CaO-TiO_2-SiO_2-ZrO_2$ interlayer.

Note: The crack appears to have grown primarily along the interlayer. The fracture surface has two distinct morphologies--(a) large glassy type particles, and (b) much finer particles.

References

1. S. L. Swartz, B. S. Majumdar, B. C. Mutsuddy, and A. Skidmore, "Joining of Zirconia Ceramics with a $CaO-TiO_2-SiO_2$ Interlayer", submitted to *Materials Letters*.

2. J. P. Hammond, S. A. David, and M. L. Santella, "Brazing Ceramic Oxides to Metals at Low Temperatures", *Weld. Res. Suppl.* 67[10] 227-s (1988).

3. D. Munz, R. T. Bubsey, and J. L. Shannon, Jr., "Fracture Toughness Determination of Al_2O_3 Using Four-Point-Bend Specimens with Straight-Through and Chevron Notches", *J. Amer. Cer. Soc.*, Vol. 63, No. 5-6, pp. 300-305 (1980).

Analytical and Experimental Evaluation of Joining Silicon Carbide to Silicon Carbide and Silicon Nitride to Silicon Nitride for Advanced Heat Engine Applications

G. A. Rossi, D. O. Patten, G. J. Sundberg, C. H. Bates, and F. J. Wu
(Norton Company)

Objective/scope

The purpose of this program is to develop techniques for producing reliable ceramic-ceramic joints and analytical modeling to predict the performance of the joints under a variety of environmental and mechanical loading conditions including high temperature, oxidizing atmospheres. The ceramic materials under consideration are silicon nitride and silicon carbide. The joining approach for silicon nitride is based on the ASEA hot isostatic pressing process while the plan for silicon carbide is to co-sinter green forms together. These joining methods were selected to produce joints which exhibit the minimum possible deviation in properties from those of the parent ceramic materials. Analytical models will be experimentally verified by measurements on experimental size and scale-up joints produced as part of this work.

Background

Because of their strength, oxidation resistance, and other desirable high temperature properties, silicon nitride and silicon carbide are under extensive study for use in advanced gas turbine and internal combustion engines. In both engine types there are requirements for joining the ceramics to themselves, other ceramics, and various engineering alloys. Existing bonding methods lack the high temperature capabilities required for use in advanced heat engines. Further, analytical modeling techniques to predict joint reliability and performance have not been developed. These technical needs have prevented consideration of economically fabricating large, complex ceramic engine components from smaller, less complicated segments. The current program will address these issues for silicon nitride to silicon nitride and silicon carbide to silicon carbide joints.

Technical progress

Silicon Nitride Joint Development

Work was continued on joining green NCX5100 (4 w/o Y_2O_3- Si_3N_4). The method by which the joints were fabricated and testing was performed has been outlined in the last semi-annual report. Various types of joints were made during this reporting period i.e. butt joint with a slip interlayer, (Butt/Slip), butt joint with no interlayer (Butt/Bare) and tongue-groove with a slip interlayer (Tongue-Groove/Slip).

High temperature (1300°C) flexural strength data obtained for the MOR bars with and without the joint are reported below.

1300°C Flexural Strengths

Joint Type	Strength (MPa)	Std. Dev. (MPa)	# of Bars
Mix 33 Join Butt/Slip	599.4	68.2	6
Mix 37 Join Butt/Slip	649.5	35.2	7
Mix 33 Join Tongue-Groove Slip	656.6	17.2	7
Mix 40 Join Tongue-Groove Slip	679.1	67.6	7
Mix 37 Join Butt/Bare	610.9	33.8	10
Mix 33 Unjoined Control	655.9	30.3	4
Mix 40 Unjoined Control	652.2	30.3	8

The sample dimensions were 3x4x50 mm (MIL 1942B) with the joint plane oriented transversely and parallel to the loading direction. Flexure testing was performed on 4 point-quarter point fixture, using a 40 mm outer span.

The mixes 33, 37 and 40 are of the same composition and were milled in small research mills. Samples of mixes 37 and 40 were densified in the same HIP cycle separate from mix 33. None of the joined specimens tested above exhibit fracture originating in the join. The 1300°C flexure strengths of joins densified in separate HIP cycles from separate mills by the same technique were reproducible. The 1300°C flexure strengths of the butt and tongue-groove joins with slip interlayers and the self-bonded butt joins compare favorably with the unjoined controls. The use of tongue-groove geometry joins will provide increased green strength necessary for handling with no loss in 1300°C flexure strength after densification. The injection molding compound bond interlayer has been ruled out due to incomplete join closure and the extremely friable nature of the green joins. The choice of a joining technique will require additional testing of joins by stress rupture. The stress rupture testing at 1370°C has recently started and limited data has been generated (see below). Room temperature flexure testing will be performed on the most promising joins after stress rupture and flexure evaluation.

The stress rupture testing has resulted in the following to date.

Stress Rupture Life (hrs.)

Sample	200 MPa	250 MPa
Mix 37 - #17		+200.0
Unjoined Control		+200.0
Mix 37 - #1, 2	+200.0	
Bare/Butt Join	+200.0	
Mix 37 - #11, 12		78.5
Slip/Butt Join		159.6

More stress rupture testing will be needed to determine the join interlayer for the remainder of the contract.

An MOR bar containing the joint (Mix 33, Butt/Slip) was carefully polished with diamond paste and submitted for SEM examination. The joint line was not visible. The same sample was then chemically etched and resubmitted for SEM, but the joint was still invisible. A similar polished bar with the joint was plasma etched and observed with the SEM, but also in this case no joint line could be detected, not even at 10 kX magnification.

Silicon Carbide Joint Development

During the first part of this six month period exploratory work has continued to identify the most promising joining techniques for silicon carbide. Several attempts were made to fabricate joints using ß-SiC powder suspensions as interlayers between green bodies. When aqueous suspensions were used, a typical "mud cracking" problem was apparent, which still persisted when surfactants and organic amines were used, in order to increase the solids loading of the slurry. The use of organic solvents, such as xylene, did not result in better joints, either. Joining attempts were also made employing a 1 mm thick wafer of a ß-SiC powder injection molding mix. The wafer was pressed between two prefired disks in a warm die, dewaxed and pressureless sintered at 2100°C. Unfortunately, no bond resulted between the parent materials. Joints were also attempted between green and fired disks without any interlayer. The green disks were prefired and machined to achieve smooth, flat mating surfaces. After sintering at 2100°C, a bond was formed, but SEM analysis showed considerable porosity in the joint line. Finally, it was found that an interlayer slip made up with about 50 w/o SiC powder and 50 w/o of an aqueous solution containing 10 w/o of an experimental Dow binder would produce good joints. The technique, abbreviated as Slip/CIP method, consists basically in applying the slip to the surface of one of the green parts to be joined, then pressing the other part by hand against the part coated with the slip and making a sandwich, which is then closed inside plastic bags and cold isostatically pressed (CIPed) at 200-350 MPa. During the isopressing step, the interlayer is still partially wet and plastic due to the presence of the binder, so that it conforms to the microasperities of the green body surface. The excess slip is extruded out of the joint area. After CIPing the part is carefully dried and fired.

Using the Slip/CIP method, green blocks of approximately 30x30x60 mm have been successfully joined on the 30 x 30 mm faces, either by pressureless sintering at 2100°C or by sintering and then glass encapsulated (ASEA) HIPing at 1900°C. 2 x 3 x 30 mm MOR bars containing the joint were then machined out of these samples and tested for strength at 25°C and 1500°C in 4 point bending. The results are reported below.

Strengths of MOR Bars With and Without Joint
(Slip/CIP Method)

JOINING OF SILICON CARBIDE TO SILICON CARBIDE
CO-SINTERING OF GREEN BILLETS WITH AND WITHOUT HIPPING

FLEXURAL STRENGTH OF TEST BARS WITH AND WITHOUT JOINT

MATERIAL	25°C (MPa)	1530°C (MPa)
CO-SINTERED (WITH JOINT)	186*	N/A
CO-SINTERED AND HIPPED (WITH JOINT)	290+	254^
SINTERED CONTROL (NO JOINT)	241	220
SINTERED AND HIPPED CONTROL (NO JOINT)	276	255

* 3 OUT OF 8 BARS BROKE AT JOINT
^ 1 OUT OF 7 BARS BROKE AT JOINT
\+ 1 OUT OF 6 BARS BROKE AT JOINT

It is apparent that post sintering HIPing considerably enhances the strength of the joint. It is also important to note that only a small fraction of the test bars broke at the joint.

Some of the MOR bars were polished to reveal the joint region by SEM. Figs. 1 and 2 show two such microstructures. In the sintered sample, the interlayer shows a higher density than the material itself. On the other hand, in the sintered/HIPed sample it appears that the material has densified more than the interlayer. Microfocus X-ray radiography was also used to check for joint defects and has revealed a generally dense joint with some localized lineal defects or high porosity regions.

Another method, besides the Slip/CIP, was investigated during this period. It consists in joining dense SiC parts by friction fitting polished, flat, mirror-like surface and firing again the part. It was demonstrated that a fairly good joint can be obtained in 13 mm diameter discs by pressureless sintering at 2100°C, as shown by the joint microstructure (SEM) of Fig. 3. A post-sintering ASEA HIP

run has demonstrated that the joint line clearly visible in Fig. 3 can be virtually eliminated, as shown by Fig. 4. Shear strengths were also measured on the sintered and sintered/HIPed joints, and the results are presented below.

Shear Strengths for SiC Joints
Made with Polished Discs (MPa)

Sample	Shear Strength	Remarks
Sintered	20	Sheared at joint
Sintered/HIPed	110	Partially sheared at joint

After the success obtained on small disks, this method was attempted on dense 25x 25x25 mm cubes. In this case, however, the two mating surfaces did not stick to each other upon friction fitting. The possible reasons are a lower density (92% of TD) compared to the disk case, or insufficient flatness, due to the unavailability of the appropriate polishing equipment. The lack of flatness is probably the reason, because the two blocks were subsequently ASEA HIPed to 98% of TD and repolished, but with the same result.

In order to overcome the problem, two blocks with the polished surfaces in contact were coated with a CVD SiC coating at Midland Materials Research, Midland, MI. The CVD coating had the dual purpose of binding the blocks together and preventing glass intrusion during the ASEA glass encapsulated HIP run. This run will be done in the near future, and if successful, MOR bars containing the joint will be machined and tested for strength.

A problem has arisen during the SiC-SiC joining experiments, i.e. occasional cracking which occurred when large billets were joined with the Slip/CIP method. These cracks emanate from the joint region and seem due to localized stresses. The possible reasons are, in our view, imperfect drying before firing or stresses generated by the fast binder burnout during firing. Whatever the reason, we feel that this problem can be overcome.

Characterization

An experimental plan was established during this period and a short summary of each major area was outlined in the April-May bi-monthly report. Finite element analysis has been employed to design the specimen to be used for all tensile characterization testing. Tensile specimens will be used in stress/strain, creep and fast fracture testing.

The NBS pin-and-clevis "dogbone" tensile specimen will be used for high temperature creep characterization tests. In addition, finite element analysis was used to design a cylindrical tensile specimen based on the ORNL geometry for non-creep characterization tests. This geometry is known to give more reliable data since it is less affected by fixture misalignment. On the other hand, a recent conversation with S.M. Wiederhorn (NBS) has provided less concern with any significant room temperature alignment problem produced by the dogbone geometry. Therefore, the final geometry to be used for non-creep tests will be weighted by the manufacturing cost.

The use of a large NBS type specimen has been proven to be not feasible for the verification and scale-up portions of the contract. Instron has expressed an interest in manufacturing a high load (+18,000 lb.) cylindrical buttonhead universal hydraulic alignment grip that can be used for the verification and scale-up phases. The Processing Contract has a common interest in the purchase of the high load assembly. Therefore, the 200 square millimeter cylindrical cross-section specimen is being modeled using finite element techniques and studied for possible use. This ORNL modified geometry may provide better verification data at a comparable cost.

The oxidation experimental plan consists basically of evaluating the room temperature strength effect after the joint is exposed to high temperature environments. Preliminary oxidation tests to monitor the weight gain/time/temperature are prepared to help optimize the results of the experimental procedure. Due to the high oxidation resistance of the materials being used, a high precision balance is required to monitor the weight. Equipment preparation is currently underway and the preliminary tests will proceed accordingly.

We are now in the process of setting up our new Instron Model 8562. A few components of the hardware are outstanding, as well as the computer used for data acquisition. These items should be received shortly. In addition, the Vibromet polisher for the slow crack growth characterization has been delivered. Specifications for the creep furnaces and load frames have been written. Expected delivery is in November, 1988.

Analytical Modeling

A detailed plan for modeling fast fracture, creep, oxidation, cyclic fatigue and thermal cycling was presented in the previous semi-annual report. During this period we have concentrated on modeling fast fracture and creep, as explained below.

FAST FRACTURE: The first part of the fast fracture modeling milestone is completed. Fast fracture modeling consists of predicting the reliability of the ceramic-ceramic joints using statistical methods. Progress in this area include an understanding of the theory developed by Batdorf and Crose [1] and implemented in the program SCARE. The theory predicts the probability of failure of a ceramic component by using three-dimensional fracture mechanics and statistical crack density function. The latter is defined by experimental results while fracture mechanics use deterministic laws. Both theories, when combined, provide a statistical package that include polyaxial mechanics of cracks, crack orientation, and experimental determination of crack density.

The four point bend and tension specimen geometries have been modeled using ANSYS. Stress distributions will be postprocessed using SCARE and compared with experimental results. This task will be done during the second fast fracture milestone.

CREEP: Creep modeling is currently underway. This task has some difficulties due to the following:

1. Creep behavior is not expected to occur until very high temperatures and after long periods of time.

2. The ceramic joints are not expected to give significant creep strains compared to the bulk material since the volume ratio is small.

3. Creep finite element modeling requires an accurate method of determining the transition between micromechanisms of deformation (grain boundary sliding or cavitation) as a function of temperature and stress and its macromechanical behavior.

Modeling this time dependent behavior will consist of treating the joint area with different creep properties from the bulk material as they become available from joint characterization experiments. B. Wilshire and R. W. Evans [2] developed the Theta Projection method as a technique to interpolate and extrapolate creep curves from limited

experimental data. This method has shown to predict reasonably well the creep behavior of ceramic materials regardless of which micromechanism is dominant. The Theta Projection method is currently being studied further and programmed in fortran code as a subroutine to be implemented in finite element analysis. Results of this finite element model can be used to predict the overall deformation of a joined structural component.

Status of Milestones

1. Complete Characterization Experimental Plan (4-30-88) - Complete

2. Complete Joint Development Work (10-31-88) - On schedule

3. Complete 2 cm^2 Joint Experimental Plan (12-31-88) - On schedule

Publications

None

References

[1] S. B. Batdorf and J. G. Crose, "A Statistical Theory for the Fracture of Brittle Structures Subjected to Nonuniform Polyaxial Stresses", J. App. Mech., Trans. ASME, June 1974, pp. 459-464.

[2] R. W. Evans and B. Wilshire, "Creep of Metals and Alloys", The Institute of Metals, book #304, UK, 1985, pp. 197-208.

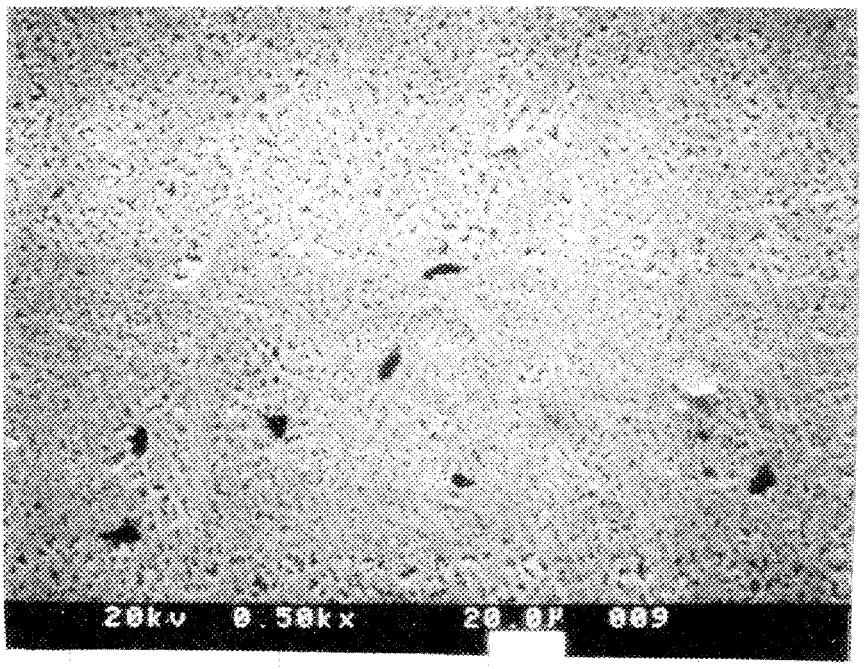

Fig 1: Microstructure (SEM) of a joint made with the slip/CIP method. Sample pressureless sintered.

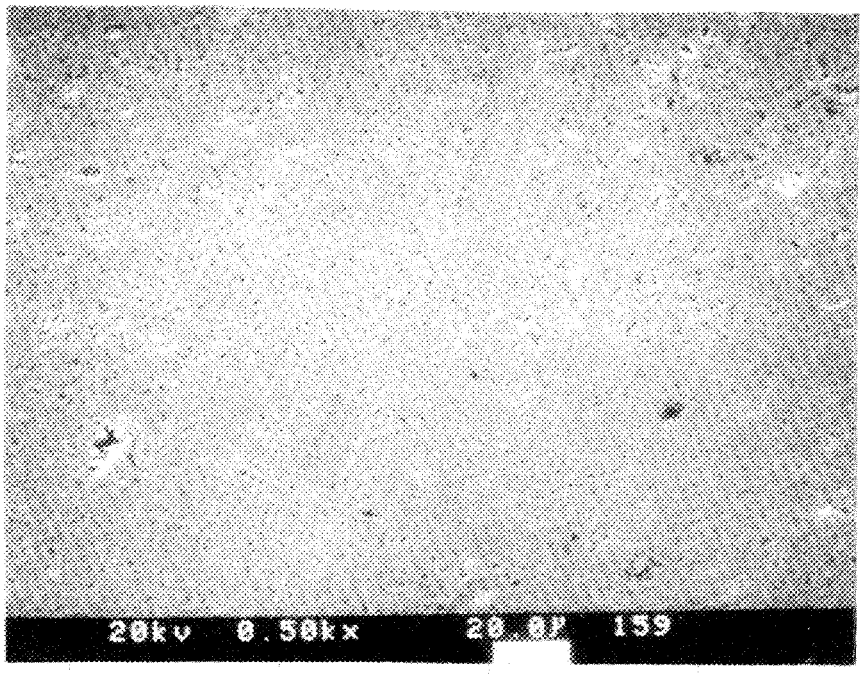

Fig. 2: Microstructure (SEM) of a joint made with the slip/CIP method. Sample sintered/ASEA HIPed.

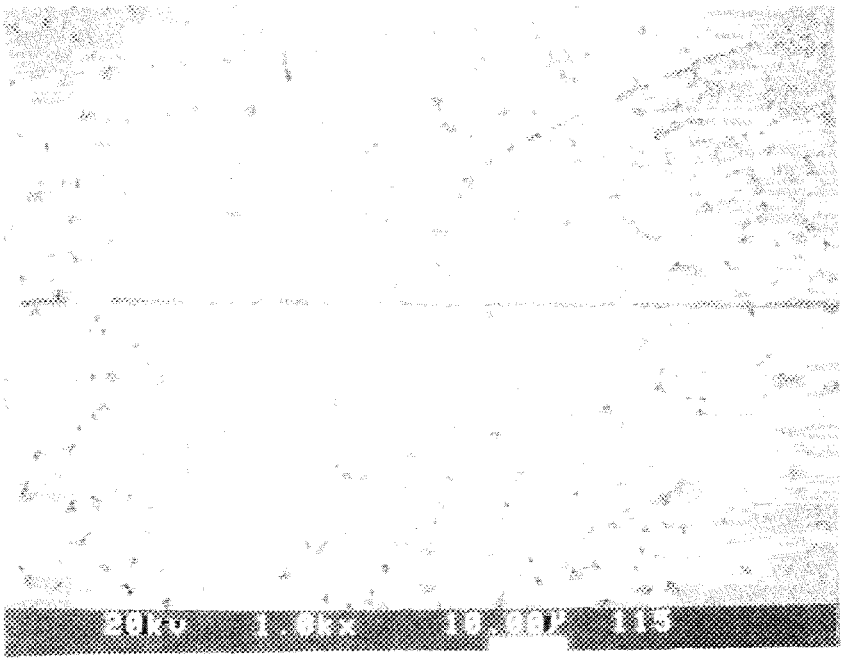

Fig. 3: Microstructure (SEM) of a joint made with dense, polished discs. Sample pressureless sintered.

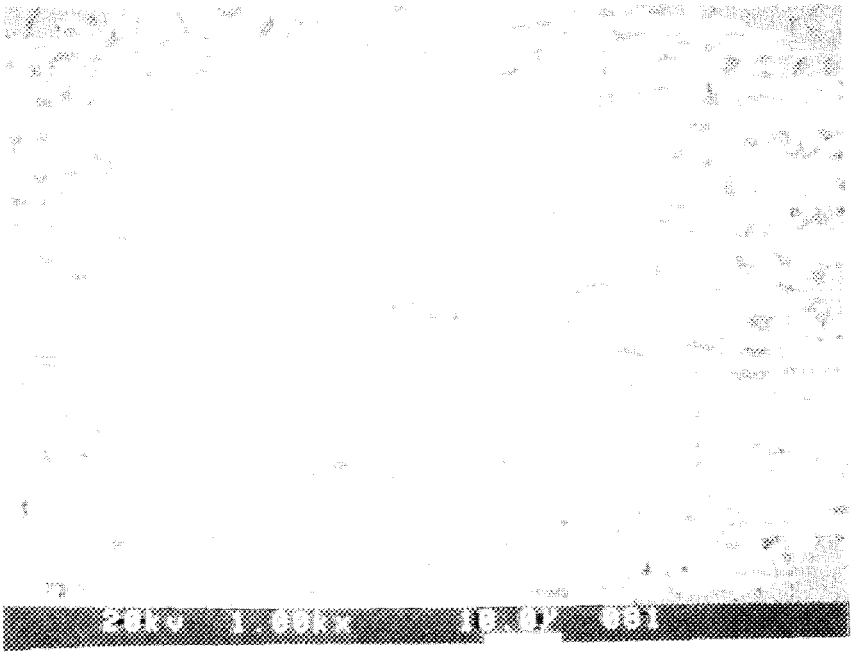

Fig. 4: Microstructure (SEM) of a joint made with dense, polished discs. Sample sintered/ASEA HIPed.

2.0 MATERIALS DESIGN METHODOLOGY

INTRODUCTION

This portion of the project is identified as project element 2 within the work breakdown structure (WBS). It contains three subelements: (1) Three-Dimensional Modeling, (2) Contact Interfaces, and (3) New Concepts. The subelements include macromodeling and micromodeling of ceramic microstructures, properties of static and dynamic interfaces between ceramics and between ceramics and alloys, and advanced statistical and design approaches for describing mechanical behavior and for employing ceramics in structural design.

The major objectives of research in Materials Design Methodology elements include determining analytical techniques for predicting structural ceramic mechanical behavior from mechanical properties and microstructure, tribological behavior at high temperatures, and improved methods for describing the fracture statistics of structural ceramics. Success in meeting these objectives will provide U.S. companies with methods for optimizing mechanical properties through microstructural control, for predicting and controlling interfacial bonding and minimizing interfacial friction, and for developing a properly descriptive statistical data base for their structural ceramics.

2.1 MODELING

2.1.1 Modeling

Microstructural Modeling of Cracks
J.A.M. Boulet (University of Tennessee, Knoxville)

Objective/scope

The goal of the study is to investigate and develop mathematical models for fracture of cracks with realistic geometry under arbitrary stress states. For brittle fracture of such cracks, interference between surface irregularities(bumps) on opposing crack faces may significantly influence fracture initiation. A sequence of elasticity problems leading to the rough-faced crack in an infinite body under arbitrary loads will be defined and solved. Application of fracture criteria to the stress field around the crack will lead to predictions of fracture-initiating loads, which will then be compared with those cited in the literature for cracks of simpler geometry subjected to the same loads.

Technical progress

We have previously reported plane strain and plane stress solutions for the problem of a Griffith crack subjected to arbitrary biaxial stress at infinity with interference of two wedge-shaped protrusions (one on each crack face) at an arbitrary position on the crack. The stress fields associated with these solutions have been used to calculate the stress intensity factors (SIF's) at both crack tips. Using the well-known biaxial form of Griffith's fracture criterion, we found that the presence of a single interference site at the middle of the crack has little influence on the predicted fracture stress.

Our model has been extended to include multiple interference sites (wedge-shaped protrusion pairs). In the computational model associated with this problem, we first find (by iteration) the contact force acting at each wedge pair. Then, we replace each wedge pair with an equivalent set of concentrated loads acting at the wedge bases. Finally, we calculate the SIF's at both crack tips due to simultaneous application of biaxial stress at infinity and the concentrated loads at all the interference sites. Calculations with multiple interference sites show that as the number of interference sites increases, so does the predicted decrease in fracture stress. As much as thirty per cent reduction in predicted fracture stress has been found.

In previously reported results, our computational model has used only normalized, dimensionless variables, with values that do not necessarily correspond to real materials. We have recently incorporated the properties of real materials such as silicon carbide and silicon nitride into the calculations. Thus, a real length scale has been established and our calculations indicate that protrusion interference is present in most cracks. For instance, any crack less than about one centimeter in length in silicon carbide experiences protrusion interference when subjected to arbitrarily oriented biaxial tensile stress.

In the model referred to above, the wedges are replaced with concentrated loads acting at their bases. This procedure gives accurate results far from the wedges. But each site must be far enough from its nearest neighbor so that its contribution to the stress field there can be accurately computed when the wedge pairs are replaced with concentrated loads. How far away is far enough? This question must be answered to determine how large the wedges can be relative to the crack size, how close an interference site can be to the crack tip, and how close two neighboring sites can be to each other, without compromising the accuracy of the concentrated load model. The question has been resolved through comparison of the stress field around the wedges with that generated by the concentrated loads. The comparison requires both analytical and numerical investigation of the behavior of the mathematical model at points on the crack face far from the wedge. The separation required between an interference site and its nearest neighbor depends on both the specific configuration of interferences sites and also the elastic porperties of the material in which the crack is presumed to exist. For silicon carbide, our calculations show that very few interference sites (often only one) can be placed in a crack without seriously degrading the accuracy of the concentrated load model.

Because protrusion interference is prevalent and increases with the number of interference sites present, it is important that the effect be modeled accurately. Because the current model is not accurate when many sites are present, a new analysis allowing accurate predictions when many interference sites are crowded into one crack should be made. In this analysis, the influence of the interference sites on the crack-tip stress fields should be found without replacing the sites by concentrated loads. Furthermore, the interference site geometry should not be limited to the wedge shape. To achieve these goals, the crack geometry assumed in the model must be changed from a Griffith (straight-line) crack to a jagged-line crack. The contact patches where interference occurs can still be taken as point load interactions.

The improved model referred to above should give accurate predictions of the fracture stress for a jagged-line crack in which interference occurs. Calculations resulting from the model could then be coupled with statistical data for real cracks from which specific jagged-line crack models could be evaluated by simulation. Such a simulation could eventually be added to existing reliability calculations and so improve the accuracy of the design process.

Status of Milestones

The milestone schedule is as follows:

2111001 Completed.

2111002 Dec-15-88

2111003 Rescheduled.

2.2 CONTACT INTERFACES

2.2.2 Dynamic Interfaces

Studies of Dynamic Contact of Ceramics and Alloys for Advanced Heat Engines

K. F. Dufrane and P. A. Gaydos (Battelle Columbus Division)

Objective/scope

The objective of the program is to develop an understanding of the friction and wear processes of ceramic interfaces based on experimental data. The supporting experiments are to be conducted at temperatures to 650 C under reciprocating sliding conditions reproducing the loads, speeds, and environment of the ring/cylinder interface of advanced engines. The test specimens are to be carefully characterized before and after testing to provide detailed input to the model. The results are intended to provide the basis for identifying solutions to the tribology problems limiting the development of these engines.

Technical progress

Apparatus

The apparatus developed for this program uses specimens of a simple flat-on-flat geometry, which facilitates specimen procurement, finishing, and testing. The apparatus reproduces the important operating conditions of the piston/ring interface of advanced engines. The specimen configuration and loading is shown in Figure 1. The contact surface of the ring specimen is 3.2 x 19 mm. A crown with a 32 mm radius is ground on the ring specimen to insure uniform contact. The ring specimen holders are pivoted at their centers to provide self-alignment. A chamber surrounding the specimens is used to control the atmosphere and contains heating elements to control the temperature. The exhaust from a 4500 watt diesel engine is heated to the specimen temperature and passed through the chamber to provide an atmosphere similar to that of actual diesel engine service. A summary of the testing conditions is presented in Table 1.

Materials

Ring and Cylinder Materials

The compositions of the various materials used in the study are presented in Table 2. A variety of monolithic and coating materials were selected to represent various chemical compositions and materials with previously demonstrated successful sliding performance.

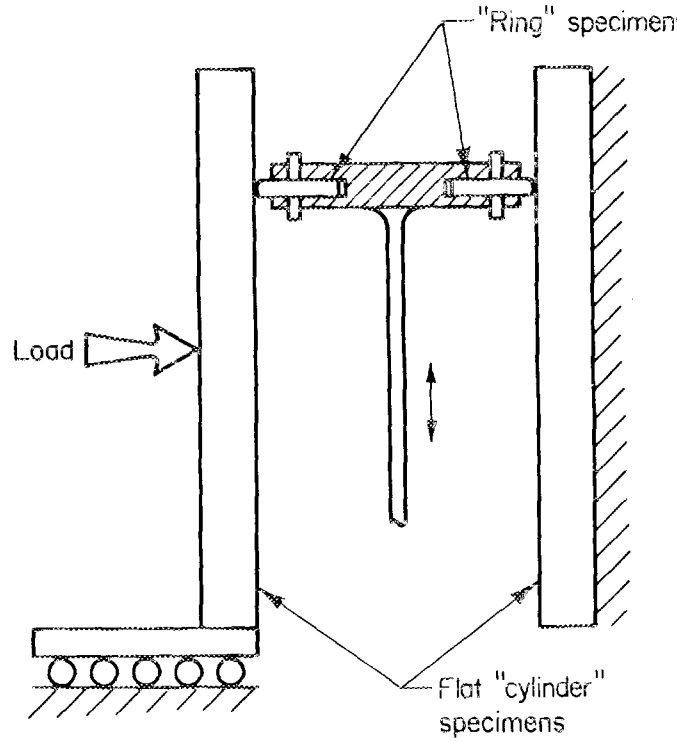

Figure 1. Test specimen configuration and loading

TABLE 1. SUMMARY OF TESTING CONDITIONS

Sliding Contact:	Dual flat-on-flat
"Cylinder" Specimens:	12.7 x 32 x 127 mm
"Ring" Specimens:	3.2 x 19 x 19 mm
"Ring" crown radius:	32 mm
Motion:	Reciprocating, 108 mm stroke
Reciprocating Speed:	500 to 1500 rpm
Average Specimen Speed:	1.8 to 5.4 m/s
Load:	to 950 N
Ring Loading:	to 50 N/mm
Atmosphere:	Diesel exhaust or other gases
Measurements:	Friction and wear (after test)

TABLE 2. MATERIALS FOR EVALUATION

Monolithic Ceramics	Coatings
YPSZ	Tribaloy 400
MPSZ	METCO 130 (13 TiO_2, 87 Al_2O_3)
ATTZ	METCO 501 (30 Mo, 12 Cr, bal Ni)
α SiC	Plasmalloy 312M ($MoSi_2$)
SiC/Al_2O_3	Cr_2O_3 (5 Cr, bal Cr_2O_3)
Sialon	Jet-Kote WC (12 Co, bal WC)
K162B (TiC - Ni/Mo)	Cr (Electroplated)
Si_3N_4	PS212 (Cr_3C_2 + BaF_2/CaF_2 + Ag)
	VR73 (WC/TaC/TiC/Co)
	VA 20 (WC/TaC/TiC/Ni)
	CA 815 (Cr_3C_2/Ni)
	Mo
	Duplex (WC and Mo)
	Ion Implanted (Cr_2O_3)

Liquid Lubricants

The primary lubricant used in the experiments has been SDL-1, a polyolester synthetic oil. This oil is subject to rapid oxidation at temperatures above approximately 260 C and produces tenacious decomposition products. While lubricant development efforts are being conducted in other contracts to formulate suitable lubricants for higher operating temperatures, the results are not likely to be available for use in this study. A polyalkyleneglycol was also investigated as a possible high temperature lubricant. This fluid also decomposes at temperatures above 260 C, but does not leave a residue as part of the oxidation process, Figure 2. Therefore, operating at higher temperatures, such as 350 to 400 C, should be possible without forming undesirable deposits.

A small quantity of experimental high temperature lubricant was also obtained from Dow Chemical. This fluid is reported to be stable at temperatures to 400 C. An additional supply has been promised to enable its evaluation in the ring/cylinder apparatus.

Solid Lubricants

Three types of high temperature solid lubricants have been procured. Two grades of carbon graphites suitable for temperatures up to 620 C will be used as sliders that may provide a dry lubricant film. Another type of solid lubricant is a lubricant-impregnated metal. Ring specimens will be formed out of an MoS_2/metal composite with a temperature capability of 400 C and will be evaluated for friction and wear characteristics.

The third approach in solid lubricants will be the manufacture of a Ga/In/WSe_2 self-lubricating compact. This compact remains thermally stable up to 800 C[1] and exhibits good friction and film transfer characteristics from room temperature to 540 C. Depending on the final strength of this composite, it may be used as a ring specimen or as a slider that supplies lubrication to the ring/cylinder interface.

Wear Experiments

Lubricant Evaluation

In the first phase of the study the need for lubrication at the ring/cylinder interface was established by the high friction coefficients and wear rates measured during dry sliding of monolithic ceramics and ceramic coatings. With lubrication, the wear rates of ceramic coatings such as Cr_2O_3 and WC tested at 260 C were found to approach those measured in heavy duty truck engines with conventional ring/cylinder materials. With the need for lubrication, the maximum operating temperature with ceramics was found to be limited by the availability of suitable lubricants. A summary of this program's wear and friction data is shown in Table 3.

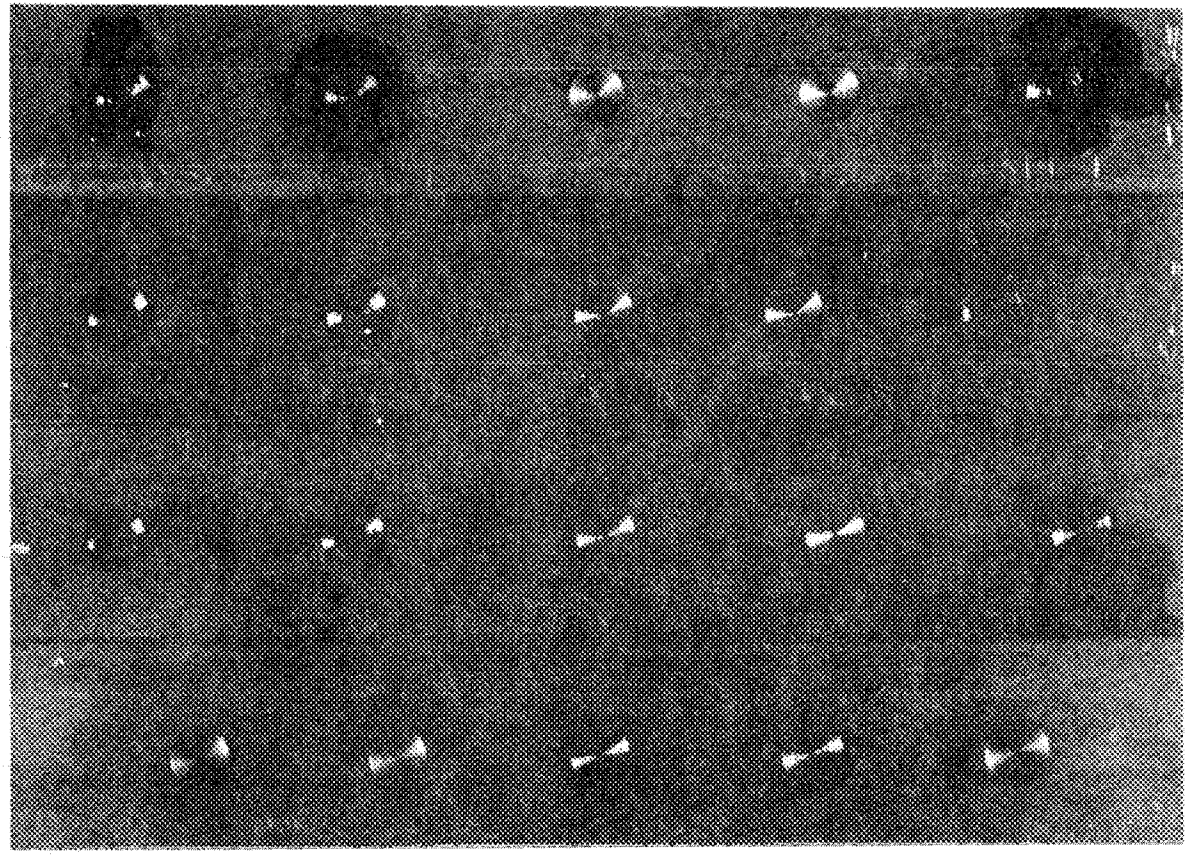

GENERIC OIL TYPE:	MINERAL	SYNTHETIC HYDROCARBON	DIESTER	POLYGLYCOL	POLYOLESTER
BRAND NAME:	PEGASUS 100/30	MOBIL 1	PLEXOL 201	UCON LB-1715	SDL-1

FIGURE 2. OIL DECOMPOSITION PRODUCTS TEST DURATION: 1 HOUR

TABLE 3. COMPARISON OF APPROXIMATE RING WEAR COEFFICIENTS

Ring Material	Cylinder Material	Lubricant	Temperature, C	Ring Loading, N/mm	Friction Coefficient	Hardness Used in Calculation, kg/mm^2	Average Ring Wear Coefficient	
							Dimensionless	$mm^3/N\text{-}m$
Cr	Cast Iron	SAE 30	100	17.5	--	975	5×10^{-9} (a)	2×10^{-10}
Cr	Cast Iron	SDL-1	100	12.3	0.03 - 0.04	975	8×10^{-8}	3×10^{-9}
WC	SiC/Al_2O_3	SDL-1	260	14.5	0.04 - 0.09	2080	3×10^{-7}	5×10^{-9}
ESA	Cr_2O_3	SDL-1	260	12.3	0.03 - 0.06	2200	6×10^{-7}	9×10^{-9}
WC	Cr_2O_3	SDL-1	260	13.9	0.03 - 0.08	2080	6×10^{-7}	1×10^{-8}
Cr_2O_3	Cr_2O_3	SDL-1	260	13.4	0.05 - 0.08	2000	1×10^{-6}	2×10^{-8}
Cr_2O_3	SiC/Al_2O_3	SDL-1	260	15.7	0.04 - 0.08	2000	1×10^{-6}	2×10^{-8}
Si_3N_4	Si_3N_4 (b)	SDL-1	260	15.7	0.04 - 0.08	2000	1×10^{-6}	2×10^{-8}
Si_3N_4	Si_3N_4	SDL-1	260	12.3	0.05 - 0.06	2000	3×10^{-6}	5×10^{-8}
αSiC	αSiC	SAE10	20	17.0	0.04 - 0.08	2700	3×10^{-6}	4×10^{-8}
Cr_2O_3	Cr_2O_3	LB625	260	12.3	0.02 - 0.16	2000	5×10^{-6}	9×10^{-8}
Cr	Cast Iron	SDL-1	260	15.7	0.07 - 0.1	975	1×10^{-5}	4×10^{-7}
Cr_3C_2	Cr_2O_3	SDL-1	260	14.0	0.13	2650	2×10^{-5}	3×10^{-7}
Cr	Si_3N_4	SDL-1	260	12.3	0.14	975	1×10^{-4}	4×10^{-6}
Cr	YPSZ	SDL-1	260	12.3	0.2 - 0.3	975	1×10^{-4}	4×10^{-6}
YPSZ	YPSZ	SAE 10	20	12.3	0.13 - 0.16	1190	2×10^{-4}	6×10^{-6}
YPSZ	YPSZ	None	540	12.3	0.3 - 0.6	1190	8×10^{-4}	2×10^{-5}

(a) Typical actual diesel truck engine experience.
(b) Surface modified by Ceraprep process.

The wear experiment initiated in the last reporting period using K162B (TiC-Ni/Mo) cylinder specimens, Cr_2O_3 - coated ring specimens, and SDL-1 (polyolester) lubricant was continued for a longer testing time at 260 C. After an additional 7.5 hrs at 500 rpm (1.8 m/s average speed) and a 12.3 N/mm ring load, the wear coefficient decreased to 1.4×10^{-7}. This represented an order-of-magnitude decrease from the previous testing period of 4 hours at 260 C and probably reflects a well broken-in sliding couple. The surfaces of the cylinder specimens were polished in the contact region, which is consistent with the low measured wear rates.

Since an operating temperature of 260 C is considered to be the upper limit for the SDL-1 (polyolester) lubricant because of the heavy and adherent carbonaceous deposits formed at higher temperatures, the upper operating temperature is being limited by the lubricant. Therefore, an exploratory experiment was conducted with LB-625 (polyglycol) to determined its suitability as a lubricant for the ceramics being studied.

The experiment with the LB-625 (polyglycol) lubricant was run using plasma sprayed coatings of Cr_2O_3 on both the ring and cylinder specimens. The 1-hour break-in at room temperature resulted in a wear coefficient of 5×10^{-6}, and 1 hour at 100 C resulted in a wear coefficient of 1×10^{-8}. On this basis, the specimens appeared to have been broken in and the wear rates decreasing. At 260 C, however, the wear coefficients increased to 3×10^{-6} and 7×10^{-6} during two 4-hour periods. The wear rates actually increased over the value calculated for the relatively high room temperature break-in period. The friction coefficients were generally less than 0.06 during the 4-hour periods at 260 C, with one brief period of 0.16. Thus, while the wear rate was high, the friction coefficient was generally quite low.

Consistent with the expected behavior of LB-625 (polyglycol), no new deposits were formed and the oil actually removed the deposits in the test chamber left by previous runs with SDL-1. However, the continued high wear rates measured with the Cr_2O_3 specimens with the LB-625 compared with previous results obtained with SDL-1 (wear coefficients of 1×10^{-6} at 260 C) raises concern regarding the application of LB-625. The higher wear rates may be the direct result of the LB-625 not containing a ZDP antiwear additive. Apparently the conventional forms of ZDP are not compatible with LB-625. In contrast, SDL-1 is reported to contain ZDP. Although ZDP has been developed and applied for use with ferrous-based materials, there is apparently sufficient chemical similarity between chromium and iron to make it effective with Cr_2O_3 coatings as well. Another experiment was conducted with LB-650X, a polyglycol that contains an antioxidant additive, to determine whether it is more effective in preventing wear of the Cr_2O_3 specimens. The experiment with the LB-650X lubricant was run on Cr_2O_3 ring and cylinder specimens that had been previously run for a total of 12 hours using the LB-625 lubricant. After two more 4-hour runs at 260 C, the wear coefficients obtained were 3×10^{-6} and 6×10^{-6}. These wear coefficients are similar to those

The LB-650X lubricant, while being more thermally stable than the LB-625, left more deposits behind when it finally did decompose.

Thus, the antioxidant additive was found to be of no benefit when the lubricant was operated above the additive's effective temperature limit. of the LB-625 tests. The coefficients of friction during these final two runs were generally less than 0.05, with one brief period of 0.14, which was similar to the results obtained with the LB-625. Because of the increased amount of deposits from the LB-650X lubricant compared with the amount formed in tests using LB-625 lubricant, further testing at elevated temperatures was done using the LB-625 fluid exclusively.

A new set of Cr_2O_3 specimens were tested to higher temperatures using LB-625 as the lubricant. After a 1-hour break-in at room temperature, the specimens were run at 316 C for one hour. The wear coefficients for the break-in and the high temperature run were 2×10^{-5} and 4×10^{-5} respectively. Friction coefficients were 0.45 for the break-in and as high as 0.12 during the run at 316 C.

The oil application rate required to maintain adequate lubrication with the polyglycol fluids was twice that required for similar tests run with SDL-1, and they were no better than SDL-1 for preventing wear. Further high temperature work will be conducted when a lubricant is developed that either contains a specially formulated antiwear additive or will accept conventional antiwear additives.

Materials Evaluation

With the lack of availability of alternate suitable high temperature lubricants, the new candidate wear materials were tested at 260 C using SDL-1 (polyolester) as the lubricant.

Wear Technology has supplied ring specimens coated by an electrospark alloying (ESA) process. The first ESA coating tried was a tungsten carbide mixed with tantalum carbide, titanium carbide, and nickel (WC+TaC+TiC+Ni). The ESA moving specimen was mated with a chromia sprayed stationary specimen. After running a total of eight hours at 260 C, the average ring wear coefficient was 6×10^{-7}, and the friction coefficient ranged from 0.03 to 0.06. While this coating showed good wear resistance, Figure 3 shows the surface cracking that occurred in the contact areas. A higher magnification micrograph of the same area, Figure 4, shows the highly polished wear surface characteristic of an extremely low wear rate.

A self-lubricating composite consisting of a wear resistant chromium carbide matrix filled with a calcium fluoride/barium fluoride eutectic and silver (PS212) was supplied by NASA Lewis Research Center. Since the composite was "self-lubricating", no additional lubricant was used. Without the temperature limitation of liquid lubricants, the tests of this material were run at 538 C.

The first test was run with self-mated PS212 ring and cylinder specimens. The test ran for ten minutes before the wear-limiting switch indicated excessive wear, and the test was shut down. The coefficient of friction during this run ranged from 0.22 to 0.27, and the ring wear coefficient was 1.2×10^{-3}. The rough surfaces,

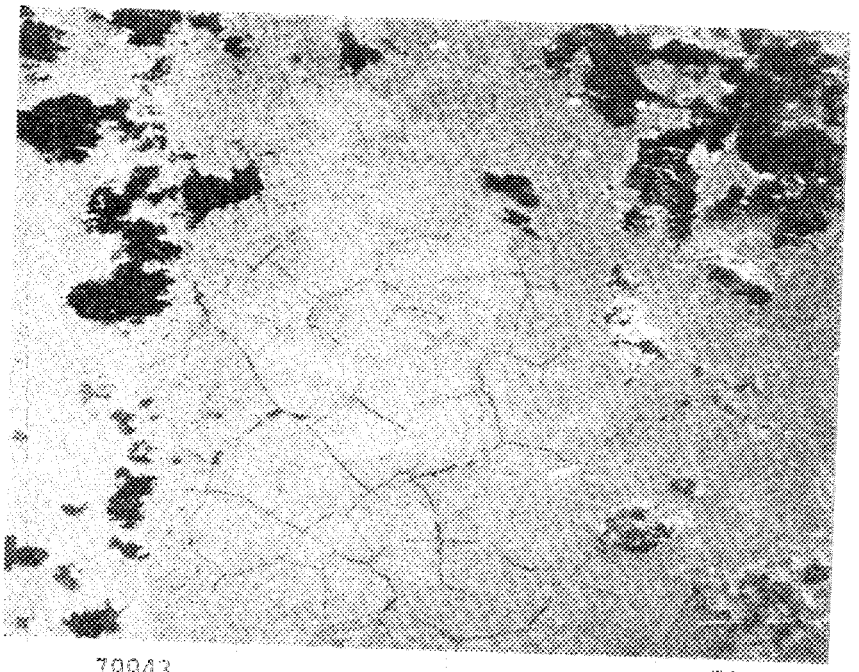

79943 50X

FIGURE 3. SURFACE CRACKING IN CONTACT AREA OF ESA VA20 RING SPECIMEN

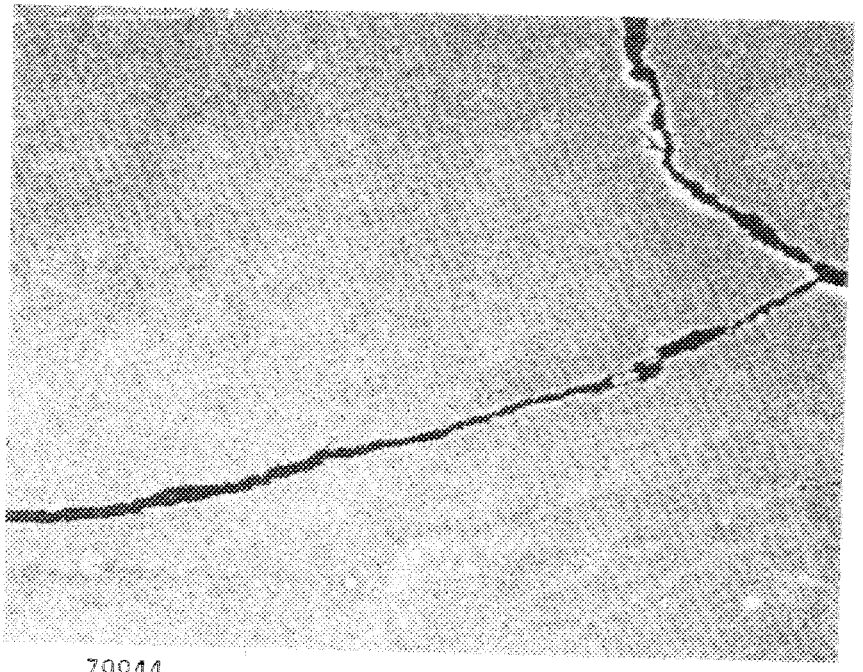

79944 1000X

FIGURE 4. HIGHLY POLISHED WEAR AREA AND SURFACE CRACKS ON ESA VA20 RING SPECIMEN

transferred material, and transverse cracks perpendicular to the sliding direction shown in Figure 5 are the kinds of surface damage typical of dry sliding with the soft, lubricious coatings.

A second test was run using silicon nitride as the ring specimens and PS212 as the cylinder ring specimens to avoid the self-mated sliding used in the first experiment. Again the test was run at 538 C without added liquid lubricant. The test ran for less than ten minutes before the ring specimen holder broke off of the sliding arm. The friction coefficient ranged from 0.13 to 0.16. A ring wear coefficient could not be measured because the ring specimens had shattered.

After repairing the experimental rig, a third test was run under the same conditions using an ESA coating of chromium carbide and nickel (Cr_3C_2+Ni). During this run the coefficient of friction ranged from 0.16 to 0.26. The ring wear coefficient was 2.4×10^{-3}, and that of the PS212 cylinder specimens was 3.2×10^{-3}. The ring coatings had worn through their thin coatings during this test, so another test was run using nitrogen-ion-implanted chromia for the ring specimens. This test also ran for only about ten minutes before the ring specimen holder broke off. A combination of the high temperatures, fatigue, and high frictional forces are thought to be the cause of these reoccurring rig failures. Friction coefficients for this test ranged from 0.26 to 0.31. The chromia ring specimens showed little wear after the short test, and their wear coefficient averaged 1.2×10^{-5}. The PS212 specimens, however, wore over 15 μm in the same amount of time, resulting in a wear coefficient of 1.2×10^{-2}.

It is apparent that the PS212 coatings, by themselves, do not provide an adequately lubricated wear surface under the severe conditions of an engine ring/cylinder interface. Another test will be run to evaluate the coating's wear resistance when lubricated with SDL-1 at the standard 260 C temperature.

Several new materials have been acquired in the past few months. A new whisker-toughened ceramic, several solid lubricants, and a prototype high temperature liquid lubricant are some of the materials that will be evaluated in the coming months. Further experiments will also be run using nitrogen ion-implanted chromia to evaluate the potential benefits of ion implantation.

Environmental Testing

Wear experiments are currently being conducted to determine which constituents of the diesel exhaust have the greatest effect on the friction and wear of ceramics in ring/cylinder applications. Ring and cylinder materials will both be plasma sprayed Cr_2O_3, the lubricant will be SDL-1 (polyolester), and environments of breathing air, nitrogen, and steam will be used. The test temperature for these tests will be 260 C. The wear results will permit a comparison of the effects of these principal exhaust constituents on friction and wear.

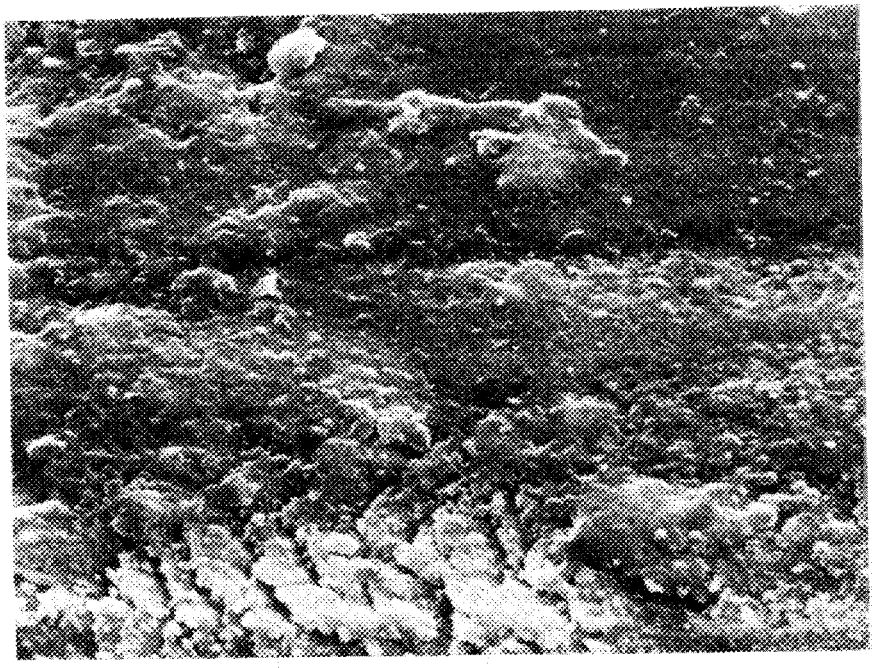

79906 5000X

FIGURE 5. WEAR SURFACE OF NASA PS212 RING SPECIMEN

Status of milestones

The study is progressing in accordance with the overall milestone schedule.

Publications

None

Reference

1. Gardos, M. N., "An Analysis of the Ga/In/WSe_2 Lubricant Compact," ASLE Transactions, Vol. 28, p. 231.

2.3 NEW CONCEPTS

Advanced Statistical Concepts of Fracture in Brittle Materials

C. A. Johnson and W. T. Tucker (General Electric Corporate Research and Development)

Objective/scope

The design and application of reliable load-bearing structural components from ceramic materials requires a detailed understanding of the statistical nature of fracture in brittle materials. The overall objective of this program is to advance the current understanding of fracture statistics, especially in the following four areas:

- Optimum testing plans and data analysis techniques.
- Consequences of time-dependent crack growth on the evolution of initial flaw distributions.
- Confidence and tolerance bounds on predictions that use the Weibull distribution function.
- Strength distributions in multiaxial stress fields.

The studies are being carried out largely by analytical and computer simulation techniques. Actual fracture data are then used as appropriate to confirm and demonstrate the resulting data analysis techniques.

Technical progress

During this reporting period, the likelihood ratio and conditional integration methods for determining confidence/tolerance bounds in Class III problems were applied to strength data of sintered SiC. The data were described in Reference 1 and the methodology was developed and reported in Reference 2. Due to limitations in Class III analyses (single specimen geometry, multiple specimen sizes), the full data set of Reference 1 (which included 3-point and 4-point bending of Mil Std 1942 A, B, and C specimens) could not be analyzed. Instead, only the three groups that were tested in 3-point bending are included here. The results are displayed graphically in Figure 1. As reported in Reference 1, fractography indicated that the strength controlling flaws were predominately located on specimen surfaces. Therefore, the specimen "size" axis is stressed area. The fracture strengths are drawn as open data points with the three different symbol types corresponding to the three specimen sizes. The Weibull modulus and sigma zero were estimated using the maximum likelihood method for combined data as described in Reference 1. The upper line is the predicted position of the median (0.5 quantile) as a function of stressed area, while the lower line is the predicted position of the 0.05 quantile behavior. Included in Figure 1 as solid circles are 95 percent confidence bounds on the 0.05 quantile. The bounds can be used to state the uncertainty in the 0.05 quantile strength for any given stressed area of interest. Class III confidence bounds such as these, however, are limited to estimates of other 3-point bend geometries. The full Class IV approaches of analysis (which are currently under development and described below) will be able to combine data from both SiC specimen geometries and make strength predictions with confidence bounds on components with arbitrary sizes and geometries.

It is interesting to point out on Figure 1 that the strength value associated with the "pinch point" of the confidence bounds (the point with the smallest uncertainty) is located essentially at the midpoint of all the measured strengths. This relationship should always be the case and is useful in visualizing bounds on other quantiles. As one considers progressively smaller quantile behaviors, the predicted line moves down and to the left, the pinch point moves to smaller effective areas or volumes, and the width of the tolerance bound increases for any size larger than that of the pinch point.

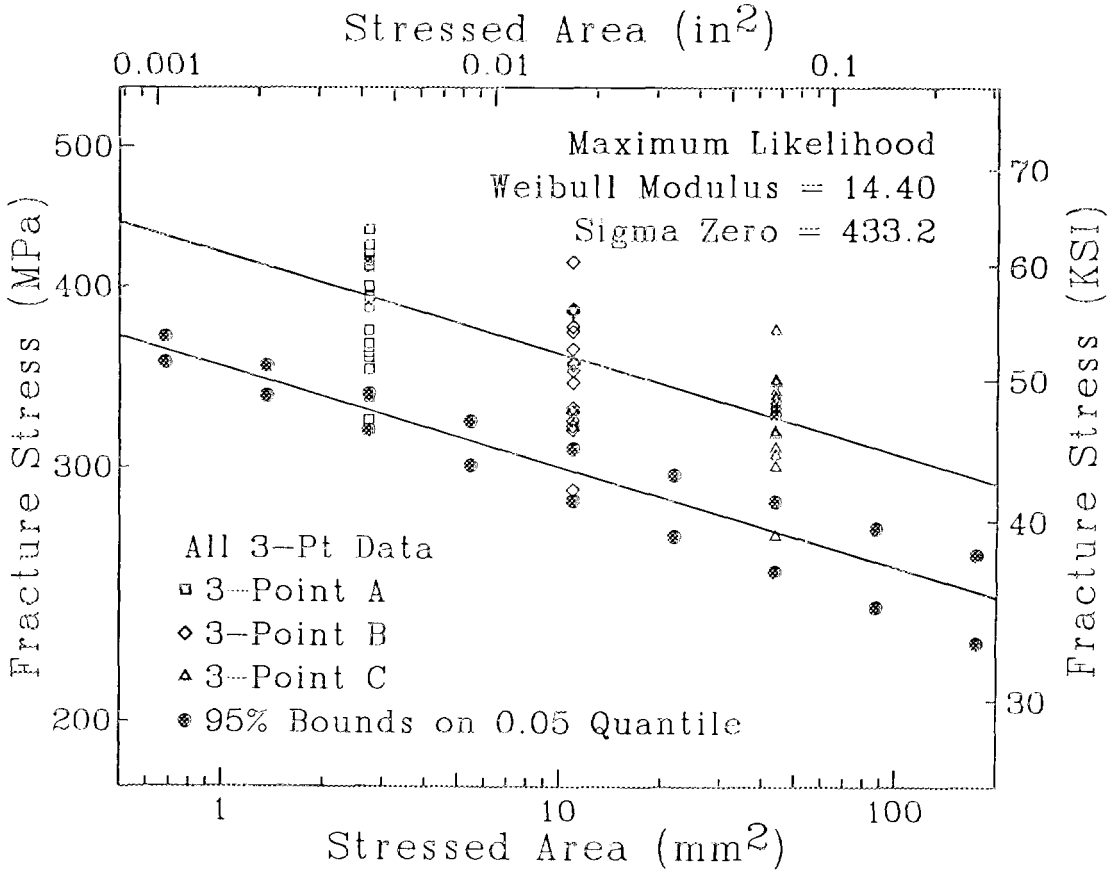

Figure 1

Also during this reporting period, effort began on development of methods for estimating confidence and tolerance bounds on Weibull parameters and strength estimates for "Class IV" problems. Class IV problems are those where the fracture data may include specimens from multiple specimen sizes and loading geometries, while the component of interest may be of yet a different size and loading configuration. Two promising classes of approaches have been identified and are being pursued. The first is based on likelihood methods and the second is based on bootstrapping methods. The following paragraphs describe these two classes of approaches and the progress in using them toward Class IV problems of strength analysis.

Classical likelihood methods such as those using asymptotic normal theory (3) are known to be very inefficient, thus requiring large sample sizes on the order of 100 or more in order to gain acceptable accuracy. Likelihood ratio techniques (4) are more efficient, requiring only 30 or so specimens in typical situations. Conditional techniques based on integration of the likelihood distribution (5) are the most efficient of this class with virtually no lower limit imposed by the accuracy of the technique. (Of course, smaller numbers of specimens contain less information and will naturally yield larger

tolerance bounds, even for an accurate method of estimating bounds.) The integration approach is much more computationally intensive than the likelihood ratio approach. Therefore, it is anticipated that the integration approach will be used when small numbers of specimens are available, while the likelihood ratio technique will be used for larger numbers.

At this time two approaches are being considered to deal with multiple specimen sizes and geometries in likelihood approaches. In the first, an attempt is being made to employ a model of equivalent sizes, so that all sizes can be relative scaled. This method would take into account all information that is known. However, it requires that the relative relationship between sizes be exact. This may not be the case, since the relationship depends among other things on the correct model of failure and multiaxial stress considerations. In the other approach, it is only assumed that the Weibull distribution, with unknown modulus and characteristic strength for each loading-geometry condition, properly describes failures. While this approach loses some information, it has the advantage of not depending on the model of failure, etc. Moreover, in this approach the integration method may again be exact.

The second class of approach being pursued uses variations of the "bootstrapping" technique (6). This technique begins with an estimator that can combine data from multiple specimen sizes and geometries and yield an estimate of the Weibull parameters. (Two such estimators have been described in Reference 1--one based on linear regression and the other on maximum likelihood.) The estimator is used on the experimental data to yield the best estimate of the adjustable parameters of the distribution. In parametric bootstrapping, these estimated parameters are then used to simulate data similar to the original but chosen randomly from a distribution with the estimated parameters. In non-parametric bootstrapping, additional data sets are generated by randomly choosing strengths from the original data with replacements (ie. a given strength can be chosen more than once in a data set). In both techniques, the generated data set is analyzed using the original estimator. By repeatedly generating and analyzing artificial data sets a large number of times, information can be gained about the variability of the estimator in analyzing data similar to the experimental data set. This, in turn, can be used to estimate confidence bounds on parameters and tolerance bounds on estimated behavior of components.

The bootstrapping technique is computationally intensive, but it offers the intriguing potential of estimating confidence and tolerance bounds on a variety of very complex problems beyond Class IV (such as those involving multiple flaw populations, multiaxial stresses, strength degradation due to slow crack growth, etc). If an estimator can be designed to estimate all the adjustable parameters of a given model, then the bootstrapping technique should be capable of estimating confidence bounds on all the parameters and tolerance bounds on estimated strengths. (It should be pointed out that the better the quality of the estimator, the smaller the width of the bounds.) As the effort proceeds, the relative advantages and disadvantages of parametric versus non-parametric bootstrapping should become evident.

References

1. C.A. Johnson and W.T. Tucker, "Advanced Statistical Concepts of Fracture in Brittle Materials", in *Ceramic Technology for Advanced Heat Engines Project, Semiannual Progress Report for Period April 1987 through September 1987,* pp 200-208.

2. C.A. Johnson and W.T. Tucker, "Advanced Statistical Concepts of Fracture in Brittle Materials", in *Ceramic Technology for Advanced Heat Engines Project, Semiannual Progress Report for Period October 1987 through March 1988.*

3. W. Nelson, *Applied Life Data Analysis*, John Wiley & Sons, New York, 1982.

4. D.R. Cox and D. Oakes, *Analysis of Survival Data,* Chapman and Hall, New York, 1984.

5. J.F. Lawless, "Construction of Tolerance Bounds for the Extreme-Value and Weibull Distributions," *Technometrics,* 17, 255-61, 1975.

6. B. Efron, "Bootstrap Methods: Another Look at the Jackknife," *The Annals of Statistics,* 7, No. 1, 1-26, 1979.

Status of Milestones

On schedule.

Communications/Visits/Travel

None.

Problems Encountered

None.

Publications

None.

3.0 DATA BASE AND LIFE PREDICTION

INTRODUCTION

This portion of the project is identified as project element 3 within the work breakdown structure (WBS). It contains five subelements, including (1) Structural Qualification, (2) Time-Dependent Behavior, (3) Environmental Effects, (4) Fracture Mechanics, and (5) Nondestructive Evaluation (NDE) Development. Research conducted during this period includes activities in subelements (1), (2), and (3). Work in the Structural Qualification subelement includes proof testing, correlations with NDE results and microstructure, and application to components. Work in the Time-Dependent Behavior subelement includes studies of fatigue and creep in structural ceramics at high temperatures. Research in the Environmental Effects subelement includes study of the long-term effects of oxidation, corrosion, and erosion on the mechanical properties and microstructures of structural ceramics.

The research content of the Data Base and Life Prediction project element includes (1) experimental life testing and microstructural analysis of Si_3N_4 and SiC ceramics, (2) time-temperature strength dependence of Si_3N_4 ceramics, and (3) static fatigue behavior of PSZ ceramics.

Major objectives of research in the Data Base and Life Prediction project element are understanding and application of predictive models for structural ceramic mechanical reliability, measurement techniques for long-term mechanical property behavior in structural ceramics, and physical understanding of time-dependent mechanical failure. Success in meeting these objectives will provide U.S. companies with the tools needed for accurately predicting the mechanical reliability of ceramic heat engine components, including the effects of applied stress, time, temperature, and atmosphere on the critical ceramic properties.

3.1 STRUCTURAL QUALIFICATION

Microstructural Analysis of Structural Ceramics

B. J. Hockey, Jr., and S. M. Wiederhorn (National Institute of Standards and Technology)

Objective/scope

The objective of this part of the program is to identify the mechanisms of failure in structural ceramics subjected to mechanical loads in various test temperatures and environments. Of particular interest is the damage that accumulates in structural ceramics as a consequence of high temperature exposure to environments and stresses normally present in heat engines.

Design criteria for the use of ceramics at low temperature differ from those at high temperature. At low temperature ceramics are elastic and brittle; failure is controlled by a distribution of flaws arising from processing or machining operations, and the largest flaw determines the strength or lifetime of a component. By contrast, at high temperature where ceramics are viscoelastic, failure occurs as a consequence of accumulated, or distributed damage in the form of small cavities that are generated by the creep process. This damage effectively reduces the cross-section of the component and increases the stress that must be supported. Such increase in stress is in a sense autocatalytic, since it increases the rate of damage and eventually leads to failure as a consequence of loss in cross section. When this happens, the individual flaw loses its importance as a determinant of component lifetime. Lifetime now depends on the total amount of damage that has occurred as a consequence of the creep process. The total damage is now the important factor controlling lifetime.

Recent studies of high temperature failure of the non-oxide ceramics intended for use for heat engines indicates that for long term usage, damage accumulation will be the primary cause of specimen failure. Mechanical defects, even if present in these materials, are healed or removed by high temperature exposure so that they have little influence on long term lifetime at elevated temperature. In this situation, lifetime can be determined by characterizing the nature of the damage and rate of damage accumulation in the material at elevated temperatures. In ceramic materials such as silicon nitride and the sialons, such characterization requires the use of high resolution techniques of analysis because of the fine grain size of these materials: hence the need for transmission electron microscopy as an adjunct to the mechanical testing of ceramics for high temperature applications is apparent.

In this project, the creep and creep-rupture behavior of several ceramic materials will be correlated with microstructural damage that occurs as a function of creep strain and rupture time. Materials to be studied include: sialons; hot-pressed silicon nitride; and sintered silicon carbide. This project will be coordinated with WBS 3.4.1.3, Tensile Creep Testing, with the ultimate goal of developing a test methodology for assuring the reliability of structural ceramics for high temperature applications.

Technical Highlights

During the past six months the importance of microstructure to the deformation and rupture of two phase materials was analyzed, particularly with regard to the kind of deformation and fracture that is likely to occur in the materials anticipated for use in heat engines. Many of these are two phase materials in which a rafractory particle or fiber is imbedded in a much less refractory matrix. Part of the study involved a review of the pertinent literature concerned with two phase deformation; part involved an analysis of data collected over the past three years on this program. A report of the work is given below.

Models of Two Phase Creep

The first paper to deal with two phase creep was the seminal paper presented by Coble[1] to explain creep by grain boundary transport. Coble assumed that creep occurred primarily by diffusion of material along grain boundaries as a consequence of chemical potential differences between boundaries that were subjected to compression and boundaries that were subjected to tension. The creep rate was found to be proportional to the grain boundary thickness and to the grain boundary diffusivity, and inversely proportion to the cube of the grain size. This theory has been further developed by others[2], and is one of the basic creep models that describe the deformation of materials at elevated temperatures.

Subsequent to Coble's work, Raj[3] and Ashby[4] noted that the process of solution re-precipitation in two phase ceramics could be described by the Coble equation, provided the grain boundary thickness was replaced by the thickness of the matrix phase separating the grains, figure 1. If the flux of material from the compressive to the tensile surface of the grains is transport-controlled, then the equation governing creep is identical to the Coble equation. If, however, the flux is interface-controlled, then the creep rate is inversely proportional to the grain size, and a surface kinetic term enters the creep equation[3]. These two mechanisms constitute solution re-precipitation, the most generally accepted mode of high temperature deformation in two phase systems.

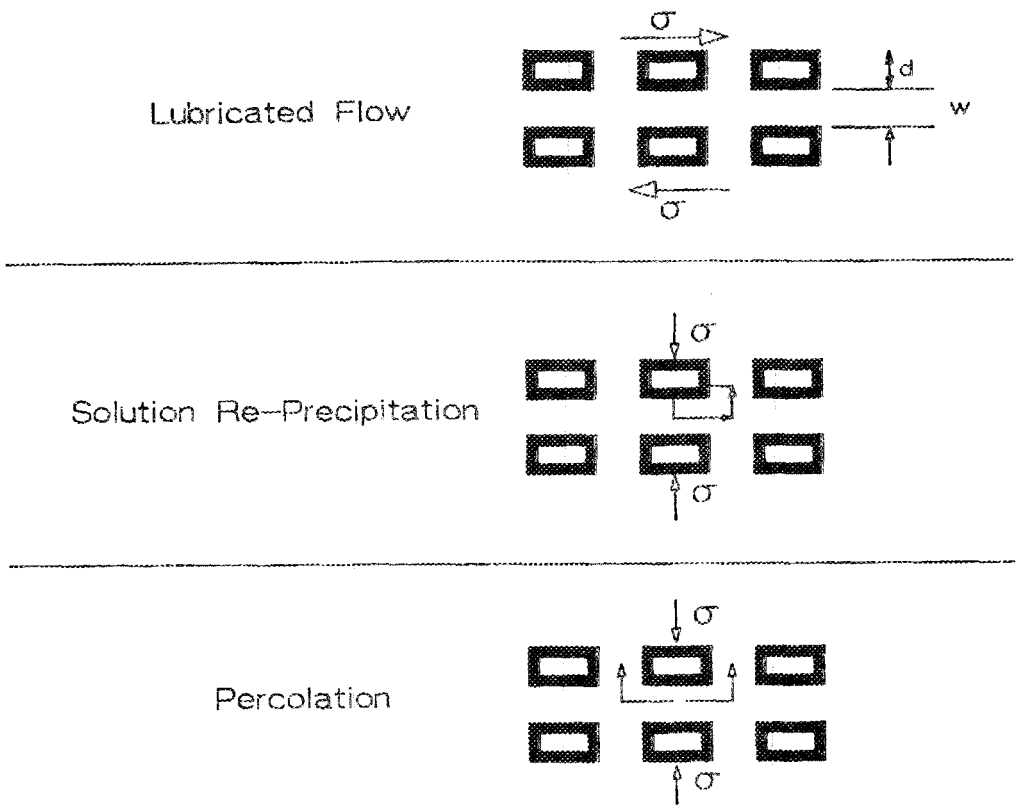

1. Models of two phase creep: lubricated flow; solution re-precipitation; percolation. After Pharr and Ashby [4].

A second class of creep models involves mass flow of the matrix phase within the two phase material. In its simplest form, the matrix phase acts as a lubricant between the hard rigid grains, which permits them to slide easily past one another, figure 1. As contact between the grains is not envisioned in this model, creep occurs only as a consequence of shear deformation within the matrix phase; as a consequence, the creep rate is proportional to the volume fraction of the matrix phase[4]. However, as grains of a two phase material are never laid out in perfect rows, lubricated flow, as described here, plays only a minor role in the deformation process. Grains constituting the solid impinge upon one another and flow gradually subsides. For continued deformation, grain rotation must occur and grains must slide over one another; as a consequence, dilatory stresses develop locally within the matrix phase[5]. To accommodate these local volume changes, the matrix must flow between the refractory grains. In regions where negative pressures develop, the forces between the solid particles are increased so that firm interparticle contact is made between adjacent grains. Creep deformation by viscous flow, sometimes known as percolation, has been described by Lange[6] and by Drucker[7], who showed that the creep rate is proportional to the cube of the volume fraction of the matrix phase. Large deformations cannot occur by percolation alone, since here too, interparticle contact gradually slows the creep process. Percolation can, however, accommodate dilation that occurs when other modes of deformation are active.

Experimental studies to elucidate the role of microstructure on the creep rate of two phase materials were conducted by Raj and his coworkers on glass ceramics[8,9]. Their studies suggest that the creep of glass ceramics is a viscous process in which the grain size dependence of the creep rate is dependent on temperature. At 950°C, the creep rate is inversely proportional to the grain size suggesting an interfacial mechanism of creep, whereas at higher temperatures, >1150°C, the creep rate is inversely dependent on the cube of the grain size, suggesting that creep was transport controlled. In a more recent, but less systematic study on vitreous bonded aluminum oxide, creep rate measurements indicated a relatively low sensitivity of the creep rate to the grain size, which is consistent with interfacially controlled creep in this material[10]. Based on these few studies, it can be concluded that both interfacial and transport controlled creep can occur in two phase ceramics.

Microstructure of Two Phase Materials

Potential problems with the above models of two phase creep arise as a consequence of differences between the microstructure envisioned in the models, figure 1, and the microstructures of real materials. These differences are of two types: (1) grains are usually not

uniform in size or shape, so that the stacking of grains and the interstices occupied by the matrix phase are also non-uniform; (2) grains in real two phase structures are usually faceted so that corners and edges, rather than flat or gently curved faces, come into contact. These differences result in creep that is inhomogeneously distributed within the body, in contrast to the assumptions of uniformly distributed stress and strain inherent in most theories of creep.

The lack of uniformity of grain size and grain shape results in uneven loading of the grains, giving rise to local stress concentrations within the microstructure. This effect was discussed by Drescher and De Jong[11], who used a physical two-dimensional model consisting of plastic disks of six different radii to model the deformation and the stress distribution developed within granular materials. Hundreds of disks were randomly stacked together between two glass plates; the stack of disks was loaded along its edges to mimic the flow of a two-dimensional granular solid. During deformation, paths of force through the stack of disks were mapped by polarized light. Birefringence patterns within the stack of disks indicated that the applied force was not transferred uniformly, since some of the disks were completely free of birefringence while others were highly birefringent. Clusters containing from 3 to 8 disks (estimated from figure 9 of Drescher and De Jong's paper) formed cells that moved in unison during deformation; strain occurred only at the boundary of each cell. Considering the variation in grain size normally observed in most ceramic materials, this model is probably an accurate reflection of creep behavior in real materials.

An example of a type of microstructure that leads to uneven loading is illustrated in figure 2a for a grade of vitreous bonded aluminum oxide containing ≈20 v/o vitreous phase[10]. Because of the faceted grain morphology, intergranular contact occurs only at points or lines determined by the faceting. Consequently, line and point contacts would be expected to control the deformation process in this material during creep. Contact due to faceting also occurs when smaller amounts of second phase are present. In vitreous bonded aluminum oxide containing only ≈8 percent second phase (figure 2b) angular boundaries and microscopically faceted surfaces of the grains also permit contact only at sharp edges rather than flat surfaces[10]. Finally, stress contours observed by transmission electron microscopy in specimens of hot pressed silicon nitride that have been deformed at elevated temperatures[12] also suggest that contact points dominate the creep behavior of this material.

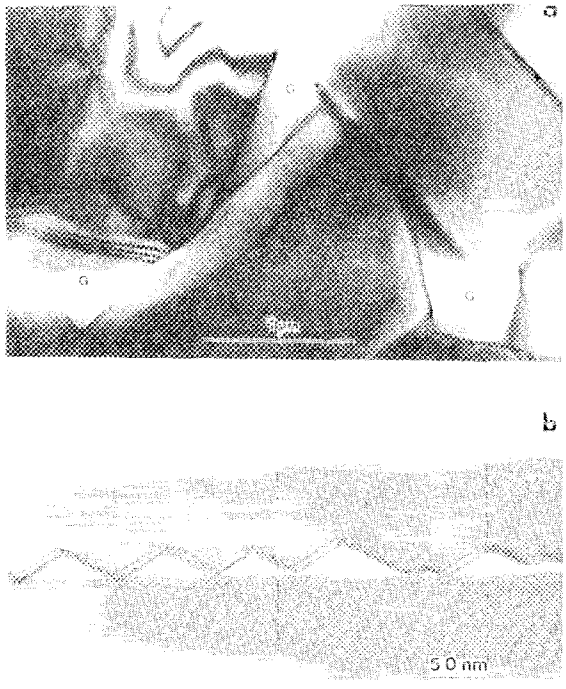

2. Microstructure of two phase materials: (a) vitreous bonded alumina containing ≈20v/o vitreous phase; (b) vitreous bonded alumina containing ≈8v/o vitreous phase. Both the faceted morphology of the grains (a) and the microscopic-scale faceting of the grain surfaces (b) preclude extensive contact between grains. Contact seems to occur more frequently at edges and corners rather than along flat or smoothly curved surfaces.

Creep of Two Phase Materials

One consequence of the microstructural features discussed above is creep asymmetry, in which the creep of two phase materials differs in tension and in compression. As shown in figure 3 for siliconized SiC (33% Si), twice as much stress is required in compression as in tension to attain the same creep rate[13][1]. Results similar to those in figure 3 have been obtained for glass ceramics[14], and for an experimental grade of SIALON[15]. In siliconized silicon carbide[13], compressive creep is probably controlled by deformation of contact points (or junctions) between grains of silicon carbide as indicated by the observation of localized deformation at contact asperities, figure 4. Dislocation glide or climb at the contact points is expected to yield a value of ≈4 for the power law creep exponent, which is consistent with the experimental data at the lower levels of applied stress. The increase in the stress exponent at the higher applied stresses is probably a consequence of the onset of general plasticity at the contact points of the silicon carbide grains.

Support for the role of silicon carbide in the deformation process is obtained from studies of compressive creep above the melting point of silicon[12]. As can be seen from figure 5, the creep rate under the conditions selected, 1430°C and 75MPa, can be extrapolated from creep measurements below the melting point of silicon. Since it is an inviscid fluid above its melting point, silicon does not support any of the load; hence, asperity deformation of the silicon carbide alone determines the rate of creep of this material in compression. In tension, however, the controlling mechanism for creep must be entirely different from that occurring in compression, since this grade of siliconized silicon carbide simply falls apart above the melting point of the silicon when subjected to a tensile load. Alternatively, the result suggests that below the melting point a substantial portion of the load is born by the silicon during tensile creep.

A number of processes can contribute to creep deformation in tension. An important factor in determining the dominant process is the strength of the points of contact between grains of silicon carbide. If these points of contact are strong enough, then the silicon carbide itself will support the applied tensile stress, and the composite material should be able to support a load above the melting point of the silicon. This behavior has been observed in a grade of siliconized silicon carbide containing less silicon than that of the material used to collect the data in figures 3 and 5[16].

---

[1] Following the procedure used by Wang and Raj[9] only 16% of the difference in the creep rates could be attributed to shear effects.

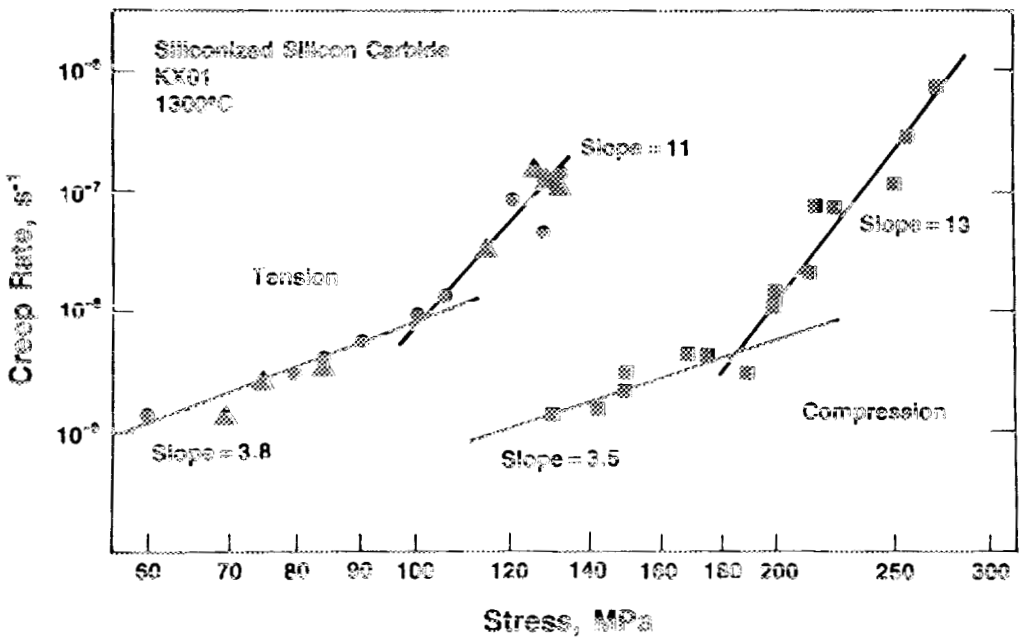

3. Creep asymmetry in siliconized silicon carbide. As can be seen, creep in tension is easier than creep in compression. At least two modes of creep are observed in both tension and compression. After Wiederhorn et al. [13].

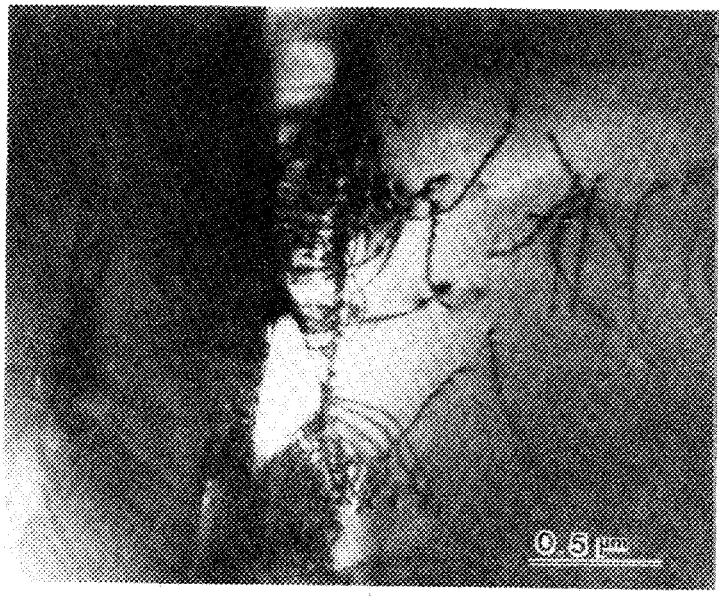

4. Localized damage at contact sites between SiC grains in siliconized silicon carbide subjected to compressive deformation. Dislocation activity is observed to be initiated at local points of contact between carbide grains.

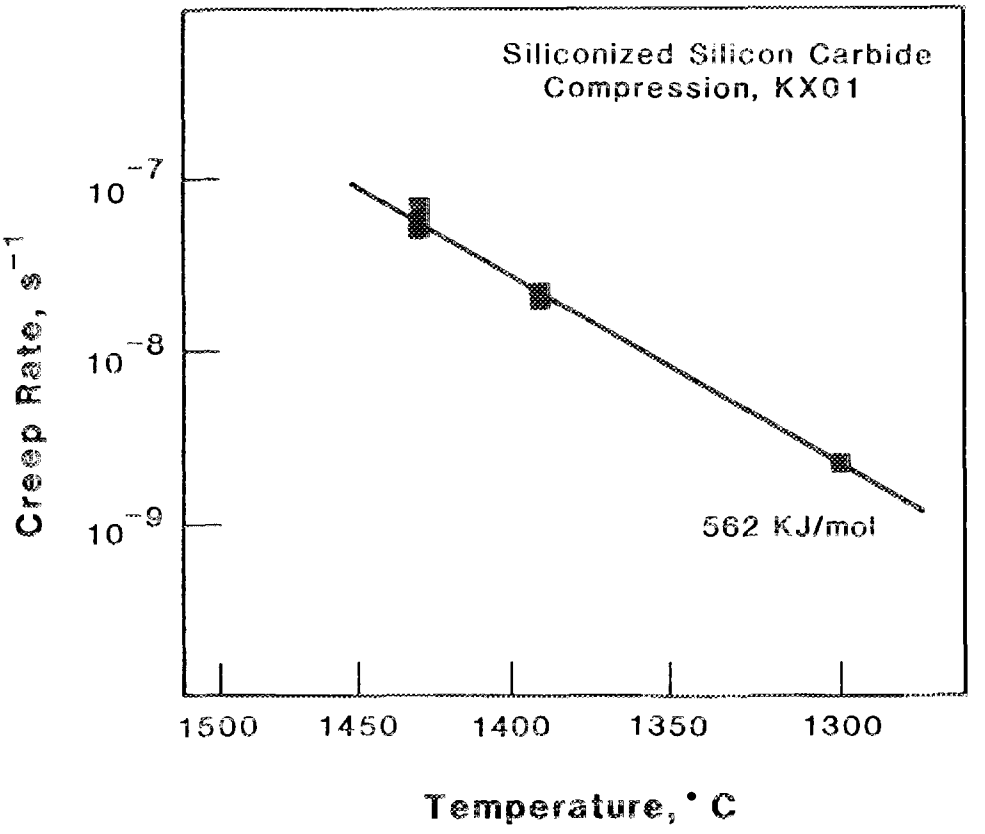

5. Compressive creep of siliconized silicon carbide as a function of temperature. The material supports a load and creeps in a predictable manner at temperatures that exceed the melting point of silicon. By contrast, specimens of this material break at very low loads above the melting point of the silicon in tension. These results are similar to those of Vaandrager and Pharr [22] on brass containing a liquid at grain boundaries. After Wiederhorn et al. [13].

If, however, these contact points are weak, they will break when subjected to sufficient tensile stress, leaving the silicon alone to support the applied stress. As a consequence of its complex microstructure, the stress distribution in the silicon is expected to be nonuniform, a consequence of which is the limitation of deformation to isolated regions in the structure that are subjected to high stresses. In this situation, creep of the composite as a whole will be determined by the deformation rate of the silicon in regions of high stress. The process envisioned is that proposed by Drescher and De Jong[11], but with the deformation occurring in the matrix rather than in the granular phase. If creep deformation in the silicon were controlled by power law creep, a stress exponent of ≈4 would also be expected in tension. However, because silicon creeps more easily than silicon carbide[17,18], the creep rate for siliconized silicon carbide in tension would be greater than that in compression for the same applied stress, thus accounting for creep asymmetry.

Any volume expansion occurring during creep deformation will also contribute to creep asymmetry in two phase ceramics. Since the average pressure of a body under stress is equal to 1/3 the trace of the stress tensor, the pressure difference between tensile and compressive loading is equal to 2/3 of the absolute value of the applied stress. This difference in pressure will work against any volume expansion occurring during creep, which will increase the stress required for creep in compression over that required in tension. Therefore, a larger applied stress will be needed to achieve the same creep rate in compression as in tension.

Changes in volume during creep may have several sources. One such source of volume expansion is the dilation that occurs as a consequence of grains sliding over one another (discussed above). Another source of volume expansion is cavitation, which occurs more easily in tension than in compression. When cavitation occurs, the creep rate is enhanced by the cavitation: $\Delta\dot{\varepsilon} = \dot{V}/3$, where V is the rate of volume increase due to cavity nucleation and growth, so that creep is faster in tension than in compression where cavitation is suppressed by the applied stress. Creep asymmetry has been attributed to cavity formation by Morell and Ashbee[14] in their study of creep and creep rupture of glass ceramics. In siliconized silicon carbide, cavitation has also been shown to play a role in enhancing tensile creep behavior at high stresses[12,19] figure 3.

The number of grains that come into contact as a consequence of the applied stress will also play a role in the creep process. Because of the overall difference in average pressure in tension and compression, more particles will be forced together in compression than in tension, thus increasing the area of contact between grains. When creep is controlled by intergranular sliding, this enhancement of the contact area increases the stress required for deformation in

compression over that required in tension. The process described is similar to that envisioned in simple sliding, where the lateral force for sliding is determined by the area of contact between the two bodies. For a sliding coefficient of friction of ≈1, which is reasonable at high temperatures[20], the stress level required for a given creep rate in compression is estimated to be ≈70 percent greater than that in tension. Differences of this magnitude have been observed for siliconized silicon carbide and for glass ceramics.

Microstructural Observations

Microstructural observations on siliconized silicon carbide deformed at elevated temperatures support the suggestion that contact sites between silicon carbide grains play an important role in the creep process. Dislocation densities within the deformed solid are generally low and their distribution is not uniform, indicating that deformation does not occur uniformly throughout the microstructure. In particular, dislocation activity in silicon carbide is concentrated primarily at contact sites between the grains of silicon carbide, figure 4. Furthermore, damage is more severe and more uniformly distributed in compression than in tension[21], supporting the idea that contact between silicon carbide grains is more intense in compression than in tension. Dislocations are also observed in the silicon at isolated locations throughout the composite. Thus, deformation within the two phase solid is not uniform, but occurs at isolated locations throughout the structure.

If deformation occurs only at contact sites, then the rate of deformation in the vicinity of contact would be controlled by geometric factors relevant to the site geometry, as for example, the area of contact and the size of the deformation zone at the contact site. For materials that facet, these geometric factors will not depend on grain size, since the geometry of the corners and edges formed from the facets should not depend on grain size. If deformation at a contact site results in a relative displacement, u, between two grains, then the strain attributable to the grain will be given by u/d, so that the creep rate of the material will be inversely proportional to its grain size, d. This dependency of creep rate on grain size is less than that predicted by transport controlled solution re-precipitation, or percolation theory, figure 1. The predicted grain size dependence of the creep rate (-1) is identical to that proposed for lubricated flow, or for interface controlled solution re-precipitation, which might be expected, since here too, deformation is localized to the interface of the solid. Thus, whereas an inverse linear dependence of creep rate on grain size indicates interface controlled creep, solution re-precipitation may not be the cause of creep as the same grain size dependence of the creep rate can be obtained from several other processes.

References:

1. R.L. Coble, "A Model for Boundary Diffusion Controlled Creep in Ceramic Materials," J. Appl. Phys., 34, 1679-82 (1963).

2. R. Raj and M.F. Ashby, "On Grain Boundary Sliding and Diffusional Creep," Metall. Trans. 2, 1113-27 (1971).

3. R. Raj, "Creep in Polycrystalline Aggregates by Matter Transport Through a Liquid Phase," J. Geophys. Res., 87, 4731-9 (1982).

4. G.M. Pharr and M.F. Ashby, "On Creep Enhanced by a Liquid Phase," Acta Metall. 31, 129-38 (1983).

5. R.L. Tsai and R. Raj, "Creep Fracture in Ceramics Containing Small Amounts of a Liquid Phase," Acta Metall. 30, 1043-58 (1982).

6. F.F. Lange, "Non-Elastic Deformation of Polycrystals with a Liquid Boundary Phase"; pp. 361-81 in Deformation of Ceramic Materials, edited by R.C. Bradt and R.E. Tressler, Plenum Press, New York, 1972.

7. D.C. Drucker, "Engineering and Continuum Aspects of High-Strength Materials"; pp. 795-833 in High Strength Materials, edited by V.F. Zackay, Wiley, New York, 1965.

8. R. Raj and C.K. Chyung, "Solution-Precipitation Creep in Glass Ceramics," Acta Metall. 29, 159-166 (1981).

9. J.-G. Wang and R. Raj, "Mechanism of Superplastic Flow in a Fine-Grained Ceramic Containing Some Liquid Phase," J. Am. Ceram. Soc. 67, 381-444 (1984).

10. S.M. Wiederhorn, B.J. Hockey and R.F. Krause, Jr., "Influence of Microstructure on Creep Rupture"; pp. 795-806 in Ceramic Microstructures '86: Role of Interfaces, edited by J. A. Pask and A. G. Evans, Plenum Press, New York, 1987.

11. A. Drescher and G. de Josselin de Jong, "Photoelastic Verification of a Mechanical Model for the Flow of a Granular Material," J. Mech. Phys. Solids, 20, 337-51 (1972).

12. F.F. Lange, D.R. Clarke, and B.I. Davis, "Compressive Creep of Si_3N_4/MgO Alloys: Part 2, Source of Viscoelastic Effect," J. Mater. Sci. 15, 611-15 (1980).

13. S.M. Wiederhorn, D.E. Roberts, T.-J. Chuang and L. Chuck, "Damage-Enhanced Creep in a Siliconized Silicon Carbide: Phenomenology," J. Am. Ceram Soc., 71, 602-608 (1988).

14. R. Morrell and K.H.G. Ashbee, "High Temperature Creep of Lithium Zinc Silicate Glass-Ceramics, Part 1, General Behavior and Creep Mechanisms," J. Mater. Sci., 8, 1253-70 (1973).

15. C.-F. Chen, Creep Behaviors of SIALON and Siliconized Silicon Carbide Ceramics," Ph.D. Dissertation, The University of Michigan, Ann Arbor, MI, 1987.

16. Y. Tsai and R.E. Tressler, "Tensile Creep Behavior of Siliconized Silicon Carbides," paper 38-B-88 presented at the 90th Annual Meeting of The American Ceramic Society, May 1-5, 1988, Cincinnati, Ohio.

17. M.M. Myshlyaev, V.I. Nikitenko, and V.I. Nesterenko, "Dislocation Structure and Macroscopic Characteristics of Plastic Deformation at Creep of Silicon Crystals," Phys. Stat. Sol. 36, 89-96 (1969).

18. P.L. Farnsworth and R.L. Coble, "Deformation Behavior of Dense Polycrystalline SiC," J, Am. Ceram. Soc., 49, 264-268 (1966).

19. D.F. Carroll and R.E. Tressler, "Effect of Creep Damage on the Tensile Creep Behavior of a Siliconized Silicon Carbide," J. Am. Ceram. Soc., in press.

20. E. Rabinowicz, pp. 90-94 in Friction and Wear of Materials, John Wiley and Sons, Inc., New York, 1965.

21. B.J. Hockey, unpublished data.

22. B.L. Vaandrager and G.M. Pharr, "Creep of Alpha Brass Containing a Liquid Grain Boundary Phase," Scr. Metall., 18, 1337-39 (1984).

Status of Milestones

To date, all milestones have been met or are on schedule. A silicon nitride material that is reinforced by silicon carbide whiskers is currently being analyzed by transmission electron microscopy. Creep data are being collected in tension and the causes of damage in the composite will be ascertained (Milestone 311101). A paper will be written on this work by 9/89 (Milestone 311102).

Publications

S.M. Wiederhorn, B.J. Hockey and D.F. Carroll, "Creep of Two Phase Ceramics," Advances in Ceramics, Accepted for Publication.

Physical Properties of Structural Ceramics

P. H. McCluskey,* R. K. Williams, R. S. Graves, and T. N. Tiegs (Oak Ridge National Laboratory)

Objective/scope

The structural ceramics which will be used in the combustion chambers of advanced heat engines must also thermally isolate the metallic parts of the engine from the high temperature combustion gases. The ceramics being considered for this application are complex materials which are toughened by the presence of a second phase. The purpose of this task is to develop an improved understanding of the factors which determine the thermal conductivities of these structural materials at high temperatures. This study is required because the thermal conductivities of the ceramics of interest are generally not known at high temperatures, and the theory has not yet been sufficiently developed to yield reliable predictions. The influences of second phase type, content, shape, and of parallel energy transport by photons are of particular importance. At present our understanding of these variables is at best only qualitative. The two areas which will be investigated are the role of photon transport at high temperatures and the influence of second phase additions.

Technical progress

Thermal diffusivity and conductivity values for several Al_2O_3-SiC whisker composites were determined. The thermal diffusivity values spanned the range 373–1473 K and thermal conductivity data were obtained between 305 and 365 K. The thermal diffusivity was observed to decrease with increasing temperature and increase with SiC whisker content. An estimate of the thermal conductivity of the whiskers was obtained from the direct thermal conductivity measurements, but attempts to derive whisker conductivity values from the thermal diffusivity data were not successful because the laser flash method lacks the required accuracy and precision.

The specimens were subjected to two different temperature profiles to investigate the effect of thermal history on diffusivity. In the most severe case, multiple 1073–373 K quenches, radial cracks were observed in the test specimens; however, there was no change in diffusivity. The lack of sensitivity to thermal cycling appears to be related to the sample size.

In recent years there has been increased interest in the area of ceramic-ceramic composites. A primary reason for this research has been to develop a new generation ceramics having higher strength, better toughness, and therefore, greater reliability.[1,2] One such system that has been shown to have improved high temperature mechanical properties is silicon carbide whisker reinforced aluminum oxide.[3,4] In this text silicon carbide whiskers [SiC(w)] can be considered as discontinuous, single crystal fibers with approximate dimensions of 0.5 μm diameter and 30 μm length.[5]

---

*Current address: New York State College of Ceramics at Alfred University, Alfred, NY 14802.

Due to their attractive mechanical properties, Al_2O_3-SiC(w) composites have been used in, or are being considered for use in, harsh applications, such as cutting tools and advanced heat engines. While mechanical properties are extremely important in these applications, of equal importance are the heat flow properties and the ability to maintain these properties. This report discusses the energy transport through these composite materials as a function of silicon carbide whisker content, and also contains results on the ability of these materials to maintain these properties after several thermal cycles.

Experimental procedures

All specimens used in the present study were machined from composites fabricated at Oak Ridge National Laboratory. The preparation is described in detail elsewhere.[5] The rice-hull-derived SiC whiskers had an average diameter of about 0.5 μm and an aspect ratio of about 50. Three different SiC(w) loadings were investigated: 10, 20, and 50 vol %. The specimens with 10 and 20 vol % SiC(w) were 100% theoretical density after hot pressing. A typical microstructure is shown in Fig. 1. Hot-pressing temperatures were 2073 K for 10 vol % and 2123 K for both the 20 and 50 vol %.

The disks used for diffusivity measurements were machined such that their diameter was 12.49 mm and the thickness approximately 1.0 mm. The disks were polished to uniform thickness (to within ±0.003 mm) across the sample. In each case, the disks were fabricated so that the direction of heat flow would be parallel to the hot-pressing axis, or perpendicular to the SiC whiskers.

Thermal diffusivity, α, was measured from 373-1473 K using the laser flash[6] techniques.* The sample was held in a resistance heated tantalum furnace under vacuum ($P < 5 \times 10^{-6}$ torr). One face of the uncoated sample was subjected to a single 50 j pulse of a glass-Nd laser,† and the rear face transient temperature response was monitored using an IR detector.‡

The procedure given by Koski[7] was used to calculate the thermal diffusivity. The one-dimensional calculations include the effects of finite pulse time and radiant heat losses and α-values are obtained at 30, 50, and 70% of the temperature rise time. These three values are averaged to yield the α-value for each pulse. The specimen temperature was monitored using a W5-Re/W26-Re thermocouple adjacent to the rear face. Before the laser flashed, the test temperature was required to vary by less than 2 K for 20 s.

Two standard samples were run to determine the accuracy and repeatability of the results. The α-values for SRM 1462 (austenitic stainless steel) were computed from the density, specific heat,[8] and thermal conductivity.[9] Thermal diffusivity values for SRM 1421 (electrolytic iron) were obtained from the literature.[10] The results obtained are shown in Fig. 2. Except at low temperatures and in the vicinity of the Curie point, the α-values for SRM 8421 are within ±4% of the accepted values. The agreement is better for SRM 1462, since all of the α-values agree with the expected results within experimental uncertainty.

---

*Dynatech Scientific, Inc., Cambridge, MA; Model: Alpha-Metric.
†Laser Applications, Inc., Winter Park, FL; Model: 9300 Pulse System.
‡Judson Infrared, Inc., Montgomeryville, PA; Model: J10DM204-R02M-15.

Y211657

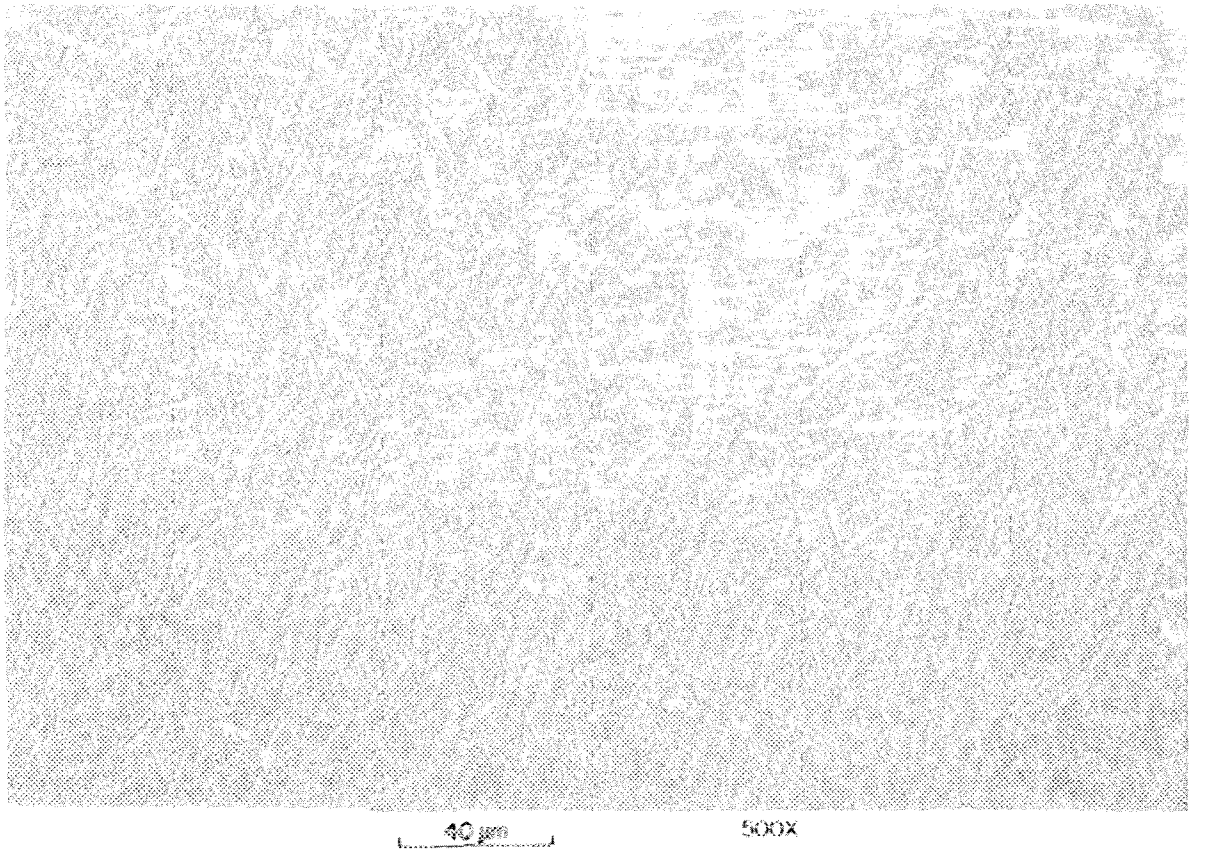

Fig. 1. Microstructure of Al_2O_3 - 20 vol % SiC whiskers. Section is perpendicular to the hot-pressing axis.

Five measurements were made at each temperature. For the composites, the range of these five values decreased from about ±3% at 373 K to ±0.7% at 1473 K. The reported α-values are the average of these five measurements. Data were collected on both heating and cooling; however, only heating data are reported since the two sets of values never differed by more than about 0.5%. Measurements were made at 373, 573, 973, 1173 and 1473 K.

The thermal diffusivity data were supplemented with direct thermal conductivity, λ, measurements which were made over a limited temperature range, 305 to 365 K. Although they only span about 60 K, these results have an absolute uncertainty of no more than about ±3%,[11] and the repeatability is about 0.3%. These direct measurements are useful when small differences in λ must be detected.

To investigate the effect of thermal cycling and thermal shock, two different temperature profiles were used. Initially, cycling was carried out in the tantalum furnace. The specimen was cycled between 773 and

ORNL-DWG 88-16274

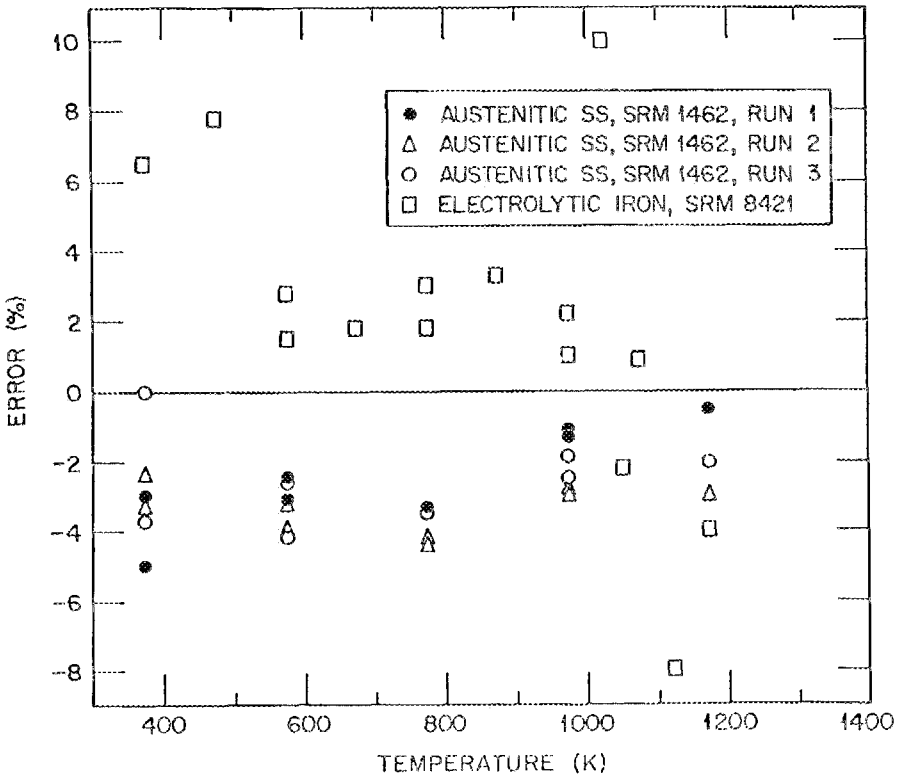

Fig. 2. Experimental thermal diffusivity data for two standard materials show satisfactory operation of the apparatus.

1473 K four times. The heating and cooling rate in this case was approximately 100 K/min. When no change in diffusivity was observed, a second, more severe treatment was employed. This second treatment involved heating the sample to 1073 K in a resistance-heated furnace, allowing a 10-min soak time, then quenching to boiling water. The diffusivity was measured after one and ten quenches.

Experimental results

The thermal diffusivity data for as-fabricated composite samples are given in Table 1, and the thermal conductivity results are shown in Table 2. The latter values were lowered by 1–2% as suggested by tests on standard samples.[12] The thermal diffusivity data are shown in Fig. 3. The thermal conductivity values shown in Table 3 were derived from these data using literature values for the specific heat[13,14] and appropriate density data. The two sets of thermal conductivity values are compared in Fig. 4, which includes other data for hot-pressed Al_2O_3[12] from the same apparatus. The results from the diffusivity apparatus appear to be a few percent too low at 373 K, and the scatter is significant.

Table 1. Measured thermal diffusivity (m^2/s) for Al_2O_3 whisker composites for each composite tested

Temperature (K)	10 vol % SiC ($\times 10^6$)	20 vol % SiC ($\times 10^6$)	50 vol % SiC ($\times 10^6$)
373	6.65	7.66	9.33
573	4.00	4.54	6.58
773	2.84	3.28	5.12
973	2.20	2.60	4.27
1173	1.79	2.13	3.50
1473	1.41	1.69	2.68

Table 2. Thermal conductivity values for an Al_2O_3 - 20 vol % SiC composite sample

Temperature (K)	Thermal conductivity ($W^{-1}m \cdot K$)
303.09	34.25
331.43	31.48
362.75	29.02

Discussion

The results presented define the effects of temperature and whisker content on the properties of the composites and also give some indication as to the stability of their properties. As shown in Table 3, the thermal conductivity decreases with temperature and increases with SiC whisker content. These variations should be consistent with the magnitudes and temperature variations of the thermal conductivities of the two components, but the thermal conductivity of SiC whiskers is not known. This uncertainty is due to the unknown role of defects in limiting the thermal conductivity of the whiskers. Although the thermal conductivity of dense, pure SiC exceeds that of Al_2O_3,[15] this may not be true if the effects of impurities and imperfections are significant. At room temperature, the range of thermal conductivity values reported for SiC samples[15] is nearly two orders of magnitude. At present, the only thermal conductivity estimate for SiC whiskers was obtained from measurements on mullite matrix composite.[16] This result indicates that the thermal conductivity of rice-hull-derived whiskers is only 5% of the value for good cubic crystals.[17]

ORNL-DWG 88-16276

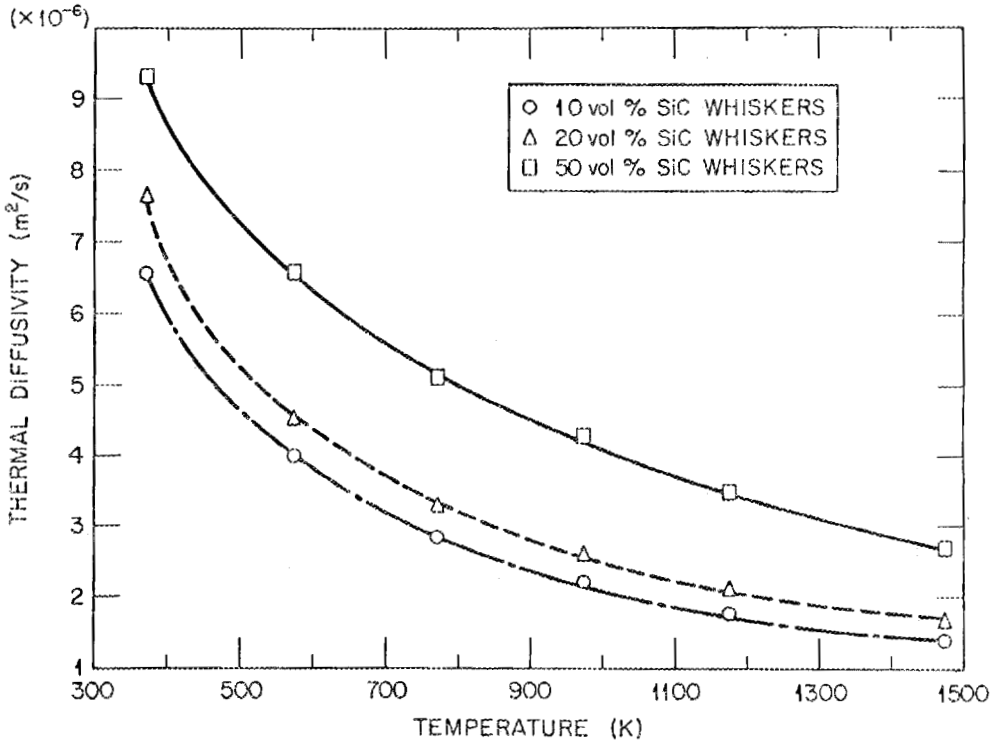

Fig. 3. Experimental thermal diffusivity data for three Al_2O_3 - SiC whisker composites.

Table 3. Thermal conductivity values for Al_2O_3 - SiC whisker composites as calculated from thermal diffusivity measurements

Temperature (K)	Thermal conductivity ($W^{-1}m \cdot K$)		
	10 vol % SiC	20 vol % SiC	50 vol % SiC
373	23.6	27.4	28.6
573	17.1	19.1	25.4
773	13.0	14.6	21.4
973	10.5	12.0	18.5
1173	8.77	10.2	15.8
1473	7.10	8.4	12.5

ORNL-DWG 88-16275R

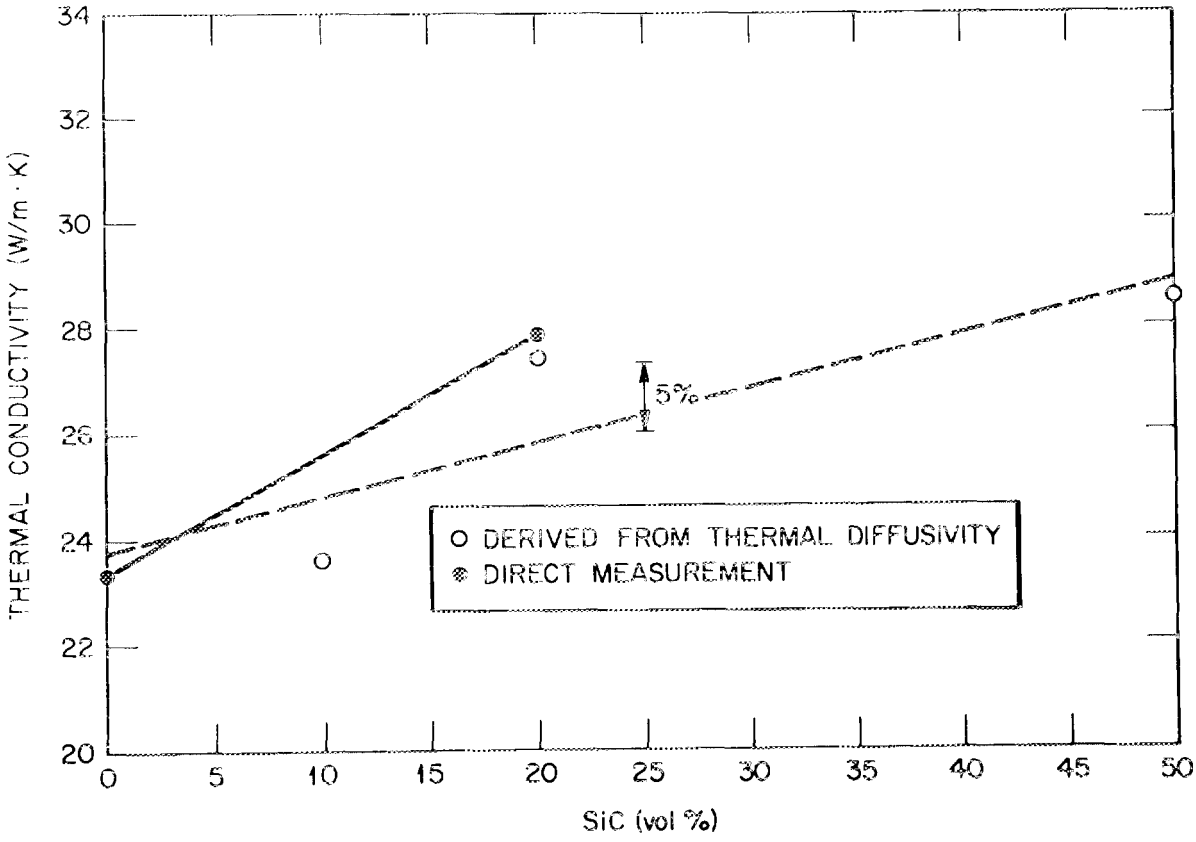

Fig. 4. Comparison of directly measured thermal conductivity values with results derived from thermal diffusivity data. The comparison is made at 373 K, and the thermal conductivity data were extrapolated from 365 to 373 K.

A similar estimate can be obtained from the direct thermal conductivity measurements for Al_2O_3 and Al_2O_3 - 20 vol % SiC shown in Table 2. The Bruggeman formula[16] for heat flow perpendicular to the aligned whiskers:

$$\left(\frac{\lambda_m - \lambda_c}{\lambda_m + \lambda_c}\right) V_m = \left(\frac{\lambda_c - \lambda_p}{\lambda_c + \lambda_p}\right) V_p \ , \qquad (1)$$

was used in the calculations. In this equation, the subscripts m, c, and p refer to the matrix phase (m), composite material (c), and whiskers (p). V_m and V_p are the volume fractions of matrix and whiskers. The results show the temperature variation expected for a phonon conductor:[12,17]

$$\lambda_{SiC}^{-1} = 0.01411 + 4.888 \times 10^{-6}\ T \ (T \text{ in K, } W^{-1}m{\cdot}K) \ . \qquad (2)$$

This result is about a factor of two higher than the value derived by Russell et al.,[16] and is about a factor of six smaller than values for the best crystals studied to date. This reduction is too large to be caused by the external boundaries of the whiskers. This effect[18,19] can only account for about a 25% reduction in the thermal conductivity. Internal planar defects spaced at an interval of about 2×10^{-8} m would be required to produce the reduction in λ.

At ambient temperature, the particle and matrix thermal conductivities only differ by about a factor of two and the calculations are not very sensitive to the choice of composite formula or whisker orientation. Fricke[20] derived formulas for oriented composites by generalizing Maxwell's equation. For similarly oriented whiskers, the Bruggeman and Fricke λ_c values differ by less than 1% for 20 vol % of dispersed phase. The Fricke equations also show that changing from heat flow perpendicular to parallel to the whiskers should alter λ_c by only about 7%.

The calculated whisker thermal conductivity values are sensitive to the accuracy of the experimental data. Changing λ_m and λ_c by 0.3% produces a 3% change in the λ_p value calculated from Eq. (1). This sensitivity arises because the calculation involves conductivity differences, and 0.3% is not unrealistic for the thermal conductivity data. For larger uncertainties the λ_p changes increases proportionately, and it should be noted that Eq. (1) allows both negative and imaginary λ_p solutions.

Experimental accuracy seems to be the factor which limits the value of λ_p values based on thermal diffusivity data. Using literature[15] data for the λ of Al_2O_3, and the composite values shown in Table 3 yields negative λ_p values at all temperatures.

As shown in Fig. 4, the λ values derived from α data on the composites appear to be too low, and there is evidence[12] that the literature data for Al_2O_3 are too high. With lower matrix conductivity materials, the λ differences are better defined and the diffusivity approach might be expected to be more successful.

The thermal diffusivity data do yield a reasonably clear picture of the effects of temperature and whisker content on the composite conductivity, and this result can be explained in terms of the matrix and whisker conductivities. The matrix conductivity is well known,[15] and the whisker conductivity can be defined by assuring that the low temperature value, ~60 $W^{-1}m \cdot K$, fixes the magnitude of this contribution while its temperature dependence is defined by other investigations[15] which have been carried out at higher temperatures. Averaging data from several investigations[14] yields:

$$\lambda_{SiC}^{-1} = 0.0073 + 2.56 \times 10^{-5}\ T\ (T \text{ in K, } W^{-1}m \cdot K) \quad . \qquad (3)$$

The temperature coefficient estimated by Slack[17] is about 70% of the value given in Eq. (3).

A comparison between the measured and estimated thermal conductivities for the composites is shown in Fig. 5. Except at the lowest temperatures, the agreement is ~10%. The difficulty at lower temperatures probably arises because the experimental data tend to be somewhat low and the literature data for Al_2O_3 seem to be too high.[12] This analysis shows that the whiskers produce a larger λ enhancement at high temperatures because the thermal conductivity of the whiskers is less dependent on temperature than that of Al_2O_3.

ORNL-DWG 89-5956

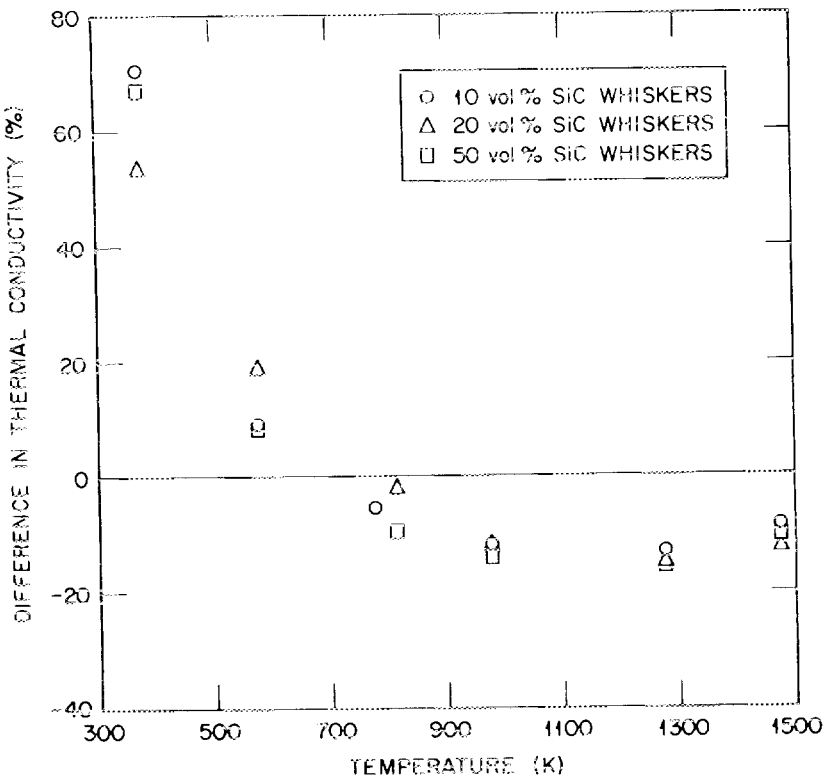

Fig. 5. Comparison of thermal conductivity values derived from thermal diffusivity measurements with values derived from composites theory and the thermal conductivities of Al_2O_3 and SiC. The comparison assumes that the measured values are correct.

Neither of the thermal treatments affected the thermal diffusivity of the composites. Samples of 10 and 20 vol % subjected to 10 quench cycles into boiling water were examined by both optical microscopy and scanning electron microscopy. Radially oriented surface cracks formed in the samples but attempts to identify microcracks by decoration with $AgNO_3$ were negative. Thus the microstructural evidence is consistent with the thermal diffusivity results. Previous studies[5] have shown that the flexural strength of 2.6-mm-thick samples is degraded by 10 quenching cycles. However, as Becher points out,[21] for the 1-mm-thick thermal diffusivity samples quenching from 700°C into boiling water may not be sufficient to generate microcracks.

References

1. K. M. Prewo, J. J. Brennan, and G. K. Layden, *Am. Ceram. Soc. Bull.* 65, 305–13 (1986).

2. P. O. Shalek et al., *Am. Ceram. Soc. Bull.* **65**, 351–56 (1986).
3. P. F. Becher and G. C. Wei, *J. Am. Ceram. Soc.* **67**, C267–C269 (1984).
4. G. C. Wei and P. F. Becher, *Am. Ceram. Soc. Bull.* **64**, 298–304 (1985).
5. T. N. Tiegs and P. F. Becher, *J. Am. Ceram. Soc.* **70**, C109–C111 (1987).
6. W. J. Parker et al., *J. Appl. Phys.* **32**, 1679–84 (1961).
7. J. A. Koski, pp. 94–103 in *Proc. 8th Symp. on Thermophysical Properties,* Vol. II ed. J. V. Sengers, American Society of Mechanical Engineers, New York, 1982.
8. E. Fitzer, *Thermophysical Properties of Solid Materials Project Section II Cooperative Measurements on Heat Transport Phenomena of Solid Materials at High Temperature,* AGARD Report No. 606, 1973, p. 58.
9. J. G. Hust and A. B. Lankford, *Update of Thermal Conductivity and Electrical Resistivity of Electrolytic Iron, Tungsten and Stainless Steel,* National Institute of Standards and Technology Spl. Publ. 260–90, 1984, p. 16.
10. Y. S. Touloukian et al., *Thermal Diffusivity*, IFI Plenum, New York, 1973, p. 82.
11. R. K. Williams et al., *J. Nucl. Mater.* **115**, 211–215 (1983).
12. R. K. Williams et al., *J. Appl. Phys.* **61**, 4894–4901 (1987).
13. National Institute of Standards and Technology, SRM-720 Data Sheet, Washington, DC (1982).
14. Y. S. Touloukian and E. H. Buyco, *Specific Heat, Nonmetallic Solids,* IFI/Plenum, New York, 1970, p. 448.
15. Y. S. Touloukian et al., *Thermal Conductivity, Nonmetallic Solids,* IFI/Plenum, New York, 1970, p. 93, 585.
16. Laura M. Russell et al., *J. Am. Ceram. Soc.* **70**, C226–C229 (1987).
17. G. A. Slack in *Solid State Physics*, ed. F. Seitz and D. Turnbull, Academic, New York, 1979, Vol. 34, p. 1.
18. P. G. Klemens, *Int. J. Thermophys.* **2**, 55–62 (1981).
19. R. A. Brito-Orta, Ph.D. Thesis (University of Connecticut, Storrs, CT, 1982).
20. H. Fricke, *J. Phys. Chem.* **57**, 934–937 (1953).
21. P. F. Becher, *J. Am. Ceram. Soc.* **64**, C17–C18 (1981).

Effect of Translucence of Engineering Ceramics on Heat Transfer in Diesel Engines

Syed Wahiduzzaman and Thomas Morel (Integral Technologies Incorporated)

Objective/scope

Ceramic materials are being used as thermal barrier materials, separating the engine metal substructure from the convective and radiative heat fluxes originating in the combustion gases. The heat transfer through the ceramic layer to the substructure will be increased by any translucence, which would allow a part of the radiation heat flux to pass through the barrier material. To quantify the effect of translucence of engineering ceramics on the heat transfer in diesel engines, Integral Technologies has conducted analytical studies using detailed computer codes which describe a realistic engine thermal environment including gas-to-wall heat fluxes, as well as the combined radiation/conduction heat transfer through a thermal barrier layer. A detailed parametric study was carried out in which the following parameters were varied, and their effect on heat barrier effectiveness was studied: 1) material absorption coefficient, 2) material conductivity, and 3) material thickness. An analysis of the results yielded bounds on critical properties, beyond which there is a reason for concern about this effect. Also, suggestions were made for methods to control any adverse effects.

In the experimental portion of this work, data were acquired describing the radiation properties of several engineering ceramics. The objective is to obtain the specific information needed for the analytical part of this work. This includes the absorption coefficient, scattering albedo and surface reflectivities of the materials. In order to obtain the data, specialized samples of the materials were fabricated. Measurements of reflectance and transmittance were obtained, and from these the desired radiation properties will be deduced using an analytical data reduction technique.

Technical progress

During this period, work was conducted on an experimental portion of a broader study undertaken to assess the effects of translucence of ceramic materials used as thermal barrier coatings in diesel engines. In an earlier analytical work a parametric study was performed, varying several radiative properties over ranges typical of engineering ceramics, thereby identifying the most important radiative properties and their impact on in-cylinder heat transfer. In the current study these properties were experimentally determined for several specific zirconia coatings considered for thermal barrier applications in diesel engines.

The methodology of this study involved formulation of a model capable of describing radiative transfer through a semitransparent medium as a function of three independent model parameters, i.e., absorption

coefficient, scattering coefficient and refractive index. A set of radiative measurements was then fitted to this model by optimization of the above model parameters. The radiative measurements were comprised of hemispherical reflectance and transmittance spectra from samples of several different thicknesses of each ceramic under collimated (unidirectional) illumination. A four-flux model was required to extract accurate radiative properties from the measurements.

For the zirconia-based ceramics investigated in this study, it was concluded that for usual coating thicknesses (1.5-2.5 mm) these ceramics are optically thick and hence, are effective as radiative heat transfer barriers. These ceramics possess high scattering coefficients and low absorption coefficients causing them to be highly reflective (60-80%) in the spectral region where thermal radiation is important. As a consequence, only a small portion of the incident energy is captured by the coating system and transmitted to the metal substrate via conduction.

The convective heat flux, which is driven by the temperature differential between the gas and the ceramic-gas interface, was found to be highly dependent on the location where radiative energy is absorbed. If a significant amount of energy is absorbed near the surface, as is the case for ceramics investigated, surface temperature is raised causing convective heat flux to be decreased. On the other hand, for ceramics that are transparent the radiative energy is absorbed at the ceramic/metal interface and consequently, the gas/ceramic interface remains relatively cool promoting convective heat transfer.

The performance of the investigated ceramics and the mechanism of heat transfer were found to depend on surface condition, specifically on soot deposition. If the surface fouling is small, the ceramics behaved as described above, i.e., as optically thick materials characterized by high scattering coefficient and low absorption coefficient. In this case, the energy transport is primarily due to convective heat transfer since only a small fraction of the incident radiant energy can be trapped by the coating. On the other hand, if the coating surface is totally covered by soot, its performance will be similar to that of a clean optically thick material characterized by small scattering coefficient and high absorption coefficient. In this case, there will be a significant increase in radiation heat transfer absorbed at the surface with an associated decrease in convective heat transfer.

Although the coatings investigated in this study were found to be optically thick at or near nominal thicknesses (2.5 mm), this is by no means representative of all engineering ceramics. For example, based on available literature data, monolithic ceramics have been found to be more transparent than the ceramics investigated in this study and, consequently, are less effective as radiation heat transfer barriers.

Based on the results, it is concluded that ceramics with high scattering and low absorption coefficients are the most suitable for

engine applications where in-cylinder surfaces can be expected to remain clean. If surfaces are expected to be sooted an opaque ceramic characterized by either high scattering coefficient and/or high absorption coefficient should be chosen in order to bring about a substantial decrease in convective heat flux. Thus, to insure the optimum thermal barrier operation for either clean or heavily sooted surfaces, a ceramic material with high scattering coefficient provides the best choice.

Status of Milestones

Report was completed and delivered to ORNL in October, 1988.

Publications

None.

Project Data Base

B. L. P. Booker (Oak Ridge National Laboratory)

Objective/scope

The objective of the task is to develop a comprehensive computer database containing the experimental data on properties of ceramic materials generated in the overall program effort. This computer system is intended to provide a convenient and efficient mechanism for the compilation and dissemination of the large amounts of data involved. The database will be made available in electronic form to all project participants. In addition, periodic hard-copy summaries of the data, including graphical representation and tabulation of raw data, will be issued to provide convenient information sources for project participants.

Technical progress

The database has expanded to 2519 test results currently on disk, and another 730 results already coded and awaiting entry. These data cover 73 materials in 11 classifications. Eleven types of test data from seven laboratories are stored at present. A detailed analysis of the current database contents is shown in Table 1.

Test data collection from the various testing laboratories has been very slow, so most of the newly entered data have come from past semiannuals and bimonthly reports. The wealth of information generated in past years contained in those sources could not be omitted from the database. One problem with this method, though, is that the authors often represented their test results only graphically, or summarized with several tests lumped together. If summarized in a table, the data was entered and marked in the specimen identification field as summary data, including how many tests were represented by the summary line, if that information was known. No attempt was made to store graphical data due to the possible error in judgment of point values and lack of corresponding test details.

Much emphasis has been placed on the need to store complete and accurate material characterization and processing information with the test data. To accomplish that, efforts are being made to record all process, chemical, and thermal histories as well as microstructural data, vendor specifications, and general intrinsic characterization information for all the materials on which tests are being, or have been, run. Table 2 contains the present file structures the system uses to store all the nontest information. Any additions or comments on those formats are welcome. Beginning with the next database summary report, each material for which test data are being reported will be listed with its characterization information in a special section of the report.

In addition to the test results and material characterization information, the system also contains notes on the apparatus and methods used on tests where such information was available. Ceramics seem to be more sensitive to testing procedures than metals and, therefore, require more extensive descriptions of the test environment. Table 3 contains the format for this information.

Table 1. CTAHE database contents as of September 30, 1988

Material	MOR	Toughness	Cyclic Fatigue	Density	X-Ray Diffraction	Welded Joint Shear	Thermal Expansion	Stress Rupture	Tensile	Interrupted Fatigue	MOE	Totals
1985 (TTZ)	165				3							168
1986H (TTZ)	155				3							158
1986S (TTZ)	125				3							128
Al2O3									3			158
Al2O3+SiCw									11			11
AMTL-A (PSZ)	3	6		3				3				15
AMTL-B (TZP)	3	3		3							18	27
AMTL-C (TTZ)				25							18	43
AMTL-D (TTZ)	3	5		3				4				15
AMTL-E (TTZ)	3	3		3							17	26
AMTL-F (FSZ)	1										20	21
AMTL-G (TTZ)				20				3				23
AMTL-H (TTZ)	3	8		3				1				15
AMTL-I (TZP)	3	3		3								9
AMTL-J (FSZ)	1	1		25								27
AMTL-K (TTZ)				25							19	44
AMTL-L (PSZ)	3	10		3				4				20
AMTL-M (TZP)	1			1								2
AMTL-N (TZP)				25								25
AMTL-P (TZP)	3	4		3								10
AMTL-Q (TZP)	1			3								4
AMTL-R (TZP)	1	1		2								4
AMTL-U1 (ZTA)	3	3						4			3	13
AMTL-U2 (ZTA)	4	4						3			4	15
AMTL-U3 (ZTA)	3	3						2			4	12
AMTL-U4 (ZTA)	2	3						4			3	12
AMTL-U5 (ZTM)	2	2									2	6
AMTL-U6 (ZTM)	2	2									2	6
CTZP	57											57
CZ-203 (TTZ)	60											60
DTA-AZ301	115											128
GTE PY6 (Si3N4)	20	4		5	26		8					63
HEXOLOY (SiC)	20	3		5	17		8					53
MS-PSZ	125		25			57				54		261
NORT/XL144 (Si3N4)	40	4		6	23		8					81
PSZ-Z201	25											25
SiC-WRAI	59											59
SiNSiCw	19	15										34
SN-4 (Si3N4)	19											19
SNW-1000			15						51			66
TASZiC (TTZ)	89				3							92
TS-PSZ	12		19						8	161		200
TZP-110	80											80
YTZP-XS241	15											15
Z-191 (TTZ)	183	1		1	3							188
Z-201(TTZ)	92				8							100
Z-701 (TTZ)	60											60
ZIRCOA 2120 (TTZ)	3	9		4								16
ZTA-XS121	13											168
TOTALS:	1596	97	59	171	89	57	24	28	73	215	110	2519

Table 2. Material characteristics information file structure

```
Material name
Material class
Batch or lot identification
Fabricator
Fabricator's identification
Vintage
Primary matrix
Stabilizer
Trace elements found
Intrinsic properties at room temperature:
  Density
  Modulus of elasticity
  Modulus of rupture
  Hardness test type
  Hardness value
  Thermal expansion coefficient
  Coefficient of friction
  Poisson's ratio
  K_IC
  Weibull modulus
Processing history:
  Powder 1 |
  Powder 2 | -------------------------> Powder characterization:
  Powder 3 |                               Powder name
  Powder 4 |                               Chemistry
  Binder                                   Supplier
  Dopants                                  Treatment
  Additives                                Particle size distribution
  Consolidation method                     Source of information
  Sintering details                        Comments
  Annealing details
  Crystalizing cycle
  Grinding details
  Polishing details
  Cleaning details
  Other notes
Microstructure:
  Grain morphology
  Grain size distribution
  Phases present --------------> Phase characterization:
  Boundary chemistry               Common phase name
  Average boundary size            Chemistry
  Boundary phase                   Quantity of phase present
  Porosity
  Other notes
```

Table 3. Test information file structure

Reference code – a link between test results and test characterization
Material
Batch or lot identification
Test type
Specimen geometry, if not included with results data
Testing apparatus
Tester
Testing facility
Information source
Other notes

The three levels of information in the database have now been defined: the first is the test data (stresses, strains, temperatures, etc.); the second is material information (microstructures, chemistries, processing histories, etc.); and the third is the test characterization information (equipment, methods, facilities, etc.). Linkage keys have been built-in to each file, or level, to facilitate access. For example, all test results are stored with a reference code for linking to test characterization information, and material and batch identifiers that point to specific materials information entries. The supplier's lot number is used for a batch code when available; otherwise a code is assigned to a set of data to distinguish it from other batches, or lots, of the same material. To facilitate using this linkage system, a user-friendly interface is being developed that will work within the dBASE III PLUS framework of the present system and alleviate some of the headaches frequently experienced in data chases.

Work during the next semiannual period will center around upgrading material characteristics and testing information on test data already in the system. Test data input will be concentrated on a select group of materials to be chosen soon; however, all test data submitted from individual laboratories will be given a higher priority for input whether or not they are on the selected list of materials. Further development of the file-linking user interface will continue as time and facilities allow.

Status of milestones

A summary report on the database contents as of September 1988 is in progress, but it is running behind schedule due to computer problems and unforeseen time constraints. The report, which will feature zirconia-based ceramics, should be completed by mid-November.

Publications

M. K. Booker, *Ceramics Technology for Advanced Heat Engines Program: A Summary Report*, ORNL/M-462, Oak Ridge National Laboratory, Oak Ridge, Tennessee (April 1988).

3.2 TIME-DEPENDENT BEHAVIOR

Characterization of Advanced Transformation Toughened Zirconias
J. J. Swab (Army Materials Technology Laboratory)

Objective/scope

Because of their unusual combination of properties, transformation toughened zirconias (TTZ), specifically yttria tetragonal zirconia polycrystal (Y-TZP), are leading candidates for cylinder liners, piston caps, head plates, valve seats and other components for the adiabatic diesel engine. These materials are age-hardened ceramic alloy systems and as such, they are likely to be susceptible to overaging and loss of strength after long times at high temperatures (i.e., close to the age-hardening temperatures). Accordingly, a task was initiated to define the extent and magnitude of the overaging (if any) at engine operating temperatures (1000-1200C) and the resulting impact on material performance.

It is also well known that Y-TZP's undergo a phenomenon at low temperatures (200-400C) which leads to decreases in strength and fracture toughness and that this phenomenon is accelerated by the presence of water. As a result, a preliminary study to try and determine the effects of this phenomenon has been included in this task.

Technical progress

MICROSTRUCTURE: Microstructural analysis of six TZPs has shown that the average grain size does not change with heat treatment time, Figure 1. This also shows, as one would expect, that the HIP'ed and hot pressed TZPs (KH and HIT) tend to be finer grained than the sintered materials. Figure 2-8 are examples of the microstructure of these TZPs. The Ceramatec CZ203 has a fine grained alumina phase, dark grains in Figure 7, dispersed throughout while the remaining materials have only zirconia present. Tsukuma and Takahata (1) have shown that the addition of alumina to TZP materials increases strength while decreasing the toughness.

Five of the six TZPs have also been examined by Gary Leatherman at Worcester Polytechnic Institute. Prof. Leatherman has used a Transmission Electron Microscope (TEM), to examine grain boundary phases which may be present. TEM results indicate that little, if any, grain boundary phases are present, Figure 9-14.

HIGH TEMPERATURE TESTING: Elevated temperature fast fracture of the most promising Y-TZPs has been completed, Figure 15. All four show a tremendous loss of strength at elevated temperatures, and the loss is greater as the temperature increases. The explanation of this is, as the temperature increases the tetragonal zirconia becomes increasingly stable. As a result there is no driving force for the tetragonal-to-monoclinic transformation, thus a reduction in strength.

The final results of the Stepped-Temperature Stress-Rupture (STSR) tests are shown in Figure 16a-g. STSR testing allows for rapid screening of stress-rupture behavior over a wide range of temperatures and stresses using a small number of specimens. The time of failure is denoted on the STSR plot using an arrow, with the applied stress that caused failure above the arrow. The symbols for the STSR plots are: (⇐) failure occurred upon loading at 800C; (→) survived full tests cycle through 1200C; and (↓) denotes the time of failure between loading but before the full cycle is completed.

Figure 16a-d, include the Y-TZPs which have normal time-dependent behavior. That is, as the applied stress decreases the time to failure increases. The first two TZPs, Hitachi and NGK-Locke, will be examined in further detail via long-time stress-rupture testing because they possess the best high temperature performance of the materials tested.

The anomalous behavior of the AC Sparkplug and Toshiba materials, Figure 16e-f, can not be explained at this time. However, the behavior of the Koransha "HIP'ed", Figure 16g, has been shown to be due to the oxygen non-stoichiometry of the material. (2)

References

1. Tsukuma, K. and Takahata, T., Advanced Structural Ceramics, Vol. 78, Ed. P.F. Becher, M.V. Swain and S. Somiya, (MRS Soc. Pittsburgh, PA, p123-35, 1987).

2. Swab, J.J., Katz, R.N. and Starita, C.J., "Effects of Oxygen Non-Stoichiometry on the High-Temperature Performances of an Yttria-Tetragonal Zirconia Polycrystal Material." Adv. Ceram. Mat., 3 [3] p283-4, (1988).

Status of Milestones

All FY88 milestones have been completed.

Publications

Swab, J.J., Katz, R.N. and Starita, C.J., "Effects of Oxygen Non-Stoichiometry on the High-Temperature Performance on an Yttria-Tetragonal Zirconia Polycrystal Material," Adv. Ceram. Mat., 3 [3] p283-4 (1988).

Katz, R.N., Quinn, G.W., Slavin, M.J. and Swab, J.J., "Time and Temperature Dependence of Strength in High Performance Ceramics," Inst. Phys. Conf. Ser. No. 89: Workshop Session, p53-62, IOP Publishing Ltd, (1988).

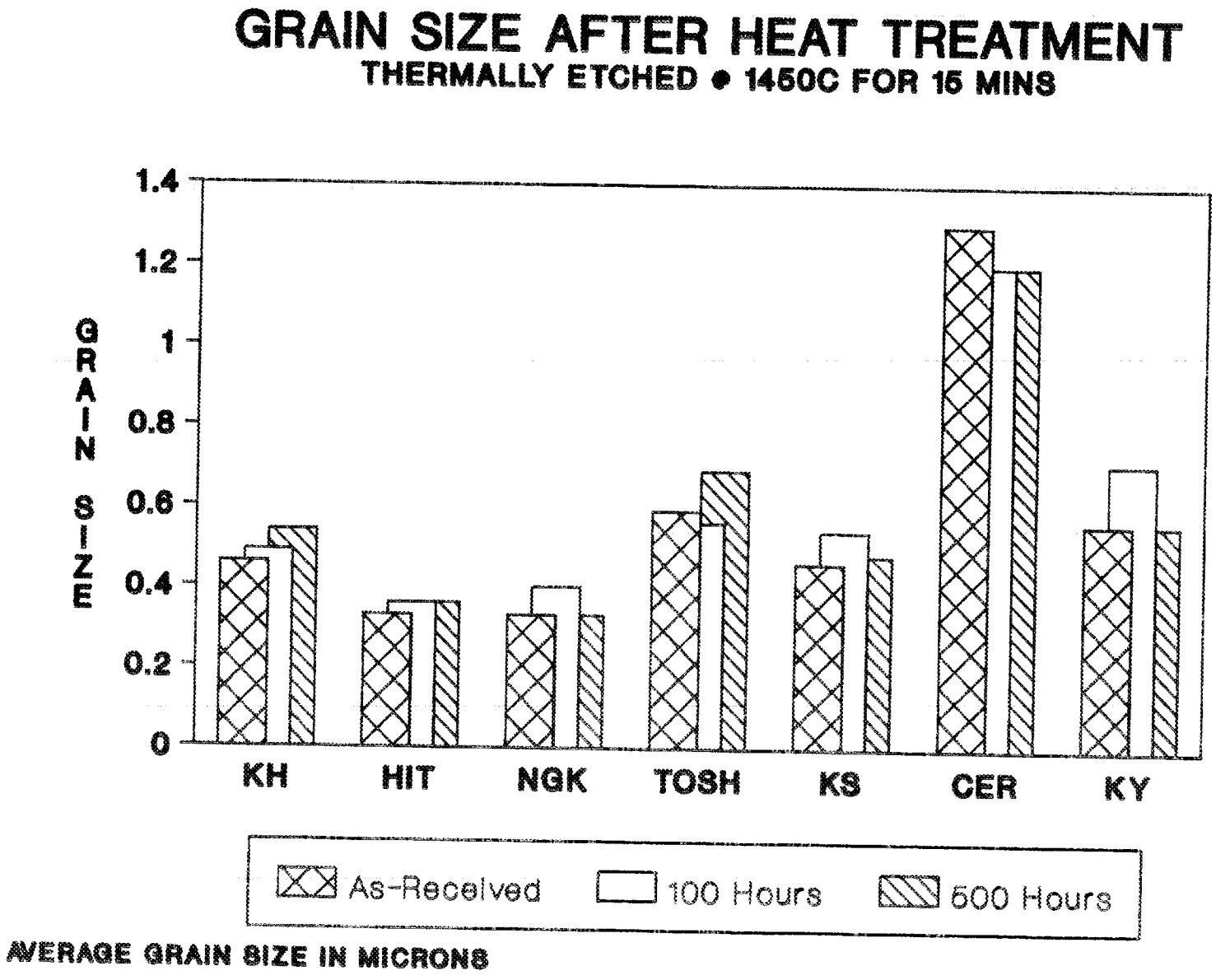
GRAIN SIZE AFTER HEAT TREATMENT
THERMALLY ETCHED • 1450C FOR 15 MINS
GRAIN SIZE
1.4
1.2
1
0.8
0.6
0.4
0.2
0
KH
HIT
NGK
TOSH
KS
CER
KY
As-Received
100 Hours
500 Hours
AVERAGE GRAIN SIZE IN MICRONS

Figure 1.

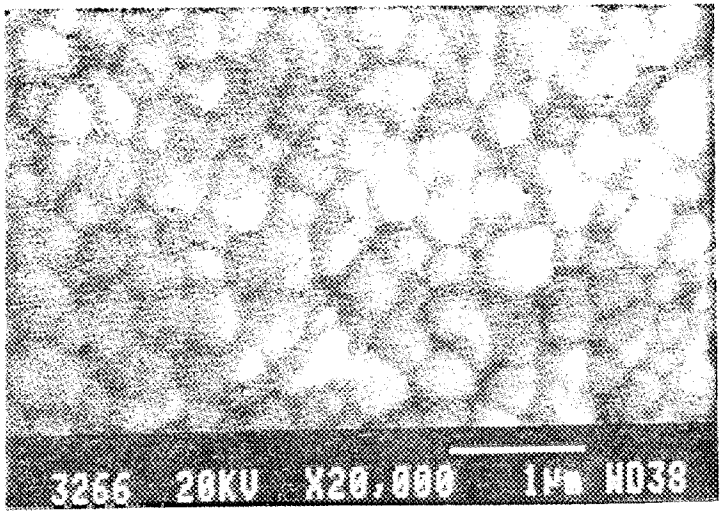

Figure 2. Koransha HIP'ed

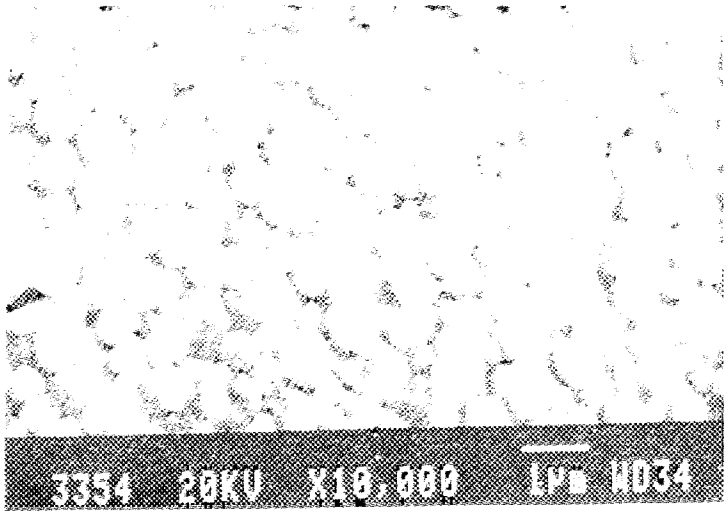

Figure 3. Hitachi

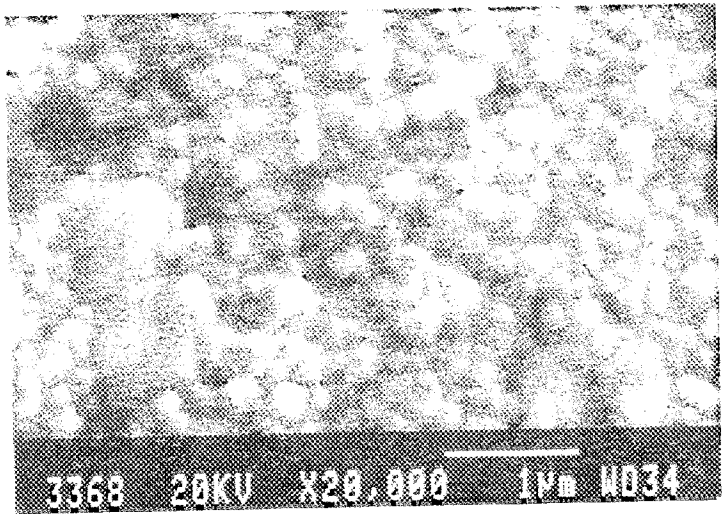

Figure 4. NGK-Locke Z-191

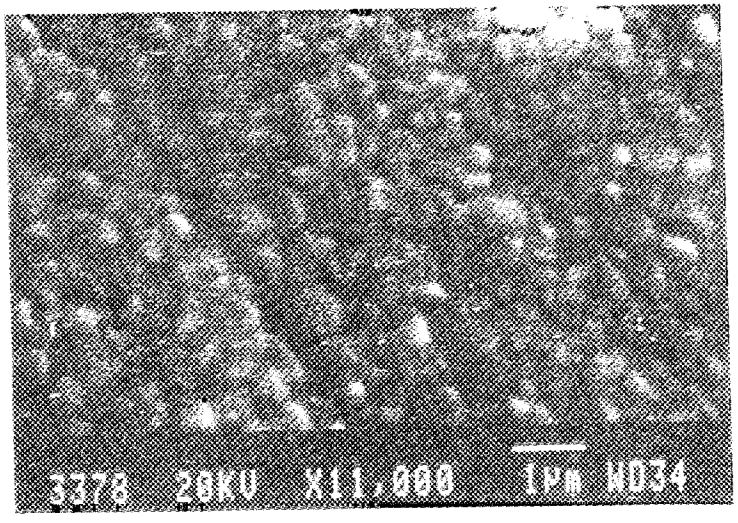

Figure 5. Toshiba "TASZIC"

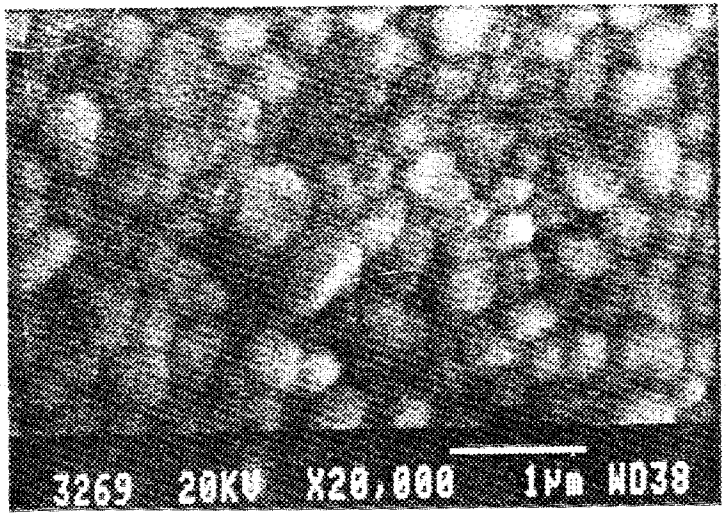

Figure 6. Koransha Sintered

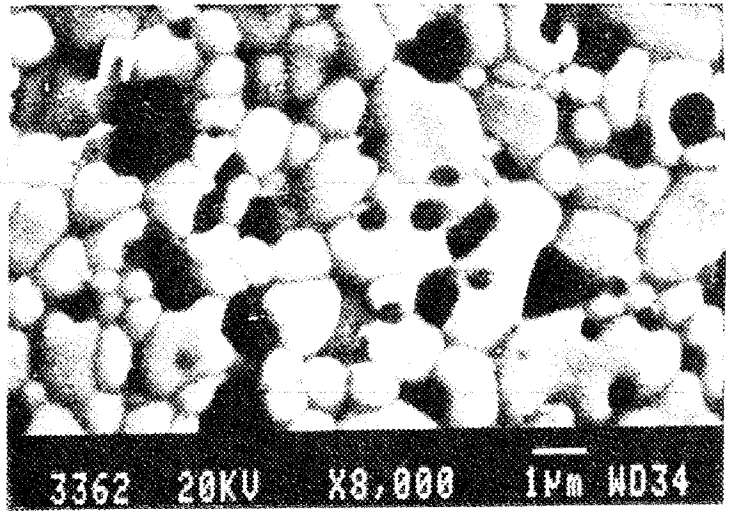

Figure 7. Ceramatec CZ203

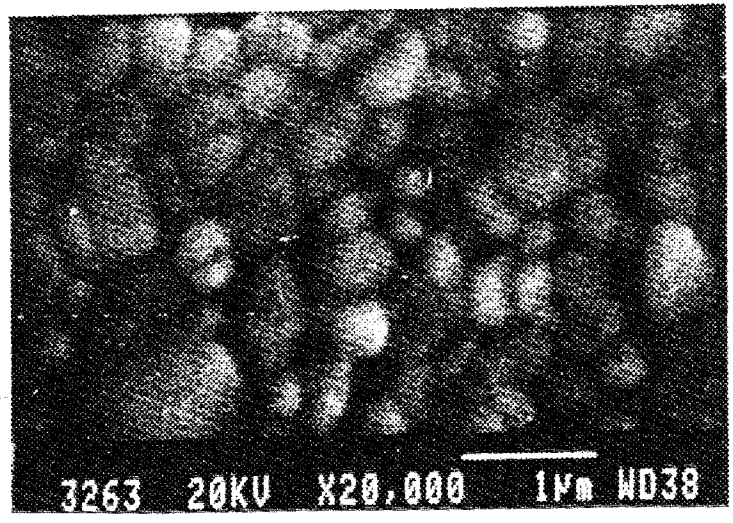

Figure 8. Kyocera Z-201

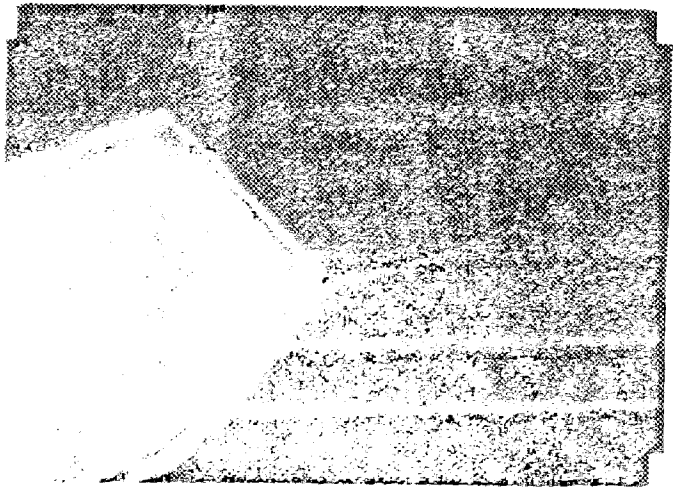

Figure 9. Koransha HIP'ed (TEM)

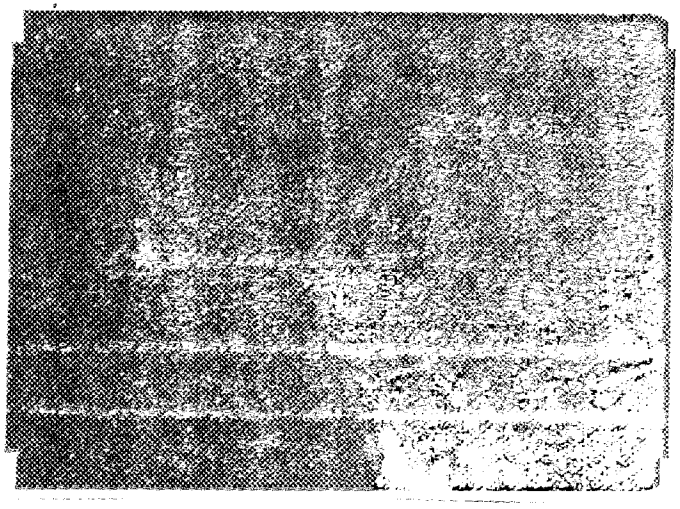

Figure 10. Hitachi (TEM)

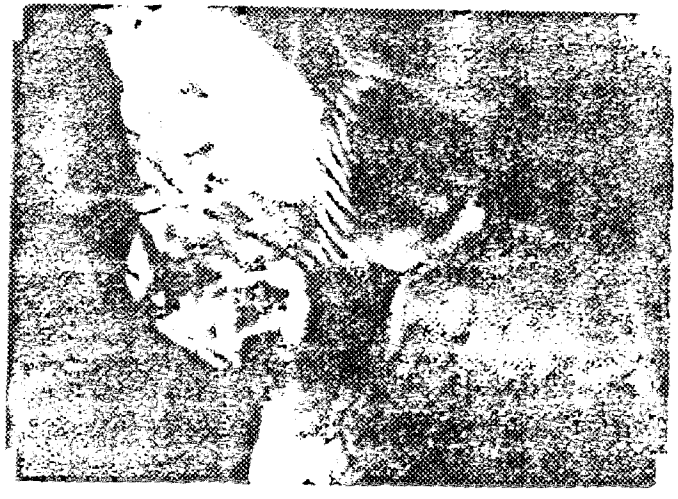

Figure 11. NGK-Locke Z-191 (TEM)

Figure 12. Toshiba "TASZIC" (TEM)

Figure 13. Koransha Sintered (TEM)

Figure 14. Kyocera Z-201 (TEM)

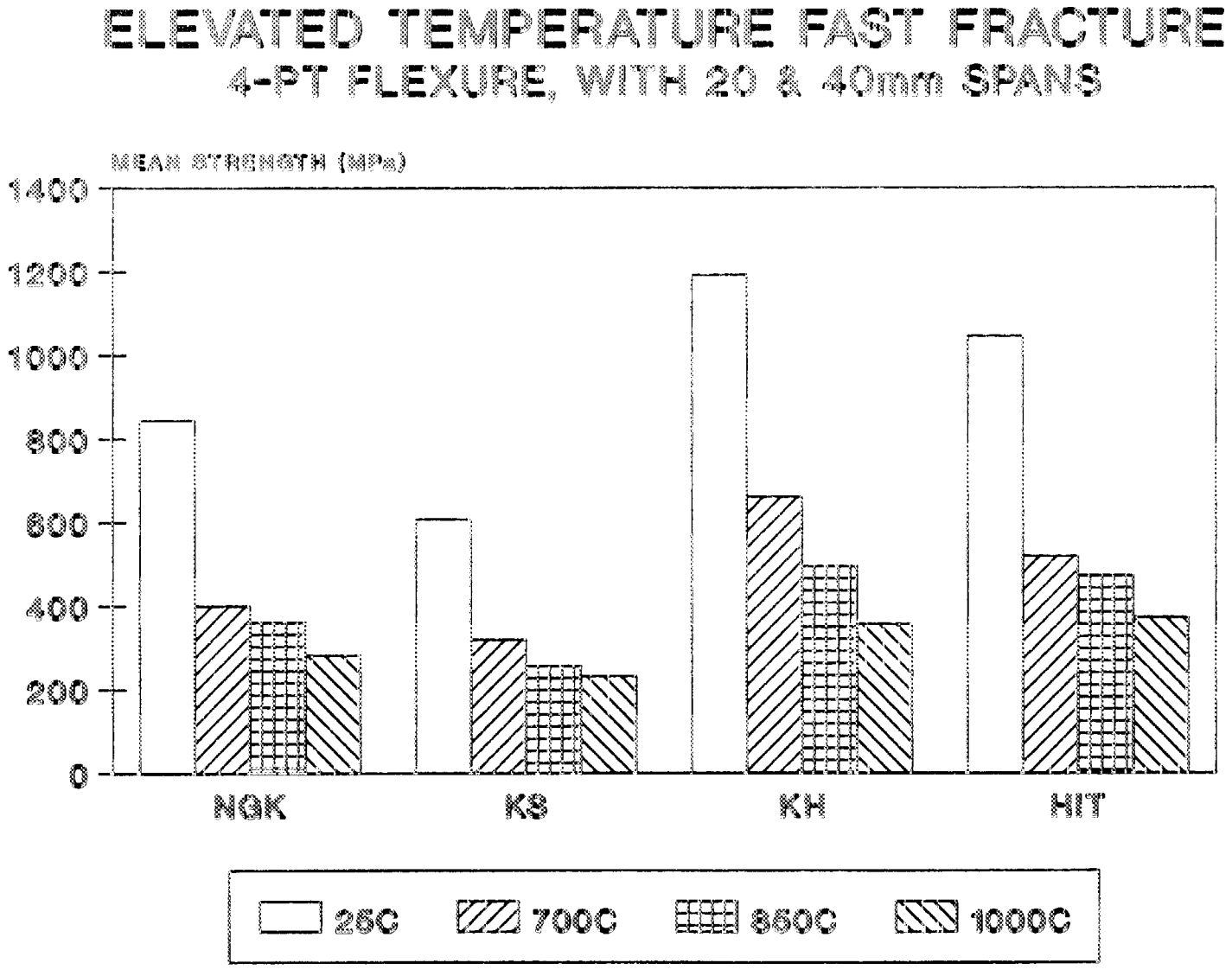
ELEVATED TEMPERATURE FAST FRACTURE
4-PT FLEXURE, WITH 20 & 40mm SPANS
MEAN STRENGTH (MPa)
1400
1200
1000
800
600
400
200
0
NGK
KS
KH
HIT
25C
700C
860C
1000C

Figure 15.

STEPPED-TEMPERATURE STRESS-RUPTURE

HITACHI 1985

STRENGTH AT 25°C = 1169 MPa

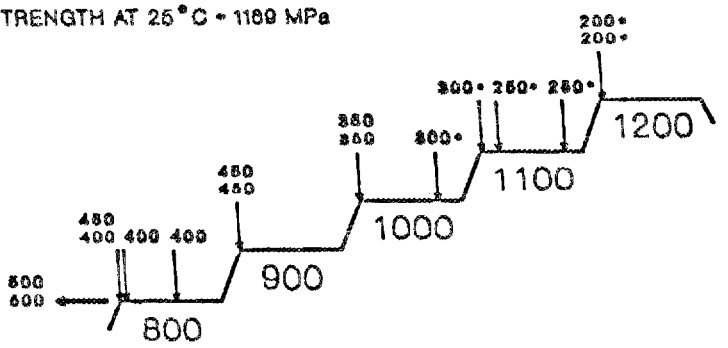

Figure 16a

NGK-LOCKE Z-191

STRENGTH AT 25°C = 873 MPa

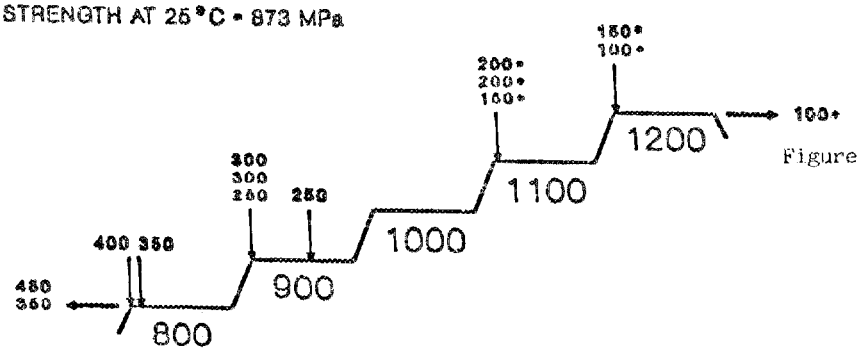

Figure 16b

KORANSHA "SINTERED" 1986

STRENGTH AT 25°C = 640 MPa

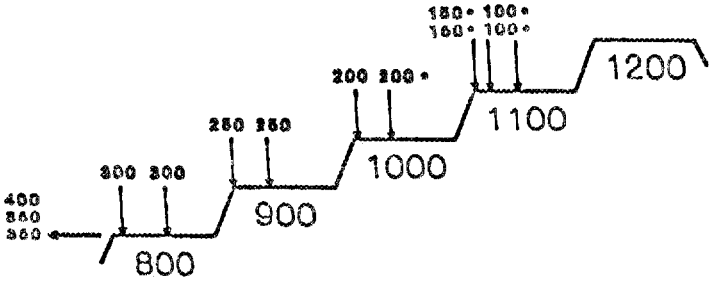

Figure 16c

- CREEP FRACTURE
- TEST TERMINATED DUE TO CREEP
- CREEP PRESENT

STRESS IN MPa
TEMPERATURE IN °C

STEPPED-TEMPERATURE STRESS-RUPTURE

KYOCERA Z-201

STRENGTH AT 25°C = 746 MPa

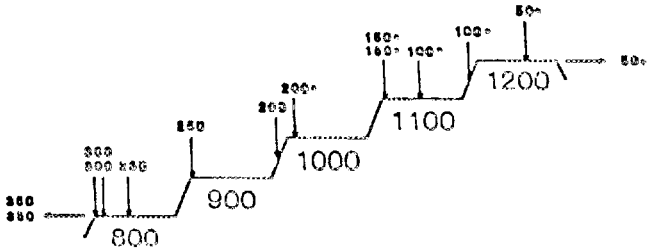

Figure 16d

AC SPARKPLUG TZP-110

STRENGTH AT 25°C = 753 MPa

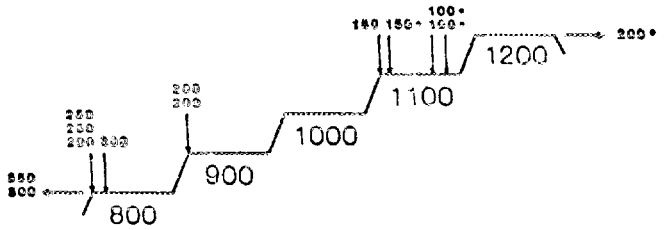

Figure 16e

TOSHIBA TASZ10

STRENGTH AT 25°C = 833 MPa

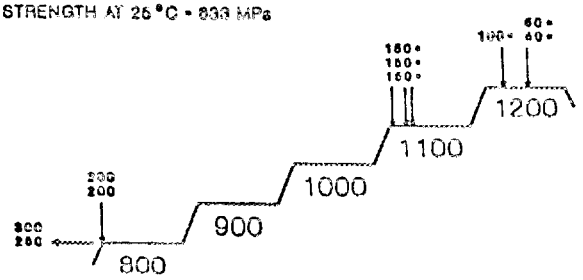

Figure 16f

KORANSHA "HIPPED" 1986: AS RECEIVED

STRENGTH AT 25°C = 1261 MPa

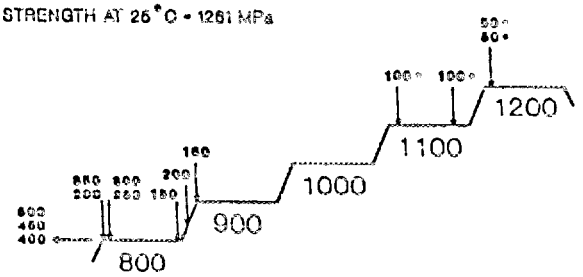

Figure 16g

- CREEP FRACTURE
- TEST TERMINATED DUE TO CREEP
- CREEP PRESENT

STRESS IN MPa
TEMPERATURE IN °C

Fracture Behavior of Toughened Ceramics

P. F. Becher and W. H. Warwick (Oak Ridge National Laboratory)

Objective/scope

Because of their excellent toughness, oxide ceramics such as partially stabilized zirconia (PSZ), dispersion-toughened alumina (DTA), and whisker-reinforced ceramics are prime candidates for many diesel engine components. The enhanced toughness of the PSZ and DTA materials is due to a stress-induced transformation (of the dispersed tetragonal ZrO_2 phase) which requires additional energy in order for catastrophic fracture to occur. However, these materials are still susceptible to slow crack growth and thus strength degradation. Also, there is evidence that at temperatures above 700°C, time-dependent aging effects can reduce the concentration of the phase involved in the transformation process leading to significant losses in toughness and strength. Again, it is essential that mechanisms responsible for both the slow crack growth and aging behavior be well understood. Similarly, the toughening behavior in whisker-reinforced ceramics and their high-temperature performance must be evaluated in order to develop materials for particular applications.

In response to these needs, studies have been initiated to examine toughening and fatigue properties of transformation-toughened and whisker-reinforced materials. Particular emphasis has been placed on understanding the effect of microstructure upon processes responsible for time-dependent variations in toughness and high-temperature strength. In addition, fundamental insight into the slow crack growth behavior associated with these materials is being obtained.

Technical progress

The time to failure (t_f) results for fine-grained (1 to 2 μm) aluminas reinforced with 20 vol % SiC whiskers at temperatures of 1000, 1100, and 1200°C in air when subjected to various applied stress (σ_{1A}) levels are shown in Fig. 1. Note first that the results include four-point flexure tests for samples taken from three to four different hot-pressed billets of alumina-20 vol % SiC whiskers. Thus, the results are displayed as data bands which simply encompass all the data. Several features of the data are noteworthy.

First is the level of applied stress required to generate failures within 6 to 10 weeks ($3.5\text{-}6 \times 10^{-6}$ s). At 1000°C at applied stresses below 80% of the 1000°C fast-fracture strength, failure did not occur for times up to 14 weeks. In fact, samples subjected to these lower stresses exibited improved fracture strengths when the tests were interrupted after 6 to 8 weeks and the samples were rapidly loaded to failure at 1000°C, as indicated in Table 1. For tests at 1100°C, applied stresses of less than 70% of the fast-fracture strength at 1000°C did not result in failure for times of up to 7 weeks. Again, samples which had not failed when subjected to stresses <70% of the fast-fracture strength exhibited increased strengths when the samples were rapidly loaded to failure at the end of the 6- to 7-week stress exposures (see Table 1).

At 1000°C and 1100°C, failure at stresses sufficient to result in time-dependent failure was characterized by a region of apparent slow

ORNL-DWG 88-12524

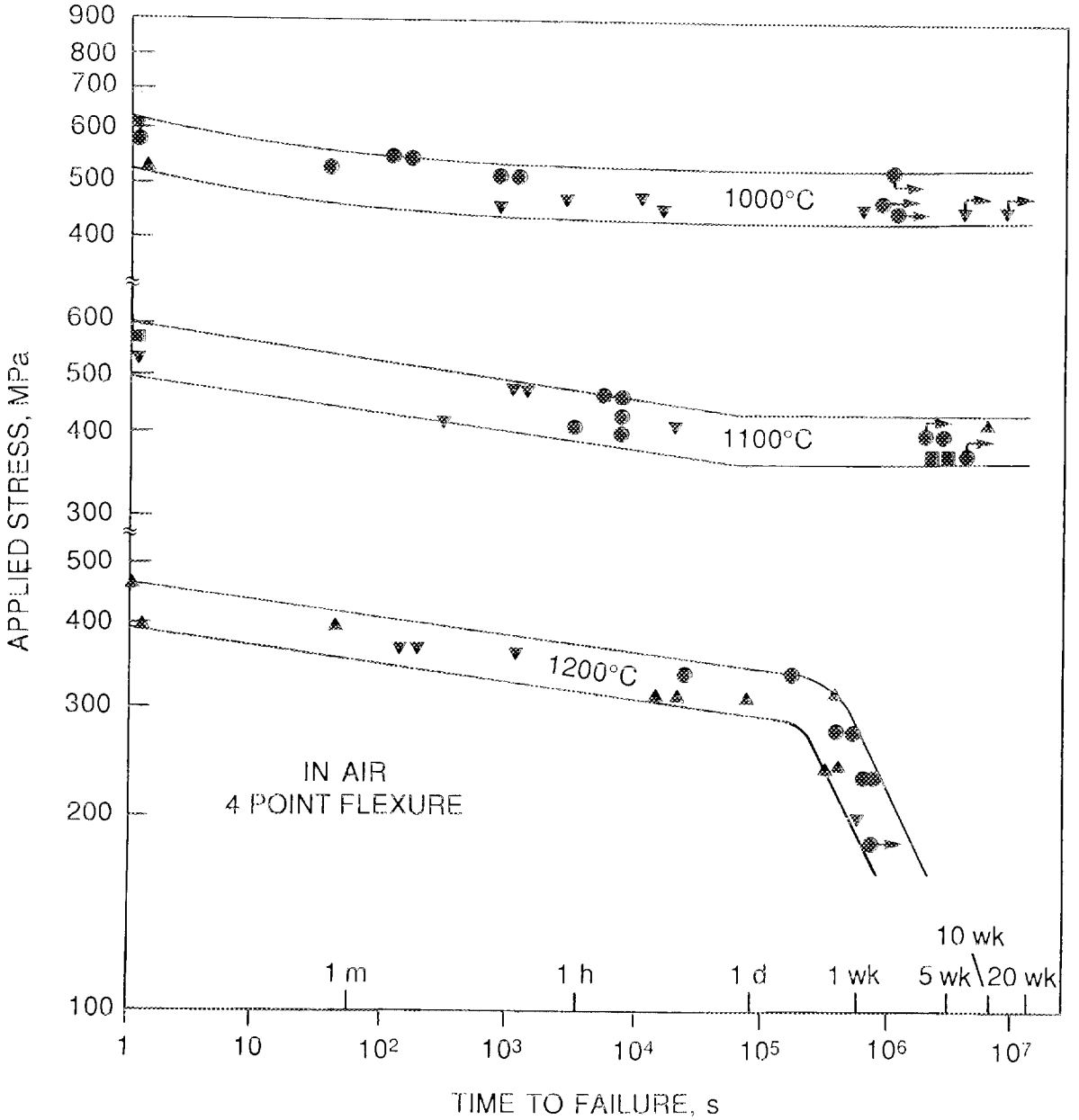

Fig. 1. Time-to-failure response for alumina ceramics containing 20 vol % SiC whiskers is a function of applied stress and temperature. At 1000 and 1100°C in air, the composites exhibit excellent resistance to failure even at very high applied stresses. At 1200°C, creep of the composites results in crack generation and failure even at very low applied stresses.

Table 1. Fracture strengths after long-term exposure at elevated temperatures

Hold time (h)	Temperature (°C)	Applied stress (MPa)	Fracture strength (MPa)
240	1000	525	840
1000	1000	365	665
1000	1100	365	620

crack growth at the stress levels approaching the fast-fracture strength. Thus, the times to failure increase with decrease in applied stress, as indicated in Fig. 1. This region was accompanied by regions of what appeared to be consistent with crack-blunting processes. This is indicated by apparent lack of any affects of changes in applied stress on times to failure as the applied stress levels approached 80% and 70%, respectively, of the fast-fracture strengths at these same temperatures (see Fig. 1).

At 1200°C, the composites exhibited times to failure which increased with decrease in applied stress over a stress range of 10 to 40% of the fast-fracture strength. The time-dependent failure at 1200°C appears to exhibit much greater applied stress sensitivity at lower applied stresses. Failure at 1200°C was accompanied by the development of multiple cracks within the constant stress region of the tensile surface of the four-point flexure specimen. In addition, permanent deflection of the specimen which survived for more than a few hours was detected. Transmission electron microscopy observations revealed that grain boundary cavities had been generated during the stressing experiments. These results were indicative of failure by creep-related damage and crack generation.

Such creep processes, quite evident in the 1200°C tests, were also present in the specimen subjected to stress (<75% of the fracture stress) for very long periods (>6 weeks) at 1000 and 1100°C. This is not unexpected, as diffusional and other processes which contribute to crack blunting will also contribute to creep deformation mechanisms that would generate cavities. Thus crack-blunting behavior must be competing with creep deformation and cavitation. At temperatures of 1100°C or less, long-term (up to 14 weeks) survival of specimens subjected to substantial stresses indicates crack blunting is controlling the material response. Increasing the temperature obviously shifts the balance toward creep deformation, cavitation, and crack generation which leads to failure. Further improvements to control this balance could include elimination or modification of impurities and increase in the matrix grain size.

Finally, one can ask the question as to how the fatigue behavior of the alumina-20 vol % SiC whisker composites compares to that of other ceramics. When considered in terms of the response of alumina ceramics,[1-4] the composites exhibit much greater fatigue resistance at these elevated temperatures. In comparison to silicon nitride ceramics (those composites also have improved fatigue resistance),[5] the composite has greater service stress capacity.

Status of milestones

The milestone on stress dependence of fatigue behavior of alumina reinforced with silicon carbide whiskers in temperature regimes where transition from crack blunting-to-creep damage occurs is complete.

The creep facilities are now in the process of being renovated/modified for future testing.

Publications

P. F. Becher et al., "Elevated Temperature Static Fatigue/Creep Rupture of Alumina Reinforced with 20 Vol % SiC Whiskers," *J. Mater. Sci.* (submitted for publication).

References

1. a. K. Jakus, S. M. Wiederhorn, and B. J. Hockey, "Nucleation and Growth of Cracks in Vitreous-Bonded Aluminum Oxide at Elevated Temperatures," *J. Am. Ceram. Soc.* **69**(10), 729–31 (1986).

   b. S. M. Wiederhorn et al., "Creep and Fracture of a Vitreous-Bonded Aluminum Oxide," *J. Mater. Sci.* **21**, 810–24 (1986).

2. B. J. Daigleigh, S. M. Joynson, and A. G. Evans, "High Temperature Failure of Polycrystalline Alumina: Failure Times," *J. Am. Ceram. Soc.* **67**(11), 759–63 (1984).

3. A. M. Cannon, W. H. Rhodes, and A. H. Heuer, "Plastic Deformation of Fine-Grained Alumina (Al_2O_3), I, Interface Controlled Diffusional Creep," *J. Am. Ceram. Soc.* **63**(1-2), 46–53 (1980).

4. B. J. Dagleigh, E. B. Siamovich, and A. G. Evans, "Duality in the Creep Rupture of a Polycrystalline Alumina," *J. Am. Ceram. Soc.* **68**(11), 575–81 (1985).

5. G. D. Guinn, "Review of Static Fatigue in Silicon Nitride and Silicon Carbide," *Ceram. Engr. Sci. Proc.* **3**(1-2), 77–98 (1982).

Cyclic Fatigue of Toughened Ceramics

K. C. Liu and C. R. Brinkman (Oak Ridge National Laboratory)

Objective/scope

The objective of this task activity is to develop, design, fabricate, and demonstrate the capability to perform tension-tension dynamic fatigue testing on a uniaxially loaded ceramic specimen at elevated temperatures.

Three areas of research have been identified as the main thrust of this task: (1) design, fabrication, and demonstration of a load train column which truly aligns with the line of specimen loading; (2) development of a simple specimen grip that can effectively link the load train and test specimen without complicating the specimen geometry and, hence, minimize the cost of the test specimen; and (3) design and analysis of a specimen for tensile cyclic fatigue testing.

Technical progress

Tensile fatigue tests of MgO-PSZ (Nilcra, MS grade)

Experimental efforts continued on tensile cyclic fatigue tests of Nilcra MS-grade MgO-PSZ at room and elevated temperatures. Due to the space limitation, the experimental details concerning specimen, test method, specimen heating, strain measurement, and test wave forms are referred to in a previous report.[1] A total of 16 tests were completed to date. Test parameters used and test results are summarized in Table 1, and the test data are plotted in Figs. 1 through 4. The closed symbols indicate that failure occurred at the test condition indicated; whereas the open symbols indicate the end point of the first step cyclic loading, and that specimen failure did not occur at the indicated test condition. Intermediate loading steps are described by the zig-zag path, which in all cases ended at the closed symbols indicating specimen failure.

The fatigue behavior of the material depicted in Figs. 1 through 4 is somewhat speculative due to the limitation in the number of test data obtained to date. General observations indicate that the fatigue curves of this material at high temperatures above 800°C would be very flat as shown in Figs. 3 and 4. Two possible reasons for this behavior may be cited. First, the fracture failure may be controlled by the critical fracture toughness of the material, hence, the number of cycles in subcritical stress loading may cause little or no fatigue damages to the specimen. Fractographic examinations of all specimens tested showed that large defects pre-existing in the test volume were the failure origin at the fracture initiating sites, as illustrated in the inserts of Figs. 1 through 4. A second reason is that the fatigue-induced slow-growth microcracks nucleated in the bulk may be impeded by increasing crack resistance due to localized transformation toughening. However, the latter reason is questionable because the toughening due to the transformation diminishes in this temperature range.

Specimen 38 that ruptured rather unexpectedly at the low strength is due to the presence of an unusually large process defect pre-existing in the gage section of the specimen.

Table 1. Results of tensile and cyclic fatigue tests of Nilcra's MgO at elevated temperatures (MS grade)

Specimen number	Tensile strength [MPa	(ksi)]	Cyclic stress to failure [MPa	(ksi)]	Intermediate cyclic stress [MPa	(ksi)]	Number of cycles at intermediate cyclic loading	Number of cycles to failure
Tests at room temperature								
26	468	(67.9)						1
39					284	(41.2)	30	(30)[a]
					353	(51.1)	7,621	(7,658)
					388	(56.2)	2,986	(10,644)
			421	(61.1)			155	10,799
Tests at 400°C								
28	341	(49.5)						1
29	440	(63.7)						1
40			238	(34.5)				1,103
41					240	(34.8)	54,135	(54,135)
					257	(37.3)	44,278	(98,413)
					271	(39.3)	32,487	(141,544)
					283	(41.0)	132,491	(274,035)
					297	(43.0)	44,129	(318,164)
					311	(45.0)	44,505	(362,669)
					325	(47.0)	44,685	(407,354)
			336	(48.8)			135	407,489
Tests at 800°C								
30	265	(38.5)						1
31	258	(37.5)						1
38	190	(27.5)						1
37					192	(27.9)	46,641	(46,641)
					210	(30.4)	88,308	(134,949)
					221	(32.0)	225,600	(360,549)
					233	(33.8)	44,263	(404,812)
					244	(35.3)	44,769	(449,581)
					258	(37.4)	130,466	(580,047)
					271	(39.3)	144,444	(724,843)
			286	(41.5)			352	724,843
Tests at 1000°C								
32	222	(32.3)						1
33	194	(28.1)						1
34					140	(20.4)	45,100	(45,100)
					154	(22.4)	44,850	(89,950)
					168	(24.4)	43,938	(133,888)
			183	(26.5)			96,657	230,545
35					161	(23.4)	46,600	(46,600)
					175	(25.4)	42,400	(89,000)
			188	(27.3)			89,735	178,735
36					180	(26.1)	49,172	(49,172)
			195	(28.2)			25,918	75,090

[a]Number of cycles accumulated at the end of intermediate loading.

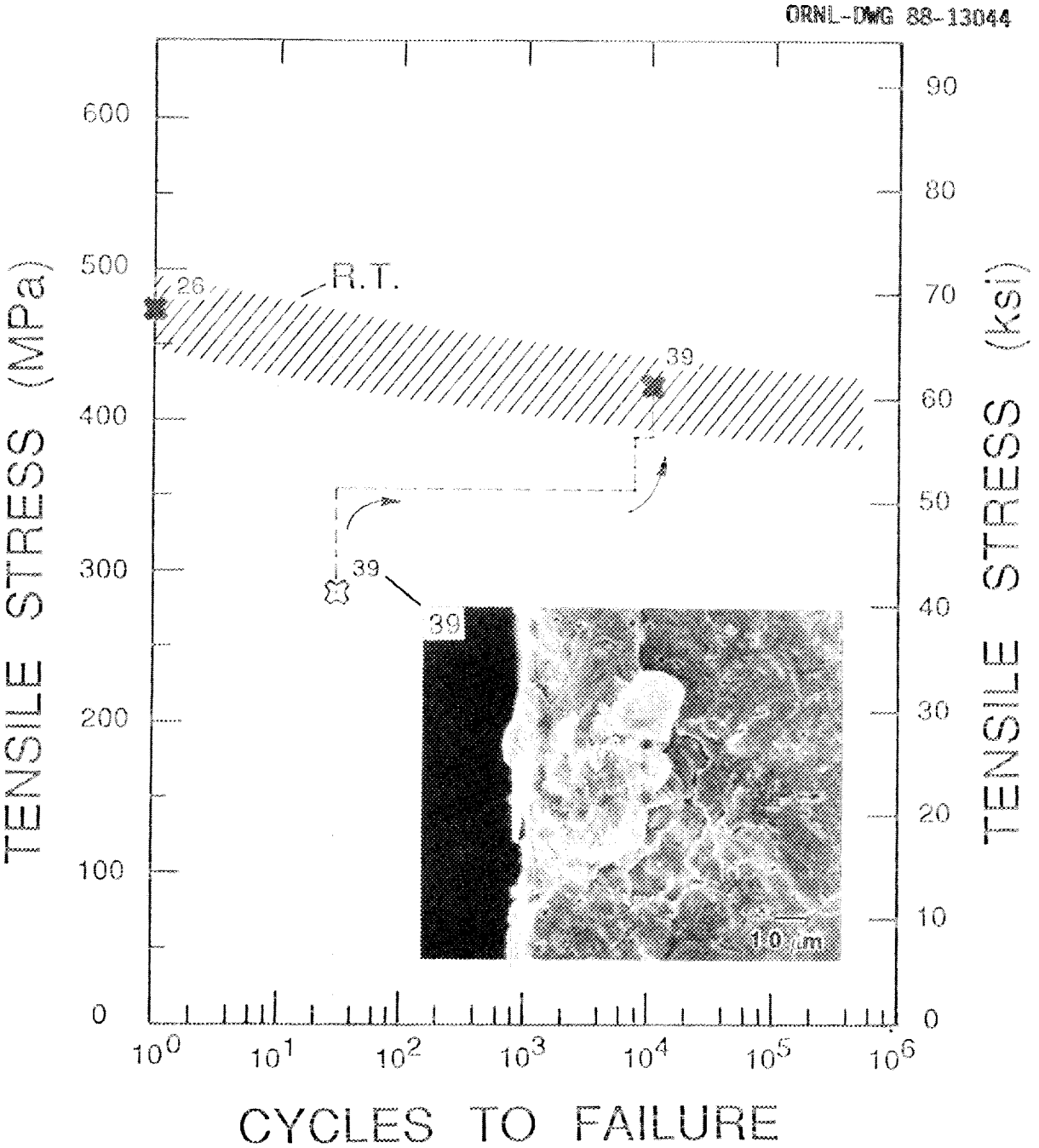

Fig. 1. Uniaxial tensile and cyclic fatigue of MgO-PSZ tested at room temperature. Fracture origin of specimen 39 is shown in the insert.

ORNL-DWG 88-13045

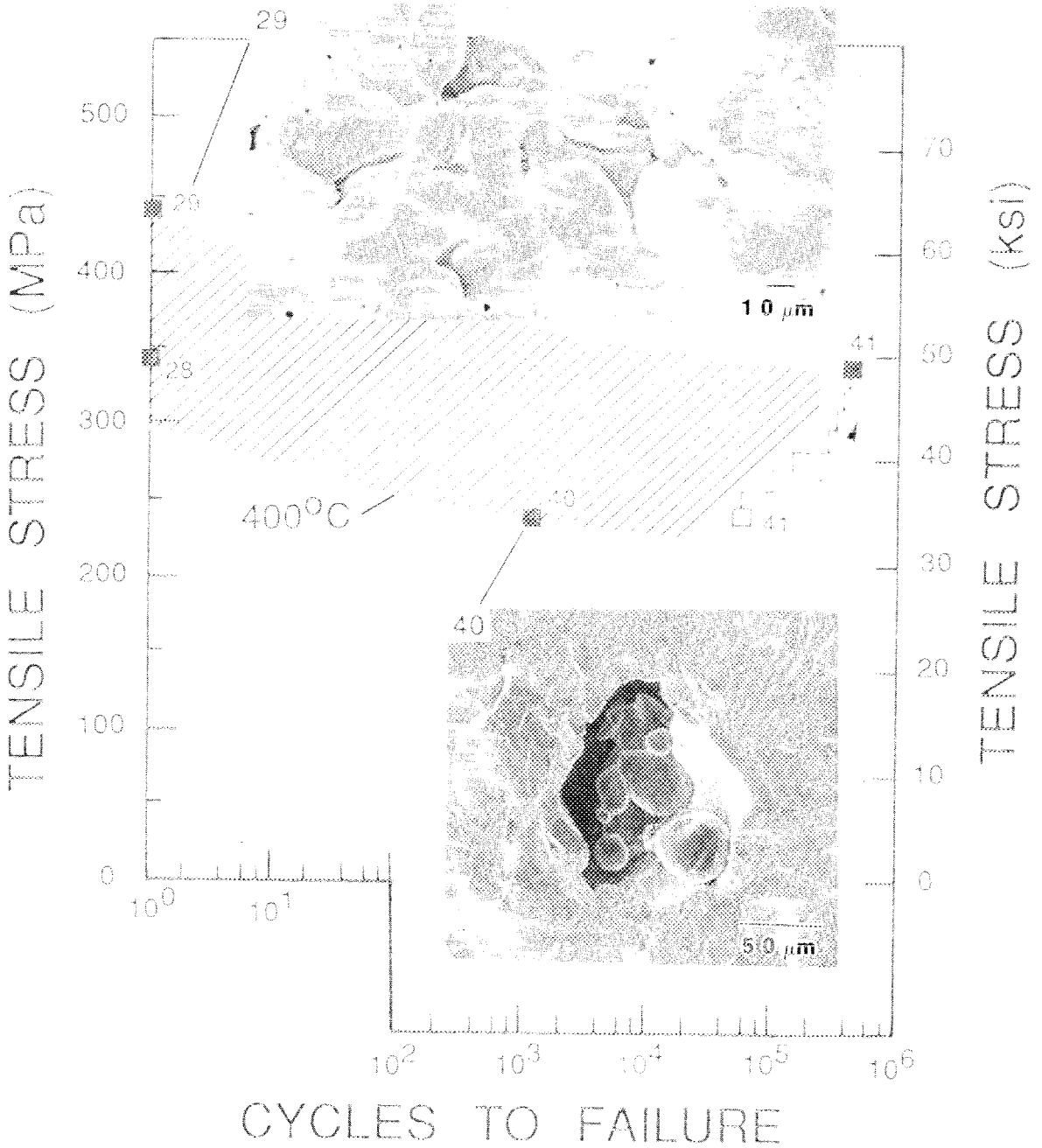

Fig. 2. Tensile and cyclic fatigue behavior of MgO-PSZ tested at 400°C. Fracture origins of specimens 29 and 40 are shown in the inserts. Smooth grain surfaces visible inside the cavity were analyzed to be rich in MgO.

ORNL-DWG 88-13046

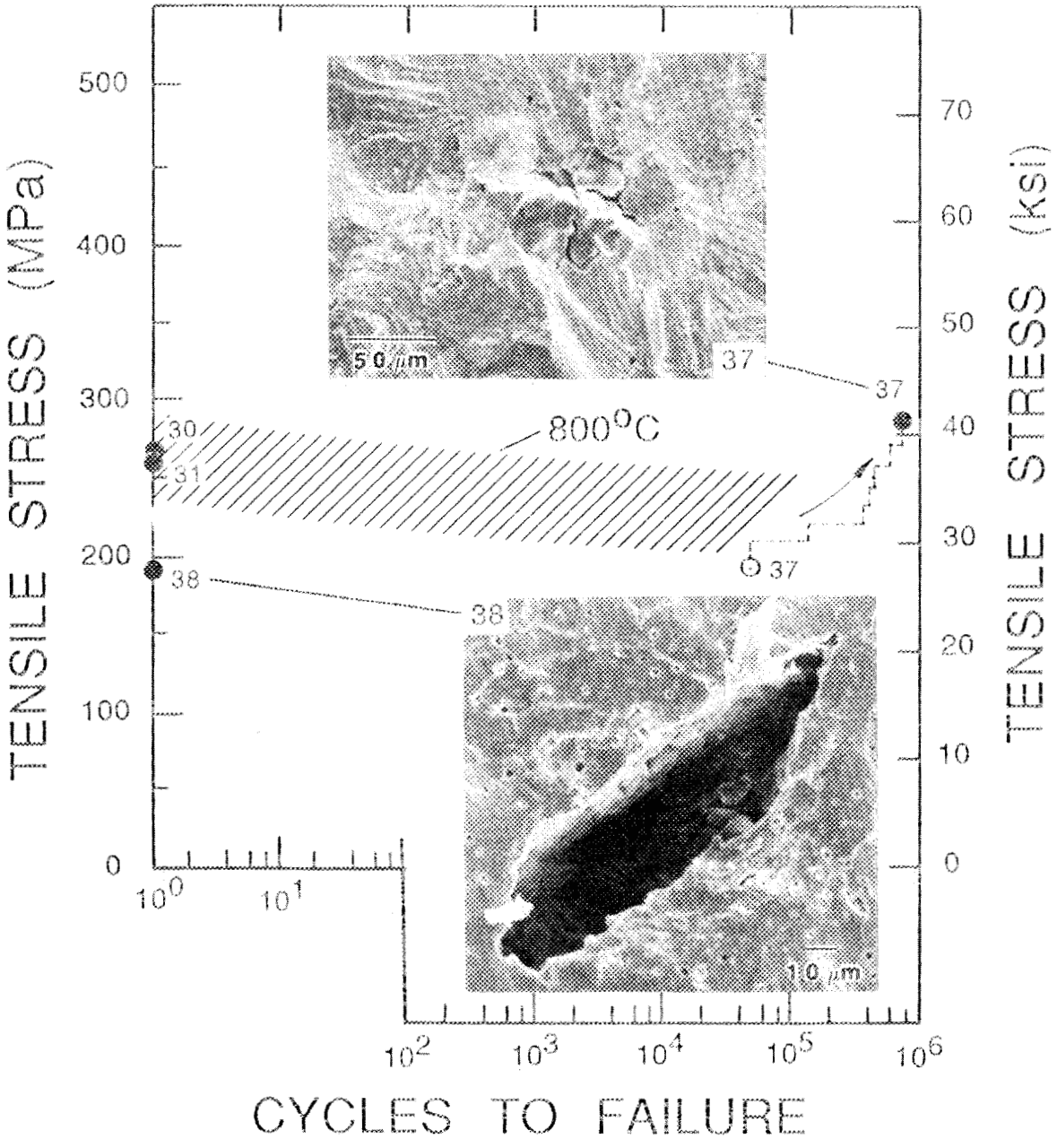

Fig. 3. Tensile and cyclic fatigue behavior of MgO-PSZ tested at 800°C. An unusually large process flaw embedded in specimen 38 acted as the fracture origin that substantially lowered its tensile strength.

ORNL-DWG 88-13047

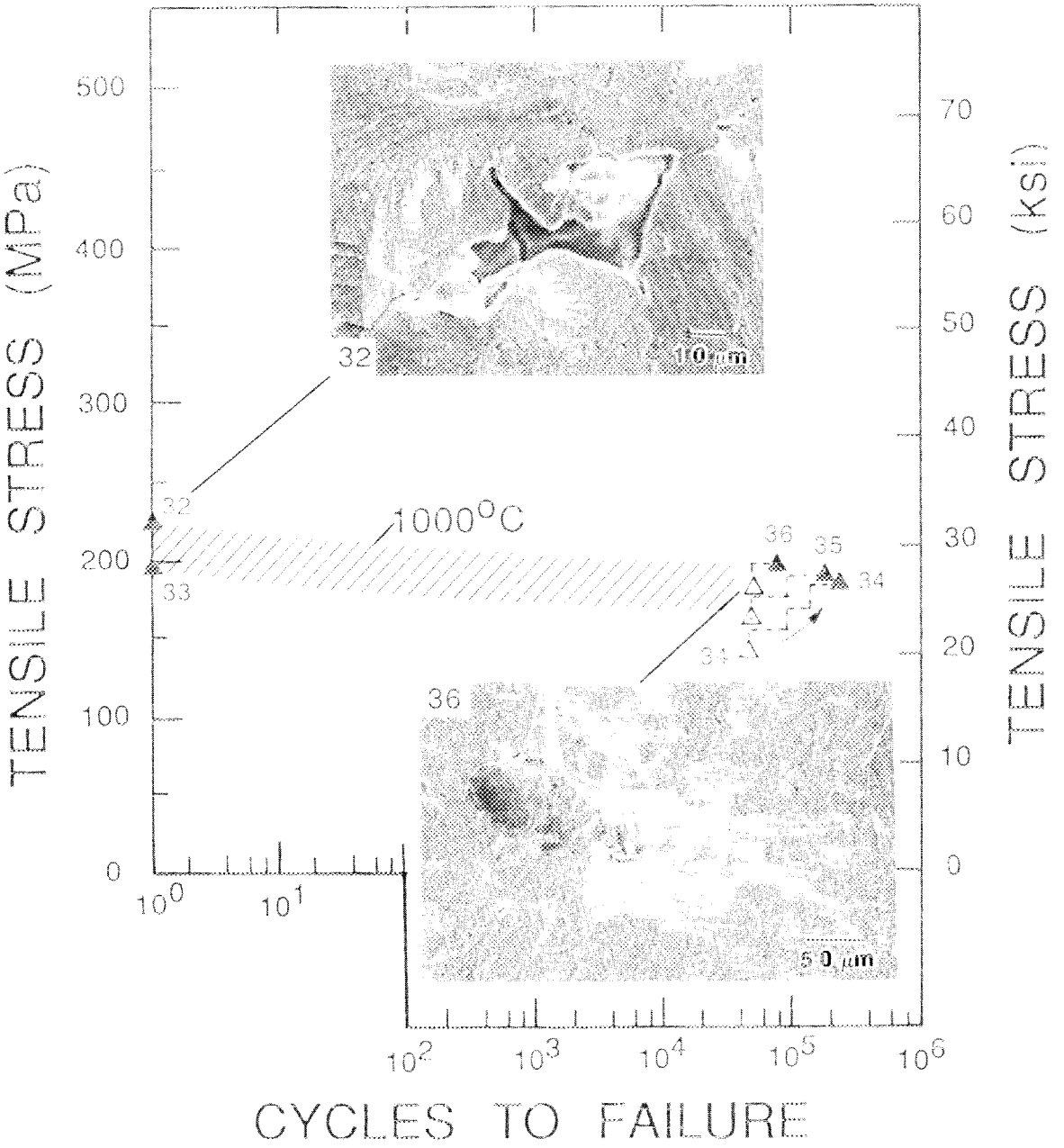

Fig. 4. Tensile and cyclic fatigue behavior of MgO-PSZ tested at 1000°C.

Specimens 34, 35, and 36 were subjected to cyclic loading in steps until failure occurred. Examinations of the stress-strain behavior indicated that all specimens behaved similarly. In all three tests, strain ratcheting resulting from the cyclic loading was much less discernable compared to that observed in TS grade PSZ. Accordingly, the total plastic strain accumulation measured at the end of the tests was also much lower than that measured in the TS grade material tested at the same temperature. Further observations indicated that the "coaxing" effects which were strongly evident in the tests of the TS grade were less obvious in the MS grade.

Evaluation of fracture toughness of TS grade PSZ in uniaxial tension

Our experimental observations indicated that large voids or inclusions were constantly the major sources of tensile fracture failures. These observations suggest that the uniaxial tensile strength of engineering ceramics, which in a practical sense cannot be devoid of any process defects, is governed by the physical characteristics of the largest defects pre-existing in the materials. An attempt was made to illustrate that experimentally determined uniaxial tensile strength can be correlated reasonably well to the fracture toughness of the material, if the complex characteristic features of the source defects can be approximated by an analytical form.

Performing precise measurements of fracture-initiating defects was difficult because they varied irregularly in shape and character. There were hardly any two defects that looked alike. To facilitate fracture mechanics analysis, all the fracture-initiating defects were treated as plane elliptical cracks defined by "2a" as the major axis and "2c" as the minor axis. The distance from the center of the fracture origin to the nearest specimen surface was measured as "b," as shown in Fig. 5. Results of the measurements are given in Table 2.

According to the Griffith-Irwin theory of fracture mechanics,[2] the critical fracture toughness, K_{Ic}, for a plane elliptical crack in an infinite solid subjected to a uniform uniaxial stress field, σ, at remote ends can be derived as follows:

$$K_{Ic} = F_1 (\phi, c/a) K_{Io} \tag{1}$$

where

$$K_{Io} = 2\sigma (a/\pi)^{\frac{1}{2}} \tag{2}$$

where K_{Io} is the stress intensity factor for a plane circular crack of radius "a" in a solid under a uniform uniaxial tensile stress, F_1 is a variable boundary correction factor, and ϕ is the angle defined as shown in Fig. 5. The value of K_{Ic} in Eq. (1) is calculated using F_1 (max), the maximum value of F_1. The above expression remains valid if the crack is situated at the center of the circular cross section having a radius "r" that is much greater than "a". If the elliptical crack is located near the surface within the range of $c/b > 0.1$, K_{Ic} is given by

$$K_{Ic} = F_2 (\phi, c/a, c/b) K_{Io} \tag{3}$$

ORNL-DWG 88-13053

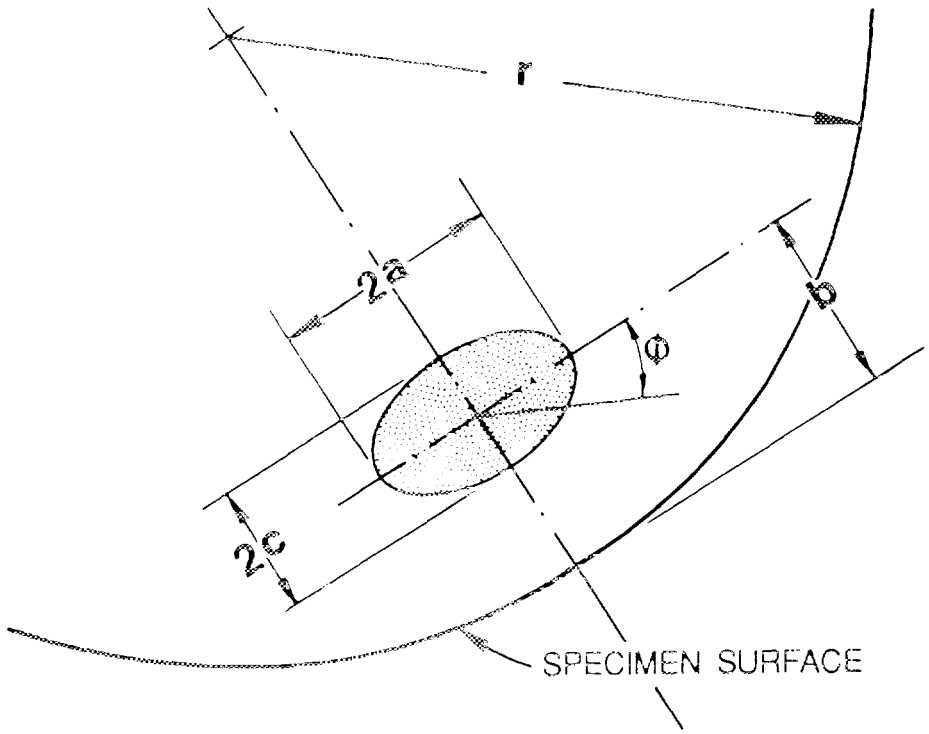

Fig. 5. Coordinate system and dimensions of an elliptical crack.

where F_2 is another correction factor which additionally accounts for the proximity to the specimen surface. For the sake of simplicity, the specimen surface is approximated as a straight edge in Eq. (3).

The values of K_{Ic} tabulated in column (h) were calculated using the Oak Ridge National Laboratory tensile strength data listed in column (e) of Table 2. In order to make meaningful comparisons with two sets of reported K_{Ic} data[3,4] which were known to have been obtained from bend tests, two sets of K_{Ic} values were calculated using the ratios of apparent bending strength (MOR) values determined from the curves given in Figs. 6(*a*) and 7(*a*) to the corresponding tensile strengths. The results were plotted in Figs. 6(*b*) (curve B) and 7(*b*) (curve D), respectively.

A comparison shows that the average K_{Ic} values (curve A) calculated from the tensile strengths are significantly lower than Nilcra K_{Ic} data (curve C) by about 55% at room temperature and by about 45% at 1000°C. The agreement between curve B, representing the average property of K_{Ic} calculated from MOR data, and curve C are respectable in view of the possible differences in monoclinic phase content and batch-to-batch variations in microstructure. The K_{Ic} data calculated from the tensile failure strength depicted by closed symbols in Fig. 6(*b*) are reasonably consistent, in particular, at high temperatures.

Table 2. Summary of critical fracture toughness (K_{Ic}) calculation

(a) Specimen number	(b) Flaw size 2a × 2c (μm)	(c) Distance from edge b (mm)	(d) Ratio c:b	(e) Tensile failure strength (MPa)	(f) K_o (MPa·$\sqrt{m}$)	(g) F_1 (max) or F_2 (max)	(h) K_{Ic} (MPa·$\sqrt{m}$)
			Room temperature				
15	100 × 100	0.55	0.09	326	2.60	1.00	2.60
16	60 × 60	0.05	0.6	448	2.77	1.03	2.85
22	155 × 230	0.14	0.82	338	3.35	1.07	3.58
18	1000 × 200	1.96	0.05	272	6.87	0.67	4.60
			Temperature = 400°C				
7	80 × 80	0.52	0.08	376	2.68	1.03	2.77
9	200 × 100	1.34	0.04	336	3.79	0.92	3.49
10	100 × 80	0.05	0.8	328	2.62	1.21	3.17
			Temperature = 800°C				
1	140 × 100	0.58	0.09	300	2.83	0.98	2.78
2	110 × 70	0.39	0.09	292	2.44	0.97	2.37
3	160 × 130	1.18	0.06	269	2.72	0.99	2.69
5	120 × 120	0.06	1.0	254	2.22	1.23	2.73
6	100 × 80	0.05	0.8	295	2.36	1.25	2.94
			Temperature = 1000°C				
12	120 × 120	0.86	0.07	244	2.13	1.0	2.13
13	130 × 80	0.06	0.67	253	2.30	1.3	2.99
14	90 × 90	0.05	0.9	270	2.04	1.23	2.52

ORNL-DWG 88-13048

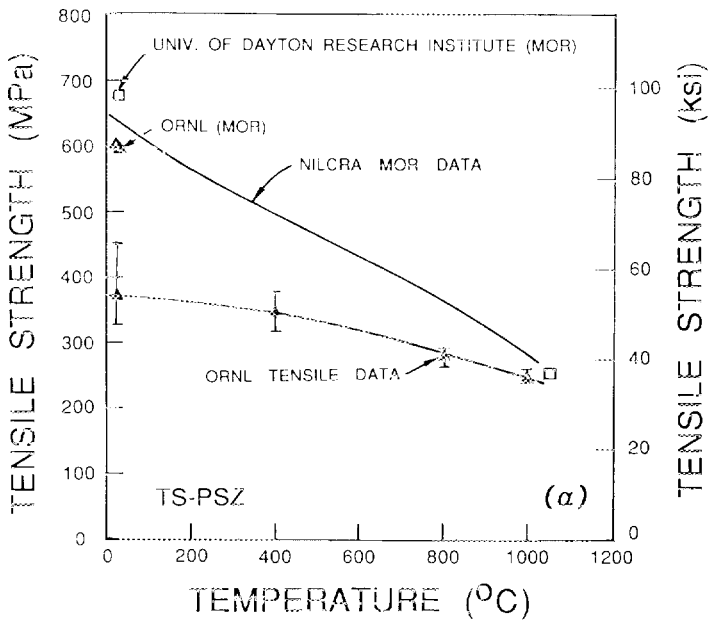

ORNL-DWG 88-13051

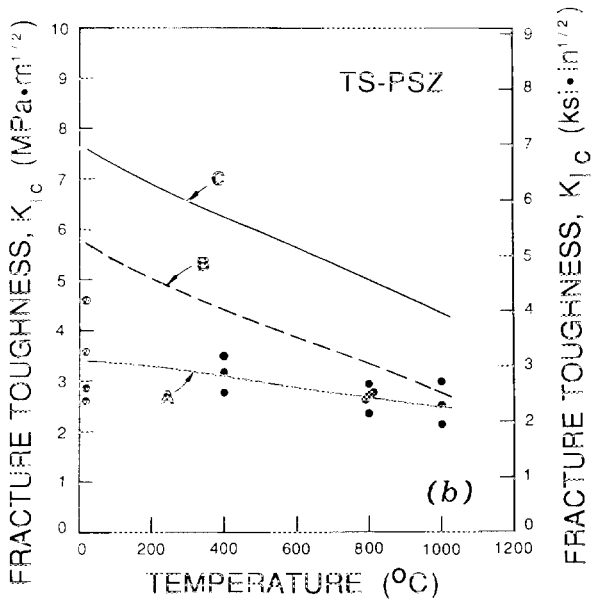

Fig. 6. (*a*) Comparison between the ORNL tensile strength and Nilcra MOR strength; (*b*) comparisons of bend-test determined and predicted K_{Ic} values: curve A – average K_{Ic} predicted from Eq. (1) using the ORNL tensile test data; curve B – average K_{Ic} predicted also from Eq. (1) but using Nilcra MOR data; curve C – Nilcra K_{Ic} data determined by bend tests.

ORNL-DWG 88-13052

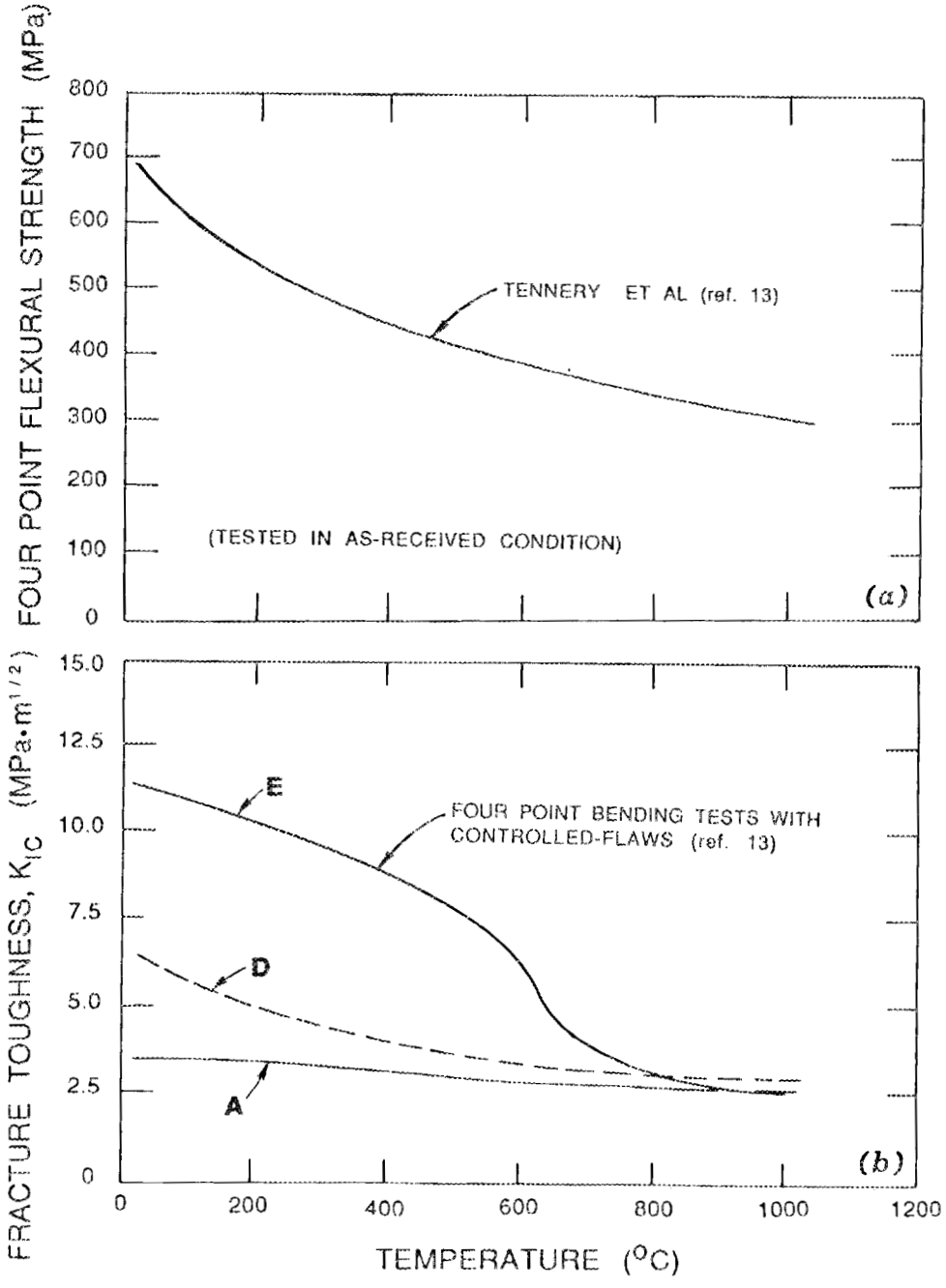

Fig. 7. *(a)* Four-point flexure strength of TS-PSZ ceramic vs temperature in air atmosphere; and *(b)* curve D – fracture toughness predicted from Eq. (1) based on MOR values taken from *(a)*, curve E – fracture toughness obtained from bend tests with controlled flaws vs temperature.

Comparative studies similar to the above were conducted also with data obtained by Tennery and his coworkers.[4] The MOR strengths used in K_{Ic} calculations are determined from the curve shown in Fig. 7(*a*). The K_{Ic} (curve D) values calculated from the MOR data were plotted in Fig. 7(*b*) for comparison with the K_{Ic} curve (curve E) determined from four-point bend tests with controlled flaws. A comparison shows that curve E is significantly higher than curve D in the lower temperature range below 600°C, but the two curves agree extremely well in the higher temperature range. It is suspected that the differences in K_{Ic} at the low temperature might have been caused by batch-to-batch variations in monoclinic phase content.

Important findings and observations

Results of fractographic studies combined with fracture mechanics analyses imply that failure stresses for TS grade PSZ in uniaxial tension are dictated most likely by the size, shape, and the location of the largest process flaw pre-existing in the test volume.

Status of milestones

Completed elevated temperature fatigue and tensile tests on advanced toughened ceramic material (Milestone 321406 scheduled on July 31, 1988).

Completed a technical report giving results of elevated temperature tests on Si_3N_4 (Milestone 321407 scheduled on September 30, 1988).

Publications

K. C. Liu, "Ceramic Specimen Heating by Induction Power," in *Proceedings of the Conference on Mechanical Testing of Engineering Ceramics at High Temperatures*, April 11–12, 1988, London, England; and in *Int. J. High Technol. Ceram.* (accepted for publication).

K. C. Liu, H. Pih, and D. W. Voorhes, "Uniaxial Tensile Strain Measurement for Ceramic Testing at Elevated Temperatures: Requirements, Problems, and Solutions," *Int. J. High Technol. Ceram.* (accepted for publication).

K. C. Liu and C. R. Brinkman, "Tensile Cyclic Fatigue Testing of Ceramic Materials at Elevated Temperatures," paper presented at the 90th Annual Meeting of the Am. Ceram. Soc., at Cincinnati, Ohio, May 1–5, 1988.

L. F. Allard, T. A. Nolan, and K. C. Liu, "Effects on Tensile Cyclic Fatigue at Elevated Temperatures on the Microstructure of Silicon Nitride Ceramics," paper presented at the 90th Annual Meeting of the Am. Ceram. Soc., at Cincinnati, Ohio, May 1–5, 1988.

K. C. Liu and C. R. Brinkman, "A Self-Aligning Apparatus for Testing Ceramic Materials in Uniaxial Tension at High Temperatures," a poster presented at the 90th Annual Meeting of the Am. Ceram. Soc., at Cincinnati, Ohio, May 1–5, 1988.

T. A. Nolan, L. F. Allard, and K. C. Liu, "Characterization of the Fracture Processes of Ceramic Materials Tested in Tensile Cyclic Fatigue at Elevated Temperatures," a poster presented at the 90th Annual Meeting of the Am. Ceram. Soc., at Cincinnati, Ohio, May 1–5, 1988.

References

1. K. C. Liu and C. R. Brinkman, "Cyclic Fatigue of Toughened Ceramics," *Ceramic Technology for Advanced Heat Engines Project Semiannual Progress Report for April through September 1987*, ORNL/TM-10701, Oak Ridge National Laboratory, pp. 232–46, March 1988.

2. D. P. Rooke and D. J. Cartwright, *Compendium of Stress Intensity Factors*, The Hillington Press, England, 1976.

3. Mechanical Properties Test Data Furnished by Nilcra Ceramics (USA), Inc.

4. V. J. Tennery et al., "Characterization of the Fatigue and Slow Crack Growth Behavior of Partially Stabilized Zirconia Ceramics," pp. 409–18 in *Proceedings of the Twenty-Second Automotive Technology Development Contractors' Coordination Meeting, P-155*, Society of Automotive Engineers, Warrendale, PA, 1985.

Rotor Data Base Generation

M. K. Ferber, M. Jenkins, and R. Martin (Oak Ridge National Laboratory)

Objective/scope

The goal of the proposed research program is to systematically study the tensile strength of a silicon nitride ceramic as a function of temperature and time in an air environment. Initial tests will be aimed at measuring the statistical parameters characterizing the strength distribution of three sample types (two tensile specimens and one flexure specimen). The resulting data will be used to examine the applicability of current statistical models as well as sample geometries for determining the strength distribution.

In the second phase of testing, stress rupture data will be generated by measuring fatigue life at a constant stress. The time-dependent deformation will also be monitored during testing so that the extent of high-temperature creep may be ascertained. Tested samples will be thoroughly characterized using established ceramographic, scanning-electron-microscope, and transmission-electron-microscope techniques. A major goal of this effort will be to better understand the microstructural aspects of high-temperature failure including:

(1) extent of slow crack growth,
(2) evolution of cavitation-induced damage and fracture,
(3) transition between brittle crack extension and cavitation-induced growth, and
(4) crack blunting.

The resulting stress rupture data will be used to examine the applicability of a generalized fatigue-life (slow crack growth) model. If necessary, model refinements will be implemented to account for both crack blunting and creep damage effects. Insights obtained from the characterization studies will be crucial for this modification process. Once a satisfactory model is developed, separate stress-rupture (confirmatory) experiments will be performed to examine the model's predictive capability. Consequently, the data generated in this program will not only provide a critically needed base for component utilization in automotive gas turbines, but will also facilitate the development of a design methodology for high-temperature structural ceramics.

Technical progress

During this reporting period, approximately 200 silicon nitride flexure specimens were received from the vendor. These samples, which were injection molded to near-net-shape form, are currently being machined to final dimensions of 3 × 4 × 50 mm.* Delivery of the silicon nitride tensile samples, which was expected in October, has been delayed until January 1989 as a result of problems with specimen preparation.

---

*GTE PY6 silicon nitride fabricated by GTE Laboratories Incorporated, Waltham, MA.

Studies aimed at examining the operational status of the eight tensile test stands to be used in this study were also initiated. A test stand consists of an electromechanical load frame with both load and strain control capabilities. A built-in trapezoidal function generator can be used to specify the desired load-time characteristics of the test. The specimen grips, which are configured for either circular (button-head) or rectangular samples, are located outside of a compact two-zone molydisilicide furnace capable of generating a maximum temperature of 1600°C. The grips are attached to the load frame using hydraulic couplers to minimize bending moments. Specimen displacement is measured with a direct contact capacitance extensometer. A personal computer is used to monitor and store various output signals including displacement, load, load error, temperature, and water flow status. A single computer can service up to four test stands. Software required for controlling the data acquisition process was developed during this reporting period.

Button-head test samples of silicon carbide and a 94% aluminum oxide were prepared from existing stock for the tests involving the tensile units. In the first test, an alumina specimen was loaded to failure at room temperature. The resulting load-displacement curve was linear to the fracture point [408 MPa (59.2 ksi)] indicating that no slipping was occurring at the extensometer contact points.

In the next test, a second alumina sample was cycled between 63 and 156 MPa at 800°C. This sample exhibited a permanent displacement during each cycle and failed after only 20 cycles. The deformation was attributed to the SiO_2 glassy phase present in the material.

In order to better characterize this creep behavior, the displacement under constant stress was measured at 800°C. The results are shown in Figs. 1 through 3 for applied stresses of 104 and 123 MPa, 164 MPa, and 84 MPa, respectively. There was little evidence of any steady-state creep behavior at the three highest stress levels. Instead, the high temperature extension appeared to be limited to primary creep followed by creep rupture. The reasons for the strain plateau at 104 MPa stress are unknown. At the lowest stress level of 84 MPa, steady-state creep was observed throughout the 72-h exposure period.

It should be noted that during testing several problems were encountered with the extensometer. First, there was considerable noise in the extensometer output as evidenced in Fig. 3. This noise, which may have resulted from electrical fluctuations associated with the furnace, limited the measurement sensitivity to approximately 1.5 μm. Second, the displacement readings exhibited periodic jumps followed by a long recovery process. These variations were found to occur in 24-h cycles. (Note: the data in Fig. 3 have been corrected for this drift.) Subsequent studies at 800°C showed that the drift in the extensometer could be correlated with periodic variations in the room temperature. Steps are now being taken to thermally isolate the extensometer housing from the ambient environment.

An SiC button-head specimen was used to examine the temperature gradients in the gage section of the sample. These temperature gradients are a result of the flow of heat from the specimen hot zone into the water-cooled grips. The maximum gradient decreased from approximately 10°C at 1200°C to less than 5°C at 1500°C.

For the final test, a dense single-phase SiC was cycled at 800°C. In this case, the load-displacement curve exhibited no permanent

ORNL-DWG 89-2126

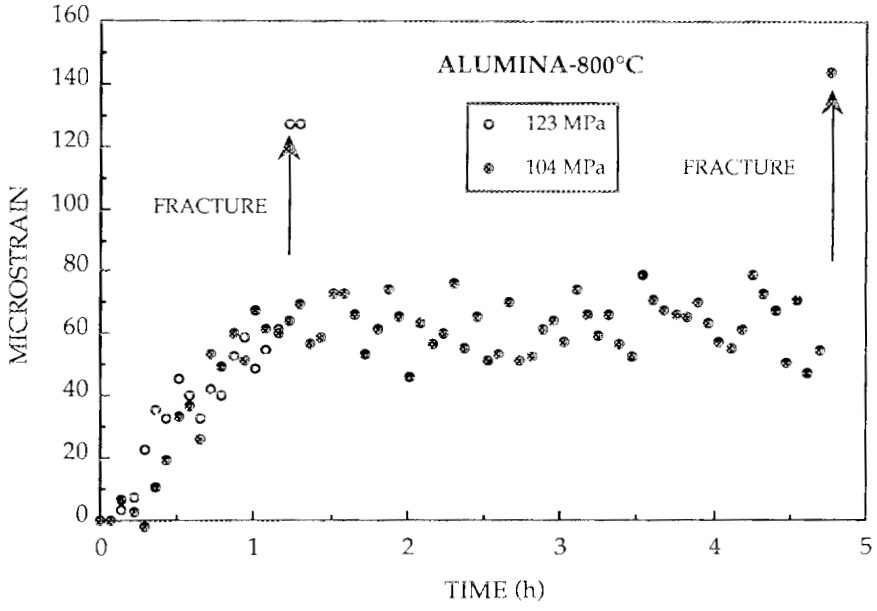

Fig. 1. Samples exposed at 800°C and stressed at 123 and 104 MPa exhibited no evidence of steady-state creep behavior.

ORNL-DWG 89-2127

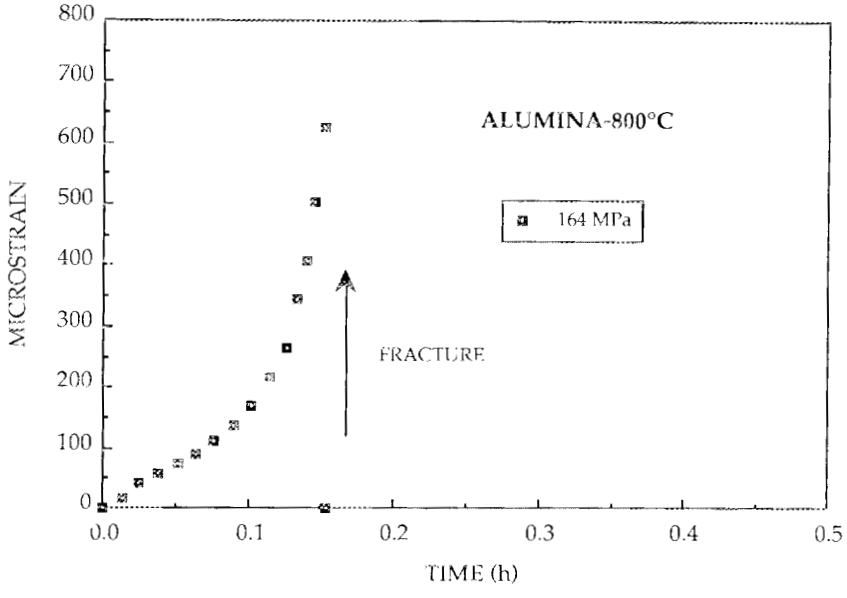

Fig. 2. Sample exposed at 800°C and stressed at 164 MPa exhibited short-term failure.

ORNL-DWG 89-2128

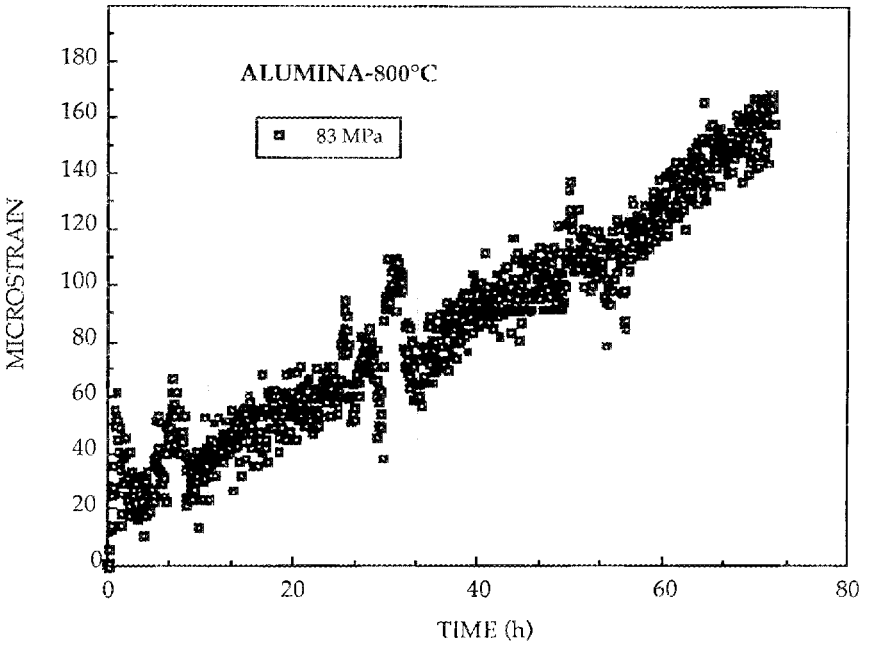

Fig. 3. Steady-state creep behavior was observed for sample exposed at 800°C and stressed at 82 MPa.

displacements. The Young's modulus was calculated to be 405 GPa, which is in good agreement with literature values.

Status of milestones

No activity.

Publications

No publications.

Toughened Ceramics Life Prediction

N. J. Shaw and J. A. Salem (NASA Lewis Research Center)

Objective/scope

The purpose of this research is to understand the room temperature and high temperature [≤1370°C (2500°F)] behavior of toughened ceramics, in particular SiC-whisker toughened Si_3N_4, as the basis for developing a life prediction methodology. A major objective is to understand the relationship between microstructure and the mechanical behavior within the bounds of a limited number of materials. A second major objective is to determine the behavior as a function of time and temperature. Specifically, the room temperature and elevated temperature strength and reliability, the fracture toughness, slow crack growth and the creep behavior will be determined for the as-manufactured material. The same properties will also be evaluated after long-time exposure to various high temperature isothermal and cyclic environments. These results will provide input for parallel materials development and design methodology development programs. Resultant design codes will be verified.

Technical progress

Experimental Procedures

Billets of HIPed RBSN (3X015) and HIPed SiC_w/RBSN (7X014), both vintage Aug., 1987, were obtained from Norton Co. and machined into MOR (3 × 4 × 50 mm) and chevron-notched (3 × 6 × 50 mm) bars for room temperature and high temperature MOR and fracture toughness determinations, creep evaluation, and oxidation and corrosion studies. These materials were prepared by mixing silicon powder with 4 wt.% Y_2O_3 and then adding 30 vol.% Tateho T44 SiC_w to a portion of the mixed powders. The powder mixtures were cast as a slurry into square plates, cold isostatically pressed, nitrided, and HIPed by the ASEA glass encapsulation method.

All MOR bars were radiographed through both the width and thickness. As-received and post-test bars of both the monolithic and composite were analyzed by TEM with particular emphasis on the intergranular phases.

The degree of whisker clustering was determined from SEM photographs of sections parallel and perpendicular to the billet face by a stereological method. Samples of SiC_w/Si_3N_4 were mounted in epoxy and ground and polished with diamond down to 1μm. The samples were removed from the mounts and etched in hot KOH for 30 s to remove the grain boundary phase. The samples were then plasma etched for 45 s with CF_4 + 4% O_2 following heating in a N_2 plasma for 20 min.(1)

Strength and fracture toughness at room and elevated temperatures were measured in 4-point bending with inner and outer spans of 20 mm and 40 mm, respectively and a loading rate of 0.5 mm·min^{-1}. Step-temperature-stress-rupture tests were performed on MOR bars with inner and outer spans of 19 mm and 38 mm, respectively. Deflection was measured by LVDTs positioned on the tensile face beneath the inner load

points and at the bar center. MOR bars cut to a length of 25 mm were exposed to 1000°C for 40 hrs. in a high velocity (Mach 0.3), pressurized (400 kPa) burner rig as a simulation of a gas turbine engine environment. For corrosion studies, 2 ppm Na was added to the gas flow to yield Na_2SO_4 deposites after reaction with sulfur in the fuel. The corrosion product was lightly ground off of the bars and the retained strength was measured at room temperature in 4-point bending with inner and outer spans of 9.5 mm and 19 mm, respectively, and a loading rate of 0.5 $mm \cdot min^{-1}$.

Results and Discussion

X-ray Radiography. X-ray radiographs of MOR bars (Figure 1) show that, while the composite structure is homogeneous, the monolithic material has significant density or compositional variations. An electron microprobe scan across a polished section of one bar showed some concentration of yttrium in a few areas and a few very small regions of high tungsten content (presumably from milling media), but no significant edge-to-edge chemical differences. No density variations across a bar could be detected by optical or scanning electron microscopy.

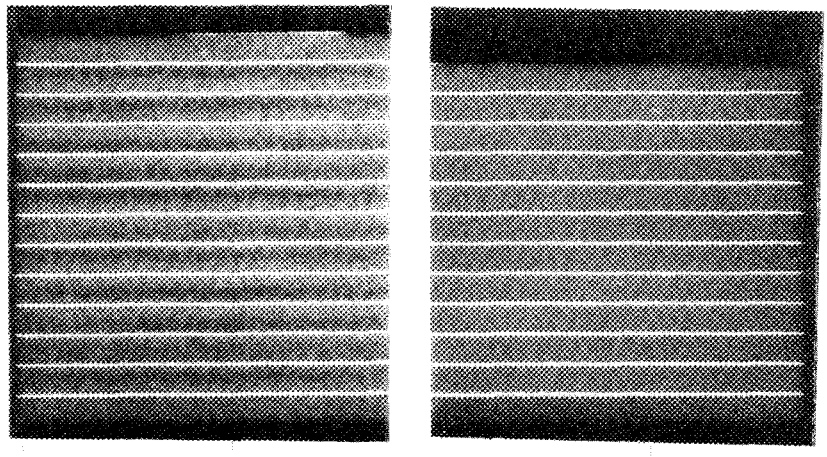

Figure 1. X-ray radiograph of machined MOR bars. View is through billet (plate) and test bar thickness. (Left) RBSN. Dark zones imply higher density or constituent with greater x-ray absorption. (Right) SiC_w/RBSN.

Whisker distribution. The polished and etched sections were observed uncoated by SEM. The SiC whiskers are slightly elevated above the matrix and appear bright against a dark background. Fourteen pictures were taken of each sample. The volume fraction of the whisker phase was measured by point counting to ascertain that the sample was properly etched. The measurements and statistical and stereological analyses were done with a semi-automatic image analyzer.(1)

One measure of whisker distribution is contiguity.(2) This is the mean value of the percent of the surface area of each whisker that is contacting another whisker. Contiguity is calculated by the equation

$$C = \frac{2S_{w-w}}{2S_{w-w} + S_{w-m}}$$

where S_{w-w} is the surface area of whisker-whisker contact and S_{w-m} is the surface area of whisker-matrix contact. The surface areas were measured by point counting. If the whiskers were completely separated, the contiguity would be 0. The contiguity of this material is 24%, indicating substantial clustering.

Transmission Electron Microscopy. Both the monolithic and the composite are fully dense and have grain boundaries with significant crystallization. The crystallized grain boundaries are Y-rich, but the many phases could not be identified. Glassy regions remain, some of which are phase separated. These regions are low in yttrium content, but seem to have accumulated many impurities, e.g., K, Ca, Cl, Na, P, S, etc., thought to have come from abrasion of a rubber mill seal. The materials also contain small, spherical W-rich particles, presumably from milling media. Many Si_3N_4 grains contain dislocations. The composite material contains large SiC grains, which are debris added with the SiC whiskers. (Norton is now taking steps to remove those large chunks before whiskers are added.) Many of the SiC whiskers are hollow and contain a Y-rich amorphous phase and small Si_3N_4 crystals. The SiC whiskers are bonded to the matrix by a glassy phase, which explains the observation of little whisker pull-out on fracture surfaces.

Strength and Fracture Toughness. Strength as a function of temperature for both the monolithic and whisker-toughened materials is illustrated in Figure 2.

The monolithic material shows constant strength, within the standard deviations, up to 1200°C. At 1400°C the strength drops rapidly. The large standard deviations in the strength data were attributed to the material variations identified by x-radiography (One bar that showed uniform density in the radiographs had a strength of 691 MPa.) The strengths measured by Norton Co. were higher, 661 MPa at R.T. and 517 MPa at 1370°C. This may have been the result of the density variations through the billets; the Norton MOR bars had the tensile face parallel to the billet face, resulting in a more uniform surface than the NASA bars, which had the tensile face perpendicular to the billet face. The failure initiating flaws were found to be slightly subsurface

---

1) Zeiss Videoplan 2, Carl Zeiss Inc., Thornwood, NY 10594

porous areas 30 - 60 μm across.

The composite material, in contrast, shows a steady decline of strength with increasing temperature. This data showed good correlation to the Norton Co. data and to the uniform structure seen by radiography. In most cases the initial failure occurred at a SiC chunk $\sim$50 μm in length.

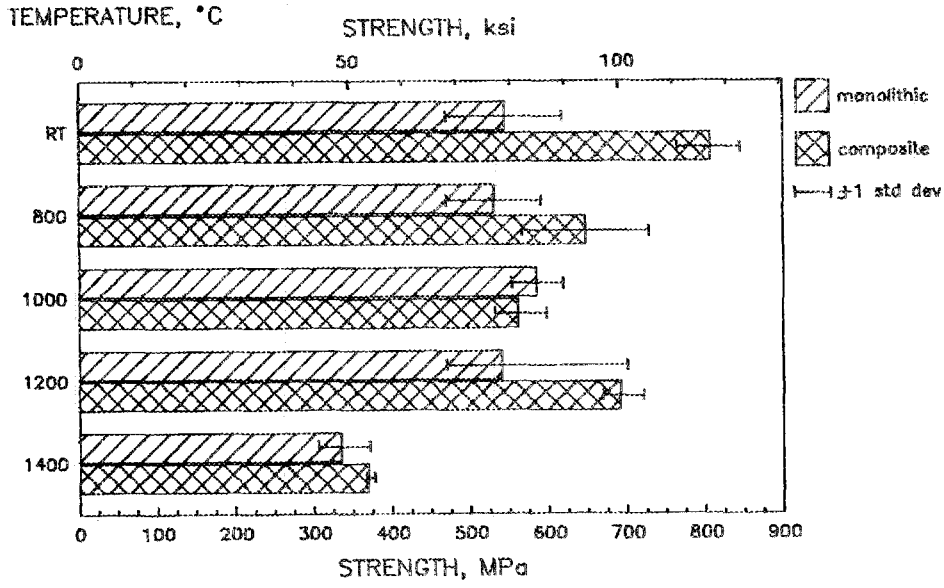

Figure 2. 4-point strength of Norton RBSN and SiC_w/RBSN.

The fracture toughness (Figure 3) reached a maximum of $\sim$7 MPa$\cdot$m$^{\frac{1}{2}}$ for both the monolithic and the composite at 1000 °C. It is conjectured that the reduced toughness at higher temperatures is due to softening of glass remaining in the grain boundary phase.

Step-Temperature-Stress-Rupture. The STSR results are given in Figure 4. The composite bars show greater deflection than the monolithic bars due to a less refractory grain boundary phase caused by impurities associated with the SiC whiskers. Failure initiating flaws were difficult to identify because of oxidation of the fracture surface, but seemed to be the same type of flaws seen in the fast fracture tests. TEM analysis of the crept bars is underway. Samples were prepared from the two bars that were tested at 200 MPa without failure. Observations made on the monolithic included: formation of small voids at triple points and grain boundaries, increased crystallization of the grain boundaries, and the presence of dislocations, although it has not yet been determined whether the dislocation density has increased over that of the uncrept material.

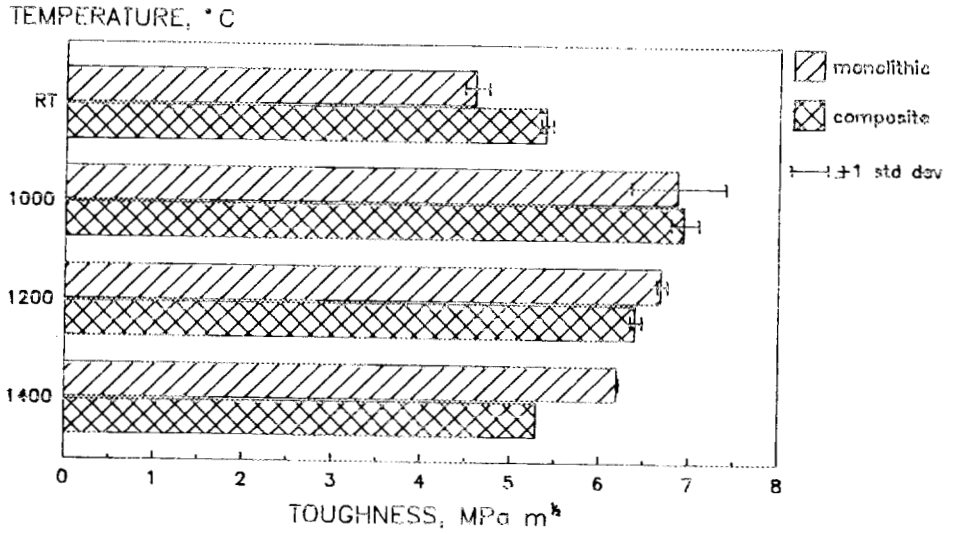

Figure 3. Chevron-notch fracture toughness of Norton RBSN and SiC_w/RBSN.

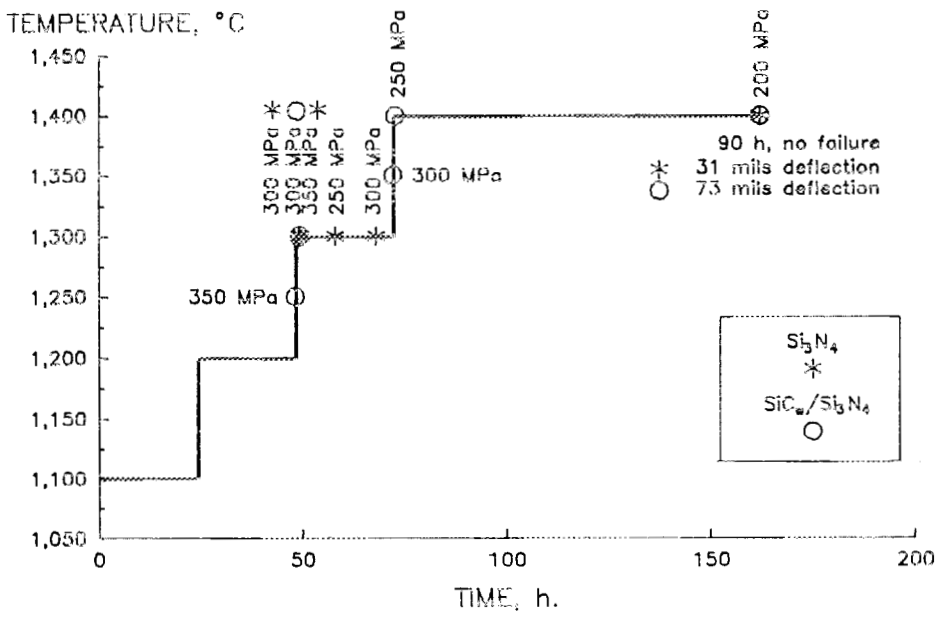

Figure 4. 4-point flexural step-temperature-stress-rupture strength of Norton RBSN and SiC_w/RBSN.

Oxidation and Corrosion. Hot corrosion occurs when sodium (an air or fuel impurity) combines with sulfur (a fuel impurity) to form sodium sulfate. Under certain conditions, Na_2SO_4 deposits on hot-gas-path components. This results in enhanced oxidation and severe corrosion. In the present study, Na impurities added to the burner flame resulted in molten Na_2SO_4 deposition, formation of substantial $Na_2O \cdot x(SiO_2)$ corrosion product, and attack of the ceramic substrate (Figure 5). The average weight of the silicate product was 11.6 ± 8.6 μg on the monolithic and 53.4 ± 6.9 μg on the composite. Room temperature bend strength of the monolithic Si_3N_4 decreased by 30% over the as-received

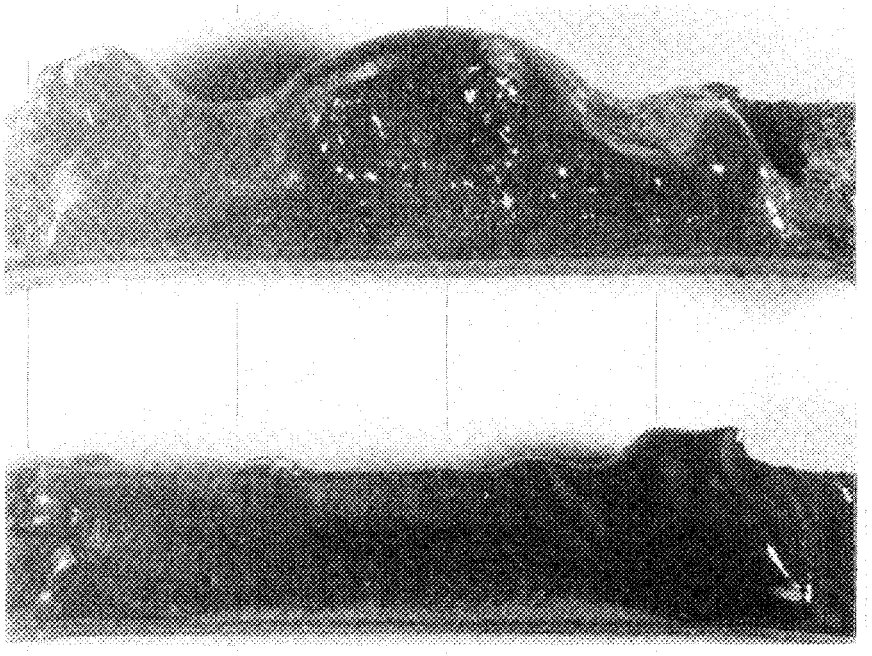

Figure 5. Corrosion product formed on SiC_w/Si_3N_4 (top) and Si_3N_4 (bottom) due to exposure to hot Na.

material (Figure 6). A comparable strength reduction of 24% was observed for monolithic GTE AY6 Si_3N_4 corroded under the same conditions. Corrosion of the SiC-reinforced composite material resulted in a strength decrease of 70%. From fractography, corrosion pits are observed as the fracture origins in both monolithic and composite materials. Burner rig oxidation (no added Na) has no effect on the monolithic Si_3N_4. However, the composite exhibited a strength reduction of 33% over as-received material. A preliminary hypothesis is that excess carbon in this developmental composite is the debilitating factor in both corrosion and oxidation. Improved processing to remove excess carbon associated with the SiC whiskers may alleviate this enhanced attack. TEM analysis of the grain boundary material in both the corroded and oxidized materials is yet to be conducted.

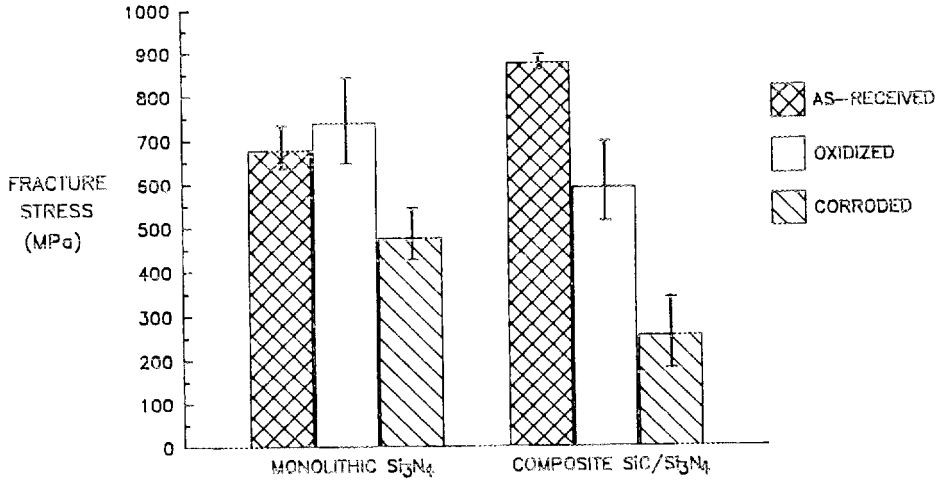

Figure 6. Room temperature 4-point bend strength of Si_3N_4 and SiC_w/Si_3N_4 after burner rig exposure.

Life Prediction. This task will provide input needed for the development and verification of a design code for whisker-toughened ceramics. The following is the abstract of paper by NASA Lewis researchers who are developing the life prediction methodology:[3]

Considerable research is underway in the field of materials science focusing on incorporating silicon carbide whiskers into silicon nitride and alumina matrices. These composites show the requisite thermal stability and thermal shock resistance necessary for use as components in advanced gas turbines and heat exchangers. This paper presents a macroscopic noninteractive reliability model for whisker-reinforced ceramic composites. The theory is multiaxial and is applicable to composites that can be characterized as transversely isotropic. Enough processing data exists to suggest this idealization encompasses a significantly large class of fabricated components. A qualitative assessment of the model is made by presenting reliability surfaces in several different stress spaces and for different values of model parameters.

Status of Milestones

321701 - order Si_3N_4 and SiC_w/Si_3N_4 from Norton Co. - complete
321702 - order second pair of materials from GCCD - complete
Remaining milestones are on schedule.

Publications

None

References

1. K. N. Siebein and W. M. Lovington, "Plasma Etching of Si_3N_4," in *Metallography of Advanced Materials*, *Microstructural Science*, *v. 16*, H.J. Cialone, G.W.E. Johnson, M.E. Blum, and G.F. van der Voort, eds., ASM International, Metals Park, OH, 1988.
2. J. Gurland, "The Measurement of Grain Contiguity in Alloys," *Trans. AIME* 212, 452-455 (1958).
3. S. F. Duffy and S. M. Arnold, "*Noninteractive Macroscopic Reliability Model for Whisker-Reinforced Ceramic Composites*," submitted to *J. Comp. Mats.*

3.3 ENVIRONMENTAL EFFECTS

Environmental Effects in Toughened Ceramics

N. L. Hecht (University of Dayton)

Objective/scope

Since 1985 the University of Dayton has been involved in a three-phase project to investigate the effects of environment on the mechanical behavior of commercially available ceramics being considered for heat engine applications. In the first phase of this project the effects of environment on the mechanical behavior of transformation toughened ZrO_2 ceramics were investigated. In the second phase, two Si_3N_4 (GTE-PY6 and Norton/TRW-XL144) and one SiC (Hexoloy α-SiC) were evaluated (see Appendix I). In the third phase, which is in progress, the tensile, flexural, and fatigue strength properties of nine SiC and Si_3N_4 ceramics (see Table 1) are being evaluated. Microstructure, chemistry, physical properties, and mechanical behavior from 25-1400°C are being investigated. A major focus of these evaluations is the flexural strength and dynamic fatigue of these materials from 1000°-1400°C.

During the past 6 months (April-September 1988) evaluations of five materials were initiated (Hexoloy α-SiC, Howmet SN-4, Kyocera SN-252, NGK EC-152, and Norton/TRW NT-154). Evaluations of Howmet SN-4 and Kyocera SN-252 were completed. In addition, activities to develop optical interferometry techniques to monitor strain and Raman spectroscopy to analyze SiC ceramics were initiated. Activities to compile a SiC and Si_3N_4 property data base from the literature were also initiated.

Experimental procedures

The research plan developed for Phase III is outlined in Table 2. Flexural strength measurements are made using two Instron Universal Testing Machines (Model 1123). Elevated temperature measurements (1000°-1400°C) are conducted in two ATS #3320 high-temperature furnaces. Flexural strengths are measured on test specimens 3 x 4 x 50 mm with the tensile surface ground and polished to a 16 microinch finish. The long

Table 1. Candidate SiC and Si_3N_4 Ceramics Selected for Evaluation.

Sohio - Hexoloy α-SiC	Cold formed (injection molded or isostatic pressing) and pressureless sintered α-SiC with additions of B and Al (200 Tensile and 200 Flexure Specimens)
Sohio - Hexoloy ST	Cold formed and pressureless sintered α-SiC and TiB_2 (60 Flexure Specimens)
GTE - PY6	Injection molded and hipped β Si_3N_4 with additions of Y_2O_3 (200 Tensile and 200 Flexure Specimens)
Norton/TRW - NT154	Sintered and HIP'ed Si_3N_4 (100 Flexure and 100 Tensile Specimens)
CVD - SiC	SiC prepared by chemical vapor deposition techniques (60 Flexure Specimens)
Howmet - SN-4	Cold formed (die pressing/isostatic pressing), sintered and HIP'ed Si_3N_4 with 10% oxide sintering aids (Al_2O_3, Y_2O_3) (60 Flexure Specimens)
Ceradyne - Ceralloy 147-3	Cold formed (isopressing/slip casting/injection molding) sintered Si_3N_4 with additions of Y_2O_3 and Al_2O_3 (60 Flexure Specimens)
Kyocera - SN252	Cold formed (isopressed/slip cast/etc.) and sintered Si_3N_4 with additions of Yb_2O_3, Y_2O_3, and Al_2O_3 (note the sintering process is controlled to promote the growth of a β Si_3N_4 whisker phase in the Si_3N_4 matrix) (60 Flexure Specimens)
NGK Spark Plug - EC-152	Gas pressure sintered Si_3N_4 with additions of Al_2O_3 and Y_2O_3 (60 Flexure Specimens)

edges of the tensile surface are rounded and polished to minimize edge failures. Flexural strength is measured using four-point bend test fixtures, and the test specimens are loaded using machine crosshead speeds of 0.004, 0.0004, and 0.00004 cm/sec. For the room temperature measurements the bend fixtures are made of steel, and for the measurements at 1000°, 1200°, and 1400°C the bend fixtures are made of SiC. The four-point bend fixtures have an outer span of 4 cm and an inner span of 2 cm.

The data from the fast, medium, and slow loading rates provide the basis for the dynamic fatigue analysis of the candidate materials. The dynamic fatigue can be characterized by a ln-ln plot of fracture strength (σ_f) versus loading rate ($\dot{\sigma}$) which is expressed by the relationship: $\sigma_f = A'\dot{\sigma}^{(\frac{1}{n+1})}$ (where A′ is a constant). The constant, n, is a measure of the stress corrosion susceptibility of the material. Large values of n are synonymous with lower stress corrosion or fatigue.

The tensile strength measurements are made using an Instron Electro-Mechanical Test System (Model 1361) equipped with Super-Grip Instron Universal Coupling and Water-Cooled Holders for High-Temperature Tensile Testing. For high temperature measurements an Instron High Temperature Short Furnace is used. The buttonhead test specimens used for the tensile strength measurements are shown schematically in Figure 1.

Fracture origins are determined by optical microscope and SEM (JOEL/SM-80 with EG&G Ortec System 5000 Microanalysis System). The strength values obtained are also evaluated by Weibull analysis. Maximum likelihood estimates of the shape parameter, m (modulus), and the scale parameter, So (the 63rd percentile for the distribution of breaking strength), are determined by this analysis.

Table 2. Research Plan

Task I Project Initiation

Phase I - Candidate Material Selection

A. Review Candidate Material Options
B. Select Two to Three Candidate Materials for Investigation and Evaluation and Establish Procedures for Specimen Preparation and Specifications for Surface Finish
C. Place Order for Flexure and Tensile Specimens

Phase II - Re-evaluate and Finalization of Testing Protocol

A. Review of Testing Protocol Technology
B. Re-evaluation of Flexure Testing Facility

Phase III - Establish Protocol for Data Storage

A. Investigate Computer Data Storage Systems
B. Establish the Data Storage Protocol to be Used

Task II Investigation of Fatigue at Elevated Temperatures

Phase I - Dynamic Fatigue -- Four Point Flexure Testing @ 1000°C/1200°C/1400°C in Air at Three Loading Rates

Phase II - Tensile Stress Rupture (static fatigue) @ 1000°C/1200°C/1400°C in Air at 2/3 the measured fast fracture tensile strength

Phase III - Analysis of Results

A. Statistical Analysis of Test Data
B. Fracture Analysis - Visual Inspection/ Microscope Examination/SEM and EDXA Examination/TEM/Auger

Task III Tensile Strength Measurements

Phase I - Measurement of Tensile Strength @ 25°C/500°C/750°C/1000°C/1200°C/1400°C

Phase II - Analysis of Test Results

A. Statistical Analysis of Tensile Test Data
B. Fracture Analysis - Visual Inspection/ Microscope Examination/SEM and EDXA/TEM

(continued ...)

Table 2. Research Plan (Concluded)

Task IV Material Characterization

A. Microstructure and Chemistry - Optical Microscopy/SEM and EDXA/XRD/Raman and IR Spectroscopy/Auger
B. Density (immersion)/Hardness (Vickers microhardness)/Coefficient of Thermal Expansion
C. Fracture Toughness - Controlled Flaw Method at 25°C/1000°C/1400°C (alternate methods of measuring K_{Ic} will be investigated)
D. Elastic Modulus - By Sonic Methods and Possible Interferometry at 25°C/1000°C/1400°C
E. Flexural Strength - Measurement of Flexural Strength in Air @ 25°C/500°C/750°C (analysis of results - statistical analysis/fracture analysis)

Task V Data Base Extension

Phase I - Review and Finalize Data Storage System to be Used

Phase II - Establish Data Storage Protocol and Format

Phase III - Initiate Data Storage Program

Task VI Project Addendum - Limited Characterization of Additional Si_3N_4 and SiC Ceramics

Phase I - Candidate Material Identification and Selection

Phase II - Materials Evaluation - High Temperature Dynamic Fatigue Evaluation (1000°C/1200°C/1400°C)

Phase III - Extended Material Analysis - Tensile Strength Measurement @ 25°C/500°C/1000°C/1400°C Data, Fracture Toughness @ 25°C and 1400°C, Flexural Strength Measurements at 25°C and 500°C, Analysis - Weibull analysis/Fracture Analysis

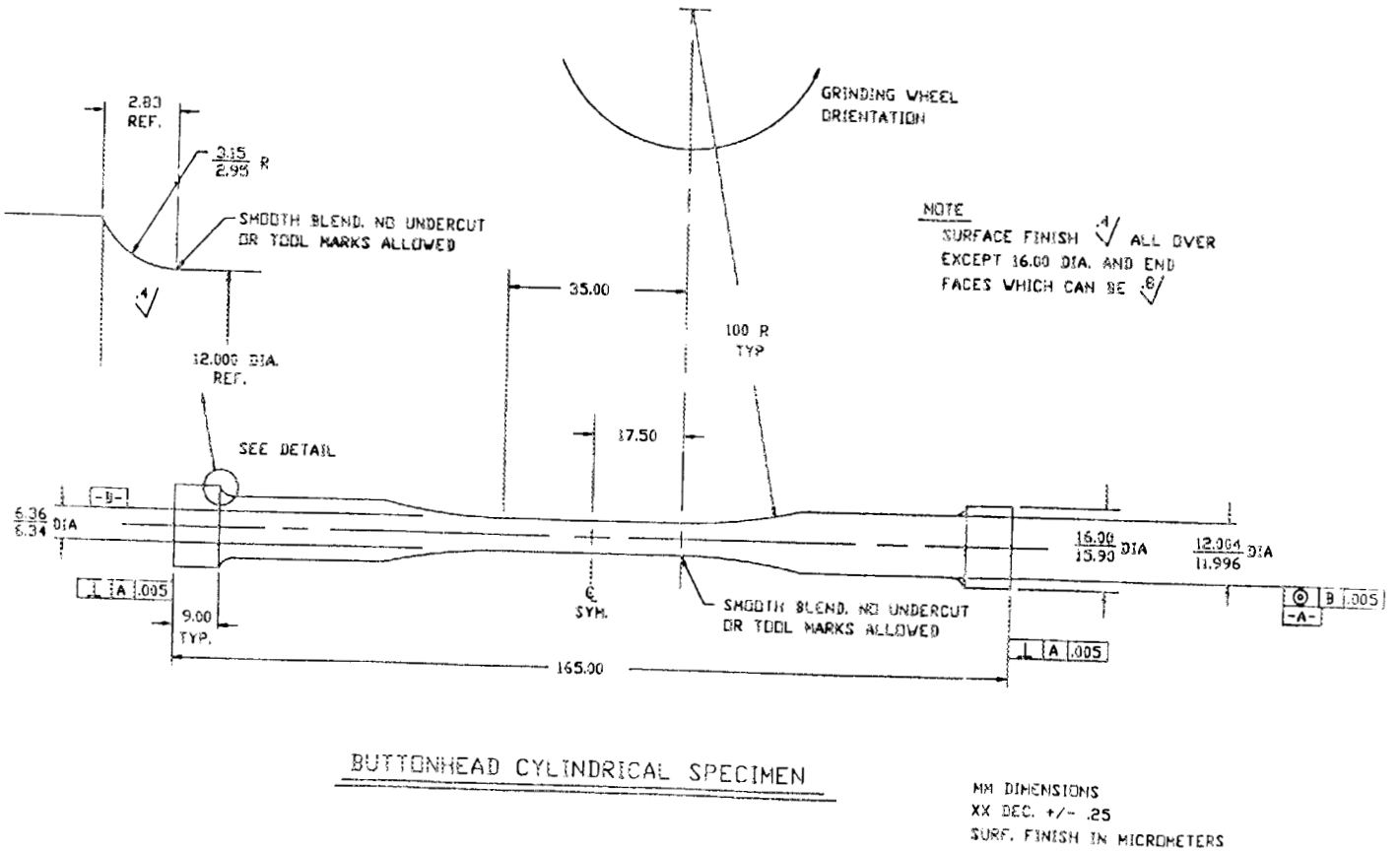

BUTTONHEAD CYLINDRICAL SPECIMEN

MM DIMENSIONS
XX DEC. +/- .25
SURF. FINISH IN MICROMETERS

Figure 1. Buttonhead cylindrical specimen.

The elastic modulus of the candidate materials is measured by a Grindo-Sonic (Model MR35T) Transient Impulse/Elastic Modulus Apparatus. The hardness of the candidate materials is measured by a Vicker's microindent hardness tester.

The microstructure and chemistry of the candidate materials are also being studied. Polished sections from representative specimens are viewed by optical microscope (Nikon Epiphot), and freshly fractured sections are viewed by scanning electron microscope (JOEL JSM-840). X-ray fluorescence (EDXA) spectra are obtained using the EG&G Ortec System 5000 attached to the JSM-840. Test specimens are also examined by x-ray diffraction using a Norelco/Philips Electronic Instruments XRD System. X-ray diffraction is conducted by CuKα radiation (40 KV, 25 μA) for analysis from 20° 2θ to 58° 2θ. In addition further chemical analysis of selected specimens is obtained using high-resolution scanning Auger spectroscopy (JOEL JAMP-30).

Thermal expansion coefficients are measured from 25°-1400°C using a Theta Industries Dilatronic II (Model 6024). Fracture toughness is measured by both the controlled flaw method and the microindent method.

Technical progress

Mechanical and physical property measurement results

The results of the physical property measurements obtained for αSiC, SN-4, and NT-154 are summarized in Table 3. The flexural strength data obtained for Howmet SN-4 and Kyocera SN-252 are summarized in Table 4. The interim flexural strength data obtained for α-SiC, EC-152, and NT-154 are summarized in Table 5. A series of bar graphs comparing flexural strength with loading rate and temperature for the four Si_3N_4 materials evaluated to date are presented in Figure 2. A similar bar graph display for Hexoloy α-SiC is presented in Figure 3.

The flexural strength data obtained for each of the candidate materials were also characterized by Weibull analysis. The results of these analyses are summarized in Table 6. The flexural strength data were also used for preparing computer-generated graphs of $\ln\sigma_f$ versus $\ln \dot{\sigma}$ and for determining n. The results of these calculations are summarized in Table 7 and the ln-ln plots obtained are shown in Figures 4 through 12.

Table 3. Physical Property Measurement Results

Property Measurement	Sohio Hexoloy α-SiC	Howmet SN-4	Norton TRW NT-154
Density (g/cc)	3.17	3.23	3.23
Young's Modulus (GPa)	427.0	204.0	310.5
Hardness (kg/mm^2)	2727	-	-
Coefficient of Thermal Expansion ($10^{-6}/°C$)	5	-	-

Table 4. Flexural Strength Measurements for Howmet SN-4 and Kyocera SN-252

Material	Temperature °C	Machine Crosshead Speed cm/sec	Flexural Strength MPa	Standard Deviation MPa	Fracture Origin
SN-4	25	0.004	977	129	Surface flaws
	1000	0.004	744	91	Surface flaws
	1000	0.00004	514	47	Surface flaws possible SCG
	1200	0.004	402	40	Surface flaws
	1200	0.00004	312	15	Surface flaws possible SCG
	1400	0.004	190	--	Severe oxidation and blistering
SN-252	1000	0.004	526	31	At surface and edges due to the presence of large whiskers
	1000	0.00004	466	26	
	1200	0.004	478	43	At surface and edges due to the presence of large whiskers
	1200	0.00004	485	35	
	1400	0.004	459	29	At surface and edges due to large whiskers
	1400	0.00004	498	29	Specimens undergo severe plastic deformation prior to fracture

Table 5. Flexural Strength Measurements for Hexoloy α-SiC, NGK EC-152, and Norton/TRW NT-154

Material	Temperature °C	Machine Crosshead Speed cm/sec	Flexural Strength MPa	Standard Deviation MPa	Fracture Origin
α-SiC	25	0.004	402	52	Tensile surface flaws
	1000	0.004	416	30	
	1000	0.0004	416	49	
	1000	0.00004	412	37	Tensile surface and edge flaws (pits/ voids and possible inclusions)
	1200	0.004	435	53	
	1200	0.0004	400	60	
	1200	0.00004	441	6	
	1400	0.004	436	48	
	1400	0.0004	415	40	
	1400	0.00004	390	36	
EC-152	1000	0.004	843	104	Surface flaws
	1200	0.004	826	35	Edge and surface flaws
	1400	0.004	389	59	Surface flaws
	1400	0.00004	269	--	Plastic deformation prior to fracture
NT-154	25	0.004	907	79	Surface/ subsurface and edge flaws
	1400	0.004	610	30	
	1400	0.00004	364	69	Plastic deformation prior to fracture

Table 6. Weibull Statistics for SiC and Si_3N_4 Specimens.

Material Designation	Temperature °C	Loading Rate MPa/sec	Weibull Modulus m	Weibull[+] Scale-data So-MPa	Weibull[*] Scale-area So-MPa
Hexoloy α-SiC	21	190	8.83	424	147
	1000	1.71	12.5	428	202
		17.1	11.03	436	186
		171	18.13	429	255
	1200	1.43	9.8	465	179
		14.3	8.67	424	144
		143	8.79	457	158
	1400	1.33	15.23	405	218
		13.3	12.18	432	200
		133	10.87	457	193
SN-252	1000	1.33	20.53	478	303
		133	19.19	540	331
	1200	1.19	19.94	499	311
		119	12.56	497	236
	1400	1.14	20.78	511	325
		114	18.68	472	285
NT-154	21	143	15.27	940	508
	1400	1.14	6.87	391	100
		114	23.11	624	415
SN-4	20	143	11.45	1025	452
EC-152	1000	133	9.86	887	343
	1200	119	24.7	842	576

[+]So-Scale-data -- The 63rd percentile for the distribution of strength for the specimens tested.

[*]So-Scale-area -- Assumes a failure resulting from a surface flaw and adjusts the scale-data to account for specimen surface area.

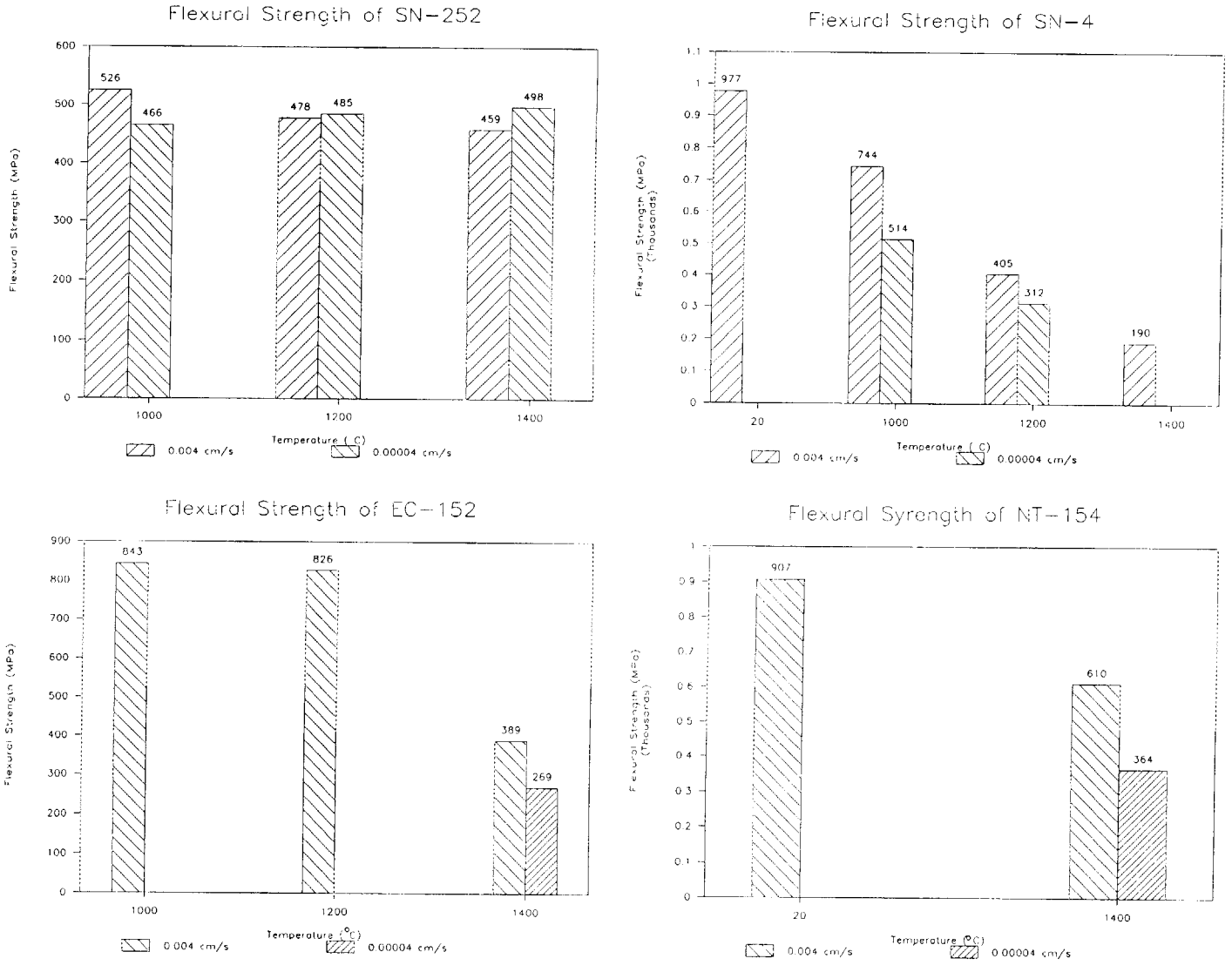

Figure 2. Bar graphs of flexural strength results for SN-252, SN-4, EC-152, and NT-154.

Table 7. Slow Crack Growth Parameter (n) Values

Material	Temperature	n Values
Sohio Hexoloy α-SiC	1000°C	Slope not significantly greater than zero
	1200°C	Slope not significantly greater than zero
	1400°C	41
Kyocera SN-252	1000°C	37
	1200°C	Slope not significantly greater than zero
	1400°C	Slope significantly less than zero (n = -58)
Howmet SN-4	1000°C	12
	1200°C	17
Norton NT-154	1400°C	7.6

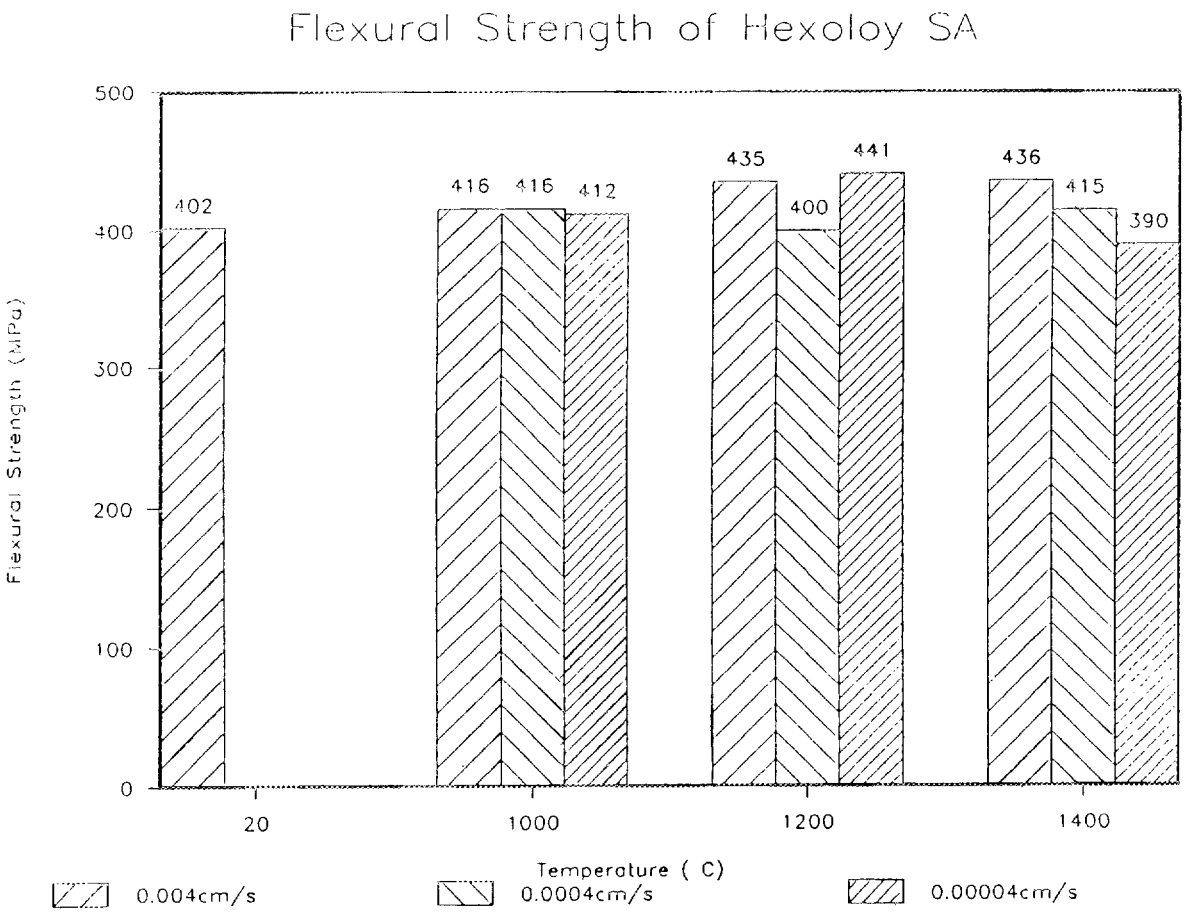

Figure 3. Bar graph of α-SiC at 1000°/1200°/1400°C.

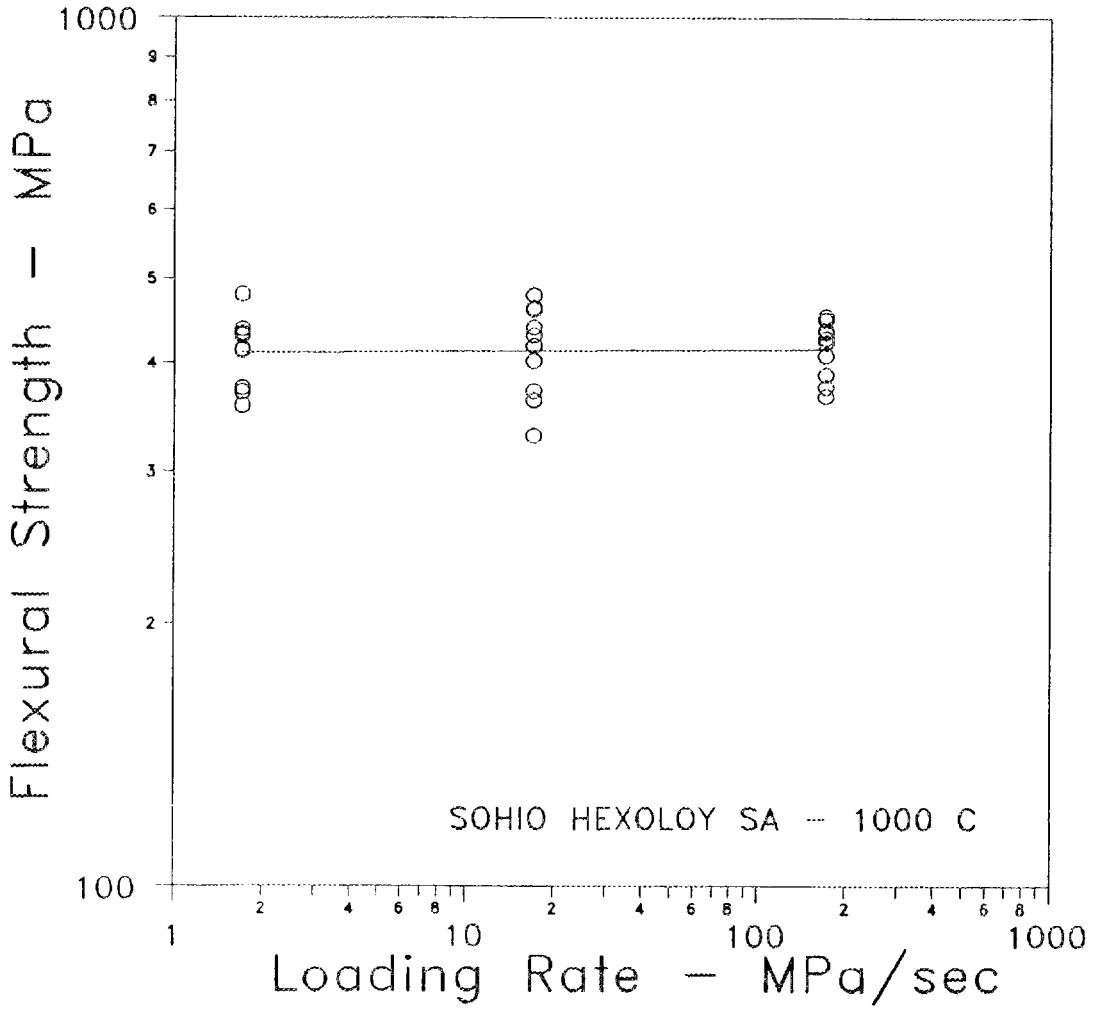

Figure 4. Flexural strength versus loading rate for Hexoloy α-SiC at 1000°C.

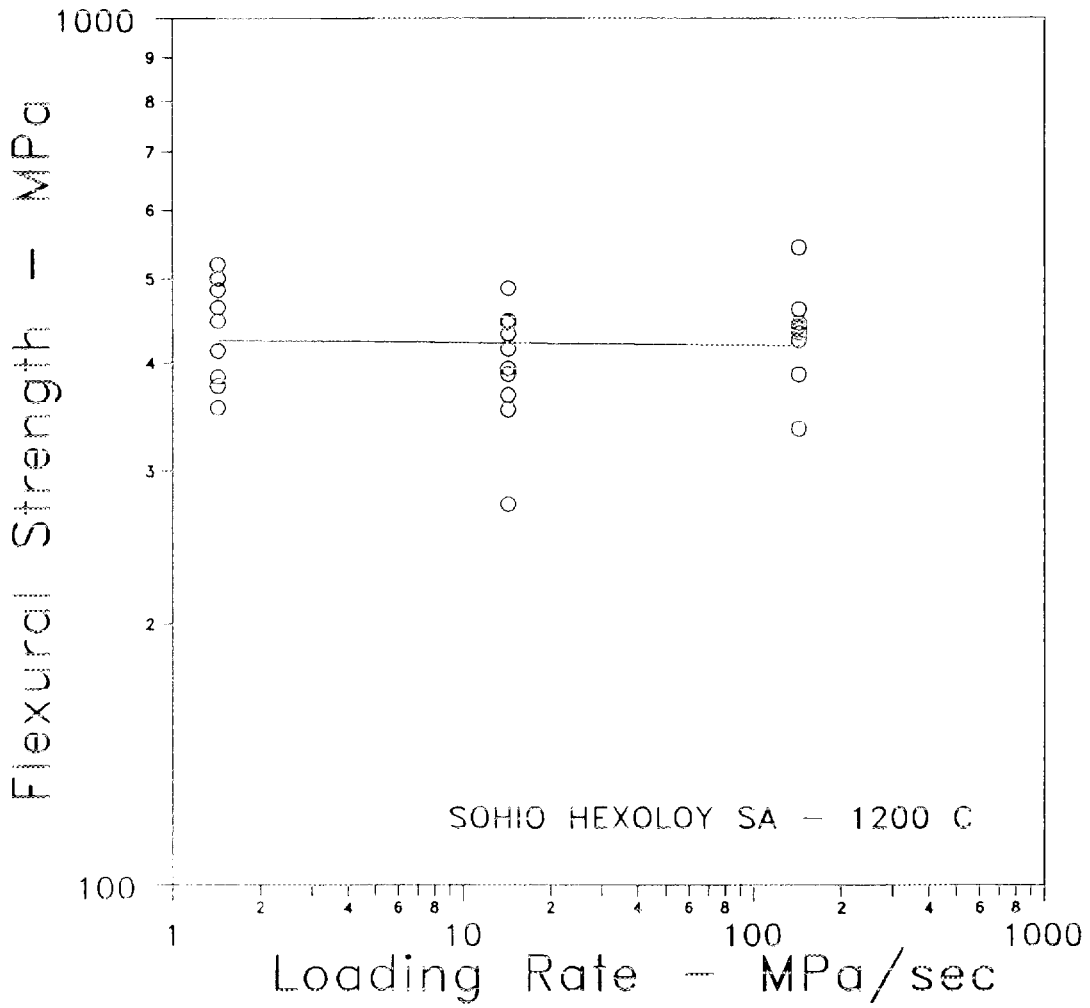

Figure 5. Flexural strength versus loading rate for Hexoloy α-SiC at 1200°C.

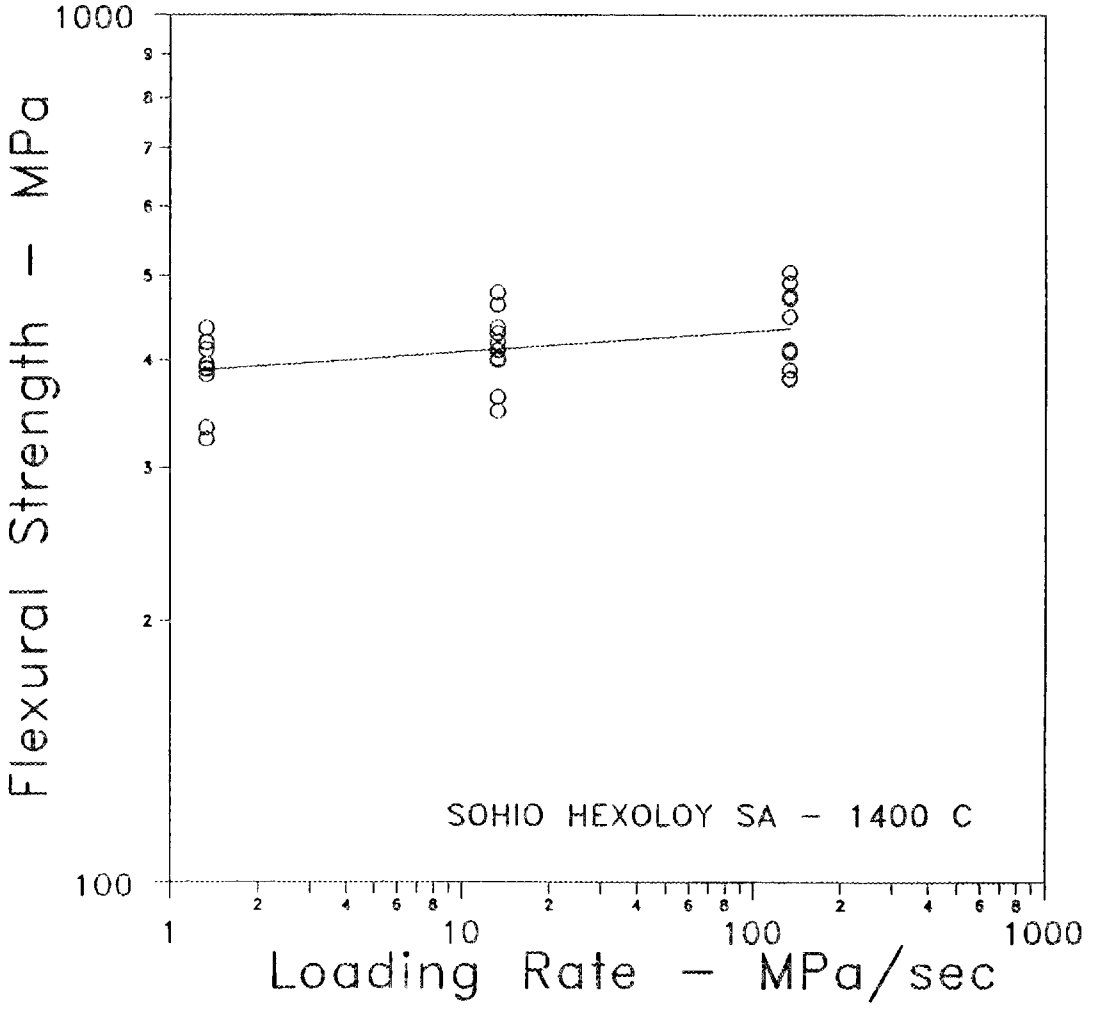

Figure 6. Flexural strength versus loading rate for Hexoloy α-SiC at 1400°C.

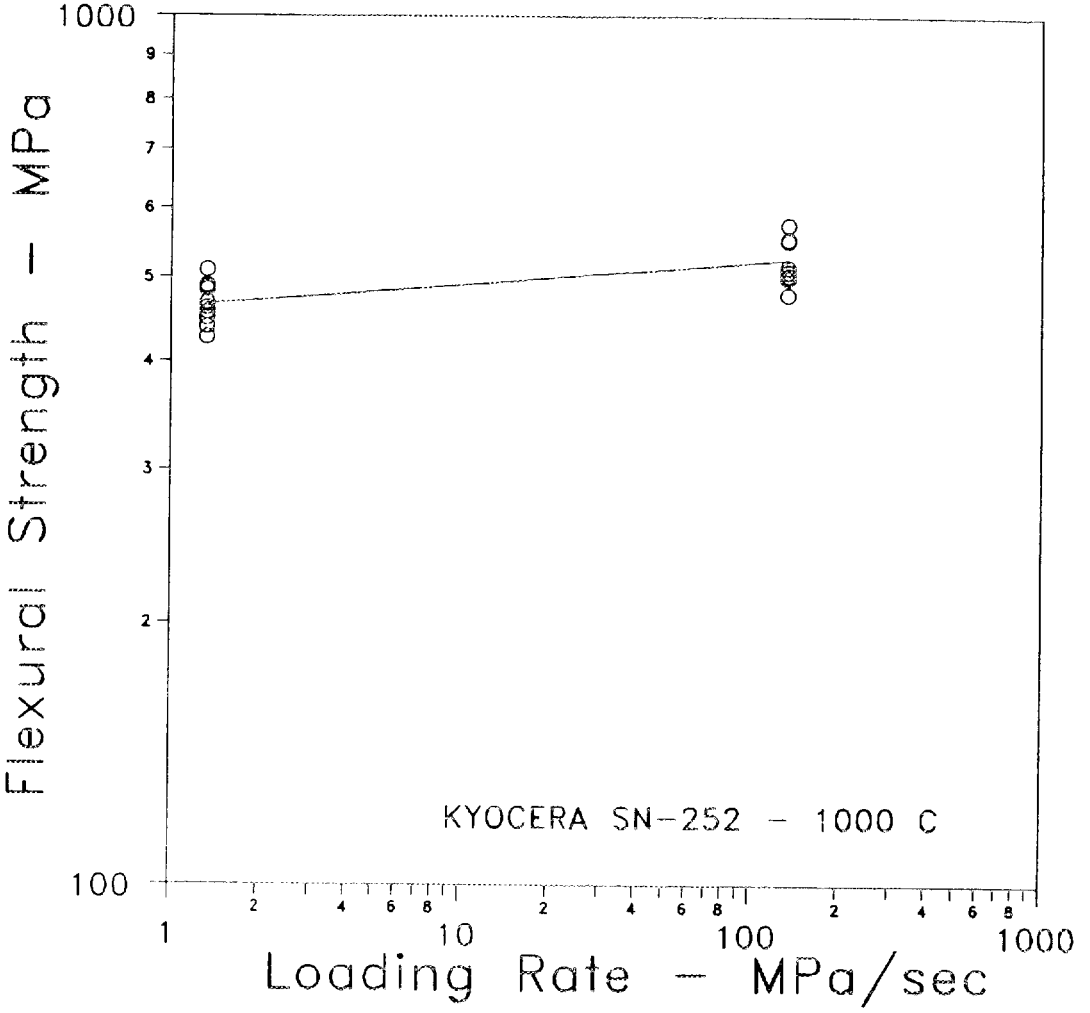

Figure 7. Flexural strength versus loading rate for SN-252 at 1000°C.

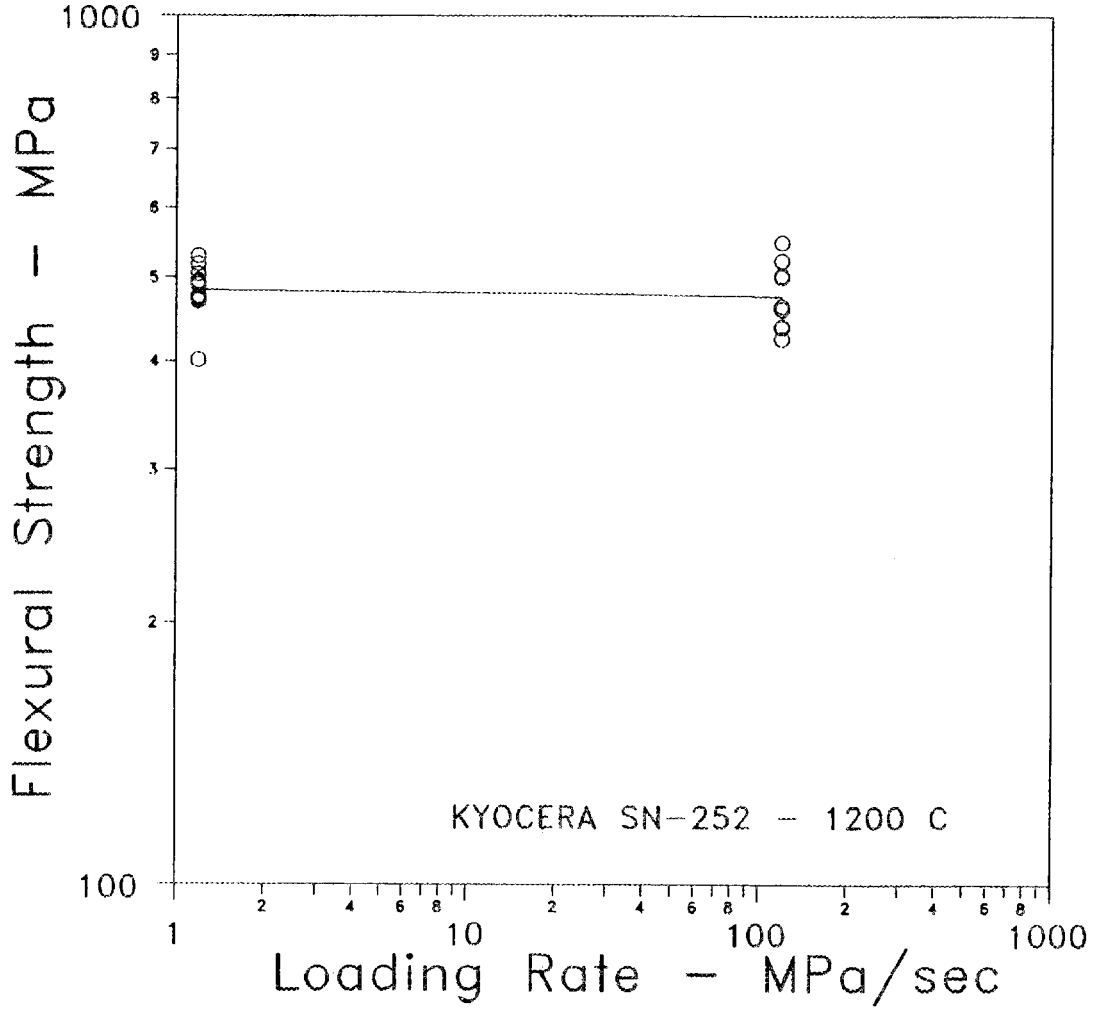

Figure 8. Flexural strength versus loading rate for SN-252 at 1200°C.

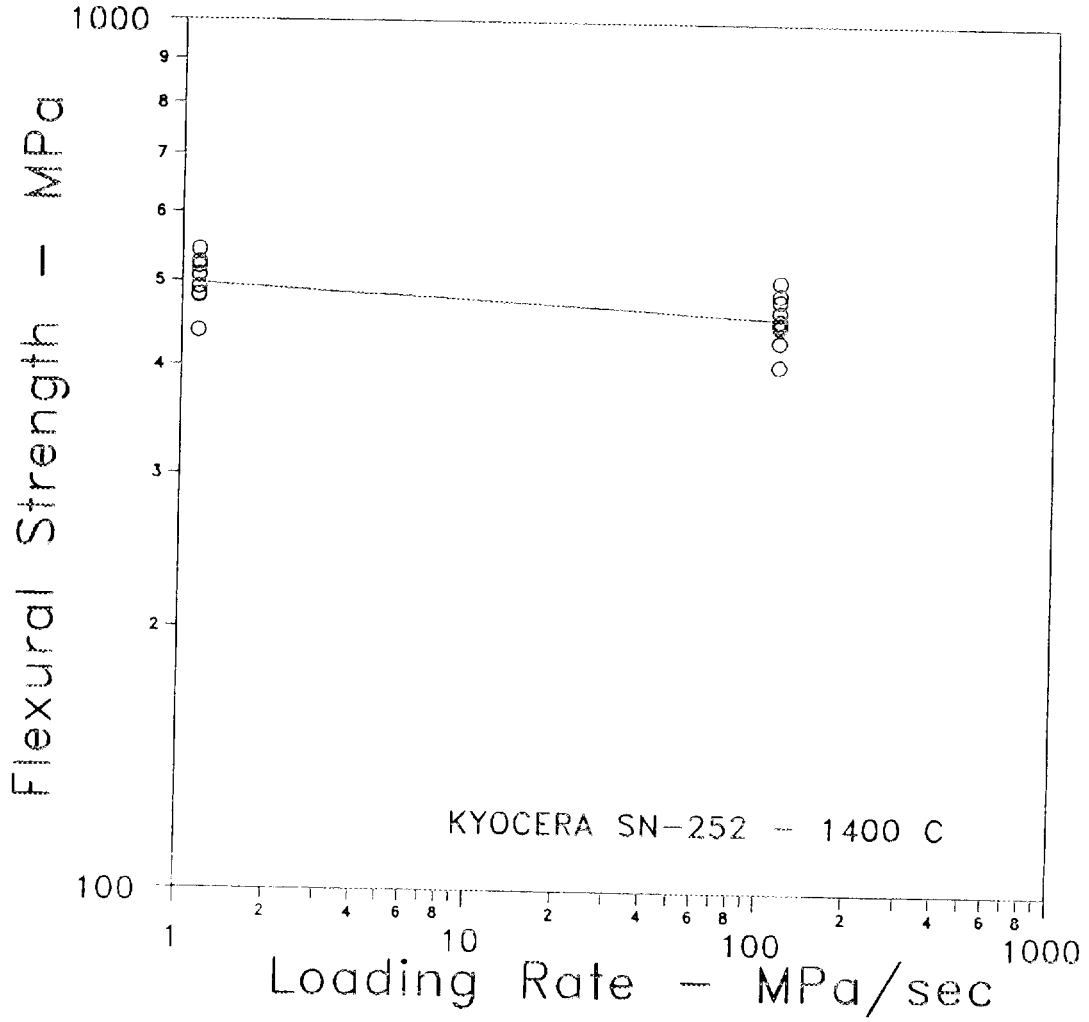

Figure 9. Flexural strength versus loading rate for SN-252 at 1400°C.

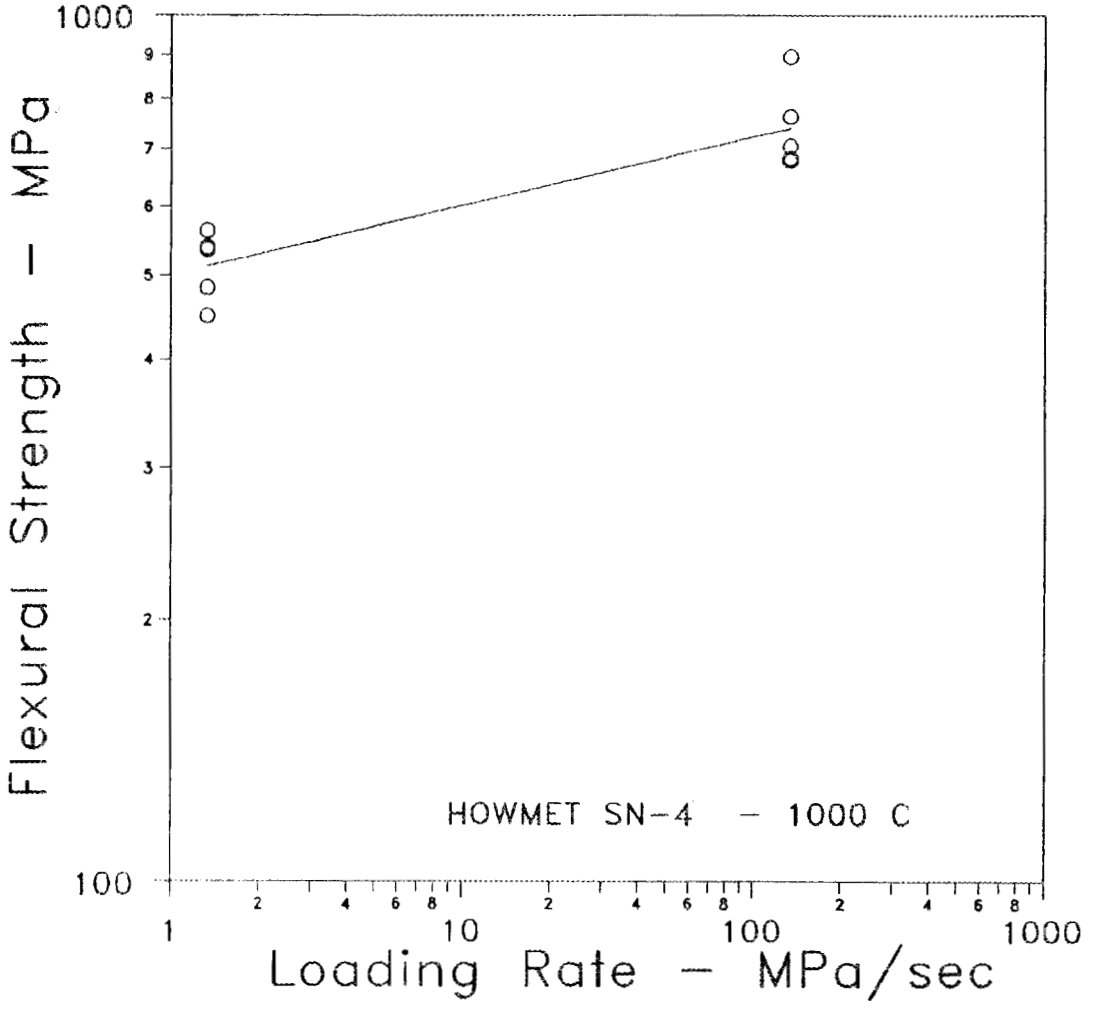

Figure 10. Flexural strength versus loading rate for SN-4 at 1000°C.

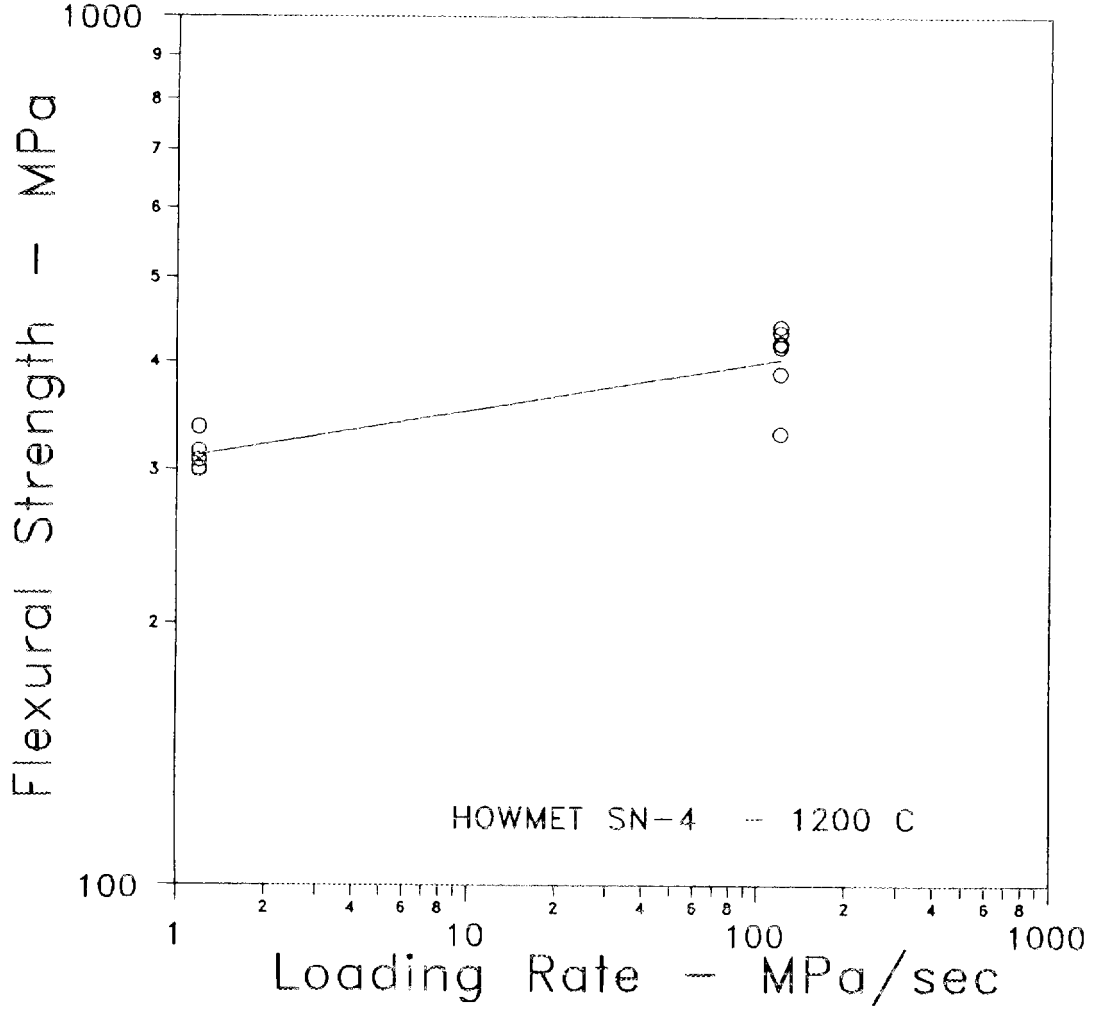

Figure 11. Flexural strength versus loading rate for SN-4 at 1200°C.

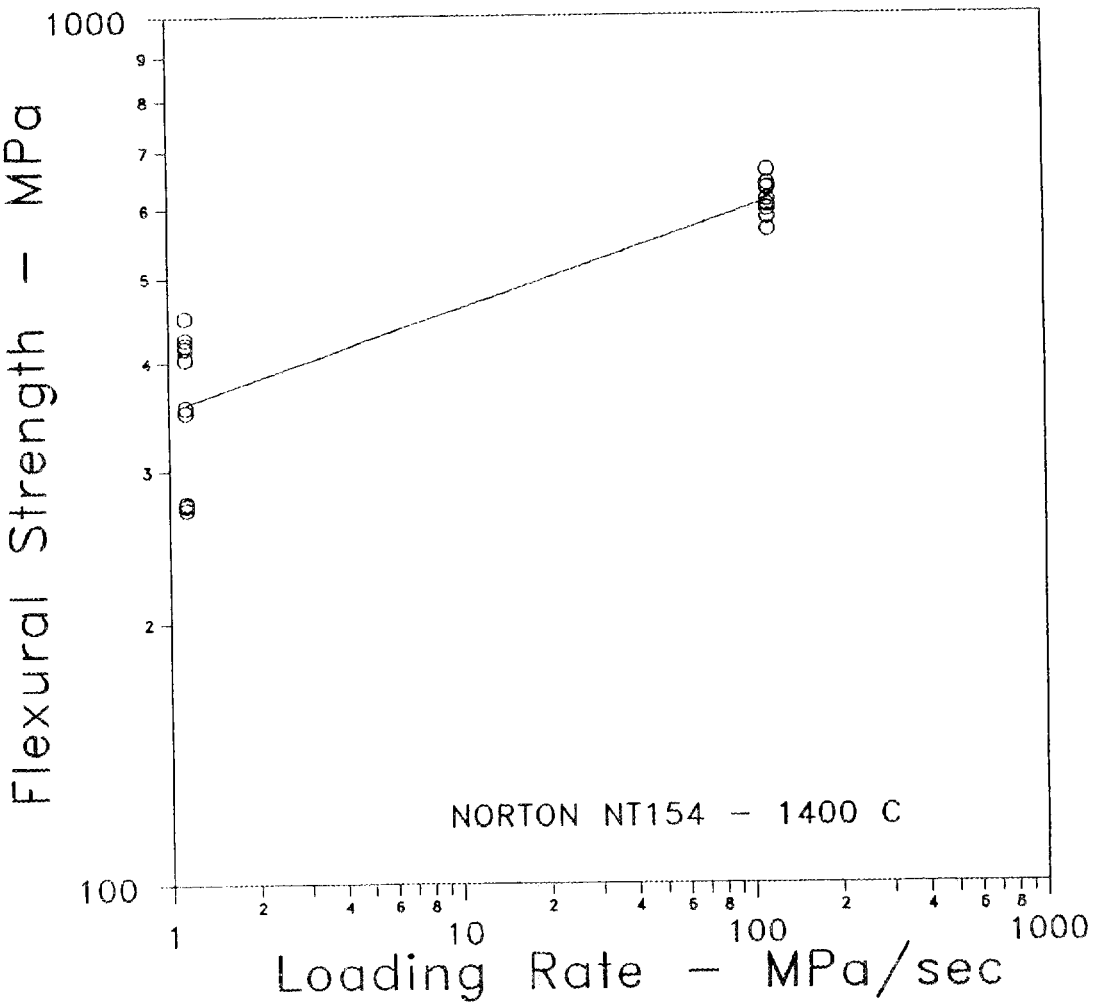

Figure 12. Flexural strength versus loading rate for Norton NT-154.

Photographs of typical fracture surfaces obtained by optical microscope and SEM were prepared. Photomicrographs of typical fracture surfaces for Hexoloy α-SiC are presented in Figures 13 through 17. Photomicrographs of typical fracture surfaces for Kyocera SN-252 are shown in Figures 18 through 20, for Howmet SN-4 are shown in Figures 21 through 26, for NGK EC-152 are shown in Figures 27 and 28, and for Norton/TRW NT-154 is shown in Figure 29. Fracture origins are identified in the fracture surface photomicrographs presented.

Representative specimens of each material as-received and after flexural testing were examined by EDXA. The results of these semiquantitative analyses are summarized in Table 8. These specimens were also examined by X-Ray Diffraction Analysis, and a summary of these results is presented in Table 9.

Room temperature (~21°C) tensile strength measurements were initiated for Hexoloy α-SiC using buttonhead specimens. The results of these tensile strength measurements are presented in Table 10. Although 23 specimens were tested, only 12 of the tests were considered valid. Eight of the test specimens failed at the buttonhead and three test specimens failed at severe radial grind marks in the gauge section.

From an evaluation of 12 test specimens it was found that all those examined had radius of curvatures below the buttonhead which were not in compliance with the specifications established by Instron. Specimens with radius of curvatures out of compliance with the specifications are subject to excessive stresses which could cause fracture just below the buttonhead (see Figure 30). For the 12 test specimens which failed in the gauge section, 10 failed at surface flaws (see Figure 31). These flaws may be due to radial grinding marks which were not completely polished out (see Figure 32).

Results of optical interferometry, Raman spectroscopy and database development

Based on initial studies it was determined that speckle interferometry offered the most effective means for monitoring strain during tensile testing. Speckle is the term used to refer to the grainy structure observed when viewing a surface illuminated with coherent light. The

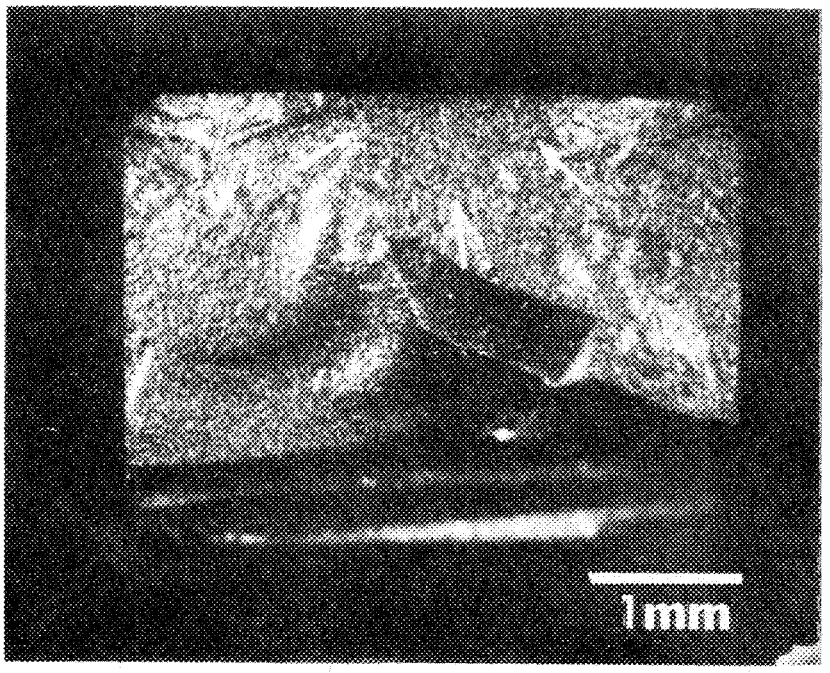

Figure 13. Typical fracture surface for Hexoloy α-SiC at 20X.

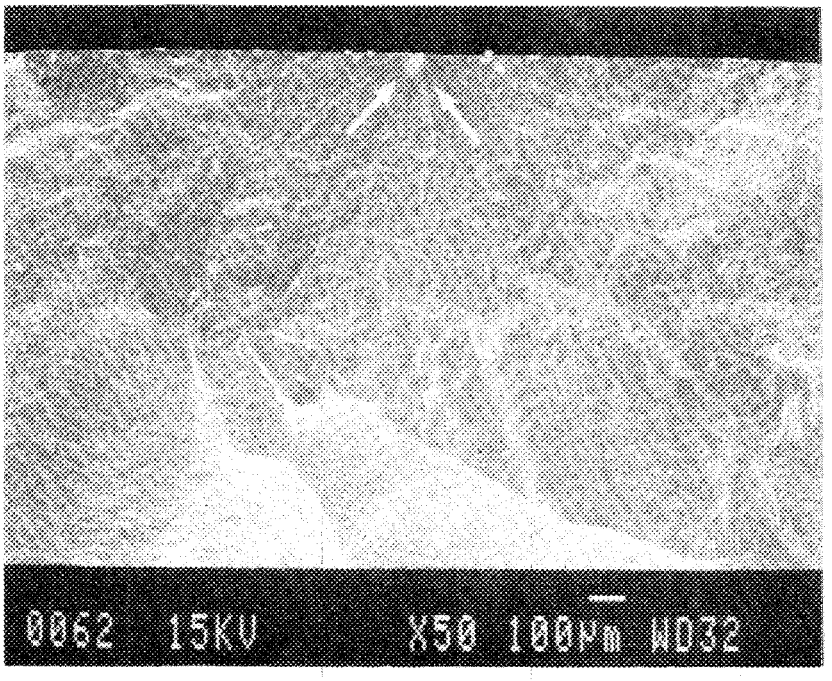

Figure 14. Typical fracture surface for Hexoloy α-SiC at 50X.

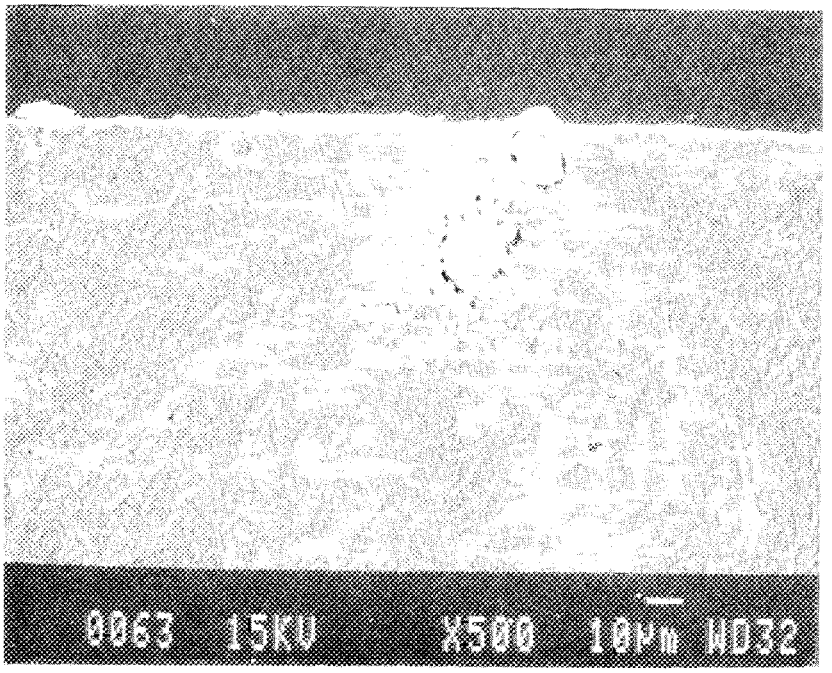

Figure 15. Typical fracture surface for Hexoloy α-SiC at 500X.

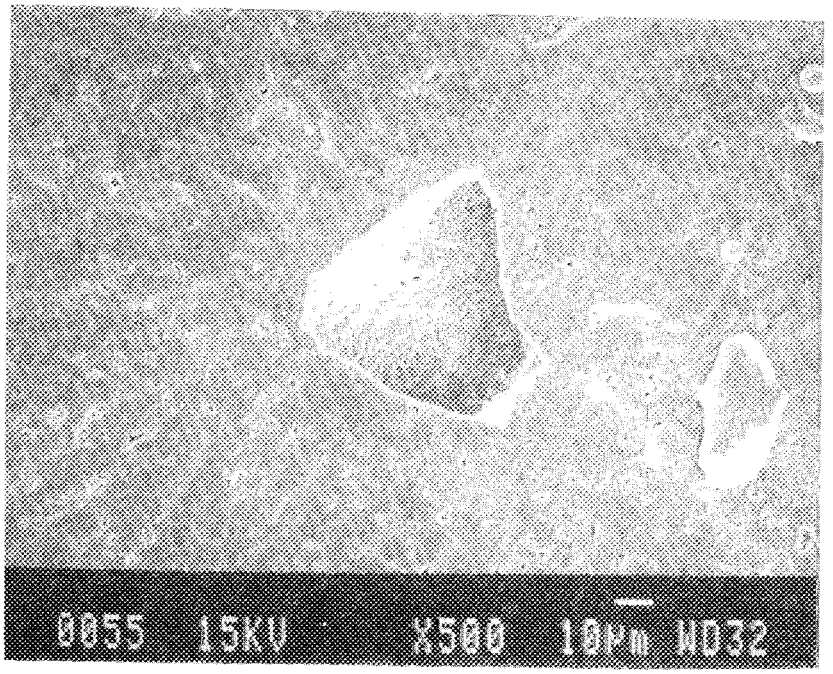

Figure 16. Subsurface flaw at the fracture origin of Hexoloy α-SiC tested at 1000°C at 500X.

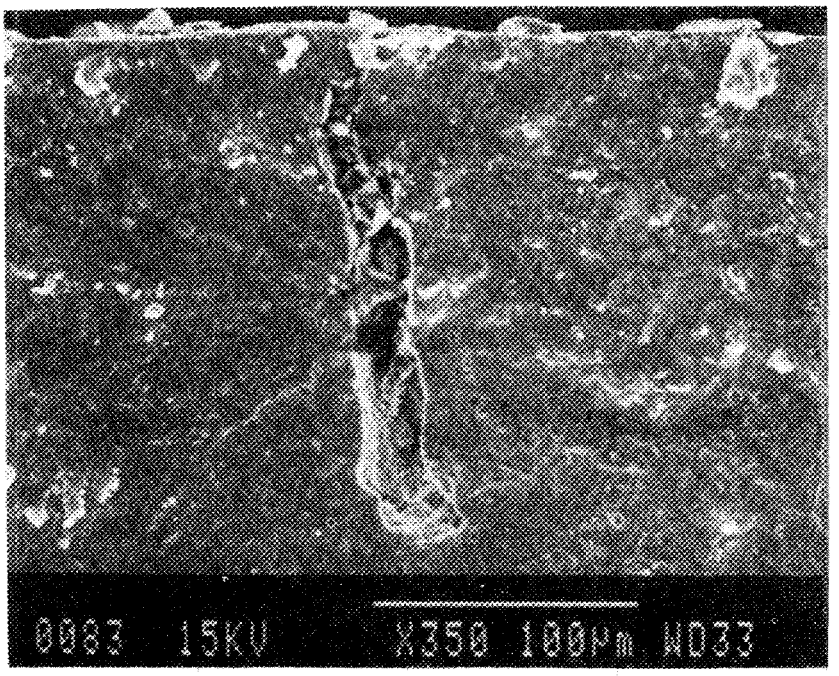

Figure 17. Surface/subsurface flaw at the fracture origin of Hexoloy α-SiC tested at 1200°C at 350X.

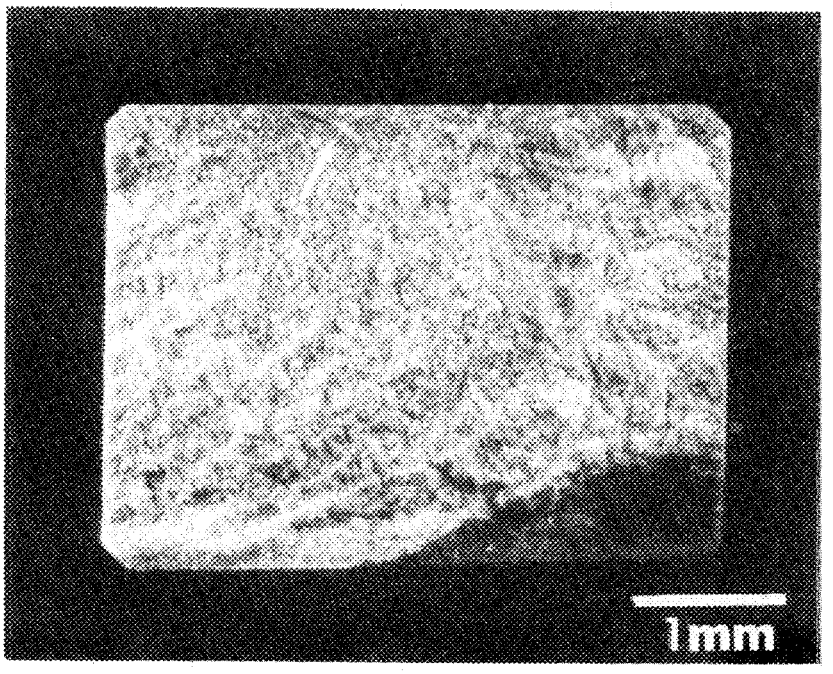

Figure 18. Typical fracture surface for Kyocera SN-252 tested at 1000°C at 20X.

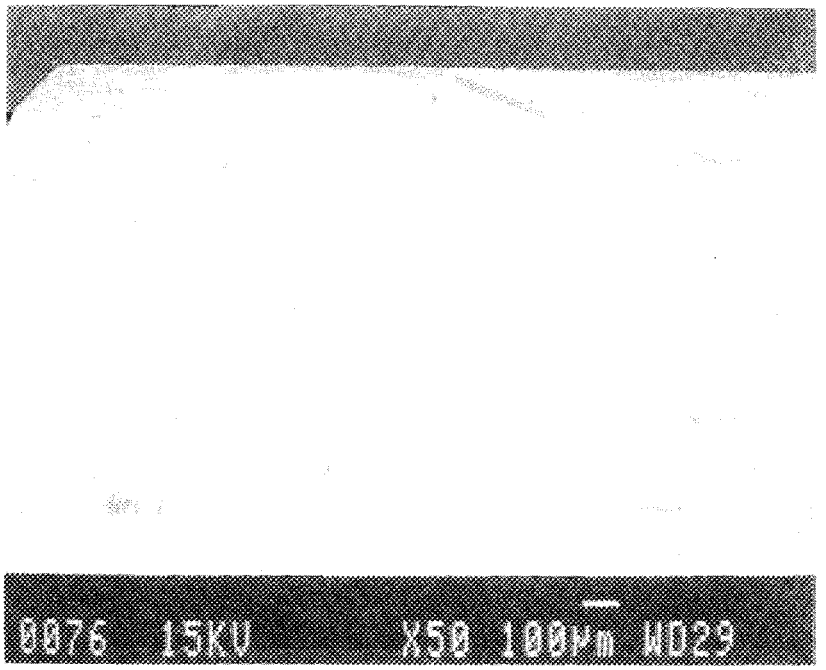

Figure 19. Typical fracture surface for Kyocera SN-252 tested at 1000°C at 50X.

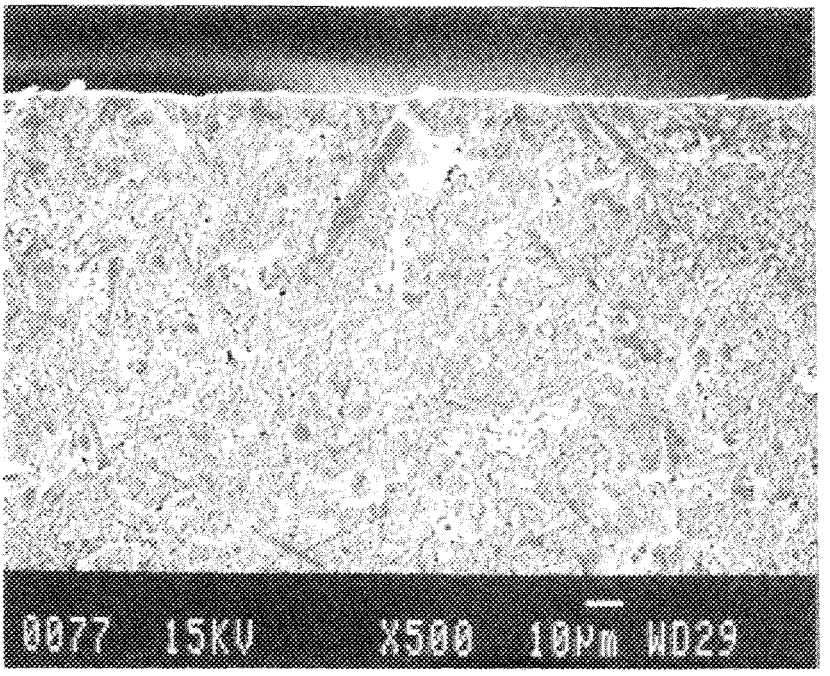

Figure 20. Typical fracture surface for Kyocera SN-252 tested at 1000°C at 500X.

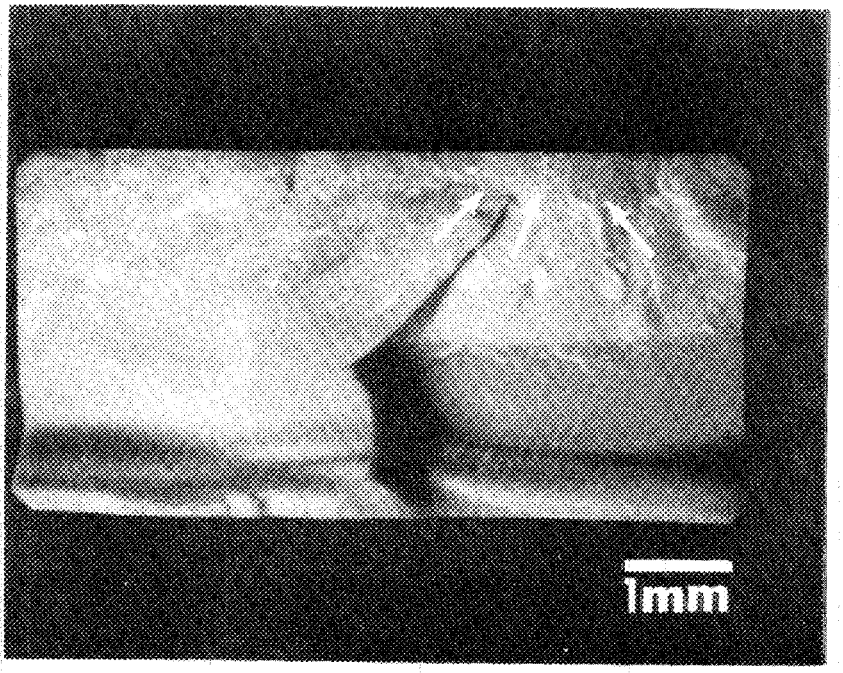

Figure 21. Typical fracture surface for Howmet SN-4 at 20X.

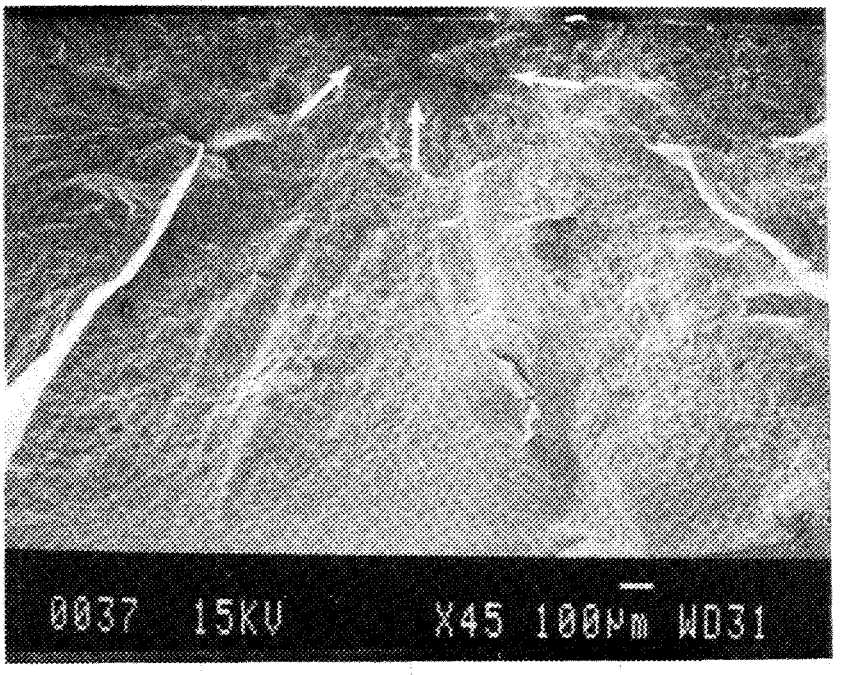

Figure 22. Typical fracture surface for Howmet SN-4 at 45X.

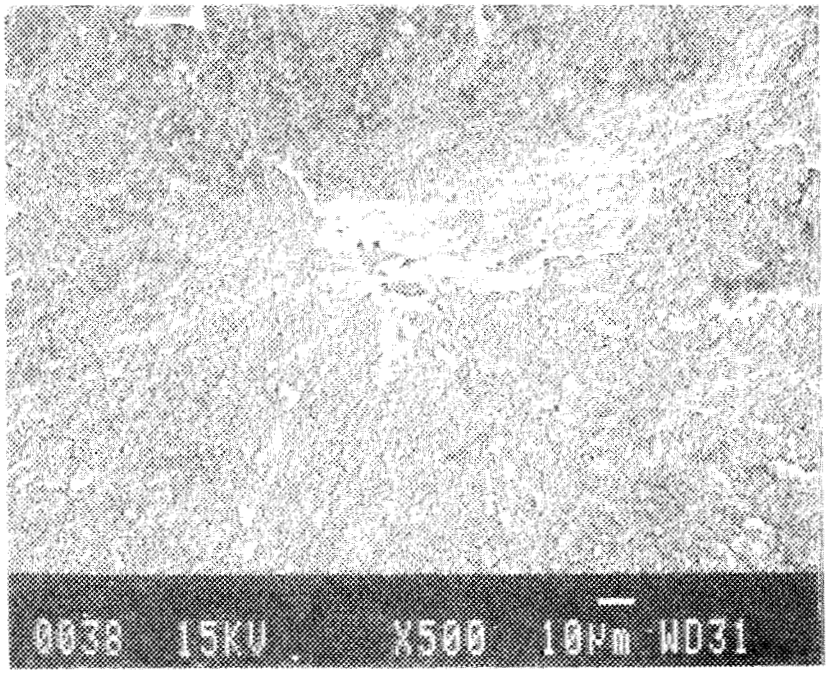

Figure 23. Typical fracture surface for Howmet SN-4 at 500X.

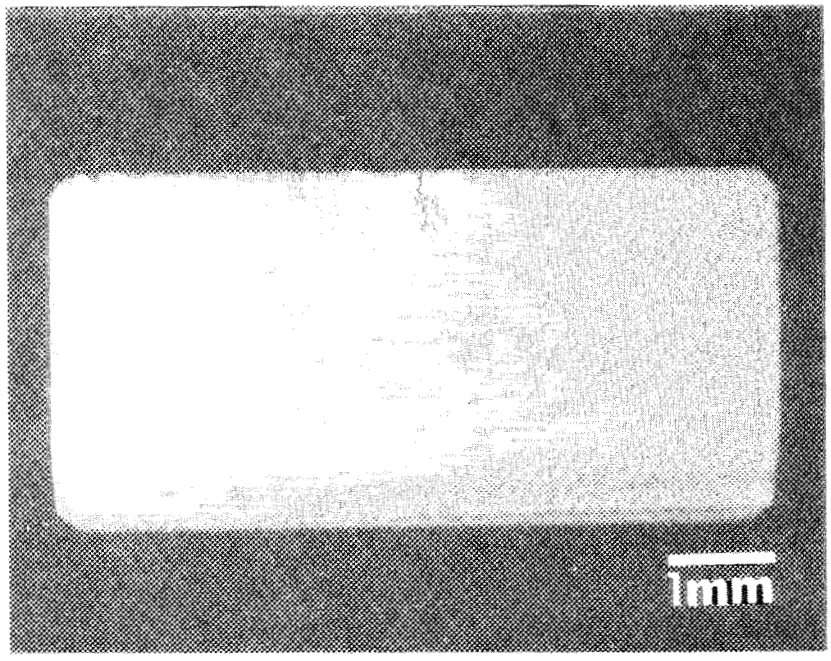

Figure 24. Fracture surface of Howmet SN-4 tested at 1200°C at 20X.

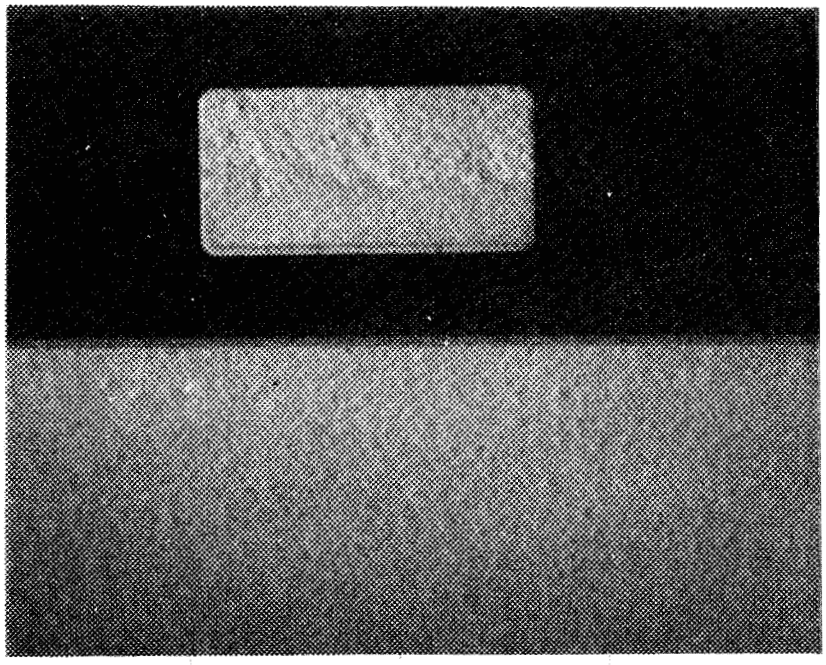

Figure 25. Top tensile surface and fracture face of Howmet SN-4 tested at 1400°C at 7X.

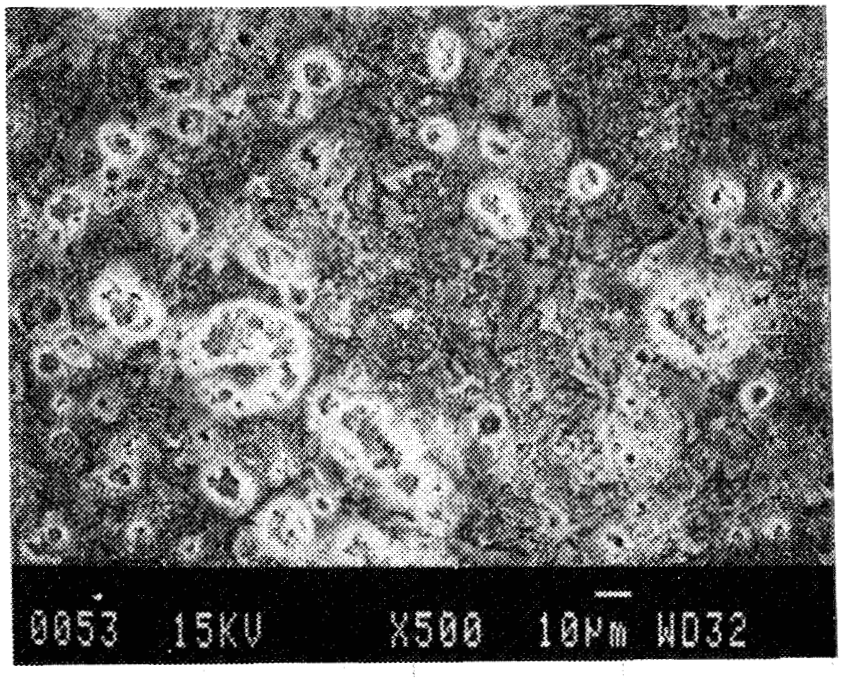

Figure 26. Fracture surface of Howmet SN-4 tested at 1400°C showing close-up of oxidized surface at 500X.

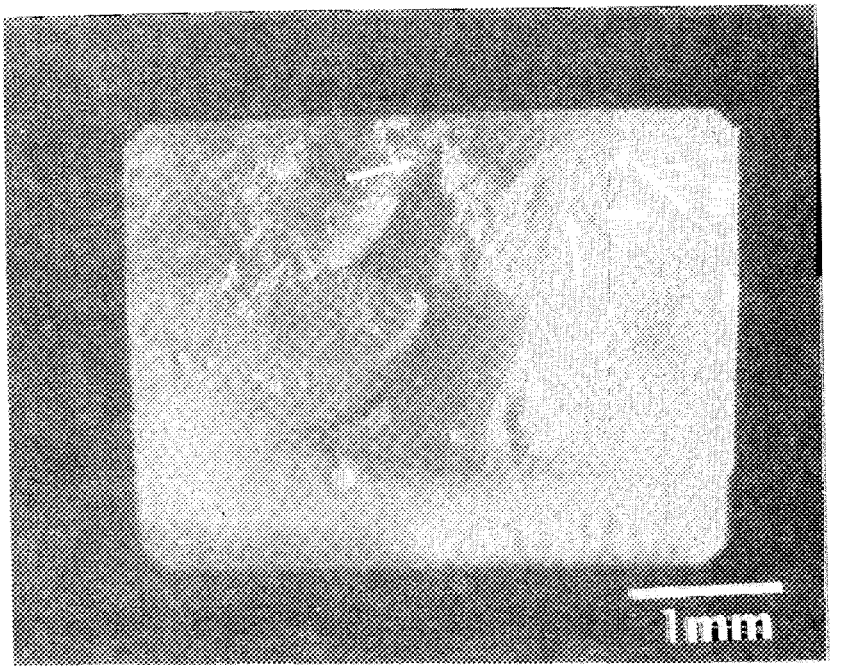

Figure 27. Typical fracture surface of NGK EC-152 tested at 1000°C at 20X.

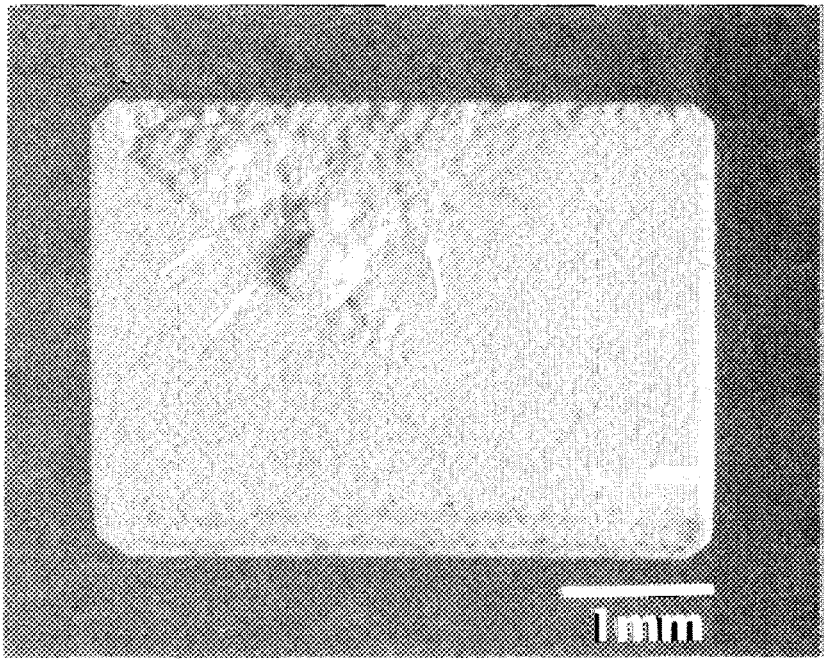

Figure 28. Fracture surface of NGK EC-152 tested at 1400°C at 20X.

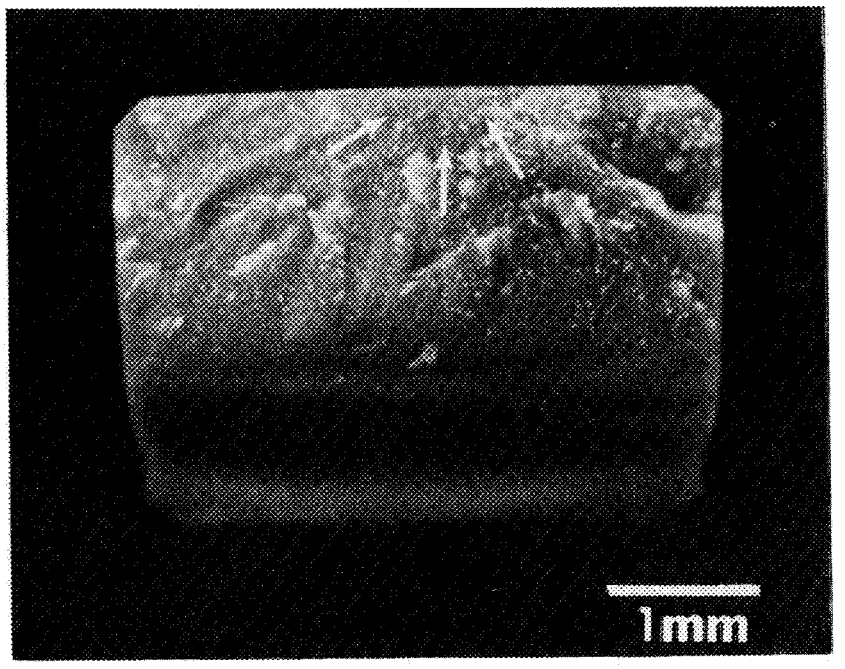

Figure 29. Typical fracture surface of Norton NT-154 tested at room temperature at 20X.

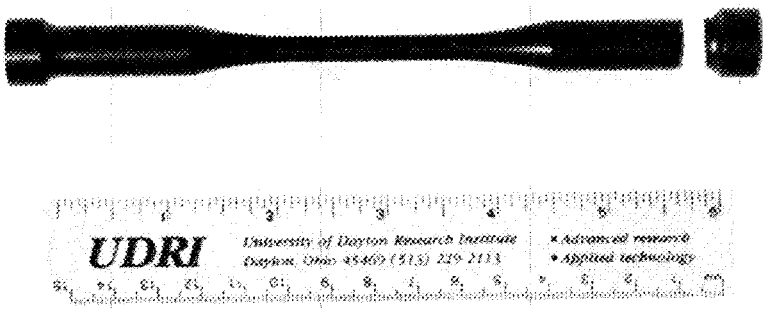

Figure 30. Typical buttonhead failure in Hexoloy α-SiC tensile specimen.

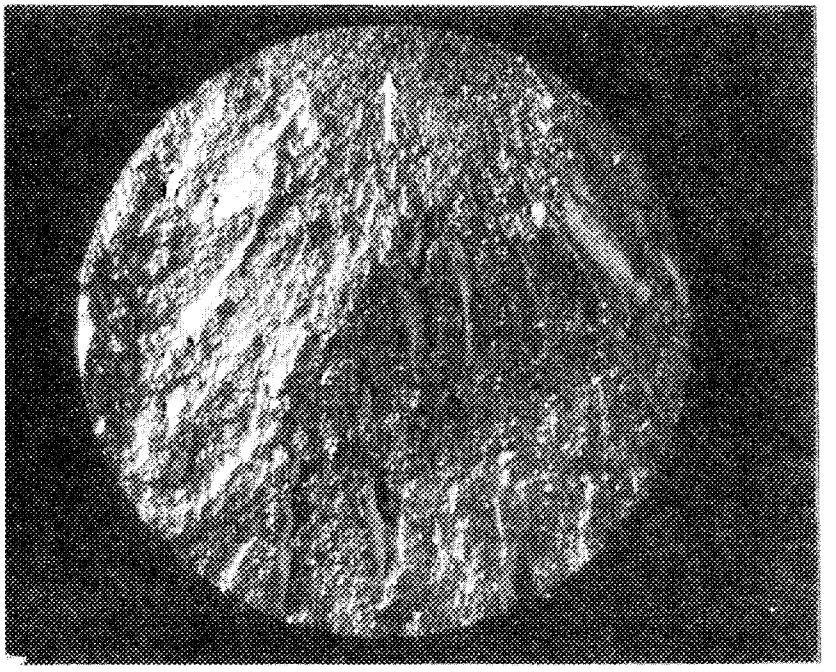

Figure 31. Typical fracture surface for a Hexoloy α-SiC tensile specimen tested at room temperature at 12X.

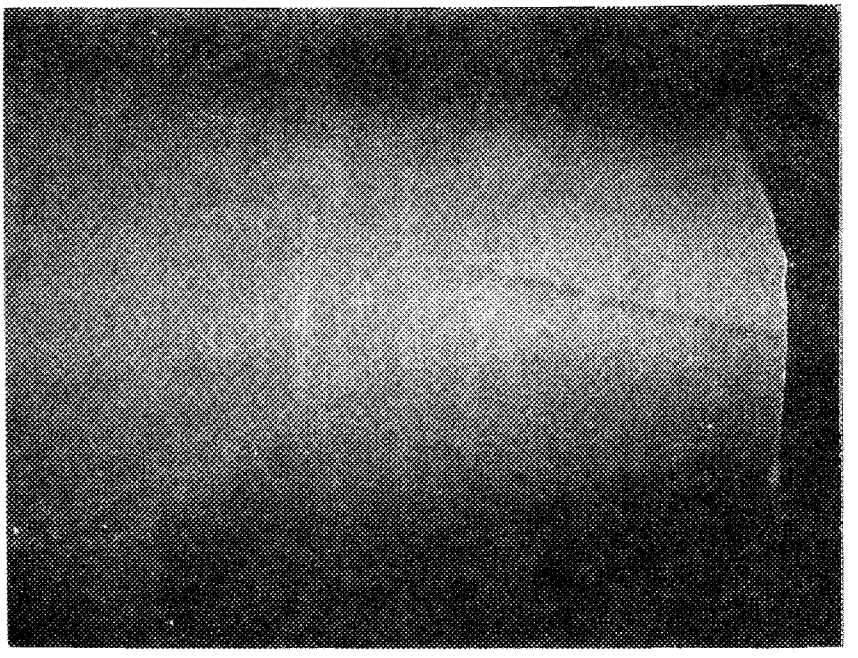

Figure 32. Typical radial grind marks observed in the guage section of the Hexoloy α-SiC tensile specimens.

Table 8. Semiquantitative Chemical Analysis of Candidate Materials

Material	Treatment Condition	Si_3N_4	Al_2O_3	Y_2O_3	Yb_2O_3	SiC
NGK EC-152	As-received	90.65	4.40	4.94	-	-
Kyocera SN-252	As-received	93.06	0.40	0.30	6.24	-
Kyocera SN-252	1000°C/fast fracture testing	77.64	trace	-	22.36	-
Kyocera SN-252	1200°C/fast fracture testing	73.74	trace	-	26.26	-
Kyocera SN-252	1400°C fast fracture testing	73.14	trace	-	26.86	-
Kyocera SN-252	1400°C alow fracture testing	65.19	trace	-	34.81	-
Howmet SN-4	As-received	90.65	5.26	4.10	-	-
Howmet SN-4	1000°C/fast fracture testing	88.82	5.20	5.98	-	-
Howmet SN-4	1000°C/slow fracture testing	90.47	4.94	4.59	-	-
Howmet SN-4	1200°C/fast fracture testing	68.50	7.83	23.67	-	-
Howmet SN-4	1200°C/slow fracture testing	66.46	9.06	24.48	-	-
Howmet SN-4	1400°C/fast fracture testing	89.71	5.16	5.13	-	-
Hexoloy α-SiC	As-received	-	-	-	-	100

Table 9. XRD Analysis of Candidate Materials

Material	2θ	D	I	2θ	D	I	2θ	D	I	2θ	D	I	Comments
	As Received			Flexure Tested at 1000°C			Flexure Tested at 1200°C			Flexure Tested at 1400°C			
Hexoloy α-SiC	34.20	2.622	24	34.35	2.611	24	34.20	2.622	19	34.25	2.618	25	α(6H)-SiC
	34.95	2.567	7	35.10	2.557	4	34.90	2.571	6	35.00	2.564	3	α(4H)-SiC
	35.75	2.512	100	35.90	2.501	100	35.75	2.512	100	35.80	2.508	100	β/α(6H)-SiC
	38.25	2.353	34	38.40	2.344	33	38.25	2.353	33	38.30	2.350	36	α(6H,4H)-SiC
	41.50	2.176	14	41.65	2.168	13	41.50	2.176	14	41.55	2.173	13	β-SiC
	45.40	1.998	6	45.60	1.989	4	45.40	1.998	6	45.45	1.996	6	α(6H)-SiC
Kyocera SN-252	21.95	4.049	3	--	--	--	--	--	--	22.15	4.013	12	Cristobalite
	23.40	3.801	26	--	--	--	23.60	3.770	21	23.85	3.731	24	β-Si_3N_4
	27.10	3.290	77	--	--	--	27.30	3.267	71	27.55	3.238	65	β-Si_3N_4
	--	--	--	--	--	--	27.75	3.215	2	--	--	--	--
	--	--	--	--	--	--	28.15	3.170	10	28.35	3.148	23	--
	29.45	3.033	36	--	--	--	29.90	2.988	8	29.55	3.023	6	Yb_2O_3
	30.85	2.898	12	--	--	--	30.35	2.945	7	30.15	2.964	12	--
	32.10	2.788	14	--	--	--	31.30	2.858	4	--	--	--	--
	32.80	2.730	5	--	--	--	32.95	2.718	21	32.65	2.743	6	--
	--	--	--	--	--	--	--	--	--	33.55	2.671	18	--
	33.75	2.656	75	--	--	--	33.90	2.644	100	34.10	2.629	100	β-Si_3N_4
	--	--	--	--	--	--	35.00	2.564	1	35.00	2.564	1	α-Al_2O_3
	36.15	2.485	100	--	--	--	36.30	2.475	88	36.50	2.462	88	β-Si_3N_4
	39.05	2.307	10	--	--	--	39.25	2.295	8	39.45	2.284	12	β-Si_3N_4
	39.65	2.273	5	--	--	--	40.35	2.235	1	40.50	2.227	13	--
	41.45	2.178	39	--	--	--	41.65	2.168	41	41.85	2.158	35	β-Si_3N_4
	--	--	--	--	--	--	--	--	--	43.20	2.094	12	α-Al_2O_3
	44.70	2.027	9	--	--	--	--	--	--	44.85	2.021	6	β-Si_3N_4
	--	--	--	--	--	--	48.05	1.893	12	48.30	1.884	18	β-Si_3N_4
	--	--	--	--	--	--	49.50	1.841	16	--	--	--	--
	--	--	--	--	--	--	50.15	1.819	17	50.30	1.814	12	β-Si_3N_4
	--	--	--	--	--	--	52.40	1.746	64	52.60	1.740	53	β-Si_3N_4
	--	--	--	--	--	--	58.15	1.586	25	58.35	1.581	12	β-Si_3N_4

Table 9. XRD Analysis of Candidate Materials (Concluded)

Material	2θ	D	I	2θ	D	I	2θ	D	I	2θ	D	I	Comments
	As Received			Flexure Tested at 1000°C			Flexure Tested at 1200°C			Flexure Tested at 1400°C			
Howmet SN-4	--	--	--	--	--	--	--	--	--	22.05	4.031	50	Cristobalite
	23.50	3.786	23	23.45	3.793	21	23.45	3.793	22	23.55	3.778	8	β-Si_3N_4
	--	--	--	--	--	--	--	--	--	26.25	3.395	17	Quartz
	27.15	3.284	76	27.10	3.29	86	27.15	3.284	81	27.20	3.278	33	β-Si_3N_4
	--	--	--	--	--	--	--	--	--	29.40	3.038	7	--
	--	--	--	--	--	--	--	--	--	32.95	2.718	8	--
	--	--	--	--	--	--	--	--	--	33.45	2.679	100	--
	33.75	2.656	77	33.70	2.659	87	33.75	2.656	85	33.80	2.652	28	β-Si_3N_4
	36.15	2.485	100	36.10	2.488	100	36.15	2.485	100	36.20	2.481	62	β-Si_3N_4
	39.05	2.307	7	39.00	2.309	8	39.05	2.307	8	39.10	2.304	6	β-Si_3N_4
	41.45	2.178	33	41.40	2.181	43	41.45	2.178	39	41.50	2.176	25	β-Si_3N_4
Norton NT-154	--	--	--	--	--	--	--	--	--	21.95	4.049	7	Cristobalite
	23.65	3.762	24	--	--	--	--	--	--	23.45	3.793	23	β-Si_3N_4
	27.30	3.267	77	--	--	--	--	--	--	27.15	3.284	80	β-Si_3N_4/Y_2O_3
	--	--	--	--	--	--	--	--	--	29.75	3.003	7	--
	33.90	2.644	98	--	--	--	--	--	--	33.75	2.656	100	β-Si_3N_4
	36.30	2.475	100	--	--	--	--	--	--	36.15	2.485	100	β-Si_3N_4
	39.25	2.295	12	--	--	--	--	--	--	39.10	2.304	9	β-Si_3N_4
	41.65	2.168	44	--	--	--	--	--	--	41.50	2.176	42	β-Si_3N_4
	48.10	1.892	17	--	--	--	--	--	--	47.95	1.897	8	β-Si_3N_4
NGK EC-152	23.45	3.793	45	23.75	3.746	17	--	--	--	--	--	--	β-Si_3N_4
	27.15	3.284	15	27.40	3.255	75	--	--	--	--	--	--	β-Si_3N_4/Y_2O_3
	29.65	3.013	65	29.90	2.988	6	--	--	--	--	--	--	Y_2O_3/$Y_2Si_3N_4O_3$
	31.95	2.801	95	32.20	2.780	11	--	--	--	--	--	--	Y_2O_3
	33.70	2.659	100	34.00	2.637	100	--	--	--	--	--	--	β-Si_3N_4
	36.10	2.488	96	36.40	2.468	85	--	--	--	--	--	--	β-Si_3N_4
	37.30	2.411	2	37.60	2.392	6	--	--	--	--	--	--	--
	39.00	2.309	11	39.30	2.292	10	--	--	--	--	--	--	β-Si_3N_4
	41.45	2.178	41	41.70	2.166	39	--	--	--	--	--	--	β-Si_3N_4
	45.45	1.996	5	45.65	1.987	6	--	--	--	--	--	--	Y_2O_3
	--	--	--	48.15	1.890	13	--	--	--	--	--	--	β-Si_3N_4

Table 10. Tensile Strength Measurements of Hexoloy α-SiC at Room Temperature

Specimen Number	Fracture Strength (MPa)	Comments
1	--	Buttonhead failure
2	251	Surface failure
3	247	Surface failure
4	294	Volume failure
5	--	Buttonhead failure
6	--	Buttonhead failure
7	307	Surface failure (possible pit)
8	253	Surface failure
9	219	Surface failure
10	277	Surface failure
11	176*	Invalid - specimen failed at grind mark
12	286	Surface failure
13	220	Surface failure
14	--	Buttonhead failure
15	247*	Invalid - specimen failed at grind mark
16	--	Buttonhead failure
17	250	Surface failure
18	--	Buttonhead failure
19	352	Surface failure
20	290	Volume failure
21	--	Buttonhead failure
22	226*	Invalid - specimen failed at grind mark
23	--	Buttonhead failure

*Average for the 12 valid test specimens - 270 MPa (± 36 MPa)

size of the image is a function of the aperture of the focusing lens, the average speckle diameter being about equal to the diameter of a diffraction limited spot in that optical system. To be able to measure motion a speckle interferometer is required, i.e., the speckle must interfere with a reference field. In-plane motion is measured in an interferometer in which two speckle fields interfere with each other, the speckle fields having been created by scattering of two beams incident on the same surface from different directions. By using the setup shown in Figure 33 the sensitivity vector, $(k_1 - k_2)$, is parallel to the surface. The measure for the sensitivity is λ_s defined by:

$$\lambda_s = \frac{\lambda}{2\sin\theta}$$

which is on the order of the wavelength of light. Conceptually the effect can be described as follows: The two incident light beams set up a stationary amplitude and phase distribution along the surface of interest, with a period of λ_s. If the surface is moved the speckle pattern will evolve in a random form until the surface has moved an integral number of periods. At that time the surface microstructure will be an identical light field to that which it saw initially, and the resulting speckle field will be identical to the original speckle field, provided that the image of the surface has not shifted by more than the correlation length of the image speckle (i.e., the average speckle dimension). Thus determining where the speckle fields in the two cases correlate can determine regions that have moved an integral number of periods of the incident field.

To implement this feature a reference specklegram is first captured by producing an image of the surface on a photographic plate and exposing the plate. The surface is then distorted and a second specklegram is captured on the same plate. Where the object surface is moved an integral number of periods of the field, the speckle will correlate and will appear sharp. In the regions between, the two speckle fields will have been random with respect to each other and that region of the photographic plate will appear indistinct. The regions of sharp speckle are contours of motion in units of the field periodicity. Since the specklegram is an image of the surface, the contours are direct surface mappings of the

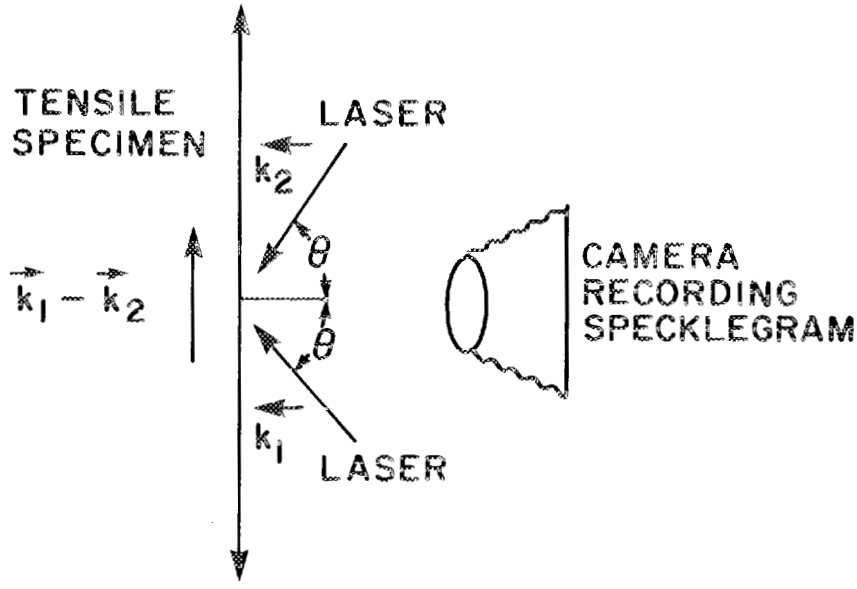

Figure 33. Speckle interferogram setup used to measure relative elongation in tensile specimen.

motion. It becomes easier to discern the regions of the correlation of the speckle fields if the photographic plate is moved slightly between exposures. Then when the developed plate is illuminated with coherent light the correlated speckle fields will effect a double slit and Young's fringes will occur in the Fourier transform plane. The uncorrelated speckle patterns will provide a diffuse scattering in the Fourier plane and a filter can be constructed to separate the two regions. Blocking the Young's fringes and refocusing the remaining light provides an image of the original surface with an intensity modulation superimposed, the fringes being contours of motion in units of the field periodicity.

A simple laboratory system was used to evaluate the system capability. A diffuse flat was used as the scattering surface. An Argon laser (514.5 nm) illuminated the surface at 45° to the surface normal. A mirror, normal to the surface, reflected half the laser beam so that it hit the surface at 90° to the initial beam. As a result the field periodicity was $1/\sqrt{2}\lambda$ (360 nm). A lens was used to focus an image of the surface onto a photographic plate with 1:1 magnification. The lens was stopped down to f/8 so that the resulting speckle would be about 10 μm, permitting 10 μm motion of the surface. A photograph of the system is shown in Figure 34. The photographic plate was moved vertically 40 μm between exposures. The developed plate was illuminated by the laser and the resulting Young's fringes are shown in Figure 35. The fringes are oriented horizontally because of the vertical shift of the plate.

In the next experiment, the plate was rotated 10° so that an incremental rotation would result in a differential in-plane motion. An incremental rotation of 0.04° about a vertical axis was made between exposures. A mask was made to block the organized scattering and to pass the region of the dark bands on either side of center. The image of the surface formed by the light that passed through the mask is shown in Figure 36. Note the intensity moduluation, which consists of vertical fringes. The fringes are contours of in-plane motion in units of 360 nm. A plot of the measured and computed motions is shown in Figure 37. Clearly the technique has demonstrated a bench-top capability of being able to measure motions with the accuracy desired for the extension tests.

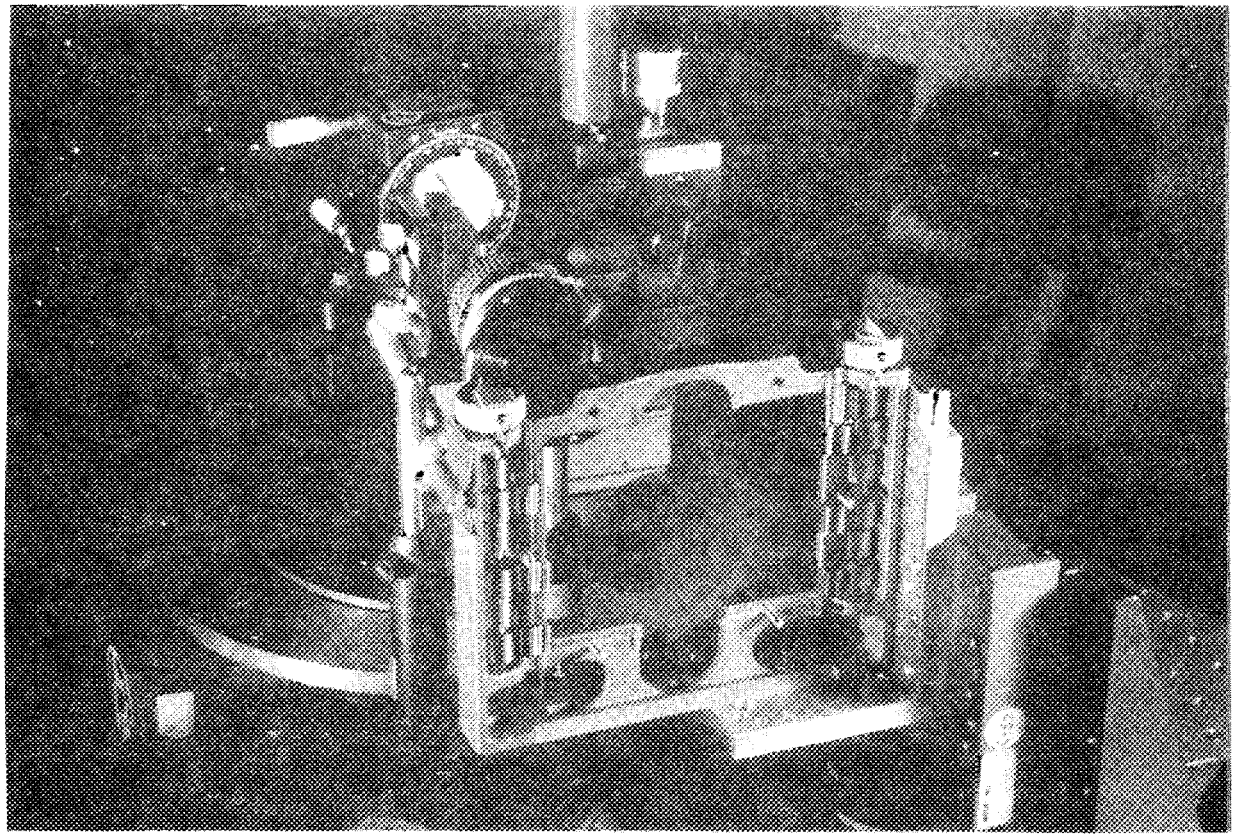

Figure 34. Photograph of experimental apparatus.

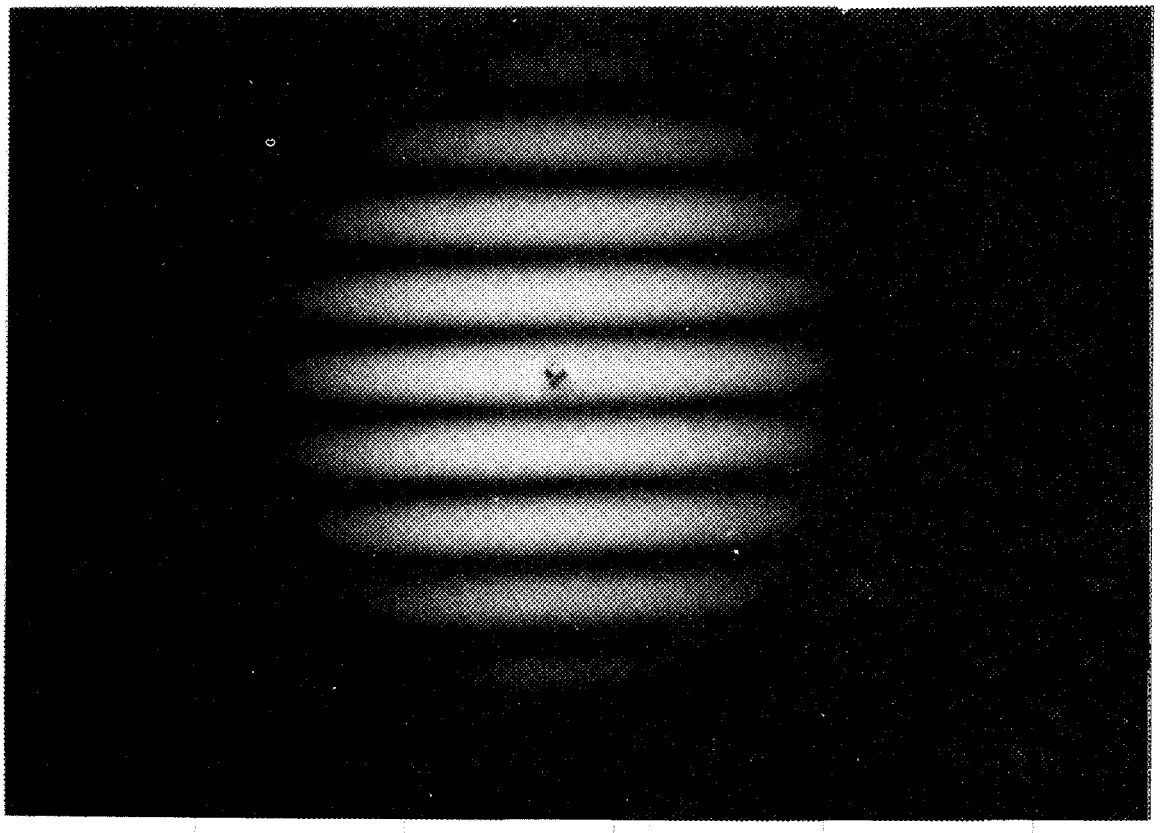

Figure 35. Young's fringes resulting from vertical shift of photographic plate.

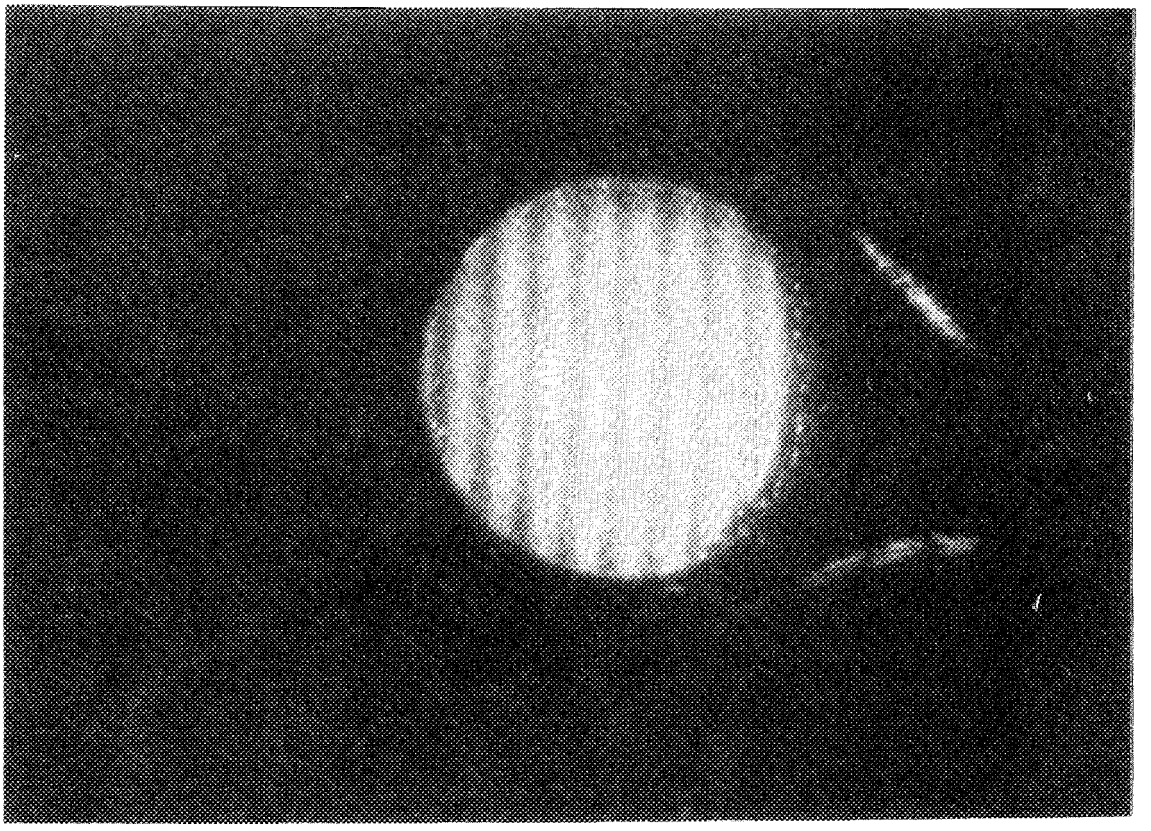

Figure 36. Speckle fringes due to planar component of specimen motion.

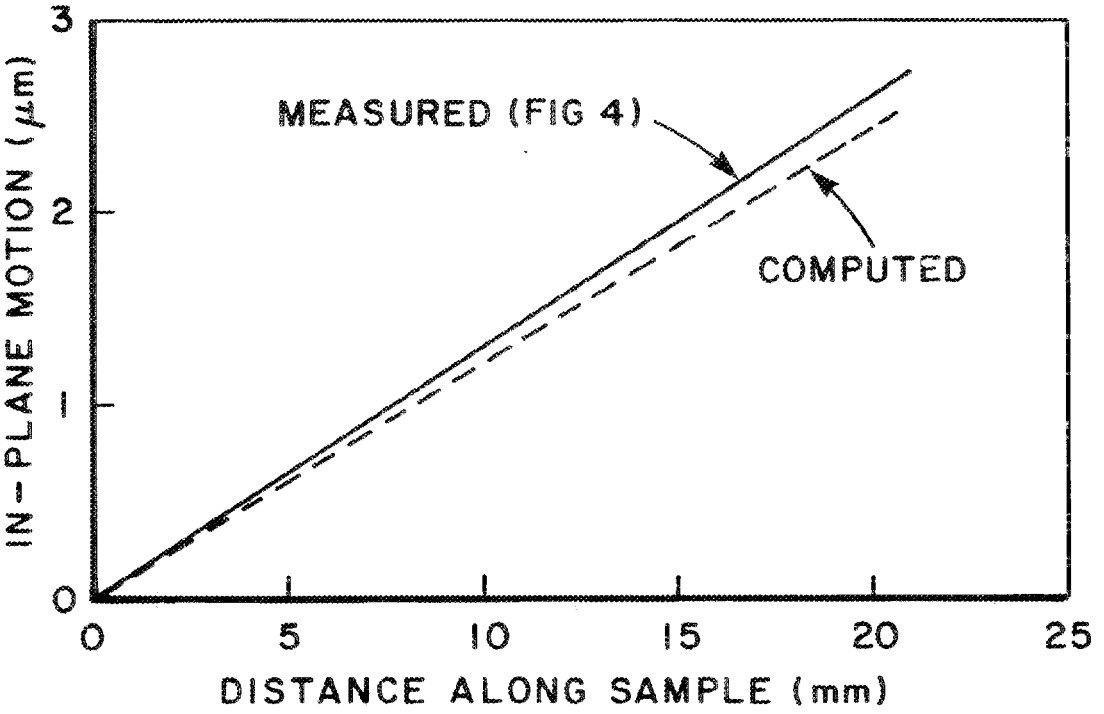

Figure 37. Comparison of measured and computed plate motion.

A test was made using a cylindrical specimen that will be used in real tests. The resulting photograph (Figure 38) is noisy but the fringes are clear. The reason for the fringe curvature is now under study.

The initial plan was to demonstrate the system using an Argon laser operating in a controlled laboratory environment. Once experience was gained the source was to be switched to a ruby laser, which would eventually be moved to the test facility for use with the tensile tester. The ruby laser would provide illumination in a short burst (20 ns), sufficiently short to be sure of freezing any motion in the specimen or the recording media. Continual maintenance and operation difficulties with the ruby laser have required that we attempt another approach. As the results with the Argon laser were quite good, we will attempt to use it as the source. The major problem will be the vibrations we expect to encounter. A mounting platform is being assembled that will be supported on vibration isolation legs. We have also experimentally determined how to record the specklegrams on 35mm roll film, instead of using the fine grain plates used in the demonstration. The roll film is a couple of orders of magnitude faster than the plates, permitting specklegrams to be captured with exposures of about 10ms. Together these changes may reduce the effects of vibrations to the point that measurements can be made. The system will be installed in the near future and simplified tests conducted.

The Raman Sepctroscopy studies have focused on the investigation of SiC ceramics. Raman scans of Hexoloy α-SiC specimens are given in Figures 39 and 40. Plot (a) was taken near a fractured edge and (b) was taken near the middle of the specimen. Raman spectra of SiC are characterized by weak signals with high background and correspondingly high noise levels. Although high background levels can be due in part to fluorescence, often in materials of this type the background as shown in Figure 39 is due to an amorphous or glassy phase. In addition to the lattice modes of the wurtzite SiC structure, hexagonal (α-phase) as well as cubic (β-phase) silicon carbide can have additional lattice modes (phonons) due to one-dimensional stacking sequence of planes. These SiC "polytypes," as they are called, can have large unit cells with many atoms and, therefore,

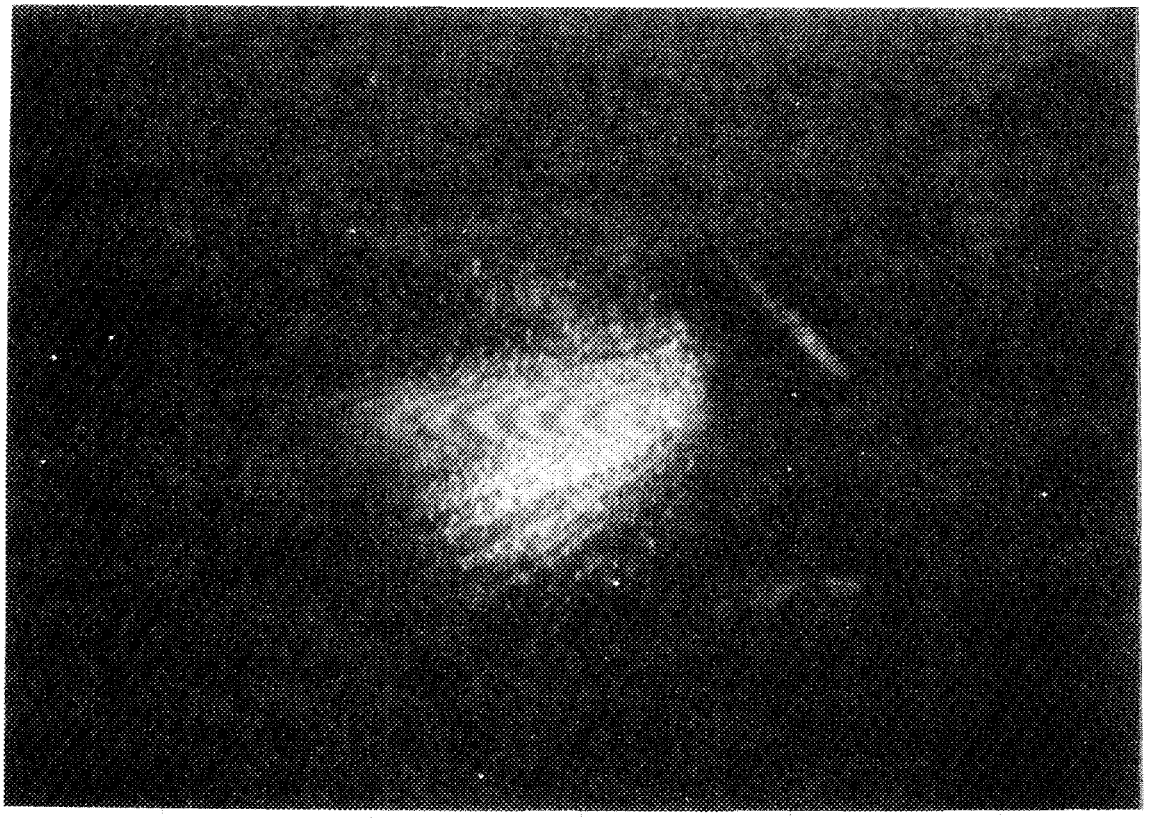

Figure 38. Speckle fringes formed by planar motion of cylindrical specimen.

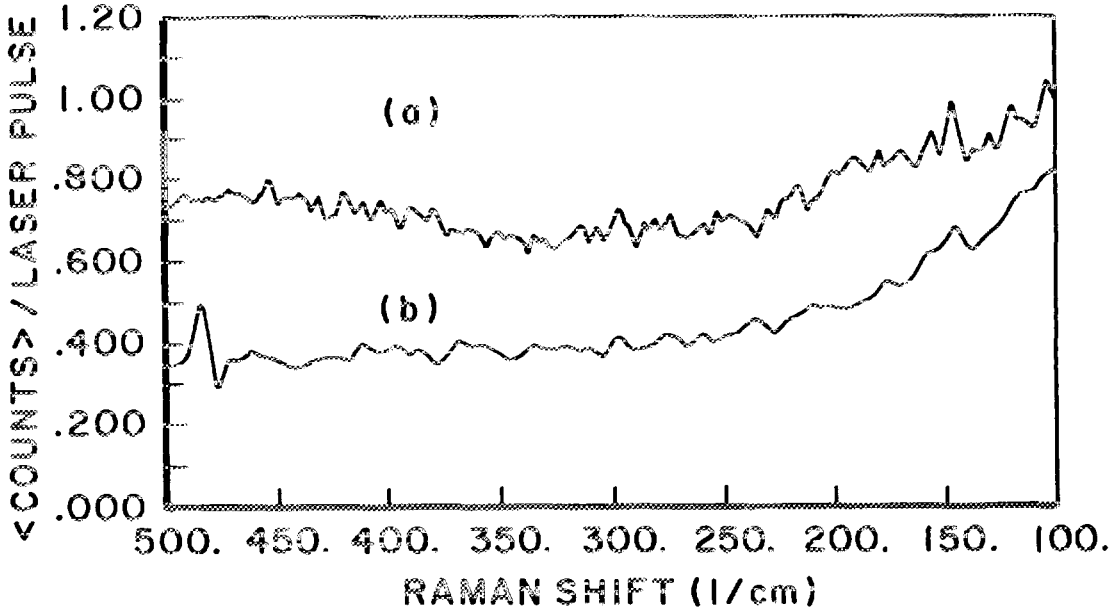

Figure 39. Spectra of two α-SiC specimens: (a) specimen No. 1-5 at a fractured edge, and (b) specimen No. 1-4 at the middle of the specimen.

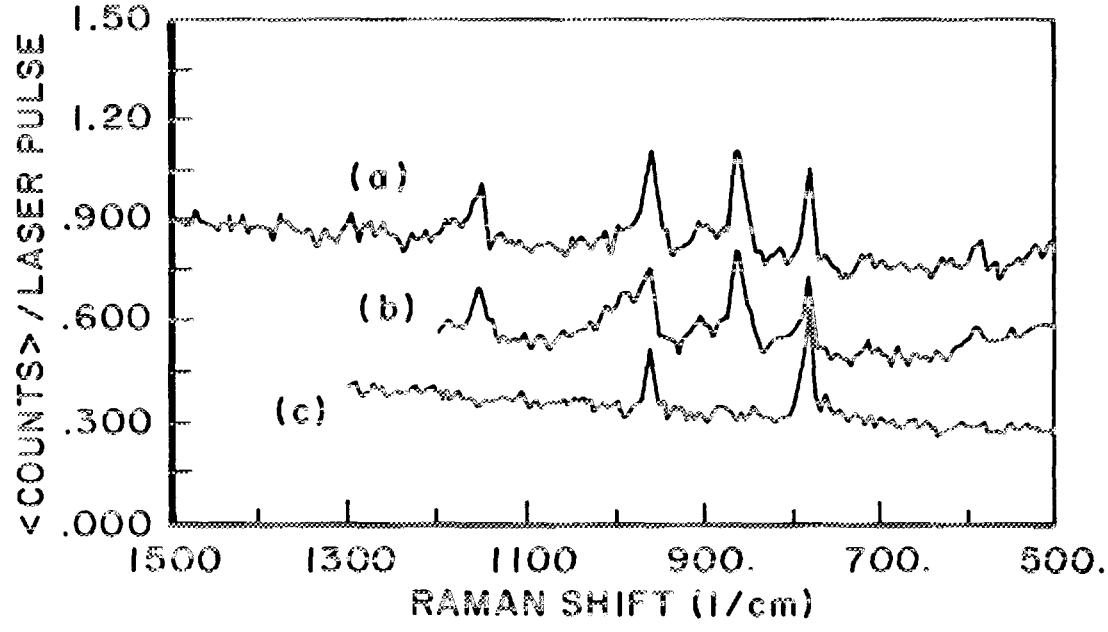

Figure 40. Spectra of two α-SiC specimens: (a) No. 1-5 near a fractured edge, (b) No. 1-5 at the middle of the specimen, and (c) No. 1-4 near the middle of the specimen.

have a large number of modes [1,2]. These structures are labeled by nH or nC where n is the number of close-packed layers in the polytype stacking sequence. For example, a common hexagonal polytype is 6H SiC.

Strong lines in the allowed modes of non-polytype (wurtzite) SiC occur for propagation of the phonon perpendicular to the c-axis , at 970 cm^{-1} (longitudinal, L), 797 cm^{-1} (transverse, T_1), and 788 cm^{-1} (transverse, T_2) [2] the first and last of which are seen in Figure 40 (c) taken from Hexoloy sample no. 1-4. The 797 cm^{-1} line is weak and can only be seen in higher resolution scans. For phonon propagation parallel to the c-axis, the L and T_2 modes shift respectively to 964 and 797 cm^{-1} while the T_1 mode does not change. These shifts are large enough to suggest the possibility of obtaining some assessment of grain orientation since line positions can be measured to within 1 cm^{-1}.

In addition to the strong lines, the 6H SiC polytype has 14 allowed lines [2]. Generally, the polytype lines are quite weak and would not be expected to be detected in these scans. Therefore, the two or more additional lines in plots (a) and (b) in Figure 40 cannot readily be assigned to a polytype. Moreover, their Raman shifts do not correlate with any nH SiC polytype. They cannot be assigned to the cubic phase since the cubic line positions nearly coincide with the hexagonal phase values for phonon propagation normal to the c-axis. Thus, it appears that they are due to the presence of a carbide or possibly a carbonate of an additive or impurity.

The appearance of the additional lines at 866 and 1150 cm^{-1} shown in Figure 40 were studied using the scanning slit. Figure 41 shows a series of four scans taken at 20 μm spaced positions on Hexoloy specimen no. 1-5. The 866 cm^{-1} line clearly disappears while the reference line at 788 cm^{-1} actually shows an increase in intensity from the 0 μm position to the 80 μm position. Furthermore, the T_1 mode at 797 cm^{-1} also becomes visible at the 80 μm position. The region scanned on the sample visually showed some kind of microscopic "blotch" on the surface where the 866 cm^{-1} line was strong.

This work with an upgraded Raman microprobe has verified the utility of the design in the studies of silicon carbide ceramics. The scanning

slit feature provides a valuable tool for characterizing the morphology of the ceramics. Clearly the extrapolation of this one-dimensional line-scanning design to a system based on a two-dimensional array detector would give the ideal scheme for this work. It is evident that these ceramics provide may opportunities for crystalline and molecular characterization using the microprobe. The basic single crystal Raman spectra for SiC are known. Thus, the work will be aimed at identifying the additional lines, exploring ways to detect the presence of the other phases, and examining the possibility of detecting orientation of SiC crystallites.

Efforts to develop a comprehensive property data base for SiC and Si_3N_4 ceramics from the literature were initiated. Data from 15 pertinent literature sources have been compiled and entered into our D base III program. This effort is continuing.

Discussion of Results

The flexural strength values measured for the Hexoloy α-SiC were higher than the average room temperature strength but lower than the average elevated temperature strength measured for the batch of specimens evaluated in Phase II. The flexural strength measured for this batch of specimens did not vary more than 50 MPa from 20°-1400°C at the three loading rates. Fracture origin for most of the specimens was observed to have occurred at tensile surface and edge flaws. A majority of the flaws observed were found to be voids or pits at or just below the surface. Pits and voids were not observed in the initial batch of specimens evaluated in Phase II.

The Howmet SN-4 material had very high room temperature flexural strength and 1000°C fast fracture flexural strength. However, above 1000°C the strength decreased dramatically and at 1400°C the material was severely oxidized. The SN-4 material also appeared to be susceptible to slow crack growth at 1000°C and 1200°C.

The Kyocera SN-252 was unique compared to the other Si_3N_4 materials evaluated. This material contained significant quantities (5-6%) of Yb_2O_3 and very small quantities (less 0.5%) of Al_2O_3 and Y_2O_3. In addition the Si_3N_4 matrix contained a whisker-reinforcing phase of β Si_3N_4 dispersed

throughout the matrix. This fibrous phase is developed during sintering by the use of a proprietary process. The chemistry of these fibers at the fracture surface was examined by scanning auger microprobe. The results of this analysis showed the whiskers to have the same Si_3N_4 compositions as the matrix (see Appendix II).

It was observed that most of the fracture origins were at large fibers located at or just below the tensile surface. We have been advised that Kyocera is working to better control the whisker development process to prevent whiskers from growing too large. The flexure specimens tested at 1400°C using the slow loading rate appeared to have undergone severe plastic deformation prior to fracture (see Figure 42). Although the material deformed the specimens fractured at strength values higher than those recorded for fracture at the fast loading rate. This behavior accounts for the negative n values calculated in Table 7.

The NGK EC-152 had impressive 1000° and 1200°C flexural strengths. However, at 1400°C the flexural strength of EC-152 decreased significantly. At 1400°C using the slow stressing rate the EC-152 specimens were subjected to plastic deformation and had lower flexural strength values than those measured at the fast stressing rate. This lower strength may be due to the occurrence of slow crack growth.

The Norton/TRW NT-154 material was also found to have the high flexural strength at both 20° and 1400°C at the fast stressing rate. However, at 1400°C using the slow stressing rate the measured flexural strength decreased significantly and the test specimens had undergone significant plastic deformation.

It is interesting to note that all of the Si_3N_4 materials tested at the slow stressing rate at 1400°C were subject to plastic deformation prior to fracture. This plastic deformation is probably due to the softening of the glassy intergranular phase formed during sintering. Two of the materials (NT-154 and EC-152) also had significantly lower flexural strengths at the slower stressing rates. The increased flexural strength measured for the SN-252 materials is probably due to the reinforcing effects of the Si_3N_4 fibers in the matrix. The lower strengths measured

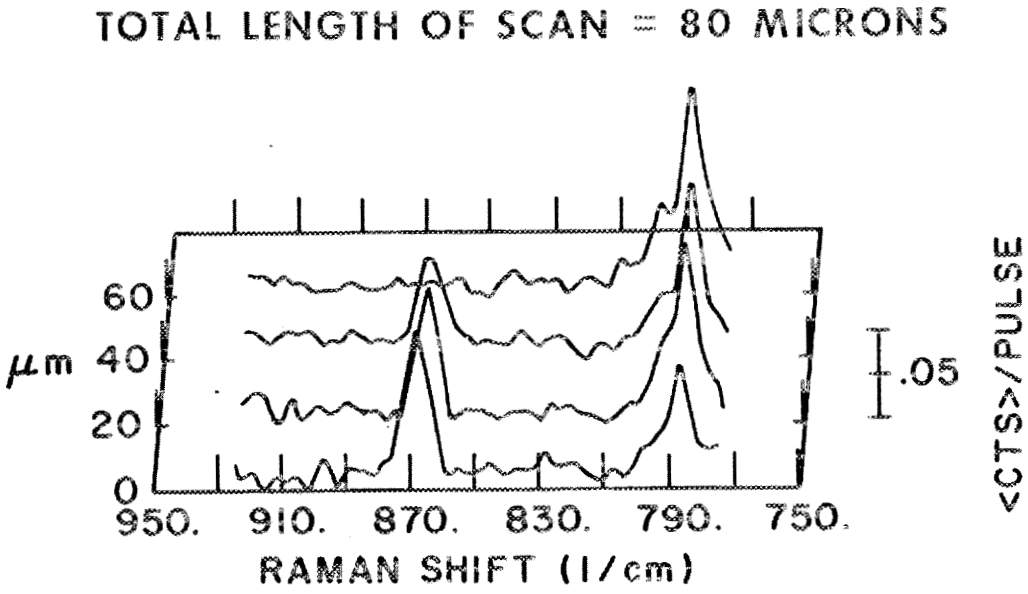

Figure 41. Spectrum of Sohio Hexoloy α-SiC No. 1-5 as a function of position.

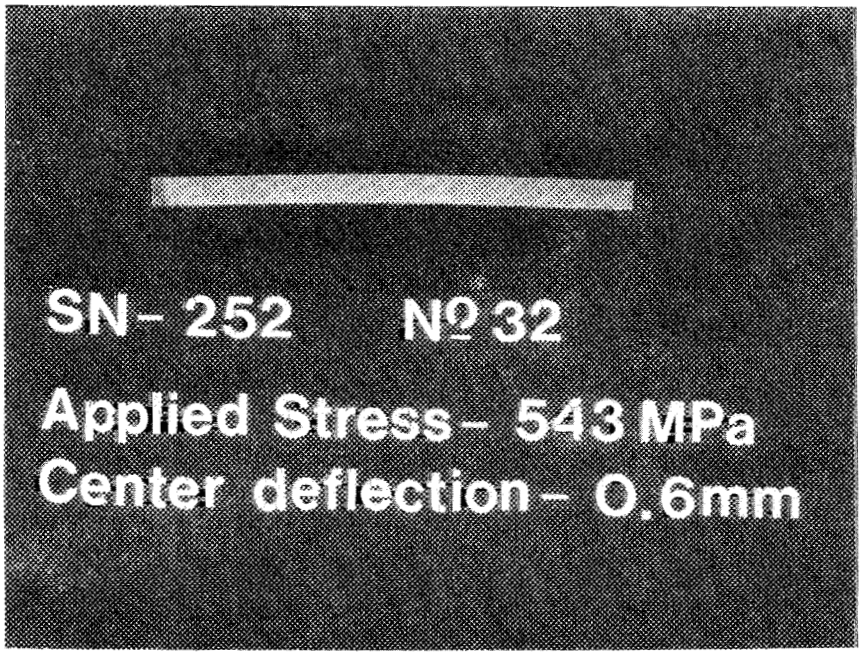

Figure 42. Plastic deformation observed for Kyocera SN-252 at 1400°C under slow loading.

for the EC-152 and NT-154 may be due to the occurrence of slow crack growth.

References

1. L. Patrick, Infrared Absorption in SiC Polytypes, Phys. Rev. 167, 809 (1968).
2. D. w. Feldman, J. H. Parker, Jr., W. J. Choyke, and L. Patrick, Raman Scattering in 6H SiC, Phys. Rev. 170, 698 (1968).

Appendix I
Results for Phase II

A. Results of Flexural Strength Measurements Made in Phase II.

Material	Temp. (°C)	Machine Crosshead Speed (cm/sec)	Strength (MPa)	Std. Dev. (MPa)	Weibull Modulus	Fracture Origin
αSiC						
	25	0.0064	331	41	9	Surface flaws.
	1300	0.0064	494	90	8	Surface flaws.
	1300	0.00004	500	77	8	Surface and edge flaws.
	1450	0.0064	500	52	10	Surface and edge flaws.
	1450	0.00004	455	59	9	Surface and edge flaws.
PY6						
	25	0.0064	641	69	11	Surface flaws.
	1450	0.0064	393	69	8	Surface, edge and subsurface flaws (mostly inclusions)[+].
	1450	0.00004	241	36	7	Flaws and inclusions[+] at or below the surface possible SCG.
XL144 (Batch 1*)						
	25	0.0064	538	97	6	Surface and edge flaws.
	1300	0.0064	604	44	13	Flaws and inclusions[#].
	1300	0.00004	551	93	9	At or below the surface.
	1450	0.0064	453	53	12	Surface and edge flaws and subsurface inclusions[#].
	1450	0.00004	213	12	6	At or below the surface SCG.

*Specimens were machined from a hot pressed billet at the University of Dayton

[o]Specimens were prepared at Norton/TRW

[#]Inclusions - Fe, Cr

[+]Inclusions - Fe, Mo, Cr, Cu

(continued ...)

Material	Temp. (°C)	Machine Crosshead Speed (cm/sec)	Strength (MPa)	Std. Dev. (MPa)	Weibull Modulus	Fracture Origin
XL144 (Batch 2°)						
	25	0.0064	787	41	22	Surface and edge flaws (mostly inclusions)
	1450	0.0064	537	76	7	Surface and edge flaws (some inclusions)

*Specimens were machined from a hot pressed billet at the University of Dayton

°Specimens were prepared at Norton/TRW

#Inclusions - Fe, Cr

+Inclusions - Fe, Mo, Cr, Cu

B. Physical Property Measurement Made in Phase II

Property Measurement	Materials: Sohio Hexoloy α-SiC	Howmet SN-4	Norton TRW NT-154
Density (g/cc)	3.17	3.24	3.24
Young's Modulus (GPa)	427	293	314
Hardness (kg/mm^2)	2558	1 58	1421
Fracture Toughness CF/MI* ($MPa \cdot \sqrt{m}$)	2.1/1.6	3.0/6.1	3.1/3.8
Coefficient of Thermal Expansion (10^{-6}/°C)	5	3.4	3.4

*MI = Microindent method.
CF = Controlled flaw method.

APPENDIX II

UNIVERSITY OF DAYTON
Research Institute
Dayton, Ohio 45469

AUGER ANALYSIS OF A FRACTURE SURFACE OF SPECIMEN SN-252 #3

Surface Science Laboratory

16 September 1988

Introduction

A specimen designated Kyocera SN-252 #30 was examined at the University of Dayton Surface Science Laboratory using its JEOL JAMP-30 Scanning Auger Microprobe. Special attention was given to the large crystallite features observed on a fracture surface. The largest crystallite is shown in Figure 1. It measures approximately 50 by 200 μm in surface area. A higher magnification secondary electron image is shown in Figure 2. It is immediately apparent that this crystallite surface is generally smooth with little evidence of residual matrix adhesion after fracture. The presence of geometric depressions along the crystallite's exposed surface is noted. These most probably resulted from smaller intersecting matrix crystallites. One such protruding crystallite is evident near the bottom of Figure 2.

Figures 3 through 5 show other regions on this fracture surface where larger crystallites have formed. These generally have the same features as those exhibited by the largest crystallite shown in Figures 1 and 2. The crystallite in Figure 4, however, appears to have a distinctive "kink" near its upper end as if it were deflected during growth.

Specimen 30 was tested in flexure at 1400°C under rapid loading conditions.

Auger Spectroscopy

Initially, difficulties were encountered in trying to acquire Auger spectra from this uncoated fracture surface. Recall that fairly large beam currents are required to stimulate a sufficient number of Auger events to enable detection compared to what is required for secondary electron microscopy (SEM) (0.1 μamps compared to 0.1 namps). The JAMP-30 instrument is both an SEM and a scanning Auger spectrometer which allows the specimen to be tilted relative to the incident primary electron beam. With some nonconductive specimens charging can sometimes be

effectively eliminated by selecting a glancing primary beam incidence angle of greater than 50°. After several attempts it was apparent that all the usual tricks used to defeat localized charging were not going to work with this specimen. Reluctantly, the specimen was coated with a thin gold/palladium film (estimated to be about 20 nm) and inserted back into the instrument. The differentially pumped "microfocus" ion gun on the instrument was used to sputter through the conductive overlayer. Electron beam parameters (3 keV and 0.1 μamps) were chosen which enabled suitable AES spectra to be acquired from the sputtered surface without specimen charging. Unfortunately these were not optimum parameters for the Si KLL peak at ~1620 eV. Consequently, standard spectra from thin films of Si_3N_4, SiO_2, and Ag were also acquired under these same beam parameters so that appropriate sensitivity factors could be acquired to enable more exact quantification. The SiLVV peak between 68 and 90 eV was used for quantification calculations. Care was taken to operate at sufficiently small beam current densities to minimize electron beam induced SiLVV peak splitting sometimes observed on thin SiO_2 films. The reader is cautioned that the quantitative results which follow are based on only a few monolayers of atoms in very localized regions of the specimen. Further, ion beam sputtering may alter localized surface chemistry by selective sputtering. The quantitative results reported here should not be extrapolated beyond the reasonable statistical limits of this technique (±10%). A much more elaborate study would be required to determine the experimental error more accurately.

Results

The large crystallite shown in Figures 1 and 2 was sputtered until the Pd peak at ~327 eV was still visible. This was taken to define the approximate native surface of the crystallite. Figure 6 shows the Auger spectrum of this surface. The surface is predominantly composed of Si and O with trace amounts of C and

Pd. Figure 7 shows an expanded view of the low energy region. This spectrum suggests the presence of a trace amount of Yb at ~178 eV which is known to be present from energy dispersive x-ray spectra.

This region was again sputtered for 9 minutes to remove the oxide layer. Figure 8 is an Auger spectrum showing the presence of silicon and nitrogen after sputtering. The complete removal of the oxide and the presence of implanted Ar are observed. Argon implantation in stoichiometric CVD grown Si_3N_4 films as a result of ion sputtering is well known suggesting that the crystallite may be near stoichiometric Si_3N_4.

An additional sputtering for 11 minutes, bringing the total sputtering time to 20 minutes, was done. Figure 9 shows the Auger spectrum at this depth. In a previous study, sputter rates for Si_3N_4 were found to be about 22.5 nm/min for this instrument suggesting that the spectra in Figures 8 and 9 represent depths of 202.5 and a 450 nm respectively (assuming a similar sputter rate for the initial oxide layer). Atomic compositions have been calculated for the native surface, after 9 minutes, and after 20 minutes of sputtering. These are summarized in Table I.

TABLE I

CALCULATED ATOMIC COMPOSITIONS OF LARGE CRYSTALLITE IN FIGURE 2.

	Si	C	Pd	Ar	O	Yb	N
At surface	30.6	5.9	1.3	---	62.1	T*	----
202.5 nm	49.3	---	---	1.4	----	-	49.3
450 nm	58.8	---	---	0.4	----	-	40.8

*T = trace

Estimated experimental error ±10%

Two smaller crystallites (shown in Figure 5) were sputtered to determine their atomic compositions for comparison to the large crystallite. Figure 10 shows a typical Auger spectrum of the lower crystallite in Figure 5 after ion sputtering to remove the gold/palladium overlayer. An Auger spectrum from the upper crystallite in Figure 5 was virtually identical to that shown in Figure 10 after the overlayer was removed. Because of their proximity, both crystallites in Figure 5 were sputtered simultaneously. Some peak splitting in the SiLVV peak is observed (Figure 11). Auger spectra from both crystallites after a 20 minute sputter etch are shown in Figures 12 and 13. Again, these spectra are virtually identical in composition. These results are summarized in Table II.

TABLE II

CALCULATED ATOMIC COMPOSITIONS OF THE TWO CRYSTALLITES FROM FIGURE 5

	C	Pd	Si	O	N	Ar
Lower crystallite surface	4	1.2	27.9	66.9	----	---
Lower crystallite after 20 min sputter	-	---	40.2	----	57.0	2.8
Upper crystallite after 20 min sputter	-	---	38.1	----	59.5	2.4

Estimated experimental error ±10%

The compositional data presented in Tables I and II were based on the SiLVV transition. As mentioned earlier, two standards (SiO_2 thermal oxide film and a thin CVD Si_3N_4 film) were used in making these calculations. These data suggest that the

crystallites have a thin SiO_2 film on their outer surface of perhaps several tens of nm. This oxide film on crystallite surfaces probably results from oxidation which occurs during the flexure testing at 1400°C.

Conclusions

Calculated bulk atomic concentrations from Auger spectroscopy for the large crystallite (Figures 1 and 2) suggest a silicon rich material at least to the depth measured. (Stoichiometric Si_3N_4 should be approximately 43 percent silicon and 57 percent nitrogen.) The smaller crystallites (Figure 5) appear to be more stoichiometric after sputtering to an equivalent depth. Whether this is a significant difference which relates to crystallite size is unknown. Other crystallites (both large and small) will have to be examined to identify whether there is a size versus composition relationship. It is clear, however, within the experimental limits of the Auger technique, that the surface oxide seen on these crystallites is near stoichiometric and quite thin. No residual oxide is observed within the bulk of the crystallites after only a short sputter. Finally, these data suggest that the large crystallites observed on this fracture surface are near stoichiometric Si_3N_4. They are mechanically linked to the substrate with little or no evidence of chemical adhesion. The substrate itself (from Figures 2 and 5) appears to be composed of many smaller interlinked elongated crystallites, presumably also Si_3N_4.

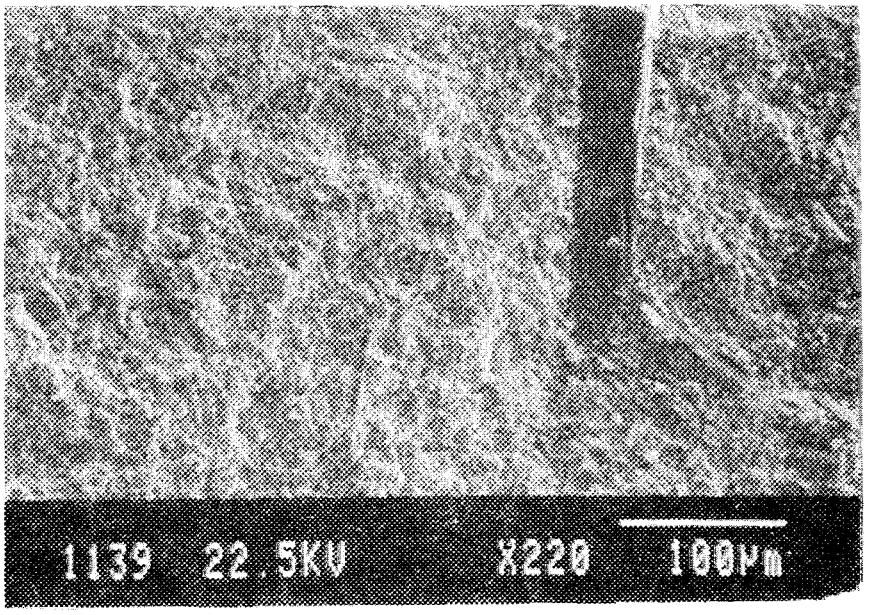

Figure 1. Secondary electron image of a fracture surface of specimen SN-252 #30. A large crystallite which extends from the upper surface to over 200 μm into the bulk is evident. Other crystallites within the bulk are also evident on this surface.

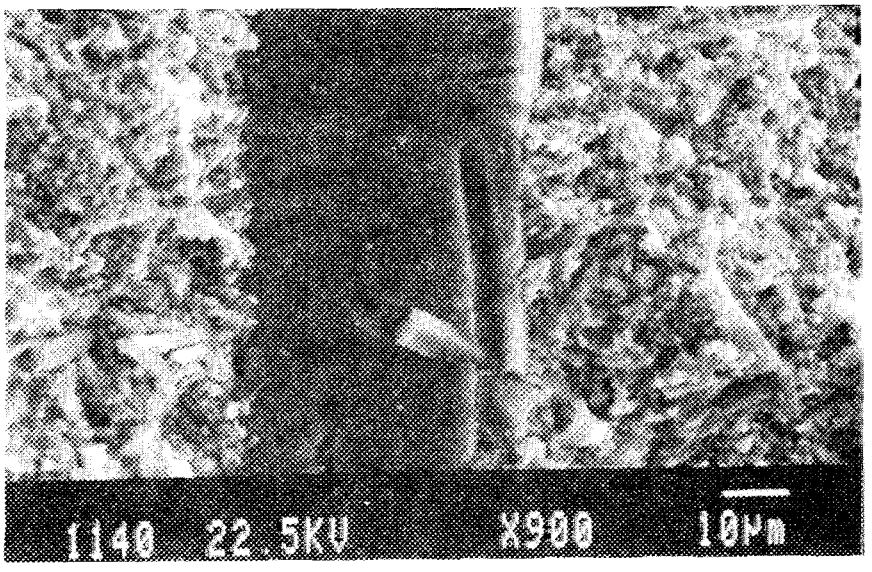

Figure 2. A 900X secondary electron image of a portion of the large crystallite from Figure 1. There is clear evidence of mechanical linkage of this crystallite to the bulk matrix and little evidence of chemical bonding (adhesion) of the matrix to the crystallite. Auger spectroscopy was used to determine the surface and near subsurface chemistry of this crystallite.

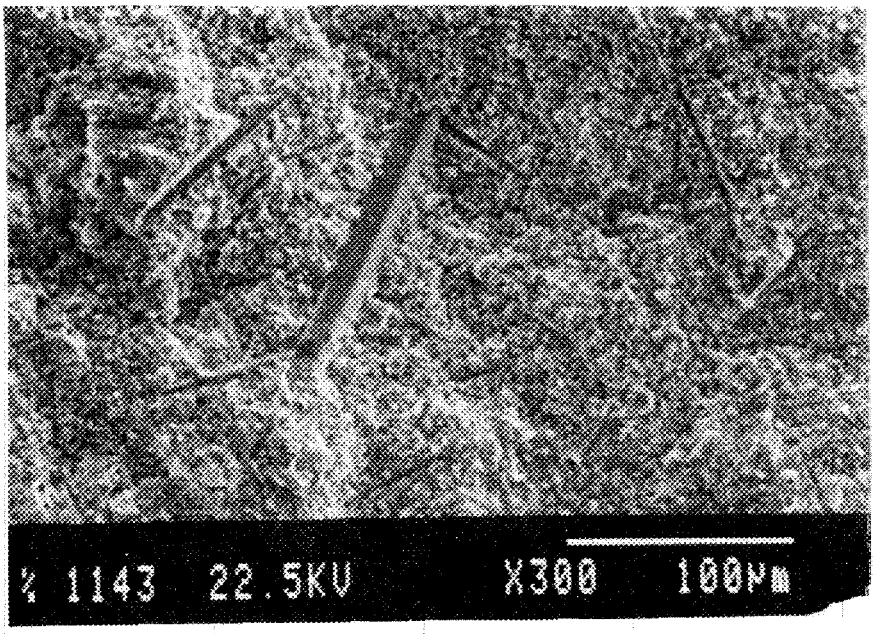

Figure 3. A secondary electron image of several other crystallites on the surface of specimen SN-252 #30. Flat crystal faces are apparently characteristic of these larger crystallites.

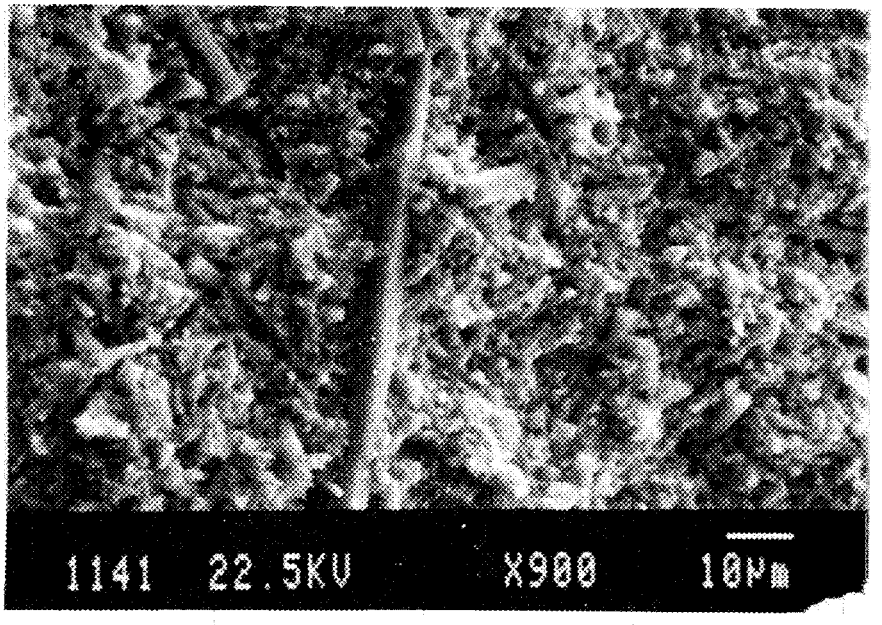

Figure 4. A secondary electron image of a smaller crystallite approximately 10 µm in linear cross section. A "kink" is observed in this crystallite as if it were deflected during growth. Other 10 µm crystallites are also seen at various angles to the fracture surface.

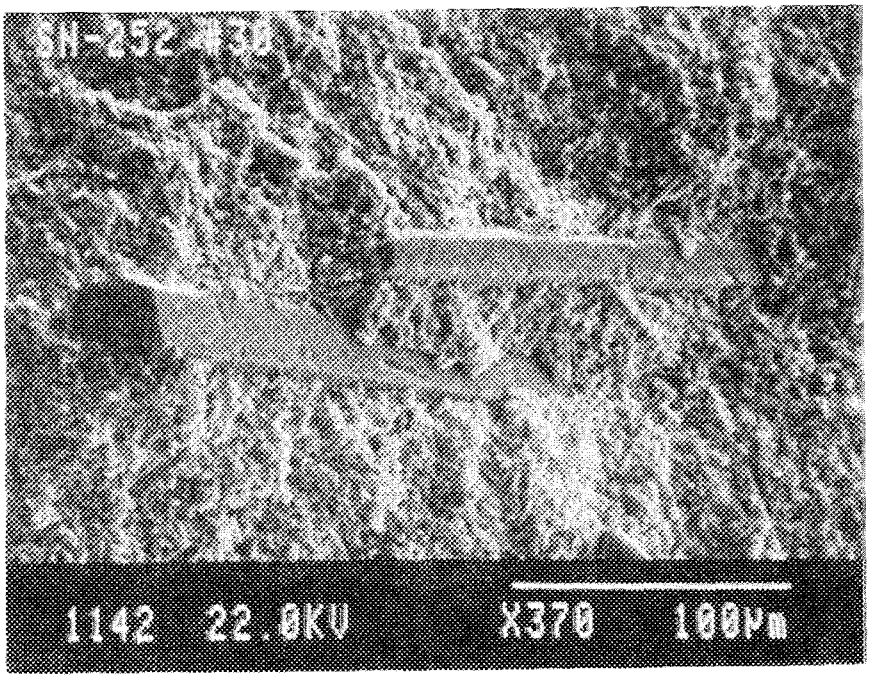

Figure 5. A secondary electron image of two more larger crystallites on the fracture surface of SN-252 #30. Auger spectroscopy in conjunction with argon ion sputtering was used to probe the surface and bulk chemistry of both these crystallites.

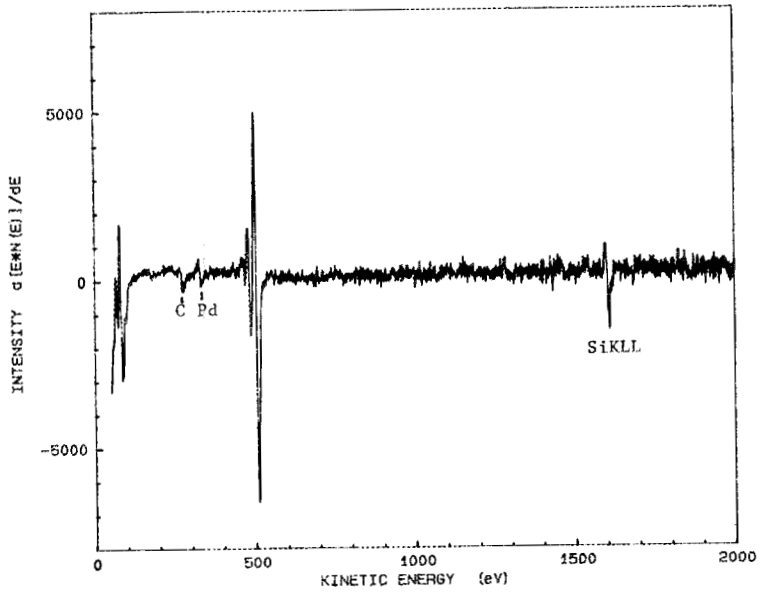

Figure 6. Auger spectrum from the surface of the large crystalline seen in Figures 1 and 2 after the Au/Pd layer has been removed by ion sputtering.

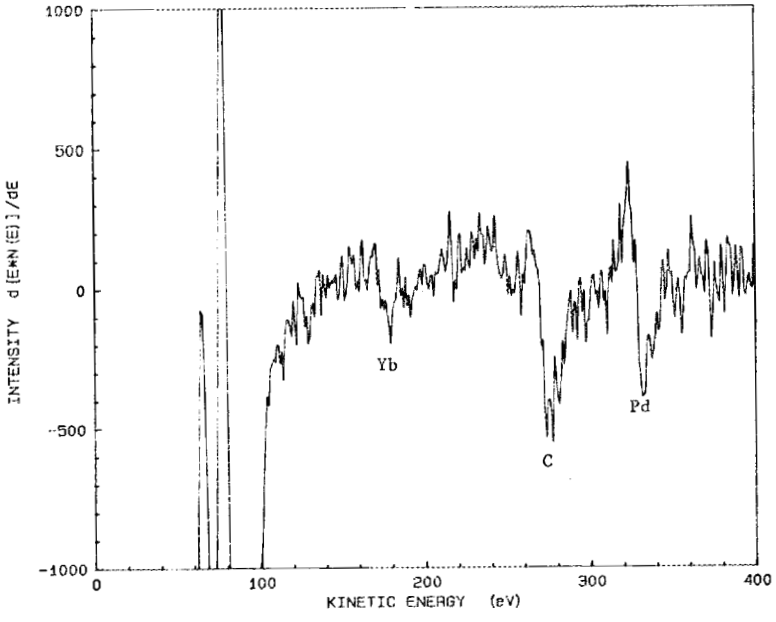

Figure 7. Auger spectrum showing an exploded view at the low energy end of the spectrum seen in Figure 6. The Pd is from the conductive overlayer. Carbon is most likely from exposure of the fracture surface to laboratory atmosphere for a considerable time. Ytterbium is one of the bulk constituent elements.

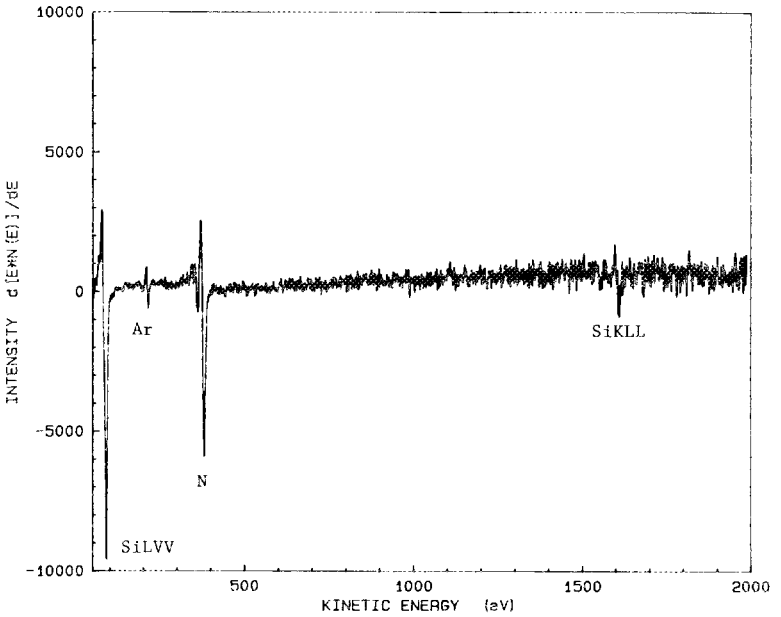

Figure 8. Auger spectrum from the surface of the large crystallite shown in Figures 1 and 2 after 9 minutes of sputtering. This surface is free of oxygen and shows some implanted Ar which is characteristic of Si_3N_4.

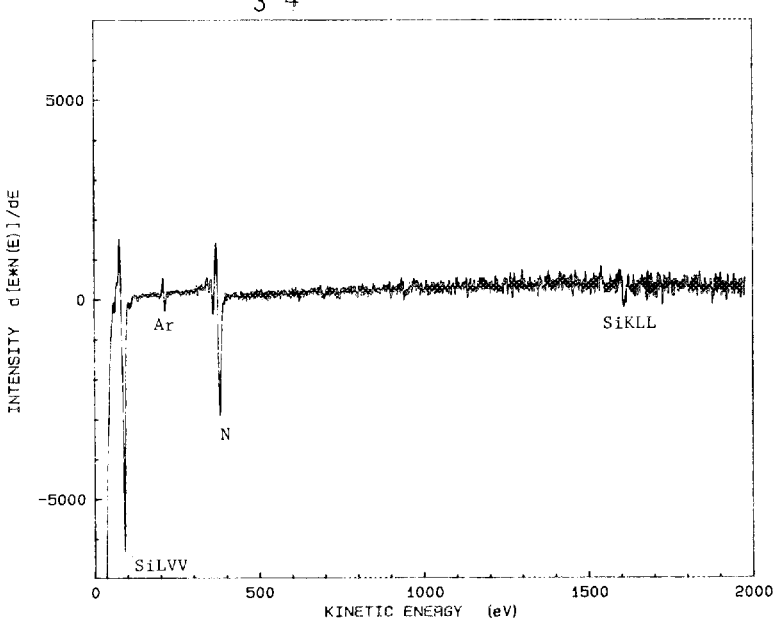

Figure 9. Auger spectrum from the large crystallite (Figure 1 and 2) after 20 minutes of ion sputtering with 3 keV Ar.

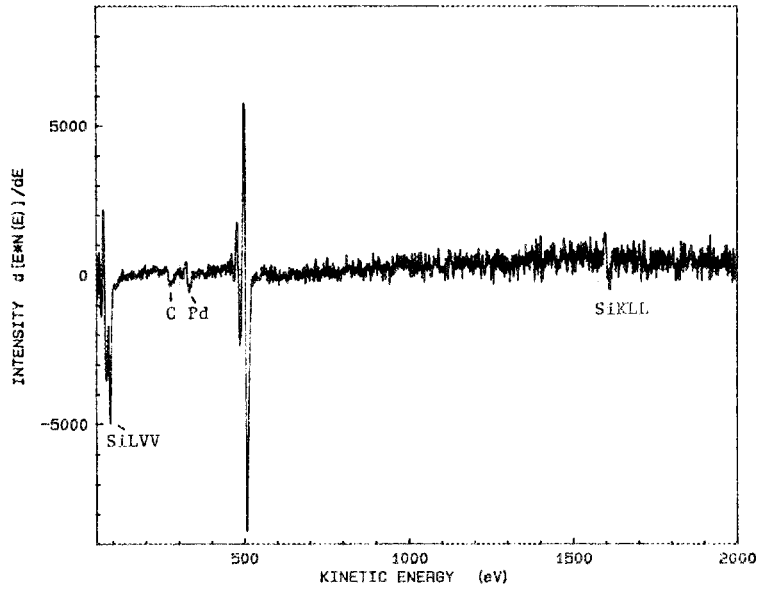

Figure 10. Auger spectrum from the surface of the lower crystalline in Figure 5 after the Au/Pd layer has been removed.

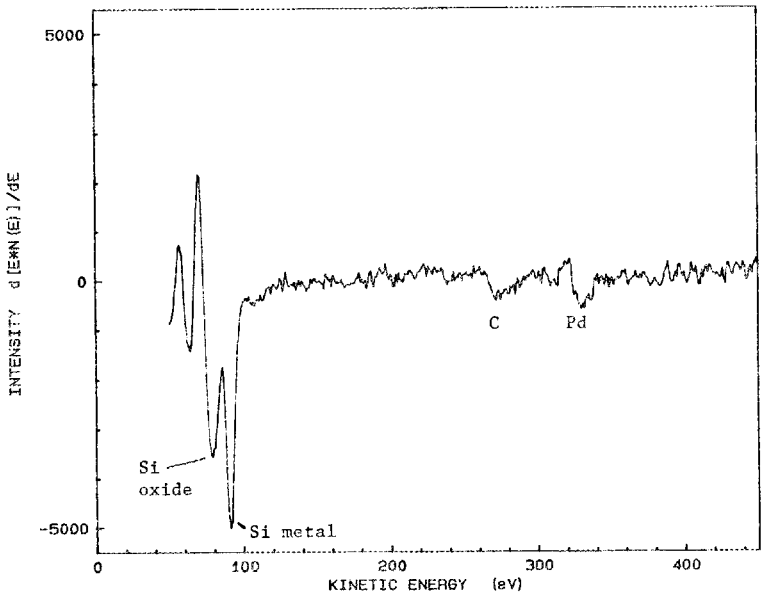

Figure 11. An exploded view of the Auger spectrum in Figure 10 showing peak splitting in the SiLVV peak. This could occur as a result of either ion beam or electron beam damage.

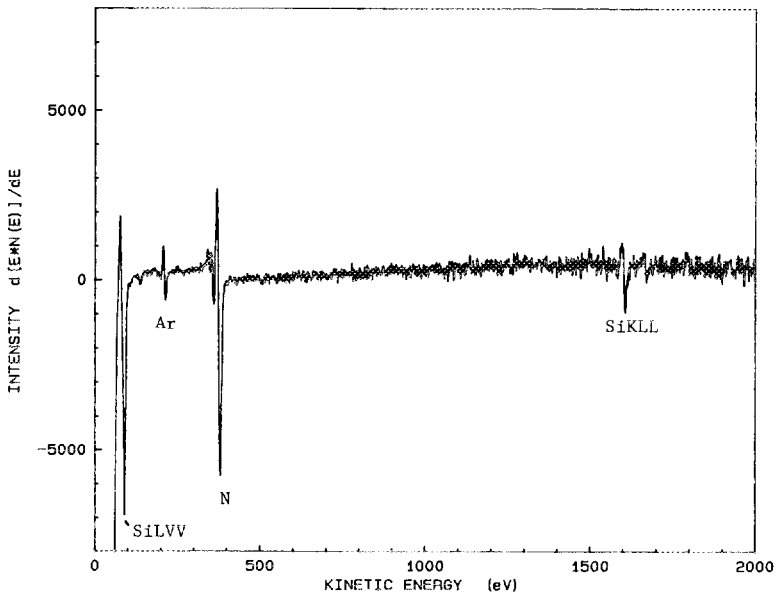

Figure 12. Auger spectrum from the lower crystalline seen in Figure 5 after a 20 minute sputter.

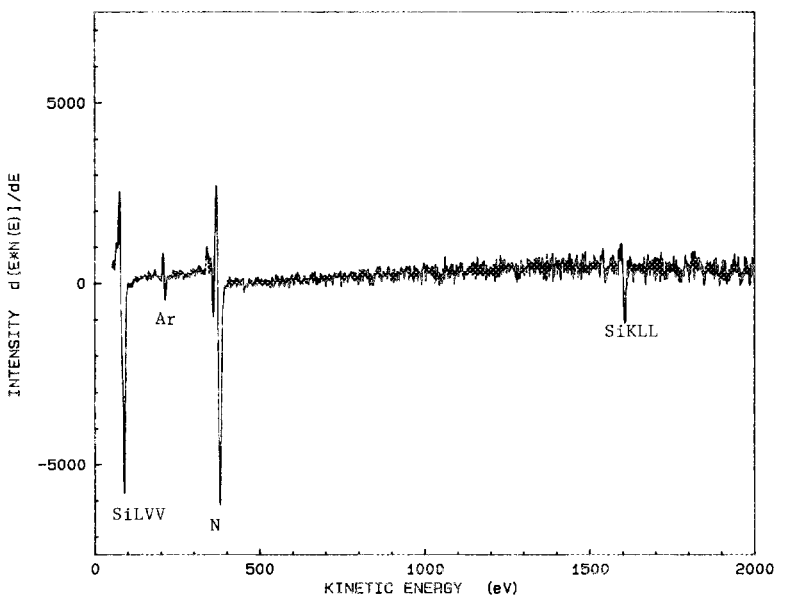

Figure 13. Auger spectrum from the upper crystallite in Figure 5 after a 20 minute sputter.

Low Heat Rejection Diesel Coupon Tests

C. R. Brinkman and W. K. Kahl (Oak Ridge National Laboratory)

Objective/scope

The objective of this task is to expose various structural ceramics to conditions found in a small diesel engine. Commercially available ceramics, as well as new candidate monolithic and whisker-toughened ceramics, will be fabricated into modulus of rupture (MOR) bars, nondestructively examined, and exposed to a variety of operating conditions within a small diesel engine. Subsequent to exposure, the bars will be nondestructively and destructively examined and the results compared to a nonexposed data base.

Technical progress

Specimens of both partially stabilized zirconia (PSZ), TS and MS grades, were exposed to the combustion conditions in two small diesel engines. The specimens were MOR bars 50 × 4.5 × 3.5 mm and were held or clamped by a special fixture during exposure at one end as shown in Fig. 1. The fixture held two bars at a time for 100 h of discontinuous engine operation. Two engines were employed for this effort, one of which was a single (engine 1) and the other a two-cylinder, 0.825-L unit (engine 2). Some specimens were given a 100-h isothermal age at 700, 750, or 800°C to act as control specimens with the engine-exposed bars. Temperatures in the engine were measured by several methods, including templugs attached to specimen surfaces, and via thermocouples inserted in a small center-drilled hole at several positions within a bar. Peak temperatures were at the surface of the bars and were near or exceeded 800°C at the unclamped ends.

Subsequent to exposure, the bars were subjected to four-point bending and the rupture strengths determined. Table 1 gives the statistical analysis and average strength values for all PSZ bars tested to date. Figures 2 and 3 are Weibull plots which compare rupture results of engine-exposed material with nonengine-exposed PSZ-TS and PSZ-MS grades, respectively. Table 1 and Figs. 2 and 3 indicate that the TS grade showed a decrease in average strength of 32% while the MS grade decreased by about 9% in comparison to average behavior of unaged material due to engine exposure.

Figure 4 compares fracture locations of representative engine-exposed material with unexposed bars. Most of the engine-exposed bars were inserted in engine 2. Note in Fig. 4 that bars exposed in engine 2 preferentially failed some 13–17 mm from the clamped or cold end of the bar in comparison to unexposed material. Some of the bars exposed in engine 1 had a gritty or sandpaperlike surface texture as can be seen in comparing surfaces of unexposed material, Fig. 5, with exposed material, Fig. 6.

Figures 7 and 8 are the result of X-ray diffraction and Raman spectroscopy studies, respectively, and show fracture strength as a function of monoclinic content. The indicated monoclinic content measurements were made near the fracture surfaces as shown. In the case of the Raman spectroscopy measurements, the apparent monoclinic content assumes that only the tetragonal and monoclinic phases are present. Figures 7 and 8 indicate a strength relationship with the higher monoclinic contents showing

ORNL-DWG 88-10552

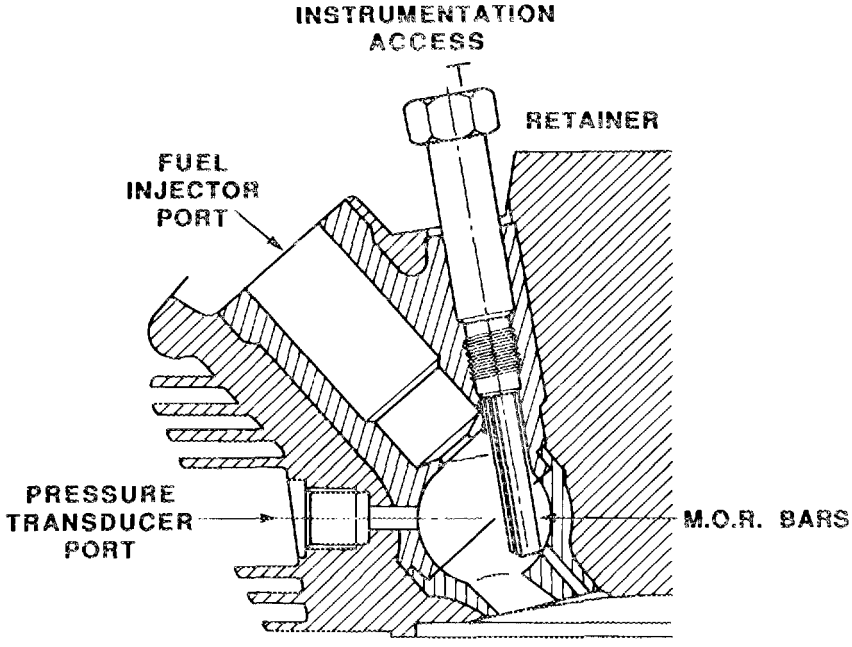

Fig. 1. Cross-sectional view of deutz cylinder head shows bars' position with respect to fuel injector.

lower strengths in the TS-grade material. Figure 9 is a plot of apparent monoclinic content measured by Raman spectroscopy as a function of distance from the cold or clamped end of two engine-exposed bars prior to being subjected to four-point bending to fracture. Note that the increased monoclinic content is in the same position in the bar as the fractures indicated in Fig. 4 for specimens exposed in engine 2. Since this is near the cold or clamped end of the bars, no explanation is currently given as to why the monoclinic content is so high in this area. Additional stress analysis of the bar during engine operation is currently under way.

Status of milestones

Milestone 331504 was completed September 15, 1988, as scheduled.

Table 1. Results of tests conducted on MOR bars after exposure to several conditions[a]

No. of observations	Material condition	Weibull modulus		y-intercept		Average strength (MPa)	Standard deviation (MPa)	Reduction in average strength[b] (%)
		Linear regression	Maximum likelihood	Linear regression	Maximum likelihood			
	PSZ-TS MOR bars after exposure							
53	As-fabricated	31.7	48.6	-202.5	-311.2	587.3	20.3	0
12	Engine exposed for 100 h	3.6	4.1	-21.7	-24.8	378.4	114.0	36
23	Pre-aged 100 h at 700°C	37.0	40.9	-233.9	-258.4	547.7	17.8	7
20	Pre-aged 100 h at 750°C	15.1	14.7	-95.5	-93.2	539.1	42.0	8
20	Pre-aged 100 h at 800°C	57.2	53.7	-359.2	-337.1	528.4	11.3	10
2	Engine exposed for 100 h/ ground and polished	--	--	--	--	459.5	60.3	22
	PSZ-MS MOR bars after exposure							
40	As-fabricated	29.2	29.8	-191.1	-195.1	683.0	28.5	0
14	Engine exposed for 100 h	17.2	20.1	-111.3	-129.9	623.2	42.6	9
20	Pre-aged 100 h at 700°C	16.4	28.2	-106.8	-182.7	641.6	40.1	6
19	Pre-aged 100 h at 750°C	19.3	24.7	-124.7	-159.6	629.4	36.5	8
20	Pre-aged 100 h at 800°C	30.0	39.4	-194.1	-254.8	635.2	24.3	7

[a]Tests were conducted with a cross head speed of 8.47×10^{-3} mm/s or a strain rate of 1.1×10^{-4} s^{-1}.

[b]Reduction in strength in comparison to as-fabricated material.

ORNL-DWG 88-11291

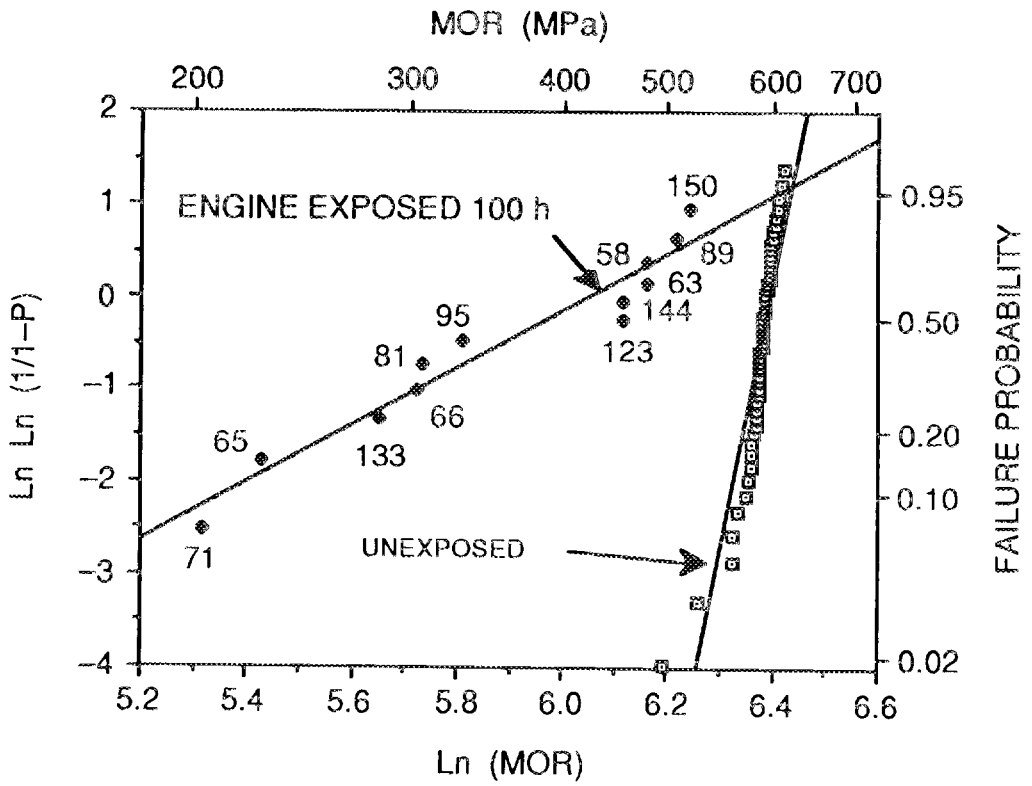

Fig. 2. Weibull plot comparing modulus of rupture (MOR) strength data for Nilcra PSZ-TS exposed to diesel engine combustion conditions and unexposed material. Numbers indicate bar numbers and specimens exposed together as pairs as follows: engine 1, 71-81 and 95-89; engine 2, 63-58, 133-123, and 144-150. Specimens 151 and 152 exposed in engine 2 were omitted for clarity.

ORNL-DWG 88-11290

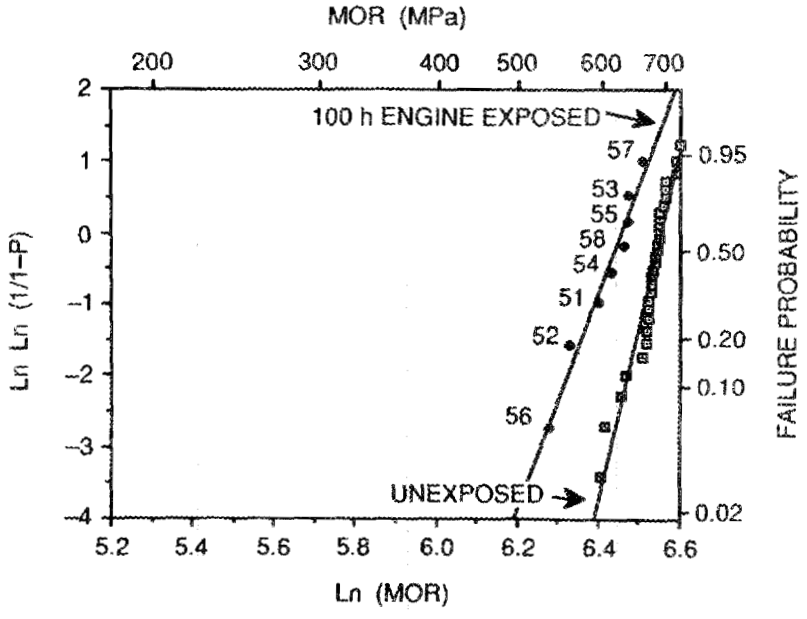

Fig. 3. Weibull plot comparing MOR strength data for Nilcra PSZ-MS exposed to diesel engine combustion conditions with unexposed material. Numbers indicate bar numbers and specimens exposed together as pairs as follows: engine 2, 41-42, 43-44, 51-52, 53-54, 55-56, 57-58, and 59-60. Specimens 45 through 50 were omitted for clarity.

ORNL-PHOTO 6233-88

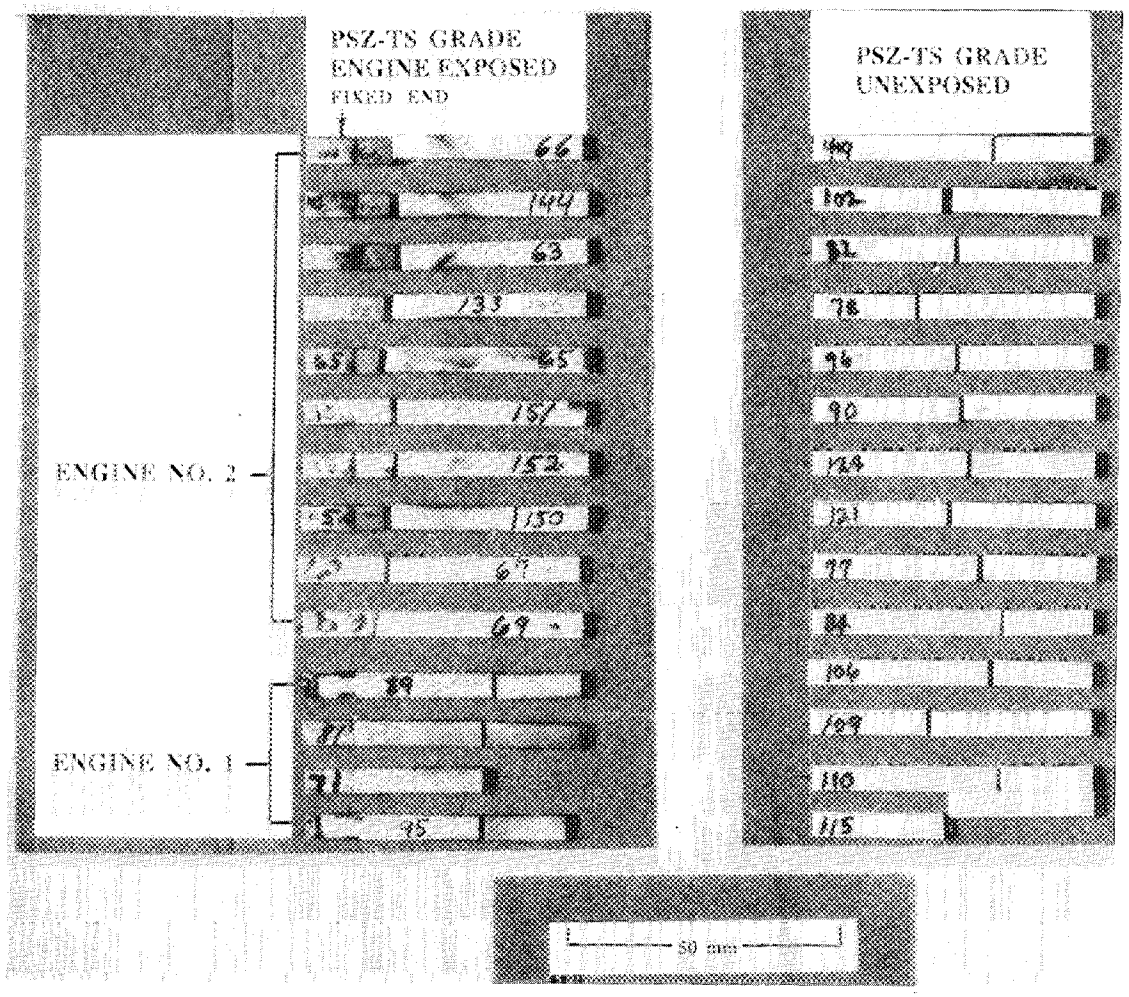

Fig. 4. Comparison of PSZ-TS MOR bars tested in the exposed and unexposed condition.

ORNL-PHOTO 6813-88

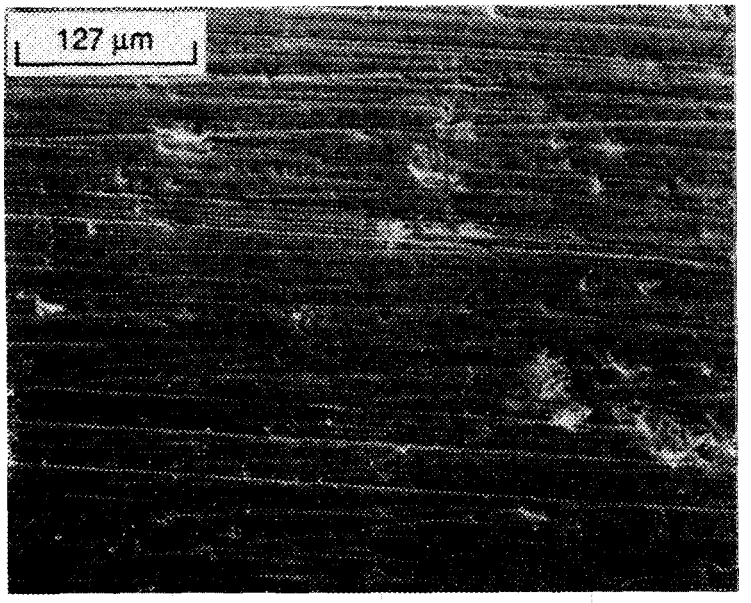

Fig. 5. As-machined surface of PSZ-TS grade, specimen 118, flexural tested in nonexposed condition.

ORNL-PHOTO 6813-88

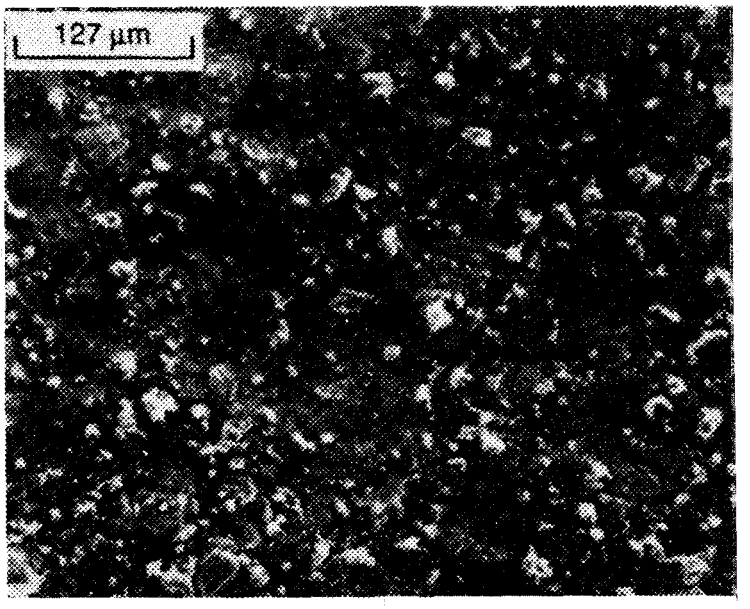

Fig. 6. As-exposed surface of specimen 71 of PSZ-TS grade after 100 h in diesel engine combustion chamber. Note gritty surface condition.

ORNL-DWG 88-13077

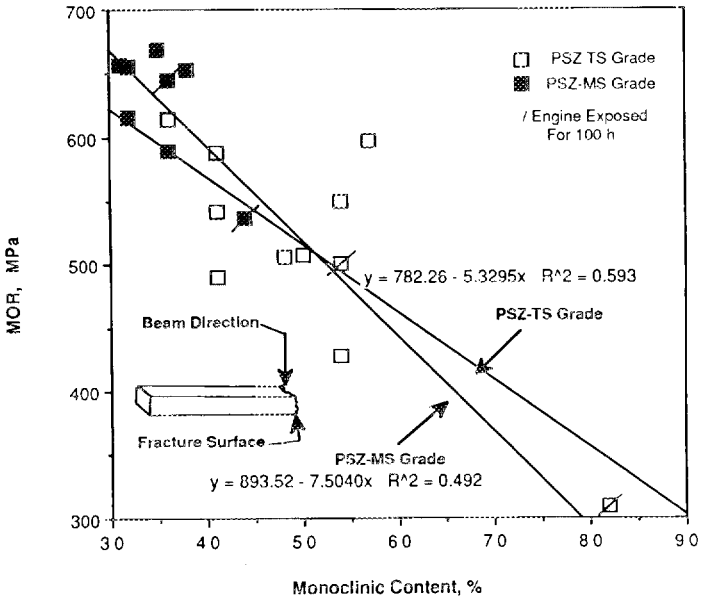

Fig. 7. Modulus of rupture (MOR) for individual bars as a function of monoclinic content from X-ray diffraction analysis.

ORNL-DWG 88-14052

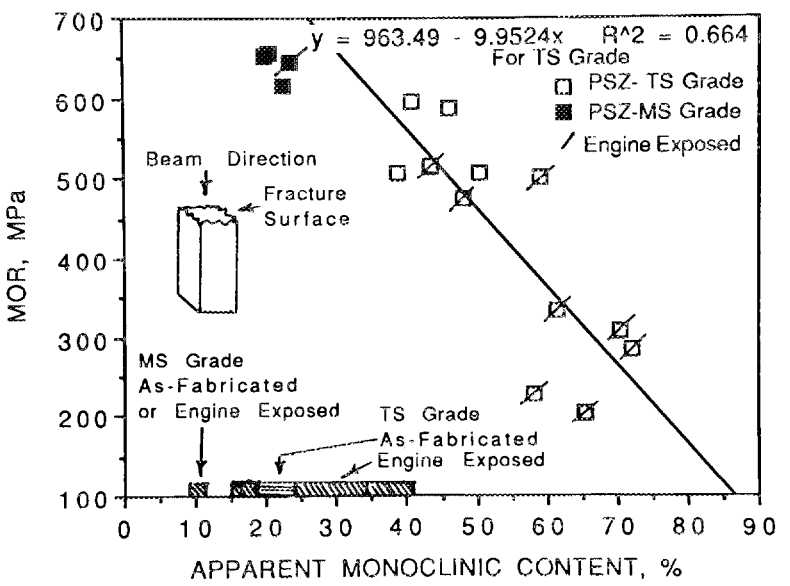

Fig. 8. Modulus of rupture (MOR) for individual bars as a function of apparent monoclinic content as determined at fracture surface by Raman spectroscopy.

ORNL-PHOTO 7121-88

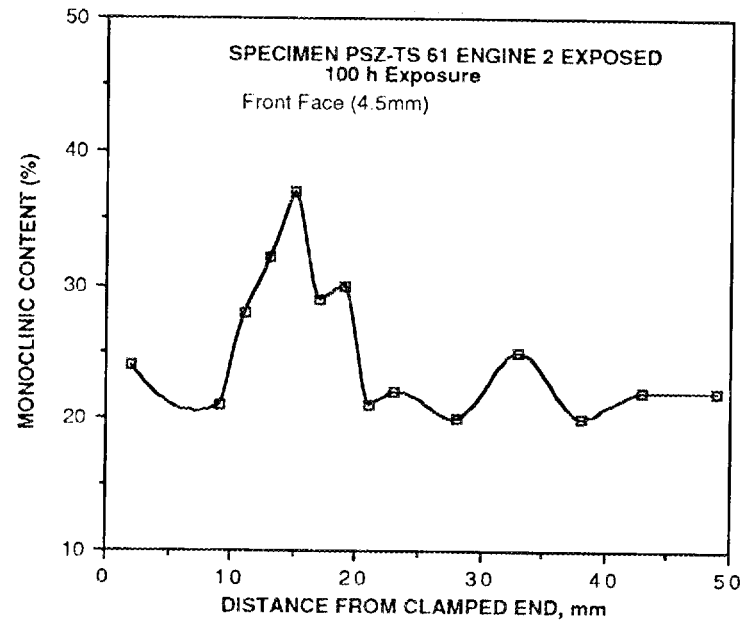

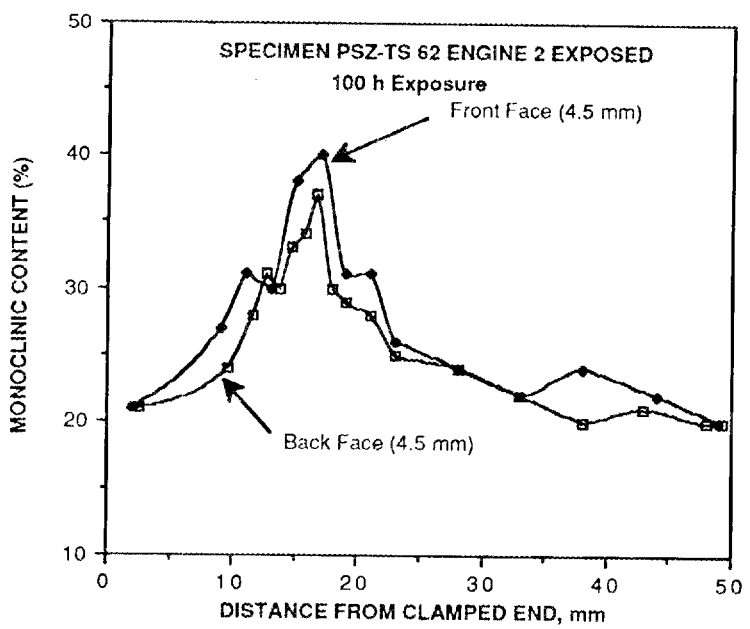

Note: Monoclinic Content Assuming Only Monoclinic And Tetragonal Phases Are Present

Fig. 9. Apparent monoclinic content shows a peak 15-17 mm from clamped end of engine-exposed bars.

3.4 FRACTURE MECHANICS

Testing and Evaluation of Advanced Ceramics at High Temperature in Uniaxial Tension

J. Sankar, V. S. Avva, And A. Sinha (North Carolina A&T State University)

Objective/scope

The purpose of this effort will be to test and evaluate advanced ceramic materials at temperatures upto 1500 °C in uniaxial tension. Testing may include fast fracture strength, along with analysis of fracture surfaces by Scanning electron microscopy. This effort will comprise of the following tasks:

Task 1. Specifications for Testing Machine and controls + (Procurement)
Task 2. Identification of Test Material (s) + (Procurement of specimens)
Task 3. Identification of Test Specimen configuration
Task 4. Specifications for Testing grips and Extensometer + (Procurement)
Task 5. Specifications for Testing Furnace (Procurement) + controls
Task 6. Development of Test Plan
Task 7. High Temperature Tensile Testing
Task 8. Reporting (Periodic)
Task 9. Final Report

It is anticipated that this program will help in understanding the behavior of Ceramic materials at very high temperatures in uniaxial tension.

Technical progress

During the reporting period, the mechanical strength characteristics of GTE SNW-1000 silicon nitride under uniaxial tension at elevated temperatures were completed. Fractography and X-Ray microanalysis of the fracture surfaces of the silicon nitride samples tested at elevated temperatures were also completed during this reporting period. The plots of the log tensile strength versus log stressing rate for three (3) testing temperatures of namely, room temperature, 900 °C and 1100 °C and at five (5) different stressing rates of 3.75, 7.5, 450, 900, and 2100 MPa/Min are given in Figure 1. From the Figure, it can be observed that there is no effect of stressing rate on the tensile strength of this material. The variation of average tensile strength versus testing temperatures for all the tested samples is shown in Figure 2. Here, the open "squares" indicate the data obtained at NCA & T and the dark "circles" indicate the data obtained at ORNL. It can be observed that the average tensile strength values obtained at A & T and ORNL matched very well, indicating the consistency of results from two different laboratories. The plot shows a decrease in average tensile strength with increasing temperature. This drop in strength is observed to be more pronounced at 1100 °C and 1200 °C than at 900 °C. This decrease could be attributed to the softening of the grain boundaries and possibly due to creep occuring

the softening of the grain boundaries and possibly due to creep occurring at these temperatures.

SEM images in Figures 3 and 4 show the fracture initiation sites of samples tested at 900 °C at stressing rates of 7.5 and 2100 MPa/Min respectively. Figures 5 and 6 show the fracture initiation sites of two samples tested at 1100 °C and at stressing rates of 7.5 and 2100 MPa/Min respectively. High magnification image of a sample tested at 900 °C (2100 MPa/Min) in Figure 7 indicates that the fracture mode is transgranular. Similarly, the high magnification image of a sample (Figure 8) tested at 1100 °C (7.5 MPa/Min) also indicates a transgranular fracture mode. However, Figure 9, the high magnification image of a sample tested at 1100 °C (2100 MPa/Min) shows areas where the grains are not sharp. This is possibly due to the partial melting of the grain boundaries which makes the grain boundaries weaker than the grain interior, resulting in partial intergranular fracture. Intergranular fracture is seen only in some areas but the fracture mode is predominantly transgranular. X-Ray microchemical analysis conducted on the fracture initiation sites of the samples tested at elevated temperatures (Figure 10) shows contaminants such as Fe, Cl, K, C, O , and Na, similar to the samples tested at room temperature.

Status of milestones

Tasks 1-7 are complete.

Publications and presentations

1. J. Sankar, A. Kelkar, A. Sinha, K. C. Liu, "Strength and Fatigue of silicon nitride in Uniaxial Tension", paper presented at the 26th Automotive Technology Development Contractor's Coordination meeting, Dearborn, Michigan, October 1988.

2. J. Sankar, A. Kelkar, A. Sinha, R. Vaidyanathan, "Room and Elevated Temperature Fractography of Silicon nitride tested under pure tension", paper presented at the 14th International Symposium for Testing and Failure Analysis, Los Angeles, California, November 1988. Proceedings published by American Society for Metals, pg. 343-353, ISTFA '88.

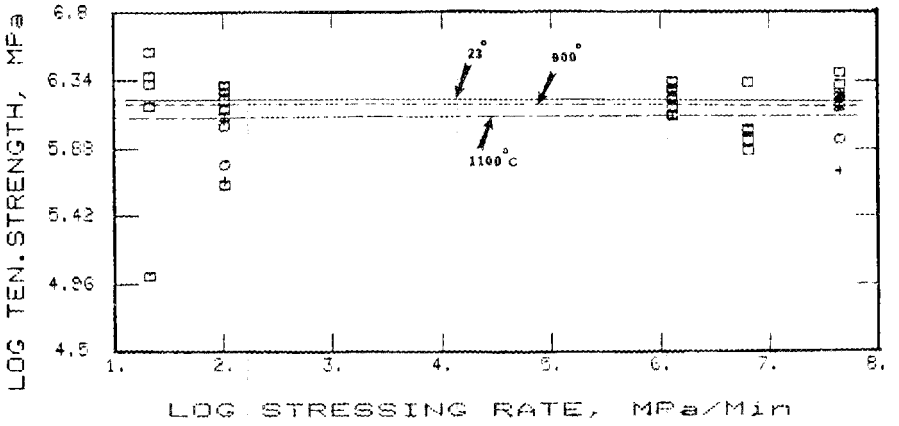

Figure 1. Plot of log tensile strength vs. log stressing rate for GTE SNW-1000 for 3 temperatures

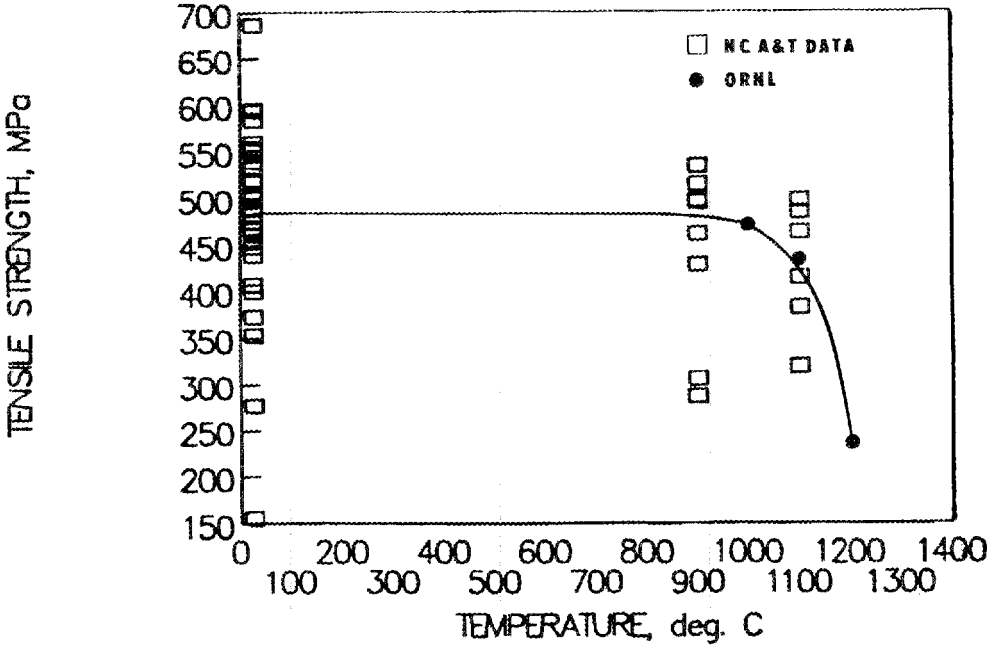

Figure 2. Variation of tensile strength vs. temperature for GTE SNW-1000

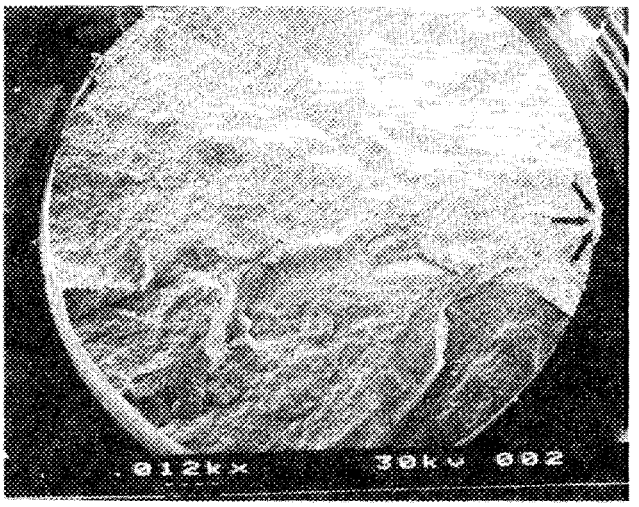

Figure 3. Fracture initiation site of a sample tested at 900 °C (7.5 MPa/Min)

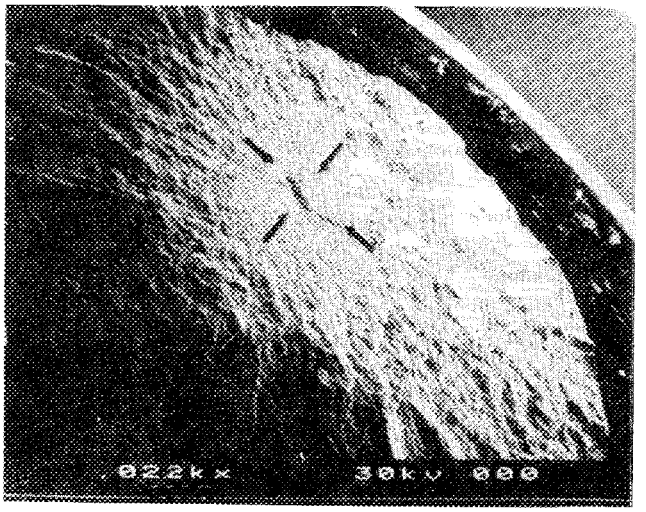

Figure 4. Fracture initiation site of a sample tested at 900 °C (2100 MPa/Min)

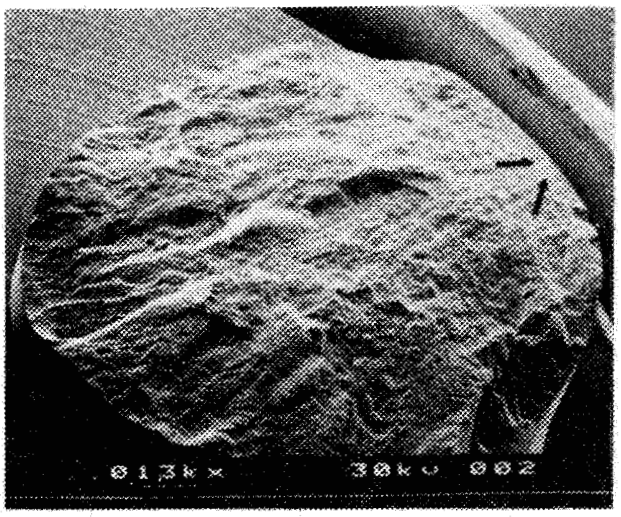

Figure 5. Fracture initiation site of a sample tested at 1100 °C (7.5 MPa/Min)

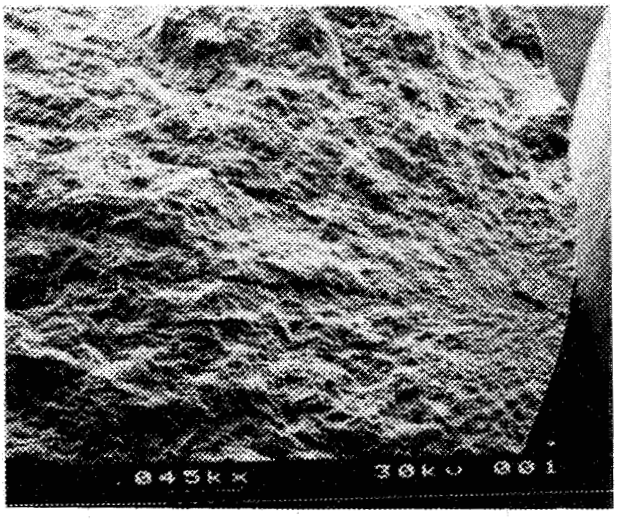

Figure 6. Fracture initiation site of a sample tested at 1100 °C (2100 MPa/Min)

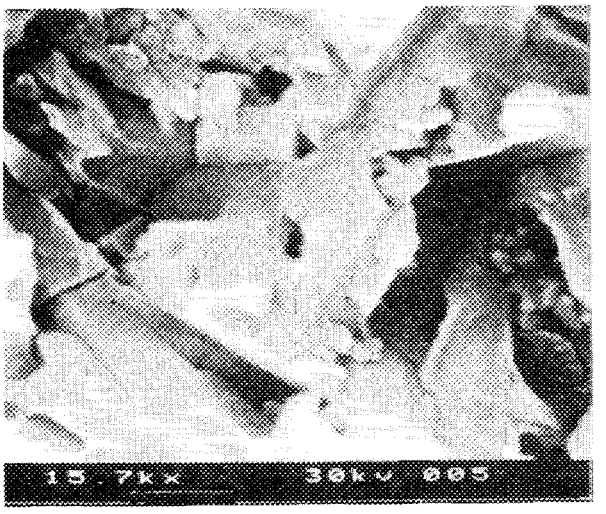

Figure 7. High magnification image of a sample tested at 900 °C (2100 MPa/Min) showing transgranular fracture mode

Figure 8. High magnification image of a sample tested at 1100 °C (7.5MPa/Min) showing transgranular fracture mode

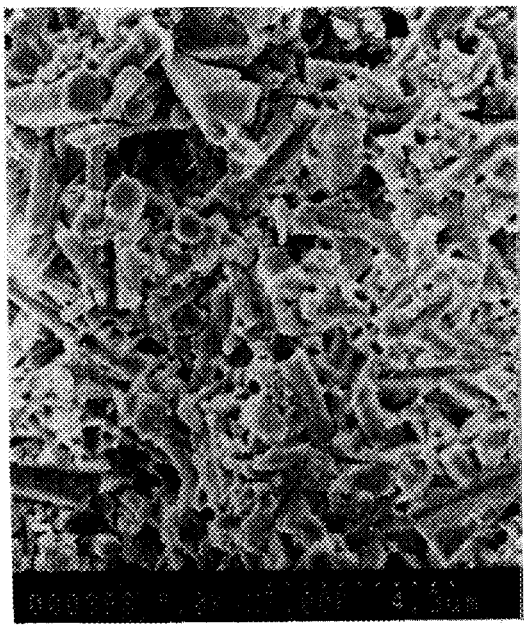

Figure 9. High magnification image of a sample tested at 1100 °C (2100 MPa/Min) showing areas of intergranular and transgranular fracture mode

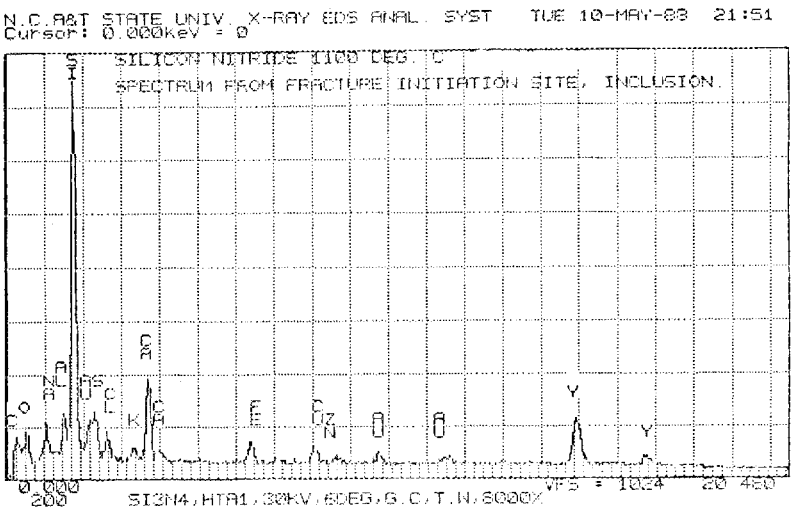

Figure 10. X-Ray spectrum acquired from the fracture initiation site of a sample tested at 1100 °C (2100 MPa/Min)

Standard Tensile Test Development

S. M. Wiederhorn, D. F. Carroll, T.-J. Chuang and D. E. Roberts
(The National Institute of Standards and Technology)

Objective/scope

This project is concerned with the development of test equipment and test procedures for measuring the tensile strength and creep resistance of ceramic materials to tensile stresses at elevated temperatures. Inexpensive techniques of measuring the creep and strength of ceramics at elevated temperatures are being developed and will be used to characterize the mechanical behavior of structural ceramics. The test methods will use self aligning fixtures, and simple grinding techniques for specimen preparation. Creep data obtained with tensile test techniques will be compared with data obtained using flexure and compressive creep techniques. The ultimate goal of the project is to assist in the development of a reliable data base and a methodology that can be used for structural design of heat engines for vehicular applications.

Technical progress

During the past 6 months, tensile test equipment was constructed to conduct creep tests at temperatures as high as 1500°C. Creep deformation is measured with a laser extensometer which follows the relative displacement of two flags attached to the garge section of each specimen. Data collection is entirely automatic, the displacements being fed into a personal computer where they are stored and then used to determine creep curves for the materials being studied. A detailed description of the equipment is given below.

Tensile Creep Apparatus

A schematic representation of the tensile creep apparatus is shown in figure 1. The tensile specimen was attached to two silicon carbide loading rods in a pin and clevis arrangement using sintered alpha silicon carbide pins. The silicon carbide loading rods extended out of the furnace and were connected via simple universal joints to an air piston that applied the load to the specimen (upper rod), and to a load cell that monitored the applied load on the specimen (lower rod). Using an optical pyrometer, no temperature difference was detected within the gauge section of the tensile specimen at temperatures greater than 1100°C. For ease of specimen loading, a clam-shell furnace was used in the creep apparatus.

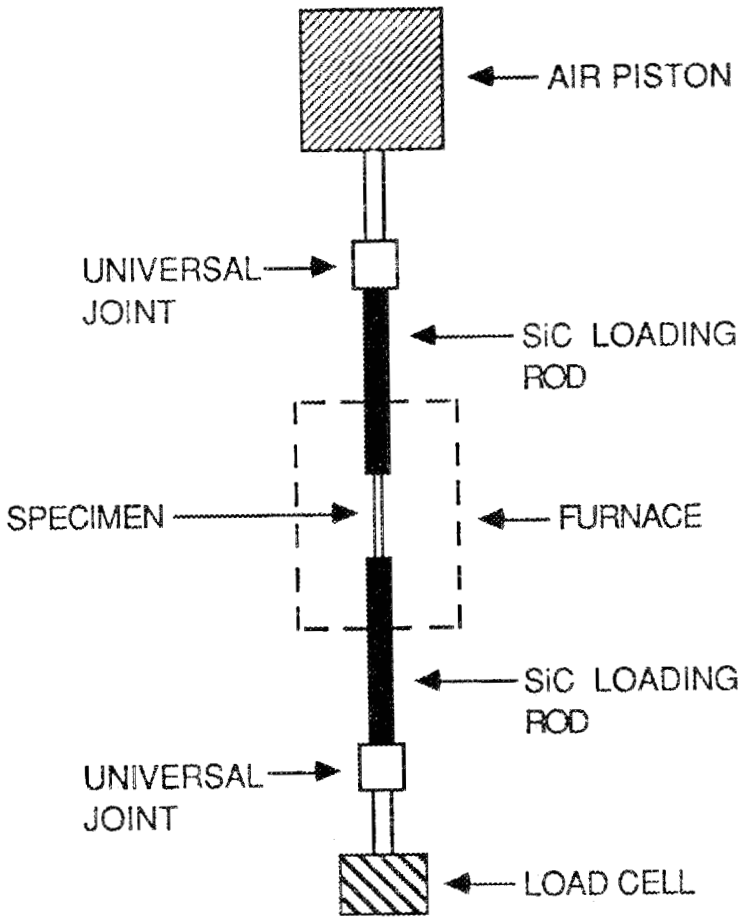

Figure 1. Schematic representation of the tensile loading apparatus.

The tensile specimen was flat and dogbone-shaped with holes at each end (figure 2) so the specimen could be pinned to the load train. Specimens were ground from a block of material with the same dimensions as the length and width of the tensile specimen. The cross-section of the block was reduced to that of the tensile specimen with a shaped grinding wheel. A thin wafering blade then cut specimens from the block with the desired thickness.

After slicing the tensile specimens from the block, holes were machined into the tensile specimens. Proper machining of the holes along the center-line of the specimen is essential, since alignment of the specimen is critically dependent on the machining. If a material has a high enough electrical conductivity, the best technique for machining the holes is wire EDM (electro-discharge machining). When holes are machined using a wire EDM, finished tensile specimens can be made at approximately 3 times the cost of conventional bend beam specimens. However, when EDM cannot be used, specimen costs are higher since more conventional grinding methods are required.

Alignment

One major concern in developing a tensile creep apparatus is the degree of alignment of the tensile specimen. An excellent review paper by Christ and Swanson [1] identifies causes of misalignment and gives examples of methods to minimize bending moments introduced by the load train. A common source of misalignment in the pin and clevis configuration occurs when the pin used to attach the tensile specimen to the loading rod, does not sit properly in the hole, but loads on the edge of the specimen (figure 3a). This type of misalignment produces a bending moment about the major face of the tensile specimen. To minimize this type of bending, the holes in the tensile specimen are tapered so that load is applied only to the center of the specimen (figure 3b). A cone-shaped copper rod, diamond paste, oil and a slow speed drill press are used to taper the holes.

Alignment about the minor face of the specimen is determined by the accuracy with which the holes are machined to the centerline of the specimen (figure 3c). The analysis by Christ and Swanson [1] was used to estimate the tolerances needed in machining the holes onto the centerline. If the centers of the holes were offset from the centerline by 0.025 mm (0.001 in), a bending stress equal to approximately 5% of the applied stress would be introduced into the gauge section of the specimen. Although based on a simple elastic analysis, this calculation indicates the machining tolerances needed to obtain good alignment in the tensile specimen.

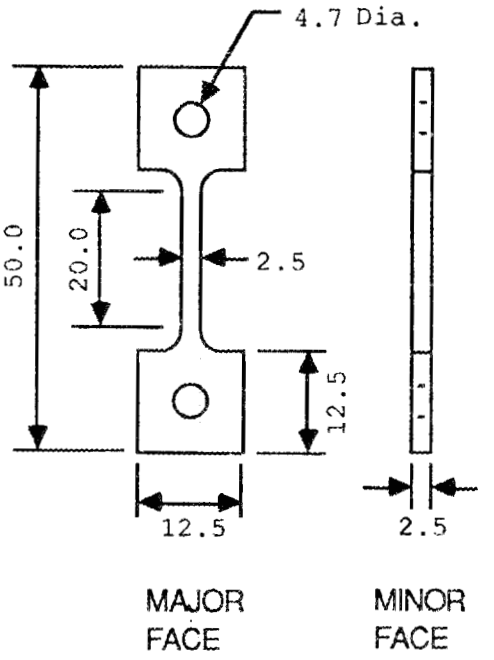

Figure 2. The major and minor faces of the flat dogbone-shaped tensile specimen. All dimensions are in millimeters.

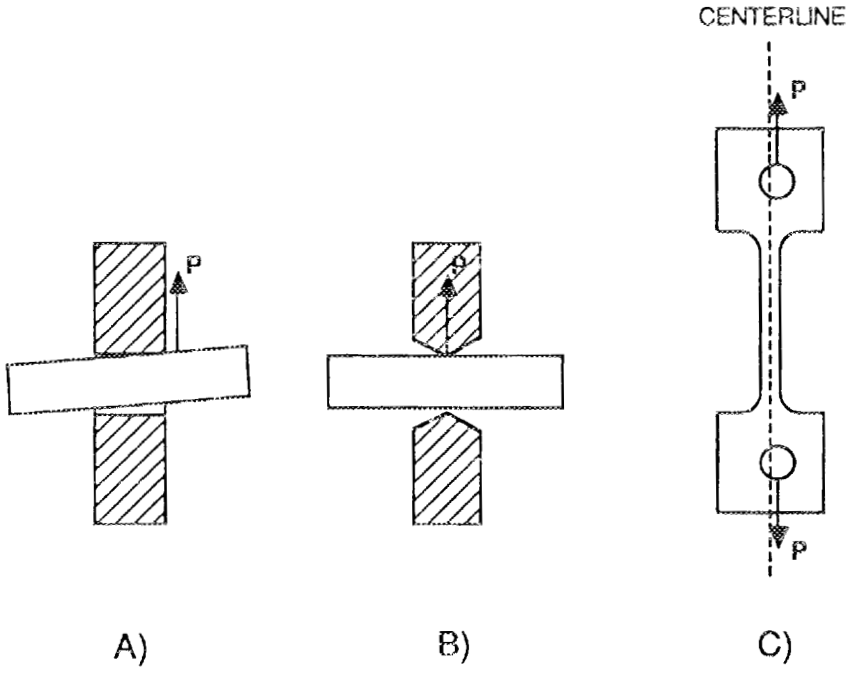

Figure 3. Common sources (a and c) and solutions (b) for misalignment in the pin and clevis gripping technique.

The degree of alignment in the tensile specimen was determined by measuring the elastic strain variation in the gauge section as a function of applied stress at room temperature. According to Christ and Swanson [1], the proper technique for determining the amount of bending in a gauge section is to simultaneously measure the strain variation on all four side of the gauge about the same perimeter of the specimen. Due to the small cross-sectional area of this specimen, it was not possible to attach four strain gauges simultaneously about the same perimeter. Therefore, the alignment was determined by measuring the strain variation between opposite faces of the gauge section. By using this technique, the amount of bending about the major and minor faces of the tensile specimen were determined as a function of applied load.

Figure 4 represents the strain variation about the major and minor faces of a typical tensile specimen as a function of applied stress. The percent elastic bending was calculated according to:

$$\% \text{ bending} = \frac{\epsilon_1 - \epsilon_o}{\epsilon_o} \times 100 \qquad (1)$$

where ϵ_1 is the elastic strain measured from one face of the gauge section, ϵ_2 is the elastic strain measured from the opposite face and ϵ_o is the average strain determined by $(\epsilon_1 + \epsilon_2)/2$.

The percent bending about the major face of the specimen was found to decrease from approximately 3.3% at 12.5 MPa to 1.0% at 50 MPa. Higher stresses were not applied to the specimen for fear of brittle fracture at room temperature. Typically, the stresses used in the creep tests were approximately 75 to 125 MPa. If the bending data are extrapolated to these stress levels, bending about the major face should be less than 1%. This result shows that good alignment can be obtained about the major face of the tensile specimen, by using the tapered hole arrangement shown in figure 3b.

The percent bending about the minor face of the specimen was also found to decrease from a level of approximately 4.2% at 12.5 MPa to 2.0% at 50 MPa. If these results are extrapolated to the stresses used in the creep studies, the elastic bending about the minor face of the specimen should be less than 2.0%. These results show that good alignment can be obtained in the minor face of the specimen if proper care is taken to machine the holes as close to the centerline as possible.

Although elastic strain gauge results indicate good alignment at room temperature, bending could still be introduced into the specimen if the upper loading rod exhibits an off-axis translation during deformation. Even though displacements of the upper loading rod during the creep test were small (<0.2 mm), it was still necessary to check the curvature of the specimen after deformation to ensure that alignment was maintained and that bending due to off-axis translation

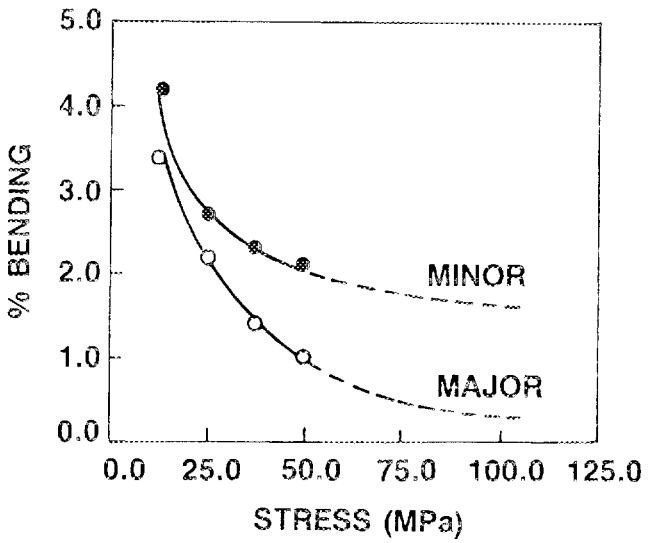

Figure 4. The percent elastic bending about the major (o) and minor (●) faces of a tensile specimen with tapered holes, as a function of applied stress.

was not introduced into the specimen. The curvature of the deformed tensile specimens was measured using a profilometer device developed by Jakus et al. [2]. This device consisted of an LVDT that was systematically dragged across the face of the tensile specimen. Any curvature in the specimen was recorded as a positive or negative displacement by the LVDT. A computer was then used to calculate the curvature of the specimen from the displacement data as a function of distance along the gauge section. This equipment was capable of measuring surface displacements over distances of 50 mm to an accuracy of 1 micron.

The curvature along the major face of a tensile specimen before and after deformation are shown in figure 5a and 5b (solid line), respectively.[1] For the as-machined specimen (figure 5a), the curvature was essentially zero with only slight variations with position on the specimen. The variation in curvature along the gauge section was a consequence of surface roughness from the machining process. After deformation to a creep strain of approximately 0.25%, there was little change in the overall curvature of the gauge section (figure 5b, solid line). The maximum curvature along the gauge section, approximately 0.06 m^{-1} (radius of 17 m), can be used to calculate a strain due to bending of ≈2-3% of the total measured strain. These results confirm that alignment in the specimen was maintained during deformation and that any effects of off-axis translation of the upper loading rod were minimal. Similar curvature results were obtained for the minor face of the tensile specimen.

For comparison, the curvature of a specimen without tapered holes is shown in figure 5b (dashed line). These results indicate the dramatic improvement that can be obtained in alignment when tapered holes are used. The initial curvature of this specimen before deformation was similar to that shown in figure 5a. After deformation to a strain of 0.5%, part of the gauge section exhibited a negative curvature of approximately -0.33 m^{-1} (radius of -3 m) while another part of the specimen exhibited a positive curvature of approximately 0.33 m^{-1} (radius of 3 m). This result indicated that the specimen was deformed into a "s" shape. Assuming the specimen had a uniform radius of curvature of 3 m, the specimen exhibited a bending strain equal to approximately 8 to 10% of the total measured creep strain. Based on these results, specimen alignment is significantly improved by using the tapered holes shown in figure 3b.

---

1 The curvature results were expressed in terms of (1/r) where r is the calculated radius of curvature. In this notation, a perfectly flat specimen ($r=\infty$) would have a curvature of 0 m^{-1}.

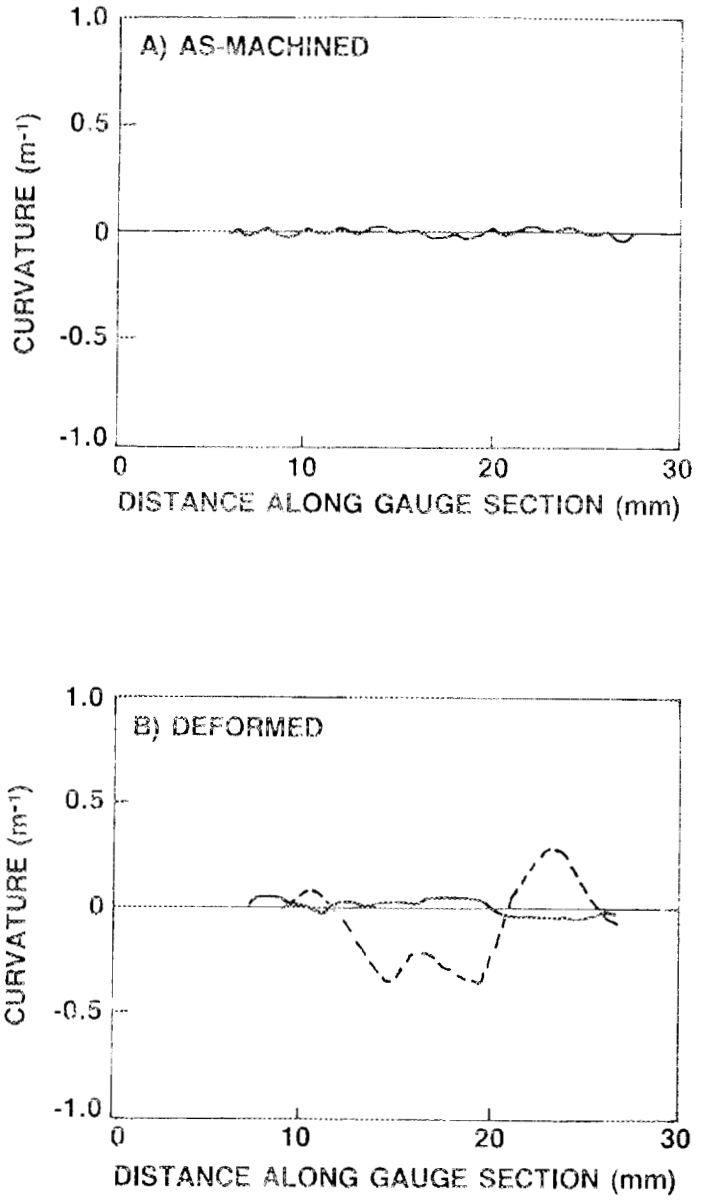

Figure 5. Curvature of a tensile specimen before and after deformation. A) As-machined specimen. B) Specimen with tapered holes deformed at 1300°C to a creep strain of 0.25% (solid line). Specimen without tapered holes deformed at 1300°C to a creep strain of 0.5% (dashed line).

Creep Measurement

Creep deformation was measured continuously using a laser extensometer.[2] In this technique, the gauge length of the specimen was marked with a set of alpha silicon carbide flags attached to the gauge section [2]. Figure 6 is a schematic representation of the flags used to mark the gauge section of the specimen. The flags were made by cutting an angled slot at one end of a rectangular piece of alpha silicon carbide, with an opening about the size of the specimen cross-section. The slotted end of the flag was then placed around the gauge section of the specimen. If the flags were machined properly, frictional forces held the flags to the gauge section of the specimen. As seen in figure 6, flags contacted the specimen along two lines, forming a well defined gauge length. A room temperature cement was then used to secure the flags to the gauge section, so the specimen could be placed into the furnace without disturbing the position of the flags. During furnace heat-up, the cement burned off leaving the flags held in place by friction. At elevated temperatures, oxidation secured the flags firmly to the gauge section.

The laser extensometer consisted of a detector and a HeNe laser (<1 mW) that scanned in a vertical line over 150 times per second. The laser was directed through a window of the furnace toward the gauge section of the specimen (figure 7). The two alpha silicon carbide flags interrupted the vertical scan as the beam passed through another window of the furnace located directly behind the specimen. A detector received the vertical scan from the furnace and sensed the interruption of the laser by the flags, thus measuring the gauge length of the specimen. By using a computer, the laser extensometer recorded the movement of the flags as a function of time. The accuracy of the laser extensometer for measurements at room temperature is better than ±2 μm. Both the laser and detector were protected from the heat of the furnace by water-cooled plates, which were attached to the front of each unit and extended to and contacted the windows of the furnace. A slot was cut into each plate just wide enough to permit passage of the laser beam.

A major problem with laser extensometry at high temperatures is air density fluctuations in the light path of the laser beam. Since the index of refraction of air depends on its density, such fluctuations lead to small random variations in the measured displacement of the flags during creep. Such density fluctuations are the result of convection currents either inside or outside of the furnace. To use laser extensometry as a method of measurement at

---

[2] Model 1102 Laser Dimension Sensor and Model 1100 Multidimensional Processor, Zygo Corporation, Middlefield, CT

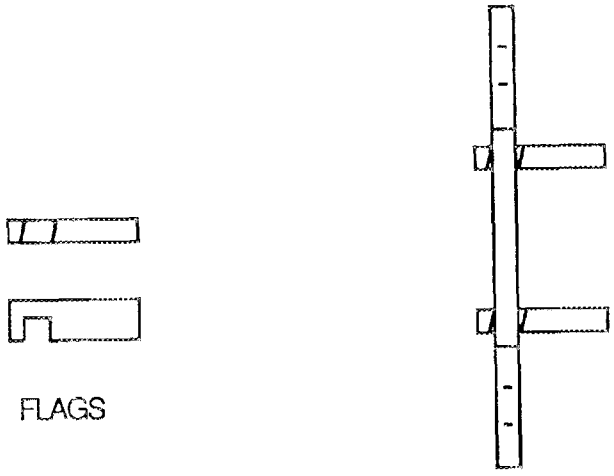

Figure 6. Schematic representation of the flags used in creep measurement technique. The flags were attached to the gauge section of the specimen. The flags contact the specimen along two lines, forming a well defined gauge length. Idea of flags originated by Chuck [15].

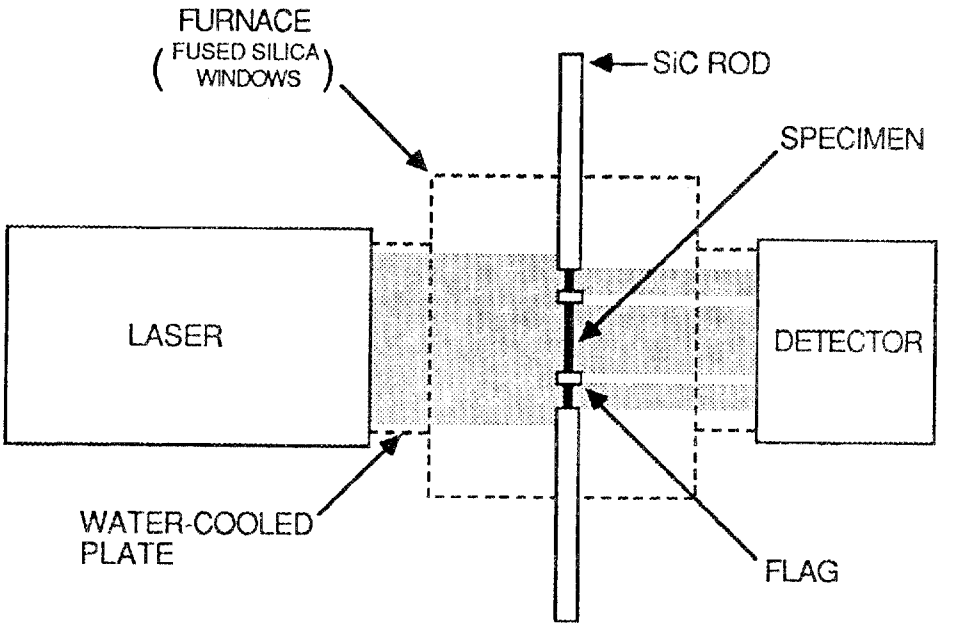

Figure 7. Schematic representation of the laser extensometer used for measuring creep deformation.

elevated temperatures, these fluctuations have to be minimized so that small amounts of creep deformation can be detected.

Two major sources of thermal fluctuation were important in the present study. Known as the chimney effect, the first source was caused by air seepage around the loading rods at their point of entry into the furnace. This source of convection currents resulted in rapid air density changes within the furnace's hot zone. The error associated with this rapid change in air density can be minimized by averaging several readings together for a single displacement measurement. Since the laser extensometer can scan 150 times per second, many readings can be easily averaged over a short period of time. Figure 8 shows an example of how averaging can eliminate error caused by convection currents for a specimen tested at 1300°C under zero applied load.[3] Two different readings were taken over a period of 1 minute. The first set of readings (open circles) represents measurements based upon an average of 10 scans, whereas the second set of readings (solid circles) represents measurements based upon an average of 1,000 scans. For the readings based upon 10 scans, the measurements recorded at one second intervals varied by 0.025 mm (25 μm) from a low of 14.495 mm to a high of 15.020 mm. Even though these measurements were based on an average of 10 scans, variations still occurred because the averaging time ($\approx$0.07 sec) was short compared to the period of fluctuations. The measurements based upon 1,000 scans (averaging time $\approx$7 sec) remained constant at 15.011 mm and did not vary within the one minute period. These measurements remained constant because the averaging time ($\approx$7 sec) was long compared to the period of fluctuations, thus allowing the effects of random fluctuations to be averaged out. These results clearly show that by averaging a sufficient number of readings, the fluctuations in measurement caused by the chimney effect can be eliminated for short periods of time (generally for periods of 1 to 3 minutes).

If tests are conducted for longer periods of time, another source of thermal fluctuations was found to affect the readings. This second source is important for creep tests that last for hundreds of hours. Figure 9 summarizes measurements taken on a specimen under zero applied load at temperatures of 600, 950 and

---

[3] In these results, the furnace was not properly insulated to reduce the chimney effect. This setup was intentional to produce a furnace environment that resulted in large displacement variations. In a normal creep test, the furnace is insulated to reduce the chimney effect so that displacement measurements based upon an average of 10 scans would not vary by more than ±2 microns over a one minute period.

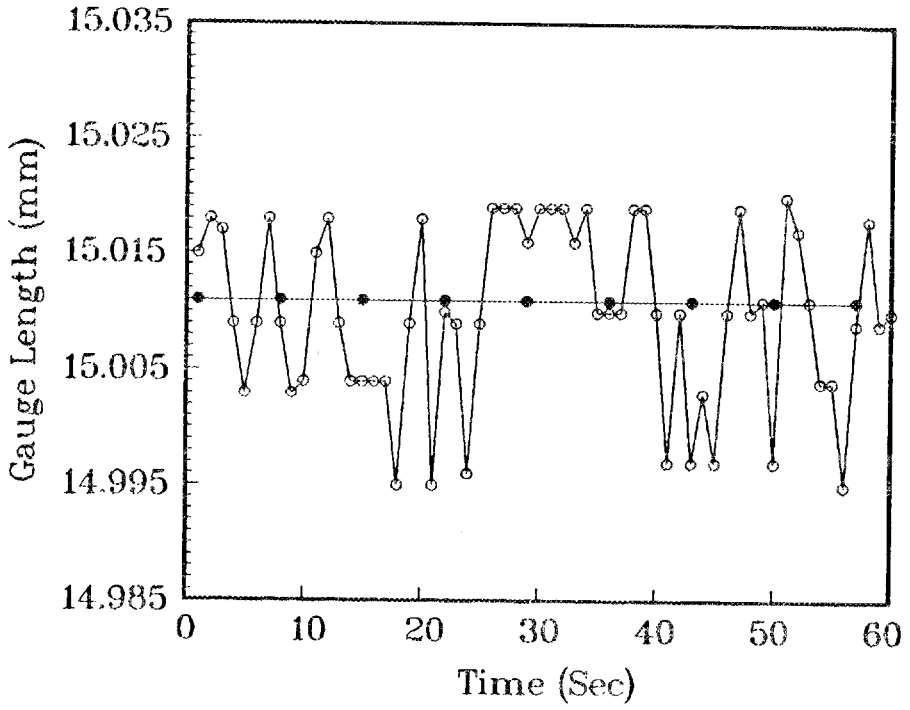

Figure 8. Gauge length measurements taken over a one minute period for a specimen at 1300°C under zero applied load (o) measurements averaged over 10 scans, (●) measurements averaged over 1,000 scans).

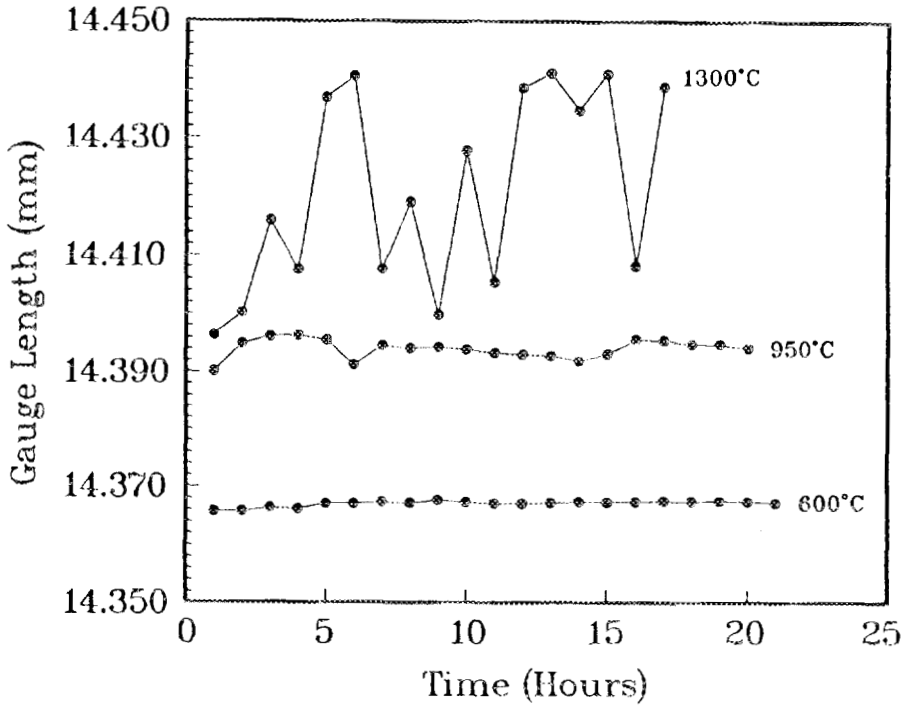

Figure 9. Gauge length measurements as a function of temperature, taken at one hour intervals over a twenty hour period. Measurements based upon an average of 1,020 scans. Fluctuations in readings at higher temperatures were due to long term changes in the air density near the windows of the furnace, and along the channel leading from the hot zone to the windows and from the windows to the laser and detector ports.

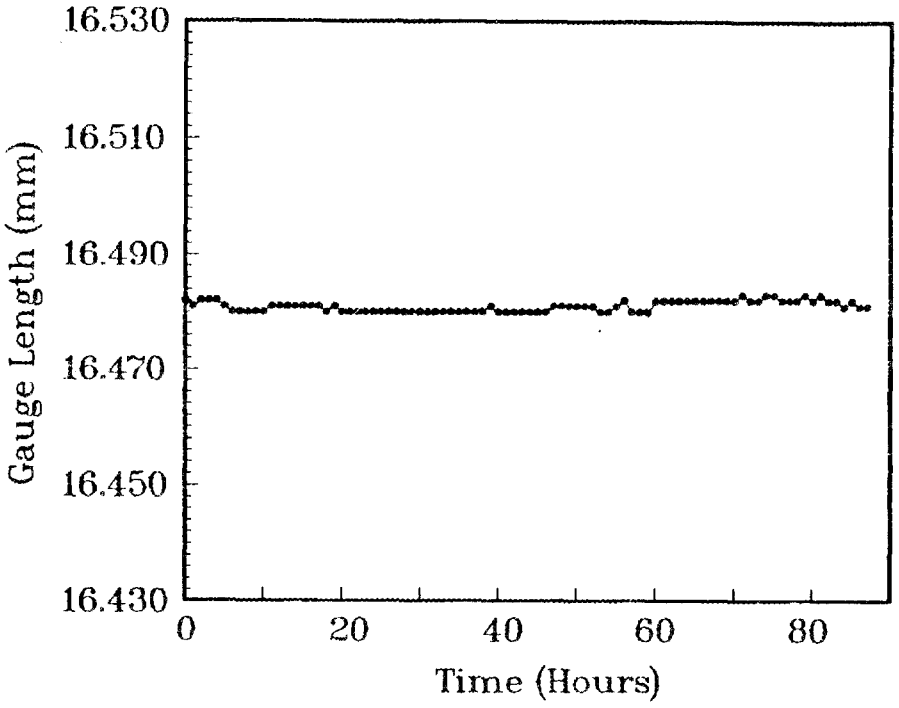

Figure 10. Gauge length measurements after furnace was modified to minimize the temperature gradient across the faces of the windows and by restricting the width of the channels leading from the hot zone to the windows and from the windows to the laser and detector ports. Measurements taken at 1300°C over a 90 hour period for a specimen under zero applied load. Each measurement was an average of 1,020 scans. The scatter in measurements during this time frame is less than ±2 μm.

1300°C.[4] Measurements were taken at one hour intervals over approximately a twenty hour period. Each hourly reading represented an average of 1,020 scans. At 600°C, the readings were relatively constant for the entire twenty hour period. As the temperature was increased to 950°C, the readings began to fluctuate with a scatter of approximately ±3 μm . At 1300°C, the readings were found to fluctuate over a 42 μm range for the twenty hour period.

This scatter was too large for laser extensometry to be an effective tool for strain measurement at elevated temperatures. This error was not due to rapid changes in the air density within the hot zone of the furnace, but to long term changes in the air density near the furnace windows. Fluctuations in the readings were reduced significantly by minimizing the temperature gradient across the faces of the windows, and by restricting the width of the channel leading from the hot zone to the windows and from the windows to the laser and detector ports. If the windows and channels were properly insulated, a very stable reading could be obtained for long periods of time. Figure 10 shows the stability that can be obtained in measurements over a ≈90 hour period for a specimen under zero applied load at 1300°C. The scatter in the measurements during this time frame were found to be less than ±2 μm.

If proper care is taken to insulate the furnace, the laser extensometer is a good technique for measuring creep deformation. Figure 11 is an example of a typical creep curve obtained for a siliconized silicon carbide at 1300°C under an applied stress of 100 MPa that was interrupted after approximately 100 hours. Each displacement measurement was an average of 25,500 scans.

Summary

A technique for measuring tensile creep deformation of ceramic materials up to temperatures of 1500°C has been developed. The tensile creep apparatus is based upon a pin and clevis arrangement to attach a flat dogbone-shaped specimen to the load train. Good alignment is obtained in the tensile specimen through careful machining and tapering of the specimen holes. The percent elastic bending was found to be less than 1% and 2% about the major and minor faces of the specimen, respectively. Creep deformation is measured continuously using a non-contacting strain measurement system that utilized a laser extensometer and a set of alpha silicon carbide flags attached to the gauge section of the specimen.

---

[4] In these results, the furnace was insulated to minimize the thermal fluctuations caused by the chimney effect.

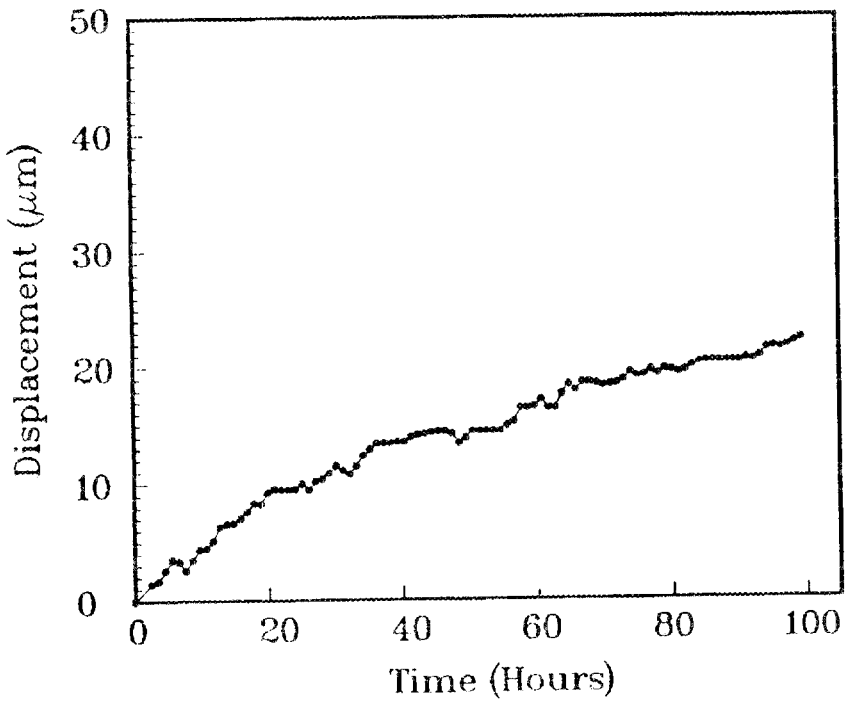

Figure 11. Typical displacement versus time curve obtained with the laser extensometer for a specimen deformed at 1300°C under applied stress of 100 MPa. Each displacement measurement was an average of 25,500 scans.

Engineering Foundation Conference

In addition to the above work on the tensile test apparatus, a technical conference on the subject Structural Ceramics - Science and Technology is being organized under the auspices of the Department of Energy and the Engineering Foundation, an organization that conducts meetings that are less formal in structure than the normal engineering meetings held on this subject. It is our plan to invite a series of speakers from industry and academia to exchange ideas on progress in the field of structural ceramics. Plans call for 2 to 3 talks in the morning and 2 to 3 in the evening on various subjects of importance to the field of structural ceramics. Each talk will be followed by a discussion, with 15 to 30 minutes allotted to each speaker. In this way, the meeting will be structured to maximize discussion after each talk. There will be no written proceedings of the meeting.

The meeting will be held on March 12-17, 1989 at the Sheraton Palm Coast Resort, Palm Coast, Florida. Topics to be covered at the meeting will include:

Reliability and Structural Design (A.G. Evans, University of California; Leonard Lindgren, Allison Gas Turbine Operations)

Fatigue of Ceramics (Rob Ritchie, University of California; Ken Liu, High Temperature Materials Laboratory)

Fracture Toughness Methodology (R. Steinbrech, Universität Dortmund)

Turbine Engines (Gene Helms, Allison)

Diesel Engines (Tom Yunoshonis, Cummins Engine Co.; C.L. Quackenbush, Norton Co.)

Turbo-Chargers (Craig Baker, Garrett)

High Temperature Testing (Malcolm S. Loveday, National Physical Laboratory; Mattison K. Ferber, High Temperature Materials Laboratory; Daniel F. Carroll, Dow Chemical Corp.)

Composite Materials (David Marshall, Rockwell Science Center; Paul Becher, High Temperature Materials Laboratory)

Non-Oxide Ceramics (Mike Lewis, University of Warwick; Arvid Pasto, GTE)

High Temperature Damage and Strength Loss (David Wilkinson, McMaster University; Georg Grathwohl, Universität Karlsruhe; Karl Jakus, University of Massachusetts).

References

1. B.W. Christ and S.R. Swanson, "Alignment Problems in the Tensile Test," J. Test. Evaluation, 4(6) 405-417 (1976).

2. K. Jakus and S.M. Wiederhorn, "Creep Deformation of Ceramics in Four Point Bending," J. Am. Ceram. Soc. 71, 832-836 (1988).

3. L. Chuck, private communication.

Status of milestones

341301 This milestone has been completed. A paper on the creep technique using laser measurements at elevated temperatures has been submitted to the Journal of the American Ceramic Society for publication.

All other milestones are on schedule (34102-34105).

Publications

1. T.-J. Chuang and S.M. Wiederhorn, "Damage-Enhanced Creep in a Siliconized Silicon Carbide: Mechanics of Deformation," J. Am. Ceram. Soc. 71, 595-601 (1988).

2. S.M. Wiederhorn, D.E. Roberts, T.-J. Chuang and L Chuck, "Damage Enhanced Creep in a Siliconized Silicon Carbide:Phenomenology," J. Am. Ceram. Soc. 71, 602-608 (1988).

3. D.F. Carroll and S.M. Wiederhorn, "A Technique for Tensile Creep Testing of Ceramics," J. Am. Ceram. Soc., Submitted

4. T.-J. Chuang, D.F. Carroll and S.M. Wiederhorn, "Creep Rupture of a Metal-Ceramic Particulate Composite," Seventh International Conference on Fracture, Accepted.

5. S.M. Wiederhorn, "Design of Advanced Ceramics for Creep Resistance," Transactions of the Canadian Council on Advanced Ceramics, Design with Engineered Ceramics, held May 26-27, 1988, Toronto, Canada, to be published as part of the proceedings of the Conference.

Fracture Toughness Determination of Thin Coatings -
J. J. Wert and R. H. Parrish(Vanderbilt University)

Objective/Scope

The goal of this program is to develop the scientific base and technology required to obtain the fracture toughness of thin coatings from microindentation.

Technical Highlights

Introduction

Microindentation fracture measurements have been a topic of interest since the mid 1970's. Techniques involving microindentation fracture have been developed to determine the fracture toughness of brittle materials. The process of determining the fracture toughness for a brittle material involves measurement of the crack lengths created by applying a load to an indenter of of known geometry. Common indenters include the Vicker's diamond pyramid indenter, the Knoop indenter and various ball and conical indenters. The crack length and other parameters such as hardness and Young's modulus are then formulated to determine the fracture toughness.

There are many factors that influence determination of the fracture toughness parameter. The magnitude of the applied load can change the stress state and cause different cracking systems to operate. It is the stress state in the material which governs the cracking system and determines the final crack length. Test environment and the materials surface finish may also bias the final results.

Understanding the complete microindentation fracture process is of prime importance to constructing an accurate model depicting this event. This entails knowing which type of cracking system is active at a particular stress level. A stress field can be generated either by an applied load or by residual stresses resulting from the elastic/plastic zone. Much of the literature discusses the various types of cracks that may accompany indentation types of tests. However few authors have gone beyond empirical formulations which are used in determine the fracture toughness parameter.

Nomenclature

There has been some confusion among the various investigators concerning nomenclature of the cracking process. Therefore, the various crack types will be described. During the indentation process, an elastic/plastic zone is produced. The stresses accompanying this zone during loading and unloading are responsible for the three basic types of cracks associated with microindentation fracture. The radial and lateral cracks are shown in Figure 1, whereas Figure 2 depicts the median crack. When the sample is viewed normal to the surface, the radial and median cracks have similar appearances.

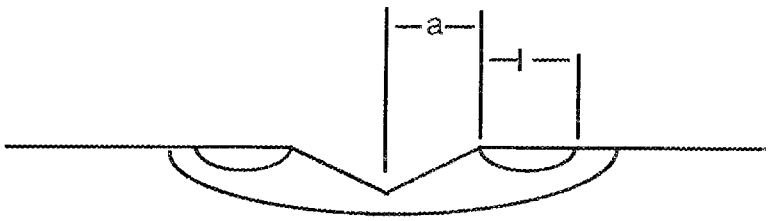

Figure 1: Geometries of radial and lateral cracks after a Vickers indentation.

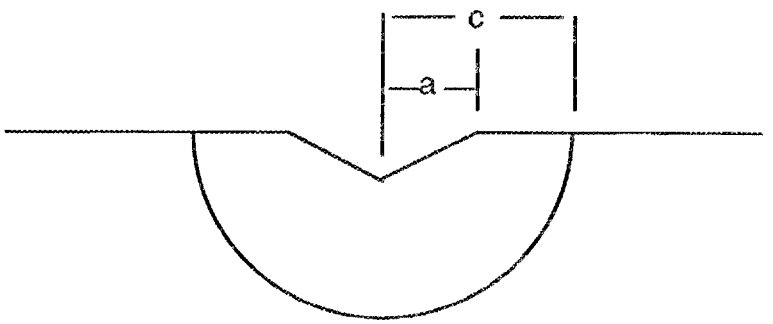

Figure 2: Geometry of a median crack after a Vicker's indentation.

Radial Cracks

The radial crack, sometimes referred to as the Palqvist crack, is a near surface crack[3]. It is often confused with the median crack because of the similar surface trace geometries. Early work by Lawn and Marshall[1] considered radial cracks as either mature median cracks or surface cracks initiating from large surface flaws. By comparison of the initiation site and geometries of the radial crack to that of the median crack, it is obvious that they are of different origins.

During loading, the radial crack is the first to initiate[4,5]. The initiation site is reported as either the elastic/plastic boundary near the surface or at a surface flaw[1]. By examining the magnitude of the stress fields Perrott[1] concluded that the initiation site is in the plastic zone. Haranoh et al.[6] conjectured that radial cracks initiate at surface flaws. They introduced different sized surface flaws by varying the materials surface finish. The applied loads for radial crack initiation were then related to the surface flaw size. They reported that the chemically-toughened specimens showed no radial cracks

with loads high enough to induce cracking in untoughened samples. However, crack initiation was reported with specimens containing surface flaws. An assumption made by Haranoh et al. was that the compressive stresses resulting from the surface finishing techniques did not penetrate to depths that would influence subsurface crack initiation.

In whatever manner the radial cracks initiate, they remain close to the surface and grow in length and depth during both loading and unloading[3]. As an exception, Perrott states that for glass, the radial cracks propagate only on unloading.

While many investigators overlooked the importance of radial cracks, Lankford[7] demonstrated that the radial crack is the earliest strength-degrading crack in brittle materials such as polycrystalline Al_2O_3. After introducing cracks in Al_2O_3 specimens with loads ranging from 25 to 500 grams, Lankford determined the depth of radial surface traces by metallurgically removing layers of the surface. He noted that one end of the trace of a crack would arrest in the elastic zone while the other end of the crack arrested close to the indenter contact zone. The two radial cracks located at the ends of a diagonal of a Vicker's indentation never connected. This demonstrates that radial cracks are independent of the median cracks and that radial cracks are of importance in strength degradation. Lankford[7] has also reported similar results observed for soda lime glass and silicon which have radial crack initiation thresholds of 25 and 5 grams respectively.

Because of the importance of radial cracks in influencing mechanical properties, Lankford[8] has suggested using radial cracks in fracture toughness evaluations at low loads. Typically, high loads are needed to initiate median cracks used to determine the fracture toughness parameter. If radial cracks could be utilized instead of median cracks, then the smaller loads needed for radial crack initiation could be used to obtain the fracture toughness measurements of thin films. Lankford[8] examined the basic fracture toughness equation of Evans and Charles[16].

$$(K_{IC}\phi/Ha^{1/2})(H/E\phi)^{0.4} = 0.129(c/a)^{-3/2}$$

where ϕ is a constraint factor
E = Young's Modulus
H = hardness

The equation was originally used with the parameter c equalling the median crack length. However, by using the radial crack length as opposed to the median crack length, Lankford determined that this same relation could be used to obtain results that were accurate to within 35%.

Niihara[9] has also used a similar approach to determine a fracture toughness equation using radial crack lengths. Through empirical analysis he modified the Evans and Charles[16] equation and the Lawn et al.[10] equation by substitution of the radial crack length for the median crack length. The result is similar to the original equations:

$$(K_{IC}\phi/Ha^{1/2})(H/E\phi)^{2/5} = 0.035(l/a)^{-1/2}$$

From fundamental fracture mechanics, Niihara has derive the fracture toughness equation for the radial crack geometry. Using a semi-elliptical crack model he derived the expression

$$(K_{IC}\phi/Ha^{1/2})(H/E\phi)^{2/5} = k_2(l/a)^{-1/2}$$

for radial cracks. The difference between the two expressions is the constant k_2. By establishing such a close match between the derived equation and the empirical equation, theoretical credibility is given to the original equations.

Median Cracks

The median crack has been the most widely studied of the three cracks[11,12]. The stresses associated with a median crack are similar to those of the radial crack. However, instead of the residual force exhibiting the peak tensile force, the largest tensile force occurs during the maximum load[1]. Typically the loads for median crack initiation are two to three orders of magnitude higher than that for the radial crack initiation. Lawn et al.[1,10] have listed a chain of events for the initiation and growth of median cracks. They describe the initiation by the typical "yield control" model of fracture mechanics. Once a critical stress level is reached a sub-surface flaw initiates a penny-shaped crack. This event commonly occurs below the indenter at the point of maximum tensile stress[13]. During increased loading, the penny-shaped crack grows on the median planes containing the major Vicker's diagonals. Once the crack intersects the surface, it begins to take on a half penny configuration by continual growth downward into the bulk and outward along the surface[14]. Depending on the residual stress field during unloading, the median cracks may either start to close or continue to grow.

Marshall and Lawn[14] have observed in soda lime glass that median cracks did not always propagate to full extension during loading. They noted that the median cracks extended fully down into the sample during loading and they extended outward during unloading to reveal the fully developed median surface trace. This is an indication of the residual stresses that may exist during and after unloading.

The loads required for median crack initiation are much larger than those required for radial cracking. The literature has not addressed the reasons for the two to three orders of magnitude difference between loads required to initiate the radial and median cracks. However, it is assumed that the stresses contributing to crack initiation at the near surface are much greater than those below the indenter due to the stress distribution.

Lateral Cracks

Lateral cracks have been the least studied of the three crack systems; however, they are important in tribological applications. Lateral fracture in brittle materials can play an important role in material removal due to solid particle erosion or abrasive wear.

The potential volume removal due to an impacting particle is related to the crack geometry. Marshall et al.[15] modeled the material removal as

$$V \sim c^2 h$$

where c = crack radius
h = crack initiation depth.

Most investigators[10,15] agree that lateral crack propagation is due to the residual stress that develops during indenter removal. The residual stresses are created by the elastic/plastic zone that is produced during loading. The relaxation of the elastic portion of the zone during unloading causes a mismatch in the material and hence a residual tensile stress. Lawn and Swain[10] modeled the plastic zone by

$$a = \left[\frac{P}{\mu \pi p_o}\right]^{\frac{1}{2}}$$

where P = load
p_o = mean contact pressure
μ = constant determined by indenter geometry
a = radius of plastic zone.

With the crack initiation site at the elastic/plastic interface, the crack depth h can be represented by the parameter a. The volume removal then becomes

$$V = c^2 a.$$

Lawn and Marshall[1] have reviewed some of the techniques that are used in modeling the propagation of a lateral crack. Their findings lead to the conclusion that many workers try to oversimplify the indentation model and consider it to be an expanding cavity in an infinite elastic/plastic medium. The expanding cavity model is not valid in this particular situation because of the presence of the free surface. The interaction of the free surface with the crack tends to cause the crack to depart from it's spherical symmetry and to grow towards the surface. Chiang et al.[4] examined Johnson's results[18] obtained by replacing the expanding cavity solution with an incompressible hydrostatic core beneath the indentation. This representation helped establish relations between the plastic zone, indentation pressure, indenter angle, hardness and Young's modulus. However, Johnson's model restricted the size of the core to that of the indentation radius and also neglected the effects of the free surface. The experimental results of Chiang et al. have shown that the indentation pressure is insensitive to a wide variation of indenter geometry. This is attributed to the minimal work hardening exhibited by the materials studied. The work hardening hypothesis assumes that the indentation volume is responsible for the plastic zone volume. The authors state that the plastic zone exhibits spherical symmetry regardless of indenter shape.

Lateral cracking is frequently observed to initiate at the elastic/plastic zone interface beneath the indenter[17] just prior to complete indenter removal[1,2]. Hagan and Swain[17] speculate that lateral crack initiation could be due to shear deformation. In a glass system, deformation of the lattice can cause atomic bonds to break and degenerate into shear cracks. The shear cracks are thought to initiate at the highly strained regions beneath the indenter which then propagate in a direction parallel to the surface. The path the crack travels is along the tensile stress trajectories and which helps to minimize the number of covalent bonds broken.

Experiments

In order to clarify what has been presented in the literature, a set of experiments were designed to study microindentation fracture. The apparatus was constructed at Vanderbilt University using a screw driven Instron tensile/compression materials testing machine. A Vicker's diamond pyramid was mounted to a 20lb load cell in order to continually measure the applied load during loading and unloading. Two capacitive displacement gages measured the axial displacement of the indenter. The samples where secured with mounting wax to a reinforced stage of a metallurgical microscope. Data acquisition consisted of two 4-1/2 digit voltmeters and a minicomputer. The materials chosen to be tested were soda lime glass, sapphire, SrF, fused silica, C axis quartz, Si(100), and Si(111). Sapphire, fused silica and quartz were chosen because of their importance as engineering materials. Most of the literature concerning microindentation

fracture reports data from experiments using soda lime glass; therefore, it was also chosen for these experiments to allow direct comparison with the results reported in the literature. The silicon samples were included because of availability and the promising results from load displacement curves generated by the Mechanical Properties Microprobe. The load displacement diagrams obtained from the MPM for silicon revealed an event near completion of the unloading cycle which may indicate a lateral crack initiation.

Examination of the load verses displacement diagrams revealed uncharacteristic curves. The last third of the unloading curve had a large decrease in slope along with dramatic changes in displacement on load reversal. The exact cause of these phenomena has not been confirmed. However, possible sources of the discrepancies may be attributed to the nonlinear stiffness of the microscope stage and the screw slack on reversal of the Instron.

The transparent materials were viewed during the test and general observations were made. Each test was taken to a maximum load of approximately 2.5kg. Median cracks were not observed to initiate during any of these tests. Radial cracks were observed to propagate on unloading while the lateral cracks initiated near the end of the unloading cycle. Both cracking systems had controlled crack front propagation.

Due to the lack of reproducible load displacement diagrams, the apparatus was reconstructed by incorporating a new Instron materials testing machine located at ORNL. The microscope stage was also redesigned to provide more structural support.

Two materials were tested using the new apparatus, soda lime glass and sapphire. The fracture response of soda lime glass was examined with loads of 10kg, 1kg, 100gr, and 10gr, while the sapphire was examined at 7kg. In general, the results were surprisingly good. However, a problem was encountered with the data obtained at the 100gr. and 10gr. loads in that the unloading curves exhibited decreasing slopes. More experimental investigation will be required to determine the origin of these anomalous results.

In spite of this problem, results of the microindentation test can provide substantial insight concerning the fracture behavior of brittle materials. Since soda lime glass is one of the more common materials used for basic research in fracture toughness, it is appropriate that this material be included in this investigation for direct comparison with the literature. Figure 3 is a load versus displacement diagram for soda lime glass obtained with the experimental apparatus described previously.

The shape of the load-displacement curve for soda lime glass is as expected. While conducting this test, and others of soda lime glass through the maximum load of 10kg., the sequence of cracking events were noted. Contrary to some data reported in the literature, radial cracks were not the first to be observed. The first type of crack noted was the median crack. For all tests performed with soda lime glass, median cracks initiated with a big "pop-in" at a load of approximately 7kg. Radial cracks did not appear until unloading and were not always located on the major diagonals. Lateral cracking initiated near completion of the unloading half cycle. The crack fronts were seen to propagate in a controlled manner during unloading for all three crack types.

For the tests conducted at 100 gram loads or less, median cracks were not observed. Figure 4 illustrates a typical curve obtained for soda lime glass indented with a load of 1kg. No fracture events were observed during loading of the sample. However, upon unloading, a radial "pop in" occurred followed by the appearance of lateral cracks.

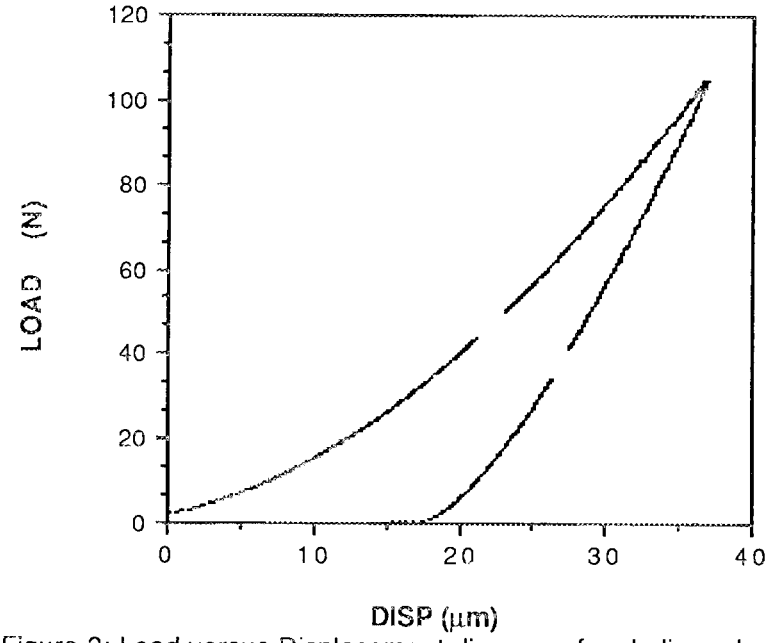

Figure 3: Load versus Displacement diagram of soda lime glass during indentation with a Vicker's indenter. (0.254 mm/min)

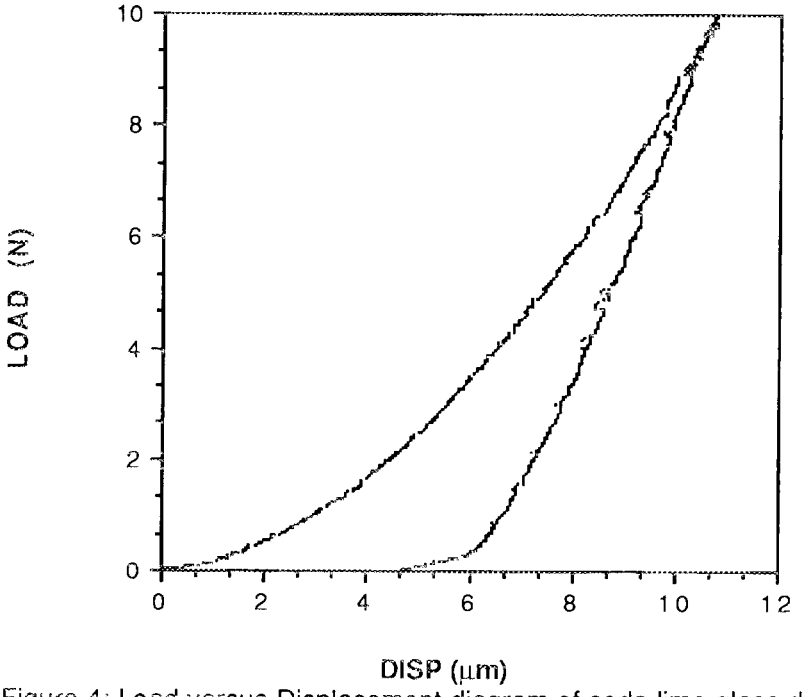

Figure 4: Load versus Displacement diagram of soda lime glass due to indentation with a Vicker's indenter.(0.0254 mm/min)

When the minimum load of 10gr was used, a different material response was observed in that no cracks were observed to initiate during either loading or unloading. However, on close examination of the indentation, a lateral crack was found to be present. Figure 5 is the corresponding load displacement diagram. The discontinuities in the curve are the result of the lack of resolution of the displacement gages.

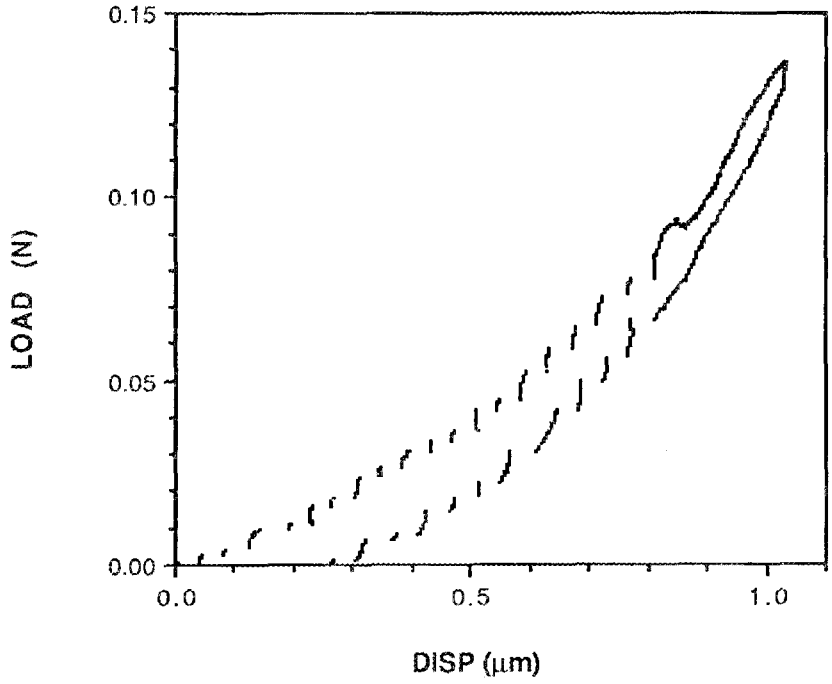

Figure 5: Load versus Displacement diagram of soda lime glass due to indentation with a Vicker's indenter.
Loading rate = 0.0025 mm/min.

The sapphire sample was loaded to approximately 7kg. At the beginning of contact, a profuse arrangement of small cracks initiated under and around the indenter. At this time, it is not known whether or not the cracks were radial. Because of the randomness and abundance of small cracks, median cracks were not observed. On unloading, lateral cracks appeared as predicted. Figure 6 is the accompanying load displacement diagram for the sapphire sample.

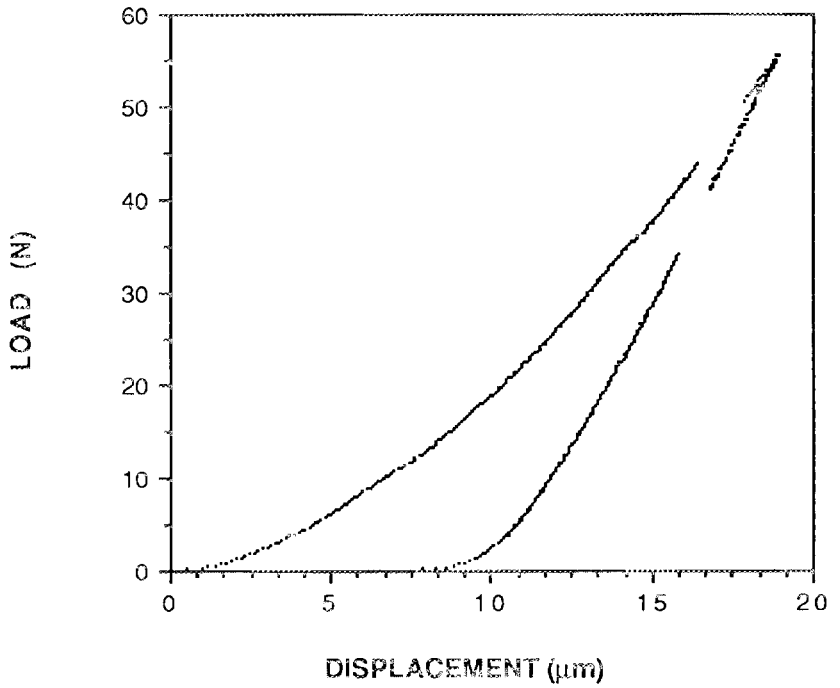

Figure 6: Load verse Displacement diagram of sapphire during Vicker's indentation. Loading rate = 0.254 mm/min.

While the data obtained for soda lime glass are useful for comparison with results available in the literature, it should be noted that it may not be representative of engineering materials. As previously shown, the indentation response of sapphire differs significantly with that of soda lime glass. Other research has shown that quartz and SrF also behave differently. In soda lime glass, median cracks are believed to initiate first. In other materials, preliminary data indicate that radial cracks are the first to develop. Further investigation is needed to determine the causes of the observed differences.

One disappointing aspect from the load/displacement results was the lack of correlation between cracking events observed optically and corresponding identifiable features in the load displacement curves. This result may be due to the dynamic characteristics of the machine used for the tests.

Future research will lead to the development of a more sensitive load and depth sensing machine. Underway is the construction of a high load head for the Materials Property Microprobe. This alteration of the MPM will enable high loads to be obtain so that the applied and residual stresses induced are adequate to initiate radial and lateral cracks. With the present ability of the MPM to discern discrete load and displacement events and the capability of higher loads, the energy release during crack formation is anticipated to be observable on the load displacement diagrams. Subsequently, the fracture toughness of a material can be determined without the need for crack length measurement or large indentation displacements. This will lead to further studies in determining the fracture toughness of thin films. Also, by knowing the energy required for the lateral crack initiation, the adherence of a thin film may be investigated.

Status of Milestones

All milestones are proceeding on schedule.

Publications

None

References

Book

1. B. R. Lawn and D. B. Marshall, Fracture Mechanics of Ceramics Vol. 3, R. C. Bradt, D. P. H. Hasselman and F. F. Lange, (1977).
2. D.B. Marshall and B.R. Lawn, "Indentation of Brittle Materials", microindentation Techniques in Materials Science and Engineering, ASTM STP 889, P.J. Blau and B.R. Lawn eds., American Society for Testing and Materials, Philadelphia, 1986, pp. 26-46.

Journal article

3. C. M. Perrott, Wear 45, p.293 (1977).
4. S. S. Chiang, D. B. Marshall, and A. G. Evans, J. Appl. Phys. 53(1), p.298 (1982).
5. E. H. Yoffe, Philosophical Magazine A 46(4), p.617 (1982).
6. T. Haranoh, H. Ishikawa, N. Shinkai, M. Mizuhashi, J. Mater. Sci. 17, p. 1493 (1982).
7. James Lankford, J. Mater. Sci. 16, p.1177, (1981).
8. James Lankford, J. Mater. Sci. Letters 1 p.493 (1982).
9. K. Niihara, J. Mater. Sci. Letters 2 p.221 (1983).
10. B. R. Lawn and M. V. Swain, J. Mater. Sci. 10 (1975).
11. B. R. Lawn, E. R. Fuller, and S. M. Wiederhorn, J. Mater. Sci. 59(5-6), (1976).
12. B. R. Lawn and E. R. Fuller, J. Mater. Sci. 10 (1975).
13. H. Ishikawa and N. Shinkai, Communications of the Am. Cer. Soc., C-124, (8), (1982).
14. D. B. Marshall and B. R. Lawn, J. Mater. Sci. 14, p.2001 (1979).
15. D. B. Marshall, B. R. Lawn, and A. G. Evans, J. Am. Ceram. Soc. 65(11), (1982).
16. A. G. Evans and E. A. Charles, J. Amer. Ceram. Soc. 59, p.371 (1976).
17. J.T. Hagan and M.V. Swain, J. Phys. D: Appl. Phys., 11, (1978).
18. K.L.Johnson, J. Mech. Phys. Solids 18, p.115 (1970).

3.5 NONDESTRUCTIVE EVALUATION DEVELOPMENT

Nondestructive Characterization

W. A. Simpson, Jr., and B. E. Foster (Oak Ridge National Laboratory)

Objective/scope

The purpose of this project is to conduct nondestructive evaluation (NDE) development directed at identifying approaches for quantitative determination of conditions (including both properties and flaws) in ceramics that affect the structural performance. Those materials that have been seriously considered for application in advanced heat engines are all brittle materials whose fracture is affected by structural features with dimensions on the order of the dimensions of their microstructures. This work seeks to characterize those features using high-frequency ultrasonics and radiography to detect, size, and locate critical flaws and to measure nondestructively the elastic properties of the host material.

Technical progress

Ultrasonics - W. A. Simpson, Jr.

We continued our studies of the beam profile produced inside typical ceramics by various ultrasonic transducers. In addition to the design of acoustic lenses, we are finding our model useful for determining the shear wave fields produced inside a ceramic by mode conversion of the primary longitudinal wave at the ceramic surface. To our knowledge, this field has not been previously studied, nor have focused shear waves been used in ceramic evaluation. Indeed, the shear wave component produced by commercial transducer designs is usually ignored during ceramic testing (being considered to be an unavoidable loss mechanism). Our preliminary results indicate that the depth of focus of the shear wave field is astoundingly great for some transducer-ceramic combinations, although the field amplitudes are less than those of the primary longitudinal fields. In addition to the increased depth of focus, the depth to which effective focus can be maintained is also greater for shear waves than for longitudinal waves, since the former wave is less severely refracted at the ceramic entry surface. Finally, for a given frequency, the wavelength of a shear wave is about one-half that of a longitudinal wave, thus making a 50-MHz shear wave about as effective as a 100-MHz longitudinal wave, if no other considerations are extant.

As mentioned above, the primary disadvantage of the shear wave field is that the amplitudes are generally lower than those of the longitudinal wave fields for commercial transducers because of the relatively poor efficiency of mode conversion at the water-ceramic interface. In addition, commercial transducers are designed to produce a given focal length for longitudinal wave energy, not for shear wave energy. We have investigated a shear wave design by "back-propagating" an aberration-free shear wave through the ceramic-water interface in order to determine the shape of the transducer element necessary to produce such a beam. It appears that the efficiency can at least be improved by judicious shaping of the transducer lens element, but it is unlikely that the efficiency will approach that of the longitudinal wave configuration for immersion

testing. Nevertheless, there may be some advantages for this type of transducer.

Figure 1 shows the calculational results obtained on the shear wave field produced in iron by a 5-MHz conventional spherically focused transducer. The grid lines are separated by one-quarter of a wavelength in iron, and the figure is centered on the "focal" point for unaberrated shear waves in the solid. The conclusions are that the depth of focus is much longer than that obtained previously for longitudinal waves, and the maximum amplitude of the field is about 6 dB lower than that at the longitudinal "focus."

Figure 2 shows the distribution of the shear wave field produced inside alumina by a 50-MHz, f/2 spherical transducer. Here the grid spacing is one-half the shear wavelength in alumina. The depth of focus is roughly comparable to that of the longitudinal field, but the field maximum occurs at a depth of almost 2.5 mm rather than the 1.1 mm previously reported for the longitudinal field of this transducer. The shear wave field can thus probe deeper into the ceramic and has a wavelength of about 125 μm as compared to a wavelength of about 210 μm for the longitudinal wave. Surprisingly, the peak amplitude of the distribution is nearly as large as for the longitudinal field.

ORNL-DWG 88-14456

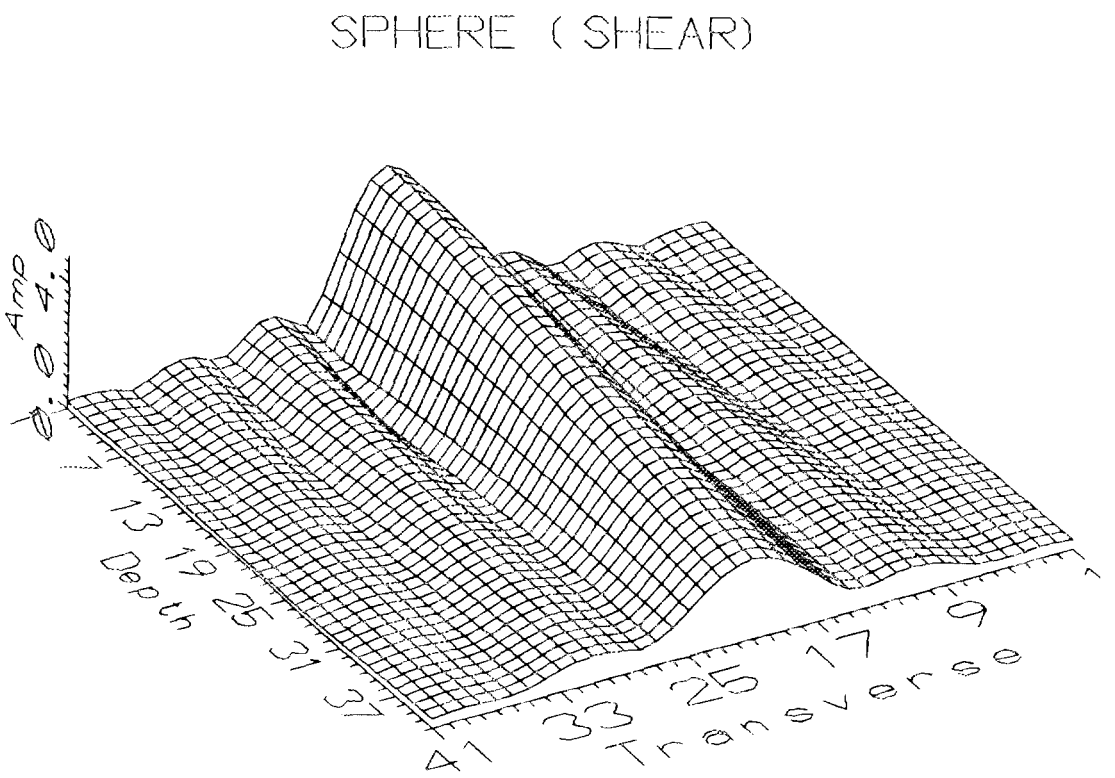

Fig. 1. Shear wave distribution produced in iron by a 5-MHz, f/3 ultrasonic transducer.

ORNL-DWG 88-14457

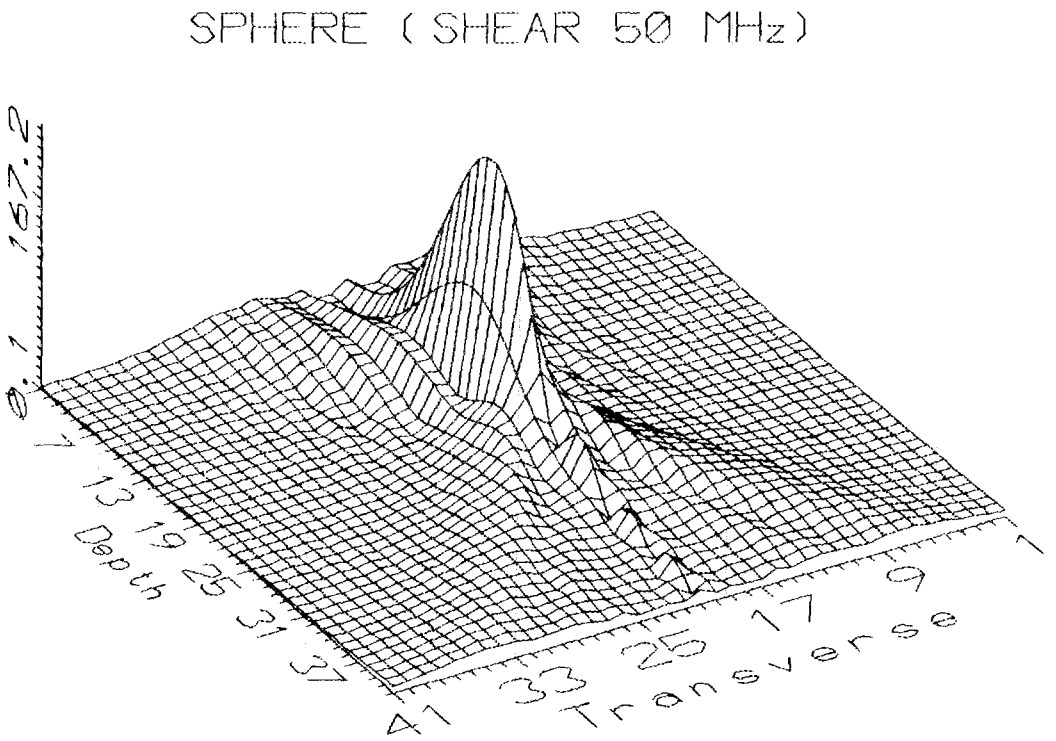

Fig. 2. Shear wave distribution produced in alumina by a 50-MHz, f/2 ultrasonic transducer.

Figure 3 shows the shear wave results obtained on an axially focused 50-MHz, f/2 transducer. The behavior of the pattern suggests that a grid spacing of one-quarter wavelength would define the distribution better, but the extreme depth of focus, combined with a peak amplitude as large as the longitudinal field for the spherically focused transducer, indicates that this lens design should give excellent results. Additional lens designs are being evaluated.

A special 50-MHz, f/0.8, high-frequency transducer designed to produce a radial surface wave has been purchased for ceramic inspection. This unit has a relatively high numerical aperture, which means that it is an efficient generator of surface acoustic waves even when the beam axis is perpendicular to the surface of the specimen. Previously, we have had to perform surface wave inspections by introducing the beam onto the sample surface at the Rayleigh critical angle. This approach is an efficient method of generating a surface wave, but it has two major disadvantages: (1) it is sensitive only to cracks whose orientations are perpendicular to the beam axis, and (2) the lack of a front-surface signal makes it difficult to gate reliably the surface wave unless the transducer-to-sample distance is maintained very accurately. With the high numerical aperture transducer, however, a radial surface wave is generated, which

ORNL-DWG 88-14458

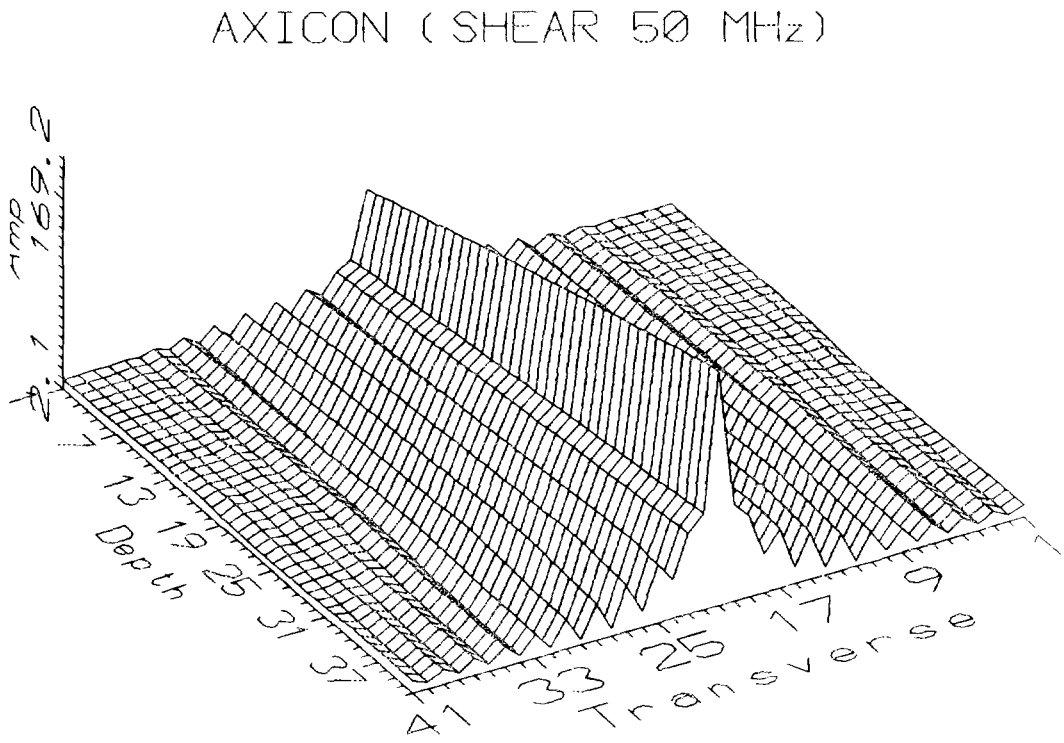

Fig. 3. Shear wave distribution produced in alumina by a 50-MHz axicon ultrasonic transducer.

means that cracks having any orientation will be detected equally well. In addition, a front-surface signal comparable in amplitude to the surface wave is also generated, and this former wave may be used to gate the surface wave in the presence of variations in the transducer-to-specimen distance.

Using the new surface wave transducer, we have repeated the examination of several alumina coupons which we earlier reported to be cracked. In addition to imaging the known cracks, we also found two smaller cracks, whose orientations were such that they were missed in the previous investigation, as well as numerous subsurface voids. All cracks were imaged with very high contrast throughout their full extent. With the new transducer, it is now possible to perform surface wave inspections as easily as volumetric inspections.

We have completed the high-frequency ultrasonic evaluation of numerous net shape ceramic specimens. For planar samples, we have previously developed techniques which can reliably detect voids as small as 25 μm at depths of 3 mm in high-velocity ceramics such as alumina, silicon nitride, and silicon carbide and at depths of almost 5 mm in slower velocity ceramics such as zirconia. As expected, however, those net shape samples having severe surface curvature greatly increased the difficulty in

detecting volumetric flaws in the 25- to 100-μm size range because of severe aberration of the ultrasonic beam. Cylindrically shaped specimens with a diameter of 25 mm or less were particularly difficult, since this configuration introduces astigmatism in addition to the spherical aberration present with planar surfaces. However, surface acoustic wave techniques, such as those used to detect surface and near-surface flaws, were much less severely affected by the surface curvature of the sample and performed nearly as well as for planar samples. For example, a silicon nitride engine wrist pin having a diameter of 22.9 mm was examined using the new surface wave transducer described above. The results were similar to those obtained on planar samples of silicon nitride (i.e., several surface and subsurface voids having diameters of ~50 μm were detected). Because the incident beam interrogates such a small region of the sample surface, these results would probably have been valid for sample diameters considerably smaller. It is only necessary to ensure that the beam axis remains normal to the sample surface at each point of the inspection (i.e., the transducer axis must accurately "follow" the curvature of the part). The sensitivity, however, seems to be little affected by changes in the surface curvature of the sample.

The beam distribution model should be particularly useful in reducing the effect of sample surface curvature described above, since the aberration introduced by propagation of the ultrasonic beam through the curved surface of the sample can be at least partially compensated by appropriate shaping of the lens surface. For example, the aberration caused by a cylindrical specimen can be minimized with a compound acoustic lens consisting of a spherical surface with an imposed cylindrical correction.

We have examined, by request, 72 silicon nitride modulus of rupture (MOR) bars for detectable voids or other defects. Both 75-MHz volumetric and 50-MHz surface wave evaluations were performed on the bars. Since these bars were sintered, we anticipated that some 25- to 50-μm indications would be found. In fact, the results indicate that this material is probably poorer than any that we have examined. All 72 bars contained numerous indications, some of which suggest voids larger than the 50-μm voids typical of sintered material. The surface wave results also detected numerous near-surface voids, and several bars were found to be cracked.

We have performed nondestructive elastic modulus measurements on a number of ceramic samples for the Ceramic Technology and Structural Ceramics groups of the Metals and Ceramics Division, Oak Ridge National Laborabory (ORNL). One particularly interesting result was obtained on a sample of partially stabilized zirconia which had a largely tetragonal phase microstructure. After measurement of the Young's modulus, the sample was returned to its owner, where it was quenched in liquid nitrogen, thus causing a phase change to monoclinic structure. The modulus was then remeasured nondestructively and found to be about 7% lower (with changes in many of the other properties as well). The sample was then annealed, forcing a return to the tetragonal phase, after which the modulus returned to nearly the original value. Since all these results were obtained on a single sample, it admirably demonstrates the advantage of nondestructive approaches.

Radiography - B. E. Foster

The purchase order for the computerized X-ray tomography system has been placed with Scientific Measurement Systems, Inc. (SMS), in Austin, Texas, and fabrication is proceeding on schedule. The purchase agreement includes several progress-payment-type milestones. The first milestone was August 15, with a requirement for completion of conceptual drawings for review and acceptance and placement of the orders for the major long-lead time items. The second milestone was completed September 22 with a review meeting at SMS. B. E. Foster is presently scheduled for hands-on training with the equipment October 23-29 (the third milestone should be completed at that time). This training is early enough in the fabrication stage of our system to permit modifications (at no extra cost) that might be desired for customizing. The other milestones are essentially on a monthly basis with the installation (by SMS personnel) date for final acceptance at ORNL set for February 15, 1989.

We received a total of 16 samples of alumina (greenware state) from the Ceramic Technology Group for radiographic inspection. In the first group of six samples, the sizes varied from 2–3 cm in diameter by 2–3 cm long. One sample (identified as No. 49) showed a very high-density strip (~1 mm wide) at one end. The other five samples (Nos. 43-47) contained a few high-density inclusions and several voids. The approximate diameters of the voids ranged from 0.25 to over 2 mm.

In the second group of ten specimens, the sample size varied from 50 mm to 3.8 cm in diameter by 3 mm to 4.5 cm long. The samples were identified as NDT Nos. 1, 2, 3, 4, and Nos. 40, 70, 117, 119, 120, and 122. The samples contained several voids ranging in size from a fraction of a millimeter to over 2 mm.

We received 20 bend specimens (two sets of ten) dimensioned as 3 × 4 × 50 mm. The set labeled 2154C was reported to have been prepared to improve homogeneity of the microstructure and to reduce critical flaw size over the set 7X014. Radiographically, we noted a significant difference between the two sets. The ten samples in set 2154C contained a large number of tiny voids or low-density stringers (appearing as inhomogeneity or fine structure mottling). The samples in set 7X014 did not show any significant indications.

Status of Milestones

Milestone 351102 was completed on schedule.

Publications

W. A. Simpson, Jr., and R. W. McClung, "An Ultrasonic Evaluation of Silicon Carbide Whisker-Resinforced Ceramic Composites," *Mater. Eval.* (submitted for publication).

Nuclear Magnetic Resonance Imaging

W. A. Ellingson, P. S. Wong, J. P. Pollinger, and H. C. Yeh
(Argonne National Laboratory)

Objective/scope

The objectives of this program are to (1) establish the feasibility of using NMR imaging systems to map organic binder/plasticizer distributions (short T_2 materials) in injection-molded green ceramics (with emphasis on Si_3N_4); (2) examine the potential of applying NMR spectroscopy to determine if there are chemical variations within and/or between batches of organic binder that affect process reliability; and (3) determine the sensitivity of NMR imaging methods to injection molding process variables as manifested in distribution of the organic binder.

Technical progress

Preparation of test phantoms

During this reporting period, two types of test phantoms (special imaging test specimens) approximately 28 mm (1.1 in.) in diameter and 13 mm (0.5 in.) in height were prepared by Garrett Ceramic Components Division of Allied-Signal Aerospace Company. Figure 1 is a schematic representation showing the details of the phantoms. In both types of phantoms, the base cylinder is the standard, as-molded GN-10 Si_3N_4 containing 15.5 wt.% binder. A set of three phantoms plus two unseeded base cylinders were prepared as scheduled. The set of three phantoms consists of two Type I phantoms (A and B versions) and one Type II phantom. X-ray images (raw films) and visual inspection of the phantoms indicated no defects. Figure 2 is a micrograph showing a 254-μm hole and a 254-μm wire used for drilling (phantom II).

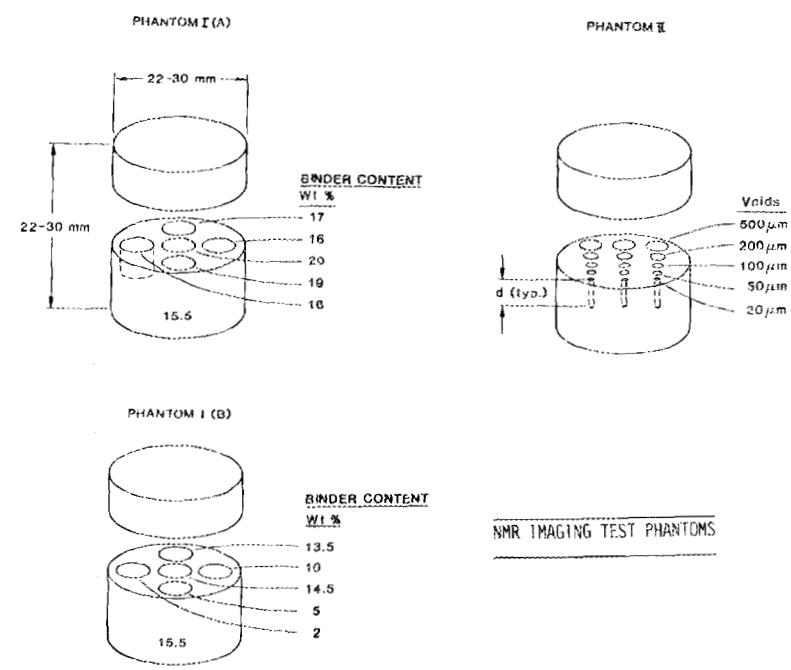

Fig. 1
Test Phantom Types
I and II.

Fig. 2

Micrograph Showing a 254-μm Hole and a 254-μm Wire (for Phantom II).

Preparation of samples containing different concentrations of organic binder

Eleven GN-10 Si_3N_4 injection molding mix powder samples, containing different concentrations 2,5,10,13.5,14.5,15.5,16,17,18,19,20 wt.% of organic binder, were prepared. These same powders were used for fabrication of test phantoms I(A) and I(B) and for spectroscopic studies (see below).

Elevated-temperature spectroscopic studies

In order to investigate the correlation between the temperature effect and the NMR signal intensity of our semi-solid organic binder, one 90°-pulse line width experiment (with a 7.1T Bruker 300AM Spectrometer) was conducted in 10°C increments between 22°C (room temperature) and 100°C on the binder alone and on the Si_3N_4 sample containing 15.5 wt.% binder. Before each experiment, samples were maintained at the indicated temperature (monitored by a thermocouple) for ~0.5-1.0h to ensure thermal equilibrium. Relative NMR spectra for binder/plasticizer (B/P) alone at 20, 40, 60, 80, and 100°C are shown in Fig. 3. A decrease in linewidth, observed as the temperature increases, should improve the spatial resolution by several orders of magnitude in the frequency-encoded dimension. Figure 4 shows the relative free induction decay (FID) signal intensity of

B/P alone and Si_3N_4 + 15.5 wt.% B/P as a function of temperature. We also used the data to investigate the correlation between T_2* (spin-spin relaxation time constant in the presence of magnetic field inhomogeneity) and temperature for both types of samples. The results are shown in Fig. 5. It should be noted that, over the temperature range studied, T_2* was shown to increase for the B/P alone, but not for a mixtures of ceramic powder and 15.5 wt.% B/P. This observation is tentatively attributed to solid-boundary effects in mixture of ceramic powder and B/P. However, the FID signal intensity does increase with temperature. This increase will enhance the S/N ratio for imaging experiments, providing that thermal equilibrium can be achieved across the sample.

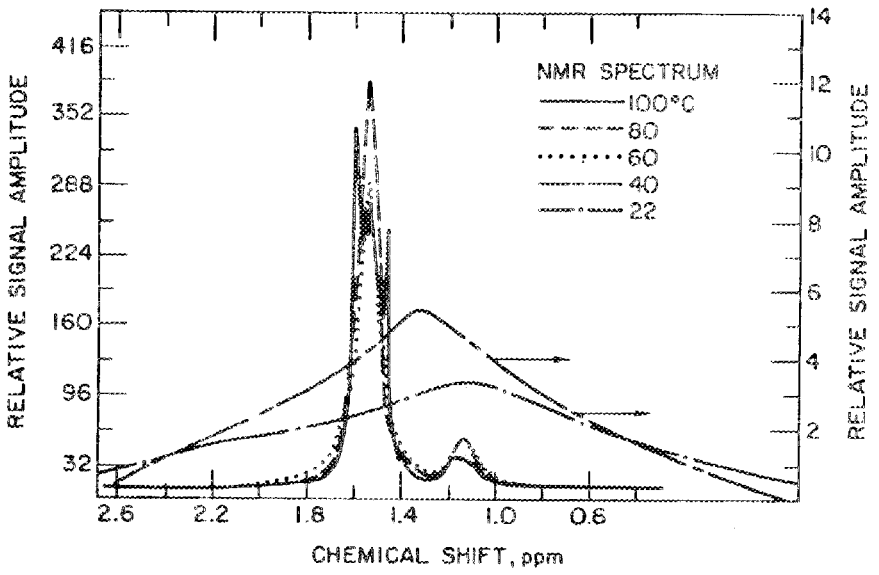

Fig. 3. Relative NMR Spectra of B/P at Various Temperatures. Scale on the right is used for data obtained at 22 and 40°C.

Room temperature spectroscopic studies on samples containing various concentrations of organic binders

To examine the potential of applying NMR spectroscopy to determine the variation of organic composition between samples, the following procedures were performed. First, we measured the NMR signal intensities for samples containing various weight % of organic using a 7.1T Bruker 300AM, binders (from part II). Second, the actual weight % of binder in each sample was analyzed by wet chemical analysis in order to confirm the weight % indicated by Garrett Ceramic Component Division of the Garrett Corporation. Third, the data were analyzed and correlated. The relative NMR signal intensities of each concentration were determined as a function of the wt.% of organic binder, as measured by wet chemical analysis. This is shown in Fig. 6. We also looked for T_2* differences among those samples. The relationship

$$\Delta_{\frac{1}{2}} \approx \frac{1}{\pi T_2^*},$$

where $\Delta_{\frac{1}{2}}$ = the full width half maximum (FWHM) of the amplitude vs. frequency trace, was used to correlate T_2*. The FWHM and T_2* results were determined for each wt.% of organic binder and these are shown in Fig. 7.

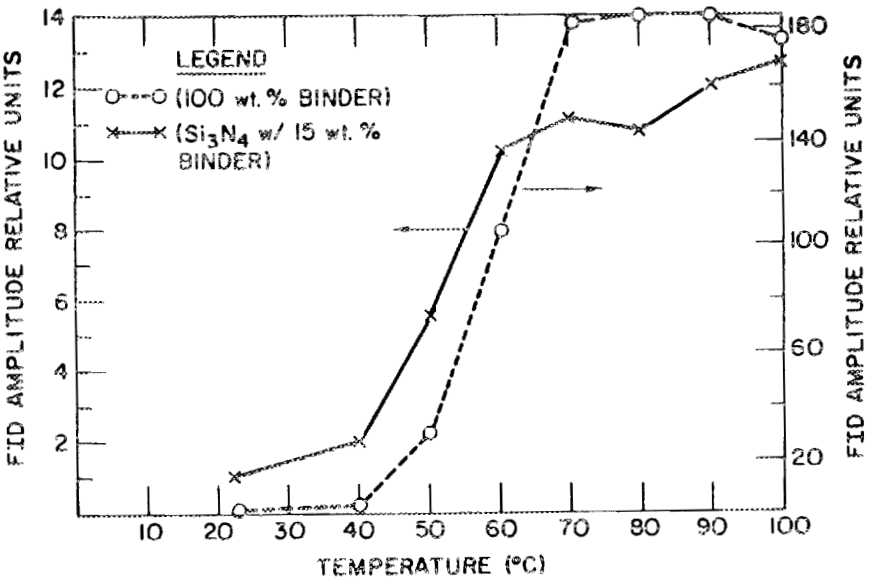

Fig. 4. Relative FID Signal Intensities of B/P Alone (Solid Line) and Si_3N_4 + 15.5 wt.% B/P (Dashed Line) as a Function of Temperature.

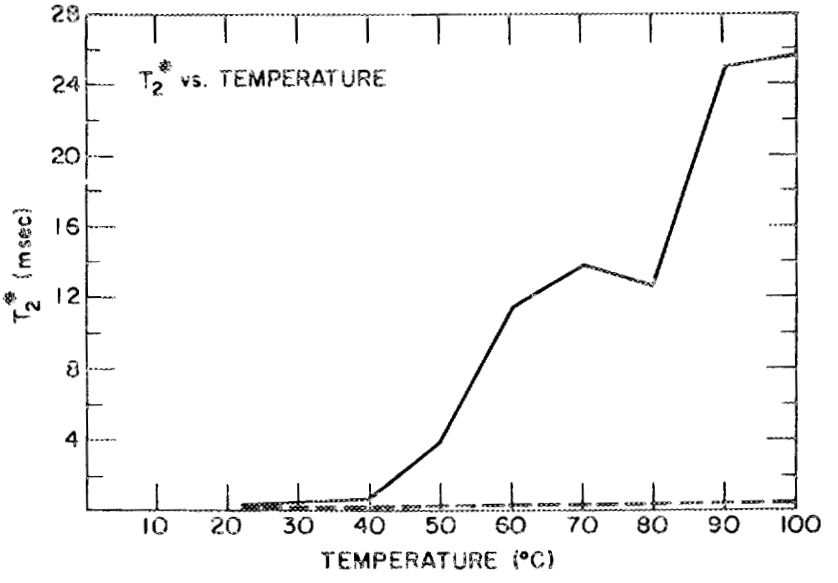

Fig. 5. Estimated T_2* of B/P Alone (Solid Line) and Si_3N_4 + 15.5 wt.% B/P (Dashed Line) as a Function of Temperature.

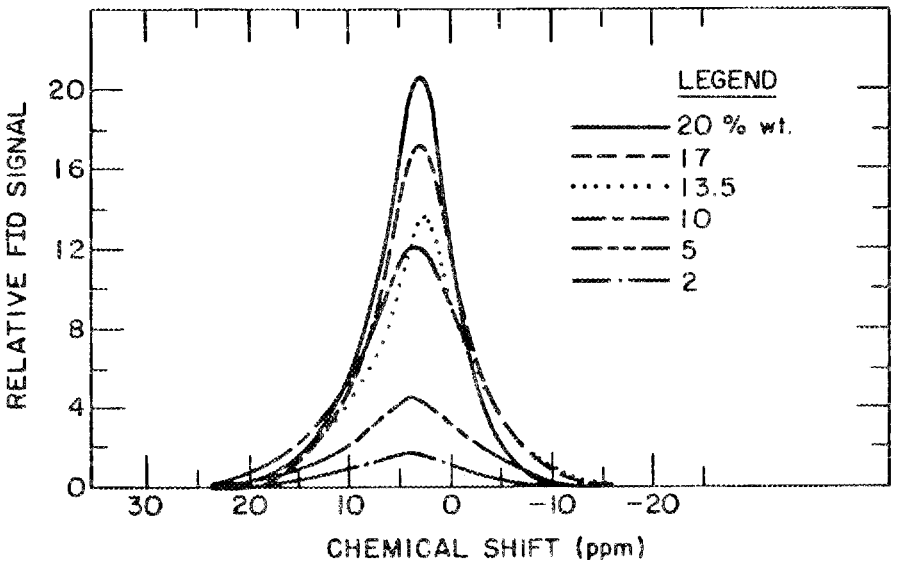

Fig. 6. Relative FID Signal Strength as a Function of B/P Concentration. Number of acquisitions = 140.

Fig. 7

FHWM and T_2* as a Function of B/P Concentration.

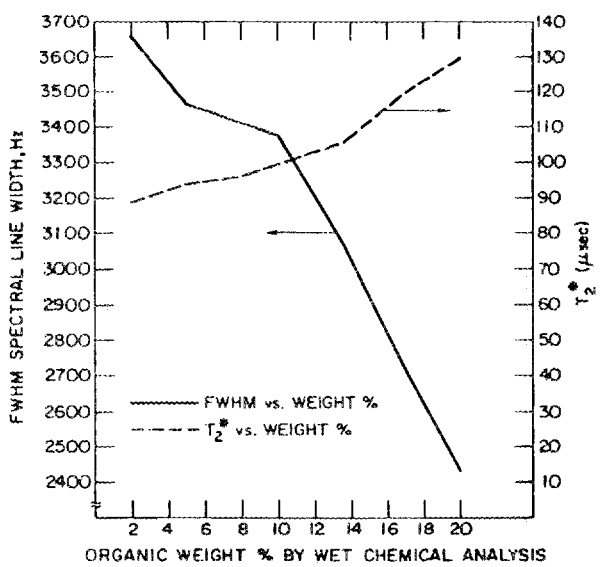

T_2 measurements (Carr-Purcell-Meiboom-Gill pulse sequence)

During this reporting period, we conducted T_2 measurements on the Si_3N_4 + 15.5 wt.% B/P mixture at 22 and 100°C. We used a Carr-Purcell-Meiboom-Gill (CPMG) pulse sequence, which is represented by

$$D_1 - t(90°)_x[\tau - t(180°)_y - \tau]_n - FID,$$

where D_1 is the time required to relax to equilibrium, τ is the variable decay time (minimum of 0.6 ms is required to allow elimination of diffusion), $t(90°)_x$ and $t(180°)_y$ are pulse durations, and n (bracketed section) is the number of 180° pulse trains, which must be an even number to provide for cancellation of 180° pulse errors. The characteristics of a CPMG pulse sequence (vs. our previously used Hahn spin-echo sequence) help to eliminate (1) 180° pulse imperfections and (2) diffusion effects which might exist on our polymeric binders.[1-3] The T_2 comparisons are shown in Table 1. We are still in the process of analyzing those preliminary data.

Table 1. T_2 Comparisons Between Hahn and CPMG Pulse Sequence

Pulse Sequence	Temperature (°C)	T_2 (msec)
Hahn	22	0.54
Hahn	100	1.84
CPMG	22	2.0
CPMG	100	3.0

Effects of weighting functions on the amplitude of the free induction decay.

After acquiring the raw NMR data, but before these data are Fourier transformed, it is often useful to multiply the raw FID data by a weighting function to optimize[2,4-5] either (a) the S/N ratio, (b) the resolution, or (c) the lineshape, depending on the desired results. Durign this period, we have investigated the following weighting functions: (1) exponential multiplication (EM), (2) Gaussian multiplication, (3) double exponential multiplication, and (4) trapezoidal multiplication (TM). The results help us select the suitable weighting function with optimal parameters when we process our raw NMR imaging data. Insofar as our imaging (short T_2, solid-state) is concerned, TM weighting function seems to play an important role. The first N_1 points are multiplied by a linear function whose value at the first point is 0 and whose value at point N_1 is 1. The last N_2 points are multiplied by a linear function whose value decreases from 1 at point $(N - N_2)$ to 0 at N, where N is the last point in the FID.

The N_1 portion of the window is sometimes used to lessen the effects of pulse breakthrough, but it can produce undesirable baseline distortion near each peak in the spectrum. Since EM with a linebroadening (LB) value greater than zero reduces noise at the end of a FID, the main use of the N_2 portion of TM is to reduce the enhanced noise produced by an EM with an LB value less than zero. The preliminary data indicate that the S/N ratio of FID decreases as N_1 increases owing to the inherent characteristics of our sample.

Imaging experiments

In earlier work,[6-8] direct NMR imaging of the B/P distribution was shown to be possible if gradient pulses and RF pulse sequence are fast enough to compensate for extremely short T_2s. All of the preliminary imaging experiments were conducted on a 2-Tesla GE chemical shift imager (CSI) which has a maximum gradient strength of 3 G/cm. The general two-dimensional spin-echo pulse sequence used is shown in Fig. 8.

Owing to the limitation of the ramp-up and ramp-down times of the gradient (most >2 msec) and phase encoding time (~3 msec), a minimum of 5-7 msec is recommended by the manufacturing company; this limitation will reduce the S/N ratio of our sample (T_2 < 1 msec) dramatically. Although attempts had been made to reduce TE to a more desirable level (3 msec) by reducing ramp-up/ramp-down and phase encoding time, the same attempts also increase eddy current (gradient switch on/off too fast) and problems associated with reconstruction of the image (phase encoding time too short). Figure 9 shows the tomographic image of the B/P phantom with five voids ranging from 1 to 5 mm in diameter. The frequency-encoding direction (y axis) indicates poor resolution due to the limitation of the readout-gradient strength (3 G/cm maximum) and the inherent characteristic of the sample (broad linewidth of ~1000 Hz).

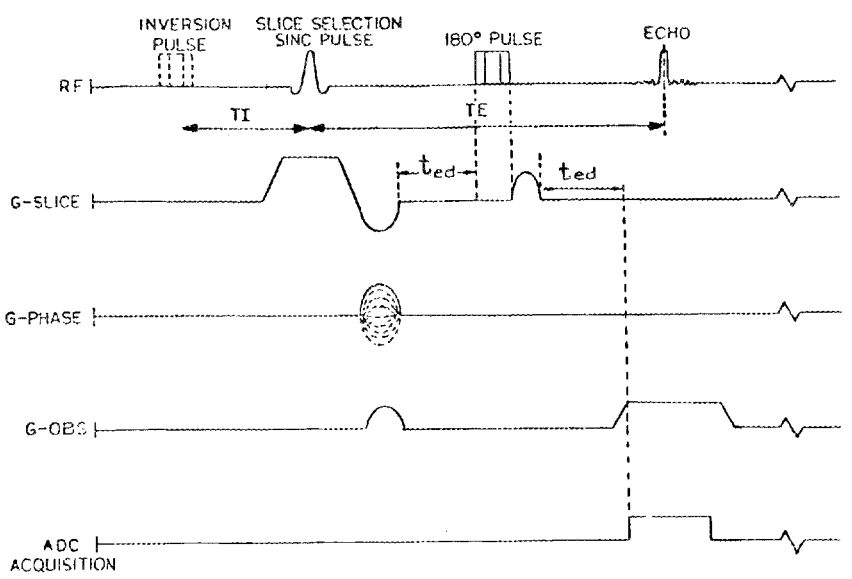

Fig. 8. Two-Dimensional Spin-Echo Pulse Sequence.

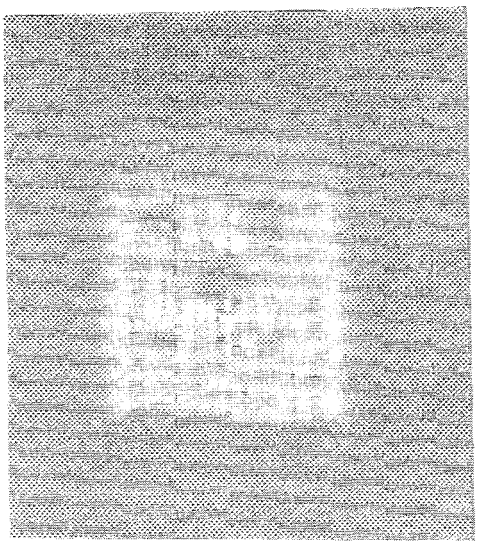

Fig. 9

Tomographic Image of B/P Phantom with five Voids (lower right, 1 mm; lower left, 2 mm; upper left, 3 mm; upper right, 4 mm; center, 5 mm). Resolution = 256 x 256; echo time = 3 msec; number of acquisitions = 4; slice thickness = 10 mm.

We are in the process of designing appropriate RF coils (capable of transmitting short pulses to uniformly excite the broad spectral line of a solid material) with more satisfactory gradient coils (capable of generating more intense and rapidly switched gradients) to overcome the limitations and problems stated above.

Status of milestones

All milestones are on schedule.

References

1. Atta-ur-Rahman, Nuclear Magnetic Resonance: Basic Principles, Springer-Verlag Publishing Co. (New York, Berlin, Heidelberg, Tokyo), 1986.

2. E. Fukishima and S. B. Roeder, "Experimental Pulse NMR: A Nuts and Bolts Approach," pp. 2217-2295 in NMR of Solids, Addison-Wesley Publishing Company (London, Amsterdam, Sydney, Tokyo), 1981.

3. S. Thomas and R. Dixon, NMR in Medicine: The Instrumentation and Clinical Application, American Institute of Physics, 1986.

4. A. E. Derome, Modern NMR Techniques for Chemistry Research, Pergamon Press, 1986.

5. General Electric Company, NMR Instruments CSI-II Series Operators Manual for CSI-II, 1986.

6. W. A. Ellingson, J. L. Ackerman, J. D. Weyand, R. A. DiMilia, and L. Garrido, "Characterization of Porosity in Green-State and Partially Densified Al_2O_3 by Nuclear Magnetic Resonance," Ceram. Eng. Sci. Proc. 8, 1987, pp. 503-512.

7. J. L. Ackerman, W. A. Ellingson, J. A. Koutcher, and B. R. Rosen, "Development of Nuclear Magnetic Resonance Imaging Techniques for Characterizing Green-State Ceramics," in Proc. 2nd Intl. Symp. on the Nondestructive Characterization of Materials, Montreal, Canada, 1986, pp. 169-178.

8. W. A. Ellingson, J. L. Ackerman, S. Gronemeyer, and L. Garrido, "Nuclear Magnetic Resonance Imaging for Detecting Binder/Plasticizers in Green-State Structural Ceramics," in Proc. 16th Symp. on Nondestructive Evaluation, 1987, pp. 231-240.

Powder Characterization

M. A. Janney, A. C. Young, and O. O. Omatete (Oak Ridge National Laboratory)

Objective/scope

The objectives of this research element are threefold: (1) to identify and characterize those aspects of the chemistry and physics of a ceramic powder (or whisker)-solvent interface that control processing, (2) to develop standard methods of analysis for item 1, and (3) to develop procedures for writing specifications for ceramic powders to include any methods of analysis developed in this project.

Technical progress

Some of the critical questions that we expect to answer during the course of this investigation are:

(1) Can a critical set of parameters be specified for a given powder that will truly qualify that powder for a particular process?
(2) Can standard electrophoresis test procedures be developed that will allow two or more independent laboratories to obtain the same set of values on the same powder for a given set of conditions?
(3) Can we determine the scientific basis to describe the chemical and physical nature of the ceramic powder-solvent interface?
(4) Can that scientific basis be translated into a set of quality-assurance (QA) tests that are meaningful to the practicing ceramic engineer?

The project is comprised of three distinct elements: (1) a round-robin characterization of electrophoretic mobility and mobility distribution, acid-base character, and perhaps other aspects of the powder to be conducted by Oak Ridge National Laboratory (ORNL) and three university partners (industrial participation in the round robin, by both ceramics firms and instrument manufacturers, will be sought on a voluntary basis); (2) special projects at each laboratory to include such investigations as determining the nature of the powder-solvent interface in both aqueous and nonaqueous solvents, adsorption onto powder surfaces, acid/base characteristics of powders in nonaqueous solvents, and controlled chemical doping of powder surfaces; and (3) adaptation and verification of analytical procedures developed during the course of these investigations to determine their usefulness in the research laboratory or industrial practice. Silicon nitride has been selected as the powder for investigation. The principal investigators for this project at ORNL have responsibility for both the administration of the subcontract work and for in-house investigations. These two responsibilities are reported separately below.

Subcontracts

Three university subcontracts have been awarded based on a competitive bid procedure. The work to be performed under the subcontracts

includes (1) participation in a round-robin characterization of electrophoretic mobility by the microelectrophoresis method and (2) special projects at each university. The university special projects are: (1) characterization of the silicon nitride-aqueous solution interface (University of Wisconsin, Madison); (2) characterization of the silicon nitride-nonaqueous solution interface (Pennsylvania State University); and, (3) surface modification of silicon nitride by controlled doping with sintering aids in the 0.1- to 5.0-wt-% range (Rutgers University). A kick-off meeting is planned for February 1989.

In-house

The in-house work is split into two parts: (1) an examination of gas chromatography as a powder surface characterization tool and (2) development of electrophoretic mobility (zeta potential) measurement as a QA tool.

Our initial chromatography work involves looking at the adsorption characteristics of chemical compounds such as alcohols, alkanes, and various other organic solvents on an alumina powder (RCHP powder). We have demonstrated that the technique of using a packed column geometry gives us reasonable and repeatable results. Further, we have demonstrated that the interactions of alcohols and phenols with the alumina surface are so strong that these probe molecules do not elute from the column even at 250°C.

In addition to our own work, Dr. Georges Guiochon (an ORNL Distinguished Scientist) and coworkers in the Division of Analytical Chemistry are working on a similar study. Currently, Dr. Guiochon is employing a surface-coated open tubular (SCOT) column instead of a capillary or packed column. The advantage of the SCOT column is a relatively low back pressure needed for operation. Lower pressure drop means a longer column and, therefore, more theoretical plates, which gives better resolution. More quantitative results can be obtained through this type of column. It is, however, more tedious to prepare such a column. A good solvent is needed to suspend the test powder in order to produce a uniform and homogeneous column coating. In cooperation with Dr. Guiochon's group, a series of chemical solvents have been used in a sedimentation experiment (0.1 g of powder in 10 mL of solvent) in search for an adequate suspension medium. Tables 1, 2, and 3 give the results for alumina, silicon nitride, and silicon carbide, respectively. The rating of the solvents is either good, fair, or poor, depending on the visual judgment of these solutions after a certain period of time. Dimethyl sulfoxide produced good suspensions for all three of the powders. Dichloroethane gave the best result for alumina powder. Both dimethyl heptanone and isopropyl alcohol also perform well for silicon nitride. As for silicon carbide, dibromomethane and butyl acetate were better than dimethyl sulfoxide. Using the data obtained from the previous powder dispersion studies, silica was suspended in a 5 wt % diethylene glycol in dibromomethane solution and used to produce a SCOT column.

In addition, a computer code is being written to relate elution peak to the adsorption isotherm. Once completed, the computer program will be able to construct an adsorption isotherm simply from either single- or multiple-pulse elution peaks, providing that the pressure drop across the column is negligible.

Table 1. Sedimentation of Reynolds RCHP alumina

Solvent	Rating	Comment
Toluene	P	Fell out immediately
Heptane	P	Fell out immediately
Dibromomethane[a]	P	Supernatant yellow, clear within 1 d, very fluffy sediment
Dichloroethane	G	Best after 16 d, milky, sediment 0.6-mL-high supernatant began to separate within 7 h, but final supernatant more cloudy than 6 (dimethyl sulfoxide)
Butyl acetate	P	Clear within 6 h
Dimethyl sulfoxide	G	Close second, thin dense sediment <0.1-mL-high, was 2 d before supernatant began to separate, still a difference in density of supernatant after 16 d
Formamide	P	Fairly clear within 2 h
Cyclohexanone[b]	F	Slightly yellow, half of supernatant fairly clear within 4 d, most fairly clear within 7 d, appears to be full of "fines" after 16 d
Dibromoethane	P	Clear within 1 d
Ethylhexyl acetate	P	Clear within 2 h
Dimethylheptanone	P	Clear within 4 d
Carbon disulfide	P	Fell out immediately
Isopropyl alcohol	P	Clear within 8 d

[a]A colorless solvent.

[b]A yellow solvent.

Table 2. Sedimentation of silicon nitride

Solvent	Rating	Comment
Toluene	P	Fell out immediately
Heptane	P	Fell out immediately
Dibromomethane[a]	P	Supernatant yellow and cloudy, extremely fluffy sediment 2 mL high
Dichloroethane	P	Clear within 4 d
Butyl acetate	P	Clear within 4 d
Dimethyl sulfoxide	G	Thin, dense sediment <0.1 mL high, milky after 27 d, best
Formamide	P	Clear within 1 d
Cyclohexanone[b]	P	Yellowish supernatant, clear of particles within 1 d
Dibromoethane	F	Very lightly cloudy, sediment fluffy, 1.8 mL high
Ethylhexyl acetate	P	A lot of "fines" in supernatant after 27 d, dense sediment 0.9 mL high
Dimethylheptanone	G	Supernatant cloudy, sediment 0.5 mL high
Carbon disulfide	P	Fell out immediately
Isopropyl alcohol	G	Supernatant cloudy, sediment 0.4 mL high

[a]A colorless solvent.

[b]A yellow solvent.

Table 3. Sedimentation of silicon carbide

Solvent	Rating	Comment
Toluene	P	Fell out immediately
Heptane	P	Fell out immediately
Dibromomethane[a]	G	Best, still very dark after 13 d, very thin sediment <0.1 mL high
Dichloroethane	P	Fell out completely within 4 d
Butyl acetate	G	Second best, still cloudy after 13 d, dense sediment 0.4 mL high
Dimethyl sulfoxide	F to G	Second best, still cloudy after 13 d, thin, dense sediment <0.2 mL high
Formamide	P	Clear within 7 h
Cyclohexanone[b]	P	Clear within 7 h, supernatant yellowish
Dibromoethane	P	Clear within 3 d, loose sediment, 0.8 mL high
Ethylhexyl acetate	P	Most fell out within 7 h
Dimethylheptanone	F	Supernatant very lightly cloudy within 6 d, dense sediment 0.5 mL high
Carbon disulfide	P	Fell out immediately
Isopropyl alcohol	P	Clear within 3 d

[a]A colorless solvent.

[b]A yellow solvent.

4.0 TECHNOLOGY TRANSFER

4.1 TECHNOLOGY TRANSFER

4.1.1 Technology Transfer

Technology Transfer
D. R. Johnson (Oak Ridge National Laboratory)

Technology transfer in the Ceramic Technology Project is accomplished by a number of mechanisms including the following:

Trade shows. A portable display describing the program has been built and used at several trade shows and technical meetings, most recently at the Annual Meeting of the American Ceramic Society, April 26–30, 1987, in Cincinnati, Ohio.

Newsletter. A Ceramic Technology Newsletter is published regularly and sent to a large distribution.

Reports. Semiannual technical reports, which include contributions by all participants in the program, are published and sent to a large distribution. Informal bimonthly management and technical reports are distributed to the participants in the program. Open-literature reports are required of all research and development participants.

Direct Assistance. Direct assistance is provided to subcontractors in the program via access to unique characterization and testing facilities at the Oak Ridge National Laboratory.

Workshops. Topical workshops are held on subjects of vital concern to our community.

International Cooperation. Our program is actively involved in and supportive of the cooperative work being done by researchers in West Germany, Sweden, and the United States under an agreement with the International Energy Agency. That work, ultimately aimed at development of international standards, includes physical, morphological, and microstructural characterization of ceramic powders and dense ceramic bodies, and mechanical characterization of dense ceramics. Detailed planning and procurement of ceramic powders and flexural test bars have been accomplished. Exchange of preliminary data on ceramic and powder characterization results has been started by those laboratories participating.

IEA Annex II Management

V. J. Tennery (Oak Ridge National Laboratory)

Objective/scope

The IEA Annex II agreement between the United States, the Federal Republic of Germany (FRG), and Sweden on structural ceramics is directed to cooperative research and development oriented to the identification and adoption of standardized methods for characterizing these materials. This agreement includes four subtasks: (1) information exchange, (2) ceramic powder characterization, (3) ceramic chemistry and structural characterization, and (4) ceramic mechanical property characterization. Each country is providing selected ceramic powders and sintered structural ceramics for use in the research work in Subtasks 2, 3, and 4 in all three participating countries. Participating laboratories in all three countries have agreed to share all resulting data with the purpose of using the knowledge gained from the work for developing standard measurement methods for characterizing ceramic powders and sintered structural ceramics.

The lack of such standard measurement methods has been an impediment to the evolution and development of structural ceramics, both from the point of view of the manufacturer and the user. This Annex II agreement was conceived to accelerate the development of standard methods for determining important properties of these evolving materials.

In the United States, many companies and their research staffs have contributed significant resources in performing the required measurements. In the United States, for example, in Subtask 2, twelve laboratories are participating; in Subtask 3, seven laboratories are participating; and in Subtask 4, eight laboratories are participating.

The research in Subtask 2 includes five ceramic powders which are being studied in this subtask. For Subtasks 3 and 4, three sintered ceramics are being studied, including one from each of the three countries. The ceramic from the United States is a silicon nitride, SNW-1000 from GTE-Wesgo, that from Germany is a hipped SiC from ESK Kempton, and that from Sweden is a silicon nitride from ASEA Cerama.

With the approaching conclusion of Annex II research, considerable discussion has been held in the United States relative to possible content of continued cooperative international research similar to that conducted under the Annex II agreement. Due to the different rates at which the research in Subtasks 2, 3, and 4 has progressed, the status of these discussions differs for each subtask. At the present time, mechanical properties research in Subtask 4 is nearest to completion and, therefore, in the United States, consideration of further research in this area is most mature. It is anticipated that research plans in the area of mechanical properties will be reviewed at the Executive Committee meeting scheduled for November 1988 in the United States and a proposal to add a Subtask 5 formulated. Results from the ceramic powder characterization research in Subtask 2 will be completed second, and it is planned to have future research plans finalized for cooperative ceramic powder characterization research by the middle of CY 1989. Results from sintered ceramic characterization in Subtask 3 will be available last in time, and it is not clear at this time if further research in this area will be supported as part of a future international agreement. The status of the research in

the areas of powder characterization, sintered ceramic characterization, and mechanical properties within the United States relative to a possible addition of a Subtask 5 is discussed later in this report.

Technical progress

The major technical status changes since the last semiannual report will be reviewed briefly.

Subtask 2, Ceramic powder characterization

The U.S. powder working group held three meetings during this reporting period: on April 6 in Pittsburgh, Pennsylvania; on May 17 in Waltham, Massachusetts; and on September 15 and 16 in Gaithersburg, Maryland. These meetings included detailed presentations of data obtained by the U.S.-participating laboratories. The earlier meetings included detailed discussions regarding problems being encountered with powder distribution by the National Institute of Standards and Technology (NIST) and measurement problems encountered by the participating laboratories. The meeting in September concluded the data submissions to NIST, which has responsibility for compiling all of the data from the 25 participating laboratories in three countries before the international meeting scheduled for early October in Berchtesgaden, FRG.

The plans for incorporating a series of zeta potential measurements on some of the ceramic powders reported in the previous semiannual report were abandoned due to lack of time and agreement among candidate participating laboratories.

NIST completed distribution of the remaining three powders to all participating laboratories. Analyses for all five powders were completed by all laboratories, and the data was submitted to NIST by the end of August 1988.

Task leaders were identified at the Orlando meeting for the purpose of helping to organize and perform the analysis of data for the powders and for identification and further discussion of problem areas in the powder measurements. These task leaders and their responsibilities are:

(1) chemical characteristics - Dr. A. Dragoo, United States;
(2) particle size distribution, density, and agglomeration - Dr. H. Hausner, FRG;
(3) surface area, permeametry, aspect ratio, isoelectric point, scanning electron microscope, and morphology - Dr. R. Pompe, Sweden.

These task leaders are organizing activities necessary to meet their responsibilities and will provide formal reports at a subtask working group meeting scheduled for October 10-11, 1988, at Berchtesgaden, FRG, just prior to the second international meeting on powder science.

Based upon the most recent agreements following receipt of the powder data by NIST, the following schedule applies to this subtask.

August 15, 1988	All powder analyses completed and results submitted to NIST
October 10-11, 1988	Data reported and reviewed at working group meeting in FRG

December 15, 1988	All data corrections due to NIST
April 30, 1989	Part I (data only) goes to printer
August 31, 1989	NIST final report Part II (data analysis) draft completed and distributed to all participants for review and comment
December 24, 1989	Part II of report published and distributed by NIST. This formally completes Subtask 2.

Subtask 3, Chemical characterization of sintered ceramics

The U.S. working group for Subtask 3 met in Cincinnati, Ohio, on May 4 to review the status of results. Dr. Hatcher of KemaNord in Sweden, who is responsible for drafting the Subtask 3 final report, reviewed the status of his work and stated that he will give a preliminary report of the results at the Executive Committee meeting in Amsterdam in June. At the Amsterdam meeting, Hatcher reported that final compilation of late data for the subtask was essentially completed and that he intends to have a final draft of the report for the subtask ready for Executive Committee action at the meeting scheduled for November in Las Vegas.

Subtask 4, Mechanical properties of ceramics

Research results from this subtask are being prepared in two reports, one written at ORNL in the United States on fractography analysis, and the second being prepared at the Kernforschungszentrum-Karlsruhe (KFK) in Karlsruhe in Germany including analysis of the fracture data. In early April, the draft report from Germany was received and distributed to the United States and Swedish participants for review and comment. The first draft of the fractography report was distributed for comment on April 26. Major difficulty was being encountered in receiving proper formatted data files from Germany, which included the specimen designators for both the Swedish and the U.S. silicon nitride ceramics. The first round of comments from U.S. reviewers were returned to Germany in early May. A revised draft of the fractography report was sent to members of the Executive Committee in all three countries on May 25. Details of the research results were presented at the Executive Committee meeting held in Amsterdam on June 8. The revised German report was received at ORNL and was sent to all U.S. participants in the subtask on June 30. Included was a questionnaire from Germany regarding the fixture designs used by U.S. participants. Based upon previous review comments, a revised version of the fractography report was sent to U.S. participants for review. Review results were received from Sweden in July on the fractography report and further communication was held with German workers via letter on July 13 concerning errors in the earlier German draft for Kolmogorov-Smirnov test results, including the confidence levels used in the draft report. Preliminary review comments on the fracture analysis report draft and the results of U.S. questionnaires were returned to Germany on August 12. Final U.S. review comments on the German report were sent to Germany in mid-September. Further communication occurred with the German workers at Karlsruhe regarding the unsatisfactory status of the German data files for Subtask 3. The final version of this German report will be reviewed at the Executive Committee meeting scheduled for November 30 in Las Vegas.

Status of Subtask 5 research plans

As stated earlier in this report, the degree of completion of each subtask has a direct bearing on the level of discussions on the purpose and need for continuation of at least some of the research under a new subtask. Further, there is evidence that other countries are interested in participating in future research, if one is approved. This potential future research is discussed in terms of a new subtask. As noted in earlier reports of this activity, Germany provided an informal proposal for mechanical property research at the working group meeting held in Dearborn, Michigan, in October 1987. Discussion of this proposal among potentially interested U.S. laboratories resulted in an alternative proposal containing a mixture of flexural and tensile strength measurement research. For example, results from the large flexure strength data sets generated in Subtask 4 indicated unexpected variations which could not be clearly attributed to "equipment variations" or to "material variations". In addition, the strong interest in developing methods for measuring the true tensile strength of structural ceramics was felt to be an appropriate subject. A proposal based upon these ideas was formulated by the author and presented to the U.S. working group at the meeting in Cincinnati on May 4, following receipt of responses from the Cocoa Beach meeting held in January.

Based upon responses received after the May meeting, a revised proposal was prepared and presented for consideration at the Executive Committee meeting in Amsterdam in June. At this meeting, a representative of the Ministry of International Trade and Industry (MITI) in Japan stated that Japan definitely wants to be a participant in any future IEA annex research on structural ceramics. During the summer, final comments were received from the U.S. industrial ceramic community, and a more or less final version of the proposal was prepared and distributed for consideration and comment to a large number of U.S. laboratories on September 12. A working group meeting to finalize the U.S. position on mechanical property research in a new subtask is scheduled for October 25 in Dearborn, Michigan. Based upon this meeting, the U.S. position will then be presented to the Executive Committee at the Las Vegas meeting at the end of November.

The research which the U.S. community is willing to support includes extensive use of strain-gauged specimens as a means for identifying load and stress asymmetries in various test machines used in determining both flexural and tensile strength of one U.S. structural ceramic material. Plans for future U.S. cooperative international research on ceramic powders will be completed by early spring.

Standard Reference Materials

A. L. Dragoo, S. G. Malghan, L.-S. Lum, D. B. Minor, J. F. Kelly, and J. C. Cline (National Institute of Standards and Technology)

Objective/Scope

Ceramics have been successfully employed in engines on a demonstration basis. The successful manufacture and use of ceramics in advanced engines depends on the development of reliable materials that will withstand high, rapidly varying thermal stress loads. Improvement in the characterization of ceramic starting powders is a critical factor in achieving reliable ceramic materials for engine applications. The production and utilization of such powders require characterization methods and property standards for quality assurance.

The objectives of the NBS program are (1) to assist with the division and distribution of five ceramic starting powders for an international round-robin on powder characterization; (2) to provide reliable data on physical (dimensional), chemical and phase characteristics of two silicon nitride powders: a reference and a test powder; and (3) to conduct statistical assessment and modeling of round-robin data. This program is directed toward a critical assessment of powder characterization methodology and toward establishment of a basis for the evaluation of fine powder precursors for ceramic processing. This work will examine and compare by a variety of statistical means the various measurement methodologies employed in the round-robin and the correlations among the various parameters and characteristics evaluated. The results of the round-robin are expected to provide the basis for identifying measurements for which Standard Reference Materials are needed and to provide property and statistical data which will serve the development of internationally accepted standards.

Technical Progress

The technical progress covered in this report includes descriptions of work on the preparation of powder samples for the IEA/ANNEX II, Subtask 2, powder characterization round-robin and of the compilation and analysis of round-robin data.

Division, Distribution and Certification of Ceramic Starting Powders. This phase of the work was completed during the previous reporting period.

Powder Characterization. X-ray sedigraph and BET analyses of all IEA powders were completed. Eight samples of each of reference silicon nitride (SNR), test silicon nitride (SNT), silicon (Si) and silicon carbide (SiC) powder samples were analyzed with the sedigraph. At least two replicates of each sample were analyzed. (BET)

In collaboration with N. L. Whitby and D. Y. H. Pui, of the Particle Technology Laboratory of the University of Minnesota, a comparison study was carried out for particle size measurements by airborne particle methods and x-ray sedigraph. Also, as a part of this

study, the use of a particle size distribution fitting routine, operating on a PC-type computer, was demonstrated. Preliminary results show that rapid, high resolution aerosol measurement techniques, particularly when augmented by distribution fitting procedures, could provide attractive alternatives to traditional time intensive methods, such as x-ray sedigraph. A preliminary draft of a paper describing this preliminary work accompanies this report.

Data Analysis. During the current reporting period powder characterization data reported to NIST by the 25 laboratories participating in the IEA/Annex II, Subtask 2, round-robin was compiled in a computer spreadsheet, verified, tabulated and plotted. A printed compilation comprising approximately 325 pages was redistributed to participating laboratories at an IEA Working Group Meeting in Berchtesgaden, FRG, on October 10. The compilation provided summary statistics, data plots, tabulations of original data, and some tables on effects of analytical procedure. The compilation covered chemical properties, particle size distribution and other physical properties; x-ray diffraction results were not included and will be issued separately. Table 1 shows the number of laboratories reporting for the three catagories of chemical properties, particle size distribution, other physical properties and quantitative x-ray diffraction. The table of contents for the compilation is attached to this report.

Meetings of the U.S. Working Group for the IEA/Annex II Powder Characterization were held at GTE Research Labs, Waltham, MA, in May and at NIST, in Gaithersburg, MD, in September. These meetings have provided an opportunity to examine powder characterization problems, to foster improved working relationships between participants and to discuss future collaborations. The September meeting was devoted largely to examining the compiled data from the participating U.S. laboratories in Annex II and to making recommendations for the combined U.S.-West German-Swedish compilation which was distributed at Berchtesgaden in October.

The IEA/Annex II Working Group Meeting of Subtask 2 established the schedule and procedures for the preparation of published materials for the subtask group's powder characterization results. Two printed documents are to be prepared: the original data and the final report and technical analysis. The following schedule was established for the publication of the original data:

1. All corrections to the compiled data are to be reported to NIST by the participating laboratories by December 15, 1988.

2. NIST will prepare the corrected compilation, including tabulations of data, summary statistics, data plots, summaries of analytical methods and selected micrographs, and submit the compilation for printing by May 1, 1989.

3. Printed copies will be distributed to the participating laboratories by September 1, 1989. General public

distribution of the data will occur once the data is released by the IEA/Annex II Executive Committee.

The technical analysis and final report will be prepared by the three national subchairman working in collaboration. They will meet on the occasions of the American Ceramic Society Coco Beach Meeting and the American Ceramic Society Annual Meeting to prepare a final draft report. They will also prepare a set of recommendations for the Chairman of Subtask 2 to present to the IEA/Annex II Executive Committee. Printed copies of the technical analysis and final report will be distributed to the participating laboratories by December 15, 1989. An in-depth statistical analysis of the round-robin data will be prepared by NIST as a separate document.

Status of Milestones

Task 1. On schedule. Subtask A completed in February. Subtask B completed in October with preparation and distribution of data compilation for IEA/Annex II. Subtask C in progress; see schedule and procedures for reporting IEA data and technical analysis in the preceding section of this report.

Publications

Nancy L. Whitby, David Y. H. Pui, Lin-Sien Lum and Alan L. Dragoo, "Powder Size Analysis Using Aerosol Measurement Techniques," to be submitted for publication in Powder Technology.

Appendix

TABLE OF CONTENTS

Cover

Table of Contents

Agenda

Participating Laboratories

Chemical Composition Code

Particle Size Code

Physical Properties Code

Chemical Properties

- Methods of Chemical Analysis
- Methods of Chemical Analysis of Silicon Nitride
- Potential Sources of Errors in Chemical Data
- Silicon Nitride Reference Powder:
  - Summary Statistics (17)

Variability in Chemical Analysis Data (4)
Plots of Data (9)
Original Data (11)
Silicon Nitride Test Powder:
Summary Statistics (12)
Plots (8)
Original Data (11)
Silicon Carbide Powder:
Summary Statistics (15)
Plots (8)
Original Data (6)
Silicon Powder:
Summary Statistics (14)
Plots (8)
Original Data (8)
Zirconia:
Summary Statistics (14)
Plots (8)
Original Data (5)
Particle Size
Silicon Nitride Reference Powder:
Summary Statistics (4)
Procedure Effects (3)
Plots (10)
Original Data (6)
Silicon Nitride Test Powder:
Summary Statistics (4)
Procedure Effects (3)
Plots (8)
Original Data (5)
Silicon Carbide Powder:
Summary Statistics (4)
Procedure Effects (3)
Plots (8)
Original Data (4)

Silicon Powder

Summary Statistics (5)

Procedure Effects (2)

Plots (8)

Original Data (4)

Zirconia Powder:

Summary Statistics (3)

Plots (5)

Original Data (3)

Physical Properties

Silicon Nitride Reference Powder:

Summary Statistics (7)

Plots (6)

Original Data (6)

Silicon Nitride Test Powder:

Summary Statistics (6)

Plots (4)

Original Data (5)

Silicon Carbide Powder:

Summary Statistics (6)

Plots (4)

Original Data (5)

Silicon Powder:

Summary Statistics (5)

Plots (4)

Original Data (5)

Zirconia Powder:

Summary Statistics (9)

Plots (4)

Original Data (4)

Table 1. Number of laboratories reporting for IEA/Annex II, Subtask 2, round-robin on powder characterization; total number of participating laboratories was 25

POWDER:	Z3YO	SNR	SN	Si	SiC
CHEMICAL PROPERTIES:					
U.S.	7	10	10	10	9
FRG	5	9	8	4	5
SWEDEN	0	1	1	1	1
PARTICLE SIZE:					
U.S.	9	12	11	10	9
FRG	2	9	6	4	6
SWEDEN	1	2	2	2	2
OTHER PHYSICAL PROPERTIES:					
U.S.	9	12	9	10	12
FRG	5	9	7	4	6
SWEDEN	2	2	2	2	2
X-RAY DIFFRACTION:					
U.S.	4	7	6	4	1
FRG	4	6	7	2	1
SWEDEN	0	2	2	1	1

Ceramic Characterization

M. D. Vaudin, E. R. Fuller, Jr., J. P. Cline and A. L. Dragoo
(National Institute of Standards and Technology)

Objective/Scope

Ceramics have been successfully employed in engines on a demonstration basis. The successful manufacture and use of ceramics in advanced engines depends on the development of reliable materials that will withstand high, rapidly varying thermal stress loads. Physical and chemical properties, phase characteristics and microstructural properties of ceramic materials determined to a large extent their mechanical and structural properties, and hence, their high temperature structural performance and reliability. The reproducibility and precision with which these properties and microstructural characteristics can be measured has not been assessed in a systematic manner for advanced ceramic materials. An initial step in such an assessment is the establishment of a data base for these ceramic properties and microstructural characteristics for a set of standardized specimens.

The objective of this task is to measure and characterize the ceramic properties (crystalline phase composition, grain-boundary properties and possible residual stresses) of a series of standard ceramic specimens to assist in the development of internationally accepted standards for ceramic characterization. This work contributes to an international interlaboratory comparison, IEA/ANNEX II, Subtask 3 on Ceramic Characterization, under the auspices of the International Energy Agency.

Technical Progress

Three materials were characterized in Subtask 3 of IEA/ANNEX II on ceramic characterization: ASEA Cerama silicon nitride, GTE SNW-1000 silicon nitride and ESK silicon carbide*. The work on the two silicon nitride materials was described in the semiannual report transmitted in April 1988. The following report describes electron microscopy observations of the microstructure and grain boundary characteristics of the ESK silicon carbide. Supporting X-ray diffraction data for the bulk phase composition is included.

---

* Certain commercial equipment, instruments and materials may be identified in this report in order to adequately specify the experimental procedure. Such identification does not imply recommendation or endorsement by the National Institute of Standards and Technology, nor does it imply that the materials or equipment identifies are necessarily the bets available for the purpose.

Electron Microscopy Observations: ESK Silicon Carbide. The ESK silicon carbide was shown by X-ray diffraction to be predominantly of the 6H polytype with a c-axis spacing of 1.5 nm. The second phase were 4H SiC (5%) and graphite (2%).

The microstructure of this material consists of grains elongated parallel to the (0001) planes (aspect ratio 3:2) and about 2-3 μm in the long dimension. Figure 1 is a <1120> selected area diffraction pattern from a SiC grain in which every sixth member of the 000L row of spots is intense, thus confirming the X-ray finding that the major phase is the 6H polytype. There are streaks between the 000L spots which indicates a high density of stacking faults. This is evident in the lattice fringe micrograph in Figure 2 in which the regular periodicity of the 6H SiC (0001) lattice fringes is interrupted at irregular intervals by faults which cause a change in the contrast and spacing of the fringes. A stacking fault in the 6H structure produces a small region of a different polytype, depending on the nature of the stacking fault. In this micrograph, the density of stacking faults was estimated as about 50/μm. If we assume that each fault produces a 1nm region of another polytype, the fraction of minority polytypes in the material by this crude estimate is about 5%. The X-ray diffraction data indicates the material contains about 5% of 4H SiC and so it can be concluded that majority of the stacking faults in this micrograph are of the type that locally produce the 4H structure.

The other major phase in this material was carbon in the form of fibrous graphite precipitates, which was detected at the level of 1% to 2% with X-ray diffraction. Using TEM it was determined that the graphite was in the form of precipitates up to 0.5 μm thick. Figure 3 is a micrograph of a fibrous graphite precipitate (as identified by selected area electron diffraction) coating a grain boundary and two triple junctions. Stacking faults are visible in the silicon carbide grains.

Figure 4 shows a thicker graphite precipitate at a four grain junction, with a very high density of stacking faults in all the grains. The morphology of these precipitates is extremely varied. They are usually associated with triple junctions or multi-grain junctions. Figure 5 shows a complex example.

In general the grains were dislocation free, but a few grains contained residual sintering damage. Figure 6 shows a small angle grain boundary that was forming in a grain; the dislocations seen in the figure were moving into the lower elastic energy configuration of the small angel boundary when the material was cooled, "freezing in" the dislocation configuration.

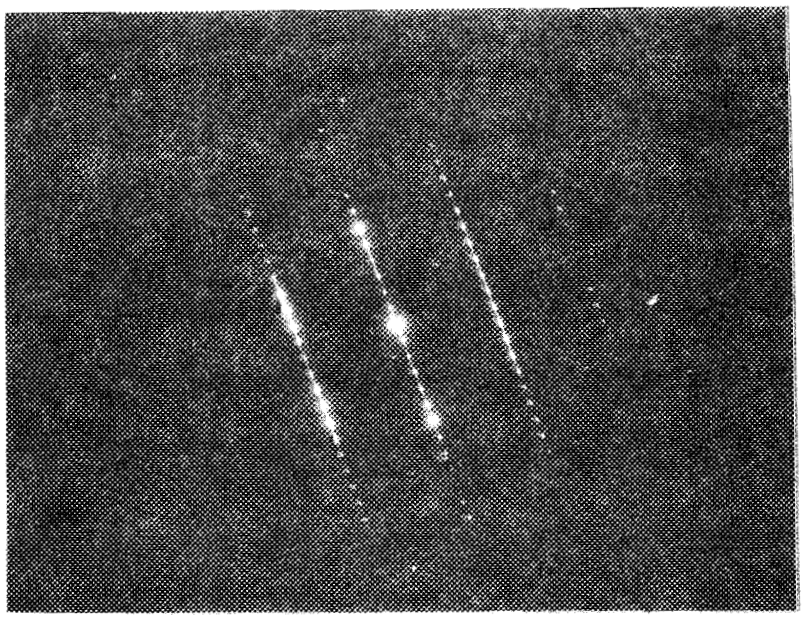

Figure 1. <1120> selected area diffraction pattern.

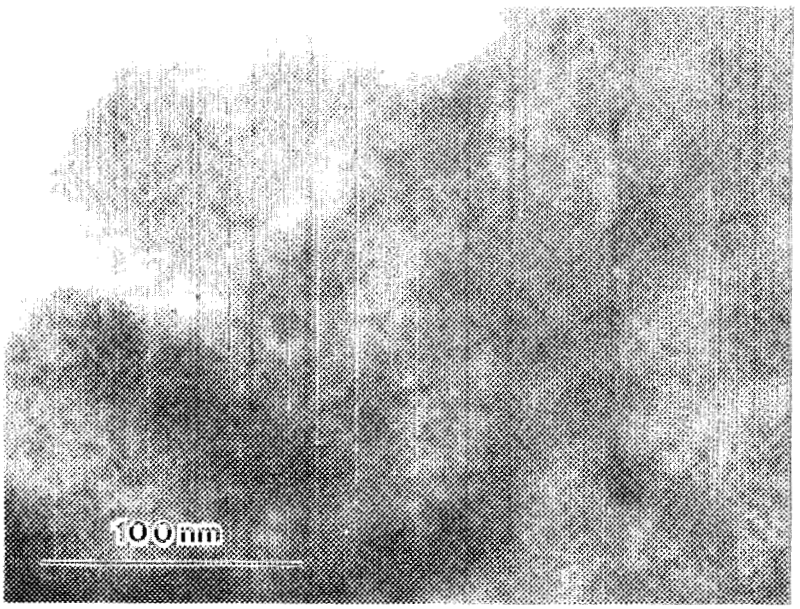

Figure 2. High resolution micrograph showing stacking faults.

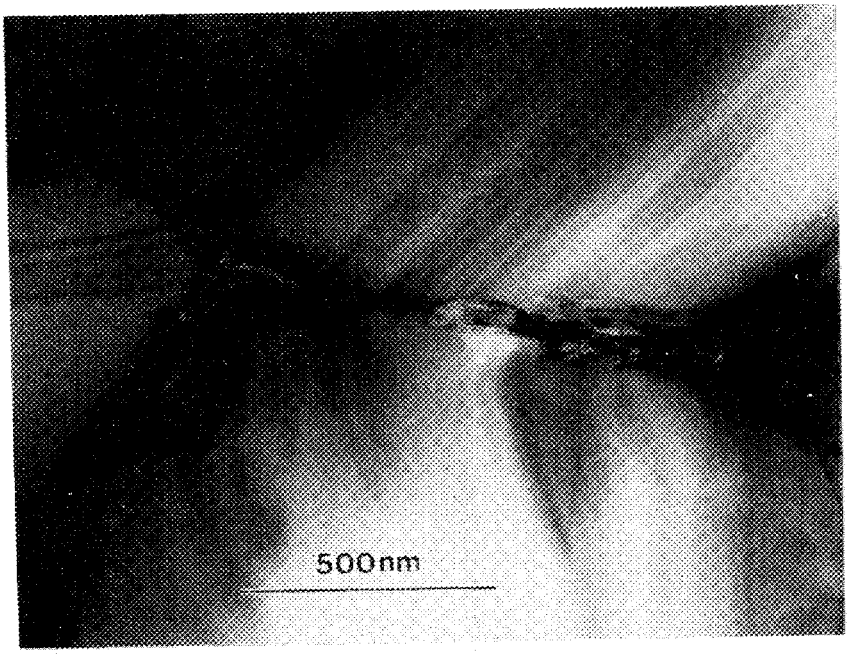

Figure 3. Fibrous graphite precipitate at grain boundary and triple grain junction between SiC grains.

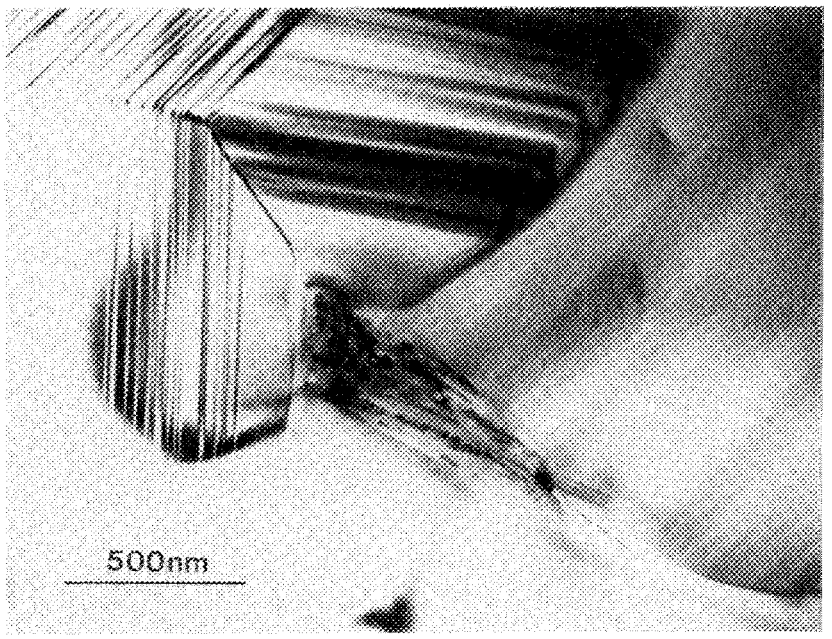

Figure 4. Graphite precipitate at four grain junction between SiC grains. Stacking faults are evident in the four grains shown in the lower portion of the micrograph.

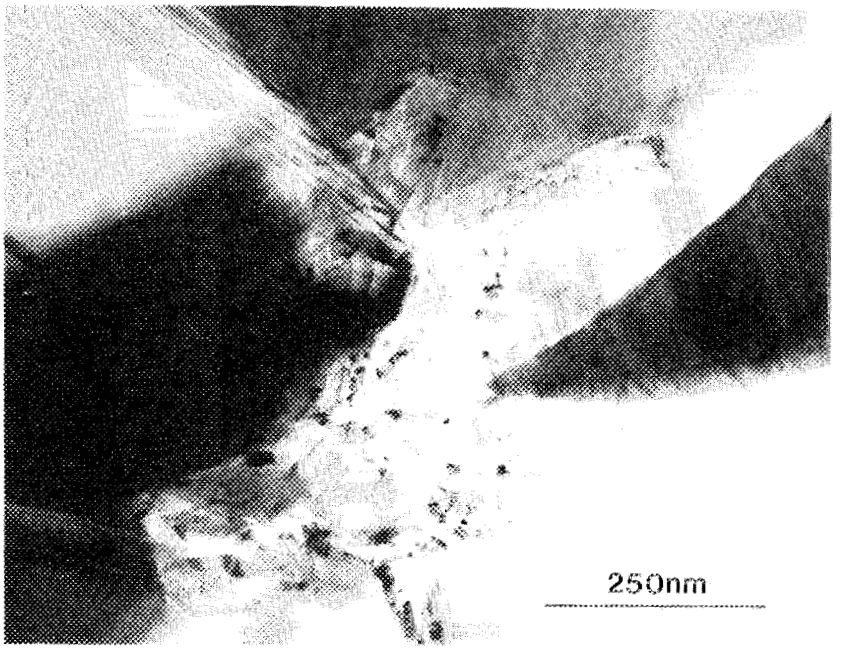

Figure 5. Graphite precipitate at junction of SiC grains. Note the complex morphology of the graphitic phase.

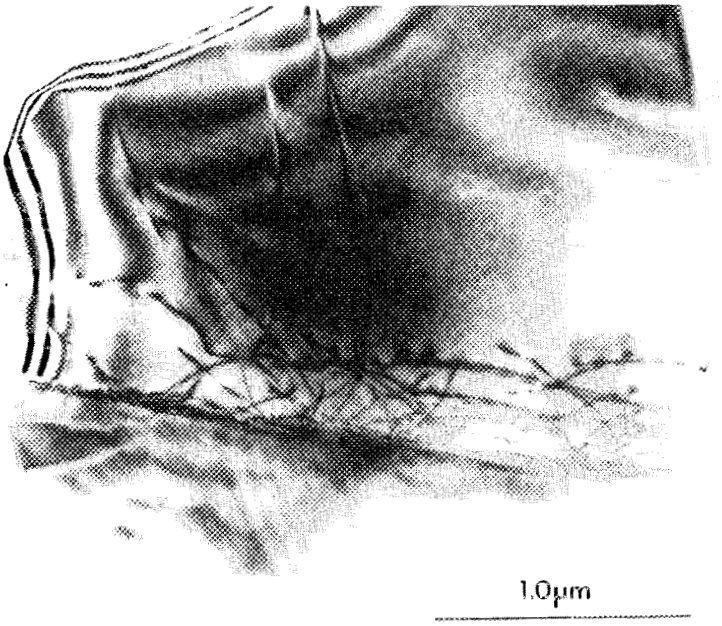

Figure 6. Small angle grain boundary and associated dislocation array quenched into a SiC grain.

X-Ray Diffraction

Qualitative x-ray diffraction analysis of a SiC specimen gave the diffraction pattern shown in Figure 7. The material was found to consist mainly of α-SiC which was estimated to consist of about 95 percent 6H polytype [JCPDS-ICDD Powder Diffraction File No. 29-1131] and 5 percent 4H [PDF No. 29-1127]. A small amount of a third phase polytype may be present as suggested by the peaks at about 45.5°, 54.5° and 71° 2-theta. The weak, broad peak at 26°, as well as the peak near 29°, may be associated with a graphitic form of carbon since none of the SiC polytypes have diffraction peaks in this range. Other weak, broad diffraction lines in the diagram may also be due to this phase. The broaden graphite diffraction lines are consistent with a thin highly disrupted (and strained) material such as that exhibited by the graphite grain boundary phase shown in Figures 3 to 5.

Measurement of surface residual stresses was attempted on the silicon carbide sample but stresses were not observed due to overlap of diffraction peaks and, possibly, to small magnitude of the effect.

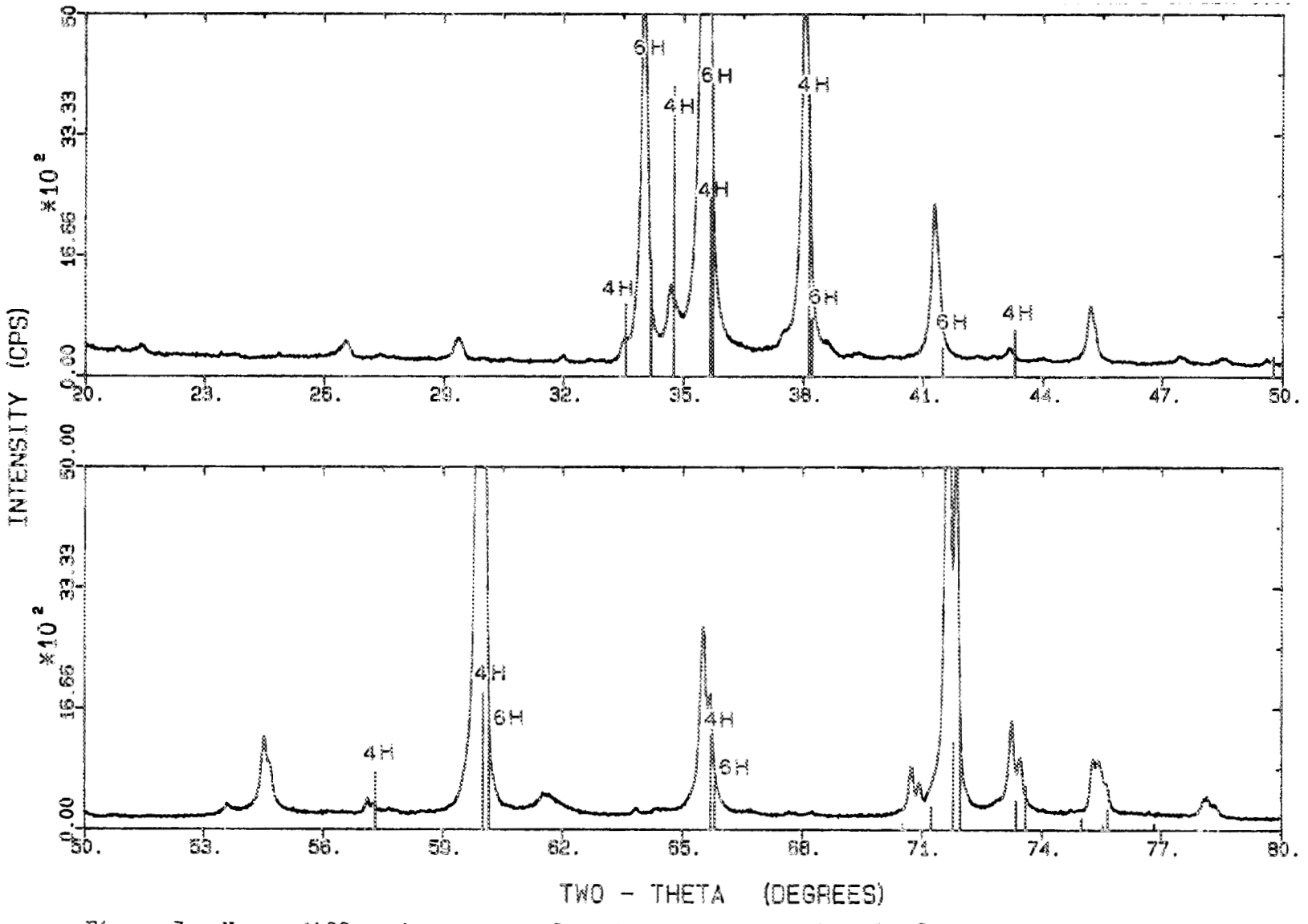

Figure 7. X-ray diffraction pattern for SiC. Positions of peaks for 4H and 6H polytypes are indicated by vertical lines.

INTERNAL DISTRIBUTION

1-2. Central Research Library
3. Document Reference Section
4-5. Laboratory Records Department
6. Laboratory Records, ORNL RC
7. ORNL Patent Section
8-10. M&C Records Office
11. L. F. Allard, Jr.
12. B. R. Appleton
13. R. L. Beatty
14. P. F. Becher
15. T. M. Besmann
16. P. J. Blau
17. A. Bleier
18. E. E. Bloom
19. K. W. Boling
20. R. A. Bradley
21. C. R. Brinkman
22. V. R. Bullington
23. R. S. Carlsmith
24. P. T. Carlson
25. J. V. Cathcart
26. G. M. Caton
27. R. H. Cooper
28. S. A. David
29. J. H. DeVan
30. J. I. Federer
31. M. K. Ferber
32. W. Fulkerson
33. R. L. Graves
34. D. L. Greene
35. M. A. Janney
36-40. D. R. Johnson
41. R. R. Judkins
42. M. A. Karnitz
43. H. D. Kimrey, Jr.
44. T. G. Kollie
45. T. B. Lindemer
46. K. C. Liu
47. E. L. Long, Jr.
48. W. D. Manly
49. R. W. McClung
50. D. L. McElroy
51. J. R. Merriman
52. A. J. Moorhead
53. T. A. Nolan
54. J. L. Rich
55. C. R. Richmond
56. J M Robbins
57. M. W. Rosenthal
58. M. L. Santella
59. A. C. Schaffhauser
60. G. M. Slaughter
61. W. B. Snyder, Jr.
62. E. J. Soderstrom
63. D. P. Stinton
64. R. W. Swindeman
65. V. J. Tennery
66. T. N. Tiegs
67. J. R. Weir, Jr.
68. F. W. Wiffen
69. R. K. Williams
70. S. G. Winslow
71. C. S. Yust

EXTERNAL DISTRIBUTION

72. Donald F. Adams
University of Wyoming
Mechanical Engineering Dept.
Laramie, WY 82071

73. Jane W. Adams
Corning Glass Works
SP-DV-21
Corning, NY 14831

74. J. Ahmad
Battelle Columbus Laboratories
Engineering Mechanics Department
505 King Avenue
Columbus, OH 43201-2693

75. Richard L. Allor
Ford Motor Company
Material Systems Reliability Division
20000 Rotunda Drive
Post Office Box 2053
Dearborn, MI 48121-2053

76. Richard T. Alpaugh
U.S. Department of Energy
Office of Transportation Systems
Forrestal Building CE-151
1000 Independence Avenue, S.W.
Washington, DC 20585

77. H. Arbabi
Brunel University
Department of Materials Technology
Uxbridge, Middlesex UB8 3PH
UNITED KINGDOM

78. V. S. Avva
NC A&T State University
Department of Mechanical Engineering
Greensboro, NC 27411

79. Kirit J. Bahnsali
U.S. Army Materials Technology Laboratory
SLCMT-EMM
405 Arsenal Street
Watertown, MA 02172

80. John M. Bailey
Caterpillar, Inc.
Research Department
Technical Center, Building L
Post Office Box 1875
Peoria, IL 61656-1875

81. Murray Bailey
NASA Lewis Research Center
21000 Brookpark Road
MS:77-6
Cleveland, OH 44135

82. R. R. Baker
Ceradyne, Inc.
3169 Red Hill Avenue
Costa Mesa, CA 92626

83. J. Gary Baldoni
GTE Laboratories, Inc.
40 Sylvan Road
Waltham, MA 02254

84. Dr. P. M. Barnard
Ruston Gas Turbines Limited
New Products Division
Firth Road
Lincoln LN6 7AA
ENGLAND

85. J. L. Bates
Battelle Pacific Northwest Laboratories
PSL/3000 Area
Richland, WA 99352

86. A. L. Bement, Jr.
TRW, Inc.
23555 Euclid Avenue
Cleveland, OH 44117

87. M. Bentele
Xamag, Inc.
259 Melville Avenue
Fairfield, CT 06430

88. Clifton G. Bergeron
University of Illinois
Department of Ceramic Engineering
204 Ceramic Building
105 South Goodwin Avenue
Urbana, IL 61801

89. Deane I. Biehler
Caterpillar, Inc.
Engineering and Research Materials
Technical Center, Building E
Post Office Box 1875
Peoria, IL 61656-1875

90. William D. Bjorndahl
TRW, Inc.
Materials Characterization and Chemical Analysis Department
Building 01, Room 2060
One Space Park
Redondo Beach, CA 90278

91. Dan Blake
Solar Energy Research Institute
1617 Cole Boulevard
Golden, CO 80401

92. Keith Blandford
Boride Products, Inc.
2879 Aero Park Drive
Traverse City, MI 49684

93. J. B. Blum
Norton Company
Advanced Ceramics
Goddard Road
Northboro, MA 01532-1545

94. Paul N. Blumberg
Ricardo-ITI
415 East Plaza Drive
Westmont, IL 60559

95. Wolfgang D. G. Boecker
Carborundum Company
Niagara Falls R&D Center
Post Office Box 832
Niagara Falls, NY 14302

96. Tibor Bornemisza
Sundstrand Turbomach
Division of Sundstrand Corporation
4400 Ruffin Road
Post Office Box 85757
San Diego, CA 92138-5757

97. Han Juergen Bossmeyer
BMW Technologies, Inc.
Watermill Center
800 South Street
Waltham, MA 02154

98. J.A.M. Boulet
University of Tennessee
310 Perkins Hall
Knoxville, TN 37996

99. Steve Bradley
Signal UOP Research Center
50 UOP Plaza
Des Plaines, IL 60016-6187

100. Raymond J. Bratton
Westinghouse Electric Corporation
R&D Center
1310 Beulah Road
Pittsburgh, PA 15235

101. Catherine E. Brown
E. 1. DuPont de Nemours & Company
Experimental Station
Information Center E302/301
Wilmington, DE 19898

102. J. J. Brown
Virginia Polytechnic Institute and State University
Department of Materials Engineering
Blacksburg, VA 24061

103. S. L. Bruner
Ceramatec, Inc.
2425 South 900 West
Salt Lake City, UT 84119

104. W. Bryzik
U.S. Army Tank Automotive Command
R&D Center, Propulsion Systems Division
Warren, MI 48090

105. S. T. Buljan
GTE Laboratories, Inc.
40 Sylvan Road
Waltham, MA 02254

106. John M. Byrne, Jr.
PPG Industries, Inc.
Corporate Development Dept.
One PPG Place
Pittsburgh, PA 15272

107. Donald J. Campbell
Air Force Wright Aeronautical Laboratory
AFWAL/POX
Wright-Patterson AFB, OH 45433

108. Larry E. Campbell
American Matrix, Inc.
118 Sherlake Drive
Knoxville, TN 37922

109. Roger Cannon
Rutgers University
Department of Ceramics
Bowser Road
Post Office Box 909
Piscataway, NJ 08855-0909

110. Harry W. Carpenter
19945 Acre Street
Northridge, CA 91324

111. David Carruthers
Allied-Signal Aerospace Company
Garrett Auxiliary Power Division
2739 East Washington Street
Post Office Box 5227
Phoenix, AZ 85010

112. Jere G. Castor
Allied-Signal Aerospace Company
Garrett Auxiliary Power Division
2739 East Washington Street
Post Office Box 5227
Phoenix, AZ 85010

113. En-sheng Chen
B&C Engineering Research
13906 Dentwood Drive
Houston, TX 77014

114. Albert A. Chesnes
U.S. Department of Energy
Office of Transportation Systems
Forrestal Building CE-151, 5G-048
1000 Independence Avenue, S.W.
Washington, DC 20585

115. Frank Childs
EG&G, Inc.
Idaho National Engineering Laboratory
Post Office Box 1625
Idaho Falls, ID 83415

116. Gilbert Y. Chin
Bell Telephone Laboratories Research & Development
Murray Hill, NJ 07974

117. Melvin H. Chiogioji
U.S. Department of Energy
Office of Transportation Systems
Forrestal Building CE-15
1000 Independence Avenue, S.W.
Washington, DC 20585

118. William J. Chmura
The Torrington Company
Corporate Research
59 Field Street
Torrington, CT 06790

119. Eugene V. Clark
Turbine Metal Technology, Inc.
7327 Elmo Street
Tujunga, CA 91042-2204

120. William L. Cleary
ORI, Inc.
1375 Piccard Drive
Rockville, MD 20850

121. Jack L. Clem
J. M. Huber Corporation
Carbon Black Division
Post Office Box 2831
Borger, TX 79008-2831

122. Harry E. Cook
Chrysler Motors Corporation
Automotive Research and Technical Planning
1200 Chrysler Drive
Highland Park, MI 48288-1118

123. Stephen Copley
University of Southern California
Materials Science Department
Los Angeles, CA 90089-0241

124. John A. Coppola
Carborundum Company
Structural Ceramics Division
Building 91-2
Post Office Box 1054
Niagara Falls, NY 14302

125. Normand D. Corbin
Norton Company
Advanced Ceramics
Goddard Road
Northboro, MA 01532-1545

126. Charles H. Craig
Defense Technology Security Administration
400 Army-Navy Drive, Suite 300
Arlington, VA 22202

127. William J. Croft
U.S. Army Materials Technology Laboratory
405 Arsenal Street
Watertown, MA 02172

128. Gary M. Crosbie
Ford Motor Company
Material Systems Reliability Division
Room S-2079, SRL
20000 Rotunda Drive
Post Office Box 2053
Dearborn, MI 48121-2053

129. Floyd W. Crouse, Jr.
U.S. Department of Energy
Morgantown Energy Technology Center
Post Office Box 880
Morgantown, WV 26505

130. Raymond Cutler
Ceramatec, Inc.
2425 South 900 West
Salt Lake City, UT 84119

131. David A. Dalman
The Dow Chemical Company
Central Research, Organic Specialties Laboratory
1776 Building
Midland, MI 48674

132. James I. Dalton
Reynolds Metals Company
Metallurgy Laboratory
Fourth and Canal Streets
Post Office Box 27003
Richmond, VA 23261

133. Stephen C. Danforth
Rutgers University
Bowser Road
Post Office Box 909
Piscataway, NJ 08854

134. Robert F. Davis
North Carolina State University
Materials Engineering
Department 232
Riddick Laboratory
Box 7907
Raleigh, NC 27695

135. Evelyn M. DeLiso
Corning Glass Works
Corning, NY 14831

136. J. Franklyn DeRidder
Omni Electro Motive, Inc.
12 Seely Hill Road
Newfield, NY 14867

137. Alan L. Dragoo
National Institute of Standards and Technology
Inorganic Materials Division
Gaithersburg, MD 20899

138. Keith F. Dufrane
Battelle Columbus Laboratories
505 King Avenue
Columbus, OH 43201

139. Edmund M. Dunn
GTE Laboratories, Inc.
40 Sylvan Road
Waltham, MA 02254

140. Jeremy D. Dunning
Indiana University
Industrial Research Liaison Program
Bloomington, IN 47405

141. Dr. Sunil Dutta
NASA Lewis Research Center
21000 Brookpark Road
MS:49-3
Cleveland, OH 44135

142. Paul N. Dyer
Air Products and Chemicals, Inc.
Post Office Box 538
Allentown, PA 18105

143. Robert J. Eagan
Sandia National Laboratories
Department 1840
Post Office Box 5800
Albuquerque, NM 87185

144. Chris A. Ebel
Norton Company
Advanced Ceramics
Goddard Road
Northboro, MA 01532-1545

145. J. J. Eberhardt
U.S. Department of Energy
Energy Conversion and
Utilization Technologies
Program
Forrestal Building CE-12
1000 Independence Avenue, S.W.
Washington, DC 20585

146. William A. Ellingson
Argonne National Laboratory
9700 South Cass Avenue
Argonne, IL 60439

147. Charles D. Estes
U.S. Senate
Committee on Appropriations
SD-152
Dirksen Senate
Washington, DC 20510

148. John N. Eustis
U.S. Department of Energy
Office of Industrial Programs
Forrestal Building CE-141
1000 Independence Avenue, S.W.
Washington, DC 20585

149. Peggy Evanich
National Aeronautics and Space
Administration
Energy Systems Office
Washington, DC 20546

150. Anthony G. Evans
University of California
College of Engineering
Santa Barbara, CA 93106

151. Robert C. Evans
NASA Lewis Research Center
Vehicular Gas Turbine and
Diesel Project Office
21000 Brookpark Road
MS:77-6
Cleveland, OH 44135

152. Katherine T. Faber
Ohio State University
Department of Ceramic
Engineering
2041 College Road
Columbus, OH 43210

153. John W. Fairbanks
U.S. Department of Energy
Office of Transportation
Systems
Forrestal Building CE-151,
5G-042
1000 Independence Avenue, S.W.
Washington, DC 20585

154. Larry Farrell
Babcock and Wilcox
Old Forrest Road
Lynchburg, VA 24505

155. Rolf Fasth
Chem Systems, Inc.
303 South Broadway
Tarrytown, NY 10591

156. H. W. Foglesong
Dow Corning Corporation
3901 South Saginaw Road
Midland, MI 48686

157. Thomas F. Foltz
Avco Corporation
Special Materials Division
Two Industrial Avenue
Lowell, MA 01851

158. Robert G. Frank
Technology Assessment Group
10793 Bentley Pass Lane
Cincinnati, OH 45140

159. Douglas W. Freitag
LTV Aerospace and Defense Company
High Temperature Materials Research
P.O. Box 225907, MS:TH-85
Dallas, TX 75265

160. P. A. Gaydos
Battelle Columbus Laboratories
505 King Avenue
Columbus, OH 43201

161. George E. Gazza
U.S. Army Materials Technology Laboratory
Ceramics Research Division
405 Arsenal Street
Watertown, MA 02172

162. Charles M. Gilmore
The George Washington University
Dept. of Civil, Mechanical, and Environmental Engineering
Washington, DC 20052

163. Paul Glance
Concept Analysis
Dupont Automotive Development Building
950 Stephenson Highway
Troy, MI 48007-7013

164. Fred M. Glaser
U.S. Department of Energy
Office of Fossil Energy
FE-14 GTN
Germantown GTN
Washington, DC 20545

165. Joseph W. Glatz
Naval Air Propulsion Test Center
Systems Technology Division
Box 7176, PE 34
Trenton, NJ 08628

166. W. M. Goldberger
Superior Graphite Company
2175 East Broad Street
Columbus, OH 43209

167. Stephen T. Gonczy
Signal UOP Research Center
Materials Science Department
50 UOP Plaza
Des Plaines, IL 60016-6187

168. Robert J. Gottschall
U.S. Department of Energy
Office of Material Sciences
ER-131 GTN
Germantown GTN
MS:G-256
Washington, DC 20545

169. Dr. Earl Graham
Cleveland State University
Department of Chemical Engineering
Uclid Avenue at East 24th Street
Cleveland, OH 44115

170. Kenneth Green
Coors Ceramics Company
17750 West 32nd Street
Golden, CO 80401

171. Robert E. Green, Jr.
The Johns Hopkins University
Center for Nondestructive Evaluation
Maryland Hall 107
Baltimore, MD 21218

172. Lance E. Groseclose
General Motors Corporation
Allison Gas Turbine Division
Post Office Box 420
Indianapolis, IN 46206-0420

173. T. D. Gulden
General Atomics
Post Office Box 81608
San Diego, CA 92138

174. P. Ulf Gummeson
Hoeganaes
River Road and Taylors Lane
Riverton, NJ 08077

175. Bimleshwar P. Gupta
Solar Energy Research Institute
Solar Heat Research Division
1617 Cole Boulevard
Golden, CO 80401

176. M. D. Gurney
NIPER
Post Office Box 2128
Bartlesville, OK 74005

177. John P. Gyeknyesi
NASA Lewis Research Center
2100 Brookpark Road
MS:49-7
Cleveland, OH 44135

178. J. J. Habeeb
Esso Petroleum Canada
Research Division
Post Office Box 3022
Sarina, Ontario N7T 7MI
CANADA

179. H. T. Hahn
Pennsylvania State University
ESM Department
227 Hammond Building
University Park, PA 16802

180. Nabil S. Hakim
Detroit Diesel Corporation
13400 West Outer Drive
Detroit, MI 48239

181. John W. Halloran
CPS Superconductor Corporation
840 Memorial Drive
Cambridge, MA 02139

182. Friedrich Harbach
Asea Brown Boveri AG
Department Functional Ceramics
Eppelheimer Str. 82
D-6900 Heidelberg 1
WEST GERMANY

183. Kay Hardman-Rhyne
DARPA
1400 Wilson Boulevard
Arlington, VA 22209

184. R. A. Harmon
25 Schalren Drive
Latham, NY 12110

185. Stephen D. Hartline
Norton Company
Advanced Ceramics
Goddard Road
Northboro, MA 01532-1545

186. Michael H. Haselkorn
Caterpillar, Inc.
Engineering Research Materials
Technical Center, Building E
Post Office Box 1875
Peoria, IL 61656-1875

187. Willard E. Hauth
Dow Corning Corporation
Composite Development Ceramics Program
3901 South Siginaw Road
Midland, MI 48640

188. Kevin L. Haynes
McDonnell Douglas Astronautics Company
Post Office Box 516, MS:107/1
St. Louis, MO 63166

189. Norman L. Hecht
University of Dayton Research Institute
300 College Park
Dayton, OH 45469-0001

190. S. S. Hecker
Los Alamos National Laboratory
Material Science and Technology Division
Post Office Box 1663
Los Alamos, NM 87545

191. Peter W. Heitman
General Motors Corporation
Allison Gas Turbine Division
Post Office Box 420, W-5
Indianapolis, IN 46206-0420

192. Richard L. Helferich
The Duriron Company, Inc.
Post Office Box 1145
Dayton, OH 45401

193. H. E. Helms
General Motors Corporation
Allison Gas Turbine Division
Post Office Box 420
Indianapolis, IN 46206-0420

194. Thomas L. Henson
GTE Products Corporation
Chemical & Metallurgical Division
Hawes Street
Towanda, PA 18848-0504

195. Thomas P. Herbell
NASA Lewis Research Center
21000 Brookpark Road
MS:49-3
Cleveland, OH 44135

196. Hendrik Heystek
Bureau of Mines
Tuscaloosa Research Center
Post Office Box L
University, AL 35486

197. Robert V. Hillery
General Electric Company
One Neumann Way
Post Office Box 156301
Cincinnati, OH 45215

198. Jonathan W. Hinton
Carborundum Company
Structural Ceramics Division
Post Office Box 1054
Niagara Falls, NY 14302

199. Joe Homeny
University of Illinois
Department of Materials Science and Engineering
Ceramics Building
105 South Goodwin Avenue
Urbana, IL 61801

200. A. T. Hopper
Battelle Columbus Laboratories
Engineering Mechanics Department
505 King Avenue
Columbus, OH 43201-2693

201. George Hsu
Jet Propulsion Laboratory
4800 Oak Grove Drive
MS:512-103
Pasadena, CA 91109

202. Shih Hsu
Digital Equipment Corporation
77 Reed Road
MS:HL02-1/L8
Hudson, MA 01749

203. Stephen M. Hsu
National Institute of Standards and Technology
Institute for Materials Science and Engineering
Gaithersburg, MD 20899

204. Harold A. Huckins
Princeton Advanced Technology, Inc.
56 Finley Road
Princeton, NJ 08540

205. Fred Huettic
Advanced Ceramic Technology, Inc.
17 Deerfield Road
East Brunswick, NJ 08816

206. O. Richard Hughes
Celanese Research Company
86 Morris Avenue
Summit, NJ 07901

207. Joseph E. Hunter, Jr.
General Motors Corporation
Research Labs, Metallurgy Department
12 Mile and Mound Roads
Warren, MI 48090-9055

208. Louis C. Ianniello
U.S. Department of Energy
Office of Materials Sciences
ER-13 GTN
Washington, DC 20545

209. Robert Ingel
Naval Research Laboratory
4555 Overlook Avenue, S.W.
Code:63-70
Washington, DC 20375

210. Robert H. Insley
Champion Spark Plug Company
Ceramic Division
20000 Conner Avenue
Detroit, MI 48234

211. Curt A. Johnson
General Electric Company
Ceramics Branch, Physical Chemistry Laboratory
Post Office Box 8
Schenectady, NY 12301

212. Larry Johnson
Argonne National Laboratory
Center for Transportation Research
Building 362
9700 South Cass Avenue
Argonne, IL 60439

213. L. A. Joo
Great Lakes Research Corp.
Post Office Box 1031
Elizabethton, TN 37643

214. A. David Joseph
Sealed Power Corporation
100 Terrace Plaza
Muskegon, MI 49443

215. Debra Joslin
University of Tennessee
Metallurgical Engineering Department
Knoxville, TN 37996

216. Dr. Adam Jostsons
Australian Nuclear Science & Technology
Lucas Heights Research Laboratory
New Illawarra Road
Lucas Heights, New South Wales
AUSTRALIA

217. Roy Kamo
Adiabatics, Inc.
630 South Mapleton
Columbus, IN 47201

218. Allan Katz
Air Force Wright Aeronautical Laboratory
Metals and Ceramics Division
Materials Laboratory, AFWAL/MLLM
Wright-Patterson AFB, OH 45433

219. R. N. Katz
U.S. Army Materials Technology Laboratory
405 Arsenal Street
Watertown, MA 02172

220. Mr. Kawaguchi
Tokai Carbon
375 Park Avenue, Suite 3802
New York, NY 10152

221. Frederick L. Kennard, III
General Motors Corporation
AC Spark Plug Division
Dept. 32-24
1300 North Dort Highway
Flint, MI 48556

222. J. R. Kidwell
Allied-Signal Aerospace Co.
Garrett Auxiliary Power Division
2739 East Washington Street
Post Office Box 5227
Phoenix, AZ 85010

223. Max Klein
Gas Research Institute
8600 West Bryn Mawr Avenue
Chicago, IL 60631

224. C. E. Knapp
Norton Company
8001 Daly Street
Niagara Falls, Ontario L2G 6S2
CANADA

225. A. S. Kobayashi
University of Washington
Department of Mechanical Engineering
MS:FU10
Seattle, WA 98195

226. rer. nat. Wolfgang Kollenberg
Projektleitung Material Rohstofforschung - PLR
Kernforschungsanlage Jülich GmbH
Postfach 1913
D-5170 Julich
WEST GERMANY

227. David M. Kotchick
Allied-Signal Aerospace Co.
AiResearch Los Angeles Division
2525 West 190th Street
Torrance, CA 90509

228. Bruce Kramer
George Washington University
Aerodynamic Center
Room T715
Washington, DC 20052

229. Saunders B. Kramer
U.S. Department of Energy
Office of Transportation Systems
Forrestal Building CE-151
1000 Independence Avenue, S.W.
Washington, DC 20585

230. D. M. Kreiner
Allied-Signal Aerospace Co.
Garrett Auxiliary Power Division
2739 East Washington Street
Post Office Box 5227
Phoenix, AZ 85010

231. A. S. Krieger
Radiation Science, Inc.
Post Office Box 293
Belmont, MA 02178

232. Pieter Krijgsman
Ceramic Design Int. Hold., Ltd.
Post Office Box 68
8050 AB Hattem
THE NETHERLANDS

233. Jack L'Amoreaux
11346 Gates Mill Drive
Knoxville, TN 37922

234. W. J. Lackey
Georgia Tech Research Institute
Energy and Materials Sciences Laboratory
Georgia Institute of Technology
Atlanta, GA 30332

235. Everett A. Lake
Air Force Wright Aeronautical Laboratory
AFWAL/POSL
Wright-Patterson AFB, OH
45433-6563

236. Hari S. Lamba
General Motors Corporation
Electro-Motive Division
LaGrange, IL 60525

237. Manfred Langer
Volkswagen AG
Forschung-Neue Technologien Werkstofftechnologie
D-3180 Wolfsburg 1
WEST GERMANY

238. James Lankford
Southwest Research Institute
Dept. of Materials Sciences
6220 Culebra Road
Post Office Drawer 28510
San Antonio, TX 78284

239. David C. Larsen
Corning Glass Works
Materials Research Department
Sullivan Park, FR-51
Corning, NY 14831

240. Dr. S. K. Lau
Carborundum Company
Technology Division
Post Office Box 832
Niagara Falls, NY 14302

241. Harry A. Lawler
Carborundum Company
Niagara Falls R&D Center
Post Office Box 832
Niagara Falls, NY 14302

242. Alan Lawley
Drexel University
Materials Engineering
Philadelphia, PA 19104

243. Daniel Lee
Temescon
2850 7th Street
Berkeley, CA 94710

244. June-Gunn Lee
Korea Advanced Institute of Science and Technology
Post Office Box 131
Dong Dac Mun, Seoul
KOREA

245. E. M. Lenoe
Air Force Office of Scientific Research
Office of Naval Research
Liaison Office, Far East
APO San Francisco, CA 96503-0110

246. Stanley R. Levine
NASA Lewis Research Center
21000 Brookpark Road
Cleveland, OH 44135

247. David Lewis
Naval Research Laboratory
Materials Science and Technology Division
4555 Overlook Avenue, S.W.
Code 63-70
Washington, DC 20375

248. Bill Long
Babcock and Wilcox
Post Office Box 1260
Lynchburg, VA 24505

249. L. A. Lott
EG&G, Inc.
Idaho National Engineering Laboratory
Post Office Box 1625
Idaho Falls, ID 83415

250. Raouf O. Loutfy
Materials and Electrochemical Research Corporation
7960 South Kolb Road
Tucson, AZ 85706

251. Bryan K. Luftglass
Chem Systems, Inc.
303 South Broadway
Tarrytown, NY 10591

252. Robert Lundberg
Swedish Institute for Silicate Research
Box 5403
S-402 29 Gothenburg
SWEDEN

253. Michael J. Lynch
General Electric Company
Medical Systems Group
Post Office Box 414, 7B-36
Milwaukee, WI 53201

254. James W. MacBeth
Carborundum Company
Structural Ceramics Division
Box 1054
Niagara Falls, NY 14302

255. Vincent L. Magnotta
Air Products and Chemicals, Inc.
Technical Diversification R&D Department
Post Office Box 538
Allentown, PA 18105

256. Tai-il Mah
Universal Energy Systems
4401 Dayton-Xenia Road
Dayton, OH 45432

257. L. Manes
Commission of the European Communities
Joint Research Centre
Ispra Establishment
1-21020 Ispra (Varese)
ITALY

258. Giel Marijnissen
Interturbine R&D
Research and Development
Post Office Box 4339
5944 ZG Arcen
THE NETHERLANDS

259. Gerald R. Martin
Fleetguard, Inc.
Cookeville, TN 38501

260. J. W. McCauley
U.S. Army Materials Technology Laboratory
SLCMT-OMM
405 Arsenal Street
Watertown, MA 02172-0001

261. Bryan J. McEntire
Norton Company
TRW Ceramics
Goddard Road
Northboro, MA 01532-1545

262. Thomas D. McGee
Iowa State University
Department of Materials Science and Engineering
Ames, IA 50011

263. H. Christopher McGowan
Advanced Ceramic Technology, Inc.
17 Deerfield Road
East Brunswick, NJ 08816

264. Malcolm G. McLaren
Rutgers University
Department of Ceramics
Busch Campus
Bowser Road
Post Office Box 909
Piscataway, NJ 08854

265. Arthur F. McLean
6225 North Camino Almonte
Tucson, AZ 85718

266. Brian L. Mehosky
British Petroleum
4440 Warrensville Center Road
Cleveland, OH 44128

267. Joseph J. Meindl
Reynolds International, Inc.
6603 West Broad Street
Post Office Box 27002
Richmond, VA 23261

268. D. Messier
U.S. Army Materials Technology Laboratory
DRXMR-MC
405 Arsenal Street
Watertown, MA 02172

269. Thomas N. Meyer
Aluminum Company of America
Alumina, Chemicals, and Ceramics Division
Alcoa Technical Center
Alcoa Center, PA 15069

270. Amar Mishra
Engelhard Corporation
CN-28
Menlo Park
Edison, NJ 08818

271. Bill Moehle
Ethyl Corporation
Ethyl Tower
451 Florida Avenue
Baton Rouge, LA 70801

272. Helen Moeller
Babcock and Wilcox
Post Office Box 11165
Lynchburg, VA 24506-1165

273. Frederick E. Moreno
Turbo Energy Systems, Inc.
2858 South Roosevelt
Tempe, AZ 85282

274. Peter E. D. Morgan
Rockwell International
Science Center
1049 Camino Dos Rios
Post Office Box 1085
Thousand Oaks, CA 91360

275. Lawrence M. Murphy
Solar Energy Research
Institute
Thermal Systems Research
Branch
1617 Cole Boulevard
Golden, CO 80401

276. Solomon Musikant
General Electric Company
Space Systems Division
Post Office Box 8555
MS:U-1219
Philadelphia, PA 19101

277. Pero Nannelli
Pennwalt Corporation
900 First Avenue
Post Office Box C
King of Prussia, PA 19406-0018

278. William D. Nix
Stanford University
Department of Materials
Science and Engineering
Stanford, CA 94305

279. Richard D. Nixdorf
American Matrix, Inc.
118 Sherlake Drive
Knoxville, TN 37922

280. S. D. Nunn
University of Michigan
Materials Science and
Engineering
Ann Arbor, MI 48109

281. Brian M. O'Connor
The Lubrizol Corporation
29400 Lakeland Boulevard
Wickliffe, OH 44092

282. W. Richard Ott
Alfred University
Center for Advanced Ceramic
Technology
Alfred, NY 14802

283. William C. Owen
Sundstrand Turbomach
Division of Sundstrand Corp.
4400 Ruffin Road
Post Office Box 85757
San Diego, CA 92138-5757

284. Muktesh Paliwal
GTE Products Corporation
Hawes Street
Towanda, PA 18848-0504

285. Hayne Palmour, III
North Carolina State University
Engineering Research Services
Division
2158 Burlington Engineering
Labs
Post Office Box 5995
Raleigh, NC 27607

286. Joseph N. Panzarino
Norton Company
Advanced Ceramics
Goddard Road
Northboro, MA 01532-1545

287. Pellegrino Papa
Corning Glass Works
Corning Technical Products
Division
Corning, NY 14831

288. R. H. Parrish
Vanderbilt University
Box 1621, Station B
Nashville, TN 37235

289. James G. Paschal
Reynolds Metals Company
Post Office Box 76154
Atlanta, GA 30358

290. Arvid E. Pasto
GTE Laboratories, Inc.
40 Sylvan Road
Waltham, MA 02254

291. Donald O. Patten
Norton Company
Advanced Ceramics
Goddard Road
Northboro, MA 01532-1545

292. James W. Patten
Cummins Engine Company, Inc.
Box 3005, Mail Code 50183
Columbus, IN 47202-3005

293. Timothy M. Pattison
Textron Lycoming
550 Main Street
MS:LSM1
Stratford, CT 06497

294. Robert A. Penty
Eastman Kodak Company
Manufacturing Technology Dept., Apparatus Division
901 Elmgrove Road
Rochester, NY 14650

295. Gary R. Peterson
U.S. Department of Energy
Idaho Operations Office
785 D.O.E. Place
Idaho Falls, ID 83402

296. R. Byron Pipes
University of Delaware
Center for Composite Materials
2001 Spencer Laboratory
Newark, DE 19716

297. Bruce J. Pletka
Michigan Technological University
Department of Metallurgical Engineering
Houghton, MI 49931

298. Robert C. Pohanka
Office of Naval Research
800 North Quincy Street
Code 431
Arlington, VA 22217

299. J. P. Pollinger
Allied-Signal Aerospace Co.
Garrett Ceramic Components Division
19800 South Van Ness Avenue
Torrance, CA 90509

300. Stephen C. Pred
ICD Group, Inc.
1100 Valley Brook Avenue
Lyndhurst, NJ 07071

301. Karl M. Prewo
United Technologies Corp.
Research Center
Silver Lane
MS:24
East Hartford, CT 06108

302. Hubert B. Probst
NASA Lewis Research Center
Materials Division
21000 Brookpark Road
MS:49-1
Cleveland, OH 44135

303. Joseph M. Proud
GTE Laboratories, Inc.
Materials Science Laboratory
40 Sylvan Road
Waltham, MA 02254

304. D. W. Prouse
Ceramatec, Inc.
2425 South 900 West
Salt Lake City, UT 84119

305. Carr Lane Quackenbush
Norton Company
Advanced Ceramics
Goddard Road
Northboro, MA 01532-1545

306. Brian Quigy
National Aeronautics and Space Administration
Energy Systems Office
Washington, DC 20546

307. George Quinn
U.S. Army Materials Technology Laboratory
405 Arsenal Street
Watertown, MA 02172

308. Dennis T. Quinto
Kennametal, Inc.
Phillip M. McKenna Laboratory
Post Office Box 639
Greensburg, PA 15601

309. S. Venkat Raman
Air Products and
Chemicals, Inc.
Contract Research Department
Post Office Box 538
Allentown, PA 18105

310. Dennis Readey
Ohio State University
2041 College Road
Columbus, OH 43210

311. Robert R. Reeber
U.S. Army Research Office
Post Office Box 12211
Research Triangle Park, NC
27709

312. K. L. Reifsnider
Virginia Polytechnic Institute
and State University
Department of Engineering
Science and Mechanics
Blacksburg, VA 24061

313. Paul Rempes
Williams International
2280 West Maple Road
Post Office Box 200
Walled Lake, MI 48088

314. Theresa M. Resetar
U.S. Army Materials
Technology Laboratory
Materials Characterization
Center
ATTN:SLCMT-OMM
405 Arsenal Street
Watertown, MA 02172

315. K. T. Rhee
Rutgers University
College of Engineering
Bowser Road
Post Office Box 909
Piscataway, NJ 08854

316. Roy W. Rice
W. R. Grace and Company
7379 Route 32
Columbus, MD 21044

317. David W. Richerson
Ceramatec, Inc.
2425 South 900 West
Salt Lake City, UT 84119

318. Scott L. Richlen
U.S. Department of Energy
Office of Industrial Programs
Forrestal Building CE-141
1000 Independence Avenue, S.W.
Washington, DC 20585

319. Paul Rieth
Ferro Corporation
661 Willet Road
Buffalo, NY 14218-9990

320. Michael A. Rigdon
Institute for Defense Analyses
1801 Beauregard Street
Alexandria, VA 22311

321. John E. Ritter, Jr.
University of Massachusetts
Mechanical Engineering Dept.
Amherst, MA 01003

322. M. Rohr
DOE/ORO
Federal Office Building
P.O. Box 2001, MS:AMERD
Oak Ridge, TN 37831

323. Giulio A. Rossi
Norton Company
Advanced Ceramics
Goddard Road
Northboro, MA 01532-1545

324. Barry R. Rossing
Lanxide Corporation
Tralee Industrial Park
Newark, DE 19711

325. Donald W. Roy
Coors Ceramics Company
Research and Development
17750 West 32nd Street
Golden, CO 80401

326. Bruce Rubinger
Gobal
50 Milk Street, 15th Floor
Boston, MA 02109

327. Robert Ruh
Air Force Wright
Aeronautical Laboratory
Metals and Ceramics
Division
Materials Laboratory,
AFWAL/MLIM
Wright-Patterson AFB, OH
45433

328. Robert J. Russell, Sr.
Norton Company
Advanced Ceramics
Goddard Road
Northboro, MA 01532-1545

329. George P. Safol
Westinghouse Electric Corp.
R&D Center
Pittsburgh, PA 15235

330. J. A. Salem
NASA Lewis Research Center
21000 Brookpark Road
Cleveland, OH 44135

331. J. Sankar
North Carolina A&T State
University
Department of Mechanical
Engineering
Greensboro, NC 27411

332. Maxine L. Savitz
Allied-Signal Aerospace Co.
Garrett Ceramic Components
Division
19800 South Van Ness Avenue
Torrance, CA 90509

333. Richard Schapery
Texas A&M University
Civil Engineering Dept.
College Station, TX 77843

334. Jim Schienle
Allied-Signal Aerospace Co.
Garrett Auxiliary Power
Division
2739 East Washington Street
Post Office Box 5227
MS:1302-2P
Phoenix, AZ 85010

335. Liselotte J. Schioler
Air Force Office of
Scientific Research
Bolling AFB
Washington, DC 20332-6448

336. Richard A. Schmidt
Battelle Columbus Laboratories
Mechanics Section
505 King Avenue
Columbus, OH 43201-2693

337. Arnie Schneck
Deere & Company Technical
Center
Post Office Box 128
Wood-Ridge, NJ 07075

338. Matthew Schreiner
ALANX Products L.P.
101 Lake Drive
Newark, DE 19702

339. John Schuldies
Industrial Ceramic
Technology, Inc.
37 Enterprise Drive
Ann Arbor, MI 48103

340-351. R. B. Schulz
U.S. Department of Energy
Office of Transportation
Systems
Forrestal Building CE-151,
5G-046
1000 Independence Avenue, S.W.
Washington, DC 20585

352. Wesley J. C. Schuster
Thermo Electron Corporation
Metals Division
115 Eames Street
Post Office Box 340
Wilmington, MA 01887

353. Murray A. Schwartz
Bureau of Mines
2401 Eye Street, N.W.
Washington, DC 20241

354. Douglas B. Schwarz
The Dow Chemical Company
52 Building
Midland, MI 48674

355. Thomas M. Sebestyen
U.S. Army Tank Automotive Command
AMSTA-RGRT
Warren, MI 48397-5000

356. Brian Seegmiller
Coors Ceramics Company
17750 West 32nd Street
Golden, CO 80401

357. S. G. Seshadri
Carborundum Company
Niagara Falls R&D Center
Post Office Box 832
Niagara Falls, NY 14302

358. Peter T. B. Shaffer
Advanced Refractory Technologies, Inc.
699 Hertel Avenue
Buffalo, NY 14207

359. Laurel M. Sheppard
Advanced Materials and Processes
Route 87
Metals Park, OH 44073

360. Dinesh K. Shetty
The University of Utah
Department of Materials Science and Engineering
Salt Lake City UT, 84112

361. Jack D. Sibold
Coors Ceramics Company
17750 West 32nd Street
Golden, CO 80401

362. Neal Sigmon
U.S. House of Representatives
Subcommittee on Interior and Related Events
Rayburn Building, Room B308
Washington, DC 20515

363. Dr. Richard Silberglitt
Quest Research Corporation
1651 Old Meadow Road
McLean, VA 22102

364. A. Sinha
North Carolina A&T State University
Department of Mechanical Engineering
Greensboro, NC 27411

365. Maurice J. Sinnott
University of Michigan
Chemical and Metallurgical Engineering
438 West Engineering Building
Ann Arbor, MI 48109-2136

366. S. R. Skaggs
Los Alamos National Laboratory
Program Office
Post Office Box 1663, MS:F-682
Los Alamos, NM 87545

367. J. Thomas Smith
GTE Laboratories, Inc.
40 Sylvan Road
Waltham, MA 02254

368. Jay R. Smyth
Allied-Signal Aerospace Co.
Garrett Auxiliary Power Division
2739 East Washington Street
Post Office Box 5227
MS:93-172/1302-2K
Phoenix, AZ 85010

369. Rafal Sobotowski
Carborundum Company
Research and Development
3092 Broadway Avenue
Cleveland, OH 44115

370. E. Solidum
Allied-Signal Aerospace Co.
Garrett Ceramics Components Division
19800 South Van Ness Avenue
Torrance, CA 90509

371. Thomas M. Sopko
Lubrizol Enterprises, Inc.
29400 Lakeland Boulevard
Wickliffe, OH 44092

372. Richard M. Spriggs
Alfred University
Center for Advanced Ceramic Technology
Alfred, NY 14802

373. M. Srinivasan
Carborundum Company
Niagara Falls R&D Center
Post Office Box 832
Niagara Falls, NY 14302

374. Gordon L. Starr
Cummins Engine Company, Inc.
Metallic/Ceramic Materials Department
Box 3005, Mail Code 50183
Columbus, IN 47202-3005

375. Harold L. Stocker
General Motors Corporation
Allison Gas Turbine Division
Post Office Box 420, T-23
Indianapolis, IN 46206-0420

376. Paul D. Stone
The Dow Chemical Company
1801 Building
Midland, MI 48674

377. Roger Storm
Carborundum Company
Niagara Falls R&D Center
Post Office Box 832
Niagara Falls, NY 14302

378. E. E. Strain
Allied-Signal Aerospace Co.
Garrett Auxiliary Power Division
2739 East Washington Street
Post Office Box 5227, MS:301-2N
Phoenix, AZ 85010

379. Thomas N. Strom
NASA Lewis Research Center
21000 Brookpark Road, 77-6
Cleveland, OH 44135

380. Jerry Strong
Albright & Wilson
Post Office Box 26229
Richmond, VA 23260

381. Richard Suddeth
Boeing Motor Airplane Company
Post Office Box 7730
MS:K-76-67
Wichita, KS 67277

382. Paul Sutor
Midwest Research Institute
425 Volker Boulevard
Kansas City, MO 64116

383. P. L. Sutton
U.S. Department of Energy
Office of Transportation Systems
Forrestal Building CE-151
1000 Independence Avenue, S.W.
Washington, DC 20585

384. J. J. Swab
U.S. Army Materials Technology Laboratory
Ceramics Research Division, SLCMT-EMC
405 Arsenal Street
Watertown, MA 02172

385. Lewis Swank
Ford Motor Company
Material Systems Reliability Division
Room S-2023, SRL
20000 Rotunda Drive
Post Office Box 2053
Dearborn, MI 48121-2053

386. Truett Sweeting
Carborundum Company
Niagara Falls R&D Center
Post Office Box 832
Niagara Falls, NY 14302

387. Stephen R. Tan
ICI Advanced Materials
Post Office Box 11
The Heath, Runcorn Cheshire
WA7 4QE
ENGLAND

388. Anthony C. Taylor
U.S. House of Representatives
Committee on Science and Technology
Rayburn Building, Room 2321
Washington, DC 20515

389. Monika O. Ten Eyck
Carborundum Technical Ceramics GMBH
Nobelstrasse 6
D4050 Monchengladbach-Wickrath
WEST GERMANY

390. John K. Tien
Columbia University
1137 S.W. Mudd Building
New York, NY 10027

391. T. Y. Tien
University of Michigan
Materials and Metallurgical Engineering
Dow Building
Ann Arbor, MI 48109-2136

392. Julian M. Tishkoff
Air Force Office of Scientific Research
(AFOSR/WC) Bolling AFB
Washington, DC 20332

393. Louis E. Toth
National Science Foundation
Division of Materials Research
1800 G Street, N.W.
Washington, DC 20550

394. Richard E. Tressler
Pennsylvania State University
Ceramic Science and Engineering Department
201 Steidle Building
University Park, PA 16802

395. W. T. Tucker
General Electric Company
Post Office Box 8
Schenectady, NY 12301

396. Donald L. Vaccari
General Motors Corporation
Allison Gas Turbine Division
2001 South Tibbs Avenue
Indianapolis, IN 46241

397. Dr. ir. O. Van Der Biest
Katholieke Universiteit Leuven
Departement Metaalkunde en Toegepaste
de Croylaan 2
B-3030 Leuven
BELGIUM

398. Edward C. Van Reuth
Technology Strategies, Inc.
10722 Shingle Oak Court
Burke, VA 22015

399. V. Venkateswaran
Carborundum Company
Niagara Falls R&D Center
Post Office Box 832
Niagara Falls, NY 14302

400. Dr. K. E. Voss
Englehard Corporation
Research Department
Menlo Park, CN-28
Edison, NJ 08818

401. John B. Wachtman, Jr.
Rutgers University
Bowser Road
Post Office Box 909
Piscataway, NJ 08854

402. Harlan L. Watson
U.S. House of Representatives
Committee on Science and Technology
Rayburn Building, Suite 2321
Washington, DC 20515

403. John D. Watson
Broken Hill Proprietary Co., Ltd.
Melbourne Research Laboratories
245 Wellington Road
Mulgrave 3170 Victoria
AUSTRALIA

404. C. David Weiss
Caterpillar, Inc.
Engineering Research Materials
Technical Center, Building E
Post Office Box 1875
Peoria, IL 61656-1875

405. James J. Wert
Vanderbilt University
Box 1621, Station B
Nashville, TN 37235

406. Albert R. C. Westwood
Martin Marietta Laboratories
1450 South Rolling Road
Baltimore, MD 21227

407. Thomas J. Whalen
Ford Motor Company
Material Systems Reliability Division
Room S-2023, SRL
20000 Rotunda Drive
Post Office Box 2053
Dearborn, MI 48121-2053

408. Sheldon M. Wiederhorn
National Institute of Standards and Technology
Inorganic Materials Division
Gaithersburg, MD 20899

409. James C. Williams
General Electric Company
Engineering Materials Technology Labs.
One Neumann Way
Cincinnati, OH 45215-6301

410. Janette R. Williams
Kollmorgen Corporation
PCK Technology Division
322 L.I.E. South Service Road
Melville, NY 11747

411. Craig A. Willkens
Norton Company
Advanced Ceramics
Goddard Road
Northboro, MA 01532-1545

412. Roger R. Wills
TRW, Inc.
Valve Division
1455 East 185th Street
Cleveland, OH 44110

413. J. M. Wimmer
Allied-Signal Aerospace Co.
Garrett Auxiliary Power Division
2739 East Washington Street
Post Office Box 5227
MS:1302-2P
Phoenix, AZ 85010

414. David Wirth
Coors Ceramics Company
Technical Operations & Engineering
17750 West 32nd Street
Golden, CO 80401

415. Thomas J. Wissing
Eaton Corporation
Engineering & Research Center
26201 Northwestern Highway
Post Office Box 766
Southfield, MI 48037

416. Dale Wittmer
Southern Illinois University at Carbondale
Department of Mechanical Engineering and Energy Processes
Carbondale, IL 62901

417. Stanley M. Wolf
U.S. Department of Energy
Conservation and Renewable Energy
Forrestal Building CE-12
1000 Independence Avenue, S.W.
Washington, DC 20585

418. George W. Wolter
Howmet Turbine Components Corporation
Technical Center
699 Benston Road
Whitehall, MI 49461

419. James C. Wood
NASA Lewis Research Center
21000 Brookpark Road
MS:500-210
Cleveland, OH 44135

420. Roger P. Worthen
Eaton Corporation
Engineering and Research Center
26201 Northwestern Highway
Post Office Box 766
Southfield, MI 48076

421. Harry C. Yeh
Allied-Signal Aerospace Company
Garrett Ceramic Components Division
19800 South Van Ness Ave.
Torrance, CA 90509

422. Thomas M. Yonushonis
Cummins Engine Company, Inc.
Box 3005, Mail Code 50183
Columbus, IN 47202-3005

423. Don Zabierek
Air Force Wright Aeronautical Laboratory
AFWAL/POTC
Wright-Patterson AFB, OH 45433

424. Charles Zeh
U.S. Department of Energy
Morgantown Energy Technology Center
Post Office Box 880
Morgantown, WV 26505

425. Anne Marie Zerega
U.S. Department of Energy
Office of Transportation Systems
Forrestal Building CE-15
1000 Independence Avenue, S.W.
Washington, DC 20585

426. Martin Zlotnick
Nichols Research Corp.
8618 Westwood Center Drive, Suite 200
Vienna, VA 22180-2222

427. Klaus M. Zwilsky
National Materials Advisory Board
National Research Council
2101 Constitution Avenue
Washington, DC 20418

428. Department of Energy
Oak Ridge Operations Office
Assistant Manager for Energy Research and Development
P.O. Box 2001
Oak Ridge, TN 37831-8600

429–438. Department of Energy
Office of Scientific and Technical Information
Office of Information Services
P.O. Box 62
Oak Ridge, TN 37831

For distribution by microfiche as shown in DOE/TIC-4500, Distribution Category UC-95 (Energy Conservation).

☆U.S. GOVERNMENT PRINTING OFFICE:1989 -648 -119/ 80193 REGION NO. 4